

# Bulletin of Materials Science

**Editor**

**K J Rao**

*Indian Institute of Science, Bangalore*

**Editorial Board**

D C Agrawal, *Indian Institute of Technology, Kanpur*

M F Ashby, *University of Cambridge, Cambridge, UK*

S Banerjee, *Bhabha Atomic Research Centre, Bombay*

D Chakravorty, *Indian Association for the Cultivation of Science, Calcutta*

A K Chatterjee, *The Associated Cement Companies Limited, Thane*

K L Chopra, *Indian Institute of Technology, Kharagpur*

A D Damodaran, *Regional Research Laboratory, Trivandrum*

B K Das, *National Physical Laboratory, New Delhi*

H Herman, *State University of New York, Stony Brook, USA*

B Ilschner, *Ecole Polytechnique Federale de Lausanne, Lausanne, Switzerland*

Indira Rajagopal, *National Aerospace Laboratories, Bangalore*

K T Jacob, *Indian Institute of Science, Bangalore*

S K Joshi, *Council of Scientific and Industrial Research, New Delhi*

S Mahajan, *Carnegie Mellon University, Pittsburgh, USA*

R A Mashelkar, *National Chemical Laboratory, Pune*

S B Ogale, *University of Poona, Pune*

Pradip, *Tata Research Development and Design Centre, Pune*

P Ramachandra Rao, *National Metallurgical Laboratory, Jamshedpur*

S Ranganathan, *Indian Institute of Science, Bangalore*

C N R Rao, *Indian Institute of Science, Bangalore*

B B Rath, *Naval Research Laboratory, Washington, USA*

R W Siegel, *Argonne National Laboratory, Argonne, USA*

R Srinivasan, *Inter-University Consortium for DAE Facilities, Indore*

G V Subba Rao, *Central Electrochemical Res. Inst., Karaikudi*

G Sundararajan, *Defence Metallurgical Research Laboratory, Hyderabad*

M S Valiathan, *Manipal Academy of Higher Education, Manipal*

I K Varma, *Indian Institute of Technology, New Delhi*

Vikram Kumar, *Solid State Physics Laboratory, Delhi*

# Bulletin of Materials

Volume 18, January–December 1995

## CONTENTS

Volume 18, No. 1, February 1995

Seminar on "Recent trends in glass and glass-ceramics"

Foreword

A first principles technique for the analysis of  
random binary alloys

Conducting glasses

Some aspects of glass–ceramic superconductors

Sol-gel glasses: some recent trends

Glass formation domains and structural properties of  
transition metal ion glasses

Ultrasonic velocity and attenuation in glass

---

Crystallographic and electrical study of the charge ordering in  
zinc copper ferrites V M

Microstructural features of  $\text{Cd}_{0.8}\text{Zn}_{0.2}\text{Te}$  thin films studied by X-ray  
diffraction and electron microscopy

*B K Samantaray, T B Ghosh, S L Shrivastava*

Dielectric measurements in vanadium doped barium titanate

*A Hanumaiah, T Bhimasankaram, S V Suryanarayana*



EPR studies on molybdenum phosphates  
 $\text{BaMo}_2\text{P}_4\text{O}_{16}$  in the temperature range 300–400 K

*G Constantin, M M Borel, A Grandjean*

Thermoelectric power in  $\text{Gd}^{3+}$ -substituted  $\text{Cu}_2\text{S}$

*C B Kolekar, P N Maiti*

Lanthanum oxide doping effect on dc electrical conductivity of  
sodium vanadate and rubidium vanadate

*D V Pawar, T S Shinde*

An analysis of the electrical conductivity of  
system

*K Singh, S D Verma*

Resistivity studies of melt spun and annealed  
twinned samples

*Kulvir Singh, D Singh*

Room-temperature low-cycle fatigue behaviour of  
aluminum

*P N Singh, C Ramachandra*

Oxidation and corrosion behaviour of laser-processed  
aluminum

*A K Pattanaik, A S Khanna, C S Haran*

Structure of vacuum deposited SnSe films

*T Subbarao, B K Samal*

## Volume 18, No. 3, June 1995

Bulk high- $T_c$  magnetometer

*Neelam*

Cone formation on Ag surface bombarded by

## Contents

Photoconductivity in crystalline phthalocyanines *Fr*

Photoconductivity in thin films of phthalocyanine *Fr*

Photoconductivity of iodine-doped single crystals of p  
*Francis P Xavier and*

Growth mechanism of  $\text{NaBrO}_3$  crystals from aqueous  
*V Surrender*

### **Rapid Communication**

Near ideal electrical switching in fast ion conducting g  
an electronic process with chemical origin *B Vaidh*

## **Volume 18, No. 4, August 1995**

### **India-Japan Seminar on New Materials**

#### **Foreword**

Computer simulation of deformation and fracture o  
molecular dynamics method

Basic studies leading to the development of an ultra  
fracture toughness low-alloy steel

*G Malakondaiah, M Sriniva*

MOVPE growth and characterization of  $\text{ZnSe}$ -  
heterostructures *Mitsuru Funato, Shizuo Fujita*

On the stability of intermetallic phases

**Volume 18, No. 5, September 1995**

Electrically conducting polymers: from fundam

Preparation of silica monolith via sol-gel rou

*A Gupta, K Biswas, A Basu Mallick,*

Preparation and characterization of gold doped  
for mechano-optical transducers

*Sanjay Tiwari, Shikha Tiwari, B*

Preparation and characterization of silver clad  
superconducting tapes with high critical curre

*U Syamaprasad, M S Sarma, A R*

*P S Mukherjee, J*

Preparation and characterization of ultra-thin  
applications

*S*

Synthesis and characterization of molecular  
aromatic diamines with various electron accep

*Ram Adha*

X-ray analysis of different starch granules

*Vasudeva Singh, R Gopalkrishne Urs, H S*

XRD and SEM studies of reactively deposite

*Johny T Abraham, Peter Koshy, V*

*P Guruswa*

Equivalent circuit models for electronic ceram

*Lakshman Pandey, Om Pa*

## **Rapid Communications**

A critical assessment of the standard molar enthalpy of formation of  $\text{NiWO}_4$

Structural and dielectric properties of a solid solution *Vandana Sharma,*

**Volume 18, No. 6, October 1995**

**Proceedings of the Sixth Annual General Meeting, 1995**

Foreword

My experiments with thin films—the nature of the interface

Electronic structure of amorphous semiconductors

Microwave ferrites for phase shifters

Cast metal matrix composites—challenges and opportunities

Novel high performance fibres

Material science aspects of phase change materials  
*L K Malhotra*

Thermal plasmas in material processing

Fatigue of brittle materials—A critical assessment

Processing of materials—monolithic to composites

A new materials processing—hydrothermal synthesis of nanomaterials

Effect of doping concentration on non  
 $\text{La}_{2-x}(\text{Ba},\text{Sr})_x\text{CuO}_4$  superconductors *Dine.*

Nucleation and growth study of copper thin  
 and wetting layers by metal-organic chemical  
*A Dutta, J Gos*

Studies on spray pyrolyzed molybdenum trioxide

$(\text{PEG})_x\text{NH}_4\text{ClO}_4$ : a new polymeric fast proton conductor

Synthesis and properties of rare earth doped  
*S*

### **Rapid Communication**

$\text{SrB}_4\text{O}_7 : \text{Bi}_2\text{VO}_{5.5}$ —A novel nanocomposite  
*M V Shankar, G N S*

### **Volume 18, No. 8, December 1995**

Materials engineering for a better global environment

Synthesis and characterization of bioactive hydroxyapatite  
 solutions using corals *T S Sar*  
*N Prasanth Kumar, K Senthamil S*

Synthesis of high-energy-density  $\text{Pr}_2\text{Fe}_{14-x}\text{Co}_x$  compounds  
 applications *S Halдар, S Ram, P Ramac*

Effect of processing on microstructure and properties of  
 $\text{Al-4.5Cu-10Pb}$  alloy

Magnetic study above the curie temperature of

## Seminar on "Recent trends in glass and glass-ceramics research"

### FOREWORD

Glasses and glass-ceramics have received considerable attention because of the wide variety of properties exhibited by them. They provide challenging and complex problems to theoreticians. Various aspects of glasses and glass-ceramics a one-day seminar on "Recent trends in glass and glass-ceramics research" was organized by the Materials Research Group of the Materials Research Society of India at the Indian Institute of Cultivation of Science, Calcutta on January 28, 1994. The seminar consisted of some of the invited talks delivered by experts in this field.

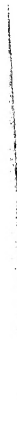
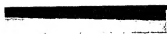
A Mookerjee examines the theoretical problem of phase transformations in alloys after introducing the augmented-space recursion method and orbital peeling technique. He applies this powerful tool to study the  $\text{Pd}_c\text{V}_{1-c}$  system.

C S Sunandana discusses the structural characteristics of glasses containing different species of alkali ions. He also discusses the mechanism of ion migration in glasses to explain the electrical conductivity as a function of alkali ion concentration as also the mixed alkali effect.

B K Chaudhuri reviews the different aspects of glass-ceramics and of high  $T_c$  superconductors. The conduction mechanism in glasses, glass formation in different oxide systems, crystallization kinetics, changes as a function of composition and its influence on properties are some of the topics covered by him.

D Ganguli introduces the basic steps involved in the sol-gel technique. He touches upon the basic issues in the definition of glass in the wake of tremendous advances made in the preparation of materials by sol-gel process. He describes briefly the preparation of new and exotic glasses with potential applications.

A Ghosh gives an account of his investigation on glasses containing some transition metal ion glasses based on unconventional compositions.



2

## A first principles technique for the analysis of random binary alloys

A MOOKERJEE\*

S.N. Bose National Centre for Basic Sciences, DB17,  
700 064, India

**Abstract.** In this communication we introduce the first principles technique coupled with the orbital peeling technique, as a powerful tool for studying cluster interactions, useful for the study of alloy phase diagrams. The study of the studied PdV system has been carried out.

**Keywords.** First principles technique; random binary alloys

### 1. Introduction

A bulk of the study of alloy phase diagrams have been based on the understanding of phenomenological models. The purpose of this study, with extensive experimental data and physical insight, is to determine the parameters felt to be crucial in the determination of alloy phase diagrams. Extrapolation (or interpolation) to make predictions. The study of physical parameters as coordinates in a parameter space. The study of systems which are in the neighbourhood of one another. The study of features. By continuity, the parameter space is divided into regions of stability. Types and numbers of coordinates used in the study are referred to several excellent reviews (Pearson 1972; Girguly *et al* 1989). Some of the popular parameters are those



random alloys, one needs a derivation for a specified alloy system. Models have been developed for energies in terms of effective multisite interactions (Gonis *et al* 1987). Within this approach, phase and phase stability reduces to the calculation of effective interactions. Traditionally there have been calculations of effective pair interactions. The first approach was the calculation and total energy determination for a disordered phase, to invert these total energies to get the effective pair interactions. Williams method (Connolly and Williams 1983) for a disordered phase, set up a perturbation for a phase associated with an ordered phase as a perturbation. This approach included the calculation of the total energy (Ducastelle and Gautier 1976), the calculation of the total energy (Garland 1977) and the concentration dependence of the work on the electronic structure. The coherent potential approximation has its own limitations. In a number of cases, subtle convergence procedures at each step are required.

Analytic generalizations beyond the coherent potential approximation (Kumar *et al* 1982) based on the cluster approximation (TCA) (Millard 1982) have been developed. Computational difficulties when cluster size is large. L6s and Repetsky (1994) proposed a *t*-matrix. However, the analyticity problem has not been established as yet. In the site approximation, de Fontaine and co-workers (1982) used direct configurational averaging (DCA) without resorting to any kind of simplification. In the multisite interactions were calculated

## 2. The formalism

### 2.1 *Effective pair interactions*

The starting point of the calculations is the expansion of the energy in terms of effective cluster interactions. The expansion for the energy of a binary alloy  $A_c B_{1-c}$  may be written as:

$$E(n_i) = E^{(0)} + \sum_{i=1}^N E_i^{(1)} \delta c_i + \sum_{i,j=1}^N E_{ij}^{(2)} \delta c_i \delta c_j + \dots$$

If  $n_i$  are the occupation probabilities for the A type of atom, the fluctuation given by  $n_i - c$ , where  $c = \langle n_i \rangle$ . The coefficients  $E_i^{(1)}$  are the renormalized cluster interactions (renormalized in the sense that self-retraced paths have been included).  $E^{(0)}$  is the energy of the effective medium.  $E_i^{(1)}$  is the interchange energy for species A and B, as a result of an interaction resulting from the interchange of a B atom with an A atom in the alloy.  $E_{ij}^{(2)}$  is the effective renormalized pair interaction with a single body interaction at  $i$ , when sites  $j$  ( $\neq i$ ) is occupied by a B atom.

The renormalized pair interactions express the correlations between the most dominant quantities for the analysis of phase stability. In the CPA-ECM, the pair interactions are included in the configuration energy expansion. The pair interactions may usually be included for a more accurate and complete description of the alloy.

At this point it is worth mentioning that our scheme of renormalized pair interactions is similar to other methods based on the effective medium. The calculation involves the determination of the effective medium as well as averaging over different configurations of the system. The averaging scheme that the different methods based on the effective medium are based on is different from one another. In the CPA-ECM the averaging is done over the CPA-ECM effective medium. In the CPA-ECM the averaging is done over the CPA-ECM effective medium.

such an assumption is not rigorously true, valid in a number of alloy systems (including Most of the works where calculations start with band structure contribution alone. Our work

The effective pair interactions can be averaged local density of states:

$$E_{ij}^{(2)} = \int_{-\infty}^{E_F} dE (E - E_F) \Delta n(E),$$

where  $\Delta n(E)$  is given by:

$$\Delta n(E) = \sum_{IJ \text{ all pairs}} \text{Im} \langle \text{Tr}(EI -$$

$\xi_{IJ}$  is  $\pm 1$  according to whether  $I = J$  or  $I \neq J$ . The averaging. There are four possible pairs  $IJ$ ,  $II$ ,  $JJ$ ,  $IJ$  and  $JI$ . The Hamiltonian of a system where all sites except the sites  $i$  and  $j$  are occupied by atoms of the same type. The local density of states can be related to the following equation:

$$\Delta n(E) = \frac{d\eta(E)}{dE},$$

where

$$\eta(E) = \log \frac{\det \langle G^{AA} \rangle \det \langle G^{BB} \rangle}{\det \langle G^{AB} \rangle \det \langle G^{BA} \rangle}$$

## 2.2 Augmented space recursion

As discussed in the previous section, the calculation of the properties within our formalism reduces to the determination of the configuration-averaged structure functions  $\langle G^{AA} \rangle$ ,  $\langle G^{BB} \rangle$ ,  $\langle G^{AB} \rangle$  and  $\langle G^{BA} \rangle$ . We shall employ the recursion coupled with the linearized tight-binding method (LMTB) (LMTO) introduced by Andersen and Jepsen (1984) for a first-principles calculation of these configuration averaged quantities. We shall take the linearized tight-binding Hamiltonian derived systematically from the LMTO method and extended to random alloys, given by:

$$\begin{aligned} H_{iL,jL}^{\beta} &= C_{iL}' \delta_{iL} \delta_{jL} + \Delta_{iL}^{1/2} S_{iL,jL}^{\beta} \Delta_{jL}^{1/2}, \\ C_{iL}' &= C_L^A n_i + C_L^B (1 - n_i), \\ \Delta_L^{1/2} &= (\Delta_L^{1/2})^A n_i + (\Delta_L^{1/2})^B (1 - n_i). \end{aligned}$$

Here  $i, j$  denote the lattice sites and  $L = (lm)$  are the orbital indices ( $l \leq 2$ ).  $C_L^A, C_L^B, \Delta_L^A$  and  $\Delta_L^B$  are the potential parameters of the alloy,  $n_i$  are the local site-occupation variables which take the value 0 or 1 according to whether the site is occupied by an A atom or B atom. The binding structure function  $S^{\beta}$  contains all the information about the binding expressed in terms of conventional structure function  $S^0$  as

$$S^{\beta} = S^0 (1 + \beta S^{\beta}).$$

The Hamiltonian described by (7) is related to the nearest-neighbour interaction by the relation

$$H^{\gamma} = E_v + h^{\gamma} = E_v + h^{\beta} - h^{\beta} o^{\beta} h^{\beta} + \dots$$

This ASA form of the orthonormalized Hamiltonian  $H^{\gamma}$  is usually truncated after the second term

$$\begin{aligned}
& + \sum_{p \neq 2} \sum_{l=1}^9 \sum_{l'=1}^9 (\Delta_{p,l}^{1/2,B} + \delta_{p,l}^{1/2,B}) \\
& + \sum_{p \neq 1,2} \sum_{q \neq 1,2} \sum_{l=1}^9 \sum_{l'=1}^9 (\Delta_{p,l}^{1/2,B} + \delta_{p,l}^{1/2,B}) \\
& (a_p^\dagger a_q + a_q^\dagger a_p).
\end{aligned}$$

We note that the Hamiltonian has both the form of the Hamiltonian, done in single site approximations (Kudoh et al., 1988). In the configuration average we will employ the same averaging on the same footing as quantum mechanics in the Hilbert space spanned by the wave functions of the different realizations of the random variables.

Let us suppose that the Hamiltonian depends on the random occupation variables  $\{n_i\}$ , which are assumed to have finite values.

$$p(n_i) = \frac{1}{\pi} \langle \gamma_0^i | ((n_i - i0)\mathbf{I} - \mathbf{M}^i) | \gamma_0^i \rangle$$

where  $\mathbf{M}^i$  is an operator defined on the  $N$  possible realizations of  $n_i$ . The augmented Hilbert space states that the configuration average of

$$\langle G(E, \{n_i\}) \rangle = \langle F | z\tilde{I} - \tilde{H}(\{n_i\}) | F \rangle$$

$\tilde{H}(\{\tilde{M}^i\})$  is the same operator function in terms of  $n_i$  and  $|F\rangle = \Pi^\otimes |\gamma_0^i\rangle$  is the configuration average state. The configuration averaging has been reduced to a single element in the augmented space  $\Psi = H(\{n_i\})$ .

## *A first principles technique for the analysis of a*

A member of the basis in  $\Pi_i^\otimes \phi_i$  has the form  $|\gamma_{\lambda_1}^1 \otimes \gamma_{\lambda_2}^2 \otimes \dots \otimes \gamma_{\lambda_N}^N\rangle$ .  $\lambda$  may be either 0 or 1. In the usual terminology of ASF the cardinality of the basis and the sequence of positions at which the basis functions are defined are called the cardinality sequence labels the basis. Thus a binary representation of the member of the basis in the configuration space is then

$$B[C, \{S_C\}] \odot B[C', \{S_{C'}\}] = \delta_{CC'} \delta\{S_C S_{C'}\}.$$

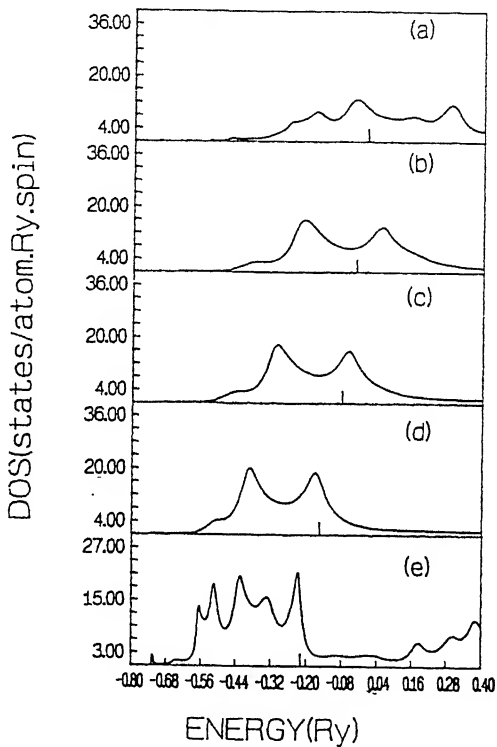
Without going into the computational details we mention that the operations of  $\tilde{H}$  on the configuration space amount to changing the sequences. Since the operations are restricted to the bits of the sequences, logical functions to define the operation of the Hamiltonian are used.

It is well known, that for a system described by a sparse matrix the continued fraction method is one of the widely used methods to generate a continued fraction expansion of the resolvent of the Hamiltonian. Haydock (1972) has mapped the continued fraction coefficients to self-avoiding walks on the configuration space. It has been shown that the dominant contribution comes from walks starting from the initial state. This allows us to work only on a finite part of the configuration space. In practice the continued fraction is evaluated to a finite number of terms by incorporating analyticity preserving terminators. Several terminators have been used in the literature and we have chosen to use the terminator of Haydock. The advantage of such a termination procedure is that the approximation preserves the herglotz properties. It is interesting to compare this with the CPA one goes to great lengths to ensure that the approximations cannot maintain the accuracy in the band structure. The continued fraction approximation preserves the first  $2(N-2)$  moments of the density of states. This represents the effect of a cluster at a distance  $(N-2)$  from the initial state. It maintains the correct band-widths, band-weights and the band edges. If we carry out recursion on the augmented

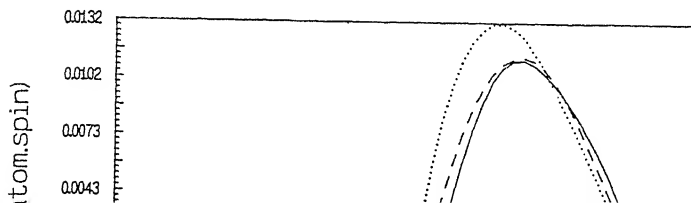
### 3. An illustrative example

We shall now illustrate the usefulness of the above prescription in calculating the pair potential  $\phi(r)$  for various values of concentration  $c$ . The calculations are done up to fourth neighbour interactions. Our choice of the system is that in transition metal alloys (apart from the fact that most strongly ordered alloys will have a half-filled  $d$ -band, or somewhere near five  $d$ -electrons), a completely empty or full  $d$  level will tend to be stable. The constituents on opposite ends of the transition metal series above prescription. Further, stability of the system can be experimentally as well as by theoretical calculations. The generalized perturbation method (Turic) and configurational averaging (Dreyssé *et al.*) are available for comparison with our results.

We now mention briefly some details of the calculation. Total energy density-functional calculations were done for the crystal structure. The Kohn–Sham equations were solved for the orbitals (LDA). The LDA was treated within the linear muffin-tin orbitals (LMTO) in the atomic sphere approximation. The orbitals were formed semi-relativistically (including spin-orbit coupling). The correlation potential of Von Barth and Hedin (1972) was used for  $l = 0, 1, 2$  orbitals, so that the occurrence of the parameters  $\Delta_l^i$  and  $\gamma_l^i$  of the constituent atoms is due to the fact that the Wigner-Seitz radius  $r_s$  of the alloy,  $r_s^{\text{alloy}}$ . These potential parameters are used in the Hamiltonian. This choice of different Wigner-Seitz radii takes into account charge self-consistency and is emphasized by Kudrnovský *et al.* (1990).



**Figure 1.** Density of states vs energy for  $\text{Pd}_c\text{V}_{1-c}$  alloys. (a)  $c = 0.0$ , (b)  $c = 0.25$  and (e)  $c = 1.0$ . The vertical lines mark the positions of the F





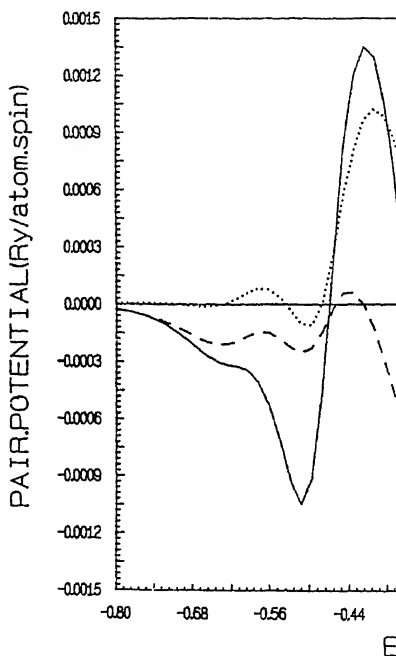


Figure 3. The  $n$  neighbour pair potential,  $n = 3$  and dotted curve,  $n = 4$  concentrations.

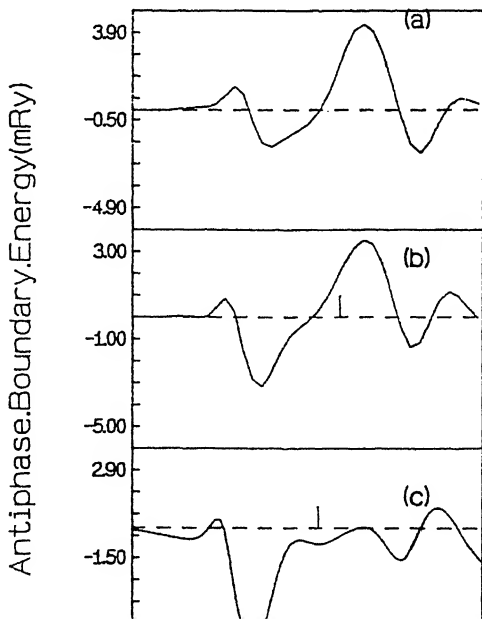
the effective pair interaction decreases with increasing number of nodes.

In figure 3 we have plotted  $V_1$ ,  $V_2$ ,  $V_3$  to demonstrate this point. This in turn

*A first principles technique for the analysis of a*

**Table 1.** Values of  $p_k$  for various superstructures at concentrations 0.25 and 0.5.

$k$	1	2	3	4	$c$
$\text{Li}_2$	0	3	0	6	0.25
$\text{DO}_{22}$	0	2	4	2	0.25
$\text{Li}_0$	2	3	4	6	0.5
$\text{A}_2\text{B}_2$	2	2	8	2	0.5



In the fcc lattice for  $c = 0.75$ , the only interactions up to fourth nearest neighbours have identical numbers of AB nearest pairs, much smaller than  $V_1$  and is given by  $V_4$ , proved rigorously by Kanamori and Kanamori of the 3d Ising model Hamiltonian that the fcc structure is stable if  $\varepsilon > 0$ . We find from our results suggesting that at this concentration DO is stable, that  $\varepsilon > 0$  for  $c = 0.25$  at  $E = E_F$  and hence is supported by the fact that an exchange of a large electron number. For  $c = 0.5$ , the  $A_2B_2$  and we find  $LI_0$  to be more stable than  $LI_1$  in energy in agreement with experiments and theory.

In conclusion our results demonstrate the feasibility of peeling in conjunction with LMTO formalism as a feasible approach to the calculation of properties of disordered alloys. However, before accepting our results further work is necessary in order to include spin, exchange and correlation effects, elastic properties and alloy phase stability. This methodology and the study still form an open problem.

## References

- Andersen O K and Jepsen O 1984 *Phys. Rev. Lett.* **52** 1635
- Asta M, Wolverton C, de Fontaine D and Dreyss C 1990 *Phys. Rev.* **B42** 4311
- Berera A 1990 *Phys. Rev.* **B42** 4311
- Bose S K, Kudrnovský J, Jepsen O and Andersen O K 1990 *Phys. Rev.* **B42** 4311
- Burke N R 1976 *Surf. Sci.* **58** 349
- Connolly J W D and Williams A R 1983 *Phys. Rev.* **B28** 2555
- Dasgupta I, Saha T and Mookerjee A 1994 *Phys. Rev.* **B50** 10444

*A first principles technique for the analysis of alloy phase*

- Turchi P E A, Stocks G M, Butler W H, Nicholson D M and Gonis A 1988 *Phys. Rev. B* **38** 1068
- Villars P, Mathis K and Hulliger F 1989 *The structure of binary compounds*, (Amsterdam: North Holland) **2** p. 1
- Wolverton C, Ceder G, de Fontaine D and Dreyssé H 1993 *Phys. Rev.* **B48** 726
- Wright H, Weightman P, Andrews P T, Folkerts W, Flipse C F J, Sawatsky G A and Padmore H 1987 *Phys. Rev.* **B35** 519



## Conducting glasses

C S SUNANDANA

School of Physics, University of Hyderabad, Hyderabad 500 134

**Abstract.** Ion-conducting tellurite glasses are built from trigonal bipyramidal units. Neutron diffraction as well as Raman and IR spectroscopic studies show a continuous transition from  $\text{TeO}_4 \rightarrow \text{TeO}_{3+1} \rightarrow \text{TeO}_3$  as the alkali content is progressively increased, non-bridging oxygens being created in the process. The transport of both single and mixed alkali tellurite glasses is satisfactorily explained by a hopping transport mechanism, based on the site-memory effect exhibited by the alkali ions.

**Keywords.** Ion conducting glasses; tellurite glasses; mixed alkali ion glasses; intercharge transport.

### 1. Introduction

Conducting glasses—essentially non-metallic in constitution (or composition)—could be of three types, depending on the nature of conducting species: (a) ion-conducting: e.g.  $\text{As}_2\text{S}_3$ ,  $\text{V}_2\text{O}_5$ – $\text{Te}_2$ ,  $\text{CuO}$ – $\text{V}_2\text{O}_5$ – $\text{TeO}_2$ , (b) ion-electron conducting:  $\text{SiO}_2$ ,  $\text{AgI}$ – $\text{Ag}_2\text{O}$ – $\text{B}_2\text{O}_3$  and (c) mixed-conducting:  $\text{Na}_2\text{O}$ – $\text{V}_2\text{O}_5$ – $\text{TeO}_2$ .

In the first category—dealt with by Ghosh (1994)—are solid electrolytes (Sunandana and Bhatnagar 1984; Sunandana and Rao 1985), used in solid state memory devices while the second category comprises solid electronic conductors (ion-electron conductors) only. The third category consists of glasses that transport both ions and electrons—a feature useful for solid state battery applications. Parameters such as  $\text{Fe}^{3+}$  often render ion conducting glasses mixed conductors (Sunandana 1990b).

In this talk we shall focus exclusively on ion-conducting

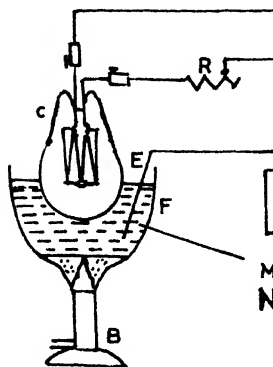


**Figure 1.** Burt's apparatus for the electrolysis of molten glass; R: variable resistance, C: crucible; B: bunsen burner. The apparatus was used to study the transport of ions through glass as dramatically

## 2. Basic structure of tellurite glass

Glass structure is important for controlling not only the potential barriers for the ion transport but also the concentration itself. This structure depends on the concentration of the alkali components. The structure of the glass includes (i) the building block i.e. the  $\text{TeO}_6$  octahedra in the glass network, (ii) the changes in the structure when an oxide component is added, and (iii) the role of non-bridging oxygens (NBOs) in the glass network.

Empirically speaking, pure  $\text{TeO}_2$  is a highly viscous liquid. The covalency of the  $\text{Te}-\text{O}$  bond is high, and the octahedral coordination of the  $\text{Te}$  is

## Conducting glasses

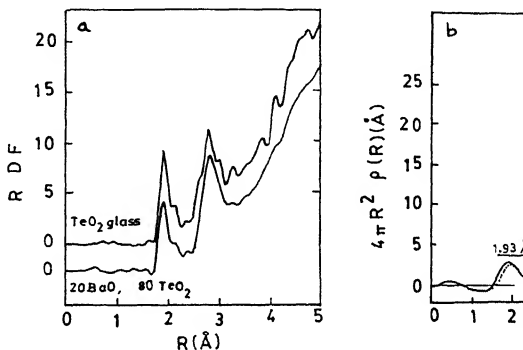
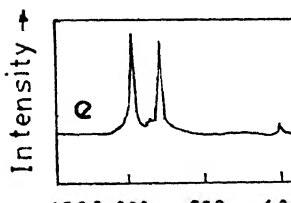
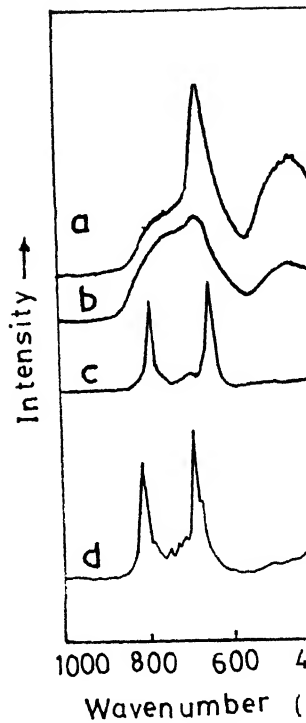


**Figure 2.** a. Radial distribution function (RDF) of  $\text{TeO}_2$  obtained by pulsed neutron total scattering. Note that the sub peaks. The position of the first varies from 1.9–2.2 Å the second is fixed at 2.18 Å. These two distances correspond to the  $\text{TeO}_4$  unit (Ueno and Suzuki 1983) and b. RDF for  $\text{TeO}_2$  from neutron diffractometry ( $\lambda = 1.06$  Å) (A: Experimental data; B: structural diffusion model for amorphous  $\text{TeO}_2$ ). The influence of Li–O distances, which is more profound after the addition of alkali-oxides, is seen in the broadening of the first and Te–O peaks, which occur at 1.93 and 2.90 Å. Note the effect of the addition of alkali-oxides (Neov *et al* 1979).

distances in  $\text{TeO}_4$  by way of the split first peak in the RDF (figure 2).

Two major conclusions that emerge from these studies are that the basic block of the  $\text{TeO}_2$  glass structure is a trigonal bipyramid (the addition of alkali-oxides the tbp gradually changes through a trigonal pyramid  $\text{TeO}_3$ , in the manner of a continuous structural change in tellurite glasses and not known to occur in borate, silicate and phosphate glasses.





## Conducting glasses

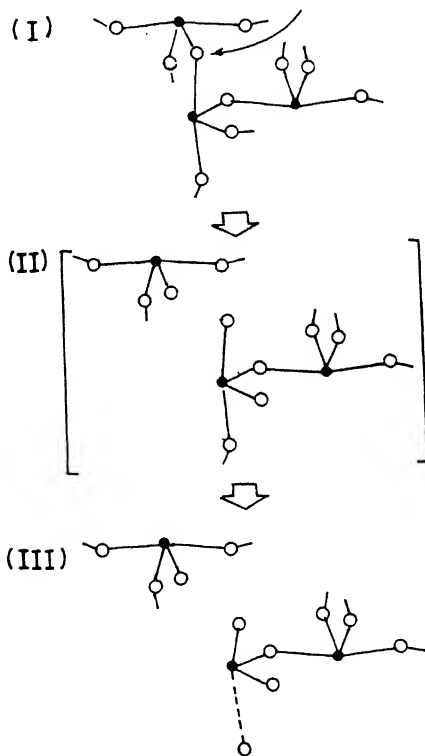


**Figure 4.** A mechanism for the structural change in the  $\text{TeO}_2$  to  $\text{TeO}_{3+1}$  polyhedra induced by addition of modifier oxide.

I:  $\text{TeO}_2$  glass structure with oxygen linked  $\text{TeO}_4$  units. ● — long bond. Arrow indicates modifier entry.

II: Breaking of I by addition of modifier oxide and creation of a new structure.

As may be noted from the above discussion of the continuous transformation of the oxide. This important defect (akin to the vacancy) plays a vital role in the alkali-ion transport in tellurite glasses.

Coming back to the '60 W bulb experiment, asked, particularly in the context of structural defects transported across tellurite glasses of different alkali-types? and (ii) what role does the concentration and mobility of these ions play?

### 3. Electrical conduction in tellurite glasses

The ionic conductivity ( $\sigma$ ) of lithium (and other alkali) is studied by a number of workers (Sunandana and Bhanu Prasad 1988; Duclot 1988; Tanaka *et al* 1988, 1991; Bhanu Prasad and Rojo *et al* 1990). Crystalline  $\text{Li}_2\text{Te}_2\text{O}_5$  (Bhanu Prasad *et al* (1981). The temperature dependence of the behaviour  $\sigma = \sigma_0 \exp(-E_a/kT)$ , indicates an underlying cause. Alkali-oxide concentration ( $\sigma_0$ ) and activation energy ( $E_a$ ) show opposite trends, the latter decreasing upon increase of sodium concentration. Do the ions occupy interstices close to NBO's in the glass? Does the  $\text{Li}^+$  ion overcome the random distribution of  $\text{TeO}_4$  units?

Before discussing the specific case of lithium, we first discuss a recently developed (Maass and Van Turnhout 1991) theory of ion transport processes in glass. This theory is based on the idea that  $\text{Li}^+$  in glass (e.g.  $\text{Li}_2\text{O}-\text{SiO}_2$ ) create a

## Conducting glasses

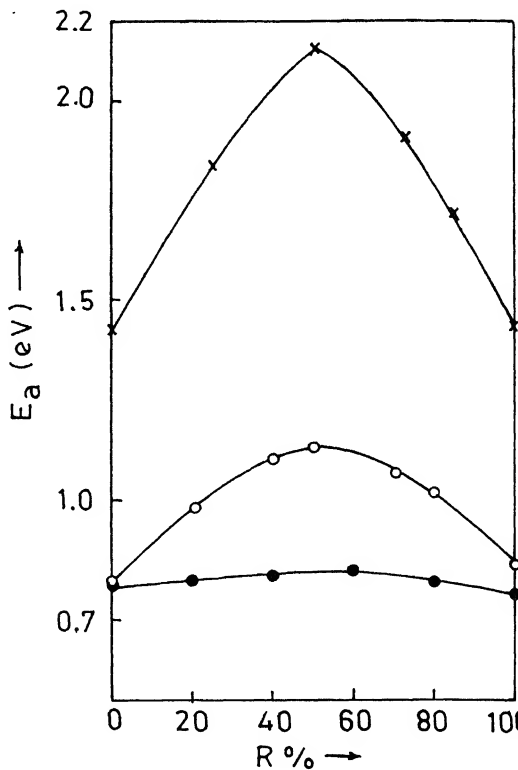


**Figure 6.** Mixed alkali effect observed in the conductivity of glasses. The curves show  $E_a$  versus  $R$  for the glasses  $30[(1-x)\text{Na}_2\text{O} \cdot x\text{K}_2\text{O}]:70\text{GeO}_2$  (x x x),  $30[(1-x)\text{Li}_2\text{O} \cdot x\text{Na}_2\text{O}]:70\text{TeO}_2$  (● ● ●).  $R$  is the ratio of the total alkali concentration (e.g.  $\text{Na}/(\text{Na} + \text{Li})$ ). The maximum  $E_a$  is observed at  $R = 0.5$ . For data sources see text.

a minimum and  $E_a$  goes through a maximum. A tentative explanation for nearly seven decades has been observed in the conductivity activation energy of (Li, Na) borate (Kawamura *et al* 1988) and germanate glasses of 30–70 composition. Note that the effect is largest in germanate glasses. (Li, Na) tellurite glasses show a similar effect. It would be interesting to study  $(70 - x)\text{GeO}_2 \cdot x\text{TeO}_2$ , to see if the effect is related to the short range order induced by peroxide ions. In the percolation-type model described by Uchino, for single and mixed alkali glasses, it gives a good fit to various glasses and the actual microstructural conductivity.

Uchino *et al* (1992) looked at ionic conduction by modelling the local structure of alkali ions using orbital calculations on clusters such as  $\text{Li}_2\text{O}$ . To simulate the local scale structure of  $\text{Li}_2\text{O}$ , Uchino *et al* have proposed an ion interchange transition model for  $\text{Li}^+$  conduction in lithium tellurite glasses (Balaya and Sunandana 1994).

In the tellurite glasses, let us assume that the NBOs and of course  $\text{Te}^{4+}$  bound by oxygen involves the following steps:

- I.  $\text{Li}^+$  (bound)  $\rightarrow$  Li (unbound)
- II.  $\text{Te}^{4+} \rightarrow [\text{Li}^+ (\text{bound})]$
- III.  $\text{Li}^+$  (bound)  $\rightarrow (\text{Te}^{4+})$
- IV.  $\text{O}^{2-} \rightarrow \text{O}^- (\text{NBO})$

## Conducting glasses

### 4. Conclusions

Ion-conducting tellurite glasses are built from trigonal Neutron diffraction as well as Raman and IR spectroscopy there is a continuous transition from  $\text{TeO}_4 \rightarrow \text{TeO}_{3+1}$  - content is progressively increased, non-bridging oxygens b Electrical conduction in both single and mixed alkali tell explained by the interchange transport mechanism, base exhibited by the glass network.

### Acknowledgement

I thank my former students Mr T Kumara Swami and Dr P the research on tellurite glasses.

### References

- Balaya P and Sunandana C S 1990a *Recent advances in fast ion con*  
B V R Chowdari *et al* (Singapore: World Scientific) p. 539  
Balaya P and Sunandana C S 1990b *Recent advances in fast ion con*  
B V R Chowdari *et al* (Singapore: World Scientific) p. 543  
Balaya P and Sunandana C S 1992 *Solid state ionics: materials and appli*  
(Singapore: World Scientific) p. 527  
Balaya P and Sunandana C S 1993 *J. Noncryst. Solids* **162** 253  
Balaya P and Sunandana C S 1994 *J. Noncryst. Solids* **175** 51  
Brady G W 1956 *J. Chem. Phys.* **27** 300  
Burt R C 1925 *J. Opt. Soc. Am.* **11** 87  
Cachau-Herriellat D *et al* 1981 *J. Solid State Chem.* **37** 352  
Ghosh A 1994 This proceedings  
Ivanov A O 1964 *Sov. Phys. Solid State* **5** 1933



# Some aspects of glass-ceramic superconductors

B K CHAUDHURI

Solid State Physics Department, Indian Association for the Cultivation of Science, Calcutta 700 032, India

**Abstract.** In this review article we have discussed, in brief, the general procedure for making glass-ceramic superconductors and some of their physical properties. All these glasses which become superconductors after properly annealing at higher temperatures are, in general, transition metal oxides (TMO) with copper ions. So the usual theoretical models of polaronic hopping conduction mechanisms are valid for explaining the semiconducting behaviour of these oxide glasses. Some of the transport properties of the glass-ceramic (GC) phases, viscosity of the glassy state, wire making feasibility etc have also been discussed in short.

**Keywords.** Glass-ceramics; superconductors.

## 1. Introduction

The semiconducting transition metal oxide (TMO) glasses, in general, have been vastly studied during the last couple of decades (Mott and Davis 1979). This is because of their probable technological applications (Hirashima *et al* 1987; Sakuri and Yamaki 1985; Nakamura and Ichinose 1987). Above all, these glasses with various compositions are relatively easy to prepare compared to other non-oxide glasses. Moreover, the cost of sample preparation is also low and for these reasons a small research group having moderate research facilities can start working on different aspects of TMO glasses. But the investigations of the structural as well as the physical properties of such glassy systems provide wealth of new informations about the basic mechanism of semiconducting behaviour in these and similar other glasses. Magnetic, optical, dielectric, and thermal properties are also equally important for all these glasses elucidating many interesting features (Mott and Davis 1979).

However, it had not been guessed earlier (before 1987) that some of the TMO glasses might even show high temperature superconducting behaviour in their crystalline (called glass-ceramic or GC) phases obtained by annealing the glass samples at higher temperatures (below the respective melting points).

After the discovery of high  $T_c$  superconductors in the Y-(Ba, Sr)-Cu-O (Bednorz and Muller 1986), Bi-Sr-Ca-Cu-O (Michel *et al* 1987; Maeda *et al* 1988) etc systems (where Cu is the transition metal atom), special importance has also been attributed to make these high  $T_c$  materials from the corresponding glassy phases. It was first shown by Komatsu *et al* (1987) that the glass made by melting Y-Ba-Cu-O oxide becomes superconductor in the corresponding GC phase. This is definitely an important discovery. This is because, the superconductors obtained by this GC route would be highly homogeneous, their grain sizes could be controlled, wires/tapes could be drawn from the glasses which could then be converted in the corresponding high  $T_c$  phases and necessary technology could be developed for the proper utilization of these wires/tapes. Mixing of the components occur at molecular level in the melts. Almost fully dense, uniform, pore-free materials can be fabricated from the glassy phase leading to high critical density of the prepared superconductors. Heat treatments of



the quenched glasses can lead to the metastable crystalline phases having properties which cannot be synthesized by the usual normal means. However, there are also certain limitations of the melt quenching approach. The components must not be volatile at about one to two hundred degrees above the melting temperature. The melt must not phase separate and not react with the container used for the melting. Recently, containerless melting technique is being used to make pure glassy phases.

Another part of research with these precursor glasses is to understand their properties and to know why these glasses become superconductors in their glassy phases while many similar TMO glasses do not show superconductivity in their respective GC phases. Therefore, proper understanding of the behaviour of these glasses is also necessary. However, this second part of research is in the rudimentary stage and we will not discuss this part in the present article.

## 2. Preparation of the glassy phase

The starting materials (carbonates and metal oxides), in general, are well mixed in appropriate proportions and then melted in Pt or crystalline  $\text{Al}_2\text{O}_3$  crucibles at 1000 and 1300°C for a few hours. Before melting, pre-heating around 500°C is essential.

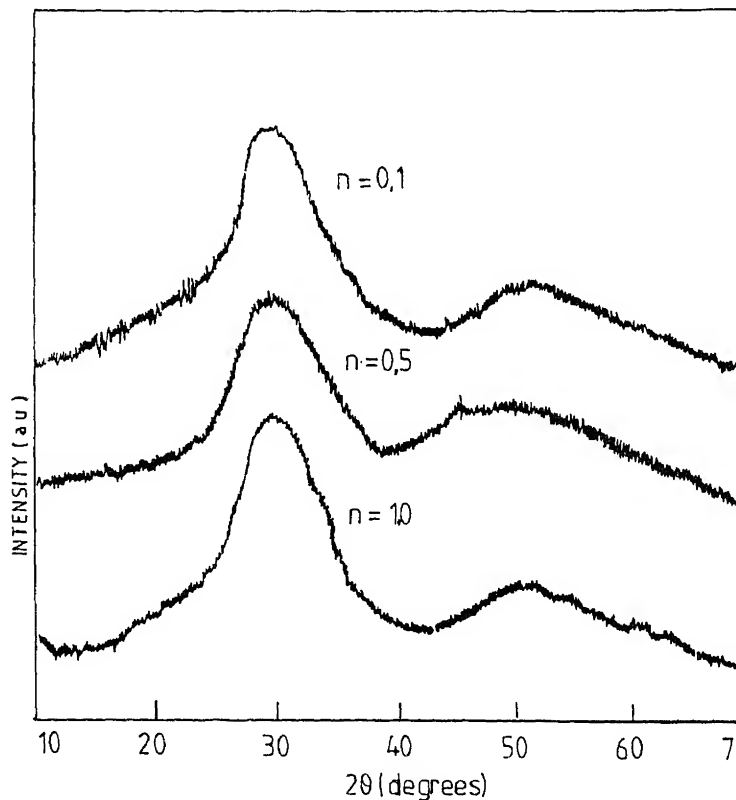


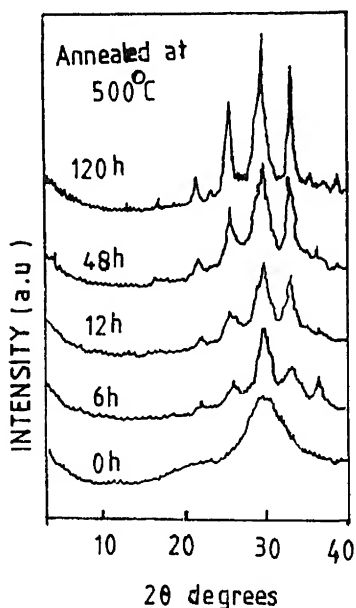
**Figure 1.** X-ray diffraction pattern of a typical Pb-doped  $\text{Bi}_{4-n}\text{Pb}_n\text{Sr}_3\text{Ca}_3\text{Cu}_4\text{O}_{15}$  ( $n = 0.5$  and  $1.0$ ) glass.

The melt is rapidly quenched by a twin roller or by pressing between two metal plates resulting in black opaque glass with metallic lustre. Now a days, containerless glass making process has also been well developed to avoid contamination effect. X-ray diffraction patterns of some typical glasses, viz.  $\text{Bi}_{4-x}\text{Pb}_x\text{Sr}_3\text{Ca}_3\text{Cu}_y\text{O}_x$  ( $x = 0.1, 0.5, 1.0$ ), are shown in figure 1 indicating an amorphous character with broad peaks. Sometimes low intensity diffraction due to some unreacted CaO etc might appear in the diffraction pattern. Furthermore, phase separation is also observed in such glasses (Chaudhuri and Som 1992; Mollah *et al* 1994). The appearance of crystalline superconducting phases with increase of annealing time is shown in figure 2. The following procedure is generally followed to make good quality glassy precursors for high  $T_c$  superconductors: (i) Mixing of the raw oxide (if carbonates are used they should be calcined around  $900^\circ\text{C}$  for 8–10 h to decompose carbonates) materials for an hour or more with pure acetone or alcohol, (ii) the mixture is pre-heated at  $500^\circ\text{C}$  for about 5 h, (iii) the preheated oxide is melted between  $1000$  and  $1300^\circ\text{C}$  for 1 to 2 h, (iv) the melt is quenched rapidly between two copper blocks to obtain the glassy precursors for high  $T_c$  superconductors and (v) the glasses thus obtained are properly heat-treated under appropriate conditions to get high  $T_c$  superconducting oxides.

We are discussing below some of the most common glasses and the corresponding superconducting glass-ceramics.

### 3. Bi–Sr–Ca–Cu–O system

Bi-based glasses have been widely used for the preparation of high  $T_c$  superconducting materials. Several glasses with different concentrations of Bi or the transition metal



ions have been prepared (Tohge *et al* 1989) and their superconducting properties studied. The glass forming region of a typical Bi-Sr-Ca-Cu-O system is shown in the phase diagram in figures 3a, b. Many other glass compositions of this group have a similar phase diagram. A wide glass forming region as shown by the broken line in figure 3 exists in this system. It is highly interesting to note that no glass forming oxide is present in this system and the glass transition temperature ( $T_g$ ) depends mainly on the  $\text{Bi}_2\text{O}_3$  concentration in the glass as shown in figure 4 for a typical  $\text{Bi}_x\text{SrCaCu}_2\text{O}_x$ . The DSC scan of a Bi-Sr-Ca-Cu-O glass showing  $T_g$  and crystallization temperature  $T_x$ , is drawn in figure 5 (Komatsu *et al* 1988). Influence of calcium content on  $T_x$  and  $T_g$  for some Bi-based glass is shown in figure 6. Tohge *et al* (1989) reported that the values of  $T_g$  and  $T_x$  decrease with increase in  $\text{CaO}$  and  $\text{Bi}_2\text{O}_3$  concentration and increase with increasing the alkaline earth (CaO and

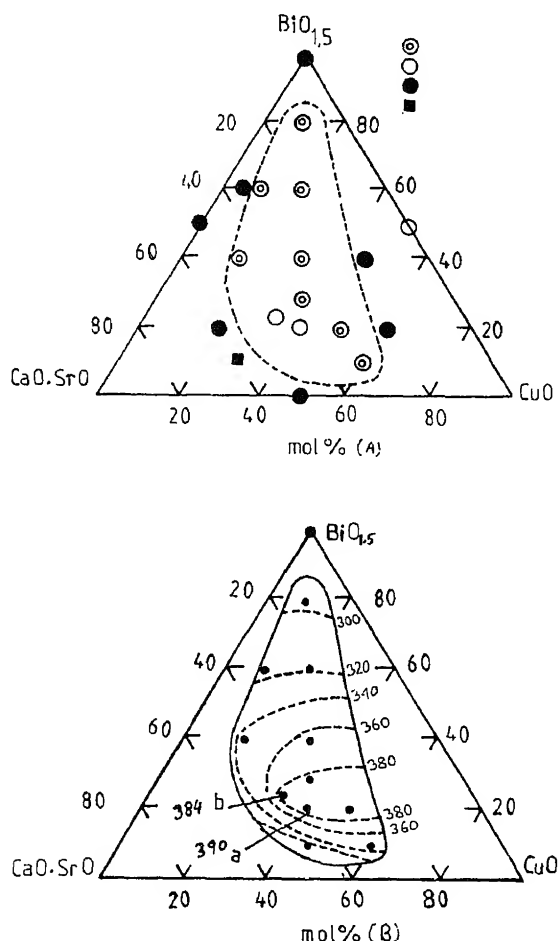


Figure 3. A. Phase diagram of a typical  $\text{BiO}_{1.5}(\text{SrO} \cdot \text{CaO})_{0.5}\text{CuO}$ ,  $\text{SrO}/\text{CaO} = 1$  composition (a)  $\text{BiSrCaCu}_2\text{O}$  and (b)  $\text{Bi}_2\text{Sr}_2\text{Ca}_2\text{Cu}_3\text{O}_y$  (Tohge *et al* 1989). B. Isotherms of  $T_g$  in  $\text{Bi}_{1-x}\text{Sr}_x\text{SrCaCu}_2\text{O}_x$ ,  $\text{CuO} \cdot \text{SrO}/\text{CaO} = 1$  (a)  $\text{BiSrCaCu}_2\text{O}$  and (b)  $\text{Bi}_2\text{Sr}_2\text{Ca}_2\text{Cu}_3\text{O}_y$  (Tohge *et al* 1989).

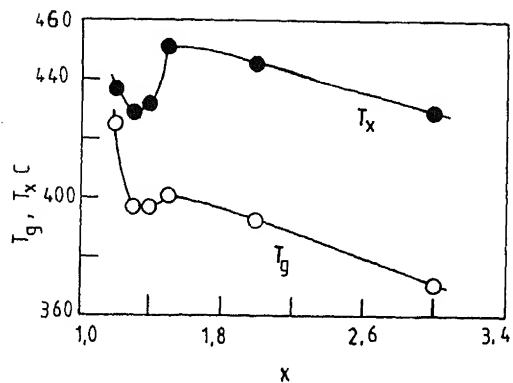


Figure 4. Effect of Bi content on  $T_g$  and  $T_x$  for the  $\text{Bi}_x\text{SrCaCu}_2\text{O}_y$  glassy precursor (Bansal and Guire 1989).

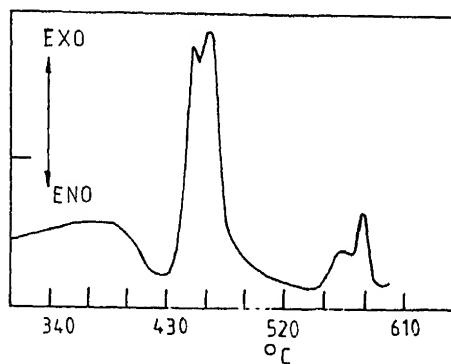


Figure 5. DSC scan of  $\text{Bi}_{1.5}\text{SrCaCu}_2\text{O}_y$  glass in inert atmosphere at a heating rate of  $10^\circ\text{C}/\text{min}$  (Komatsu *et al* 1989).

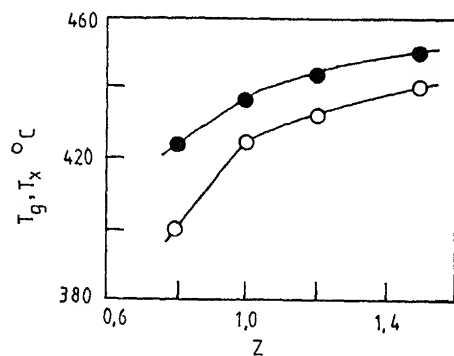


Figure 6. Influence of calcium content on  $T_x$  and  $T_g$  for the  $\text{Bi}_{1.2}\text{SrCa}_z\text{Cu}_2\text{O}_y$  glasses (Komatsu *et al* 1989).

content. The difference  $T_x - T_g$  called thermal stability factor is large for glasses with large  $\text{Bi}_2\text{O}_3$  content. Therefore,  $\text{Bi}_2\text{O}_3$  plays an important role in glass formation and also in thermal stability which is required for making glass fibre or glass

#### 4. Bi-Pb-Sr-Ca-Cu-O system

This is another very important glassy precursor for high  $T_c$  superconductors. The superconducting transition temperature  $T_c$  more than 115 K with  $T_{c0} = 100$  K. The values of  $T_g$  and  $T_x$  (figure 7 for a typical Pb doped glass) increase slowly with increase of  $\text{Bi}_2\text{O}_3$  content and reach a maximum for  $x = 3.0$  (figure 8) and decrease with further increase of bismuth content.

#### 5. Bi-Sr-Ca-Li-Cu-O system

This is another glassy system almost similar in its behaviour with that of the Sr-Ca-Cu-O type system discussed above. The main functions of Li doping are to decrease the glass melting temperature as well as glass annealing temperature for making them superconductors. The superconducting transition temperature is also increased in such systems by about 5–10 K.

#### 6. Y-Ba-Cu-O system

It is very difficult to make glass with these oxides ( $\text{Y}_2\text{O}_3$ ,  $\text{BaCO}_3$  and  $\text{CuO}$ ) because of their high melting temperature (1300–1400°C) and high quenching rate. However, a little  $\text{B}_2\text{O}_3$  (1–5 wt%) good quality glass of such system can be prepared. In this case, however, the superconducting transition temperature is reduced below 100 K. However, there is some report that rapid quenching of small droplets of  $\text{YBa}_2\text{Cu}_3\text{O}_7$  melt on steel plates resulted (Koo *et al* 1889) in an amorphous material which has  $T_g = 330^\circ\text{C}$  and  $T_x = 780^\circ\text{C}$ .

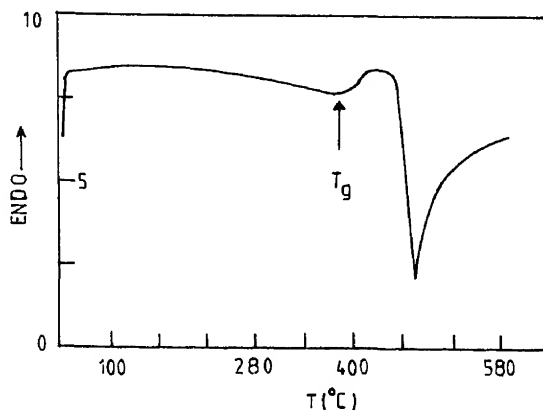


Figure 7. DSC scan of  $\text{Bi}_{1.5}\text{Pb}_{0.5}\text{Sr}_2\text{Ca}_2\text{Cu}_3\text{O}_y$  glass recorded at a heating rate of 10 K/min in argon (Bansal 1990).

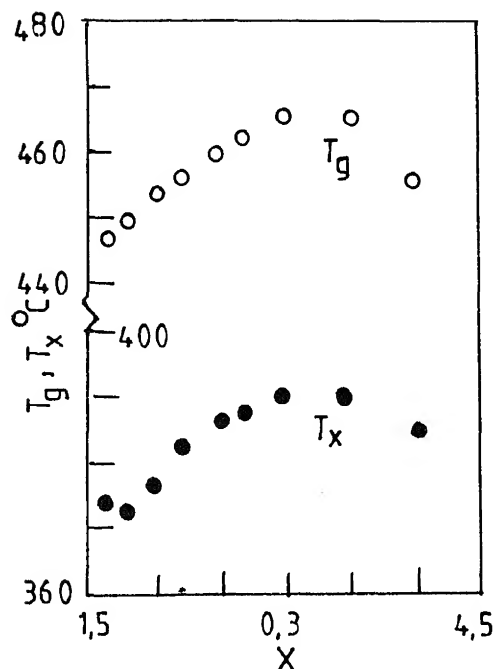


Figure 8. Dependence of  $T_g$  and  $T_x$  of  $\text{Bi}_x\text{Pb}_{0.4}\text{Sr}_2\text{Ca}_2\text{Cu}_3\text{O}_y$  glasses on their bismuth content (Komatsu *et al* 1990).

## 7. Tl-Ba-Ca-Cu-O system

Report on the preparation of  $\text{Tl}_2\text{Ba}_2\text{CaCu}_2\text{O}$  and  $\text{Tl}_2\text{Ba}_2\text{Ca}_2\text{Cu}_3\text{O}_x$  glasses (Nassau *et al* 1989) is available in the literature. But loss of  $\text{Tl}_2\text{O}_3$  during melting makes it difficult to get superconducting glass-ceramic phases.

## 8. Ba-K(Li, Na)-Bi-O type non copper oxide system

This is a new glass system showing very interesting semiconductor-metal-semiconductor like transition even in the glassy phase (Bera *et al* 1994; Mollah *et al* 1994).

## 9. Ba-Pb-Bi-O-type non-copper oxide system

This is also a new and very interesting glassy precursor for high  $T_c$  superconductors. These glasses can be prepared with different concentrations of Pb showing non-linear physical properties (Sadhukhan *et al* 1994). Recently, many other glasses like V-Bi-St-Ti-O, V-Bi-Ba-Ti-O, V-Bi-Cr-Sr-Ca-O etc have also been discovered showing some superconducting behaviour (around 20 K or below) in their glassy phases. However, elaborate investigations of such glasses have not yet been made. It is apparent that in the near future more and more glassy precursors for high  $T_c$

superconductors with many interesting physical and structural properties were discovered. But the main problems related to the understanding of the mechanism of such superconducting transitions in these oxide glasses and the peculiar behaviour exhibited by some of these glassy precursors for high  $T_c$  superconductors, metal-insulator behaviour (Bera *et al* 1994), increase of ac conductivity superlinear behaviour in the low temperature region (Mollah *et al* 1994) etc. are not clear.

## 10. Glass viscosity

Temperature dependence of glass viscosity is very important for a successful drawing of the glass fibres. Generally, beam-bending technique has been used for the determination of viscosity in the glass transition range of the glasses like  $\text{Bi}_x\text{Sr}_{1-x}\text{Ca}_{1-x}\text{O}_y$  ( $x = 1.5$  to  $2.7$ ) (Tatsumisago *et al* 1990). The temperature dependence of viscosity follows an Arrhenius behaviour with an activation energy,  $E_0$  of 800 to 9980 J/mol. Glasses with lower Bi content showed lower  $E_0$ . Such a large value of  $E_0$  indicates that from the Bi-Sr-Ca-Cu-O system glass fibres can be drawn only at around the glass softening point rather than from the pure melt because of high fluid viscosity in water. Since the range  $T_x - T_g$  is very narrow for these glasses, crystallization may be the main problem for drawing fibres at around the glass softening point. However, an increase in the Bi content in the glass lowers the value of  $E_0$  and hence facilitates drawing glass fibres. Unfortunately, addition of Bi to a large extent lowers the value of  $T_c$ . So an appropriate choice of the composition of glasses is necessary for successful drawing of the glass fibres and then making them superconductors after properly annealing at a higher temperature. Temperature dependence of viscosity in a very narrow temperature range is shown in figure 9 where the shaded region indicates the allowable fibre drawing range. The temperature dependence of viscosity for  $\text{Bi}_4\text{Sr}_3\text{Ca}_3\text{Cu}_4\text{O}_y$  glass is shown in figure 10. The temperature dependence of melt viscosity has been measured for the  $\text{Bi}_2\text{Sr}_2\text{Ca}_1\text{Cu}_2\text{O}_y$  glass. The melt viscosity

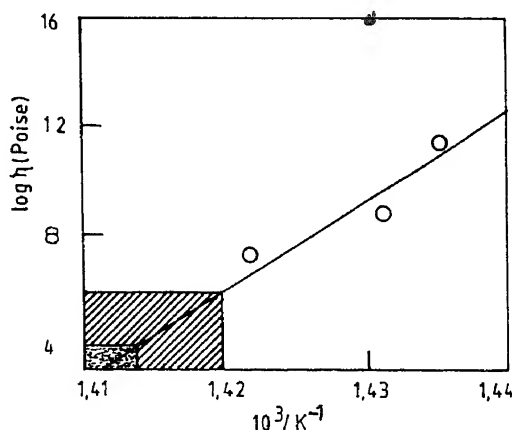


Figure 9. Temperature dependence of viscosity of the melt quenched  $\text{Bi}_{1.5}\text{Sr}_{1.5}\text{Ca}_1\text{O}_y$  glass. The allowable drawing range is shown as in the shaded region (Onishi *et al* 1990).

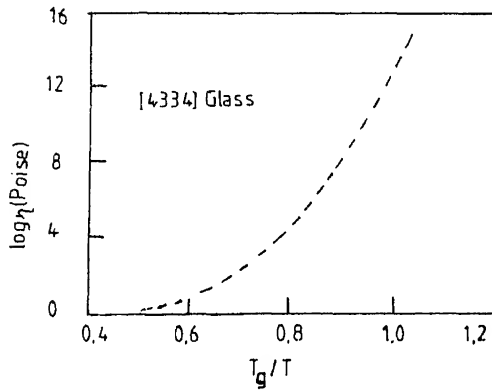


Figure 10. Temperature dependence of viscosity for the melt and glass of  $\text{Bi}_4\text{Sr}_3\text{Ca}_3\text{Cu}_4\text{O}_y$  composition (Zheng *et al* 1991a, b).

varies from 45 to 100 Poise in the temperature range of 885 to 985°C (LeBeau *et al* 1989).

### 11. Crystallization process from glassy phase

Crystallization process or crystallization kinetics is important for a successful drawing of the glass fibres. Non-isothermal (Tatsumisago *et al* 1989a, b; Tohge *et al* 1989; Bansal 1990) or isothermal (Zheng and Mackenzie 1991) differential scanning has been used to study the kinetics of crystallization in the Bi-based oxide glasses leading to superconductivity in their ceramic phases. The isothermal crystallization of a glass can be expressed by the Avrami equation (Avrami 1939) viz.

$$x = 1 - \exp[-(kT)^n],$$

where  $x$  is the volume fraction crystallized after time  $t$ ,  $n$  the Avrami parameter which depends on the crystal growth morphology, and  $k$  the crystallization rate constant which can be expressed as the activation energy,  $R$  the gas constant and  $T$  the isothermal absolute temperature. The values of  $E_a$  for crystallization of glasses of various compositions are found to vary from 290 to 489 kJ/mol. The value of the Avrami exponent for crystallization of the  $\text{Bi}_4\text{Ca}_3\text{Sr}_3\text{Cu}_4\text{O}_y$  glass was found (Zheng and Mackenzie 1991) to be close to 3 suggesting a three dimensional crystal growth at a constant number of nucleation state.

### 12. Crystal phases obtained under heat treatment of glasses

Time, temperature and atmosphere have great influence on the crystal formation from the glass phase under heat treatment studied by several researchers. Some results on the Bi-based glasses are discussed below. When a glass sample is heat-treated, it takes quite a long time to become crystalline, and this crystallization is not a continuous process leading to the final single superconducting phase. Several factors are involved



to control the different phase formations. Composition, phase separation in the melt, annealing time, temperature, heating rate, cooling rate etc are important parameters to get a single superconducting crystalline phase from a typical glass phase under investigation.

Several authors (Tohge *et al* 1989; Tatsumisago *et al* 1990) have studied the  $T$ – $T$ – $T$  diagram of the Bi–Sr–Ca–Cu–O system. A typical  $T$ – $T$ – $T$  diagram for the  $\text{BiSrCaCu}_2\text{O}_y$  glass is shown in figure 11. The symbol is a mixture of crystalline phase. Figure 12 shows the  $T$ – $T$ – $T$  diagram for the  $\text{Bi}_2\text{Sr}_2\text{Ca}_2\text{Cu}_3\text{O}_y$  glass composition. The transformation behaviour of the cast material of  $\text{Bi}_2\text{Sr}_2\text{CaCu}_2\text{O}_x$  composition into the 2212 superconducting phase is different in air and nitrogen atmospheres. Due to a large fraction of copper present as Cu(I) in these glasses, the crystallization mechanism is affected

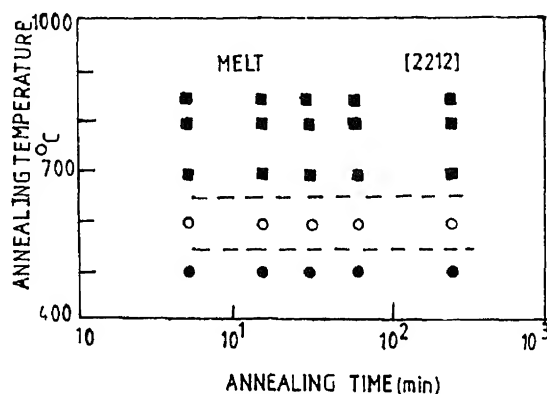


Figure 11.  $T$ – $T$ – $T$  diagram for  $\text{BiSrCaCu}_2\text{O}_y$  glass (●, glass; ○, 10 K phase; □, phase). (Tohge *et al* 1989).

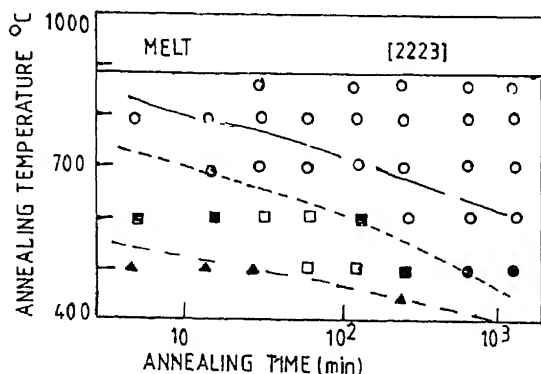


Figure 12.  $T$ – $T$ – $T$  diagram for  $\text{Bi}_2\text{Sr}_2\text{Ca}_2\text{Cu}_3\text{O}_y$  glass. ▲: glass +  $\text{Cu}_2\text{O}$  + (CaO +  $\text{Cu}_2\text{O}$ ):80 K phase + CaO +  $\text{CuO}$ :80 K phase + CaO +  $\text{Cu}_2\text{O}$  +  $\text{CuO}$ ; ○:80 K phase (Komatsu *et al* 1989).

oxygen partial pressure. The amount of Cu(I) ions in these glasses depends on the cooling rate and thus their crystallization behaviour is affected by condition of glass making. The glass preparation conditions have an effect (Zheng *et al* 1991a, b) on the ratio Cu(I)/Cu (total) in the glass which in turn affects the glass structure and its crystallization mechanism. The glasses melted at lower temperature have lower values of this ratio and yield larger crystallites. The value of this ratio also changes with increase/decrease of melting time. So it is always advisable to melt all glass compositions of a particular base glass at fixed temperature, if possible, and quench them for making superconducting samples.

The initial crystallization phase precipitating out of a glass depends on the composition and also on the ratio  $\eta = \text{Cu(I)}/\text{Cu (total)}$ . The initial crystallization phase from the  $\text{Bi}_4\text{Sr}_3\text{Ca}_3\text{Cu}_4\text{O}_y$  glass is 2201 phase. The glasses with low  $\eta$  value produces large 2201 crystals and *vice versa*. It might be possible to control crystallization by controlling the atmosphere and the ratio  $\eta$  since crystal growth needs oxygen and the size of the crystal depends on ratio  $\eta$ . Continuous glass fibre drawing is possible (Zheng *et al* 1991a, b) by using higher values of  $\eta$ . In this connection we would like to mention that all these glasses with Cu ions behave like transition metal oxide glasses and are semiconducting in nature as mentioned earlier (Som *et al* 1992). The semiconductivity arises due to the presence of mixed valence states of Cu. Elaborate investigations of the semiconducting properties of the Bi-based Li and Pb doped glasses have been carried out in our laboratory (Mollah *et al* 1993, 1994).

A single phase 110 K superconductor has been prepared (Shi *et al* 1988, 1989) by crystallization of  $\text{Bi}_2\text{Sr}_2\text{Ca}_3\text{Cu}_4\text{O}_y$  and  $\text{Bi}_2\text{Sr}_2\text{Ca}_4\text{Cu}_5\text{O}_y$  glasses by annealing at 870°C in air. The starting composition as well as annealing temperature are important for obtaining a 110 K phase. The 80 K and the  $\text{Ca}_2\text{CuO}_3$  phases first coprecipitate from the glass. The 110 K phase nucleates and grows at the interface between these two phases which is controlled by interface diffusion of calcium and copper.

Like undoped Bi–Sr–Ca–Cu–O system Pb doped system has also been elaborately studied (Mollah *et al* 1993, 1994). Thorough investigations of  $T-T-T$  diagrams for the  $\text{Ba}_{1.8}\text{Pb}_{0.2}\text{Sr}_2\text{Ca}_2\text{Cu}_3\text{O}_y$  and  $\text{Ba}_{1.6}\text{Pb}_{0.4}\text{Sr}_2\text{Ca}_2\text{Cu}_3\text{O}_y$  glasses were conducted by Tatsumisago *et al* (1990). The  $\text{Ca}_2\text{PbO}_4$  phase is formed in the Bi–Pb–Sr–Ca–Cu–O glass on short term annealing at 855°C. However, on long term annealing the  $\text{Ca}_2\text{PbO}_4$  phase disappears and 110 K phase is formed. It therefore appears that  $\text{Ca}_2\text{PbO}_4$  plays an important role on the formation of the high  $T_c$  phase in the Pb doped glassy precursors for high  $T_c$  superconductors.

### 13. Dependence of $T_c$ and $J_c$ on the processing conditions

It has already been mentioned that if the glasses of our present interest are annealed at a higher temperature (above  $T_g$ ) they become crystalline and ultimately superconducting depending on various factors like glass melting temperature, quenching rate, atmosphere, and also on the cooling rate. Therefore, it is not very easy to satisfy all the conditions at a time for achieving high  $T_c$  and high  $J_c$  values for a particular glass concentration. Furthermore, superconducting properties as well as  $J_c$  values also depend on the glass compositions. That is, if all the processing conditions are similarly maintained for two different compositions of the Bi–Sr–Ca–Cu–O glasses

the glass melting temperature, superconducting transition temperature etc also on the additives like Pb, K, Li, iodine etc. Some typical results on the dependence of  $T_c$  and  $J_c$  on some of the above mentioned factors are discussed below in

Figure 13 shows the variation of  $T_{c0}$  (zero resistance temperature) of  $\text{Bi}_x\text{SrCaCu}_2\text{O}_y$  glasses annealed at  $840^\circ\text{C}$  for 45 h in air and then furnace cooled. There are optimum values of  $x$  for which  $T_{c0}$  is maximum. However, the glasses  $\text{Bi}_{1.2}\text{SrCa}_z\text{Cu}_2\text{O}_y$  annealed under the same condition show variation of  $T_{c0}$  with  $z$  (calcium content) as shown in figure 14. Here  $T_{c0}$  does not depend very much on the Ca content of the glass. The variation of electrical resistivity of a typical  $\text{Bi}_{1.2}\text{SrCaCu}_2\text{O}_y$  sample is shown in figure 15 where the sample is annealed at various temperatures.  $T_c$  increases with increase of annealing temperature, but for very high temperature annealing  $T_c$  decreases appreciably.

The effect of annealing time on  $T_c$  and  $J_c$  for the  $\text{Bi}_2\text{Sr}_2\text{CaCu}_2\text{O}_y$  (or 2212) sample annealed at  $820^\circ\text{C}$  in air is shown in figures 16 and 17. Weak links at the boundaries are responsible for low values of  $J_c$  in the glass-ceramic superconductors.

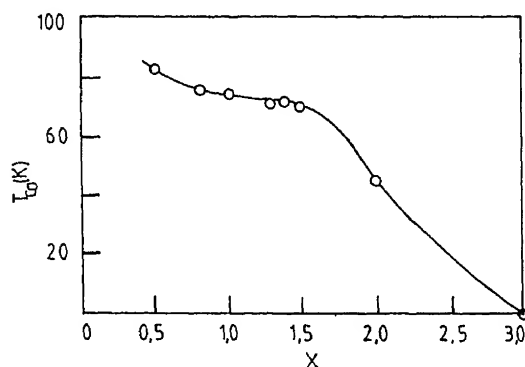


Figure 13. Superconducting transition temperatures,  $T_c(R=0)$ , of  $\text{Bi}_x\text{SrCaCu}_2\text{O}_y$  glasses annealed at  $820^\circ\text{C}$  for 40 h in air and furnace cooled (Komatsu *et al* 1989).

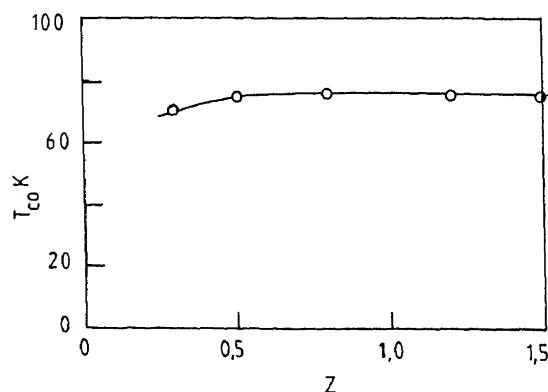


Figure 14. Superconducting transition temperatures,  $T_c(R=0)$ , of  $\text{Bi}_{1.2}\text{SrCa}_z\text{Cu}_2\text{O}_y$  glasses annealed at  $820^\circ\text{C}$  for 40 h in air furnace cooled (Komatsu *et al* 1989).

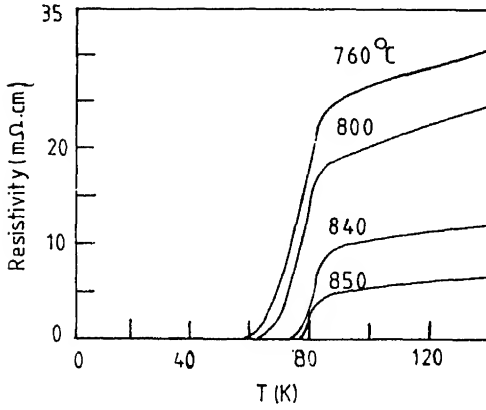


Figure 15. Variation of resistivity of a typical  $\text{Bi}_{1.2}\text{SrCaCu}_2\text{O}_y$  glass with annealing temperature ( $T_{c0}$ , zero resistance).

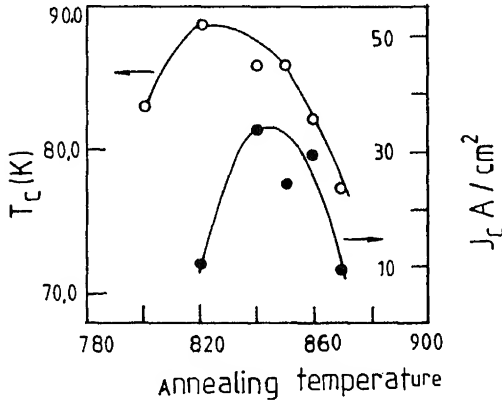


Figure 16. Effect of annealing temperature on critical current density ( $J_c$ ) and  $T_c$ .

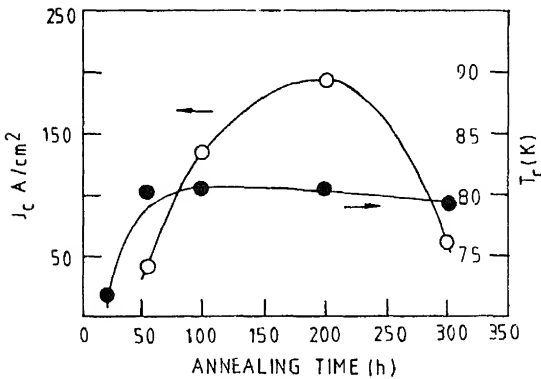


Figure 17. Values of critical temperature  $T_c$  and critical current density  $J_c$  (77 K, zero magnetic field) of  $\text{Bi}_2\text{Sr}_2\text{CaCu}_2\text{O}_y$  glass samples annealed at 820°C in air for various times and furnace cooled (Komatsu *et al* 1990).

Recently, efforts are being made to reduce the density of weak links at the grain boundaries. Air, oxygen or vacuum annealed samples have different  $T_c$  values (Bari and Li 1991). Annealing in  $O_2$  greatly enhances  $T_c$  of  $Bi_4Sr_3Ca_3Cu_4O_x$  type glasses to a value of 110 K. The vacuum annealed sample has small  $T_c$  (75 K or so) and a very low  $T_{c0}$ .

The rate at which a sample is cooled after annealing at higher temperature largely affects the superconducting transition temperature. The  $Bi_{1.5}SrCaCu_2O_y$  glass, for example, annealed at 840°C for 90 h in air followed by fast cooling showed (Bari and Guire 1989; Guire *et al* 1990) semiconducting behaviour in the normal state. On the other hand, similar sample annealed similarly and cooled slowly showed metallic behaviour in the normal state. The glass sample annealed at 840°C for 200 h is superconducting at 77 K. However, it is interesting to note that the  $BiSrCaCu_2O$  glass sample annealed at 850°C for 24 h in oxygen and cooled rapidly (Komatsu *et al* 1988) showed a sharp superconducting transition and higher  $T_c$ , whereas the furnace cooled sample showed a broad transition with a tail and low  $T_c$  value. The effect of cooling conditions on the superconducting properties of  $Bi_{1.2}SrCaCu_2O_y$  and  $Bi_2Sr_2CaCu_2O_y$  glass-ceramics have also been investigated. Two glass samples of  $Bi_{1.2}SrCaCu_2O_y$  compositions were annealed at 880°C for 20 h in air and one sample was rapidly quenched in air and the other was furnace cooled. The temperature dependence of electrical resistivities of these samples is shown in figure 18. The quenched sample has a high normal state resistivity with a sharp drop at 90 K followed by a long tail which persists to very low temperature. On the other hand, the furnace cooled sample showed a much smaller value of normal state resistivity. It also exhibited a sharp drop in resistivity at 105 K indicating the formation of a high  $T_c$  phase followed by a sharp drop at 85 K with  $T_c$  at 68 K (zero resistance value). The effect of cooling condition on the value of  $T_c$  of the glass-ceramics obtained by annealing a glass of  $Bi_2Sr_2CaCu_2O_y$  composition at 820°C for 48 h in air differs from that of similar glass like  $Bi_{1.2}Sr_2CaCu_2O_y$ . The normal state resistivity of the furnace cooled sample was smaller than that of the air cooled sample. But the former showed a  $T_c$  (zero resistance value) of 85 K compared with 88 K for the latter. The reason for this difference in behaviour is not clear. The influence of various cooling rates on  $T_c$  of  $BiSrCaCu_2O_y$ ,  $Bi_2Sr_2Ca_2Cu_3O_y$ ,  $Bi_3Sr_3Ca_3Cu_4O_y$  and  $Bi_3Sr_3Ca_4Cu_5O_y$  glasses annealed for

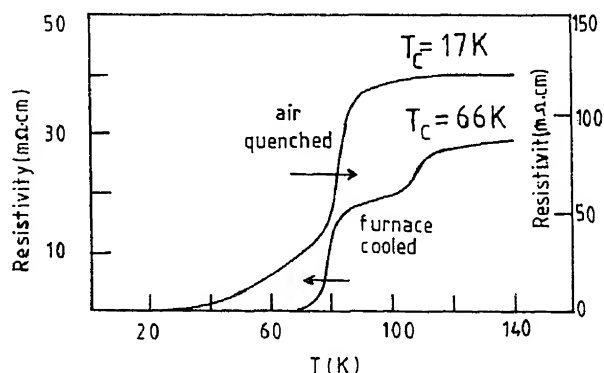


Figure 18. Temperature dependence of electrical resistivity of  $Bi_{1.2}SrCaCu_2O_y$  samples annealed for 20 h in air.

or 48 h at 870–888°C in air, O<sub>2</sub>, or vacuum has also been studied (Som *et al* 1992; Chatterjee *et al* 1994). The  $T_c$  (onset) increased with decrease in cooling rate.

The Pb and Li doped Bi–Sr–Ca–Cu–O systems have also been elaborately investigated in recent years because of the fact that addition of Pb or Li reduces the glass transition temperature as well as increases the superconducting transition temperature as mentioned earlier. Temperature dependence of resistivity of Pb doped  $\text{Bi}_{4-n}\text{Pb}_n\text{Sr}_3\text{Ca}_3\text{Cu}_4\text{O}_x$  (with  $n = 0.1, 0.5$  and  $0.1$ ) is shown in figure 19. These glass ceramics are obtained by annealing the glasses at 840°C for 24 h in air. All the samples show  $T_c$  between 110 and 115 K which is about 10 to 15° higher than the corresponding undoped systems. Similar curves with Li doped  $\text{Bi}_4\text{Sr}_3\text{Ca}_{3-z}\text{Li}_z\text{Cu}_4\text{O}_x$  systems have also been studied (Mollah *et al* 1993). Interesting informations are obtained from the thermoelectric power (TEP) measurements of both the glass and the glass ceramics. For the glasses thermopower is negative (electronic carrier) but for the superconducting glass-ceramics the thermopower is found to be positive (hole carriers). In figure 20 we have shown the temperature dependence of thermoelectric power of the Pb-doped  $\text{Bi}_4\text{Sr}_3\text{Ca}_3\text{Cu}_4\text{O}_x$  glass-ceramics. Choice of correct starting composition to prepare the 110 K superconducting phase in the bismuth system is also very important.  $\text{Bi}_{1.84}\text{Pb}_{0.34}\text{Sr}_2\text{Ca}_2\text{Cu}_3\text{O}_y$  composition results in the formation of the 75 K phase whereas 110 K phase is mainly produced in the  $\text{Bi}_{1.84}\text{Pb}_{0.3}\text{Sr}_2\text{Ca}_2\text{Cu}_4\text{O}_y$ . Recently, we have been successful in preparing 110 to 115 K phase in the Pb doped

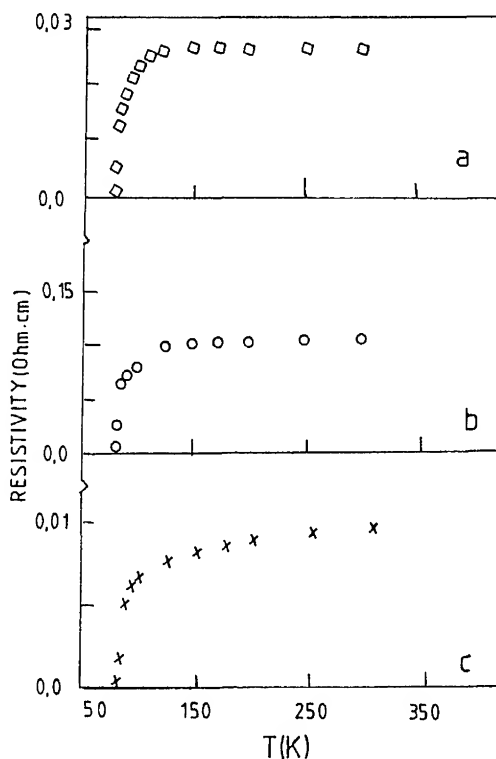


Figure 19. Temperature dependence of resistivity of (a)  $\text{Bi}_{1.84}\text{Pb}_{0.34}\text{Sr}_2\text{Ca}_2\text{Cu}_3\text{O}_y$ , (b)  $\text{Bi}_{1.84}\text{Pb}_{0.3}\text{Sr}_2\text{Ca}_2\text{Cu}_4\text{O}_y$ , and (c)  $\text{Bi}_{1.84}\text{Pb}_{0.3}\text{Sr}_2\text{Ca}_2\text{Cu}_4\text{O}_y$ .

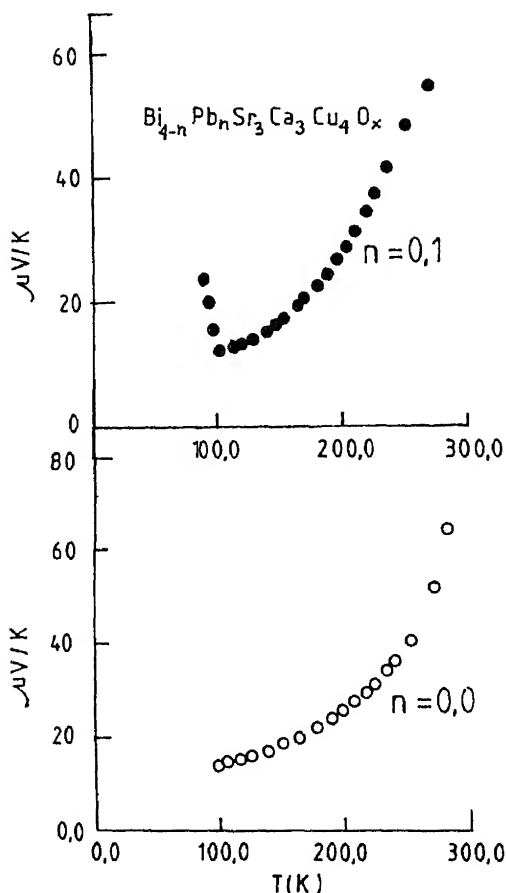


Figure 20. Temperature dependence of thermopowers of  $\text{Bi}_{4-n}\text{Pb}_n\text{Sr}_3\text{Ca}_3\text{Cu}_4\text{O}_x$  ceramics ( $n = 0.0, 0.1$ ).

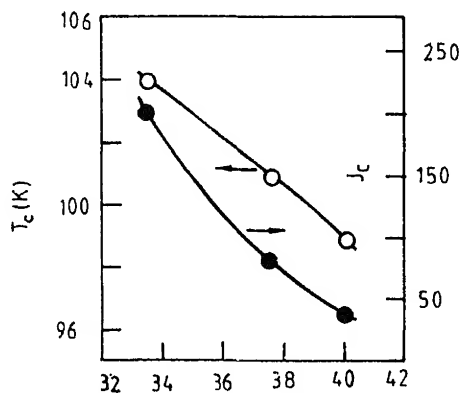
$\text{Bi}_4\text{Sr}_3\text{Ca}_3\text{Cu}_4\text{O}_x$  glass-ceramics (Bose 1994; Chatterjee *et al* 1994; Mollah 1994). It has also been shown by Baker *et al* (1989) that superconducting phase is obtained from the  $\text{Bi}_4\text{Sr}_3\text{Ca}_3\text{Cu}_4\text{O}_x$  glassy precursor. The influence of Pb content on the superconductivity of the nominal compositions  $\text{BiPb}_x\text{Sr}_2\text{Ca}_2\text{Cu}_3$ ,  $\text{Bi}_{1-x}\text{Pb}_x\text{Sr}_2\text{Ca}_2\text{Cu}_3$ ,  $\text{Bi}_{1-x}\text{Pb}_x\text{Sr}_2\text{Ca}_2\text{Cu}_{3.6}\text{O}_y$ , etc systems have also been elaborately investigated. The optimum value of  $x$  for higher  $T_c$  was found to be 0.35. At higher PbO concentration  $\text{Ca}_2\text{PbO}_4$  formed which caused the formation of a low  $T_c$  phase. PbO can be added until the  $\text{Ca}_2\text{PbO}_4$  is formed in the glass-ceramic phase. Pure 2223 phase has been formed with Pb addition (Hatano *et al* 1988; Kozawa *et al* 1988; Luo *et al* 1990). However, the effect of Pb substitution is not well understood. Pb is considered to be partially substituted (Takano *et al* 1988) into the bismuth oxide planes of the crystal structure of the 110 K phase. The effect of this substitution is to stabilize the lattice and to facilitate the formation of the pure 2223 phase. Addition of PbO or LiO lowers the melting point as well as increases the viscosity of the glass probably by acting as a fluxing agent. The Pb atoms are easily incorporated

into the structure probably because Bi in the  $3^+$  oxidation state and Pb in the  $2^+$  state have the same outer electronic shell configuration of  $6s^2 6p^0$  (Bansal 1992). On the other hand, substitution of the bigger  $Pb^{2+}$  cation (ionic radius = 1.20 Å) for  $Bi^{3+}$  (ionic radius = 0.96 Å) probably results in the distortion of the crystal lattice.

Values of critical temperature  $T_c$  and critical current density  $J_c$  (at 77 K and zero magnetic field) of a typical  $Bi_{0.8}Pb_{0.2}SrCaCu_xO_y$  ( $x = 1.5, 1.8$  and  $1.2$ ) glass-ceramics annealed at  $840^\circ\text{C}$  in air is shown in figure 21. Excess amount of CaO or CuO always reduces  $J_c$  values in the glass-ceramics. The Pb-doped high  $T_c$  phase has been observed with high resolution transmission electron microscopy and it was found that Pb atoms were located in the Bi–O layers with an atomic ratio of Pb/Bi being 0.1. It is also observed that for low Pb/Bi ratio, Pb atoms incorporated into the structure of both the low  $T_c$  and high  $T_c$  phases, whereas for high Pb content ( $x > 0.25$ ) the Pb rich phase appeared. From all such considerations it appears that a value of  $x \sim 0.2$  would be the optimum substitution of Pb for Bi for the formation of the high  $T_c$  phase in the  $Bi_{1-x}Pb_xSrCaCu_{1.5}O_y$  system. This might be closely related to the maximum Pb content incorporating in the high  $T_c$  phase. This is in agreement with the results of many other researchers. The optimum starting glass composition appears to be  $Bi_{1.6}Pb_{0.4}Sr_2Ca_2Cu_3O_y$ . When annealed at  $840\text{--}945^\circ\text{C}$  in air for a long time, a large volume fraction of the 110 K phase is formed in this glass which shows a  $T_{c0}$  at 107 K along with high  $J_c$  value. There are definitely other possible glass compositions for preparing superconductors with high  $T_c$  and high  $J_c$  values.

#### 14. Superconducting wires, tapes, films from glass phase

We have already discussed in our previous review (Chaudhuri and Som 1992) the development of superconducting wires or tapes from the glassy phases. Glass precursor approach for the preparation of high  $T_c$  superconducting fibres is very interesting (Zheng *et al* 1989, 1991a, b; Onishi *et al* 1989, 1990, 1991; Komatsu *et al* 1990; Miller *et al* 1990; Chaudhuri *et al* 1989; Bose 1994). So far this technique has been





used for making fine rods, tapes and thick films of the Bi-Sr-Ca-Cu-O or Pb-Ca-Cu-O glassy phases. Continuous glass fibres with diameter  $\sim 110 \mu\text{m}$  have successfully drawn (Zheng *et al* 1991) with [4334] glass. The superconducting value after heat treatment of about 12 h is about 85 K. Figure 22 shows some drawn fibres from the glass melt. The  $J_c$  values for such superconducting wires are relatively small (100 to 200 A/cm<sup>2</sup>). Glass fibres of several diameters have also been drawn from the Pb doped Bi-Sr-Ca-Cu-O glassy phase (Komatsu *et al* 1990).  $T_c$  as high as 109 K and  $J_c = 1480 \text{ A/cm}^2$  (Komatsu *et al* 1990). Attempts have been made for fabrication of long fibres from melts of 2212 phase and 1112 phase using a gas jet fibreization technique. Glass fibres of short lengths have also been prepared (Zheng *et al* 1989) by spinning a melt of 4334 glass. Another technique for making glass wire by depositing glass melt on Pt wires has also been made (Bhaugikar *et al* 1991). Interesting development has been made in recent years to make filaments or powder by spraying the liquid melts. Another technique involves glass coating on metal or ceramic surfaces and subsequent annealing to make high temperature superconductors.

## 15. Summary and conclusion

We have reviewed some of the properties of the glass-ceramic superconductors prepared and studied by different researchers. Most of the studies on the GC phases have been concentrated on the Bi-Sr-Ca-Cu-O based systems either undoped or doped with Pb, Li etc. Y-Ba-Cu-O and Tl-Ba-Ca-Cu-O systems have not been well studied in their respective GC phases as they are difficult to prepare the respective glassy phase. However, homogeneous glass is formed when Y-Ba-Cu-O is mixed with appropriate amount of  $\text{B}_2\text{O}_3$  and PbO. Crystalline Y-Ba-Cu-O can be nucleated in this glass by proper annealing treatment. Such studies are being carried out in recent years. Because of the presence of transition metal ions ( $\text{Cu}^{1+}$  and  $\text{Cu}^{2+}$ ) in all the glassy phases showing semiconducting behaviour are almost similar in their behaviour with those of usual TMO glasses. Superconductivity in the glassy phase has not been observed in any of the glasses down to 8 K or so. However, very re-

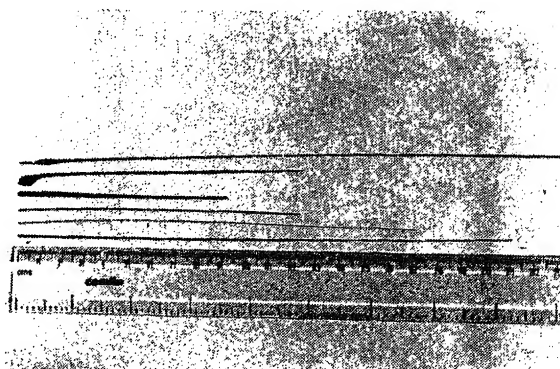


Figure 22. Glass fibres drawn from melt of 4334 glass.

we have observed some increase in the conductivity of the Pb-doped  $\text{Bi}_{4-n}\text{Pb}_n\text{Sr}_3\text{Ca}_3\text{Cu}_4\text{O}_x$  glasses in the low temperature (below 150 K) region but they do not show superconductivity down to 10 K. Moreover, the ac conductivity ( $\sigma_{ac}(\omega)$ ) of the TMO glasses show the general behaviour like  $\sigma_{ac}(\omega) \propto \omega^s$  (where the exponent is  $\leq 1$ ). But most of the glasses becoming high  $T_c$  superconductors show slightly greater value of  $s$  than unity in the low temperature region. Furthermore, these glasses also show quite large glass transition temperature, and Debye type dielectric relaxation behaviour. In the Bi-based glasses one also observes the presence of  $\text{BiO}_3$  and  $\text{BiO}_6$  structural units.  $\text{Bi}_2\text{O}_3$  acts as the glass former and plays an important role increasing the thermal stability factor ( $T_x - T_g$ ) with increase of  $\text{Bi}_2\text{O}_3$  in the glass which is essential for drawing glass fibres from the melts. Very interesting behaviour was shown by the Ba-K (Li or Na)-Bi-O based glasses. Most of these glasses showed non-linear variations of dc and ac conductivities and even semiconductor-metal-semiconductor like transition was exhibited between 300 and 340 K (depending on concentrations). These glasses also showed superconductivity in their ceramic phases (when annealed in oxygen atmosphere). The strong electron-phonon interaction can be attributed to explain the above mentioned non-linear behaviour. However, proper understanding of the behaviour of these and similar other glasses becoming high  $T_c$  superconductors in their GC phases has not been possible. The nature of carriers in these glasses are negative as observed from the thermoelectric power measurements but with the increase of crystallinity (by annealing) the nature of carrier changes from negative to positive in the superconducting GC phase. More elaborate microstructural and spectroscopic studies of such glasses might be interesting to elucidate the causes as to why these glasses unlike many TMO glasses become superconductors in their GC phases.

### Acknowledgement

The author is grateful to Miss Gargi Banerjee (JRF, DAE), S Chatterjee (JRF, UGC), D K Modak (SRF, CSIR) and S Mollah (Post Doc., CSIR) for their various help and cooperation.

### References

- Avrami M 1939 *J. Chem. Phys.* **7** 1103
- Baker R C, Hung W H and Steinlink H 1989 *Appl. Phys. Lett.* **54** 371
- Bansal N P 1990 *J. Appl. Phys.* **68** 1143
- Bansal N P and Guire De 1989 NASA Cr 185139
- Bednorz J G and Muller K A 1986 *Z. Phys.* **B64** 189
- Bera A K, Banerjee G, Ghosh A K, Modak D K and Chaudhuri B K 1994 *Phase Trans.* (in press)
- Bhargava A, Varshneya A K and Snyder R L 1991 *Mat. Letts.* **11** 313
- Bose K 1994 *Preparation and characterization of some high  $T_c$  superconducting composites*, Ph.D. Thesis, Jadavpur University, Calcutta
- Chaudhuri B K and Som K K 1992 *Indian J. Phys.* **A66** 37
- Chaudhuri B K, Som K K and Sengupta S P 1989 *J. Mater. Sci.* **8** 520
- Chatterjee S, Banerjee S and Chaudhuri B K 1994 *Phys. Rev.* **B** (communicated)
- Gan F and Li G 1991 *J. Non-Cryst. Solids* **130** 67
- Guire de M R, Bansal N P and Kim C J 1990 *J. Am. Ceram. Soc.* **73** 1165
- Hatano T, Aota K, Ikeda S, Nakamura K and Ogawa K 1988 *J. Appl. Phys.* **27** L2055

- Hirashima H, Watanabe Y and Yoshida T 1987 *J. Non-Cryst. Solids* **95 & 96** 825
- Komatsu T, Kamai K, Matsusita K, Tanaka M, Iwai Y, Kawakami A, Kaneko Y and Yamashita T 1988 *Jap. J. Appl. Phys. Lett.* **26** L1272, L1148
- Komatsu T, Imai K, Goto R, Matsusita K and Yamashita T 1988 *Jap. J. Appl. Phys.* **27** L533
- Komatsu T, Ohki T, Matsusita K and Yamashita T 1989 *J. Ceram. Soc. Jap.* **97** 251
- Komatsu T, Hirose C, Ohki T and Matsusita K 1990 *J. Am. Ceram. Soc.* **73**-3569
- Koo H S, Xu R and Mackenzie J D 1989 *J. Mater. Res.* **4** 911
- Koyama S, Endo U and Kawai T 1988 *Jap. J. Appl. Phys.* **27** L1861
- LeBeau S E, Righi J, Ostenson J E, Sanders S C and Finnemore D K 1989 *Appl. Phys. Lett.* **55**
- Luo J S, Faudot F, Chevalier J P, Portier R and Michel D 1990 *J. Solid State Chem.* **89** 94
- Maeda M, Tanaka Y, Fukutomi M and Asano T 1988 *Jap. J. Appl. Phys.* **27** L209
- Michel C, Hervieu M, Borel M M, Grandin A, Deslandes F, Provost J and Raveau B 1987 *Z. Phys.* **421**
- Michel C, Hervieu M, Borel M M, Grandin A, Deslandes F, Provost J and Raveau B 1987 *Z. Phys.* **421**
- Miller T A, Sanders S C, Ostenson J E, Finnemore D K, LeBeau S E and Righi J 1990 *Appl. Phys. Lett.* **56** 584
- Mollah S 1993 *Preparation and characterization of some transition metal oxide glasses becoming superconductors in their glass-ceramic phases*, Ph.D. Thesis, Jadavpur University, Calcutta
- Mollah S, Som K K, Bose K and Chaudhuri B K 1993 *J. Appl. Phys.* **73** 931
- Mollah S, Bera A K, Chakraborty S and Chaudhuri B K 1994 *Phys. Rev.* **B49** 1243
- Mollah S, Chatterjee S, Chakraborty S and Chaudhuri B K 1994 *Philos. Mag.* (in press)
- Mott N F and Davis E A 1979 in *Electronic processes in non-crystalline materials* (Oxford: Clarendon Press) 2nd Ed.
- Nakamura S and Ichinose N 1987 *J. Non-Cryst. Solids* **95 & 96** 849
- Nassau K, Miller A E, Gyorgy E M and Siegrist T 1989 *J. Mater. Res.* **4** 1330
- Onishi M, Kohgo T, Chigusa Y, Watanabe K, Kyoto M and Watanabe M 1990 *Jap. J. Appl. Phys.* **29** L1081
- Onishi M, Kyoto M and Watanabe M 1991 *Jap. J. Appl. Phys.* **30** L988
- Onishi M, Khgo T, Chigusa Y, Kyoto M and Watanabe M 1989 *Jap. J. Appl. Phys.* **28** L2204
- Sadhukhan M, Bera A K and Chaudhuri B K 1994 *J. Non-Cryst. Solids* (communicated)
- Sakuri Y and Yamaki J 1985 *J. Electrochem. Soc.* **132** 512
- Shi D, Blank M, Patel M, Kinks D G, Mitchell A W, Vandervoot K and Claus H 1988 *Physica* **C156** 151
- Shi D, Jang M, Vandervoorz K and Claus H 1989 *Phys. Rev.* **B39** 9091
- Som K K 1991 *Studies of some semiconducting oxide glasses and some high  $T_c$  superconducting compounds*, Ph.D. Thesis, Jadavpur University, Calcutta
- Som K K, Mollah S, Bose K and Chaudhuri B K 1992 *Phys. Rev.* **B45** 1655
- Takano M, Takada J, Oda K, Kitaguchi H, Miura Y, Ikeda Y, Tomii Y and Mazaki H 1988 *Jap. J. Appl. Phys.* **27** L1081
- Tatsumisago M, Angell C A, Tsuboi S, Akamatsu Y, Tohge N and Minami T 1989a *Appl. Phys. Lett.* **55** 2268
- Tatsumisago M, Angell C A, Tsuboi A, Akamatsu Y, Tohge N and Minami T 1989b *Appl. Phys. Lett.* **55** 6000
- Tatsumisago M, Tsuboi S, Tohge N and Minami T 1990 *Appl. Phys. Lett.* **57** 195
- Tohge N, Tsuboi S, Tatsumisago M and Minami T 1989 *Jap. J. Appl. Phys.* **28** L1742
- Zheng H and Mackenzie J D 1991 *Phys. Rev.* **B43** 3048
- Zheng H, Xu R and Mackenzie J D 1989 *J. Mater. Res.* **4** 911
- Zheng H, Colby M W and Mackenzie J D 1991a *J. Non-Cryst. Solids* **127** 1679
- Zheng H, Hu Y and Mackenzie J D 1991b *Appl. Phys. Lett.* **59** 1679

## Sol-gel glasses: some recent trends

D GANGULI

Sol-Gel Laboratory, Central Glass and Ceramic Research Institute, Calcutta 700 032, India

**Abstract.** The basic experimental steps in the preparation of sol-gel glass as developed in recent times, and their relevance have been discussed taking high purity silica glass as an example. Current developments in sol-gel derived ultra-low expansion glasses, rare earth doped laser glasses, semiconductor-doped non-linear glasses, gradient index lenses, microoptics and organic molecule-doped (mainly dyes) glasses for sensor and other applications have been discussed in brief.

**Keywords.** Sol-gel; silica glass; doped silica; silicate glasses.

### 1. Introduction

Production of glasses by the basic procedure of melting–cooling–annealing and its variants is a historically evolved industrial practice. While such procedures are convenient for producing most of the commercial glasses, some special glasses are indeed known to be less amenable to them. Some of the difficulties acknowledged by the classical glass melting technique are: (i) Requirement of high temperature facilities (2000°C or more) for glasses for special applications, e.g. pure silica, doped (e.g. rare earths) silica and titania-silica glasses, (ii) requirement of special refractories for the high-melting glasses, (iii) corrosion of refractories and the resulting contamination of glass in case of low viscosity melts and (iv) preferential vaporization of raw materials and consequent defects and shift from target composition.

For special glasses, therefore, alternative simpler routes have been looked for. While chemical vapour deposition has been proved to be a powerful technique specially for high melting glasses, sol-gel processing has also enjoyed wide attention because of its built-in versatility and simplicity, and specially, the relatively low temperature of operation.

The advantages of sol-gel processing have been discussed by many authors, and will not be elaborated here; it is sufficient to mention that all the difficulties for special glasses, as listed above, can be overcome by the sol-gel process. Homogeneity of multicomponent sol-gel glasses is, of course, a critical issue, and merits separate discussion.

The present paper will attempt to highlight some critical issues in sol-gel glass making, as also describe selectively and in brief some of the current trend-setting activities in the development and application of sol-gel glasses.

### 2. Sol-gel glass .... glass?

Since the virtual rejection of the ASTM definition of glass as an inorganic product of

a piece of silica gel as silica glass (Scholze 1991)! The question if a 'glass' which melting history behind it would exhibit a  $T_g$  has been answered in the affirmative of some sol-gel glasses (Mackenzie 1982; Weinberg 1986) as examples. Wide acceptance of adequately dried (dehydroxylated) and densified gels as 'glass' has of course come through approximate matching of their ambient (e.g. refractive index, hardness, density) and some above-ambient (e.g. thermal expansion, high temperature viscosity) properties with those of the corresponding melt-derived dry and dense glasses. These issues have been addressed by Weinberg (1986) and Brinker and Scherer (1989).

The journey of a bulk gel to a glass by thermal densification is accompanied by the following progressive changes which can be completed under the best of conditions (e.g. optimum gel structure, atmosphere of heating, maximum temperature, heating schedule): (i) Expulsion of volatiles including molecular water, (ii) elimination of water generated by OH-OH reaction, (iii) elimination of pores, specially micropores, (iv) substantial reduction of surface area and (v) reorientation of (and elimination of) the structural elements towards a stable, glass-like structural state.

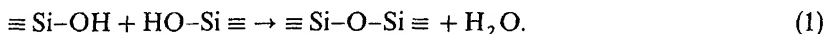
At intermediate stages (e.g. thermal treatment well below  $T_g$ ), the above process is only partially complete and the host of intermediate materials that can be produced in this way remain away from the targeted dry and dense products in all their properties. The sol-gel literature is replete with examples of such intermediate products, partially densified, hydroxyl-containing silica and silicate thin films baked at high temperatures (400°–500°C). The issue has been examined in some detail by Brinker and Pantano (1990). Such materials are loosely described as glass and the process probably continues until more rigid boundary conditions are defined for glass. The process of exactly duplicating a homogeneous and dense melt-glass, substantial elimination of Si-OH non-bridging oxygens and near-complete to complete densification of a compositionally homogeneous starting gel seem to be the basic necessities. When these goals are achieved to a satisfactory level, the structural features also approach the glasslike state in a cooperative fashion. Subtle but clear and progressive evolution of the structural features of a gel towards those of the corresponding melt-glass has been recorded via vibrational spectroscopy and comparison between the two made by X-ray diffraction by different workers (Bertoluzza *et al* 1982; Yoshino *et al* 1990; Karim *et al* 1992; De *et al* 1993a).

### 3. Silica glass: a case in point

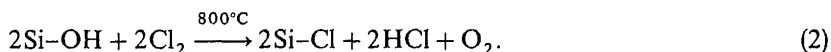
The most intensive efforts in developing sol-gel processes for glassmaking have been put in recent times in the area of high purity silica glass. The reasons for this selection are not only in the general necessity for developing a low temperature process, but also in the wide applicability of the material; optical communication is one important area where dense, low-hydroxyl and low-defect silica glass is required. Various sol-gel processes have been developed for silica glass (Matsuyama *et al* 1984; Rabinovich *et al* 1988; Shoup 1988; Clasen 1987, 1988; Toki *et al* 1988; Hench *et al* 1992; Kundu *et al* 1993b), though some major features are common to all of them. This is discussed below.

A dry xerogel ready for conversion to glass has a density somewhere in the approximate range 0.6–1.5 g/cm<sup>3</sup> (fully dense silica glass has a density of 2.2 g/cm<sup>3</sup>) depending on the starting material and preparative procedure. The

pore surface at this stage is usually covered with hydroxyl groups. Further hydroxyl (Si-OH) is generated by decomposition of molecular water present in the pores during thermal treatment. Such hydroxyl groups react at elevated temperatures:



The escape of water vapour thus generated must be monitored and minimized to avoid cracking of the gel. Two routes are used: (i) vacuum treatment at an early stage of gel-glass conversion so as to decrease the content of molecular water at a later stage and (ii) OH-Cl, OH-F or Cl-F exchange by passing suitable gases during heating to minimize formation of  $\text{H}_2\text{O}$  by OH-OH reaction, e.g.



Re-oxidation is often necessary for decreasing the chloride content, so that bubbling by chlorine evolved during use at high temperatures can be avoided. Chlorine, however, helps removal of metallic impurities via formation of volatile metal chlorides during glass preparation (MacChesney *et al* 1987a). Fluorine, on the other hand, decreases the refractive index of the glass (so-called 'down doping' in optical fibres) and helps avoidance of bubble formation at high temperature. Helium is used as the scavenging gas at the final stage of pore elimination. When all these steps are rigidly followed, an essentially hydroxyl-free or low-hydroxyl and pore-free glass is obtained.

The steps described above form the basic outline for silica gel-glass conversion, though gels may have been obtained from different starting materials, viz. silicon alkoxides (Matsuyama *et al* 1984; Hench *et al* 1992), fumed silica (Clasen 1988; Rabinovich 1988), a combination of the two (Toki *et al* 1988; Kundu *et al* 1992; De *et al* 1993b) and alkali silicates (Shoup 1988, 1991). It must be mentioned here that silica glasses prepared by the above routes are usable at high temperatures (softening for joining, melting for fibre drawing etc) in the same way as a melt-derived, defect-free glass without bloating or bubbling. They thus earn full credit for behaving like a 'normal' glass.

The sol-gel process for silica glass has been used in the last decade for the development of low-loss optical communication fibres. Two approaches have been pursued: development of all-gel-derived fibres, and fibres with gel-derived material as an optically passive part. Kitagawa *et al* (1987) obtained fibres from F-doped gel-glass tubes in which fluorine was removed from the internal surface. The fibres thus derived recorded a minimal loss of 0.43 dB/km. MacChesney *et al* (1987b) on the other hand used a hybrid system where an overclad of a thick gel tube was provided on commercial  $\text{GeO}_2$ -doped core and  $\text{SiO}_2$  clad; the reported loss of the fibre was about 0.4 dB/km. An F-doped, gel-derived substrate tube was used by MacChesney *et al* (1985) to obtain fibres showing a minimal loss of 0.28 dB/km.

Another area in which important developmental work has been carried out recently using sol-gel silica or silicate glass is micro-optics and optics with complicated shapes (Shoup 1991; Hench and Noguees 1994). Some items which have been developed using

singlets and arrays) and (iv) sinusoidal diffraction gratings. Development of silica micro-optics has made it necessary to cast a hard look at the shrinkage behaviour of gels obtained from sols of different characteristics (viscosity, surface tension etc.) to optimize the designs of moulds with micron-level features for sol casting. This issue has been discussed by Hench and Nogués (1994). Other developmental techniques used in recent times include stamping (Tohge *et al* 1988) and laser densification (Hench and Fabes 1992) of silica and silicate gel films before gel-glass conversion.

#### 4. Other glasses

A large variety of two- to multicomponent oxide glasses have been synthesized by sol-gel processing. Surveys have been made by James (1988) and Rabinovich (1993) among others. Among these, two compositional areas can be selected as examples because of their potentiality in direct practical use. The current status in both cases is discussed below with typical examples. Finally, brief mention is made of dye-doped and semiconductor-doped glasses, and GRIN lenses as end-use materials.

##### 4.1 $\text{TiO}_2$ - $\text{SiO}_2$ glasses

Low-titania (5–10 wt%) silicate glasses are well-known for high melting temperature and ultra low thermal expansion (ULE). Various sol-gel techniques have been employed to prepare such glasses. In a recent work, Deng *et al* (1988) dispersed silica in a titania sol to obtain a gel and densified the gel at 1500°C to convert it to a ULE glass. Abe *et al* (1988) used partially complexed titanium isopropoxide in tetrahydrofuran solution of silicic acid as starting materials to incorporate up to 50 wt%  $\text{TiO}_2$  without crystallization at 1000°C. Minehan *et al* (1989) used organotin-derived colloids of  $\text{TiO}_2$  and  $\text{SiO}_2$  to obtain tape cast or pressed bodies which were converted to glass via sintering. In a very recent work, 6–7 wt%  $\text{TiO}_2$  was incorporated in ULE sol-gel glass (typically  $+0.96$  to  $-0.61 \times 10^{-7}/^\circ\text{C}$ ) by using a new organotin control chemical additive and a combination of Ti-isopropoxide and chloride (Ganguli *et al* 1994).

##### 4.2 Rare earth doped silica glasses

The available combinations of high thermal shock resistance of silica glass and the optical behaviour of some rare earth (RE) ions in glass have prompted several groups to develop RE doped silica glass for laser and filter applications. Most of such work involves incorporation of  $\text{Nd}^{3+}$  in alkoxide-derived silica glass (Pope and Mathur 1988; Mathur and Pye 1990; Moreshead *et al* 1990; Thomas *et al* 1992) but also other RE dopings (Patra and Ganguli 1993; Rabinovich *et al* 1993).

The basic difficulty of uniformly dispersing the RE ions proved to be a stumbling block in an otherwise easy process, but recent work (Thomas *et al* 1992) has produced a chemical solution with apparently high potential. Sol-gel laser glass rods produced

### 4.3 Dye-doped glasses, semiconductor-doped glasses and GRIN lenses

Introduction of organic molecules and enzymes in gels and converting the gels to partially densified 'glasses' is currently a very active area of sol-gel research. Various optical and chemical sensors have been developed by doping of molecules in porous silica glass (Rottman *et al* 1992). Other areas relate to development of fluorescent and photochromic materials (Zink and Dunn 1991).

Sol-gel processing has also proved to be a very convenient way of doping quantum sized semiconductor (notably CdS) crystals in glass. Intensive efforts are currently going on for developing new optically non-linear materials by this route (Nogami *et al* 1990, 1991). The sulphide nanocrystals are generated *in situ* or via H<sub>2</sub>S treatment of monolithic silica or silicates.

Finally, the sol-gel technique is also being extensively used (Yamane 1990) for the development of radial graded index (r-GRIN) lenses. The basic technique commonly involves leaching of silicate (TiO<sub>2</sub>-SiO<sub>2</sub>, GeO<sub>2</sub>-SiO<sub>2</sub>, PbO-SiO<sub>2</sub> etc) gel rods followed by their densification to glass, so as to obtain a progressive change in refractive index from the core to the margin.

The above account is but a condensed and truncated review of the global activity in sol-gel glassmaking, and only aims at indicating the major visible trends in this rapidly growing field.

### Acknowledgement

Thanks are due to my colleagues at the Sol-Gel Laboratory for many useful discussions.

### References

- Abe Y, Sugimoto N, Nagao Y and Misono T 1988 *J. Non-Cryst. Solids* **104** 164
- Aizawa M, Nosaka Y and Fujii N 1994 *J. Non-Cryst. Solids* **168** 49
- Almeida R M and Pantano C G 1990 *J. Appl. Phys.* **68** 4225
- Bertoluzza A, Fagnano C, Morelli M A, Gottardi V and Guglielmi M 1982 *J. Non-Cryst. Solids* **48** 117
- Brinker C J and Scherer G W 1990 *Sol-gel science: the physics and chemistry of sol-gel processing* (Boston: Academic Press) pp. 760-777
- Clasen R 1987 *J. Non-Cryst. Solids* **89** 335
- Clasen R 1988 *J. Mater. Sci. Lett.* **7** 477
- De G, Kundu D, Karmakar B and Ganguli D 1993a *J. Non-Cryst. Solids* **155** 253
- De G, Kundu D, Karmakar B and Ganguli D 1993b *Mater. Lett.* **16** 231
- Deng Z, Breval E and Pantano C G 1988 *J. Non-Cryst. Solids* **100** 364
- Doremus R H 1973 *Glass science* (New York: Wiley) p. 1
- Hench L L and Nogués J L 1994 in *Sol-gel optics: processing and applications* (ed.) L C Klein (Boston: Kluwer) p. 59
- Hench L L, Wilson M J R, Balaban C and Nogués J L 1992 in *Ultrastructure processing of advanced materials* (eds) D R Uhlmann and D R Ulrich (New York: Wiley) p. 159
- James P F 1988 *J. Non-Cryst. Solids* **100** 93
- Kamiya K, Wada M, Matsuoka J and Nasu H 1992 in *Structure and formation of glasses* (ed.) S Sakka (Kyoto: Proc. Japan-Russia-China Seminar) p. 17
- Kitagawa T, Shibata S and Horiguchi M 1987 *Electron. Lett.* **23** 1295
- Kundu D, De G, Karmakar B, Patra A and Ganguli D 1992 *Bull. Mater. Sci.* **15** 453



- MacChesney J B, Johnson D W Jr., Lemaire P J, Cohen L G and Rabinovich E M 1985 *J. Appl. Technol.* **LT-3** 942
- MacChesney J B, Johnson D W Jr., Fleming D A, Walz F W and Kometani T Y 1987a *Mater. Lett.* **22** 1209
- MacChesney J B, Johnson D W, Fleming D A and Waltz F W 1987b *Electron. Lett.* **23** 1005
- Mackenzie J D 1982 *J. Non-Cryst. Solids* **48** 1
- Mathur A and Pye L D 1990 *SPIE* **212** 1327
- Matsuyama I, Susa K, Satoh S and Suganuma T 1984 *Bull. Am. Ceram. Soc.* **63** 1408
- Minehan W T, Messing G L and Pantano C G 1989 *J. Non-Cryst. Solids* **108** 163
- Moreshead W V, Nogues J-L R and Krabill R H 1990 *J. Non-Cryst. Solids* **121** 267
- Nogami M, Nagasaka K and Kato E 1990 *J. Am. Ceram. Soc.* **73** 2097
- Nogami M, Zhu Y Q, Tohyama Y, Nagasaka K, Tokizaki T and Nakamura A 1991 *J. Am. Ceram. Soc.* **74** 2097
- Patra A and Ganguli D 1993 *J. Mater. Sci. Lett.* **12** 116
- Pope E J A and Mackenzie J D 1988 *J. Non-Cryst. Solids* **106** 236
- Rabinovich E M 1988 in *Sol-gel technology for thin films, fibres, preforms, electronics and special coatings* (ed.) L C Klein (New Jersey: Noyes Publications) p. 260
- Rabinovich E M 1994 in *Sol-gel optics: processing and applications* (ed.) L C Klein (Boston: Kluwer Academic Publishers) p. 1
- Rabinovich E M, Bruce A J, Kopylov N A and Trevor P L 1993 *J. Non-Cryst. Solids* **160** 126
- Rottman C, Ottolenghi M, Zusman R, Lev O, Smith M, Gong G, Kagan M L and Avnir D 1990 *J. Non-Cryst. Solids* **113** 293
- Secrist D R and Mackenzie J D 1964 in *Modern aspects of the vitreous state* (ed.) J D Mackenzie (London: Butterworths) vol. 3 p. 149
- Scholze H 1991 *Glass—nature, structure, properties* (New York: Springer-Verlag) p. 3
- Shoup R D 1988 in *Ultrastructure processing of advanced ceramics* (ed.) J D Mackenzie and D L Bieganski (New York: Wiley) p. 347
- Shoup R D 1991 *Bull. Am. Ceram. Soc.* **70** 1505
- Taylor D J and Fabes B D 1992 *J. Non-Cryst. Solids* **147** & **148** 457
- Thomas I M, Payne S A and Wilke G D 1992 *J. Non-Cryst. Solids* **151** 183
- Tohge N, Matsuda A, Minami T, Matsuno Y, Katayama S and Ikeda Y 1988 *J. Non-Cryst. Solids* **100** 479
- Toki M, Miyashita S, Takeuchi T, Kanbe S and Kochi A 1988 *J. Non-Cryst. Solids* **100** 479
- Weinberg M C 1986 in *Better ceramics through chemistry II* (eds.) C J Brinker, D E Clark and D L Bieganski (Pittsburgh: Materials Research Society) p. 431
- Yamane M 1990 *SPIE* **1328** 133
- Yoshino H, Kamiya K and Nasu H 1990 *J. Non-Cryst. Solids* **126** 68
- Zink J I and Dunn B J 1991 *J. Ceram. Soc. Jap.* **99** 878

## Glass formation domains and structural properties of nonconventional transition metal ion glasses

A GHOSH

Solid State Physics Department, Indian Association for the Cultivation of Science, Calcutta 700 032, India

**Abstract.** Glass formation domains and structural properties of some binary transition metal ion glasses based on nonconventional network formers  $\text{Bi}_2\text{O}_3$  and  $\text{PbO}$  have been investigated. With the same network former, the glass formation domains depend on the transition metal ions. Homogeneous glasses with random network structure were obtained, as evidenced by the composition dependent density, molar volume and glass transition temperatures. Significant information about possible structural units in these glasses has been obtained from the IR spectra of these glasses.

**Keywords.** Glass formation domain; transition metal; nonconventional glass; glass transition temperature; molar volume; density; IR spectra.

### 1. Introduction

Oxide glasses based on nonconventional network formers like  $\text{PbO}$  and  $\text{Bi}_2\text{O}_3$  are of great interest because they form amorphous materials without traditional network formers like  $\text{P}_2\text{O}_5$ ,  $\text{B}_2\text{O}_3$ ,  $\text{GeO}_2$ ,  $\text{SiO}_2$  etc and they can be used to produce glass-ceramics, layers for optical and optoelectronic devices, thermal and mechanical sensors, reflecting windows etc (Dimitriev *et al* 1986; Mianxve and Peinan 1986; Aegerter *et al* 1990; Takahashi and Yamaguchi 1990). Fajans and Kreidl (1948) pointed out that  $\text{Pb}^{2+}$  and  $\text{Bi}^{3+}$  cations are highly polarizable and the asymmetry of their polyhedra inhibits crystallization processes in the melts in which they participate. Multicomponent glasses based on  $\text{PbO}$  or  $\text{Bi}_2\text{O}_3$  have been successfully synthesized and their structures studied (Bishay and Maghrabi 1969; Dumbaugh 1978, 1986; Morikawa *et al* 1981; Rao *et al* 1984; Dimitriev *et al* 1986). The recently reported (Zheng and Mackenzie 1988; Tatsumisago *et al* 1990; Onisi *et al* 1991; Yuan *et al* 1991) multicomponent cuprate glasses in which  $\text{Bi}_2\text{O}_3$  is the main glass former are of particular interest because they can be used to produce high temperature superconductor glass-ceramics with controllable microstructure. In this paper, glass formation domains and structural properties of some  $\text{Bi}_2\text{O}_3$  and  $\text{PbO}$  based nonconventional binary glasses containing transition metal ions such as V, Fe and Cu have been discussed. It is worth mentioning that these glasses exhibit semiconducting properties arising from the presence of multivalent states of the transition metal ions in the glassy materials and thus, have many applications, such as memory and threshold switching, ferrites, cathode materials, etc (Nakamura and Ichinose 1987; Ghosh 1988; Livage *et al* 1990; Sakuri and Yamaki 1990).

### 2. Experimental

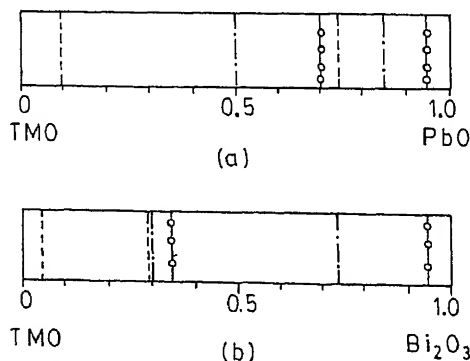
Different binary glass compositions studied were prepared from reagent grade chemicals  $\text{Bi}_2\text{O}_3$ ,  $\text{PbO}$ ,  $\text{V}_2\text{O}_5$ ,  $\text{Fe}_2\text{O}_3$  and  $\text{CuO}$ . The binary mixtures of the

appropriate chemicals were melted in alumina crucibles for 2 h at temperature depending on compositions. Glasses were obtained either by pouring the melt on a twin-roller or by pressing the melts between two brass plates depending on the systems and compositions. All the prepared glasses were tested for their amorphous structure using X-ray diffraction and scanning electron microscopy. Glass transition and crystallization temperatures were obtained from differential thermal analysis. Density was measured using Archimedes' principle. The IR spectra of the glasses in KBr matrices were recorded in the range  $200\text{--}4000\text{ cm}^{-1}$  in a Perkin-Elmer spectrophotometer. Final glass compositions were estimated either by gravimetric absorption or by chemical analysis. The concentrations of the reduced transition metal ions were determined by either chemical analysis or magnetic measurements.

### 3. Results and discussion

#### 3.1 Glass formation domain

Two systems of glasses of compositions  $(\text{PbO})_{1-x}(\text{TMO})_x$  and  $(\text{Bi}_2\text{O}_3)_{1-x}(\text{TMO})_x$  where  $\text{TMO} = \text{V}_2\text{O}_5$ ,  $\text{Fe}_2\text{O}_3$  and  $\text{CuO}$  and  $x$  is the mol fraction of TMO were studied. The glass formation domains for these two systems of glasses are shown in figure 1. It is clear that among the PbO based glasses, the glass formation domain  $0.25 \leq x \leq 0.90$  for the  $\text{PbO-V}_2\text{O}_5$  system is the largest, while the domain  $0.05 \leq x \leq 0.15$  is the smallest for the  $\text{PbO-Fe}_2\text{O}_3$  glasses. The  $\text{PbO-CuO}$  glasses have intermediate glass formation domain  $0.15 \leq x \leq 0.50$ . On the other hand, for the  $\text{Bi}_2\text{O}_3$  based glasses, the  $\text{Bi}_2\text{O}_3\text{-CuO}$  system has the largest glass formation domain  $0.05 \leq x \leq 0.70$ , while the glass formation domain  $0.70 \leq x \leq 0.95$  is the smallest for the  $\text{Bi}_2\text{O}_3\text{-V}_2\text{O}_5$  glasses. The glass formation domain for the  $\text{Bi}_2\text{O}_3\text{-Fe}_2\text{O}_3$  system is intermediate as for  $\text{PbO-Fe}_2\text{O}_3$  system. However, a larger glass formation domain for the  $\text{Fe}_2\text{O}_3$  system has been reported using much faster quenching rate (Tanaka 1989). It is noted that glass formation occurs in the  $\text{Bi}_2\text{O}_3\text{-V}_2\text{O}_5$  system for low  $\text{V}_2\text{O}_5$  content.



## 2 Analyzed glass compositions

Wet chemical and atomic absorption spectroscopic analysis showed that all glass compositions changed slightly from the batch compositions due to evaporation loss. These measurements coupled with the magnetic measurements indicated that in all glass compositions, transition metal ions exist in two oxidation states, e.g.  $V^{4+}$  and  $V^{5+}$ ,  $Cu^+$  and  $Cu^{2+}$  and  $Fe^{2+}$  and  $Fe^{3+}$  for the vanadate, cuprate and ferric glasses, respectively. However, the concentrations of the reduced ions depend on the glass compositions. The fraction of the reduced ion concentration was observed to be the highest for cuprate glasses, while it was the lowest for ferric glasses.

## 3 Density and molar volume

The variation of density and molar volume of the two systems of glasses are shown in figures 2 and 3 respectively. It is clear from figure 2a that for the PbO based glasses, the density increases with the increase of PbO content. The density for the PbO–CuO glasses is higher than that for the PbO– $V_2O_5$  glasses. For the  $Bi_2O_3$  based glasses, the variation of density with composition is small for all glass compositions (figure 2b). The density of  $Bi_2O_3$ –CuO glasses is comparable with that of the  $Bi_2O_3$ – $Fe_2O_3$  glasses, while the density for the  $Bi_2O_3$ – $V_2O_5$  glasses is the lowest. On the other hand, the variation of the molar volume of the PbO–CuO glass system (figure 3a) with composition shows opposite trends to the variation of density, while for the other glass systems (figures 3a and b), molar volume changes with composition in a fashion similar to the density. Thus for the glass systems studied, except for PbO– $V_2O_5$  with PbO content  $> 50$  mol%, the density and the molar volume change monotonically with composition. This indicates that all the glass systems are probably in a single phase with random network structure and that the geometry and topology of the random network do not change significantly with compositions.

## 4 Glass transition temperatures

The glass transition temperatures ( $T_g$ ) determined from the differential thermal analysis curves are shown in figure 4, as a function of compositions. Figure 4a indicates

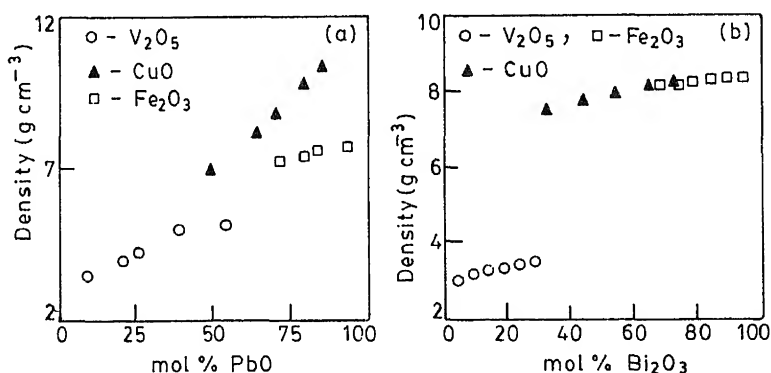


**Figure 2.** Variation of density with glass composition: (a) PbO–TMO glasses and (b)  $Bi_2O_3$ –TMO glasses.

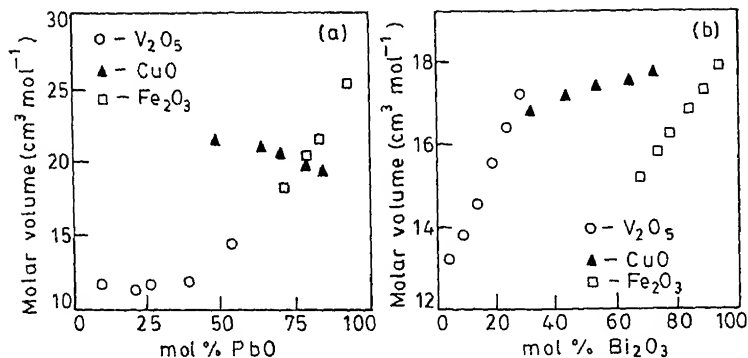


Figure 3. Variation of molar volume with glass compositions: (a) PbO-TMO glasses and (b)  $\text{Bi}_2\text{O}_3$ -TMO glasses.

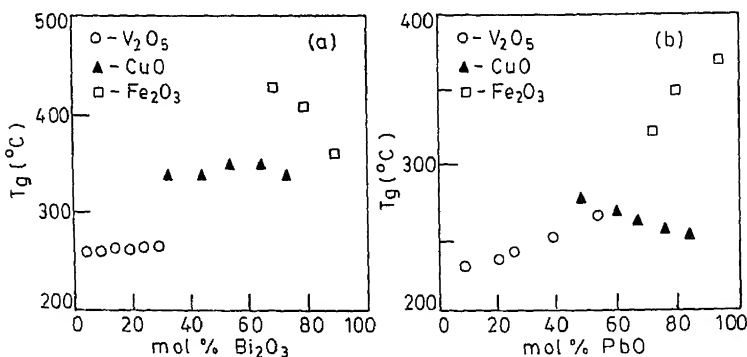


Figure 4. Composition dependence of the glass transition temperature ( $T_g$ ): (a)  $\text{Bi}_2\text{O}_3$ -TMO glasses and (b) PbO-TMO glasses.

that the  $T_g$  increases with  $\text{Bi}_2\text{O}_3$  content in the  $\text{Bi}_2\text{O}_3$ - $\text{V}_2\text{O}_5$  and  $\text{Bi}_2\text{O}_3$ - $\text{CuO}$  glasses, while  $T_g$  decreases for the  $\text{Bi}_2\text{O}_3$ - $\text{Fe}_2\text{O}_3$  glasses. The  $T_g$  also increases with PbO content in PbO- $\text{V}_2\text{O}_5$  and PbO- $\text{Fe}_2\text{O}_3$  systems while  $T_g$  decreases slightly for the PbO- $\text{CuO}$  system (figure 4b). Since glass transition temperature depends on the strength and connectivity of the network, it is clear from figure 4 that the strength and connectivity of the network increase with the increase of PbO or  $\text{Bi}_2\text{O}_3$  content in all glass systems except for the  $\text{Bi}_2\text{O}_3$ - $\text{Fe}_2\text{O}_3$  systems. In the  $\text{Bi}_2\text{O}_3$ - $\text{CuO}$  and PbO- $\text{CuO}$  systems, however, the variation of  $T_g$  with composition is small. The effect of the coulombic field of substitution can account for such a small variation in  $T_g$ . The increase of  $T_g$  with  $\text{Bi}_2\text{O}_3$  or PbO content in the vanadate glass system also suggest a continuous change of the glass matrix having a 2D vanadate layer structure into a more complicated 3D structure (Mandal and Ghosh 1993). These conclusions are also supported by the IR results.

### 3.5 Infrared spectra

Infrared (IR) spectra of the glass compositions yield important information about structural units. The spectra of several glass compositions have been reported elsewhere

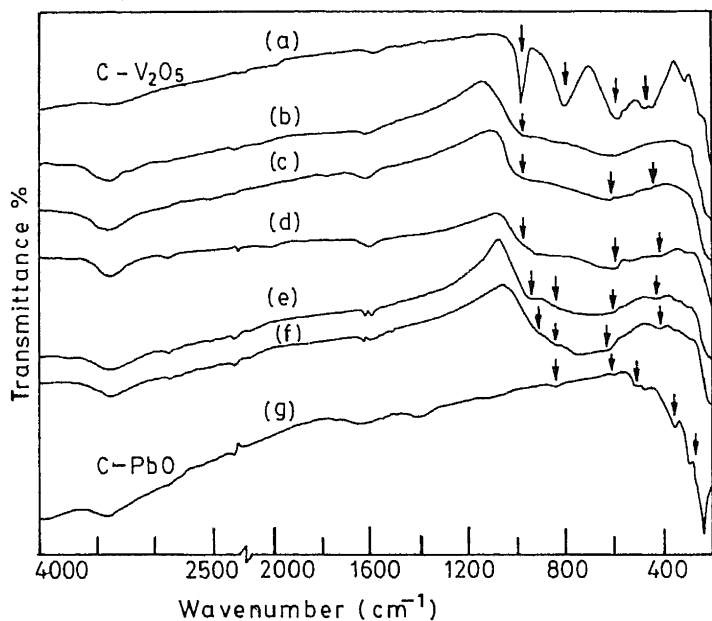
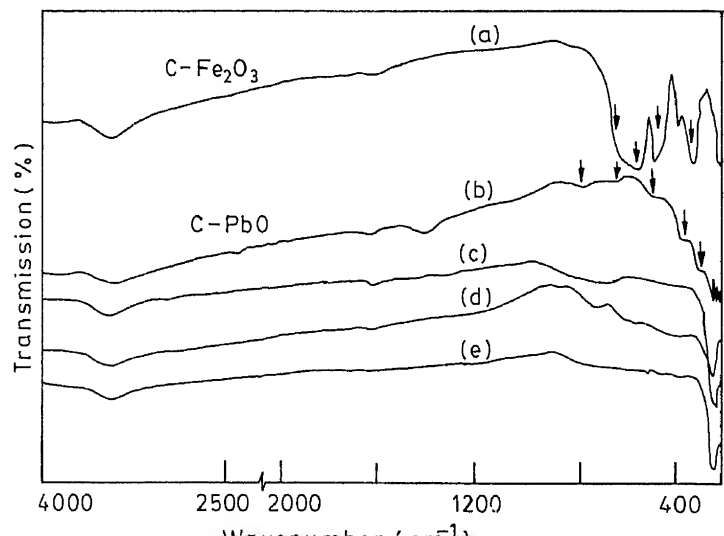


Figure 5. Room temperature IR spectra of  $\text{PbO-V}_2\text{O}_5$  glasses: (a) Crystalline  $\text{V}_2\text{O}_5$ , (b) 90 mol%  $\text{V}_2\text{O}_5$ , (c) 80 mol%  $\text{V}_2\text{O}_5$ , (d) 70 mol%  $\text{V}_2\text{O}_5$ , (e) 60 mol%  $\text{V}_2\text{O}_5$ , (f) 50 mol%  $\text{V}_2\text{O}_5$  and (g) crystalline  $\text{PbO}$ .



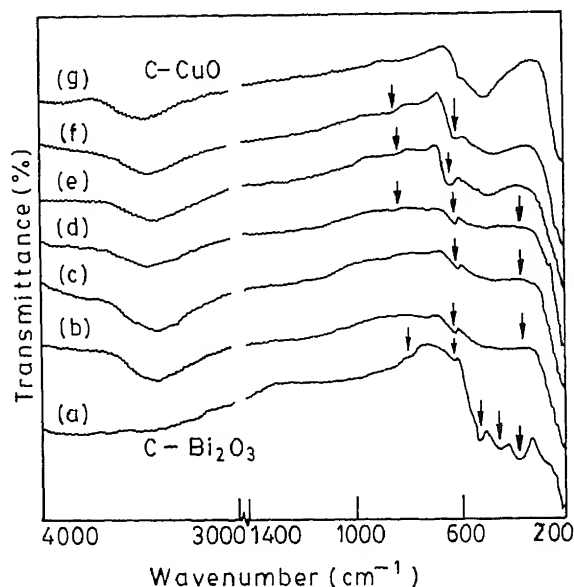


Figure 7. Room temperature IR spectra of  $\text{Bi}_2\text{O}_3$ -CuO glasses: (a) crystalline  $\text{Bi}_2\text{O}_3$ , (b) 27 mol% CuO, (c) 35.4 mol% CuO, (d) 46 mol% CuO, (e) 56 mol% CuO, (f) 68 mol% CuO and (g) crystalline CuO.

(Mandal and Ghosh 1993; Hazra and Ghosh 1995). For briefness, IR spectra of glass systems for different compositions are shown in figures 5–7.

**3.5a  $\text{PbO-V}_2\text{O}_5$  and  $\text{Bi}_2\text{O}_3\text{-V}_2\text{O}_5$  glass systems:** It is clear from the IR spectra of  $\text{PbO-V}_2\text{O}_5$  glasses presented in figure 6 that the band at  $1020\text{ cm}^{-1}$  for the bond vibration of the crystalline  $\text{V}_2\text{O}_5$  becomes very weak for the glass compositions and shifts to lower frequencies with increasing PbO content. Also new bands appear in the range  $950\text{--}970\text{ cm}^{-1}$ . For PbO content  $>40\text{ mol}\%$ , the band at  $1020\text{ cm}^{-1}$  vanishes and new bands appear at  $950\text{ cm}^{-1}$  and  $430\text{ cm}^{-1}$ . According to the mechanism suggested earlier (Dimitriev *et al* 1983), the  $\text{Pb}^{2+}$  ions occupy position between V-O-V layers and have a direct influence on the isolated V=O bond of the groups of the crystalline  $\text{V}_2\text{O}_5$ . This leads to a drop in the wave numbers down to  $970\text{--}950\text{ cm}^{-1}$  for the compositions with PbO content below 40 mol% and thus in these glass compositions, unaffected  $\text{VO}_5$  polyhedra are preserved along with affected  $\text{VO}_5$  polyhedra. However, for glass compositions with PbO content  $>40\text{ mol}\%$ , only affected  $\text{VO}_5$  polyhedra are present. The IR spectra of the  $\text{Bi}_2\text{O}_3\text{-V}_2\text{O}_5$  glasses, reported earlier (Ghosh 1987) indicate that the band at  $1020\text{ cm}^{-1}$  for the V=O bond vibration in the  $\text{VO}_5$  polyhedra is observed for glass compositions with 95 mol%  $\text{V}_2\text{O}_5$ . However, with decreasing  $\text{V}_2\text{O}_5$  content, this band becomes very weak shoulder at  $1000\text{--}980\text{ cm}^{-1}$ . Thus for these compositions,  $\text{Bi}^{3+}$  ions occupy positions between vanadate layers and chains and thus affect directly V=O bonds similar to  $\text{Pb}^{2+}$  ions in  $\text{PbO-V}_2\text{O}_5$  glass compositions.

weak compared to the crystalline PbO and Fe<sub>2</sub>O<sub>3</sub>. However, weak bands at 820 cm<sup>-1</sup> and 630 cm<sup>-1</sup> are observed in all glass compositions. These bands also correspond to the bands of crystalline PbO for Pb–O bond vibration in PbO<sub>4</sub> tetrahedra. The band at 350 cm<sup>-1</sup> corresponding to the orthorhombic PbO is not observed in the glass compositions. It may be noted from figure 6 that the bands corresponding to the Fe–O bond are not significant in the glasses. However, Mössbauer studies (Mandal *et al* 1994, 1995) indicate the presence of FeO<sub>4</sub> tetrahedra in all glass compositions and the Fe–O bond covalency is large compared to the conventional ferric glasses.

The IR spectra of the Bi<sub>2</sub>O<sub>3</sub>–Fe<sub>2</sub>O<sub>3</sub> glasses have been reported earlier (Ghosh 1987). The bands at 840 cm<sup>-1</sup>, 540–620 cm<sup>-1</sup>, 470 cm<sup>-1</sup> and 350 cm<sup>-1</sup> are observed in all glass compositions, suggesting that these glasses are built up of BiO<sub>3</sub> pyramidal unit similar to Bi<sub>2</sub>O<sub>3</sub>–CuO glasses. Mössbauer studies (Tanaka *et al* 1989) showed that Fe exists as Fe<sup>3+</sup> ions in FeO<sub>4</sub> tetrahedra (isomer shift < 0.4 mms<sup>-1</sup>) and the covalency of Fe–O bond decreases with the increase of Fe<sub>2</sub>O<sub>3</sub> content in the glass compositions.

### 3.6 Bi<sub>2</sub>O<sub>3</sub>–CuO and PbO–CuO glass systems

For all glass compositions, four fundamental absorption bands at 830 cm<sup>-1</sup>, 620 cm<sup>-1</sup>, 450 cm<sup>-1</sup> and 350 cm<sup>-1</sup> are observed in the IR spectra (figure 7). These absorption bands are characteristic of BiO<sub>3</sub> pyramidal units of the crystalline Bi<sub>2</sub>O<sub>3</sub>. The intensity of these bands, however, decreases and broadens significantly for the glass compositions due to their disordered structure. Thus the IR spectra suggest that the glass compositions consist of BiO<sub>3</sub> pyramidal units. The symmetric vibration bands at 830 cm<sup>-1</sup> and 450 cm<sup>-1</sup> for the glasses have higher wave numbers compared to the vibrational bands of fused Bi<sub>2</sub>O<sub>3</sub>, suggesting that the stronger Bi–O bonds are present in the glass compositions caused by the polarization effects. These observations for the binary bismuth cuprate glasses are in sharp contrast to the multicomponent bismuth cuprate glass compositions (Zheng *et al* 1989), in which both BiO<sub>6</sub> octahedral and BiO<sub>3</sub> pyramidal units are present depending on compositions. In these glasses with increasing SrO and CaO contents, a conversion of BiO<sub>6</sub> units to BiO<sub>3</sub> units was observed producing nonbridging oxygen atoms. For the PbO–CuO glasses, IR bands have been observed at 830 cm<sup>-1</sup>, 620 cm<sup>-1</sup> and 460 cm<sup>-1</sup> corresponding to the bands of crystalline PbO and this might be due to Pb–O bond vibration in the PbO<sub>4</sub> tetrahedra. However, the presence of the band at 720 cm<sup>-1</sup>, which is absent in either PbO or CuO, is not clear at the moment.

### 3.7 Magnetic properties

Magnetic susceptibility of all glass compositions showed paramagnetic character of these materials and increased with the increasing transition metal ion. The magnetic properties of these materials arise from the paramagnetic transition metal ions with 3d electrons. The concentrations of the reduced transition metal ions estimated from magnetic susceptibility data were found to be close to their estimates from the chemical analysis.



#### 4. Conclusions

Glass formation domains and structural properties of some binary transition glasses based on nonconventional glass network formers PbO and Bi<sub>2</sub>O<sub>3</sub> have been studied. Glass formation domains depend on the glass systems as evidenced by X-ray diffraction studies. The composition dependence of density and molar volume shows that the prepared glasses are homogeneous with random network structure. The variation of the glass transition temperature indicates that the strength of the network structure depends on the nature of transition metal ions and glass composition. The structural units building up of these glasses have been obtained from Raman spectra.

#### Acknowledgement

The author wishes to thank Mr S Mandal and Mr S Hazra for their help.

#### References

- Aegerter M, Serra E, Rodinques A, Kordas G and Moore G 1990 SPIE-Sol-Gel optics, 13
- Bishay A and Maghrabi C 1969 *Phys. Chem. Glasses* **10** 1
- Dimitriev Y, Mihailov V and Gatif E 1986 *Phys. Chem. Glasses* **34** 114
- Dimitriev Y, Dimitrov V, Arnaudov M and Topalov D 1983 *J. Non-Cryst. Solids* **57** 147
- Dumbaugh W H 1978 *Phys. Chem. Glasses* **19** 21
- Dumbaugh W H 1986 *Phys. Chem. Glasses* **27** 119
- Fajans K and Kreidl N 1948 *J. Am. Ceram. Soc.* **31** 105
- Ghosh A 1987 *Preparation and characterization of some semiconducting glasses from the study of physical properties*, Ph.D. Thesis, Jadavpur University, Calcutta
- Ghosh A 1988 *J. Appl. Phys.* **64** 2652
- Hazra S and Ghosh A 1995 *Phys. Rev.* **B50**
- Livage J, Jolivet J P and Tronc E 1990 *J. Non-Cryst. Solids* **121** 35
- Mandal S and Ghosh A 1993 *Phys. Rev.* **B48** 9388
- Mandal S, Hazra S and Ghosh A 1994 *J. Mater. Sci. Lett.* **13** 1054
- Mandal S, Hazra S, Das D and Ghosh A 1995 *J. Non-Cryst. Solids* (in print)
- Mianxve W and Peinan Z 1986 *J. Non-Cryst. Solids* **84** 334
- Morikawa H, Jegondez J, Mazieres C and Revolevschi A 1981 *J. Non-Cryst. Solids* **44** 107
- Nakamura S and Ichinose N 1987 *J. Non-Cryst. Solids* **95-96** 849
- Onisi M, Kyoto M and Watanabe M 1991 *Jpn. J. Appl. Phys.* **30** L988
- Kao K J, Wong J and Rao B G 1984 *Phys. Chem. Glasses* **25** 57
- Sakuri Y and Yamaki J 1990 *J. Electrochem. Soc.* **132** 512
- Tanaka K, Kamiya K and Yoko T 1989 *J. Non-Cryst. Solids* **109** 289
- Takahashi Y and Yamaguchi K 1990 *J. Mater. Sci.* **25** 3950
- Tatsumisago M, Tsuboi S, Tohge N and Minami T 1990 *J. Non-Cryst. Solids* **124** 167
- Yuan L R *et al* 1991 *Jpn. J. Appl. Phys.* **30** L1545
- Zheng H and Mackenzie J D 1988 *Phys. Rev.* **B38** 7166
- Zheng H, Xu R and Mackenzie J D 1989 *J. Mater. Res.* **4** 911

## Ultrasonic velocity and attenuation in glass

U S GHOSH

Department of Solid State Physics, Indian Association for the Cultivation of Science, Calcutta 700 032, India

**Abstract.** Ultrasonic velocity and attenuation in glasses exhibit anomalous properties and the current theory most successful in explaining these anomalous properties in the high temperature range has been presented. The model considers that the disorder inherent in amorphous network results in a double well potential corresponding to two equilibrium configurations and a particle is ascribed to move in the double-well potential. Acoustic behaviours in glasses have been interpreted in terms of a thermally activated relaxation process. Improvement of this basic model has also been discussed. Mention has also been made of some behaviours at high temperature that need further research for convincing explanation.

**Keywords.** Ultrasonic velocity and attenuation; double-well potential; thermally activated relaxation.

### 1. Introduction

For the last twentyfive years, studies on physical properties of glass have attracted the attention of solid state physicists mainly because glasses exhibit a number of properties strikingly different from their crystalline counterpart. In many cases, the differences become very prominent at extremely low temperature. These properties are: specific heat, thermal conductivity, thermal expansion, acoustic velocity, acoustic absorption, third order elastic constants, pressure coefficients of velocity to name a few (Krause and Kurkjian 1968; Hunklinger and Arnold 1976; Kul'bitskaya and Shutilov 1976; Anderson 1981; Pohl 1981; Hunklinger and Schickfus 1981).

In the present article, we shall confine our discussion to only within the behaviour of ultrasonic velocity and attenuation in glasses.

### 2. Anomalous properties of acoustic velocity in glass

For dielectric crystals, it is well known that

$$dC/dT = 0 \quad \text{at} \quad T \approx 0, \quad (1)$$

and  $dC/dT$  is negative (magnitude very small) above  $T = 0$  where  $T$  is the absolute temperature and  $C$  the elastic constant. As a result similar variation is found in acoustic velocity as a function of temperature in dielectric crystals. The situation is quite different in glasses: (i) a strong variation with both positive and negative temperature coefficient of sound velocity is found between 0.2 K and 5 K (Hunklinger and Arnold 1976; Hunklinger and Schickfus 1981). Within this temperature range the variation shows a maximum, (ii) beyond 5 K sound velocity falls gradually, attains a minimum between 50 K and room temperature depending on the nature of the glass and then rises with positive temperature coefficient (Hunklinger and Arnold 1976; Hunklinger and Schickfus 1981). At higher temperature (of course below  $T_g$ ,

of minimum and subsequent rise of velocity with the temperature is for glasses containing high concentration of tetrahedral structures (Kul'bitskaya 1975; Hunklinger and Arnold 1976; Kul'bitskaya and Shutilov 1976; Hunklinger and Schickfus 1981), (iii) the value of sound velocity at high temperature before  $T_g$  may considerably exceed the value at 0 K (Hunklinger and Arnold 1976; Hunklinger and Schickfus 1981), (iv) below 1 K, dependence of velocity on temperature is logarithmic (Hunklinger and Arnold 1976; Hunklinger and Schickfus 1981), (v) some glasses such as  $B_2O_3$ ,  $As_2S_3$  in which the random glass network is composed of planar units instead of three dimensional tetrahedral structures do not show the variation indicated above in (ii) and (iii). Sound velocity falls monotonically with temperature in these cases (Hunklinger and Arnold 1976; Kul'bitskaya and Arnold 1976; Hunklinger and Schickfus 1981).

### 3. Anomalous properties of acoustic absorption

Information regarding acoustic absorption is obtained from the measurement of ultrasonic attenuation of ultrasonic wave as it passes through the medium. It is known that in dielectric crystal ultrasonic attenuation at temperatures above 30 K for which  $\omega\tau_{th} \gg 1$  is independent of temperature where  $\omega$  is the frequency of the ultrasonic wave and  $\tau_{th}$  is the life time of the thermal phonons (Hunklinger and Arnold 1976). At low temperature for which  $\omega\tau_{th} \ll 1$ , the attenuation coefficient in dielectric crystal varies even faster than  $T^4$  and becomes practically negligible below 10 K (Hunklinger and Arnold 1976; Hunklinger and Schickfus 1981). A strikingly different behaviour is found in glasses (Hunklinger and Arnold 1976; Hunklinger and Schickfus 1981). Not only that the magnitude of attenuation is much larger in glass than in crystals, but the variation of ultrasonic attenuation with temperature shows a large peak around 50 K or above depending on the nature of the glass. The peak height of attenuation is proportional to the frequency and the peak shifts slowly towards higher temperature with increasing frequency. A quadratic frequency dependence of absorption is found on the high temperature side of the peak. At low temperature around 5 K a second smaller peak or shoulder appears which shifts rapidly towards higher temperature with increasing frequency. At still lower temperatures there is a decrease of absorption, the attenuation drops rapidly as  $T^3$  becomes independent.

### 4. Theoretical treatment

The most successful model to explain the above mentioned low temperature behaviour in glass has been put forward by Anderson *et al* (1972) and Phillips (1972). This situation has been reviewed in a beautiful article by Jackle *et al* (1976). It assumes the existence of an ensemble of two-level system (TLS) in glass with a broad distribution of level splitting. This also accounts for the presence of low energy excitations with approximately constant density of states in addition to phonons as indicated by the specific heat studies in glass, which show excess specific heat at low temperatures than that predicted by Debye theory. These TLS are considered as belonging to structural defects which, at very low temperatures, are frozen in place.

Anderson and Bömmel (1955) indicated that in an amorphous network because of inherent disorder certain atoms or groups of atoms can occupy two different configurational states i.e. particles of unspecified nature constituting localized structural defects are able to move in a double well potential having two minima corresponding to two equilibrium configurations, and the two possible configurations of the defect in either of the two wells of the double well potential represent the two states of the defect. At low temperature only the two lowest energy levels with an energy separation determined by quantum mechanical tunnelling through the barrier are important. At high temperatures the two defect configurations should actually be treated as thermodynamical states involving a thermodynamical average over some vibrational degrees of freedom. At high temperature the double well potential should correctly be interpreted as free energy curve rather than potential energy curve.

At extremely low temperature when ultrasonic phonon interacts with TLS, transition between the two states are possible by tunnelling in which a resonant phonon is absorbed or emitted, this ultimately causes a net ultrasonic absorption which gradually decreases with increase of the acoustic intensity and finally saturates due to increase of the population of upper level. At a slightly higher temperature, but still a very low temperature, another process of sound attenuation involving relaxation via tunnelling becomes important: the ultrasonic wave disturbs the thermal equilibrium of TLS, the disturbed TLS relaxes via the emission and absorption of resonant phonon.

At high temperature, a different process which can be described as a structural relaxation via thermally activated transition overriding the barrier height of the double-well potential becomes important. Thus, in glass two types of defects are distinguished: (1) tunnelling defect which is a structural defect but for which resonant absorption or emission of phonon occurs at very low temperature in a tunnelling process which may involve relaxation also and (2) thermally activated defects which are also structural defects but which when disturbed from its original state of thermal equilibrium by ultrasonic induced strain relaxes via thermally activated transition requiring higher temperatures. It is to be noted that both the types of defects are basically two state defects.

In the present article we are concerned with ultrasonic propagation behaviour in the high temperature range and hence we deal with the thermally activated defects only. The thermally activated relaxation process has profound effect on ultrasonic velocity and attenuation in the higher temperature region and the observed behaviour in this temperature region are explained with the help of this relaxation process.

## 5. A simple model for the microscopic origin of double well potential

We now discuss a simple but interesting model given by Bridge and Patel (1986) regarding the microscopic origin of the two well potentials based on central force theory. Consider a three dimensional network of A-O-A bonds (A = cation, O = anion, for example an oxygen atom) in which A-O-A angles are not necessarily  $180^\circ$ . For a perfect crystalline arrangement all A-A and A-O separations (bond lengths) are the same and the central force theory predicts that all atoms of a particular kind move in identical symmetric interatomic potential wells each of which has a single central minimum for each atom corresponding to its equilibrium position and for sufficiently small vibrations, the motion of each atom is harmonic while at large

amplitudes anharmonic effect appears causing flattening of the bottom of the well. This is the picture in crystalline arrangement. For the amorphous case there is always a distribution of A-A separations (denoted by  $R$ ) with values both greater than or less than the equilibrium crystalline value. There may also be a distribution of A-O bond lengths about the crystalline value. Bridge and Patel (1986) then developed their model for the microscopic origin of two well potentials in a glass network in the case of both longitudinal and transverse vibrations of the anions according to the simple classical central force theory, cations being considered to be too heavy to move. To illustrate the model we consider the simple case of longitudinal vibrations of the anion (O atom) in the linear system A-O-A.

For a diatomic molecule of the type (A-O), the mutual potential energy  $U$  at any instant is of the form

$$U = -\frac{a}{r} + \frac{b}{r^m}, \quad (2)$$

where  $6 < m < 12$ ,  $r$  = A-O separation at any instant of motion,  $a$  and  $b$  are constants for a given molecular type which are obtained from the following relations, (i)

$$\left(\frac{dU}{dr}\right)_{r=r_0} = 0, \quad (3)$$

which gives

$$b = (a r_0^{m-1})/m, \quad (4)$$

and (ii)

$$U_0 = -\frac{a}{r_0} \left(1 - \frac{1}{m}\right), \quad (5)$$

where  $U_0$  is the bond energy at the equilibrium interatomic separation  $r_0$  (the crystalline value).

Next we consider the linear arrangement of three atoms (A-O-A) consisting of an anion in the middle of the two cations separated by a distance  $R$ . At any instant of motion of the anion, one A-O separation is denoted by  $r$  and the other is  $(R-r)$ . We assume that the potential energy of the system at any instant is given by the superposition of two potentials of the form given by (2) i.e.

$$U = \left(-\frac{a}{r} + \frac{b}{r^m}\right) + \left(-\frac{a}{R-r} + \frac{b}{(R-r)^m}\right). \quad (6)$$

If we define an elongation factor  $e$  by  $e = (R/2r_0)$  i.e. cation-cation separation divided by equilibrium separation  $2r_0$  (crystalline value), then

$$U = -a \left[ \frac{1}{r} + \frac{1}{2er_0 - r} \right] + b \left[ \frac{1}{r^m} + \frac{1}{(2er_0 - r)^m} \right]. \quad (7)$$

The quantity  $U/2$  may be regarded as the mutual potential energy of half the anion atom plus one of the cation atoms and is taken as the potential in which the anion atom moves, each cation being considered infinitely heavy. It should be noted that direct

interaction between the cation atoms has been ignored as it is a function of  $R$  only cannot affect the variation of  $U$  with  $r$  and is therefore of no interest to us.

Bridge and Patel (1986) considered the case of P-O-P system in  $P_2O_5$  glass and calculated the variation of  $U/2$  with displacement of the O-atom for various fixed values of  $e$  using the  $a$  and  $b$  values evaluated from (4) and (5) and the known values of bond energy  $U_0$  and bond length  $r_0$  in  $P_2O_5$  crystal and taking  $m=9$ . This is shown in figure 1. It was observed that a single minimum in the potential energy occurs for  $e < 1$  and also for  $e$  slightly greater than unity. However a two-well potential develops for  $e \geq 1.2$  i.e. elongation of P-P separation ( $R$ ) with respect to the crystalline value  $2r_0$  exceeds 20%. For an elongation of 38% ( $e = 1.38$ ) a potential barrier of about 0.1 eV, the correct order of magnitude to explain the acoustic loss in  $P_2O_5$  glass, occurs.

A similar calculation was carried out by Bridge and Patel (1986) for transverse displacement of the anion atom in the linear system A-O-A and it was found that for  $e > 1$ , a single minimum in the potential occurs, but for  $e < 1$  two wells appear with a barrier of the right order of magnitude required to explain the acoustic loss with a small contraction (negative elongation) of  $\sim 6\%$  ( $e = 0.94$ ) in  $P_2O_5$  glass. For the case of non- $180^\circ$  A-O-A system in phosphate glass, Bridge and Patel (1986) further showed that the central force theory leads to double-well potential when  $e$

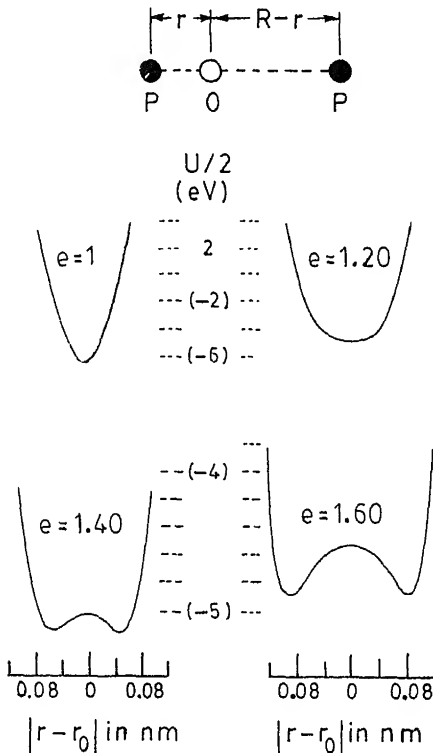


Figure 1. Potential wells for motion of oxygen atoms parallel to P-O-P, in phosphorus pentoxide glass.

values for the P-P separation is greater than certain critical value for longitudinal motion and less than a different critical value for transverse motion.

## 6. Relaxation effects on ultrasonic velocity and attenuation

The relaxation effects of the defects in glass have their origin in the coupling of these defects with the elastic strain field. An ultrasonic wave through a glass causes an elastic strain which in turn causes a relative shift in energy (or free energy) between the two states of a defect. As a result the equilibrium of the defect is disturbed or in other words thermal inequilibrium takes place. A relaxation process sets in to restore the equilibrium. Now, relaxation is essentially a readjustment of occupation number of the two states of the defect (occupation number of a state is the probability with which the state is occupied). Therefore relaxation is described in terms of the time dependent occupation numbers  $P_1$  and  $P_2$  of the two states designated as states 1 and 2, state 1 being considered to be higher in energy and because of the condition that  $P_1 + P_2 = 1$  always, a complete description of the two states can be given in terms of occupation number  $P_1$  of state 1 alone. Denoting the equilibrium value of the occupation number by a superscript (0), i.e.  $P_1^{(0)}$  and  $P_2^{(0)}$  for the two states and free energy of the two states before the application of the strain field by  $F_1$  and  $F_2$  we have

$$\frac{P_1^{(0)}}{P_2^{(0)}} = \frac{e^{-\beta F_1}}{e^{-\beta F_2}} = e^{-\beta(F_1 - F_2)} = e^{-\beta(\Delta F)}, \quad (8)$$

where

$$\beta = \frac{1}{kT}, \quad k = \text{Boltzmann constant, } \Delta F = F_1 - F_2,$$

and

$$P_1^{(0)} + P_2^{(0)} = 1. \quad (9)$$

From (8) and (9)

$$P_1^{(0)} = [e^{\beta \Delta F} + 1]^{-1} = f(\Delta F) \text{ say.} \quad (10)$$

The time dependence of the occupation number of the two states at any instant  $t$ ,  $P_1(t)$  and  $P_2(t)$  are determined by the rate equation

$$\frac{d}{dt} P_1(t) = -P_1(t) W_{12}(t) + P_2(t) W_{21}(t), \quad (11)$$

where  $W_{12}$  and  $W_{21}$  are the probabilities for transition per unit time from state 1 to state 2 and *vice versa*.  $W$ 's may be time dependent because of the action of the time dependent perturbation by the acoustic field. An elastic strain  $e(t)$  caused by the sound wave affects the two states of a defect and changes their free energies and also  $\Delta F$  and hence their occupation numbers. We characterize this change of free energy difference for a strain of unit strength by a deformation potential  $D$ , defined by

$$\Delta F(e) = \Delta F + D \cdot e, \quad (12)$$

i.e.

$$D = \frac{\partial [\Delta F(e)]}{\partial e}$$

In (12)  $\Delta F$  refers to the equilibrium value. At every moment the relaxation processes aim at instantaneous equilibrium for which occupation number is not  $P_1^{(0)}$  but  $P_1^{(l)}$  defined by the occupation number that would be obtained at the equilibrium temperature for a free energy difference  $\Delta F(e)$  (and not  $\Delta F$ ) and analogous to (10) we will have

$$\begin{aligned} P_1^{(l)} &= f[\Delta F(e)] = f(\Delta F + D \cdot e) \\ &= f(\Delta F) + \frac{\partial f(\Delta F)}{\partial(\Delta F)} \cdot D \cdot e, \end{aligned} \quad (13)$$

which gives the relation between the instantaneous and absolute equilibrium values of occupation number as

$$P_1^{(l)} = P_1^{(0)} + \frac{\partial f(\Delta F)}{\partial(\Delta F)} \cdot D \cdot e. \quad (14)$$

Our aim is to find the complete deviation of  $\delta P_1$  of occupation number  $P_1(t)$  at any instant  $t$  from the absolute equilibrium value of  $P_1^{(0)}$  i.e.

$$\delta P_1 = P_1(t) - P_1^{(0)}.$$

Note that  $P_1(t)$  refers to neither the instantaneous nor the absolute equilibrium value. Noting that the relaxation time is given by

$$\tau^{-1} = W_{12}^{(0)} + W_{21}^{(0)}, \quad (15)$$

it can be shown [10] that

$$\frac{d}{dt}[P_1(t) - P_1^{(0)}] + \frac{P_1(t) - P_1^{(0)}}{\tau} = \frac{1}{\tau} \frac{df(\Delta F)}{d(\Delta F)} D \cdot e, \quad (16)$$

considering the time dependence of  $e$  as  $e \sim e^{-i\omega t}$  where  $\omega$  is the frequency of the sound wave, the solution of (16) gives

$$\delta P_1 = P_1(t) - P_1^{(0)} = \frac{df(\Delta F)}{d(\Delta F)} D \cdot e (1 - i\omega\tau)^{-1}. \quad (17)$$

This change of  $\delta P_1$  in the occupation number causes a feed back on the elastic stress  $\sigma$  and our next aim is to find this contribution of  $\delta\sigma$  due to the change in  $\delta P_1$  i.e.  $\partial\sigma/\partial P_1$ .

Now

$$\sigma = \frac{1}{\Omega} \left( \frac{\partial \mathcal{F}}{\partial e} \right)_{T, P_1}, \quad (18)$$

where  $\Omega$  is the volume of the undeformed solid and we have postulated a free energy function  $\mathcal{F}$  of the whole system containing  $N$  defects with  $T, e, p$  as independent variables. The free energy function  $\mathcal{F}$  of the whole system should not be confused with free energy  $F_1$  or  $F_2$  of the defect states

$$\mathcal{F}(T, e, P_1) = \mathcal{F}'(T, e, P_1) - TS(P_1), \quad (19)$$



where  $\mathcal{F}'$  is the free energy function excluding entropy contribution  $S(p_1)$  associated with the probability distribution of the defects between their two states. To find  $\partial\sigma/\partial P_1$  we first find  $\partial\mathcal{F}'/\partial P_1$ . We have

$$\mathcal{F}' = NP_1 F_1 + NP_2 F_2 = NP_1 (F_1 - F_2) + NF_2,$$

$$\frac{\partial\mathcal{F}'}{\partial P_1} = N(F_1 - F_2) = N\Delta F,$$

$$\sigma = \frac{1}{\Omega} \left( \frac{\partial\mathcal{F}}{\partial e} \right)_{T, P_1} = \frac{1}{\Omega} \left( \frac{\partial\mathcal{F}'}{\partial e} \right)_{T, P_1},$$

$$\begin{aligned} \frac{\partial\sigma}{\partial P_1} &= \frac{1}{\Omega} \frac{\partial}{\partial P_1} \left( \frac{\partial\mathcal{F}'}{\partial e} \right) = \frac{1}{\Omega} \frac{\partial}{\partial e} \left( \frac{\partial\mathcal{F}'}{\partial P_1} \right) = \frac{1}{\Omega} \frac{\partial}{\partial e} (N\Delta F), \\ &= \frac{N}{\Omega} \frac{\partial}{\partial e} (\Delta F) = nD, \end{aligned}$$

where  $n$  is the number of defects per unit volume.

Thus the defect contribution  $\delta\sigma$  to the stress due to the change of the occurrence number is given by (using (17) and (20))

$$\delta\sigma = nD\delta P_1 = nD^2 \frac{df(\Delta F)}{d(\Delta F)} e(1 - i\omega\tau)^{-1}.$$

The dynamical contribution  $\delta C(\omega)$  of the two state defects to the complex, frequency dependent elastic constant  $C$  is

$$\delta C(\omega) = \frac{\delta\sigma}{e} = nD^2 \frac{df(\Delta F)}{d(\Delta F)} \frac{1 + i\omega\tau}{1 + \omega^2\tau^2},$$

$$\text{Re } \delta C(\omega) = nD^2 \frac{df(\Delta F)}{d(\Delta F)} \frac{1}{1 + \omega^2\tau^2},$$

$$\text{Im } \delta C(\omega) = nD^2 \frac{df(\Delta F)}{d(\Delta F)} \frac{\omega\tau}{1 + \omega^2\tau^2}.$$

Where the complex elastic constant  $C$  is written as

$$C = C_\infty + \delta C(\omega),$$

( $C_\infty$  is the elastic constant without interaction of the defects with sound wave,  $C_\infty$  is the elastic constant at infinite relaxation time). From the relation  $C_\infty = \rho v_\infty^2$ ,

$$C = C_\infty + \delta C(\omega) = \rho [v_\infty + \delta v(\omega)]^2,$$

where  $\rho$  is the density, it is easy to show that

$$\text{Re } \delta C(\omega) = 2\rho v_\infty \text{Re } \delta v(\omega),$$

where  $v_\infty$  = velocity of sound wave without interaction i.e. at infinite relaxation time.

$\text{Re } \delta v(\omega)$  = Real part of the change of velocity from  $v_\infty$  due to relaxation effect. Experimentally it is the real part of velocity which is measured as phase velocity. Hence from (23) and (25), the relaxation effect on sound velocity (omitting the argument  $\omega$  in  $\delta v(\omega)$ )

$$\delta v = -\frac{\text{Re } \delta C(\omega)}{2\rho v_\infty} = -\frac{1}{2\rho v} n D^2 \frac{df(\Delta F)}{d(\Delta F)} \cdot \frac{1}{1 + \omega^2 \tau^2} \dots \quad (26)$$

(omitting the suffix  $\infty$  in  $v_\infty$  in the final expression).

Again, it can be shown that  $\text{Im } C$  which arises entirely from  $\text{Im } \delta C(\omega)$  in our case is related to the dissipation factor  $Q^{-1}$  as follows:

$$\begin{aligned} Q^{-1} &= \frac{2\alpha v}{\omega} = -\frac{1}{\rho v^2} \text{Im } C = -\frac{1}{\rho v^2} \text{Im } \delta C(\omega), \\ &= -\frac{1}{\rho v^2} n D^2 \frac{df(\Delta F)}{d(\Delta F)} \cdot \frac{\omega \tau}{1 + \omega^2 \tau^2}, \end{aligned} \quad (27)$$

( $\alpha$  = attenuation coefficient).

It should be noted that in (26) and (27)  $v$  refers to the velocity without interaction of the sound wave with the defects and it is obtained from the experimental result of velocity at extremely low temperature (liquid helium) and  $\delta v$  is the change of sound velocity from this value due to the interaction (i.e. relaxation effect). The variation  $\delta v$  of the sound velocity and the dissipation factor  $Q^{-1}$  arising out of the relaxation effect as given by (26) and (27) refer to one kind of defect only. Because of the amorphous phase there will be several kinds of defects having different values of  $\tau$  which depends on activation energy  $V$  (barrier height between the two wells of the double-well potential), and we will have a distribution function  $P(V)$  of the activation energy  $V$ . Further, we have using (10)

$$\frac{df(\Delta F)}{d(\Delta F)} = -\beta \frac{e^{\beta \Delta F}}{(e^{\beta \Delta F} + 1)^2}, \quad \beta = \frac{1}{kT}.$$

In the temperature range of our interest  $kT \gg \Delta F$  and

$$\frac{df(\Delta F)}{d(\Delta F)} \approx -\beta/4 = -\frac{1}{4kT}.$$

The relaxation effects on sound velocity and absorption then become

$$\frac{\partial v}{v} = -\frac{D^2}{8\rho v^2 kT} \int_0^\infty \frac{P(V) dV}{1 + \omega^2 \tau^2}, \quad (28)$$

$$Q^{-1} = \frac{D^2}{4\rho v^2 kT} \int_0^\infty \frac{P(V) \omega \tau}{1 + \omega^2 \tau^2} dV. \quad (29)$$

Here  $v$  refers to the sound velocity without interaction (i.e. at extremely low temperature say liquid He).

For the evaluation of (28) and (29) we need an expression for  $\tau$ . From reaction theory, rate of an activated process is proportional to  $e^{-\beta(F_a - F_i)}$  where  $F_a$  reaction threshold and  $F_i$  the free energy of the initial state. The transition probabilities  $W_{12}$  and  $W_{21}$  are then

$$W_{12} = \omega_{a1} e^{-\beta(F_a - F_1)},$$

$$W_{21} = \omega_{a2} e^{-\beta(F_a - F_2)}.$$

At equilibrium

$$P_1^{(0)} W_{12}^{(0)} = P_2^{(0)} W_{21}^{(0)},$$

and

$$\frac{P_1^{(0)}}{P_2^{(0)}} = \frac{e^{-\beta F_1}}{e^{-\beta F_2}}.$$

Using these equations at equilibrium, we have

$$\omega_{a1} = \omega_{a2} = \omega_a^{(0)} \text{ say}$$

and

$$\frac{1}{\tau} = W_{12}^{(0)} + W_{21}^{(0)} = \omega_a^{(0)} e^{-\beta(F_a - F_1)} [1 + e^{-\beta(F_1 - F_2)}].$$

The energy difference  $(F_a - F_i)$  corresponds to barrier height  $V$ , hence

$$\tau = \tau_0 e^{V/kT} (1 + e^{-(\Delta F/kT)})^{-1}, \quad \tau_0 = \frac{1}{\omega_a^{(0)}}.$$

At high temperature for which  $\Delta F \ll kT$ ,

$$\tau = \tau(0) e^{V/kT}, \quad \tau(0) = \frac{1}{2} \tau_0.$$

## 8. Improvement of the theory

Earlier theoretical works using (28), (29) and (31) or (30) considered (a) a symmetric double-well potential for which the two minima were equal in energy, (b) a gaussian distribution  $P(V)$  for the barrier height only, (c) a low barrier cut-off is needed to produce a peak in  $Q^{-1}$ . In vitreous silica, a cut-off for  $V$  below 125 K, and a  $\sim 410$  K of the gaussian distribution are needed for agreement with experiment. (d) frequency dependence of attenuation was not satisfactory.

The theory has been improved by Gilroy and Phillips (1981) so as to give satisfactory agreement with the experiment. The model is based on an asymmetric double well potential having distribution for both barrier height and asymmetry. This model has the advantage that no low barrier cut off is required contrary to the symmetric double well model. The same variations in local environment that produce variations in the barrier height in glass are also expected to produce inequ-

potential wells having unequal depths in the double well potential curve. Thus the improved theory considered (i) asymmetry parameter  $\Delta$  of the wells given by  $\Delta =$  the difference in energy of the two potential minima and a distribution of  $\Delta$  denoted by  $n(\Delta)$ , (ii) no lower cut off for  $V$ , (iii) distribution of  $V$  of the form  $g(V) = (1/V_0)e^{-V/V_0}$  where  $V_0$  is the energy value of the order that corresponds to glass transition temperature  $T_g$ . Gilroy and Phillips (1981) choose  $n(\Delta)$  as a constant  $n_0$ , valid for temperature below  $T_g$  and (iv) further in their analysis relaxation time  $\tau$  was expressed as

$$\tau = \tau_0 e^{V/kT} \sec h(\Delta/2kT), \quad (32)$$

which is a natural consequence of the introduction of asymmetry in (30). With the introduction of asymmetry, (30) may be written as

$$\tau = \tau_0 e^{(V - \Delta/2)/kT} (1 + e^{-(\Delta/kT)})^{-1} \quad (33)$$

where  $V$  is now the barrier height from the lower well,  $V - \Delta/2$  is the average of the barrier heights measured from the two inequivalent wells and  $\Delta F$  should be replaced by  $\Delta$  when asymmetry parameter is taken into consideration. It is worthwhile to note that (33) can be shown to be identical in form with (32).

Improved theory of Gilroy and Phillips (1981) gives

$$\frac{\delta v}{v} = -\frac{D^2}{8\rho v^2 kT} \int_0^\infty \int_0^\infty \frac{1}{1 + \omega^2 \tau^2} \sec h^2\left(\frac{\Delta}{2kT}\right) n(\Delta) g(V) d\Delta dV, \quad (34)$$

$$Q^{-1} = \frac{D^2}{4\rho v^2 kT} \int_0^\infty \int_0^\infty \frac{\omega \tau}{1 + \omega^2 \tau^2} \sec h^2\left(\frac{\Delta}{2kT}\right) n(\Delta) g(V) d\Delta dV. \quad (35)$$

Gilroy and Phillips (1981) gave the approximate solution of (34) and (35) in closed form as follows

$$\frac{\delta v}{v} = -\frac{D^2}{4\rho v^2} n_0 [1 - (\omega \tau_0)^{kT/V_0}], \quad (36)$$

$$Q^{-1} = \frac{D^2}{4\rho v^2} n_0 \pi \frac{kT}{V_0} (\omega \tau_0)^{kT/V_0}. \quad (37)$$

$Q^{-1}$  as a function of temperature shows a maximum when  $dQ^{-1}/dT = 0$  which leads to

$$\omega \tau_0 = e^{-(V_0/kT_m)}$$

i.e.

$$\ln \omega + \ln \tau_0 = -\frac{V_0}{kT_m}. \quad (38)$$

Where  $T_m$  is the temperature at which the  $Q^{-1}$  peak occurs and

$$Q_{\max}^{-1} = \frac{\pi n_0 D^2 kT_m}{4\rho v^2 V_0 e}. \quad (39)$$

The relaxation effects on both the sound velocity ( $\delta v/v$ ) and dissipation ( $Q^{-1}$ ) contain the same parameters such as  $(n_0 D^2)/\rho v^2$ ,  $\tau_0$  and  $V_0$ . While  $Q^{-1}$  is obtained from the

attenuation coefficient which is directly measured in the ultrasonic attenuation experiment, the relative variation of velocity  $\delta v/v$  at any temperature  $T$  is obtained from the velocity measurements  $v_T$  at temperature  $T$  and  $v_{\text{He}}$  at temperature of liquid helium where relaxation effect is practically nil. i.e.

$$\frac{\delta v}{v} = \frac{v_T - v_{\text{He}}}{v_{\text{He}}}.$$

Gilroy and Phillips (1981) were able to fit their theory with experiments on vitreous silica by adjusting suitable values of these parameters consistent with other experimental data. However, the parameters  $\tau_0$  and  $V_0$  can be obtained from a plot of  $\ln \omega$  vs  $\ln Q^{-1}$ . If attenuation experiments are performed at different frequencies. From (38) there should be a straight line which should yield  $\ln \tau_0$  and  $V_0/k$  from its intercept and slope. Bridge and Patel (1986) in their studies on ultrasonic relaxation in molybdenum phosphate glasses of different composition also used the expression of  $Q^{-1}$  analogous to (35), but instead of going for an analytic solution they adopted a method of numerical computation of the relevant integrals in order to fit the experimental curve. Recently Mukherjee *et al* (1993) carried out ultrasonic investigation of a binary system of  $V_2O_5$ - $GeO_2$  glasses of different compositions and evaluated the parameters necessary to interpret the attenuation ( $Q^{-1}$ ) experiment successfully following Gilroy and Phillips (1981) theory.

## 9. Present status of the theory

It is worthwhile to mention here that Gilroy and Phillips (1981) had to consider an additional term in their theory for the variation of velocity, additional term to account for the temperature velocity variation which cannot be explained by the relaxation theory. It should be noted that (36) indicates a negative value of  $\delta v$  i.e. sound velocity decreases due to relaxation effect from its value without relaxation (the negative value of  $\delta v$  is apparent if we note that  $\omega\tau_0 \ll 1$ ) and the magnitude of this decrease in  $\delta v$  increases as  $T$  increases. Hence the linear rise of velocity with temperature at higher temperatures cannot be explained by this theory, nor can it explain a value of velocity at higher temperature greater than that without relaxation effect i.e. greater than the value at extremely low temperature (say He temperature). This is why Gilroy and Phillips (1981) had to consider additional term indicating a rise of velocity with temperature observed in quartz glass. While the theory of the relaxation effects on attenuation (i.e.  $Q^{-1}$ ) as given by (37) adequately explains the attenuation behaviour of glasses, the theory can explain the initial decrease of  $(\delta v/v)$  with increasing temperature in the region below the temperature at which the minimum occurs but cannot account for the almost linear rise on the higher temperature side without including a small additional term as mentioned above. In the case of vitreous silica attempt has been made by Dienes (1958) to relate this increase of  $v$  with  $T$  at higher temperature to the anomalous small thermal expansion coefficient of glass compared to that of crystalline counterparts. The small thermal expansion coefficient of vitreous silica leads to positive temperature coefficient of elastic moduli and hence a positive temperature coefficient of velocity. But such explanation in terms of small thermal expansion fails in many other glasses where thermal expansion is not small but comparable to the value for their crystalline counterparts.

glass and are associated with the freezing of natural fluctuations of the order parameter of liquid glass at temperatures close to  $T_g$ . When the rate of cooling is high, the viscosity of a glass forming substance may be so high that the order fluctuations are not dispersed but are frozen at temperature  $T_g$  and are thus retained in the solid state. Moreover, cooling below  $T_g$  may further increase the tensile stresses between the regions of higher and lower order i.e. it may enhance the local elastic inhomogeneities. Kul'bitskaya *et al* (1975, 1976) showed that the effective macroscopic elastic constant  $C_{\text{eff}}$ , which governs the velocity of propagation of ultrasonic wave in such an elastically inhomogeneous medium, is equal to an average value of  $C_0$  from which is subtracted a positive quantity  $\Delta_f^2$  proportional to the mean square amplitude of the spatial fluctuations of the elasticity i.e.

$$C_{\text{eff}} = C_0 - \Delta_f^2.$$

With the increase of temperature both  $C_0$  and  $\Delta_f^2$  decreases. If the correction  $\Delta_f^2$  decreases more rapidly than  $C_0$  as the temperature is increased, resulting in homogenization of glass structure, the macroscopic elastic constant  $C_{\text{eff}}$  may increase producing positive temperature coefficient of velocity. The above mechanism of the formation of microscopic elastic inhomogeneity in glasses suggest that the temperature dependence of  $\Delta_f^2$  should be more pronounced in high  $T_g$  glasses and this is why some doubt has arisen about the validity of this mechanism in the case of  $\text{BeF}_2$  where  $T_g$  is small, 592 K (i.e. slightly greater than that of  $\text{B}_2\text{O}_3$  for which  $T_g = 513$  K and temperature coefficient of velocity is always negative), yet showing a positive temperature coefficient of velocity even more pronounced than in vitreous silica. The situation regarding positive temperature coefficient of velocity in the high temperature region observed in many glasses is not yet fully clear and is still of theoretical interest.

## References

- Anderson A C 1981 in *Amorphous solids, low temperature properties* (ed.) W A Phillips (Berlin: Springer Verlag) p. 27
- Anderson O L and Bömmel H E 1955 *J. Ceram. Soc.* **38** 125
- Anderson P W, Halperin B I and Verma C 1972 *Philos. Mag.* **25** 1
- Bridge B and Patel N D 1986 *J. Mater. Sci.* **21** 3783
- Dienes G J 1958 *J. Phys. Chem. Solids* **7** 290
- Gilroy K S and Phillips W A 1981 *Philos. Mag.* **B43** 735
- Hunklinger S and Arnold W 1976 *Phys. Acoust.* **12** 155
- Hunklinger S and Schickfus M V 1981 in *Amorphous solids, low temperature properties* (ed.) W A Phillips (Berlin: Springer Verlag) p. 91
- Jackle J, Piche L, Arnold W and Hunklinger S 1976 *J. Non-Cryst. Solids* **20** 365
- Krause J T and Kurkjian C R 1968 *J. Am. Ceram. Soc.* **51** 226
- Kul'bitskaya M N and Shutilov V A 1976 *Sov. Phys. Acoust.* **22** 451
- Kul'bitskaya M N, Nemilev S V and Shutilov V A 1975 *Sov. Phys. Solid State* **16** 2319
- Mukherjee S, Maiti A, Ghosh U S and Basu C 1993 *Philos. Mag.* **B67** 823
- Phillips W A 1972 *J. Low Temp. Phys.* **7** 351
- Pohl R O 1981 in *Amorphous solids, low temperature properties* (ed.) W A Phillips (Berlin: Springer Verlag) p. 27



# Crystallographic and electrical study of the chromium substituted ferrous zinc copper ferrites

V M NANOTI and D K KULKARNI

Department of Physics, Institute of Science, Civil Lines, Nagpur 440 001, India

**Abstract.** The structural and electrical properties of the oxidic spinel  $\text{Zn}_{0.5}\text{Cu}_{0.5}\text{Fe}_x\text{Cr}_{2-x}\text{O}_4$  ( $x = 0.8, 0.9, 1.0, 1.1$ ) have been investigated through X-ray diffraction, electrical resistivity, and thermoelectric measurements.

X-ray diffraction data showed formation of single spinel phase with cubic structure. D.C. resistivity measurements from room temperature to 850 K was carried out and activation energy for all the compositions evaluated. Thermoelectric measurements showed  $p$ -type semiconducting nature in all the samples.

**Keywords.** X-ray diffraction; activation energy; Seebeck coefficient; mixed ferrites.

## 1. Introduction

Many mixed metal oxides with spinel structure were investigated as they exhibit interesting structural, magnetic and electrical properties. The spinel structure consists of a cubic close packed cage of ions with metallic ions occupying 8 tetrahedral (A) and 16 octahedral (B) interstitial sites. Properties of these spinels were controlled by the type of ions and their preferences for tetrahedral (A) and octahedral (B) sites. The Zn-Cu ferrites have aroused considerable interest due to their interesting electrical and magnetic properties. According to Mitra *et al* (1992), a number of  $\text{Fe}^{+2}$  ions are generally formed during sintering process responsible for hopping mechanism. Van Uitert (1955) reported evaporation of  $\text{Zn}^{+2}$  ions from Zn ferrites, which increases the probability of formation of  $\text{Fe}^{+2}$  ions. In the present work  $\text{Zn}_{0.5}\text{Cu}_{0.5}\text{Fe}_x\text{Cr}_{2-x}\text{O}_4$  system was applied for the study of structural as well as electrical properties.

## 2. Experimental

Four samples of the spinel series  $\text{Zn}_{0.5}\text{Cu}_{0.5}\text{Fe}_x\text{Cr}_{2-x}\text{O}_4$  with  $x = 0.8$  to  $1.1$  in the steps of  $0.1$  were prepared by conventional ceramic technique using AR grade oxides viz.  $\text{Fe}_2\text{O}_3$ ,  $\text{Cr}_2\text{O}_3$ ,  $\text{ZnO}$  and  $\text{CuO}$ . The oxides were mixed in proper molar proportions to yield the desired stoichiometry. The mixture was ground in acetone and presintered at  $1000^\circ\text{C}$  for 16 h and slowly cooled. Then the samples were again mixed properly and refired at  $1000^\circ\text{C}$  for another 100 h and annealed initially at the rate of  $100^\circ\text{C/h}$  up to  $500^\circ\text{C}$  and then cooled naturally. The X-ray diffractograms of the powdered samples were then taken using Philips X-ray diffractometer and Cu-K radiation with wavelength  $1.542 \text{ \AA}$ . The X-ray patterns showed a single spinel phase with cubic structure. X-ray intensity calculations were carried out for the site distribution.

DC resistivity of the samples was measured using LCR bridges [Meghommeter Model RM 160/3 (BPL India) and Digital LCR meter VLCR-17 (Vasavi Electronics)]. Pellets were prepared by mixing 4% polyvinyl acetate (PVA) as a binder under 2



tonnes/cm pressure. Initially pellets were heated at 300°C for 3 h and then at 1 by gradual rise in temperature. The final sintering was carried out for 3 h and sample was furnace cooled. A thin layer of silver paste was applied over each pellet for good electrical contacts. Measurements were carried out from room temperature to 850 K. Thermoelectric measurements were carried out by sandwiching thick pellets between two copper rods from room temperature to 850 K.  $\log \rho$  vs  $10^3/T$  and  $\alpha$  (mV) vs  $T$ (K) were also plotted to find out  $\Delta E$  and Seebeck coefficients respectively.

### 3. Results and discussion

X-ray patterns of all the compounds showed a single spinel phase with cubic structure. X-ray intensity calculations were carried out. In such mixed systems determination of oxidation states, degree of inversion, cation distribution and anionic parameter are difficult. The intensities of reflections. The most sensitive planes were taken to be indicators for the adjustment parameters for bigger size anions which were of fixed oxidation states.

As none of the compounds had high conductivity or low activation energy, the possibility of mixed valences of same metal ion was remote. Intensity calculations

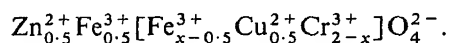
**Table 1.** Lattice parameter ( $a$ ), X-ray density ( $dx$ ),  $d_{B-B}$  distances, activation energy ( $\Delta E$ ) and Seebeck coefficient ( $\alpha$ ) for the system  $Zn_{0.5}Cu_{0.5}Fe_xCr_{2-x}O_4$ .

$x$	$a$ (Å)	$dx$ (g/cc)	$d_{B-B}$ (Å)	$\Delta E$ (eV)	$\alpha$ ( $\mu$ V/K)
0.8	8.3443	5.4086	2.9502	0.67	+ 410
0.9	8.3490	5.3792	2.9518	0.61	+ 355
1.0	8.3522	5.3890	2.9529	0.58	+ 310
1.1	8.3549	5.3929	2.9539	0.53	+ 280

**Table 2.** Comparative study of X-ray intensities for the compound  $Zn_{0.5}Cu_{0.5}Fe_{0.9}Cr_{1.1}O_4$  ( $a = 8.3490 \pm 0.0001$ ).

Angle $2\theta$	' $d$ ' (obs)	$hkl$	$I/I_{max}$ (obs)	$I/I_{max}$ (cal)
23.1700	4.8203	111	5.65	5.63
38.2700	2.9531	220	50.84	50.79
45.1725	2.5204	311	100.00	100.00
47.3600	2.4102	222	5.03	5.02
55.2225	2.0886	400	10.72	10.70
69.1825	1.7051	422	6.08	6.05
74.2050	1.6047	333	14.19	14.02
81.9100	1.4768	440	15.93	15.91
94.2875	1.3205	620	2.06	2.06
99.0150	1.2729	533	3.38	3.36
100.6050	1.2581	622	2.06	2.04
120.4425	1.1153	642	2.19	2.15
125.8775	1.0870	553	4.83	4.81

were carried out for all possible cation distributions and the highest matching intensities lead to the cation distribution with following oxidation states.



Details of observed and calculated peak intensities are listed in table 2. Typical X-ray patterns for one of the samples is also shown in figure 2. Lattice parameters 'a' for all the compositions are listed in table 1. Lattice parameter for the compound  $\text{Zn}_{0.5}\text{Cu}_{0.5}\text{FeCrO}_4$  is reported as 8.3522 Å (Nanoti *et al* 1993).

All the compounds showed room temperature resistivity of the order of  $10^4$  ohm.cm. The relationship

$$\rho = \rho_0 \exp(\Delta E/kT),$$

[Wilson's law] is obeyed indicating semiconducting nature of all the compounds. Plots of  $\log \rho$  vs  $10^3/T$  showed no break indicating stable oxidation states. Activation

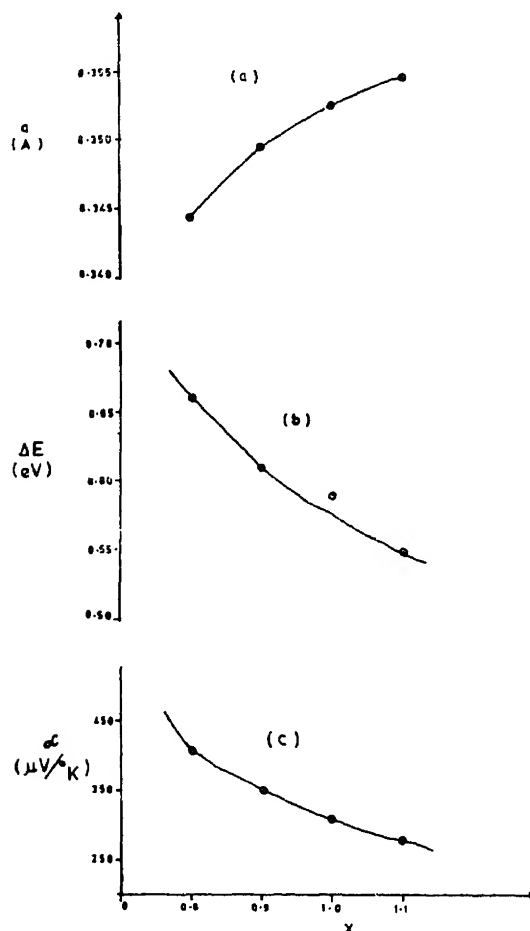


Figure 1. Plot of (a) lattice parameter 'a' vs x, (b) activation energy  $\Delta E$  vs x and (c) Seebeck coefficient  $\alpha$  vs x.

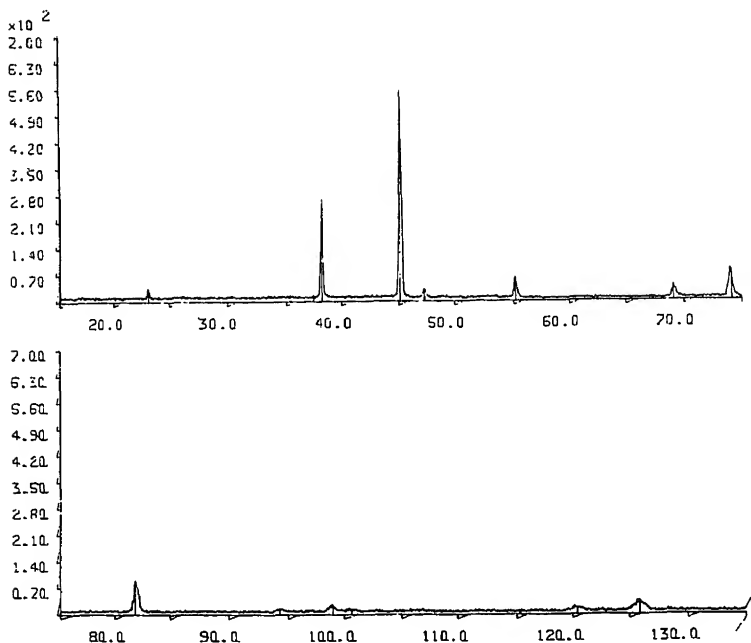


Figure 2. XRD pattern for the compound  $\text{Zn}_{0.5}\text{Cu}_{0.5}\text{Fe}_{0.9}\text{Cr}_{1.1}\text{O}_4$ .

energy for the system was found to vary between 0.53 eV to 0.67 eV (figure spinels  $d_{A-A}$  and  $d_{A-B}$  distances are longer than  $d_{B-B}$  distances. Therefore electron conduction took place by hopping of charge carriers (holes) mostly between B-sites).

A cursory glance at table 1 shows that  $E$  decreases with increasing  $x$  which may be due to several reasons, such as, small number of  $\text{Fe}^{2+}$  ions are generally formed during sintering process, which increases the conductivity due to increased hopping between  $\text{Fe}^{+2}$  and  $\text{Fe}^{+3}$  ions (Mitra *et al* 1992).

Smith and Wijn (1959) and Van Uitert (1955) found that a small amount of oxygen evaporates from the surface grains of zinc ferrites which increases the probability of formation of  $\text{Fe}^{+2}$  ions. Electrical properties of ferrites are explained on the basis of tunneling of electrons amongst  $\text{Fe}^{+2}$  and  $\text{Fe}^{+3}$  ions aligned on B-sites (Srinivasan and Srivastava 1981). It has been assumed that electrons which participate in the  $\text{Fe}^{+2} \leftrightarrow \text{Fe}^{+3} + e^-$  exchange process are strongly coupled to the lattice and do not move from one site to other due to phonon-induced transfer mechanism, developed by Srivastava (1981). Bates and Steggels (1975) found that theoretically calculated values of resistivity and Seebeck coefficients for Zn-Cu ferrites from the above mechanism agree well with the experimental results. Electrical conductivity and Seebeck coefficient data of polycrystalline ferrous zinc ferrite and ferrous zinc copper ferrite studied as a function of temperature have been satisfactorily analyzed on the basis of the above mechanism of electron transport based on a phonon assisted electron tunneling. Conduction in the present system can be attributed to above reason. Thermoelectric measurements are carried out from room temperature to 493 K. Seebeck coefficient of the system was varied between  $+280 \mu\text{V/K}$  to  $+410 \mu\text{V/K}$ . All compounds

*p*-type semiconductors. *p*-type semiconductivity exhibited by compounds can be attributed to loss of some ZnO during firing process creating vacancies at A site. In such a case very small amount of  $\text{Cu}^{+2}$  may go to A-site. Such a possibility for gallium migrating from B to the A site has been reported by Lotgering (1966) and O'keeffe (1961). As a result of this  $\text{Zn}^{+2}$  deficient compounds may be formed having vacancies at B-sites, which will trap holes giving rise to *p*-type of conduction.

## References

- Bates C A and Steggels P 1975 *J. Phys.* **C8** 2283  
Lotgering F K 1966 *Phys. Chem. Solids* **27** 139  
Mitra R, Puri R K and Mendiratta R G 1992 *J. Mater. Sci.* **27** 1275  
Nanoti V M, Prakash C S and Kulkarni D K 1993 *Proceedings of DAE SSP symp., Bombay* p. 168  
O'keeffe M 1961 *Phys. Chem. Solids* **21** 172  
Smith J and Wijn H P J 1959 *Ferrites* (New York: Wiley-Inter Science) p. 299  
Srinivasan G and Srivastava C M 1981 *Phys. Status Solidi* **b103** 665  
Van Uitert L G 1955 *J. Phys.* **31** 883



# Microstructural features of $\text{Cd}_{0.8}\text{Zn}_{0.2}\text{Te}$ thin films studied by X-ray diffraction and electron microscopy

B SAMANTA, U PAL\*, B K SAMANTARAY, T B GHOSH,  
S L SHARMA and A K CHAUDHURI

Department of Physics and Meteorology, Indian Institute of Technology, Kharagpur 721 302, India

\*Universidad Complutense, Departamento Fisica de Materiales, Facultad de Ciencias Fisicas, 28040 Madrid, Spain

**Abstract.** Thin films of synthesized  $\text{Cd}_{0.8}\text{Zn}_{0.2}\text{Te}$  have been deposited on glass substrate at different substrate temperatures. Different microstructural parameters like crystallite size, rms strain, dislocation density, stacking fault probability and stacking fault energy are determined by XRD, SEM, TEM and TED. XRD and XPS have been used to determine the composition. Variations of the microstructural parameters with film thickness and substrate temperature have been studied in order to obtain optimum growth condition for maximum particle size and least microstructural defects. An effort has been made to correlate the experimental results.

**Keywords.** Thin film;  $\text{Cd}_{1-x}\text{Zn}_x\text{Te}$ ; X-ray diffraction; electron microscopy.

## 1. Introduction

$\text{Cd}_{1-x}\text{Zn}_x\text{Te}$  is one of the II–VI ternary semiconductor materials whose band gap can be tailored to any value between 1.45 eV and 2.23 eV (Pal *et al* 1989; Saha *et al* 1989). It is a promising material for high efficiency tandem solar cells (Rohatgi *et al* 1989), switching (Patel 1986) and other optoelectronic devices (Dean 1979; Svob and Marfaing 1986). It is also the most suitable substrate material for epitaxial growth of  $\text{Hg}_{1-x}\text{Cd}_x\text{Te}$  because both these materials have similar structure, with lattice parameters varying almost linearly with composition (Bruder *et al* 1990).

Several studies have been carried out to find bulk as well as thin film properties of CdTe and ZnTe. However, very little is known about the thin film properties of  $\text{Cd}_{1-x}\text{Zn}_x\text{Te}$ . The present work aims at the synthesis of  $\text{Cd}_{0.8}\text{Zn}_{0.2}\text{Te}$ , deposition of thin  $\text{Cd}_{0.8}\text{Zn}_{0.2}\text{Te}$  film of different thicknesses at different substrate temperatures and characterization of the deposited films for various microstructural parameters such as crystallite size, microstrain, stacking fault probability and stacking fault energy and dislocation density. These parameters are determined from X-ray diffraction (XRD), scanning electron microscopy (SEM), transmission electron microscopy (TEM) and transmission electron diffraction (TED) studies.

## 2. Experimental

### 2.1 *Preparation of the material*

$\text{Cd}_{0.8}\text{Zn}_{0.2}\text{Te}$  was synthesized from its constituent elements (spectroscopically pure) taken in a carbon coated quartz ampoule. The ampoule with the charge was sealed under vacuum ( $\approx 10^{-5}$  torr) and suspended in a vertical tantalum furnace at 1123 K

to start the reaction. After 6 h, the temperature was sharply raised to 1433 K (above the melting point) (Steininger *et al* 1970) in order to avoid constitutional supercooling effect. After 6 h, the furnace was slowly cooled to room temperature.

From XRD data of the synthesized material, the interplanar spacings ( $d_{hkl}$ ) were determined. These values lie between those of CdTe (8 F) and ZnTe (8 F) as expected for ternary compound. The notation within the parentheses (as described in the ASTM standard method for assigning phase designation) indicate the Bravais lattice of the materials to be fcc with 8 atoms in each unit cell. Using the Nelson–Riley plot [ $1/2(\cos^2\theta/\sin\theta + \cos^2\theta/\theta)$  vs  $a$ ] the lattice parameter  $a_0$  was calculated. The value of  $a_0$  so obtained was  $0.6405 \pm 0.0005$  nm. Assuming the linearity of the Vegard's law, the composition was found to be  $\text{Cd}_{0.80}\text{Zn}_{0.20}\text{Te}$ . The composition so obtained was accurate within 10 at%.

The composition of the bulk material was also estimated by electron spectroscopy for chemical analysis (ESCA). X-ray photoelectron spectra (XPS) were recorded on a VG ESCA LAB MK II spectrometer using  $\text{AlK}_{\alpha}$  (1486.6 eV) radiation operated at 12 kV, 10 mA. All scans were recorded at 25 eV pass energy at an analyzer chamber pressure of  $10^{-9}$  torr. Before recording the spectra, the specimen was cleaned with  $\text{Ar}^+$  ions. For quantitative analysis, the area under each photoelectron peak was estimated after correcting for background. Atomic percentages were obtained using the published sensitivity factors (Wagner *et al* 1981). Because of the uncertainties in the sensitivity factors and of the background selection, the quantitative estimates were found to be accurate within 15 at% (Wagner *et al* 1981) within the XPS detection limit of  $\approx 5$  nm from the surface. Under the instrumental conditions employed, the energy resolution of the spectrometer was 0.92 eV. For the analysis, the  $\text{Cd}(3d_{5/2})$ ,  $\text{Zn}(2p_{3/2})$  and  $\text{Te}(3d_{5/2})$  photoelectron peaks were taken into consideration. The peaks were identified by the electron binding energy position of the pure elements. The binding energy of carbon 1s peak at 285 eV was taken as the energy reference (Sternberg 1983). Composition of the bulk material was thus determined to be  $\text{Cd}_{0.76}\text{Zn}_{0.24}\text{Te}$ .

## 2.2 Thin film deposition

Thin films of different thicknesses were deposited on properly cleaned glass substrates at different temperatures by vacuum ( $10^{-5}$  torr) evaporation of the synthesized material from a tantalum boat. The rate of deposition was always maintained at about 60 nm/min. The film thicknesses were measured by a Taylor–Hobson Fom Talysurf.

## 2.3 X-ray line profile analyses

XRD patterns of various films were obtained by a Philips X-ray diffractometer (PW1729) using monochromatic  $\text{CuK}_{\alpha}$  radiation. Ni filter was used for obtaining monochromatic  $\text{CuK}_{\alpha}$  radiation. The XRD patterns showed that the films had preferred (111) orientation. The peak heights due to other planes were considerably smaller than those of the bulk sample. The values of the lattice constant calculated

**Table 1.** Microstructural parameters for  $\text{Cd}_{0.8}\text{Zn}_{0.2}\text{Te}$  thin films deposited at different substrate temperatures ( $T_s$ ).

Subs. temp $T_s$ (K)	Film thickness (nm)	Lattice constant (nm)	Particle size (nm)	rms strain ( $10^{-3}$ )	Stacking fault prob.	Stacking fault energy (mJ/m <sup>2</sup> )	Dislocation density (lines/m <sup>2</sup> ) $10^{14}$
300	240	0.6410	33	8.2	0.061	8.81	50.7
	320	0.6418	52	7.6	0.052	8.89	29.1
	460	0.6412	77	7.0	0.044	8.91	18.6
	610	0.6404	117	6.4	0.036	9.09	11.2
	710	0.6408	152	6.1	0.031	9.60	8.2
	800	0.6410	119	6.8	0.039	9.48	11.7
375	980	0.6410	150	6.9	0.037	10.29	9.4
475	800	0.6416	165	4.7	0.026	6.80	5.8
575	850	0.6410	174	5.0	0.026	7.69	5.8

tails of the peaks, so a careful adjustment of the background was carried out (Mitra and Misra 1966). Assuming that the broadening of the line profile is due to the crystallite size and strain only, the variance is given by (Klug and Alexander 1974):

$$W_{2\theta} = \frac{S\lambda\sigma}{2\pi^2 p \cos \theta} + 4 \tan^2 \theta \langle e^2 \rangle, \quad (1)$$

where  $W_{2\theta}$  is the variance calculated in  $2\theta$  scale,  $p$  the particle size,  $\sigma$  the angular range over which the intensity is appreciable,  $\langle e^2 \rangle$  the mean squared lattice strain,  $\lambda$  the wavelength of the radiation used,  $\theta$  the Bragg angle and  $S$  the Scherrer constant whose value for the cubic constant can be taken to be unity. For calculating the variance a suitable background was drawn. The angular range of this profile in radians was the first value (maximum) of  $\sigma$ . This range was then divided into several divisions. A new background line was then drawn by reducing the profile by one division from each end. This new range was the next  $\sigma$  and corresponding  $W_{2\theta}$  was calculated. Thus several  $\sigma$  and corresponding  $W_{2\theta}$  were computed. The error in the range values lies within  $\pm 3.492 \times 10^{-4}$  radian. The particle size ( $p$ ) and the rms strain  $\langle e^2 \rangle^{1/2}$  can be calculated from the slope and intercept of the straight line respectively. A typical variance ( $W_{2\theta}$ ) vs range ( $\sigma$ ) plot is shown in figure 1.

The lower limits of dislocation density ( $\rho$ ) for the films were calculated using the method suggested by Williamson and Smallman (1956).

Stacking fault probability ( $\alpha$ ) is the fraction of layers undergoing stacking sequence faults and hence one fault is expected in  $1/\alpha$  layers. Stacking fault probability  $\alpha$  is determined by Fourier analysis of the X-ray line profile using the formula (Warren 1969):

$$\frac{1}{D_{(\text{eff}, 111)}} = \frac{1}{D} + (\sqrt{3}/4) \frac{(1.5\alpha + \beta)}{a}. \quad (2)$$

Here  $D_{(\text{eff}, 111)}$  is the average crystal dimension obtained from the intercept of the initial slope on the axis of abscissae of  $A_L^S$  vs  $L$  plot,  $A_L^S$  being the size coefficient and



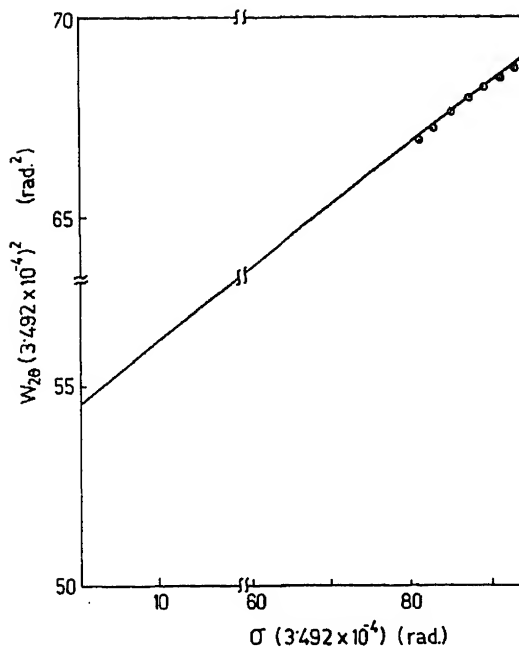


Figure 1. Variance ( $W_{2\theta}$ ) vs angular range ( $\sigma$ ) plot for  $\text{Cd}_{0.8}\text{Zn}_{0.2}\text{Te}$  thin films thickness 710 nm deposited at 300 K.

$L$  being the real distance along the columns of cells perpendicular to reflecting  $D$  is the true particle size,  $a$  the lattice parameter and  $\beta$  the twin fault probability which is assumed to be zero in this case.

Occurrence of stacking faults also gives rise to shift in the peak positions of samples with respect to the ideal positions of a fault free sample in the XRD pattern. Warren and Warekois (1955) have given a relation connecting  $\alpha$  with the shift  $\Delta(2\theta)$ :

$$\alpha = \frac{2\pi^2}{45\sqrt{3} \tan \theta_{111}} \Delta(2\theta_{111}^0).$$

The value of  $\alpha$  determined by Fourier coefficient technique is used here to calculate the  $\Delta(2\theta_{111}^0)$  value in (3). Thus we obtained the corrected peak position ( $2\theta_0$ ) line profile for stacking fault free sample. Taking this  $2\theta_0$  as the reference profile and after proper correction for geometrical profile, centroids of the peaks were obtained. Then  $d_{hkl}$  values were calculated.

From the stacking fault probability, the stacking fault energy can be calculated with the empirical expression suggested by Reed and Schramm (1974).

The surface morphology was studied with a Camscan series II DV electron microscope. SEM photographs of the thin films were taken after etching the surface of the films by bromine (1%) methanol vapour in order to reveal the surface properly. SEM photographs for few typical films are shown in figures 2a–c.

TEM and TED patterns of films deposited at different substrate temperatures were obtained with the help of a JEOL, JEM 200CX electron microscope using 200 keV electrons. The films having thickness less than 100 nm were etched from the

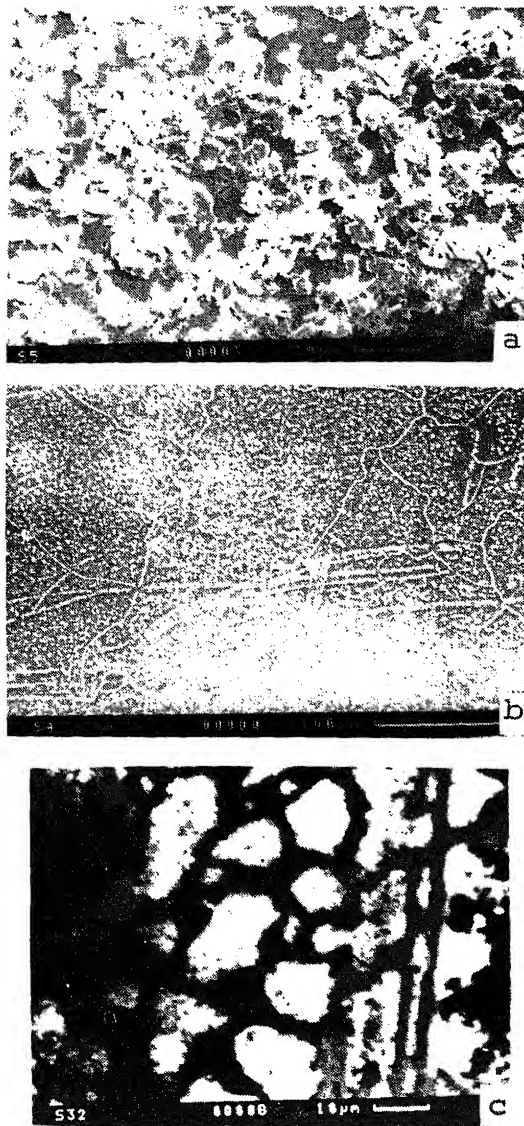


Figure 2. a. SEM photograph of thin film having thickness 710 nm deposited at 300 K, b. thin film having thickness 240 nm deposited at 300 K and c. thin film having thickness 850 nm deposited at 575 K.

substrates using  $\text{HNO}_3 + \text{HF} + \text{H}_2\text{O}$  (3:2:2) solution and were studied by transmission electron microscope.

### 3. Results and discussions

XRD pattern of the synthesized material shows peaks corresponding to the cubic phase only. From Nelson-Riley plot, the lattice constant  $a_0$  is found to be 0.6405 nm.

The XRD patterns of the films deposited at different substrate temperatures (375, 475, and 575 K) reveal the preferential growth of the crystallites with (111) parallel to the substrate. Peaks due to the planes (220) and (311) are also observed and found to be very weak. No peak corresponding to the hexagonal phase appears in the XRD patterns. In the present investigation, as observed from TEM and XRD photographs, hexagonal phase appears with the cubic phase for all the films studied. The appearance of lamellas within the grains in TEM photographs are very clear. It is also clear from TED and TEM studies that the hexagonal phase increases with increasing substrate temperature.

From Nelson–Riley plots for the films, lattice constants  $a_0$  are calculated and tabulated in table 1. XRD analysis does not show much deviation in  $a_0$  or  $c$  content ( $x$ ) values of the  $\text{Cd}_{1-x}\text{Zn}_x\text{Te}$  films from those for the bulk material.

From the XRD patterns of the films deposited at room temperature, the crystallite size, rms strain, dislocation density, stacking fault probability and stacking energy have been calculated and tabulated in table 1. Variations of crystallite size and rms strain with film thickness are shown in figure 3. It is seen that the cry-

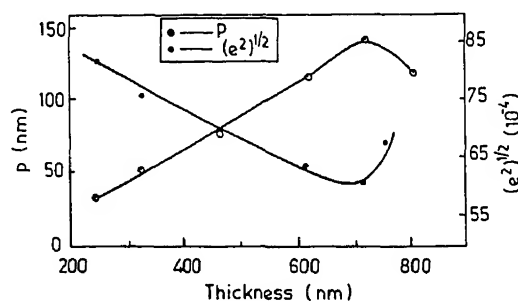
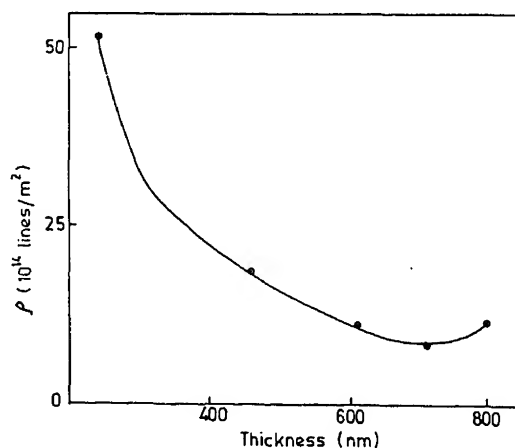


**Figure 3.** Variations of particle size ( $p$ ) and rms strain  $\langle e^2 \rangle^{1/2}$  with the thickness of films deposited at 300 K.



size increases with the film thickness and achieves its maximum value at thickness  $\approx 700$  nm. This is also seen from the SEM photographs (see figures 2a–b) where the maximum average grain size is found to be  $\approx 3000$  nm. The rms strain is found to decrease with the film thickness ( $\approx 6 \times 10^{-3}$  at thickness  $\approx 700$  nm).

The variation of dislocation density with film thickness is shown in figure 4. Dislocation density decreases with the film thickness and achieves its minimum value at  $\approx 700$  nm. Dislocation network can be seen in the SEM photograph of very thin film (figure 2b). Dislocation network is not observed in the SEM photographs for films having thickness  $> 240$  nm. Variations of stacking fault probability and stacking fault energy with film thickness are presented in figure 5. The stacking fault probability decreases and hence stacking fault energy increases up to thickness of 700 nm. With the increase of film thickness particle size increases due to coalescence of small crystals. But for thicker films ( $> 700$  nm) stacking fault probability sharply increases with the increase of thickness. This was also observed for CdTe films by Saha *et al* (1988). The large concentration of stacking faults give rise to the growth of microcrystallites of hexagonal phase which probably inhibits the growth of fcc crystallites. This may be the cause of the optimum film thickness ( $\approx 700$  nm) for particle size and rms strain.

From table 1 it is clear that the particle size increases with the substrate temperature. The increase of grain size with the substrate temperature is also very clear from SEM (figures 2a–c), TEM and TED photographs (figures 6 and 7). Appearance of spotty TED rings at higher substrate temperature (see figure 7b) indicates the increase in crystallite size with increase in substrate temperature.

The  $d_{hkl}$  values determined from TED patterns of the films deposited at different substrate temperatures are given in table 2. Hexagonal planes are indicated by hexagonal notations.

The zinc content ( $x$ ) value obtained from the XPS peak area ratios of the bulk sample is 0.24. The estimated  $x$  values for different films are within the range from 0.21 to 0.29. These  $x$  values are obtained by normalizing the atomic percent of Zn

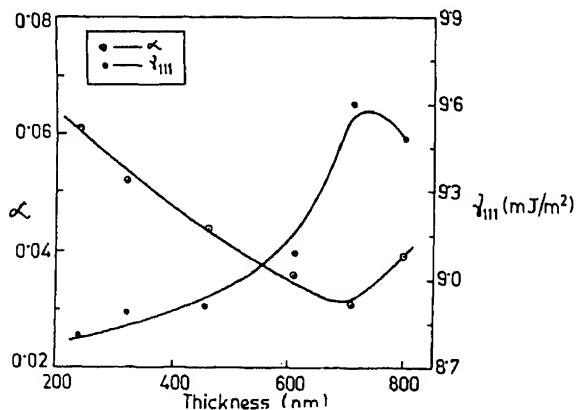


**Figure 5.** Stacking fault probability ( $\alpha$ ) and stacking fault energy ( $\gamma_{111}$ ) vs thickness of the thin films deposited at 300 K.

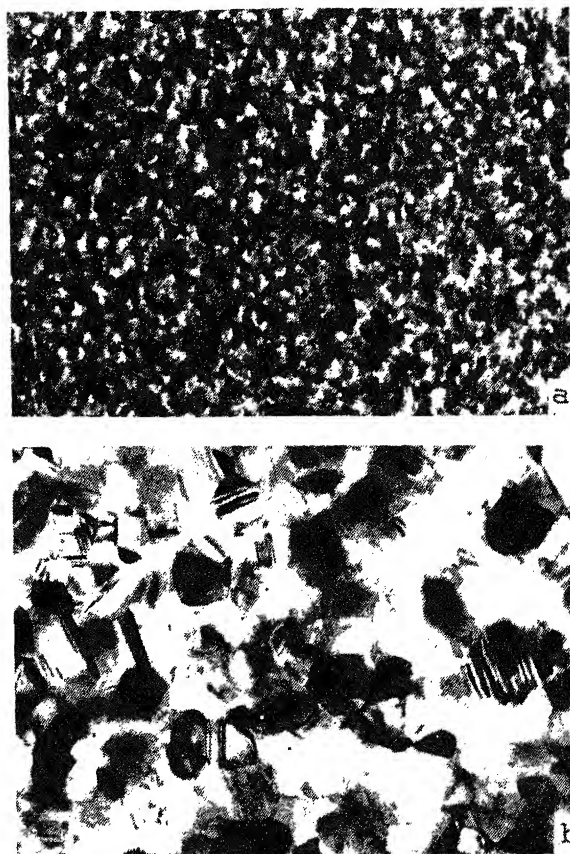


**Figure 6.** TEM photographs (with magnification  $\times 66000$ ) of  $\text{Cd}_{0.8}\text{Zn}_{0.2}\text{Te}$  deposited at (a) 300 K and (b) 575 K.

and Cd present in the samples. A maximum deviation of nearly 10 at% from the stoichiometric value of Te is observed. However, this is well within the expected accuracy limit. In table 3, atomic percent of the elements estimated from XPS analyses are given. No systematic variation of the composition with the film thickness or the substrate temperature is observed. This may be due to the insensitivity of the technique to determine such a small variation. However, for all the films and the bulk sample, the  $x$  values estimated by XPS analyses are higher than the corresponding  $x$  values obtained from XRD data.

The rms strain, dislocation density, stacking fault probability and stacking fault energy values decreased with the substrate temperature. Initially the decrease was quite sharp but it became marginal at higher substrate temperatures. This is because of the fact that when the substrate is kept at a higher temperature, dislocations get more thermal energy and have a higher mobility.

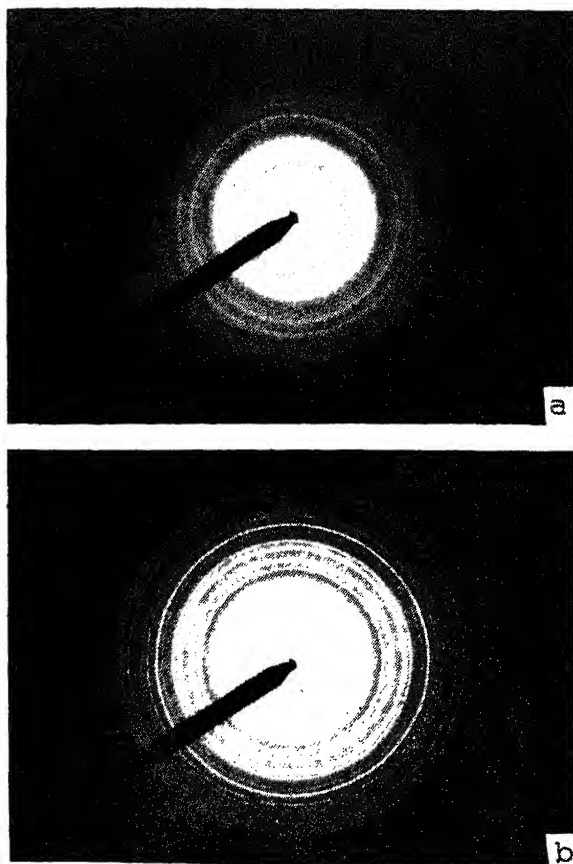


Figure 7. TED photographs of  $\text{Cd}_{0.8}\text{Zn}_{0.2}\text{Te}$  thin films deposited at (a) 300 K and (b) 575 K.

## Conclusion

Hexagonal phase appears along with the cubic phase even for the  $\text{Cd}_{0.8}\text{Zn}_{0.2}\text{Te}$  films deposited at room temperature. The proportion of hexagonal phase increases with the substrate temperature. The stacking fault probability in the films decreases with the thickness causing an increase of stacking fault energy. At higher substrate temperatures particle size becomes larger and stacking fault probability decreases. Therefore we may conclude that for  $\text{Cd}_{0.8}\text{Zn}_{0.2}\text{Te}$  thin films least microstructural defects are observed for optimum thickness of  $\approx 700$  nm and at 575 K substrate temperature. At this temperature films with very large crystallite size and least dislocation density can be obtained. TED also shows single crystal type spots in the diffraction pattern of the film deposited at this temperature.

**Table 2.** Interplanar spacing values obtained from TED patterns of thin films deposited at different substrate temperatures ( $T_s$ ).

$T_s = 300$ K		$T_s = 375$ K		$T_s = 475$ K		$T_s = 575$ K	
$d_{hkl}$ (nm)	$hkl$	$d_{hkl}$ (nm)	$hkl$	$d_{hkl}$ (nm)	$hkl$	$d_{hkl}$ (nm)	$hkl$
0.371	111	0.372	111	0.371	111	0.371	111
0.210	10 $\bar{1}$ 3	0.211	10 $\bar{1}$ 3	0.266	10 $\bar{1}$ 2	0.268	10 $\bar{1}$ 2
0.193	311	0.147	331	0.226	220	0.227	220
0.146	331	0.138	20 $\bar{2}$ 4	0.193	311	0.209	10 $\bar{1}$ 3
0.1227	511	0.1231	511	0.189	20 $\bar{2}$ 1	0.193	311
0.1135	440	0.1137	440	0.159	400	0.189	20 $\bar{2}$ 1
0.1080	531	0.1081	531	0.148	331	0.159	400
0.1010	620	0.1010	620	0.1267	21 $\bar{3}$ 3	0.146	331
		0.0975	533	0.1231	511	0.130	422
		0.0922	444	0.1132	440	0.1229	511
		0.0836	731	0.1082	531	0.1133	440
				0.1015	620	0.1076	531
				0.0977	533	0.1045	13 $\bar{4}$ 3
				0.0897	711	0.1010	620
				0.0858	642	0.0976	533
				0.0832	731	0.0920	444
						0.0894	711
						0.0854	642
						0.0833	731

**Table 3.** Composition analyses.

Substrate temperature (K)	Film thickness (nm)	Cd atom (%)	Zn atom (%)	Te atom (%)	Value of x obtained	
					ESCA	XPS
300	240	38	13	49	0.25	0.25
	320	36	13	51	0.27	0.27
	460	40	14	46	0.26	0.26
	610	39	13	48	0.25	0.25
	710	40	11	49	0.22	0.22
	800	39	12	49	0.24	0.24
375	980	32	13	55	0.29	0.29
475	800	38	10	52	0.21	0.21
575	850	39	11	50	0.22	0.22

## References

- Bruder M, Schwarz H-J, Schmitt R, Maier H and Omöler M 1990 *J. Cryst. Growth* **101** 266  
 Dean P J 1979 *J. Lumin.* **18-19** 755  
 Klug H P and Alexander L E 1974 *X-ray diffraction procedures for polycrystalline and amorphous materials* (New York: Wiley-Interscience Pub.) p. 661  
 Mitra G B 1964 *Acta Crystallina* **17** 765

- Pal U, Saha S, Chaudhuri A K, Rao V V and Banerjee H D 1989 *J. Phys. D: Appl. Phys.* **22** 965
- Patel N G 1986 *J. Mater. Sci.* **21** 2097
- Reed R P and Schramm R E 1974 *J. Appl. Phys.* **45** 4705
- Rohatgi A, Ringel S A, Sudharsanan R, Meyers P V, Liu C H and Ramanathan V 1989 *Solar Cells* **27** 219
- Saha S, Pal U, Samantaray B K and Chaudhuri A K 1988 *Thin Solid Films* **164** 85
- Saha S, Pal U, Chaudhuri A K, Rao V V and Banerjee H D 1989 *Phys. Status Solidi* **114** 721
- Seah M P 1983 in *Practical surface analysis* (New York: John Wiley and Sons, Inc.) p. 181
- Steininger J, Strauss A J and Brebrick R F 1970 *J. Electrochem.* **117** 1305
- Svob L and Marfaing Y 1986 *Solid State Commun.* **58** 343
- Wagner C D, Davis L E, Zeller M V, Taylor J A, Raymond R A and Gale W C H 1981 *Surf. Interface Anal.* **3** 211
- Warren B E 1969 *X-ray diffraction* (Massachusetts: Addition-Wesley) p. 293
- Warren B E and Warekois E P 1955 *Acta Metallogr.* **3** 473
- Williamson G N and Smallman R E 1956 *Philos. Mag.* **1** 34





## Dielectric measurements in vanadium doped barium titanate

A HANUMAIAH, T BHIMASANKARAM,  
S V SURYANARAYANA and G S KUMAR

Department of Physics, Osmania University, Hyderabad 500 007, India

MS received 9 March 1994; revised 3 November 1994

**Abstract.** Ceramic samples of  $\text{Li}_{0.1}\text{Ba}_{0.95}(\text{V}_x\text{Ti}_{1-x})\text{O}_3$ , where  $x = 0$  to  $0.2$  were prepared by solid state reaction method. The samples were characterized by XRD. The dielectric measurements have been carried out on the sintered disks as a function of the frequency (100 Hz–1 MHz) and temperature (300–420 K). The variation of dielectric constant with temperature indicates a diffuse phase transition in all the samples studied.

**Keywords.** Dielectric; diffuse phase transition; doped barium titanate.

### 1. Introduction

The ferroelectrics with diffuse phase transition were first discovered in the solid solutions of barium titanate–barium tin oxide (Smolenskii and Isupov 1954). The broadening of the phase transition is a very common phenomena in solid solutions (Smolenskii 1970; Lines and Glass 1977) and other disorder structures. The ferroelectric–paraelectric phase transitions in these systems are not abrupt but they are gradual diffuse transitions occurring over a temperature range called Curie range. In this region the ferroelectrics exhibit unusual dielectric and ferroelectric characteristics. This behaviour is attributed to structural disorder and compositional fluctuations in the crystalline systems studied (Smolenskii 1984). The diffuse transitions do not occur at high temperatures where the defects are more mobile in the lattice. The presence of impurities also affect the phase transition temperatures of ferroelectric materials, for example, Zr-doped  $\text{BaTiO}_3$  (Gallogher 1963). The impurity ions which replace either Ba or Ti to some extent do show changes in dielectric constant and transition temperatures. In this present work  $\text{Li}_{0.1}\text{Ba}_{0.95}(\text{V}_x\text{Ti}_{1-x})\text{O}_3$  has been prepared and investigated for the variation of its dielectric constant with temperature and frequency.

### 2. Experimental

Lithium barium titanate  $\text{Li}_{0.1}\text{Ba}_{0.95}\text{TiO}_3$  and lithium barium vanadium titanate used in the present study were prepared by solid state double sintering method. Reagents of  $\text{Li}_2\text{CO}_3$ ,  $\text{BaCO}_3$ ,  $\text{V}_2\text{O}_5$  and  $\text{TiO}_2$  were mixed in appropriate proportions to obtain  $\text{Li}_{0.1}\text{Ba}_{0.95}\text{V}_x\text{Ti}_{1-x}\text{O}_3$  ( $x = 0$  to  $0.2$ ). The components were homogeneously mixed, ground to a fine powder and calcined at  $1050^\circ\text{C}$  for 2 h. The presintered mixture was then ground, mixed with 2% poly vinyl alcohol as a binder, pressed into pellets of diameter 11 mm and thickness 2 mm, using a pressure of  $1 \times 10^9 \text{ N/m}^2$ . The pellets were initially kept at  $400^\circ\text{C}$  for 2 h to eliminate the binder and were sintered at  $1150^\circ\text{C}$  for 1 h in a linearly programmable furnace. Lithium in the place of barium has been used to lower the sintering temperature of  $\text{BaTiO}_3$  (Subba Rao *et al* 1981). Using a

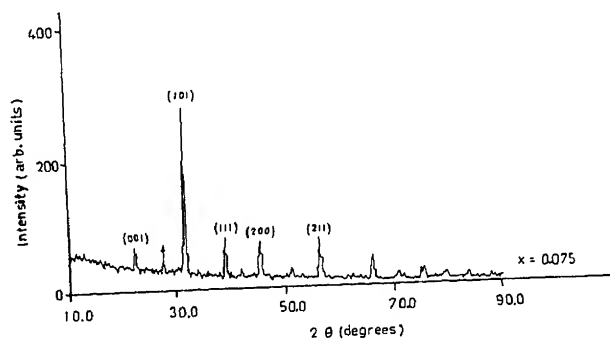
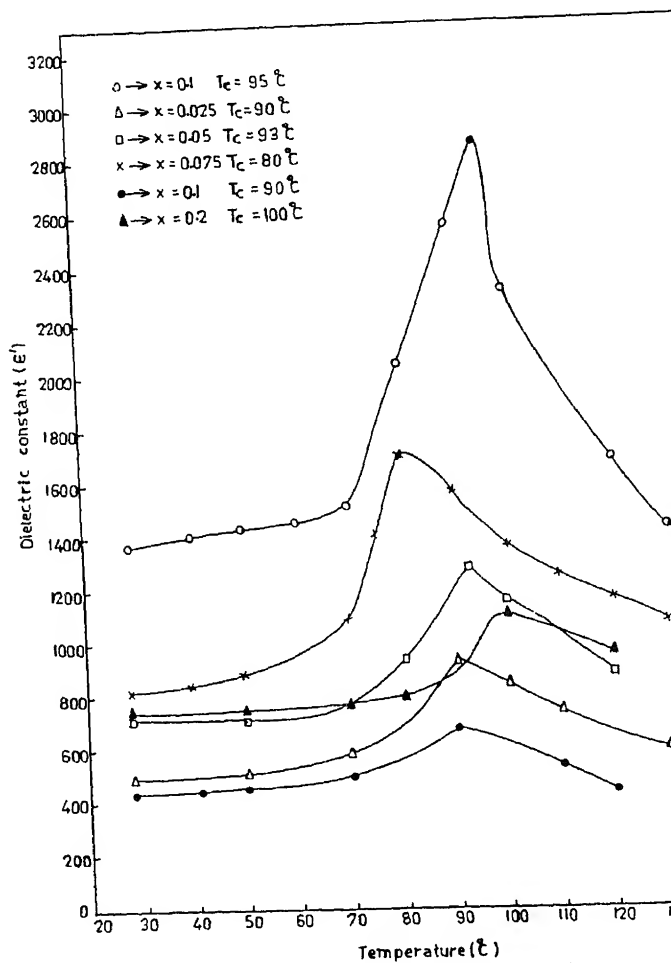


Figure 1. X-ray diffractogram of lithium barium vanadium titanate ( $x = 0$ )



recorded employing a scan speed of 4 deg/min. The dependence of  $\epsilon$  in all the samples was measured employing HP 4192A impedance analyser as a function of temperature from ambient to 150°C.

## 5. Results

The XRD pattern shown in figure 1 for sample with  $x = 0.075$  indicated the formation of the single phase with tetragonal symmetry but there was one peak (marked in figure 1) which could not be identified to any particular phase. This peak could not be identified with any peak of  $V_2O_5$ . A similar type of XRD pattern was observed in other samples, however, the intensity of unidentified peak increased with the increase of vanadium content. The lattice parameters of the samples were computed and found to be almost equal to that of barium titanate.

The density of the sample determined by loss of weight method indicated that as the concentration of vanadium increased, the density was found to decrease. The variation of  $\epsilon'$  with temperature is presented in figure 2. As the concentration of vanadium was increased the Curie temperature  $T_c$  was found to decrease from 95°C–80°C. It was also noticed that there was a fall of peak value  $\epsilon'_c$  with vanadium content. The transitions are not found to be sharp as can be seen in figure 2. This type of behaviour of  $\epsilon'$  is associated with diffuse phase transition (DPT). Such transition is not associated invariably with Curie-Weiss law and an alternative expression was suggested by Uchino and Nomura (1982) which is given as

$$1/\epsilon' = 1/\epsilon'_c + [(T - T_c)^2/2\epsilon'_c\delta^2],$$

where  $\epsilon'_c$  and  $\delta$  are maximum dielectric constant and intensity of DPT respectively. From the knowledge of  $\epsilon'_c$ ,  $T_c$ , and  $\epsilon'$ , the value of  $\delta$  can be computed in the present case. The value of  $\delta$  thus computed is given in table 1. The diffuse transition is more pronounced in samples with higher vanadium concentration. As  $\epsilon = \epsilon' - j\epsilon''$ , the  $\epsilon''$  data are plotted as a function of temperature at 1 kHz frequency (figure 3). The results are identical with those obtained by Issac Robin *et al* (1992) in the case of lithium barium zirconate titanate system.

The variation of dielectric constant with temperature at different frequencies for the sample  $x = 0.1$  is shown in figure 4. We observed that the  $T_c$  for all the frequencies is the same and not much of dispersion occurs in the frequency range studied. Therefore it can be assumed that the sample behaviour resembles to that of a relaxor ferroelectric.

**Table 1.** Dielectric data of lithium barium vanadium titanate ( $Li_{0.1}Ba_{0.95}V_xTi_{1-x}O_3$ ).

$x$	Density (g/cc)	$\epsilon'_{RT}$	$\epsilon'_c$	$T_c$	$\delta$
0.0	5.58	1364	2854	95	27
0.025	5.58	491	926	90	29
0.05	5.44	720	1280	93	37
0.075	5.37	810	1700	80	28
0.1	5.35	425	670	90	28
0.2	5.33	740	1100	100	32

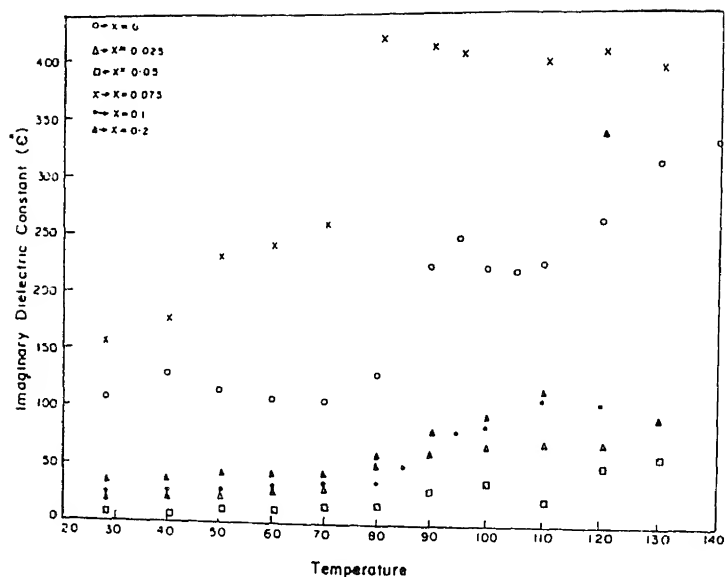


Figure 3. The variation of imaginary dielectric constant ( $\epsilon''$ ) with temperature at 1 kHz frequency. ( $\circ$ ,  $x = 0.0$ ;  $\Delta$ ,  $x = 0.025$ ;  $\square$ ,  $x = 0.05$ ;  $\times$ ,  $x = 0.075$ ;  $\bullet$ ,  $x = 0.1$ ;  $\blacktriangle$ ,  $x = 0.2$ )

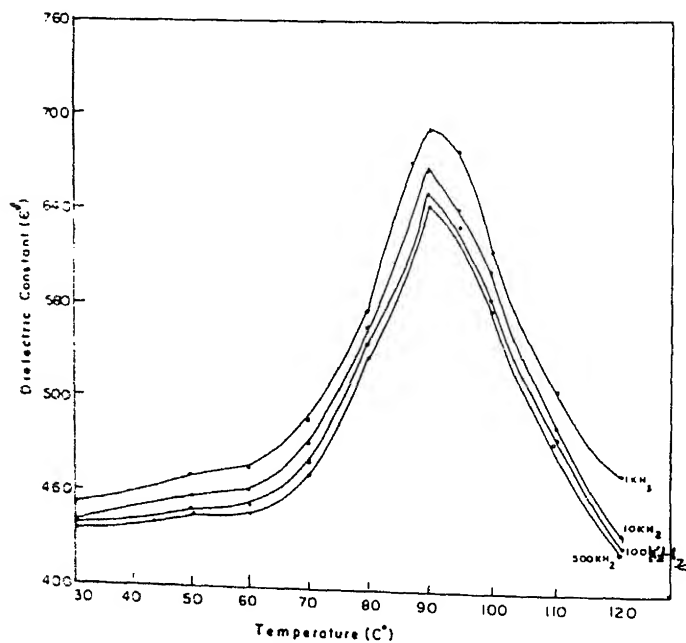


Figure 4. The variation of dielectric constant ( $\epsilon'$ ) with temperature at different frequencies ( $x = 0.1$ ).

## Acknowledgement

The authors thank the University Grants Commission, New Delhi, for financial assistance through a sponsored project.

## References

- Gallogher 1963 *J. Am. Ceram. Soc.* **46** 359  
Issac Robin A, Prasad Rao A V and Sambasiva Rao K 1992 *Indian J. Pure Appl. Phys.* **30** 267  
Lines M E and Glass A M 1977 *Principles and applications of ferroelectrics and related materials* (Oxford: Clarendon Press) p. 285  
Smolenskii G A and Isupov V A 1954 *Dokl. Akad. Nauk. SSSR* **97** 653  
Smolenskii G A 1970 *J. Phys. Soc. Jap.* **S28** 26  
Smolenskii G A 1984 *Ferroelectrics* **53** 129  
Subba Rao P S V, Sambasiva Rao K and Bhanumati A 1981 *J. Mater. Sci. Lett.* **6** 389  
Uchino K and Nomura S 1982 *Ferroelectrics Lett. Sect.* **44** 55

# Bulletin of Materials Science

## Editor

K J Rao

*Indian Institute of Science, Bangalore*

## Editorial Board

D C Agrawal, *Indian Institute of Technology, Kanpur*  
M F Ashby, *University of Cambridge, Cambridge, UK*  
S Banerjee, *Bhabha Atomic Research Centre, Bombay*  
D Chakravorty, *Indian Association for the Cultivation of Science, Calcutta*  
A K Chatterjee, *The Associated Cement Companies Limited, Thane*  
K L Chopra, *Indian Institute of Technology, Kharagpur*  
A D Damodaran, *Regional Research Laboratory, Trivandrum*  
B K Das, *National Physical Laboratory, New Delhi*  
H Herman, *State University of New York, Stony Brook, USA*  
B Ilschner, *Ecole Polytechnique Federale de Lausanne, Lausanne, Switzerland*  
Indira Rajagopal, *National Aerospace Laboratories, Bangalore*  
K T Jacob, *Indian Institute of Science, Bangalore*  
S K Joshi, *Council of Scientific and Industrial Research, New Delhi*  
S Mahajan, *Carnegie Mellon University, Pittsburgh, USA*  
R A Mashelkar, *National Chemical Laboratory, Pune*  
S B Ogale, *University of Poona, Pune*  
Pradip, *Tata Research Development and Design Centre, Pune*  
P Ramachandra Rao, *National Metallurgical Laboratory, Jamshedpur*  
S Ranganathan, *Indian Institute of Science, Bangalore*  
C N R Rao, *Indian Institute of Science, Bangalore*  
B B Rath, *Naval Research Laboratory, Washington, USA*  
R W Siegel, *Argonne National Laboratory, Argonne, USA*  
R Srinivasan, *Inter-University Consortium for DAE Facilities, Indore*  
G V Subba Rao, *Central Electrochemical Res. Inst., Karaikudi*  
G Sundararajan, *Defence Metallurgical Research Laboratory, Hyderabad*  
M S Valiathan, *Manipal Academy of Higher Education, Manipal*  
I K Varma, *Indian Institute of Technology, New Delhi*  
Vikram Kumar, *Solid State Physics Laboratory, Delhi*

## Editor of Publications of the Academy

V K Gaur

*C-MMACS, NAL, Bangalore*

### Subscription Rates

(Effective from 1989)

	Subscription Rates		
	1 year	3 years	5 years
All countries except India (Price includes AIR MAIL charges)	US\$ 100	\$ 270	\$ 400
India.....	1 year Rs. 75	10 years Rs. 400	

All correspondence regarding subscription should be addressed to **The Circulation Department**, Academy.

### Editorial Office

Indian Academy of Sciences, C V Raman Avenue,  
P. B. No. 8005, Bangalore 560 080, India

Telephone: 334 254  
Telex: 845-2178 A  
Telefax: 9180-334

© 1995 by the Indian Academy of Sciences. All rights reserved.

Cover: SEM showing fracture characteristics of LCF tested sample. For details, see p. 161

## A new phenomenon: the transient metastable graphitization of alloyed white iron

G I SILMAN\* and A A ZHUKOV\*\*

\*Materials Science at the Briansk Institute of Technology, 241000, Russia

\*\*Machine-Building Technology at the Vinnitsa Technical University, 286 021, Ukraine

MS received 28 September 1994

**Abstract.** In previous papers the case of stable-mottled irons has been analyzed. Hereunder a different case is looked into, when the mottled structure is a transient metastable state. Then the sequence of transformations during isothermal graphitizing annealing of some alloyed white irons can be summed up as follows:

'White' structure  $\rightarrow$  mottled structure  $\rightarrow$  'White' structure  
(metastable) (metastable) (stable)

In the transient mottled state the alloys have a much lower hardness and can be machined before the final heat treatment.

A simplified theoretical approach to this phenomenon is being offered.

**Keywords.** Cementite; graphite; stable states; metastable states; non-equilibrium crystallization.

### 1. Introduction

Alloyed white cast irons can have metastable white and mottled structures which transform to the more stable white structure. Such a transition is possible for the simple reason that alloyed white iron is chemically inhomogeneous because of non-equilibrium crystallization. Then in certain parts of the alloy we will have a predominance of carbide-stabilizing elements (of the Cr type) and here the initial 'white' state of the alloy will be a stable one. In other parts of the alloy there will be a predominance of graphitizing elements (of the Si type) and then the initial state of the alloy will be a metastable one. Because of low diffusivity of the mentioned elements (especially Cr) at temperatures of the solid state a short graphitizing anneal may provoke a partial graphitization in the second type of local microvolumes, while at long annealing times the system may become homogenized and will return to the 'white' state, but this time thermodynamically stable.

To such a qualitative explanation we can add the following theoretical approach, using 'geometrical' thermodynamics (Zhukov 1971, 1979; Silman *et al* 1983, 1986a).

### 2. Theory

Let us consider a simpler case of a ternary Fe–C–Cr system (figure 1). When the Cr-content is low these alloys may initially have a metastable austenite (A) + cementite (C) structure (chilled iron) at supercritical temperature ( $> A_1$ ), but after graphitizing annealing, the stable structure is austenite (A) + graphite (G). In figure 1 these alloys pertain to zone A + G.



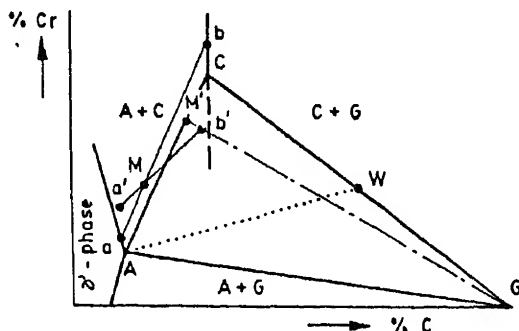


Figure 1. An isothermal section of the Fe-C-Cr phase diagram at a temperature under the solidus (schematic).

High-Cr alloys cannot graphitize and if austenite is still the high-temperature state of the solid (Fe, Cr) + <C> solution, they pertain to zone A + C on the left side of figure 1.

An intermediate state is described in figure 1 by the A + G + C tie-line triangle inside which we have the corresponding three-phase equilibrium. Here graphitization of an initially chilled alloy can proceed only to a certain extent. Along the A + C side of this triangle this extent is equal to zero, along the A + G side it is equal to 100% and along the median AW it is 50%. The mechanism of partial graphitization in the latter case is very simple. During the first stages of such a process part of the Cr-alloyed cementite is transformed into austenite. The partition ratio  $\langle Cr_C \rangle / \langle Cr_A \rangle$  is larger than 1.0 (because the A + C tie-lines have a positive slope in figure 1 and chromium is accumulated in the carbide phase). Therefore more <Cr> is transferred by diffusion into the latter until it is fully stabilized by this additional portion of chromium. So graphitization stops at 50% if the alloys' descriptive points lie along the AW median.

This theory does not take into account kinetic circumstances. The latter inevitably appear because the diffusivity of Cr and Fe atoms is much smaller than that of C atoms. It has been shown in earlier works that in the Fe-C-Cr system the equilibrium partition coefficient  $\langle Cr_C \rangle / \langle Cr_A \rangle$  in as-cast alloys rarely attains 70–80% of the equilibrium value (Silman *et al* 1983, 1986a). Then the following phenomenon takes place.

Let us suppose that in figure 1 alloy M is situated in the A + C zone and therefore pertains to a totally stable carbide system austenite 'a' + cementite 'b' (see tie-line ab drawn in figure 1 slightly to the left side of the AC tie-line of the AGC tie-line triangle). Now let us suppose that due to kinetic circumstances the partition of Cr between phases has not been fully attained (see tie-line a'b' in figure 1 drawn through point M with a smaller slope). Then point b' finds itself inside the AGC triangle and carbide b' is able to partly graphitize (the ratio between graphitized and ungraphitized zones may reach a maximum of  $M'C/AC$ ).

This partly graphitized state is a transient one. It can subsist only until the b' carbide phase remains impoverished in chromium.

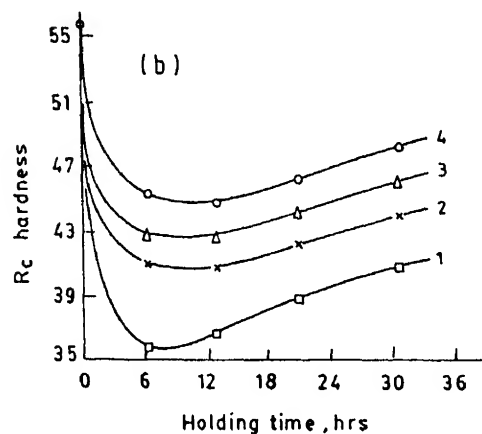
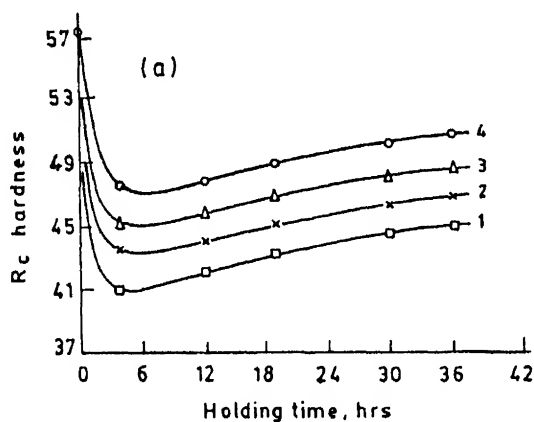
## Experimental

The chemical composition of the investigated alloys is given in table 1. Specimens with a 10 mm dia were cast into green sand moulds and in steel gravity die-moulds. In all cases the metal was chilled and there was no graphite in its microstructure.

The specimens were then subjected to graphitizing annealing in vacuum at 1050°C. The influence of annealing time on the  $R_c$  hardness of alloys (after cooling in air of the evacuated and sealed silica-glass ampoules) is shown in figure 2.

**Table 1.** Chemical composition of alloys.

No. of alloys	Content of elements (wt.%)			
	C	Si	Cr	Mn
1	3.19	1.86	1.86	0.72
2	3.29	1.85	2.11	0.72
3	3.38	1.93	2.58	0.93
4	3.38	2.07	2.90	1.03



#### 4. Discussion and conclusions

The shape of the curves obtained in figure 2 shows that a transient partly graphitized state has been attained in all cases after an intermediate annealing length of time (3 – 6 h). Continued annealing (up to 36 h) produced an opposite effect of carbidization of the partly graphitized metal.

These results were corroborated by metallography, which showed the appearance of temper carbon in the metal and then its disappearance.

The lowest hardness in the partially graphitized state was found in gravity die-cast metal of alloy 1. With a hardness of  $R_c 36$  this metal has an acceptable level of machinability. After machining the parts can be subjected to 'carbidizing' annealing which brings the hardness to  $> R_c 40$ . Or else we can use such alloys as heat-resistant, prone to age-hardening during exploitation.

The authors have patented in the former USSR the practical applications of the phenomena described above (Silman *et al* 1986b).

#### Acknowledgement

The authors wish to thank for attention to this work Prof. P Ramachandra Rao, Director, National Metallurgical Laboratory, Jamshedpur. One of the authors (AAZ) is indebted to the Tata Iron and Steel Co., for financial assistance.

#### References

- Silman G I, Zhukov A A and Zhavoronkov Yu V 1983 in *Questions of formation of metastable structures of alloys* (Ukraine: Dnepropetrovsk State University) pp. 161–172
- Silman G I, Zhukov A A and Zhavoronkov Yu V 1986a in *Thermodynamics of cast alloys structure formation* (Kiev: Institute of Foundry Problems) pp 104–107
- Silman G I, Zhukov A A, Zhavoronkov Yu V and Frolov M S 1986b Soviet Patent No. 246346 (special series)
- Zhukov A A 1971 *Geometrical thermodynamics of iron alloys* (Moscow: Metallurgia) pp 272
- Zhukov A A 1979 *Geometrical thermodynamics of iron alloys* (Moscow: Metallurgia) pp 232

## Spectroscopic characterization of polysilicon solar cells

S B MANAMOHANAN, R K GARG, S PARTHASARATHI and  
M M PRADHAN

National Physical Laboratory, Dr K S Krishnan Marg, New Delhi 110 012, India

MS received 6 June 1994

**Abstract.** Polysilicon ingots were made by float zone, using solar grade silicon (SOG-Si) prepared by acid leaching of metallurgical grade silicon (MG-Si). Impurity contents of the MG-Si and SOG-Si were analysed by emission spectroscopy and Fourier transform infrared spectroscopy. The main metal impurities Ca, Al, Fe, Cu, Mn, Mg, V, Ti and Zn and non-metal impurities C, O and B present in the two types of samples were determined. Elemental analysis for a knowledge of the impurity content is important to correlate its effect on the spectral response and diffusion length of minority carrier, and to determine solar cell process reliability. Spectral response and diffusion length for float zone silicon solar cell have been determined.

**Keywords.** Polysilicon; solar cell; spectral response; diffusion length.

### 1. Introduction

Effects of impurities in polysilicon on solar efficiency parameters have been studied by many investigators (Hunt and Dosaj 1979; Koliwad *et al* 1979; Davis *et al* 1980; Pivac 1988). The principal effect of the impurities is a degradation of spectral response (SR), lifetime and diffusion length (DL) (Davis *et al* 1980). Solar-grade silicon (SOG-Si) was prepared from metallurgical grade silicon (MG-Si); float zone (FZ) and Czochralski (CZ) were prepared from SOG-Si. The relevant impurities in these grades of materials were characterized by emission spectroscopy and FTIR spectroscopy. Spectral response and diffusion length were determined for cells fabricated from FZ material.

### 2. Experimental

#### 2.1 Emission spectroscopy

Emission spectroscopy characterization for R&D programmes enables a multielement scan at reasonable cost (Wang 1968, 1972). The emission spectra were recorded using a C Z Jena PGS 2 plane grating spectrograph. The excitation unit was a Universal arc pulse generator UBI 2. The spectra of the samples and SiO standards from SPEX were recorded on AGFA-Gevaert 34B50 photographic plates.

Four categories of samples  $S_1$ ,  $S_2$ ,  $S_3$  and  $S_4$  were taken.  $S_1$  represents MG-Si;  $S_2$ ,  $S_3$  and  $S_4$  represent SOG-Si after acid leaching with different acid concentrations. They were powdered and arced in specpure cavity electrodes from SPEX at 230 V, 8 A.

#### 2.2 FTIR spectroscopy

The spectra for oxygen and carbon concentrations were recorded with a Digilab FTIR spectrophotometer in the range  $2000\text{ cm}^{-1}$  to  $400\text{ cm}^{-1}$ . As per the requirement of

infrared measurements, the FZ and CZ silicon were taken in the form of wafers, and mirror polished on both sides to prevent scattering losses of the infrared.

### 2.3 Spectral response

The experimental set-up for the spectral response is the same as described elsewhere (Kishore *et al* 1989).

## 3. Results and discussion

### 3.1 Material characterization

Samples  $S_1$ ,  $S_2$ ,  $S_3$  and  $S_4$  were characterized by emission spectroscopy semiquantitatively for Ca, Fe, Al, Mg, V, Mo, B, Mn, Ti and Cu. The impurity concentrations are given in table 1. The table shows that the MG-Si ( $S_1$ ) is very impure. After acid leaching with aqua regia in three concentrations, the impurities in SOG-Si material ( $S_2$ ,  $S_3$ ,  $S_4$ ) so obtained go below ppm detection levels except for traces of Al, Mg and Ca.

Koliwad *et al* (1979) reported that the copper segregates at the grain boundary, and that the efficiency of fine-grained silicon solar cell increases with increase in copper content, whereas in coarse-grained silicon the efficiency decreases with increase in copper content.

The SOG-Si material was further processed by float zone to obtain FZ material, and by Czochralski to obtain CZ. The CZ and FZ materials were characterized by FTIR spectroscopy for oxygen and carbon concentration (Pivac 1988). Oxygen is important, as the electrical conductivity of the material depends on oxygen concentration (Mead and Lowry 1980; Newman 1986; Pizzini *et al* 1990). Table 2 shows that the oxygen concentration in FZ material is less than half of the oxygen concentration in CZ material.

**Table 1.** Emission spectroscopic data for four samples of silicon (MG-Si and SOG-Si).

Element	MG-Si	SOG-Si (after acid leaching)		
	$S_1$	$S_2$	$S_3$	$S_4$
Ca	3000	300	100	50
Fe	2000	ND	ND	ND
Al	400	200	50	20
Mg	50	30	20	5
V	ND	ND	ND	ND
Mo	ND	ND	ND	ND
B	ND	ND	ND	ND
Mn	500	ND	ND	ND
Ti	500	ND	ND	ND
Cu	50	ND	ND	ND

Table 2. FTIR analysis of silicon (CZ and FZ) samples.

Samples	Carbon	Oxygen
Silicon (CZ)	$5.83 \times 10^{17}$ atom/cm <sup>3</sup>	$8.94 \times 10^{17}$ atom/cm <sup>3</sup>
Silicon (FZ)	$6.60 \times 10^{17}$ atom/cm <sup>3</sup>	$4.18 \times 10^{17}$ atom/cm <sup>3</sup>

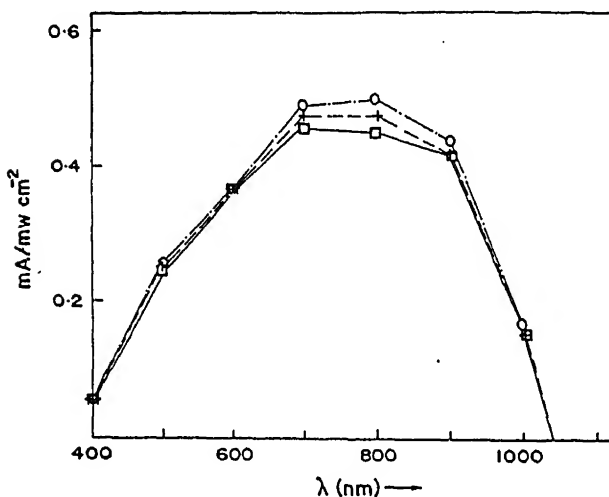


Figure 1. Spectral response curves for FZ silicon solar cells from bottom (-□-□-□-□-), middle (-+--+--+--) and top (-○-○-○-○-) portions.

### 3.2 Device evaluation

The photocurrent measurement at each wavelength relative to the number of incident photons at that wavelength is the spectral response (SR) (Stokes and Chu 1977). SR provides us the most important diagnostic information for solar cell efficiency next to the  $I$ - $V$  characteristics (Gummel and Smits 1990). An accurate measurement of SR may be used to study cell quantum yield, degradation of minority carrier diffusion length (MCDL) and base material inhomogeneities (Wendy 1981).

The diffusion length (DL) can be obtained from SR values (Agarwala *et al* 1980). MCDL is an important parameter for optimizing the solar cell efficiency in the cell fabrication process. The DL is determined by plotting  $\lambda/I_{sc}$  against the reciprocal absorption coefficient  $\alpha^{-1}$  of silicon, where  $I_{sc}$  is the short circuit current.  $I_{sc}$  is required in the evaluation of cells under development and production and also in the design of photovoltaic systems.

Spectral response measurements were done on three polysilicon solar cells fabricated as described by Jain *et al* (1981). The material for one solar cell was drawn from the bottom portion of the FZ material, the second cell from the middle, and the third from the top. SR curves are shown in figure 1. The curves show that for the bottom portion, the cell has the lowest SR indicating that the impure fraction has accumulated at the bottom. The top portion cell has a higher SR indicating a higher

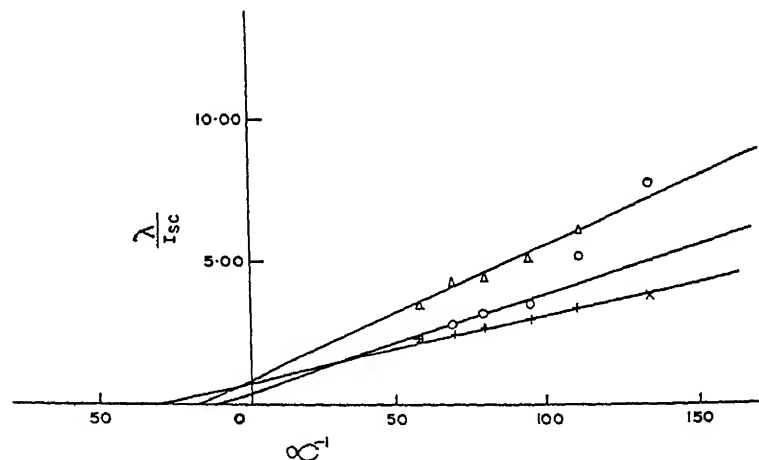


Figure 2. Minority carrier diffusion length (negative intercepts of  $\alpha^{-1}$  axis) for FZ from bottom (O-O-O-O-O), middle ( $\Delta$ - $\Delta$ - $\Delta$ - $\Delta$ ) and top (-x-x-x-x-) portions.

purity. Thus there is a gradation of purity increasing from bottom to the top of the material. The diffusion lengths DL of the above cells are shown in figure 2 as intercepts in the negative axis of  $\alpha^{-1}$ . The value of DL is 25  $\mu\text{m}$  for the top portion, 13  $\mu\text{m}$  for the middle and 10  $\mu\text{m}$  for the bottom portion cell.

In conclusion, solar cells with higher spectral response and higher efficiencies can be obtained from the upper portion of FZ silicon material.

## References

- Agarwala A, Trivedi V K, Agarwala S K and Jain S C 1980 *Solid-State Electron.* **23** 1021
- Davis J D, Rohatgi A, Hopkins R H, Blais P D, Choudhury P Rai, McCormick J J and Mallon J 1980 *IEEE Trans Electron Devices* **ED27** 677
- Gummel H K and Smits F M 1990 *Solar Cells* **29** 103
- Hunt L P and Dosaj V D 1979 *Proc. 2nd E.C. Photovoltaic Solar Energy Conference* p. 98
- Jain G C, Singh S N, Kotnala R K and Arora N K 1981 *J. Appl. Phys.* **52** 4821
- Kishore R, Shastri V D P and Manamohan S B 1989 *4th International Photovoltaic Science & Conference, Australia*
- Koliwad K M, Daud T and Liu J K 1979 *Proc. 2nd E.C. Photovoltaic Solar Energy Conference* p. 71
- Mead D G and Lowry S R 1980 *Appl. Spectrosc.* **34** 167
- Newman R C 1986 *Proc. MRS Symposium* p. 403
- Pivac B 1988 *J. Phys. D (Appl. Phys.)* **21** 1241
- Pizzini S, Gandolfi A, Farina S and Branchforti M 1990 *Mater. Sci. Eng.* **B7** 69
- Stokes E D and Chu T C L 1977 *Appl. Phys. Lett.* **30** 425
- Wang M S 1968 *Appl. Spectrosc.* **22** 761
- Wang M S 1972 *Appl. Spectrosc.* **26** 364
- Wendy Ann Orr 1981 *Characterization of materials and electrical properties of polycrystalline silicon for photovoltaic applications*, Ph.D. Thesis, p. 34

## Thermoluminescence of cement

R K GARTIA, S INGOTOMBI and S DORENDRAJIT SINGH

Department of Physics, Manipur University, Imphal 795 003, India

MS received 4 June 1994; revised 14 November 1994

**Abstract.** Cement is found to be a thermoluminescent material. The glow curves of ordinary portland cement obtained from two different sources are found to be qualitatively similar. White cement (J K Brand) exhibits intense thermoluminescence (TL) compared to Birla white brand. The emission of J K white cement seems to be mainly due to Mn impurities which enters the product through limestone, the major ingredient in the preparation of cement. The possible use of TL as a spectroscopic technique to characterize cement is discussed.

**Keywords.** Thermoluminescence; cement; spectroscopic characterization.

### 1. Introduction

Thermoluminescence (TL), the emission of light following the previous absorption of energy from radiation, is a phenomenon which is exhibited by a large number of insulating and semiconducting solids. It has found wide application in practical areas like radiation dosimetry, dating of archaeological and geological materials (Horowitz 1983; Aitken 1985; McKeever 1985). However, several novel and at first sight, unlikely applications have also appeared in literature from time to time. Amongst such attempts relevant to the present study are the possible applications of TL in quality control in industry and forensic science (Nambi 1977). Nambi (1977) gave examples of the fact that in principle TL could be used in quality control of industrial products like glass, ceramics and semiconductor. Keeping these facts in mind the TL response of cement exposed to gamma radiation has been tested.

Though the principal constituent of cement is limestone, there are a variety of cements differing in chemical characteristics which are used for specific purposes. In this investigation we have studied portland cements from only three sources viz. Hundung (Manipur), Bokajan (Assam) and Gotan (Rajasthan). The possible applications of TL of cement are discussed keeping the experimental observations of the glow curves of the material.

### 2. Experimental

#### 2.1 TL recording system

All the TL curves are recorded using the commercial recording system model TL 1404 (Indotherm Instruments Pvt. Ltd., Bombay). It is a system capable of providing linear heating at any desired rate that can be varied continuously from 10°C/min to 1000°C/min. The sample can be heated up to 600°C. However, in the present case the sample is heated to a maximum of about 450°C to avoid the undesirable black body radiation. The heating rate in most cases is about 175 to 200°C/min. The glow curves are recorded on a two pen strip chart recorder.



## 2.2 The material

Cements from three sources are studied. They are (i) Portland Cement of the Hundung Mini Cement Plant (Ukhrul Dist., Manipur), (ii) two varieties of portland cements from the Bokajan cement factory (Assam) commercially sold as portland cement (PC) and ordinary portland cement (OPC) and (iii) white portland cement having rapid hardening properties obtained from the J K white cement works (Gotan, Dist. - Nagpur, Rajasthan) and the Birla white portland cement works (Kharia Khangar, Dist., Jodhpur).

## 2.3 The source of excitation

Excitation of the cements is done by irradiating it with  $\gamma$ -rays obtained from  $\text{Co}_{60}$  source with dose rate of 0.5675 Gy/s. In all the cases reported here the dose of radiation is 4 kGy.

## 3. Results and discussions

TL curves of cement irradiated with a dose of 4 kGy are shown in figure 1. The glow curve of Hundung cement exhibits four glow peaks around 120, 150, 240 and 325°C for a linear heating rate ( $\beta = 200^\circ\text{C}/\text{min}$ ). The glow curves of two varieties of Bokajan cement also exhibit four peaks around the same temperature range. However, in the later case in one sample the 150 and 240°C peaks are highly overlapped showing a flat zone over a temperature range of 150 to 270°C (figure 1, curve b). TL curves of

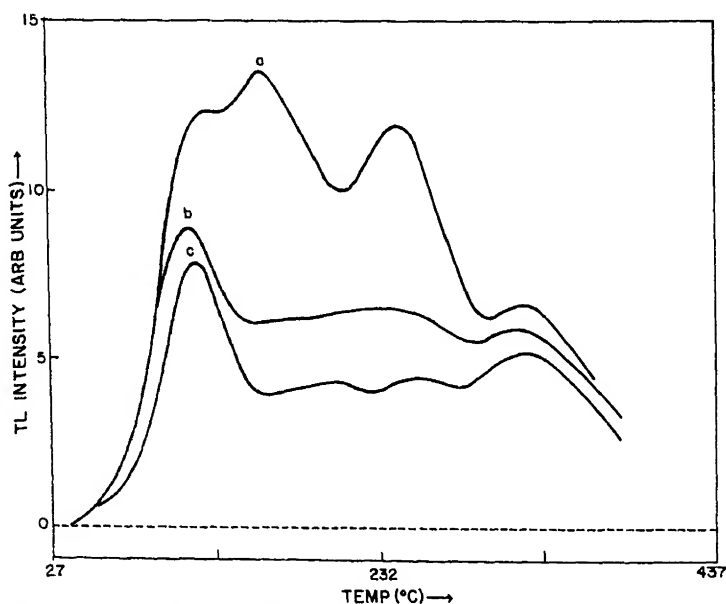


Figure 1. TL curves of different varieties of cement irradiated with 4 kGy. (a) Hundung cement, (b) Bokajan cement (PC), (c) Bokajan cement (OPC).

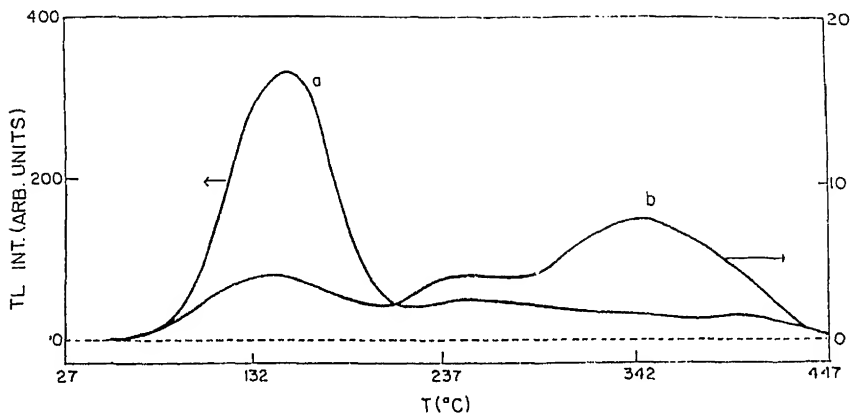


Figure 2. TL curves of J K white (curve a) and Birla white (curve b) cements irradiated with 4 kGy ( $\beta = 180^\circ\text{C/min}$ ).

J K white cement and Birla white cement recorded under almost similar condition exhibit a peak in the temperature range  $140\text{--}155^\circ\text{C}$  along with two peaks (figure 2). TL curve of J K white cement (curve a, figure 2) has a very intense peak at around  $155^\circ\text{C}$  with two weak peaks around 225 and  $400^\circ\text{C}$ . On the other hand Birla white cement (curve b, figure 2) shows three peaks at around 142, 242 and  $349^\circ\text{C}$  in such a way that the third peak around  $349^\circ\text{C}$  is more intense than the first peak at  $142^\circ\text{C}$ . These results show that cement can be termed as a thermoluminescent material exhibiting number of TL peaks between room temperature ( $27^\circ\text{C}$ ) to  $450^\circ\text{C}$ . Now the question that arises is: what are the possible applications of the phenomenon of TL that is exhibited by this commonly used building material.

The first criteria required for any possible application of TL is the stability of the signal. This has been checked for the Hundung cement (as a representative of ordinary variety) and the J K white (as a representative of white variety). Figure 3 shows the effect of room temperature ( $27^\circ\text{C}$ ) fading of TL of Hundung cement. As expected the lower temperature peaks viz. 120 and  $150^\circ\text{C}$  peaks decrease in intensity but the higher temperature peaks viz. 240 and  $325^\circ\text{C}$  peaks are quite stable showing  $\approx 14\%$  loss when stored for three days at room temperature (figure 3). The fading is still less ( $\approx 4\%$ ) for the higher temperature peak in case of white cement (figure 4). In short these experiments demonstrate that the higher temperature TL peaks of cement are quite stable when stored at room temperature.

Though as early as 1938 the application of TL in the control of feldspars in ceramic product has been described (Nambi 1977), such attempts have not received attention of the industries. Recently it has been demonstrated that if properly calibrated the technique of TL can make it a simple but powerful tool for estimating the level of mixed phases in feldspar (Prescott *et al* 1990). Ordinary portland cement consists essentially of tricalcium silicate, dicalcium silicate, tricalcium aluminate; and tetracalcium aluminato ferrites. Since the present work has shown that cement is thermoluminescent showing rather consistent glow pattern for samples collected from two different sources (figure 1) its TL behaviour may also find applications in estimating the mixed phases as shown in the case of feldspar. It might also be possible to ascertain whether a particular sample has come from a known source which may find application in

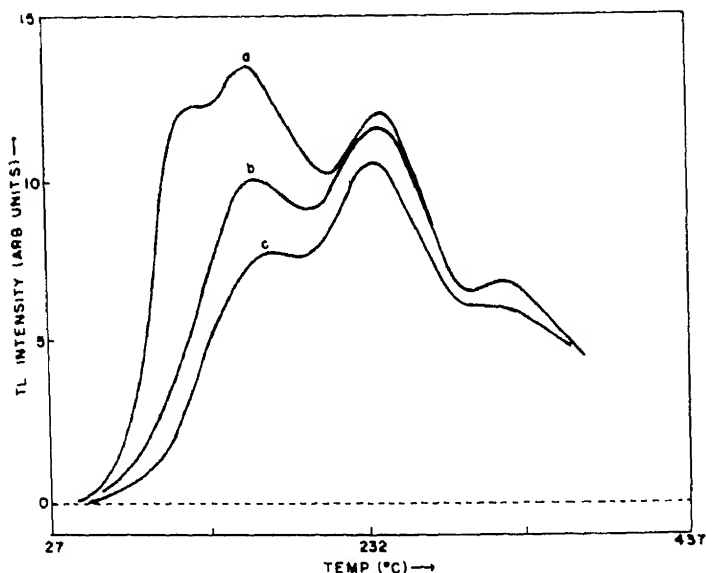


Figure 3. Effect of room temperature (27°C) fading of TL of Hundung cement. Curve 'a' is a TL glow curve with no fading. Curves 'b' and 'c' are TL glow curves with 1 and 3 days fading ( $\beta = 200^\circ\text{C}/\text{min}$ ).

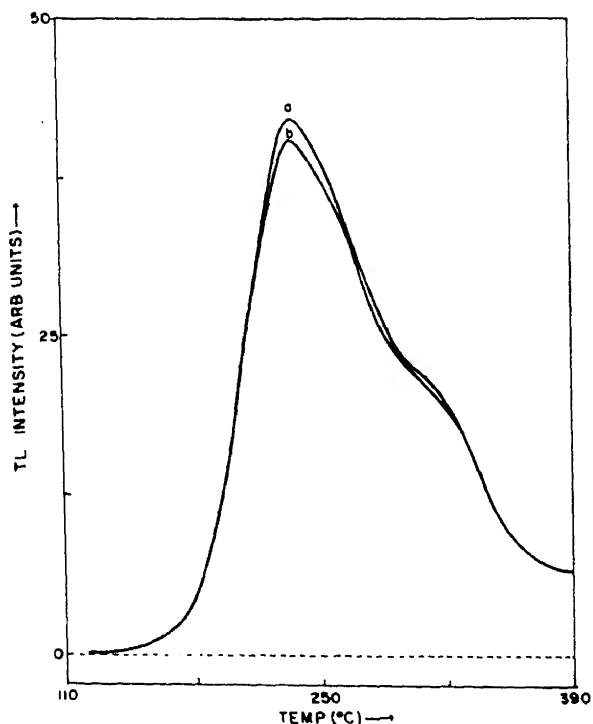
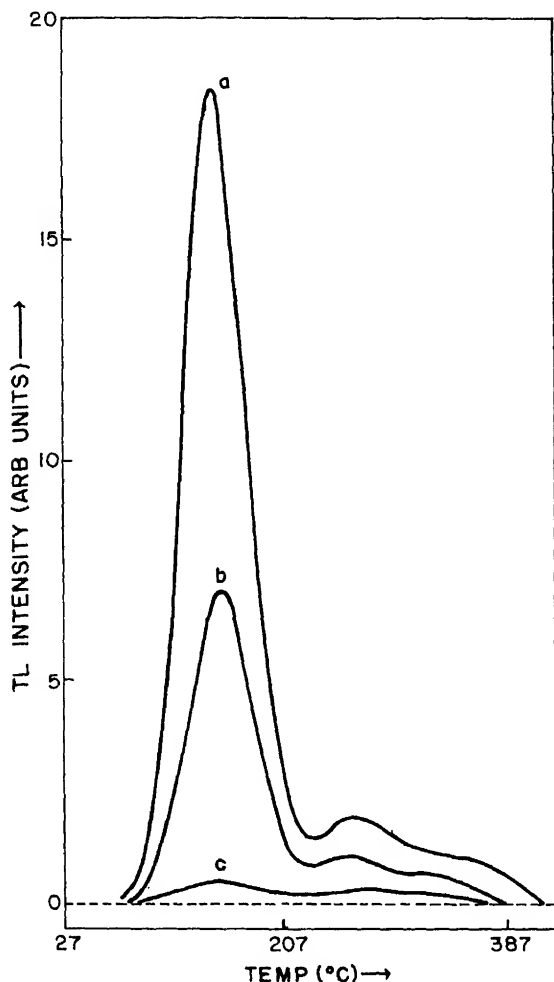


Figure 4. Effect of room temperature (27°C) fading of high temperature TL cement irradiated with 4 kGy of gamma radiation. Curve 'a' is with no fading and curve 'b' is with 3 days fading (In both cases the low temperature peak has been thermally cleared).

detecting forgery (an area of forensic science). The present preliminary study of cement is hoped to pave a way in that direction.

The glow curves of most materials are complex (McKeever 1985). In that sense the glow curves of cement, if one takes into its various constituent compounds, is rather simple. This is more so in case of white cement. Its relative high sensitivity has tempted us to investigate its glow curve in more detail. Because of the intense glow (orange-red as seen by naked eyes), it has been possible to examine the TL emission with the help of filters. It has been found that most of the emission is in the red region though emission is also found in the green and blue regions. The glow curve of white cement recorded using different filters is shown in figure 5. The TL emission of white cement occurring mostly in red region can be explained on the basis that limestone is one of the major input in cement production and its TL emission consists of a broad peak centred around 5950–6350 Å depending upon the



**Figure 5.** Monochromatic TL curves of white cement ( $\beta = 180^\circ\text{C}/\text{min}$ ). Curves a, b and c correspond to TL recorded using red, green and blue filters respectively.

Mg and Mn constituents (Sankaran *et al* 1983). This emission has been attributed essentially to Mn impurity which is a well known luminescent centre in many phosphors. Therefore, the TL emission in cement most probably takes place at Mn impurity site which enters the product through the use of limestone.

Ordinary portland cement is grey in colour because of the presence of iron oxide. On the other hand white cement contains lesser amount of iron oxide. White cement is manufactured in the same way as ordinary portland cement except using China clay (Kaolin) together with limestone free from certain specified impurities. The results of the chemical analysis of the samples used in the present work is shown in table 1

Table 1. Chemical analysis of cements used.

Sample	LOI (%)	SiO <sub>2</sub> (%)	Fe <sub>2</sub> O <sub>3</sub> (%)	Al <sub>2</sub> O <sub>3</sub> (%)	CaO (%)	MgO (%)
Hundung OPC (Manipur)	2.60	19.50	4.05	6.50	61.00	1.60
Bokajan PPC (Assam)	10.35	21.07	3.90	5.10	52.72	1.70
Bokajan PPC (Assam)	4.45	21.09	4.05	5.20	58.00	2.34
J K white (Gotan, Rajasthan)	7.43	21.93	0.33	5.08	59.11	2.30
Birla white (Jodhpur)	2.57	21.87	0.31	5.24	63.99	1.17

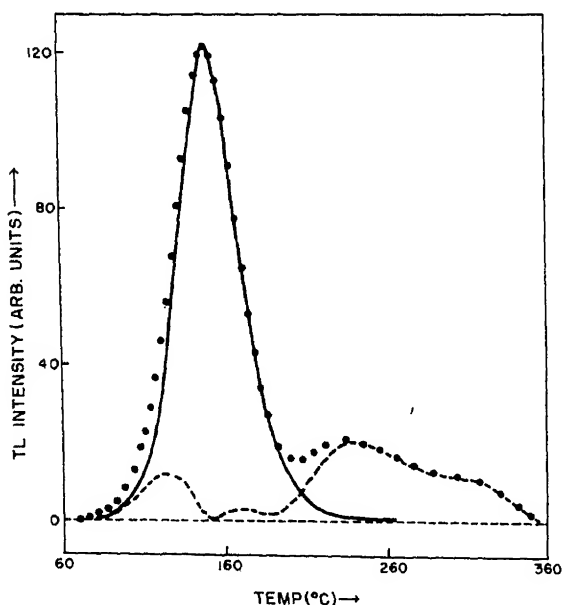


Figure 6. Curve fitting of the most intense TL peak of white cement ( $\beta = 90^\circ\text{C}/\text{min}$ ). ●, experimental curve; ---, numerically generated curve ( $E = 1.2\text{ eV}$ ,  $s = 2.2 \times 10^{13}/\text{s}$  and  $b = 2.0$ ); ----, difference curve showing the existence of additional peaks.

which shows that white cement contains iron oxide though it is one order of magnitude less compared to ordinary cement. Iron is a well known quencher. Since TL of Birla white cement is less intense (one order of magnitude) than that of J K white cement though they contain similar amount of  $\text{Fe}_2\text{O}_3$ , it is doubtful if iron impurities play any definite role in TL of cement. This is possible if iron is present in the  $\text{Fe}_2\text{O}_3$  phase and not as an impurity.

TL of a complex system like cement is expected to be highly complex. Surprisingly this is not so (figures 1 and 4). Analysis of glow curve emitted by more than one kind of compound is of no meaning. However, if one can fit any glow peak to simple models (Randall and Wilkins 1945; Garlick and Gibson 1948; Chen 1969), one can conclude that the particular peak most probably has its origin to a specific constituent. Keeping this in mind the intense peak of white cement has been analyzed. The irradiated sample is stored for three days to allow the unstable component to decay. TL of such a sample is recorded with  $\beta = 90^\circ\text{C/s}$ . The intense peak occurs at  $150^\circ\text{C}$  (figure 6). The symmetry factor (also known as shape factor) of the peak is found to be 0.52 showing that it follows second order kinetics (Chen 1969). Curve fitting of this peak using the second order kinetics equation (Garlick and Gibson 1948) yields  $E = 1.2\text{ eV}$ ,  $s = 2.2 \times 10^{13}/\text{s}$  (figure 6). This demonstrates that this peak is elementary in nature originating from a specific constituent of cement which needs to be identified. This requires further work.

#### 4. Conclusions

The results can be summarized as follows:

- (i) Cement is a thermoluminescent material.
- (ii) Since the TL of ordinary variety of cement obtained from two different sources are qualitatively similar, TL may be used as a spectroscopic technique to characterize the material, which may find use in quality control and forensic science.
- (iii) Mn impurity seems to be the luminescent centre. This is certain at least in the case of white cement.

#### References

- Aitken M J 1985 *Thermoluminescence dating* (London: Academic Press)  
Chen R 1969 *J. Electrochem. Soc.* **116** 1254  
Garlick G F J and Gibson A F 1948 *Proc. Phys. Soc.* **A60** 574  
Horowitz Y S 1983 (eds) *Thermoluminescence and thermoluminescent dosimetry* (Florida: CRC Press) p. 1  
McKeever S W S 1985 *Thermoluminescence of solids* (London, New York: Cambridge University Press)  
Nambi K S V 1977 *Thermoluminescence: Its understanding and applications* (Sao Paulo, Brasil: INF, IEA, 54 CPRD - AMD 1 Inst. de Energia Atomica)  
Prescott J R, Akbar R A and Gartia R K 1990 *Spectroscopic characterization of minerals and their surfaces* (eds) Leila M Coyne, W S Stephen, S W S McKeever and David F Blake, ACS Symposium Series 415 (Washington: American Chemical Society) Ch. 10  
Randall J T and Wilkins M H F 1945 *Proc. R. Soc.* **A184** 366  
Sankaran A V, Nambi K S V and Sunta C M 1983 *Proc. Indian Natl. Sci. Acad.* **49** 18



## The rate of corrosion of concrete reinforcement and possibilities of its mathematical modelling

V ŽIVICA

Institute of Construction and Architecture of the Slovak Academy of Sciences, Bratislava, Slovak Republic

MS received 6 May 1994; revised 20 October 1994

**Abstract.** The paper describes a method for the mathematical modelling of steel reinforcement corrosion rate. This method is based exclusively on experimental results and expression of the influence of significant corrosion factors in the form of functional relations. The method takes into account the reality of the effects of corrosion factors, their contingency and complexity, and various circumstances occurring in practice. It represents one way towards the development of methods for the prediction of service life of reinforced concrete and structures.

**Keywords.** Concrete reinforcement corrosion; corrosion rate; corrosion factors; relative humidity; chloride concentration; mathematical modelling.

### 1. Introduction

The design of concrete structures is usually based on empirical relationships between material and properties of concrete and experience with the behaviour of building materials. A new approach of concrete design is based on the prediction of its service life. Though this approach is not often used it has increasing importance in the design of concrete. The motivating factors are the increasing air pollution in recent years, importance of energy and material saving, and last but not least the growing number of cases of damage in old concrete structures and rising demands to calculate the service life of reinforced concrete structures. The steadily increasing interest in the service life prediction of concrete structures is shown for example in the papers by Müller (1985), Masters (1986) and Eurin (1988).

One approach is to obtain quantitative values about service life of concrete structures for mathematical models based on the chemistry and physics of degradation processes (Clifton 1990). Several models have been developed for prediction of service life of concrete subjected to degradation processes. Atkinson developed a model for leaching degradation (Atkinson 1985). This author and Odler and Gasser (1988) developed a model based on the mechanism of sulphate attack. The range of usefulness of any mathematical model depends upon the adequacy of the conceptual models upon which it is based. The adequacy and the success of the modelling can be limited by the following factors: (i) problems of application of theoretical data and relationships to real, heterogeneous concrete systems and (ii) simplification of degradation processes and taking into consideration only some degradation rate factors. However, it is a well-known fact that deterioration rate of concrete is a result of the interaction of the aggressive of medium and resistance of concrete. These factors alone represent a set of several partial factors.

An approach exclusively based on experimental results of studies on the influence of individual factors of aggressivity of medium and concrete resistance on the corrosion



rate allows the possibility of avoiding the shortcomings of modelling and increasing its usefulness. Morinaga (1990) chose this approach for prediction of service life of reinforced concrete structures.

Jambor's method also belongs to the category of mathematical modelling of deterioration, which is based on experimental results (Jambor *et al.* 1983). According to this method, the degree and rate of deterioration of concrete can be expressed as a product of functional relations, which themselves express the influence of the individual factors on the destruction processes. The method represents an open system, which enables the gradual completion of the functional relations product. This is a significant point in the preference of the method, because it enables increasing the capability for various circumstances that occur in practice.

It is assumed that for the utilization of the method in practice, at least a knowledge of the influence of the most important factors of deterioration process and its rate, and the expression of their influence in corresponding functional relations are required.

The significance of corrosion of steel reinforcement in the service life of reinforced concrete is indisputable. For prediction of service life of reinforced concrete also several mathematical models have been developed. These models take into consideration the depassivation rate expressed by the penetration rate of aggressive substances, chlorides,  $\text{CO}_2$  or other aggressive gases—through the concrete cover to the reinforcement surface (Grunau 1970; Alekseev 1978). These models allow determination of the approximate time of depassivation of reinforcement or the initiation of corrosion. However, information about the actual state of the reinforcement and the corrosion rate is missing. This is an important shortcoming.

Knowledge of the character of reinforcement corrosion enables for its quantitative description and expression of corrosion rate a realistic parameter which represents the quantity of corroded steel. This parameter enables determination of a significant criterion for the state of reinforcement, the value of cross-section decrease of reinforcement, which represents an important parameter for evaluation of the service life of reinforcement concrete.

In connection with mathematical modelling and prediction of service life of reinforced concrete, attention is being increasingly paid to the utilization of electrochemical methods. On the basis of results with the so-called electrochemical cell a model of a two-step mechanism has been developed by Tuutti (1971) for corrosion of reinforcement steel in concrete.

The object of this paper is an attempt to model the rate of concrete reinforcement corrosion mathematically on the basis of experimental results.

## 2. Experimental

Mortar prisms  $40 \text{ mm} \times 40 \text{ mm} \times 60 \text{ mm}$  with embedded corrosion sensors for improved method of electrical resistance measurement (IER method) were used in the study. The method was improved by developing a so-called "corrosion sensor". This sensor is embedded in the cement composite test specimen or in the concrete structure and enables one to check the condition of reinforcement. The structure of the sensors excludes disturbing effects during the measurement and increases the sensitivity of the method and the reliability of the test results. The method is described in detail elsewhere (Živica 1993).

The composition of the mortars used was as follows: Portland cement: sand 1:3, w/c 0.6, portions of  $\text{CaCl}_2$  admixture 0, 1, 2, 4 and 8% based on cement.

After moulding, the test specimens were cured for 24 h at relative humidity (RH) of 95%. After this time the curing regime was as follows: a part of the test specimens were cured at RH of 95% and the rest at RH of 65 and 35%. The temperature of curing was  $20 \pm 2^\circ\text{C}$ .

The cement used was Portland cement class 400 according to the Standard ČSN 72 2121 corresponding to the recommendation ISO-R597. The sand used was silica sand according to Standard ČSN 72 1208 corresponding to the recommendation ISO/R 697-1968. For preparation of the corrosion sensors steel sheet Class 11 373 according to Standard ČSN 41 1373 was used.

For the study of corrosion rate of steel the IER method was used. Further the method of electrode potential using the calomel saturated reference electrode (SCE) was used (Yambor and Živica 1982).

### 3. Results and discussion

The values of changes of electrical resistance of sensors ( $\Delta R$ ) and their electrode potential (EP) and weight of mortar test specimens are given in table 1. In table 2 the results of visual inspection of the corrosion sensors after the test are given. The test mortar prisms were crushed and the state of the embedded sensors was evaluated.

The results obtained show that EP values of the sensors at the beginning of the tests were in good relation to the mortar composition as indicated by the EP value of  $-254\text{ mV}$  (SCE), the corrosively passive state of steel in mortar without  $\text{CaCl}_2$  admixture, and by EP values of  $-447$ ,  $-491$ ,  $-512$  and  $-513\text{ mV}$  (SCE), the corrosively active state of steel in mortars with 1, 2, 4 and 8%  $\text{CaCl}_2$  admixture respectively. With time the EP values decreased with good correlation between EP values and  $\text{CaCl}_2$  content in mortars. From the point of view of corrosion process of steel it is important to determine the duration of the corrosively active state of steel or of the EP values of the sensors in corrosively active range i.e. above  $-300$  to  $-350\text{ mV}$  (SCE). The results show that in the mortar with 1%  $\text{CaCl}_2$  admixture the corrosively active state existed for only a very short time of under 28 days. A highly passive EP value of  $-240\text{ mV}$  (SCE) was reached after 28 days of curing. In the mortars with 2 and 4%  $\text{CaCl}_2$  admixture, the corrosively active state of steel lasted from 56 to 70 days, but with  $\text{CaCl}_2$  at 8% the corrosively active state remained throughout the duration of the test, i.e. 84 days, and EP was  $-478\text{ mV}$  (SCE) at the end of the test.

The obtained EP values are in good relation with the  $\Delta R$  values. Increase in  $\Delta R$  indicates steel corrosion in  $\text{CaCl}_2$  mortars with corrosively active EP values. The intensity of the increase in  $\Delta R$  values or the corrosion rate of steel was proportionate to the level and duration in corrosively active range of EP values. It can be seen that with time the  $\Delta R$  values of sensors embedded in mortars with  $\text{CaCl}_2$  admixture increased, indicating steel corrosion. The intensity of  $\Delta R$  increased and curing time decreased.

Figure 1 confirms the role of relative humidity (RH) in the electrochemical state of embedded steel and its corrosion rate. Below RH 65% corrosion rate is negligible, but above this value there is a significant increase in corrosion rate. The turning

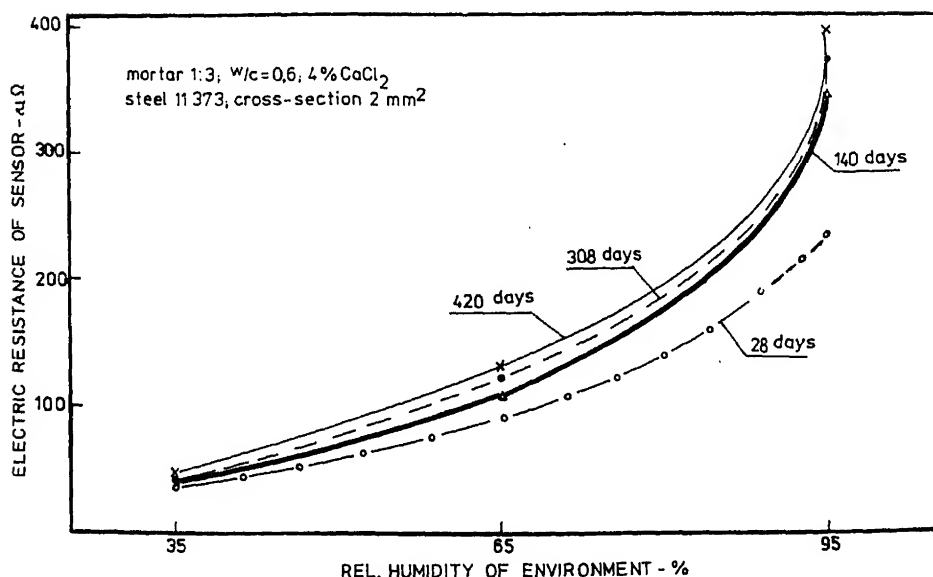
Table 1. Weight of mortar test specimens, and electrode potential (EP) and change of electrical resistance ( $\Delta R$ ) of corrosion sensors.

d of lar e g ays	Without admixture				1% CaCl <sub>2</sub> admixture				2% CaCl <sub>2</sub> admixture				4% CaCl <sub>2</sub> admixture				8% CaCl <sub>2</sub> admixture			
	Weight (g)	EP(SCE) (mV)	$\Delta R$ ( $\mu\Omega$ )	Weight (g)	EP(SCE) (mV)	$\Delta R$ ( $\mu\Omega$ )	Weight (g)	EP(SCE) (mV)	$\Delta R$ ( $\mu\Omega$ )	Weight (g)	EP(SCE) (mV)	$\Delta R$ ( $\mu\Omega$ )	Weight (g)	EP(SCE) (mV)	$\Delta R$ ( $\mu\Omega$ )	Weight (g)	EP(SCE) (mV)	$\Delta R$ ( $\mu\Omega$ )		
	555.72	-264	—	583.60	-447	—	576.57	-491	—	552.55	-512	—	572.53	-513	—	—	—	—		
	551.20	-153	+27	580.67	-240	+36	574.78	-355	+160	552.80	-305	+234	574.28	-499	+322	—	—	—		
	552.50	-122	+26	580.33	-224	+47	574.58	-340	+215	556.50	-260	+244	574.34	-502	+426	—	—	—		
	553.00	-154	+26	580.01	-222	+52	574.61	-343	+250	557.35	-308	+250	574.48	-475	+510	—	—	—		
	553.08	-142	+26	580.07	-224	+59	574.76	-279	+267	557.30	-331	+302	574.77	-469	+580	—	—	—		
	558.66	-143	+26	579.87	-214	+63	574.73	-256	+287	557.40	-275	+327	574.84	-478	+673	—	—	—		

ing. relative humidity 95%, 20  $\pm$  2°C

**Table 2.** Results of visual inspection of the corrosion sensors and final values of electrical resistance of the sensors.

Relative humidity (RH) and time of curing	Kind of mortar			
	Without admixture		4% CaCl <sub>2</sub> admixture	
	Corroded area (%)	$\Delta R$	Corroded area (%)	$\Delta R$
RH 95% 644 days	3.5	+ 38.7 (448 days)	18	+ 451
RH 65% 644 days	0	- 0.30	89	+ 145
RH 35% 642 days	0	+ 0.20	30	+ 45

**Figure 1.** Relationship between electrical resistance of corrosion sensors and relative humidity of environment.

point around RH of 65% is in good accordance with the well-known RH values given elsewhere.

The influence of RH of environment on steel corrosion rate can be expressed by the functional relation (FR)

$$F_H = e^{a_h} e^{b_h H}, \quad (1)$$

where  $F_H$  is FR of degree of corrosion of steel in concrete with RH of the environment,  $H$  is relative humidity of environment in %, and  $a_h$ ,  $b_h$  are experimental coefficients.

$$F_H = e^{2.87e^{0.0068T}} \quad (2)$$

The course of the marked curves in figure 2, expressing the dependence of  $\Delta R$  values on curing time, can be expressed by the functional relation

$$F_T = a_T T^{b_T}, \quad (3)$$

where  $F_T$  is FR of degree of corrosion of steel with curing time of concrete in the given environment.  $T$  is curing time (days), and  $a_T$  and  $b_T$  are experimental coefficients. This FR was expressed as a supplementary coefficient for the  $F_H(1)$ . After the numbering of the functional relation (3), the following equation was obtained for the curve for RH value of 95% in figure 2:

$$F_T = 0.50 T^{0.21}. \quad (4)$$

The dependence of  $\Delta R$  values of sensors on  $\text{CaCl}_2$  content in mortar is shown in figure 3. This is given by the functional relation

$$F_C = \frac{C}{a_c + b_c C} + c_c, \quad (5)$$

where  $C$  is the proportion of  $\text{CaCl}_2$  admixture in mortar expressed in percentage, based on cement content, and  $a_c$ ,  $b_c$ ,  $c_c$  are experimental coefficients.

After the numbering of function relation (5), the following equation was obtained

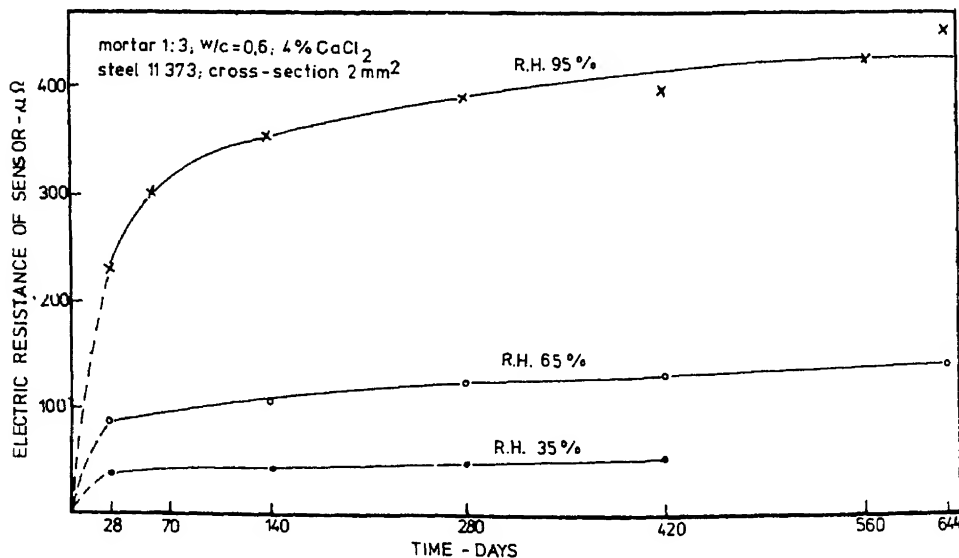


Figure 2. Relationship between electrical resistance of corrosion sensors and time of curing of the test specimens.

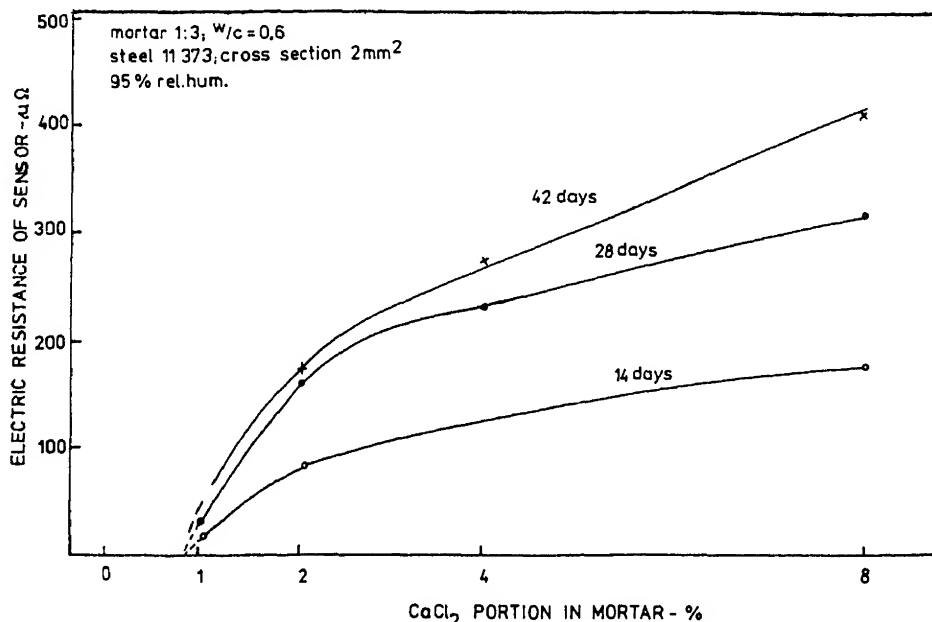


Figure 3. Relationship between electrical resistance of corrosion sensors and  $\text{CaCl}_2$  proportion in mortar.

for the 28-day curve in figure 3:

$$F_c = \frac{C}{1.80 + 0.45 C} - 0.15. \quad (6)$$

According to the principle of Jambor's method the degree of corrosion of steel reinforcement expressed as  $\Delta R$  is given by the product of functional relations (1), (3) and (5):

$$\Delta R_{\text{cal}} = F_H \cdot F_C \cdot F_T, \quad (7)$$

$$= e^{a_k e^{b_k h^H}} \cdot \left( \frac{C}{a_c + b_c C} + c_c \right) \cdot a_T T^{b_T}, \quad (8)$$

$$= e^{2.87 e^{0.0068 H}} \cdot \left( \frac{C}{1.80 + 0.45 C} - 0.15 \right) \cdot 0.50 T^{0.21}. \quad (9)$$

Table 3 gives the comparison of the experimental and calculated results according to (9). It can be seen that the results show some differences. The heterogeneity of steel corrosion process seems to be the main cause of the differences. Increasing the number of test specimens and frequency of measurement can probably reduce the differences and increase the adequacy of the mathematical modelling.

**Table 3.** Calculated and experimental values of  $\Delta R$  of sensors and  $\text{CaCl}_2$  proportion in mortar.

Time (days)	$\text{CaCl}_2$ (%)		
	2	4	8
28	147*	234	353
	160	234	322
56	170	270	408
	250	250	510
70	178	283	425
	267	302	570
140	205	326	492
	—	354	—
308	242	384	580
	—	388	—
420	258	409	618
	—	397	—
644	282	447	675
	—	451	—

\* $\Delta R$  calculated  
 $\Delta R$  experimental

estimated by IER method:

$$\Delta CS = \frac{CS \cdot \Delta R}{R_0}, \quad (10)$$

where  $CS$  is initial cross-section of the steel of the sensor and  $R_0$  its initial electrical resistance.

From a practical point of view, to predict the service life of reinforced concrete materials in aggressive environments it is important to know the time  $T_{cr}$  which represents the time when the critical value of the cross-section reduction of reinforcement  $\Delta CS_{cr}$  or the related  $\Delta R_{cr}$  is reached. Using (7) and (8) it is possible to calculate  $T_{cr}$ :

$$T_{cr} = \left( \frac{\Delta R_{cr}}{a_T \cdot F_H \cdot F_C} \right)^{1/b_T}, \quad (11)$$

when  $\Delta R_{cr}$  is given by the critical value of cross-section reduction of reinforcement.

#### 4. Conclusions

1. The experimental process and mathematical modelling described the allow evaluation of the rate of corrosion of concrete reinforcement and service life of reinforced concrete materials under conditions that occur in practice.

2. A precondition for application of the mathematical modelling is knowledge of the functional relations expressing the influence of the aggressive environmental factors and the resistance of reinforced concrete. These factors include concentration of aggressive components, relative humidity, temperature, reinforced concrete quality (concrete porosity, thickness of concrete cover, kind of reinforcement steel, etc.) Obtaining the functional relations requires experimental study. By increasing the number of functional relations the efficiency of the modelling method can be increased.
3. In this paper it has been shown the possibility of the expression of the influence of relative humidity of environment, chloride concentration in mortar and time of the existence of reinforced material in given circumstances in the form of functional relations. Using these relations the possibility of calculation of rate of corrosion of concrete reinforcement and service life of reinforced concrete materials also has been shown.
4. It must be emphasized that the results of the IER method are of effective value. This is highlighted by the well-known uneven damage developed along corroding concrete reinforcement rods (pitting corrosion).
5. On the basis of the results obtained under the experimental conditions, equations (2), (4) and (6) were numbered. Therefore, the goodness of fit of these equations is the best in the cases when the composition of reinforced cement-based material and actual conditions are identical with the experimental conditions. These are: cement sand mix ratio of 1:3 or ca 500 kg of cement on 1 m<sup>3</sup> of mortar, w/c 0.6, use of Portland cement with mineralogical composition C<sub>3</sub>S 59.0%, C<sub>2</sub>S 14.2%, C<sub>3</sub>A 8.4% and C<sub>4</sub>AF 9.8% (according to Bogue), curing temperature 20°C. Under these conditions it is possible to calculate the steel corrosion rate as a function of the proportion of CaCl<sub>2</sub> in cement-based material in range of 1 to 8% and of relative humidity. With increasing difference between experimental and actual conditions the goodness of fit of the given equations and the reliability of the calculation decrease.
6. For the validity of the numbered equations the dependence on and sensitivity of the experimental coefficients to the composition of cement-based materials is important. It is well known that the most important factor in corrosion of embedded steel is the quality of pore structure of cement-based materials. This represents a final result of the used composition and processing. It is evident that the rate of contingent steel corrosion must be considerably sensitive to the used composition and processing and, understandably, so must be the sensitive experimental coefficients in the numbered equations expressing this rate. It can be expected that by using technologies aimed at densifying of pore structure and inhibition of corrosion process (decreasing of w/c values, application of plasticizing agents, and the like) the corrosion rate will be decreased. Therefore, it can be expected that the values of experimental coefficients will be changed in proportion to the change of steel corrosion rate and the applied technique of measurement of the quality of pore structure of cement-based materials.



- Clifton J R 1991 *Proceedings of the 5th International Conference on Durability of Building Materials and Components*, Brighton (eds) J M Baker, P J Nixon, A J Majumdar and H Davies, E and F N Spon (London: Chapman and Hall)
- Eurin P 1988 *Mater. Struct.* **21** 131
- Grunau B 1970 *Das Baugewerbe*, p. 1340
- Jambor J and Živica V 1982 *Stavebnický časopis* **30** 563
- Jambor J, Živica V, Vargová M and Bágel Ľ 1983 *Stavebnický časopis* **31** 601
- Masters L W 1986 *Mater. Struct.* **19** 417
- Morinaga S 1991 *Proceedings of the 5th International Conference on Durability of Building Materials and Components* Brighton, UK (eds) J M Baker, P J Nixon, A J Majumdar and H Davies, E and F N Spon (London: Chapman and Hall) p. 5
- Müller F K 1985 *Mater. Struct.* **18** 463
- Odler I and Gasser M 1988 *J. Ceram. Soc.* **71** 1015
- Tuutti K 1971 *Proceedings of RILEM Symposium Quality Control of Concrete Structures*, vol. 1 *Service life of structures*, Stockholm
- Živica V 1993 *Mater. Struct.* **26** 318
- ČSN 72 2121 Portland cement (in Czech)
- ISO-R 597 Definitions and Terminology of Cements
- ČSN 72 1208 Testing sands (in Czech)
- ISO/R 697, 1968 Method of Testing of Cements Compressive and Flexural Strengths of Plasticity (Rilem-Cembureau Method)
- ČSN 41 1373 Steel 11373 (in Czech)

## EPR studies on molybdenum phosphates $\text{Mo}_2\text{P}_4\text{O}_{15}$ , $\text{NaMo}_3\text{P}_3\text{O}_{16}$ and $\text{BaMo}_2\text{P}_4\text{O}_{16}$ in the temperature range 300–42 K

B B DAS\*<sup>†</sup>, G COSTENTIN, M M BOREL, A GRANDIN,  
A LECLAIRE and B RAVEAU

Laboratoire de Cristallographie et Sciences des Matériaux, CRISMAT-ISMRA, Boulevard du Marechal Juin, 14050 Caen, Cedex, France

<sup>†</sup>Present address: School of Chemistry, University of Hyderabad, Central University P.O., Hyderabad 500 134, India

MS received 27 January 1994; revised 8 August 1994

**Abstract.** EPR studies of molybdenum phosphates,  $\text{Mo}_2\text{P}_4\text{O}_{15}$ ,  $\text{NaMo}_3\text{P}_3\text{O}_{16}$  and  $\text{BaMo}_2\text{P}_4\text{O}_{16}$  in the range 300–42 K was carried out. Delocalization of  $4d^1$  electron on a  $\text{Mo}^{5+}$  site in the  $\text{MoO}_6$  octahedra occurs due to tunneling process. This gives rise to unresolved EPR lineshapes in all the cases except in  $\text{Mo}_2\text{P}_4\text{O}_{15}$ . The slight indication of hyperfine structure in  $\text{Mo}_2\text{P}_4\text{O}_{15}$  is due to less feasibility of delocalization of the  $4d^1$  electron, as  $\text{MoO}_6$  octahedron is connected through a  $\text{PO}_4$  group to only three octahedra as compared with higher numbers in the case of others. The negative g-shift is observed in all the cases due to positive sign of the spin-orbit coupling constant. The decreasing trend in  $g_{\text{iso}}$ -values in  $\text{Mo}_2\text{P}_4\text{O}_{15}$  and  $\text{NaMo}_3\text{P}_3\text{O}_{16}$  with decreasing temperature is observed, whereas in  $\text{BaMo}_2\text{P}_4\text{O}_{16}$  the  $g_{\text{iso}}$ -value increases with decreasing temperature.

**Keywords.** EPR; electron delocalization; molybdenum phosphates; exchange interaction.

### 1. Introduction

Until recently it has been observed that the molybdenum phosphates have great ability to stabilize  $\text{Mo}^{5+}$  state (Kierkegaard and Westerlund 1964; Leclaire *et al* 1983; Costentin *et al* 1992). Further, the mixed valent states of molybdenum viz.  $\text{Mo}^{5+}$  and  $\text{Mo}^{6+}$  in phosphate matrix are not very common in literature (Costentin *et al* 1991). The  $\text{Mo}^{5+}$  state with  $4d^1$  electronic configuration is an interesting paramagnetic probe to study these phosphate structures by electron paramagnetic resonance (EPR) spectroscopy. In this paper, we report a comparative study on molybdenum phosphates such as  $\text{Mo}_2\text{P}_4\text{O}_{15}$  (Costentin *et al* 1992),  $\text{NaMo}_3\text{P}_3\text{O}_{16}$  (Costentin *et al* 1991) and  $\text{BaMo}_2\text{P}_4\text{O}_{16}$  (Costentin *et al* 1990) by EPR spectroscopy in the temperature range 300–42 K.

### 2. Experimental

For the preparation of  $\text{BaMo}_2\text{P}_4\text{O}_{16}$  (Costentin *et al* 1990), first  $\text{BaCO}_3$ ,  $\text{H}(\text{NH}_4)_2\text{PO}_4$  and  $\text{MoO}_3$  were mixed in appropriate proportions to obtain the composition  $\text{Ba}_2\text{Mo}_{1.667}\text{P}_4\text{O}_{16}$  and heated in air at 600 K to eliminate  $\text{CO}_2$ ,  $\text{H}_2\text{O}$  and  $\text{NH}_3$ . Then required amount of molybdenum was added to the product and heated at 1173 K for 48 h in an evacuated silica ampoule. For  $\text{NaMo}_3\text{P}_3\text{O}_{16}$  (Costentin *et al* 1991), first an appropriate mixture of  $\text{Na}_2\text{CO}_3$ ,  $\text{H}(\text{NH}_4)_2\text{PO}_4$  and  $\text{MoO}_3$  was heated at 673 K in air.

\*To whom all correspondence should be addressed.

finely ground mixture was heated in evacuated silica ampoule at 873 K for 48 h. While for  $\text{Mo}_2\text{P}_4\text{O}_{15}$ , first an appropriate mixture of  $\text{H}(\text{NH}_4)_2\text{PO}_4$  and  $\text{MoO}_3$  was heated at 873 K. Then the resulting product was mixed with an appropriate amount of molybdenum, sealed in an evacuated silica ampoule and heated at 1073 K for 96 h.

Variable temperature X-band EPR spectra of the powdered samples at 300 K, 77 K and 4.2 K were recorded using a Bruker spectrometer system (ER 200D) fitted with a double cavity  $\text{TE}_{110}$ . The low temperature spectra at 4.2 K were recorded using SMC-TBT (France) cryostat. At all the temperatures 100 kHz magnetic field modulation was used. The measured g-values were calibrated with respect to the Bruker strong pitch ( $g = 2.0028$ ).

### 3. Results and discussion

In figures 1–3 we present the EPR spectra recorded at 300 K, 77 K and 4.2 K of the  $\text{Mo}_2\text{P}_4\text{O}_{15}$ ,  $\text{NaMo}_3\text{P}_3\text{O}_{16}$  and  $\text{BaMo}_2\text{P}_4\text{O}_{16}$  systems, respectively. From the figures we observe that in the case of these molybdenum phosphates the EPR lineshapes are unresolved except in the  $\text{Mo}_2\text{P}_4\text{O}_{15}$  where there is slight indication of hyperfine structures. We explain these lineshapes considering the structure of these phosphates. The crystal structure of  $\text{Mo}_2\text{P}_4\text{O}_{15}$  is discussed elsewhere (Contentin *et al* 1992). It consists of  $\text{MoO}_6$  octahedra sharing five of their corners with  $\text{P}_4\text{O}_{13}$  tetrphosphate groups and the sixth oxygen is free. Further, its structure can be described by the

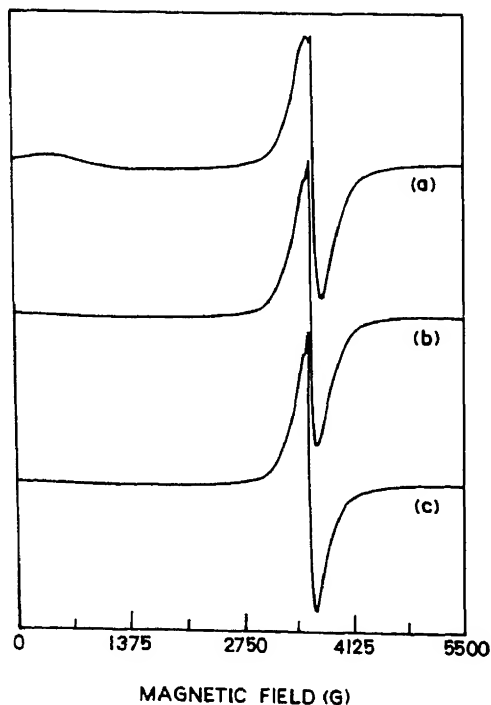


Figure 1. EPR spectra of  $\text{Mo}_2\text{P}_4\text{O}_{15}$  recorded at (a) 300 K, (b) 77 K and (c) 4.2 K.

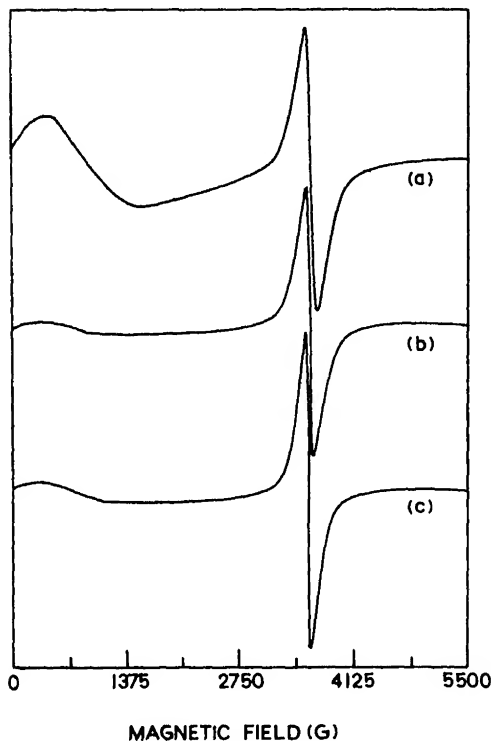


Figure 2. EPR spectra of  $\text{NaMo}_3\text{P}_3\text{O}_{16}$  recorded at (a) 300 K, (b) 77 K and (c) 4.2 K.

stacking of the  $[\text{Mo}_2\text{P}_4\text{O}_{15}]_\infty$  layers parallel to (012). This shows that in the matrix the  $\text{MoO}_6$  octahedra containing the  $\text{Mo}^{5+}$  sites are essentially separated by a  $\text{PO}_4$  group. Thus through a  $\text{PO}_4$  group the two  $\text{Mo}^{5+}$  sites in two adjacent  $\text{MoO}_6$  octahedra are separated by a distance of about  $5 \text{ \AA}$  (Costentin *et al* 1992). Thus the overlap of  $4d$  wavefunctions of two  $\text{Mo}^{5+}$  sites occurs to a substantial extent for the delocalization of the  $4d^1$  electron by quantum mechanical tunneling process. However, the presence of a  $\text{P}_2\text{O}_7$  group restrict the number of  $\text{MoO}_6$  octahedra separated by a  $\text{PO}_4$  group around a  $\text{MoO}_6$  octahedron to 3 (Costentin *et al* 1992). Thus due to this network of the  $[\text{Mo}_2\text{P}_4\text{O}_{15}]_\infty$  layers, the delocalization of the  $4d^1$  electron is hindered to an extent for the indication of the hyperfine structure due to the electronic spin and Mo nuclear spin ( $I = 5/2$ ) interaction, as observed in the case of  $\text{Mo}_2\text{P}_4\text{O}_{15}$  (figure 1).

The structure of the molybdenophosphate,  $\text{NaMo}_3\text{P}_3\text{O}_{16}$  which contains  $\text{Mo}^{5+}$  and  $\text{Mo}^{6+}$  is described elsewhere (Costentin *et al* 1991) from its single-crystal X-ray diffraction studies. In this case, the  $\text{MoO}_6$  octahedra containing the  $\text{Mo}^{5+}$  sites are connected through corner-shared  $\text{PO}_4$  groups forming  $[\text{MoPO}_8]_\infty$  chains along  $\bar{a}$ . In addition,  $\text{MoO}_5$  bipyramids containing the  $\text{Mo}^{6+}$  sites are connected through corner-shared  $\text{PO}_4$  tetrahedra forming  $[\text{MoPO}_7]_\infty$  chains along  $\bar{a}$ . Thus the host-matrix is described by the association of these chains connected through  $\text{PO}_4$  groups, forming five-sided tunnels where the  $\text{Na}^+$  ions are located. From the above structure, we explain that the  $4d^1$  electron on a  $\text{Mo}^{5+}$  site in the octahedra are delocalized along the  $[\text{MoPO}_8]_\infty$  chains by tunneling process as described above in the case of  $\text{Mo}_2\text{P}_4\text{O}_{15}$ .

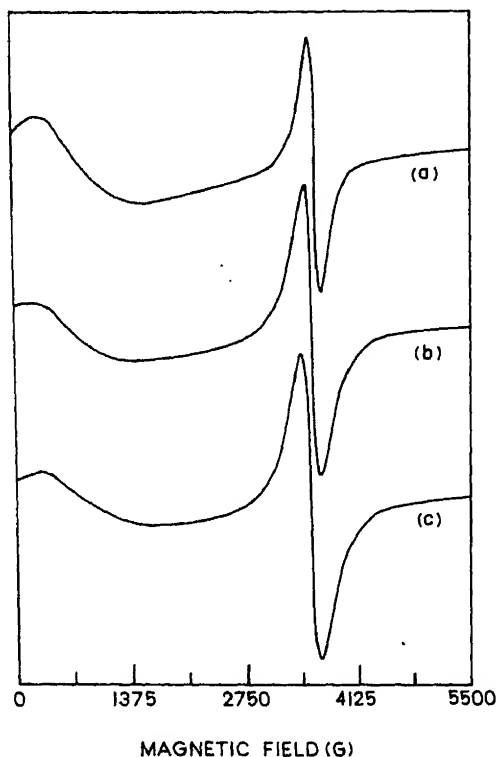


Figure 3. EPR spectra of  $\text{BaMo}_2\text{P}_4\text{O}_{16}$  recorded at (a) 300 K, (b) 77 K and (c) 4.2 K.

Thus due to this delocalization of the  $4d^1$  electron we observe the unresolved EPR lineshapes at 300 K, 77 K and 4.2 K in the  $\text{NaMo}_3\text{P}_3\text{O}_{16}$  system (figure 2). However, it is important to note that in the case of  $\text{Mo}_2\text{P}_4\text{O}_{15}$  the delocalization of the  $4d^1$  electron in the  $[\text{Mo}_2\text{P}_4\text{O}_{15}]_\infty$  layer is through the  $\text{MoO}_6$  octahedra connected through  $\text{PO}_4$  groups in a zig-zag way, whereas in the case of  $\text{NaMo}_3\text{P}_3\text{O}_{16}$ , the delocalization of  $4d^1$  electron is through  $\text{MoO}_6$  octahedra connected by  $\text{PO}_4$  groups forming  $[\text{MoO}_8]_\infty$  chains. Thus, there is difference in the delocalization pathways for the  $4d^1$  electron on  $\text{Mo}^{5+}$  sites in the  $\text{Mo}_2\text{P}_4\text{O}_{15}$  and  $\text{NaMo}_3\text{P}_3\text{O}_{16}$  systems and this difference is reflected through the observed EPR lineshapes for  $\text{Mo}_2\text{P}_4\text{O}_{15}$  (figure 1) and  $\text{NaMo}_3\text{P}_3\text{O}_{16}$  (figure 2). In the case of  $\text{Mo}_2\text{P}_4\text{O}_{15}$  there is indication of hyperfine interaction, whereas in  $\text{NaMo}_3\text{P}_3\text{O}_{15}$  unresolved EPR lineshapes are observed.

We now explain the observed unresolved EPR lineshapes of  $\text{BaMo}_2\text{P}_4\text{O}_{16}$  (figure 3) in the light of its structure as described elsewhere (Costentin *et al* 1990) from its single-crystal X-ray diffraction studies. In this case, each  $\text{P}_2\text{O}_7$  group shares two corners with the same  $\text{MoO}_6$  octahedra containing the  $\text{Mo}^{5+}$  sites forming  $[\text{MoP}_2\text{O}_{11}]$  units and the host-matrix can be described from these structural units which share their corners leading to  $[\text{MoP}_2\text{O}_{10}]_\infty$  chains along  $\bar{b}$ . From this structure, we visualize that there are essentially chains of  $\text{MoO}_6$  octahedra connected through corner-shared  $\text{PO}_4$  groups running along  $\bar{b}$  in  $[\text{MoP}_2\text{O}_{10}]_\infty$  chain (Costentin *et al* 1990). Thus delocalization of the  $4d^1$  electron of  $\text{Mo}^{5+}$  sites in  $\text{MoO}_6$  octahedra occurs along the  $[\text{MoP}_2\text{O}_{10}]_\infty$  chains by tunnelling process as described above in

$\text{Mo}_2\text{P}_4\text{O}_{15}$  and  $\text{NaMo}_3\text{P}_3\text{O}_{16}$  systems. As a result, we observed the completely unresolved EPR lineshapes for  $\text{BaMo}_2\text{P}_4\text{O}_{16}$  (figure 3) as in  $\text{NaMo}_3\text{P}_3\text{O}_{16}$  discussed above.

Again from figures 1–3 we observe that at lower fields there is distortion of the base lines of the EPR lineshapes in the case of  $\text{Mo}_2\text{P}_4\text{O}_{15}$ ,  $\text{NaMo}_3\text{P}_3\text{O}_{16}$  and  $\text{BaMo}_2\text{P}_4\text{O}_{16}$ . However, this distortion of the base lines is found to be very less in the case of  $\text{Mo}_2\text{P}_4\text{O}_{16}$  (figure 1) where it is observed only at room temperature. But in the case of  $\text{NaMo}_3\text{P}_3\text{O}_{16}$  (figure 2) and  $\text{BaMo}_2\text{P}_4\text{O}_{16}$  (figure 3) the distortion is nearly the same at room temperature but at 77 K or 4.2 K the distortion is more prominent in the case of  $\text{BaMo}_2\text{P}_4\text{O}_{16}$  as compared with that of  $\text{NaMo}_3\text{P}_3\text{O}_{16}$ . This distortion of the base lines at lower fields is explained in terms of electron exchange interaction by considering the structures of the molybdenum phosphates,  $\text{Mo}_2\text{P}_4\text{O}_{15}$  (Costentin *et al* 1992),  $\text{NaMo}_3\text{P}_3\text{O}_{16}$  (Costentin *et al* 1991) and  $\text{BaMo}_2\text{P}_4\text{O}_{16}$  (Costentin *et al* 1990) as reported earlier. It is known that in all the above three molybdenum phosphates each  $\text{MoO}_6$  octahedron has a free oxygen at the apex. The distance between the two free oxygens of the two adjacent octahedra in the above three cases are shown in table 1. Again, in the case of  $\text{NaMo}_3\text{P}_3\text{O}_{16}$  the  $\text{Na}^+$  ions in the five-sided tunnels are essentially surrounded by 9 oxygen atoms, whereas in the case of  $\text{BaMo}_2\text{P}_4\text{O}_{16}$ , the  $\text{Ba}^{2+}$  ions in the cages are surrounded by 10 oxygen atoms. The effective ionic radii (Shannon and Prewitt 1969) of  $\text{Na}^+$  ion with 9 coordinations and  $\text{Ba}^{2+}$  ion with 10 coordinations are 1.32 Å and 1.52 Å, respectively. Due to the proximity of the two free oxygen atoms in the two adjacent  $\text{MoO}_6$  octahedra in the host lattices exchange of electrons occurs between the two free oxygen atoms (Costentin 1992) and this exchange is favoured by the intervening ion present between the oxygen atoms. It appears plausible that such exchange interaction is of fairly low magnitude and affects the EPR lineshapes at lower fields. Thus in the case of  $\text{Mo}_2\text{P}_4\text{O}_{15}$ , the O – O distance of 2.55 Å (table 1) without any intervening ion, the base line distortion due to the exchange interaction is observed only at room temperature (figure 1), whereas at lower temperatures at 77 K or below the magnitude of the exchange interaction becomes too low to distort the EPR base lines. In the cases of  $\text{NaMo}_3\text{P}_3\text{O}_{16}$  (figure 2) and  $\text{BaMo}_2\text{P}_4\text{O}_{16}$  (figure 3) in spite of the fairly large O – O separations (table 1) of 5.81 Å and 4.36 Å, respectively, due to the presence of  $\text{Na}^+$  ions in  $\text{NaMo}_3\text{P}_3\text{O}_{16}$  and  $\text{Ba}^{2+}$  ions in  $\text{BaMo}_2\text{P}_4\text{O}_{16}$  the exchange interaction is higher in both the cases as compared with that of  $\text{Mo}_2\text{P}_4\text{O}_{15}$  at room temperature. As a result, the base line distortions at room temperature in  $\text{NaMo}_3\text{P}_3\text{O}_{16}$  and  $\text{BaMo}_2\text{P}_4\text{O}_{16}$  are more than in the case of  $\text{Mo}_2\text{P}_4\text{O}_{15}$ . However, in  $\text{NaMo}_3\text{P}_3\text{O}_{16}$ , the O – O separation of 5.82 Å with smaller  $\text{Na}^+$  ion of ionic radius

**Table 1.** Distance between the two free oxygen atoms of two adjacent  $\text{MoO}_6$  octahedra of the molybdenum phosphates studied.

System	O – O distance between the free oxygen atoms of two adjacent $\text{MoO}_6$ octahedra (Å)
$\text{Mo}_2\text{P}_4\text{O}_{15}$	2.55
$\text{NaMo}_3\text{P}_3\text{O}_{16}$	5.81
$\text{BaMo}_2\text{P}_4\text{O}_{16}$	4.36

System	$g_{\text{iso}}$ -values			$A_{\text{iso}}$ -values ( $\times 10^{-4}$ cm	
	300 K	77 K	4.2 K	300 K	77 K
$\text{Mo}_2\text{P}_4\text{O}_{15}$	1.921	1.917	1.915	51.5	39.3
$\text{NaMo}_3\text{P}_3\text{O}_{16}$	1.917	1.915	1.914	—	—
$\text{BaMo}_2\text{P}_4\text{O}_{16}$	1.920	1.923	1.925	—	—

1.32 Å as compared with O – O separation of 4.36 Å with in between  $\text{Ba}^{2+}$  ion of radius 1.52 Å in  $\text{BaMo}_2\text{P}_4\text{O}_{16}$ , the exchange interaction is lower in  $\text{NaMo}_3\text{P}_3\text{O}_{16}$  than in  $\text{BaMo}_2\text{P}_4\text{O}_{16}$  at 77 K and 4.2 K. This is also in agreement with our observed EPR lineshapes of  $\text{NaMo}_3\text{P}_3\text{O}_{16}$  (figure 2) and  $\text{BaMo}_2\text{P}_4\text{O}_{16}$  (figure 3).  $\text{NaMo}_3\text{P}_3\text{O}_{16}$  has less distortion than in the case of  $\text{BaMo}_2\text{P}_4\text{O}_{16}$  at 77 K and 4.2 K. From the extent of the distortion of the base lines in all the above three cases we conclude that the exchange interaction in the systems decreases with decreasing temperature. However, in the range of 77–4.2 K, the exchange interaction is of same magnitude in each case of the three molybdenum phosphates studied.

In table 2, we report our calculated  $g_{\text{iso}}$ -values of  $\text{Mo}_2\text{P}_4\text{O}_{15}$ ,  $\text{NaMo}_3\text{P}_3\text{O}_{16}$  and  $\text{BaMo}_2\text{P}_4\text{O}_{16}$  systems and  $A_{\text{iso}}$ -values of  $\text{Mo}_2\text{P}_4\text{O}_{15}$  system from the EPR spectra recorded at 300 K, 77 K and 4.2 K, respectively. The table shows that in all the cases the observed  $g_{\text{iso}}$ -values are less than the free electron  $g$ -value of 2.0023. The negative deviation is due to the positive sign of the spin-orbit coupling constant for the  $4d^1$  electron at a  $\text{Mo}^{5+}$  site in the matrices. The table also shows that the observed  $g_{\text{iso}}$ -values in the case of  $\text{Mo}_2\text{P}_4\text{O}_{15}$  and  $\text{NaMo}_3\text{P}_3\text{O}_{16}$  decrease with temperature from 300 K to 4.2 K. This behaviour is explained as follows: as the temperature decreases the Mo–O bond length of the  $\text{MoO}_6$  octahedra also decreases. Thus the size of the  $\text{MoO}_6$  octahedra having the paramagnetic  $\text{Mo}^{5+}$  sites decreases. As an overall effect, in the change of the value of the spin-orbit coupling constant for the molybdenum  $4d^1$  electron at the site, the molybdenum  $4d$  orbital contribution to bonding in the  $\text{MoO}_6$  unit and the crystal field splitting energy, the decrease in the  $g_{\text{iso}}$ -value with temperature compared with the value at 300 K is observed, whereas in the case of  $\text{BaMo}_2\text{P}_4\text{O}_{16}$  the overall change in the above parameters results in the increase in  $g_{\text{iso}}$ -value with decreasing temperature.

As discussed earlier, we observed the slight indication of hyperfine structure in the case of  $\text{Mo}_2\text{P}_4\text{O}_{15}$  (figure 1). Table 1 shows that the isotropic hyperfine splitting constants at 77 K or 4.2 K are less than that at 300 K. This we rationalize as we have discussed earlier that as temperature decreases the size of the  $\text{MoO}_6$  octahedra decreases due to the shortening of the Mo–O bonds. The O atom is more electronegative than the Mo atom. Thus the average radial distance of the  $4d^1$  electron from the Mo nucleus increases. As a result, due to reduced hyperfine interaction we observed lower  $A_{\text{iso}}$ -values at 77 K and 4.2 K as compared with the value at 300 K. However, this shortening of the Mo–O bond does not occur to a significant extent between 77 K to 4.2 K, as a result we observed the nearly same  $A_{\text{iso}}$ -values at 77 K and 4.2 K (table 2).

#### 4. Conclusions

From our above studies, we draw the following major conclusions. The unresolved EPR lineshapes are due to the delocalization of the molybdenum  $4d^1$  electron of the  $\text{Mo}^{5+}$  site in the matrix by tunneling process. The slight indication of the hyperfine structure in the case of  $\text{Mo}_2\text{P}_4\text{O}_{15}$  is due to the less feasibility of delocalization of the  $4d^1$  electron as a  $\text{MoO}_6$  octahedron having the  $\text{Mo}^{5+}$  site connected through a  $\text{PO}_4$  group to three other  $\text{MoO}_6$  octahedra. The observed  $g_{\text{iso}}$ -values decrease with temperature in  $\text{Mo}_2\text{P}_4\text{O}_{15}$  and  $\text{NaMo}_3\text{P}_3\text{O}_{16}$  whereas the  $g_{\text{iso}}$ -value increases with decreasing temperature in  $\text{BaMo}_2\text{P}_4\text{O}_{16}$ .

#### References

- Costentin G 1992 Ph.D. Thesis, Universite de Caen, Caen, France  
Costentin G, Borel M M, Grandin A, Leclaire A and Raveau B 1990 *J. Solid State Chem.* **89** 83  
Costentin G, Borel M M, Grandin A, Leclaire A and Raveau B 1991 *J. Solid State Chem.* **95** 168  
Costentin G, Leclaire A, Borel M M, Grandin A and Raveau B 1992 *Z. Kristallogr.* **201** 53  
Kierkegaard P and Westerlund M 1964 *Aca. Chem. Scand.* **18** 2217  
Leclaire A, Monier J C and Raveau B 1983 *J. Solid State Chem.* **71** 147  
Shannon R D and Prewitt C T 1969 *Acta Crystallogr.* **B25** 925





# Thermoelectric power in $\text{Gd}^{3+}$ -substituted Cu–Cd ferrites

C B KOLEKAR, P N KAMBLE and A S VAINGANKAR

Post-Graduate Department of Physics, Shivaji University, Kolhapur 416 004, India

MS received 23 March 1994; revised 2 August 1994

**Abstract.** Polycrystalline  $\text{Cd}_x\text{Cu}_{1-x}\text{Fe}_{2-y}\text{Gd}_y\text{O}_4$  ferrites for  $y = 0.0$  and  $0.1$  were prepared by ceramic technique. X-ray diffractograms of powder samples show cubic symmetry with  $x \geq 0.2$  for  $y = 0.0$  and  $0.1$ , while compositions with  $x = 0.0$  for  $y = 0.0$  and  $0.1$  are tetragonal. The thermopower measurements for  $\text{Gd}^{3+}$ -undoped ferrites in the temperature range 300 K to 788 K show  $n$ -type conductivity for  $x \geq 0.2$ . The substitution of  $\text{Gd}^{3+}$  changed  $n$ -type conductivity of the compositions to  $p$ -type. The mobilities calculated show decreasing trend on  $\text{Gd}^{3+}$  substitution. The values of activation energy  $\Delta E$  and drift mobility  $E_d$  suggest polaron formation in substituted samples. The conduction mechanism is explained on the basis of localized model and formation of  $\text{Gd}^{3+} + \text{Fe}^{2+}$  stable pairs at B site and  $\text{Cu}^{1+} + \text{Fe}^{3+}$  at A site.

**Keywords.** Charge transport; mobility; Seebeck coefficient;  $p$  and  $n$  conductivity.

## 1. Introduction

Charge transport properties are important for magnetic materials such as spinel ferrites, which possess high application potential. These properties in Cu–Cd ferrites have been discussed by Mazen *et al* (1985) and Kulkarni *et al* (1986), who reported  $n$ -type conductivity for  $\text{Cd} \geq 0.2$  in Cu–Cd ferrites and conduction mechanism respectively. Thermoelectric power in copper-containing ferrites was also studied (Ahmed *et al* 1988; Patil *et al* 1993). The substitution of  $\text{Fe}^{3+}$  by  $\text{Al}^{3+}$  in nickel ferrites changes  $n$ -type conductivity to  $p$ -type and increases the activation energy  $\Delta E$  when more than 50% replacement is done (Ahmed *et al* 1991). Similar trends have also been reported by Nicolau *et al* (1970) in  $\text{Al}^{3+}$ - and  $\text{Cr}^{3+}$ -substituted ferrites. The trivalent substitution reduces the number of  $\text{Fe}^{3+}$  ions on octahedral B site, which are responsible for Verwey conduction and therefore the above results are expected. An analogous observation on  $\text{Gd}^{3+}$ -substitution in Cu–Cd ferrites has already been reported from this laboratory (Kolekar *et al* 1994). Here we present our investigation of thermopower on the same system, i.e.  $\text{Gd}^{3+}$ -substituted Cu–Cd ferrites.

## 2. Experimental

Polycrystalline samples of  $\text{Cd}_x\text{Cu}_{1-x}\text{Fe}_{2-y}\text{Gd}_y\text{O}_4$  ( $x = 0.0, 0.2, 0.4, 0.6, 0.8, 1.0$ ) for  $y = 0.0$  and  $0.1$  were prepared by standard ceramic route using AR grade oxides. By mixing the ingredients with acetone base were presintered in platinum crucible at  $750^\circ\text{C}$  for 12 h. Final sintering in powder form was done at  $975^\circ\text{C}$  for 48 h in two cycles. The samples were furnace-cooled at a rate of  $80^\circ\text{C}/\text{h}$ . Structural characterization was done by X-ray, IR, AAS and microstructural analysis by SEM. Pellets of 1 cm diameter were prepared by cold pressing, applying about 5 ton/inch<sup>2</sup> hydraulic pressure. Good-quality pellets were obtained using PVA binder and maintaining the

pressure for about 10 min each time. Thermopower measurements were carried out on these pellets of about 2 mm thickness, using silver foils for better contact. Measurements of Seebeck coefficient  $\alpha$  from room temperature to 788 K were carried out.

### 3. Results and discussion

The X-ray diffraction analysis of the system shows that the compositions  $x \geq 0.2$  for  $y = 0.0$  and  $0.1$  are cubic spinels while  $x = 0.0$  for  $y = 0.0$  and  $0.1$  are tetragonal distorted with  $c/a > 1$ . For all the samples of Cu–Cd ferrites ( $y = 0.0$ ) there are no ambiguous reflections in the diffractograms exhibiting the formation of single-phase compounds. On substitution of  $\text{Gd}^{3+}$  the same materials show the presence of an additional line indicating separate phase. This phase is identified as due to  $\text{GdFeO}_3$  (ASTM 15 196), i.e. gadolinium iron oxide of orthorhombic character. This phase formation is favoured in such type of compounds which may be due to high

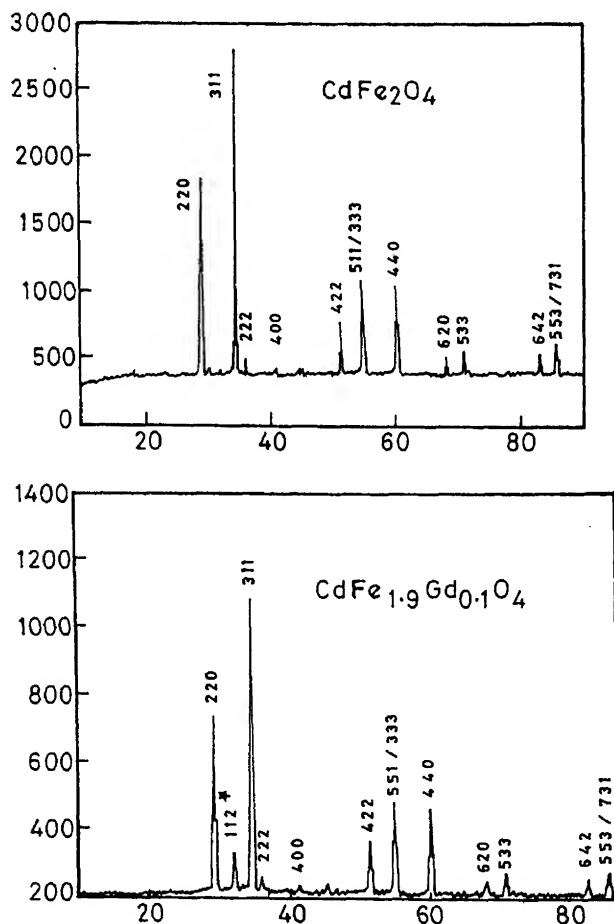


Figure 1. Typical X-ray diffractograms of the ferrites under investigation.

reactivity of gadolinium with iron. Similar results in substituted copper ferrites have already been reported (Belov *et al* 1983; Otari *et al* 1991). Typical X-ray diffractograms are presented in figure 1. The asterisk mark on the diffractogram shows plane corresponding to  $GdFe_2O_3$  structure.

The values of lattice parameters  $a$  and  $c$  are obtained using extrapolation function of  $\cos \theta$  and  $2\theta$ . These values are presented in table 1. With increasing  $Cd^{2+}$  the values of lattice constant  $a$  were found to increase. This is expected because the ionic radius of  $Cd^{2+}$  (0.99 Å) is higher than that of  $Cu^{2+}$  (0.70 Å). However, on substitution of  $Gd^{3+}$  no significant change in lattice constant was observed, which may be due to comparable ionic volumes of  $Cd^{2+}$  and  $Gd^{3+}$  (1.11 Å) and further because the amount of  $Gd^{3+}$  per formula unit is rather small. Further it was observed that the axial ratio,  $c/a$ , in tetragonally distorted copper ferrite is lowered on  $Gd^{3+}$  substitution. This can be attributed to migration of  $Cu^{2+}$  ions to tetrahedral A site on  $Gd^{3+}$  substitution, which are found to occupy octahedral B site (Kolekar *et al* 1994). This affects the total number of  $Cu^{2+}$  ions occupying B site which reduces cooperative Jahn-Teller distortions thereby reducing  $c/a$  (Hankiewicz *et al* 1990). A typical cation distribution obtained from magnetization study is presented in table 2.

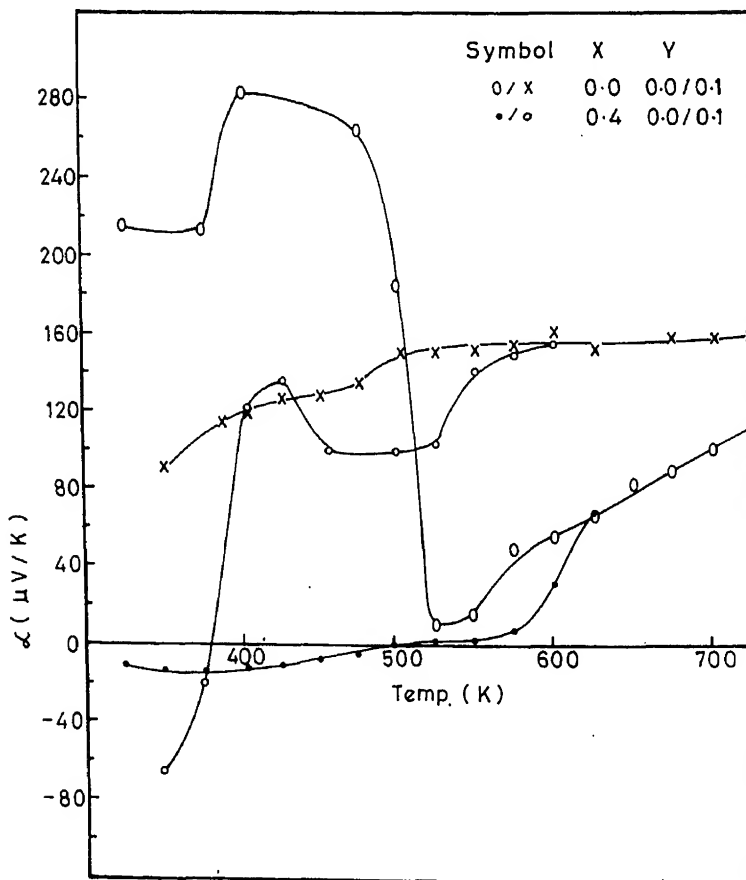
The chemical analysis done by atomic absorption flame technique using a computerized Perkin Elmer spectrophotometer model 371 to verify the proportions of ingredient elements showed that the weight proportions were correct in the final product. This suggests that the stoichiometry in the compounds is perfectly maintained. This is further supported by the observed value of  $c/a$  which should be of the order of 1.055 to maintain the stoichiometry in the compounds (Kokekar *et al* 1994). The IR study shows two distinct absorption bands  $\nu_1$  and  $\nu_2$  in the frequency range  $300\text{ cm}^{-1}$  to  $700\text{ cm}^{-1}$ . The substitution of  $Gd^{3+}$  shifts the centre frequency of the bands and some band broadening is also observed indicating the occupancy

**Table 1.** Structural and electrical data of  $Cd_xCu_{1-x}Fe_{2-y}Gd_yO_4$  ferrites for  $y = 0.0$  and  $0.1$ .

Composition		Lattice parameters (Å)	Activation energy $E$ (eV)		$(E_d)$ (eV)
$x$	$y$		Ferri	Para	
0.0	0.0	$a = 8.25$	0.4628	0.6610	0.688
		$c = 8.70$			
0.0	0.1	$a = 8.26$	0.5288	0.8058	0.4133
		$c = 8.56$			
0.2	0.0	8.47	0.3999	0.7273	0.5952
0.2	0.1	8.46	0.6516	0.6762	0.8266
0.4	0.0	8.53	0.2974	0.7934	0.93
0.4	0.1	8.51	0.6610	0.8266	
0.6	0.0	8.57	0.2288	0.4011	0.3968
0.6	0.1	8.56	—	0.744	0.6163
0.8	0.0	8.64	—	0.4296	0.4313
0.8	0.1	8.62	—	0.5219	0.62
1.0	0.0	8.69	—	0.3009	0.3674
1.0	0.1	8.69	—	0.4904	0.744

**Table 2.** Typical cation distribution of  $\text{Cd}_x\text{Cu}_{1-x}\text{Fe}_{2-y}\text{Gd}_y\text{O}_4$  ferrites for  $y = 0.0$  and  $0.1$ .

Composition		Cation distribution
x	y	
0.0	0.0	$(\text{Cu}_{1.9}\text{Fe}_{0.89})[\text{Cu}_{0.81}\text{Fe}_{1.21}]\text{O}_4^{2-}$
0.0	0.1	$(\text{Cu}_{0.30}\text{Fe}_{0.70})[\text{Cu}_{0.70}\text{Fe}_{1.2}\text{Gd}_{0.1}]\text{O}_4^{2-}$
0.2	0.0	$(\text{Cd}_{0.2}\text{Cu}_{0.30}\text{Fe}_{0.50})[\text{Cu}_{0.50}\text{Fe}_{1.50}\text{Gd}_{0.0}]\text{O}_4^{2-}$
0.2	0.1	$(\text{Cd}_{0.2}\text{Cu}_{0.36}\text{Fe}_{0.44})[\text{Cu}_{0.44}\text{Fe}_{1.46}\text{Gd}_{0.1}]\text{O}_4^{2-}$
1.0	0.0	$(\text{Cd}_{1.0})[\text{Fe}_{2.0}]\text{O}_4^{2-}$
1.0	0.1	$(\text{Cd}_{1.0})[\text{Fe}_{1.9}\text{Gd}_{0.1}]\text{O}_4^{2-}$

**Figure 2.** Temperature dependence of Seebeck coefficient for  $\text{Cd}_x\text{Cu}_{1-x}\text{Fe}_{2-y}\text{Gd}_y\text{O}_4$  ferrite system ( $x = 0.0, 0.4$ ).

of  $Gd^{3+}$  on octahedral B site. The details of IR study of this system have already been reported (Kolekar *et al* 1994).

The thermoelectric measurements were carried out in the temperature range 300 K to 788 K. The Seebeck coefficient  $\alpha$  was calculated using the relation  $\alpha = \Delta U / \Delta T$ , where  $\Delta U$  is change in thermoemf and  $\Delta T$  the temperature difference between hot and cold ends. The drift mobility ( $\mu_D$ ) of charge carriers was calculated using the relation (Eatah *et al* 1987)

$$\exp(\alpha/k/e)/\rho = 2N_0 e \mu_D, \quad (1)$$

where  $e$  is the electric charge,  $N_0$  the number of  $Fe^{3+}$  ions, and  $k$  the Boltzmann constant.

The temperature dependence of Seebeck coefficient for  $y = 0.0$  and  $0.1$  is presented in figures 2 and 3. The dependence of mobility ( $\mu_D$ ) on temperature is presented in figures 4 and 5 for the same concentrations. From figures 2 and 3 it can be seen that addition of cadmium in copper ferrite changes the conduction from  $p$ -type to  $n$ -type. An analogous result on Cu-Cd ferrites has been reported in the literature (Mazen

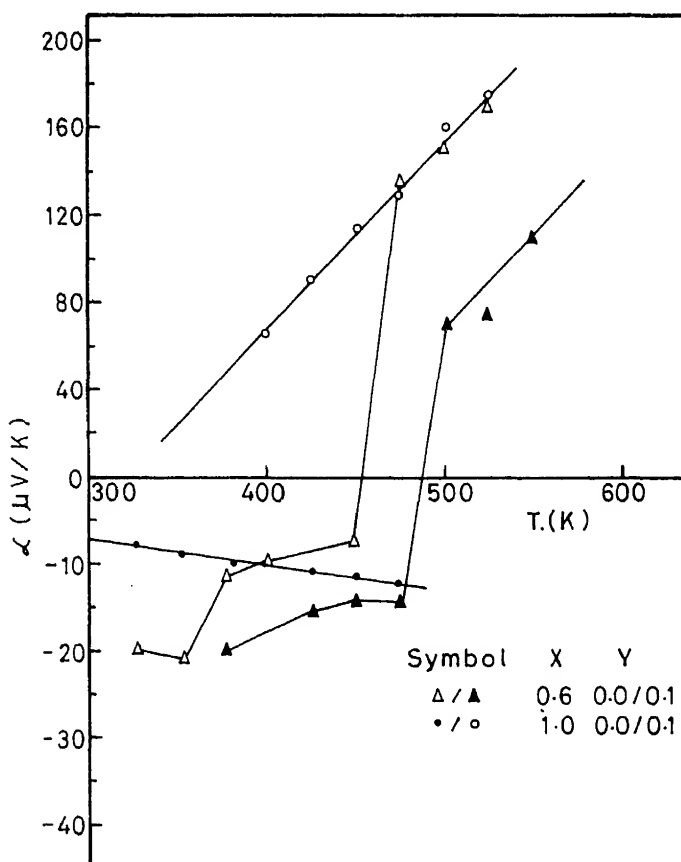


Figure 3. Temperature dependence of Seebeck coefficient for  $Cd_xCu_{1-x}Fe_{2-y}Gd_yO_4$  ferrite

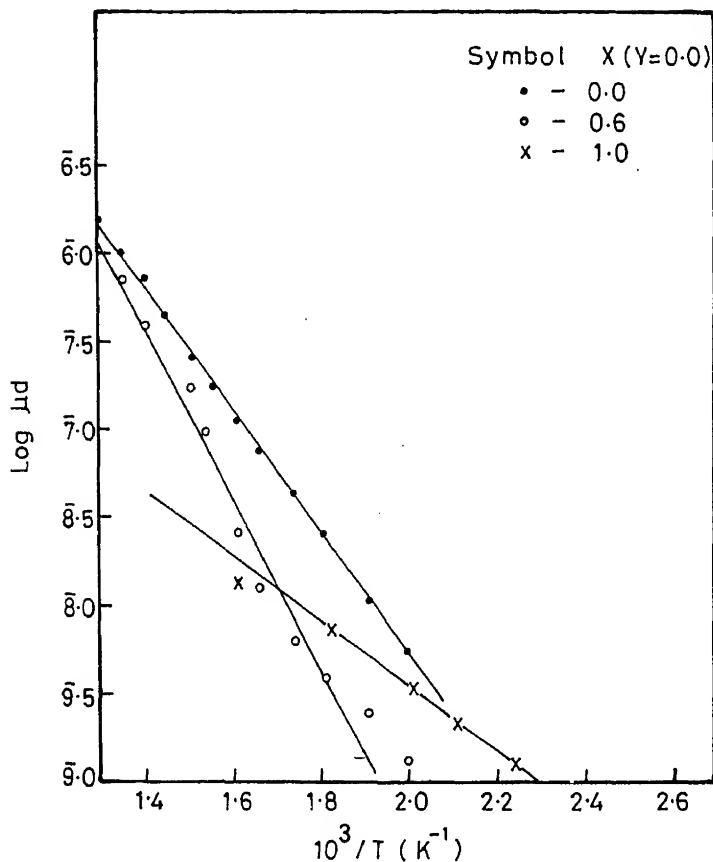


Figure 4. Dependence of log mobility on temperature for Cu-Cd system.

*et al* 1985). The cadmium ferrite is *n*-type and copper ferrite is *p*-type; therefore predominance of either of the charge carriers in mixed Cu-Cd ferrites depends upon the molar weight percentage of these elements, so also the oxygen stoichiometry and concentrations of  $\text{Fe}^{3+}$  in the solid solution. The iron-excess ferrites show *n*-type conductivity while iron-deficit compositions show *p*-type conductivity (Van Uitert 1955, 1956). It is because of the fact that, the conduction process in these ferrites is due to electron transfer from  $\text{Fe}^{2+} \rightleftharpoons \text{Fe}^{3+}$  at B site, the lowering of  $\text{Fe}^{3+}$  concentrations reduces the number of charge carriers and the vacancies of  $\text{Fe}^{3+}$  at B sites act as holes on respective cations giving rise to increase of hole conductivity. The substitution of  $\text{Gd}^{3+}$  for  $\text{Fe}^{3+}$  in Cu-Cd ferrites also influenced the mechanism of charge transport, by exhibiting *p*-type conductivity.

From figures 2 and 3 it can be seen that substitution of  $\text{Gd}^{3+}$  changes the *n*-type conductivity to *p*-type. Further, from our resistivity study it is shown that the electron conduction which is favoured in  $\text{Fe}^{2+} \rightleftharpoons \text{Fe}^{3+}$  is not favoured in  $\text{Fe}^{2+} \rightleftharpoons \text{Gd}^{3+}$ , thus forming  $\text{Gd}^{3+} + \text{Fe}^{2+}$  stable pairs at B site. The contribution to charge transport in substituted copper ferrites therefore may come from  $\text{Cu}^{2+} \rightleftharpoons \text{Cu}^{1+}$  which leads to *p*-type conductivity (Patil *et al* 1993).

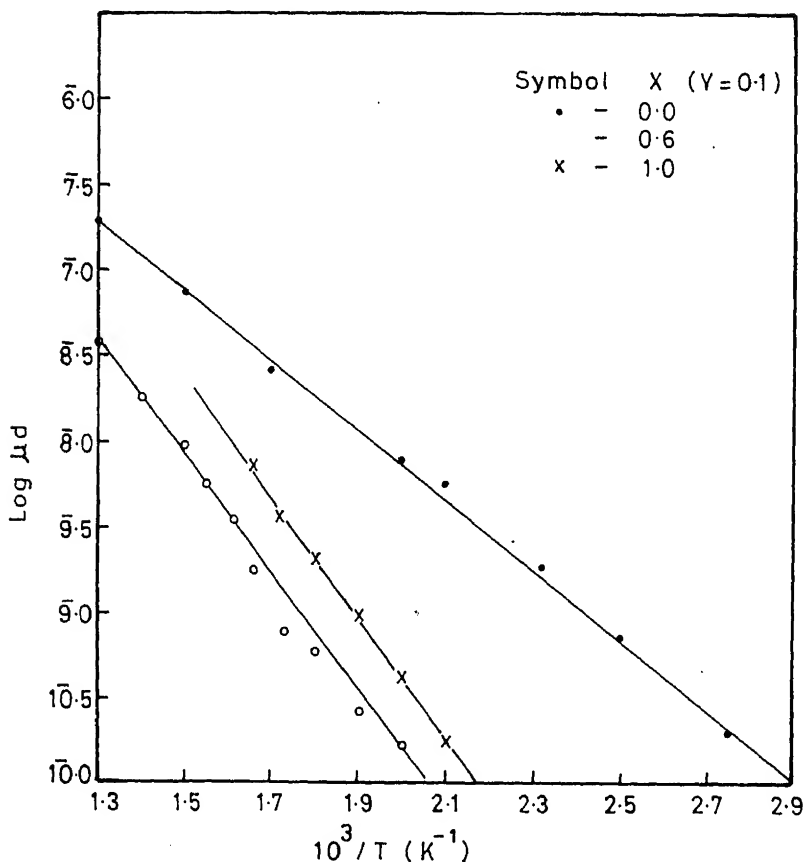


Figure 5. Dependence of log mobility on temperature for  $Cd_xCu_{1-x}Fe_{2-y}Gd_yO_4$  ferrite system for  $y = 0.1$ .

The dependence of mobility ( $\mu_D$ ) on temperature (figures 4, 5) obeys the exponential relation

$$\mu_D = \mu_0 \exp(-E_d/kT), \quad (2)$$

where  $E_d$  is the activation energy for electron drift and  $k$  the Boltzmann constant. The values of  $E_d$  calculated from figures 4 and 5 are presented in table 1. The values of activation energy  $E$  from dc resistivity plots are shown in the same table for comparison. The values of  $\Delta E$  and  $E_d$  are larger in Gd-substituted ferrites than in Cu-Cd ferrites. The values of  $\Delta E$  and  $E_d$  are greater than 0.4 eV and much greater than ionization energy of  $Fe^{2+}$  to  $Fe^{3+}$  (0.1 eV), which suggests the possibility of existence of polaron. The existence of small polaron in ferrites has been discussed by a number of workers (Vishwanathan and Moorthy 1990; Patil *et al* 1993). Conduction in substituted ferrites can be explained on the basis of localized model in which charge carriers are localized at lattice sites of cations because of strong electron-phonon interaction and so also from the magnetic interaction between the charge carriers and magnetic sublattices (Eatah *et al* 1987; Patil *et al* 1993). In addition to these,



localization may occur due to distortion because of the voluminous  $Gd^{3+}$  ion and formation of  $Fe^{2+} + Gd^{3+}$  stable pairs at B site and  $Cu^{1+} + Fe^{2+}$  at A site.

From the measurements on mobility of charge carriers, we found that it is decreased on  $Gd^{3+}$  substitution. This is expected since ferrites behave as semiconductors in which the mobility depends on the resistivity ( $\rho$ ) rather than on number of charge carriers. The observed increase in  $\Delta E$  and  $\rho$  on Gd substitution from our dc electrical conductivity study (Kolekar *et al* 1992) supports these results.

### Acknowledgement

One of the authors (CBK) is thankful to UGC, New Delhi, for the award of a teacher fellowship.

### References

- Ahmed M A, El-Nimr M K, Tawfik A and Aboelata A M 1988 *J. Mater. Sci. Lett.* **7** 639  
 Ahmed M A, El-Nimr M K, Tawfik and El-Hasab A M 1991 *Phys. Status Solidi* **123** 501  
 Belov K P, Antoshina L A and Markosyan A S 1983 *Sov. Phys. Solid State* **25** 1609  
 Eatah A I, Ghani A A, Shahat M E and Faramaway E E I 1987 *Phys. Status Solidi* **a104** 793  
 Hankiewicz J, Pajak Z and Radomski J 1990 *J. Magn. Magn. Mater.* **83** 475  
 Histake K N, Nakayama K and Ohta K 1973 *Jpn. J. Appl. Phys.* **12** 1116  
 Kolekar C B, Kamble P N and Vaingankar A S 1994 *J. Magn. Magn. Mater.* **138** 211  
 Kolekar C B, Kamble P N and Vaingankar A S 1994 *Indian J. Phys.* **A68** 529  
 Kolekar C B, Kamble P N and Vaingankar A S 1994 *Indian J. Pure Appl. Phys.* (communicated)  
 Kulkarni V R, Todkar M M and Vaingankar A S 1986 *Indian J. Pure Appl. Phys.* **24** 294  
 Mazen S A, Ghani A A and Ashour A H 1985 *Phys. Status Solidi* **a88** 343  
 Nicolau D, Bunget I, Rosenberg M and Beiciu I 1970 *IBM J. Res. Develop.* **14** 248  
 Otari S M, Patil S A, Saudagar M K, Patil B L and Sawant S R 1991 *Solid State Commun.* **78** 39  
 Patil B L, Sawant S R, Suryavanshi S S and Patil S A 1993 *Bull. Mater. Sci.* **16** 267  
 Van Uitert L G 1955 *J. Chem. Phys.* **23** 1882  
 Van Uitert L G 1956 *J. Chem. Phys.* **24** 306  
 Vishwanathan B and Moorty V R K (eds) 1990 *Ferrite materials science and technology* (New Delhi: Narosa Publ. House)

## Lanthanum oxide doping effect on dc electrical conductivity of ferroelectrics sodium vanadate and rubidium vanadate

D V PAWAR, T S MAGDUM and S H CHAVAN\*

Department of Physics, Shivaji University, Kolhapur 416004, India

MS received 17 June 1994; revised 19 September 1994

**Abstract.** The temperature dependence of dc electrical conductivity was measured by two-probe technique in the vicinity of phase transition point for ferroelectrics sodium vanadate and rubidium vanadate doped with different concentrations of  $\text{La}_2\text{O}_3$ . These materials show a sharp change in conductivity at their phase transition temperatures. The results were found to obey the conventional exponential law and the activation energies were calculated for ferroelectric and paraelectric states. It was found that activation energy in ferroelectric phase is smaller than in the paraelectric phase. The activation energy increases slowly with increase in doping concentration of  $\text{La}_2\text{O}_3$  up to 0.1 mol%, however, it decreases with further increase in doping concentration, in both ferro and para states. The dc electrical conductivity below the Curie temperature is of mixed type (ionic-electronic) while it is electronic type above the Curie temperature.

**Keywords.** Ferroelectrics; conductivity; phase transition; activation energy.

### 1. Introduction

Electrical conductivity is one of the important electrical characteristics of dielectric materials required not only for practical applications but also for the interpretation of various physical phenomena.

It was reported by Grawford (1959) that almost all ferroelectric materials which possess high Curie temperature lose their piezoelectric properties at temperatures considerably below their Curie points. Guruvich and Rez (1960) showed that the increase in electrical conductivity of these materials at high temperatures was due to loss of piezoelectric properties. The structural aspects of alkali metal vanadates were reported by Feigelson *et al* (1972) and they have shown that  $\text{NaVO}_3$  belongs to the monoclinic system with space group Cc at room temperature. The crystal chemistry of  $\text{M}^+\text{VO}_3$  ( $\text{M}^+ = \text{Li}, \text{Na}, \text{K}, \text{NH}_4, \text{Rb}, \text{Cs}$  and  $\text{Tl}$ ) pyroxenes were studied by Hawthorne and Calvo (1977) who concluded that  $\text{NaVO}_3$  is monoclinic with space group Cc while  $\text{RbVO}_3$  is orthorhombic with space group Pbcm.

The electrical conductivity of the rare earth vanadate  $\text{LnVO}_3$  ( $\text{Ln} = \text{La} - \text{Lu}$  and  $\text{Y}$ ) compound was studied by Sakai *et al* (1976). Verma and Lal (1981) reported that the heavy rare-earth tungstates are mixed (ionic-electronic) conductors. The electrical transport in light and heavy rare earth vanadates was studied by Gaur and Lal (1985, 1986).

The aim of present communication is to study the dependence of dc electrical conductivity of sodium vanadate and rubidium vanadate doped with different concentrations (0.025 to 3 mol%) of lanthanum oxide.

\*For correspondence

## 2. Experimental

The  $\text{NaVO}_3$  and  $\text{RbVO}_3$  ceramics used in this investigation were prepared stoichiometric mixture of  $\text{M}_2^+ \text{CO}_3$  ( $\text{M}^+ = \text{Na, Rb}$ ) and vanadium pentoxide by the usual ceramic technique following the method adopted by Feigelson (1972). These stoichiometric mixtures were slowly heated in a platinum crucible in a global furnace and fired at  $750^\circ\text{C}$  for 5 h and then cooled gradually to room temperature. The modified vanadates were prepared by taking different concentrations of  $\text{La}_2\text{O}_3$  (99.9% purity) as an additive. Every batch was dry mixed and then wet-mixed with ethyl alcohol in an agate mortar. After complete evaporation of alcohol, the batches were heated in a platinum crucible at  $750^\circ\text{C}$  for 5 h in a global furnace and cooled to room temperature. The ceramic samples were ground to pass 120 mesh sieve. Crystallinity was confirmed with X-ray diffraction.

Sample pellets were prepared in the form of disc of 1 cm diameter and about 1 mm thickness by applying  $7.6 \times 10^7 \text{ kg/m}^2$  pressure using a hydraulic press. The pellets were sintered on a platinum foil at  $500^\circ\text{C}$  for 4 h. The two opposite faces of the pellet were polished and silvered with air-drying silver paste to achieve good electrical contact.

The experimental set-up consists of global furnace, a digital dc microvoltmeter (VMV 15) with picoammeter adaptor, a transistorized power supply unit to provide a dc electrical field, digital multimeter and a temperature controller. To ensure ohmic contacts between electrodes and pellet interfaces were ohmic, the current ( $J$ )-electric field ( $E$ ) characteristics for all samples at constant temperature were studied. The  $J$ - $E$  characteristics are linear up to the electric field of 200 V/cm. Above this critical field, the increase of  $J$  with  $E$  becomes non-linear. The linear plot up to 200 V/cm indicates the ohmic contact. In all measurements the electric field (100 V/cm) was maintained below the critical field (200 V/cm). The measurement of dc electrical conductivity was based on the dc resistivity data obtained by two-probe method. The pellet was slowly heated in a furnace by applying dc voltage of 100 V in series with pico-ammeter. The dc electrical conductivity was obtained from resistivity data in the vicinity of phase transition points. To ensure whether conduction is ionic, electronic or mixed (ionic-electronic), the variation of dc electrical conductivity with time at a constant temperature was studied both in the ferroelectric and paraelectric states.

## 3. Results and discussion

The results of the measurement of dc electrical conductivity in pure and doped  $\text{NaVO}_3$  and  $\text{RbVO}_3$  obey the well known equation

$$\sigma = \sigma_0 \exp(\Delta E/kT),$$

where  $\Delta E$  is the activation energy,  $\sigma_0$  a constant,  $\sigma$  the electrical conductivity,  $T$  the temperature and  $k$  the Boltzmann constant. The variation of  $\log \sigma$  with temperature for pure  $\text{NaVO}_3$  and doped with different concentrations of  $\text{La}_2\text{O}_3$  (0.025, 0.05, 0.1, 0.5, 1 and 3 mol%) is shown in figure 1, while for pure  $\text{RbVO}_3$  and doped

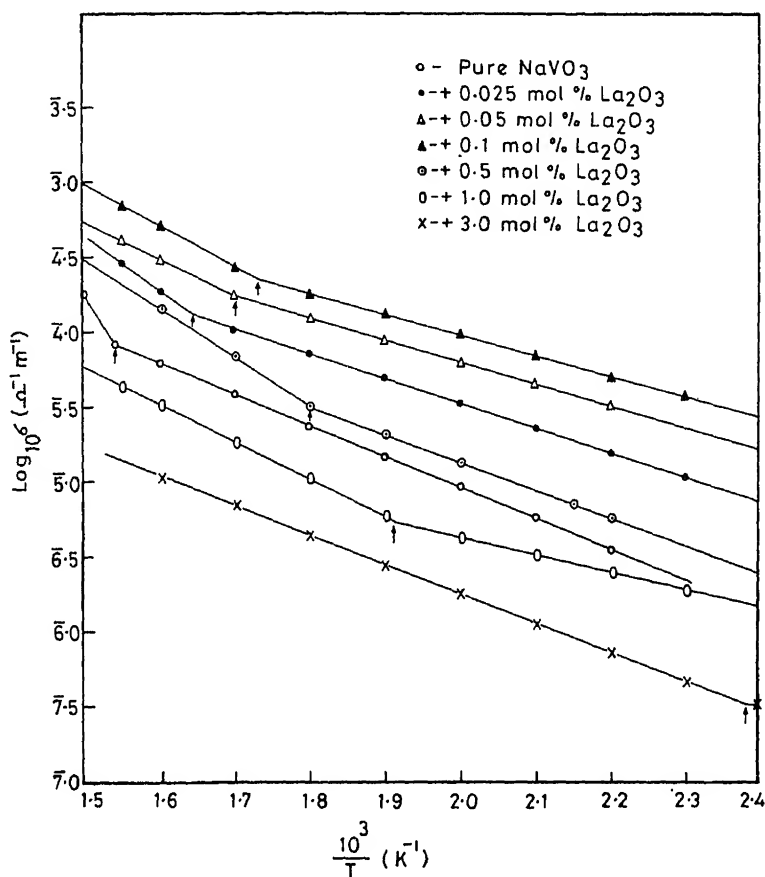


**Figure 1.** Variation of logarithmic conductivity (in  $\Omega^{-1}\text{m}^{-1}$ ) with  $1/T$  for pure and doped  $\text{NaVO}_3$ .

A sharp change in conductivity is observed at the transition temperature ( $T_c$ ). These transition temperatures ( $T_c$ ) are ferroelectric Curie temperatures of respective samples, 648 K for  $\text{NaVO}_3$  and 643 K for  $\text{RbVO}_3$  which we have confirmed by hysteresis loop method (Sawyer and Tower 1930) and dielectric constant measurements. These temperatures are in good agreement with those reported previously (Patil *et al* 1989, 1990). The doping of  $\text{La}_2\text{O}_3$  to  $\text{NaVO}_3$  and  $\text{RbVO}_3$  shows noticeable shift in the Curie temperature to lower temperature (figures 1 and 2) and is in good agreement with the results obtained by Gopala Krishnan and Seshamma (1991).

Figures 1 and 2 reveal that the magnitude of conductivity increases with increase of dopant content at low  $\text{La}_2\text{O}_3$  concentrations (0.025, 0.05, 0.1 mol%) and exhibits a maximum at 0.1 mol% and then decreases for higher dopant concentrations from 0.5 to 3 mol% of  $\text{La}_2\text{O}_3$ . The enhancement in dc electrical conductivity for addition of 0.1 mol% of  $\text{La}_2\text{O}_3$  in  $\text{NaVO}_3$  and  $\text{RbVO}_3$  ceramics is attributed to a rather more solid state interaction that takes place in the materials. This might be due to the increase of density with addition of  $\text{La}_2\text{O}_3$  up to 0.1 mol% (table 1). Doping with

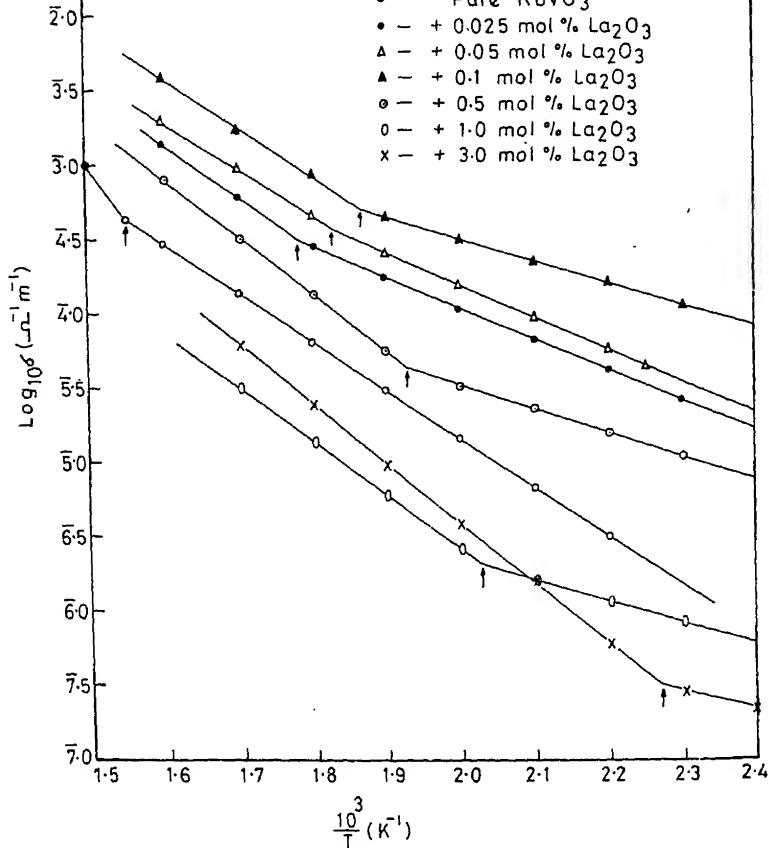


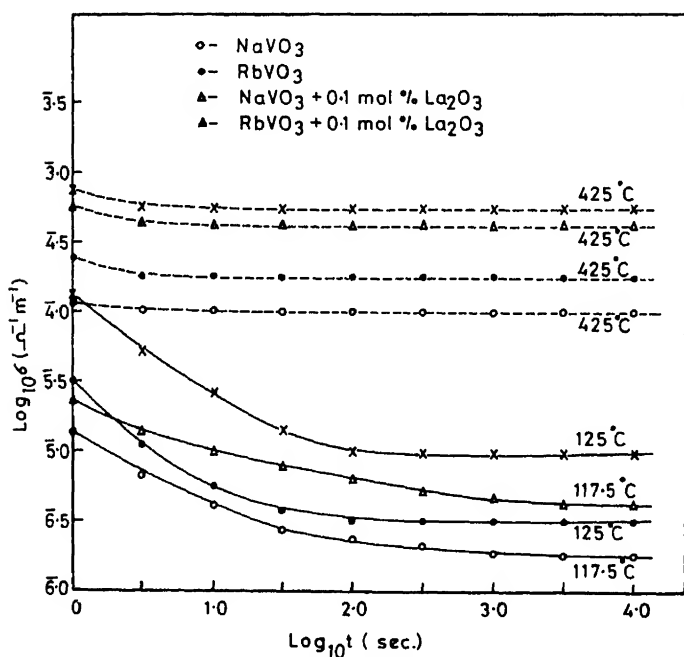
Figure 2. Variation of logarithmic conductivity (in  $\Omega^{-1}\text{m}^{-1}$ ) with  $1/T$  for pure and doped  $\text{RbVO}_3$ .

that the 0.1 mol% doping may represent the solubility limit of  $\text{La}_2\text{O}_3$  in  $\text{NaVO}_3$  as well as  $\text{RbVO}_3$  lattices. Similar results were reported by Weston *et al* (1969) for  $\text{Fe}_2\text{O}_3$  doped PZT and by Tawfik *et al* (1978) for Al doped  $\text{BaTiO}_3$  ceramics. Thus increase in conductivity for doping up to 0.1 mol% is because of the increasing concentration of cation vacancies in  $\text{NaVO}_3$  and  $\text{RbVO}_3$ . Here  $\text{Na}^+$  and  $\text{Rb}^+$  ions are considered solely mobile ions on account of their low equivalent weights compared to  $\text{La}^{3+}$ . The activation energies, both in ferroelectric and paraelectric states, and the experimental densities are summarized in table 1 for  $\text{NaVO}_3$  and  $\text{RbVO}_3$  ceramics doped with  $\text{La}_2\text{O}_3$ . Table 1 reveals that the activation energy in paraelectric state is higher than in the ferroelectric state.

The contribution to electrical conductivity is due to migration of ions or electrons or both. To investigate the nature of electrical conductivity, one has to distinguish the principal charge carriers. It is well known that, the dc electrical conductivity in a pure ionic conductor decreases with time and tends to zero after a very long time. In case of pure electronic conductor, the conductivity is independent of time, while in mixed (ionic-electronic) conduction, the dc electrical conductivity first decreases

**Table 1.** Activation energies and densities of  $\text{NaVO}_3$  and  $\text{RbVO}_3$ .

La <sub>2</sub> O <sub>3</sub> content (mol.%)	Activation energy (eV)		Ceramic density (× 10 <sup>3</sup> kg/m <sup>-3</sup> )
	Ferro	Para	
NaVO <sub>3</sub>			
0.000	0.70	1.65	2.50
0.025	0.33	0.79	2.59
0.050	0.30	0.53	2.66
0.100	0.29	0.60	2.72
0.500	0.38	0.70	2.70
1.000	0.25	0.50	2.67
3.000	0.20	0.41	2.62
RbVO <sub>3</sub>			
0.000	0.63	1.48	3.08
0.025	0.43	0.69	3.09
0.050	0.42	0.62	3.16
0.100	0.30	0.60	3.35
0.500	0.31	0.72	3.23
1.000	0.31	0.70	3.17
3.000	0.27	0.77	3.10

**Figure 3.** Variation of  $\log \sigma$  with  $\log t$  for  $\text{NaVO}_3$ ,  $\text{RbVO}_3$ ,  $\text{NaVO}_3 + 0.1 \text{ mol\% La}_2\text{O}_3$  and  $\text{RbVO}_3 + 0.1 \text{ mol\% La}_2\text{O}_3$ .

with time and then acquires a constant value after a long time. Figure 3 represents the variation of  $\log \sigma$  with  $\log t$  at a constant temperature, both in ferroelectric and paraelectric states, for pure  $\text{NaVO}_3$  and  $\text{RbVO}_3$  and doped with 0.1 mol%  $\text{La}_2\text{O}_3$ .

Figure 3 reveals that the dc electrical conductivity below transition temperature is of mixed type (ionic-electronic) while above transition temperature it is electronic. Similar type of conductivity behaviour was reported by Chavan and Kulkarni (1993) and Rasal *et al* (1993).

#### 4. Conclusions

- (i) The dc electrical conductivity of all samples increases exponentially with increasing temperature, both in ferroelectric and paraelectric regions.
- (ii) A sharp change in electrical conductivity is observed at phase transition temperature indicating the ferroelectric Curie temperature of respective samples.
- (iii) The addition of  $\text{La}_2\text{O}_3$  to  $\text{NaVO}_3$  and  $\text{RbVO}_3$  shows noticeable shift of Curie temperature to lower temperature.
- (iv) The activation energies of all the samples are higher in the paraelectric region than in the ferroelectric region.
- (v) The nature of electrical conductivity is of mixed type (ionic-electronic) in the ferroelectric region and electronic in the paraelectric region.

#### References

- Chavan S H and Kulkarni A J 1993 *J. Phys. Status Solidi* **a35** 307  
 Feigelson R, Martin G and Johnson B J 1972 *Crystal Growth (Germany)* **13/14** 686  
 Gaur K and Lal H B 1985 *J. Mater. Sci. (Poland)* **20** 3167  
 Gaur K and Lal H B 1986 *J. Mater. Sci. (USA)* **21** 2289  
 Gopala Krishnan R and Seshamma S 1991 *Bull. Mater. Sci.* **14** 1349  
 Grawford A E 1959 *Br. Commun. Electronics* **6** 516  
 Guruvich V M and Rez I S 1960 *Sov. Phys. Solid State* **2** 624  
 Hawthorne F and Calvo C 1977 *J. Solid State Chem.* **22** 157  
 Patil V V, Kashid A P and Chavan S H 1989 *Bull. Mater. Sci.* **12** 133  
 Patil N B, Patil R T and Chavan S H 1990 *Indian J. Pure Appl. Phys.* **28** 276  
 Rasal S P, Magdum T S, Pawar D V and Chavan S H 1993 *Ferroelectrics* **139** 57  
 Sawyer C B and Tower C H 1930 *Phys. Rev.* **35** 269  
 Sakai T, Adachi G, Shiohara J and Shinike T 1976 *Mater. Res. Bull.* **11** 1295  
 Tawfik A, Sekina M M A and El-Nimr M K 1978 *Indian J. Phys.* **A52** 164  
 Verma B and Lal H 1981 *Mater. Res. Bull.* **16** 1679  
 Weston T B, Webster A H and McNamara N H 1969 *J. Am. Ceram. Soc.* **52** 253

# An analysis of the electrical conductivity of the $\text{Ag}_2\text{SO}_4\text{--K}_2\text{SO}_4$ binary system

K SINGH, S D WACHASUNDER<sup>†</sup> and S S BHOGA<sup>††</sup>

Department of Physics, Nagpur University, Nagpur 440 010, India

<sup>†</sup> National Environmental Engineering Research Institute, Nagpur 440 020, India

<sup>††</sup> Department of Physics, Hislop College, Nagpur 440 001, India

MS received 26 April 1994; revised 26 September 1994

**Abstract.** Electrical conductivity of the  $\text{Ag}_2\text{SO}_4\text{--K}_2\text{SO}_4$  binary system shows three maxima at 20, 70 and 90 mole% of  $\text{K}_2\text{SO}_4$  added to  $\text{Ag}_2\text{SO}_4$ . The first and the third maxima have been explained in the light of intragrain percolation due to lattice distortion, whereas, the second maximum by the surface percolation. The limit of solid solubility has been set at 20 mole% on the basis of evidences obtained from XRD, DTA and SEM techniques.

**Keywords.** Ionic conductivity; solid solubility; lattice distortion.

## 1. Introduction

The study of alkali metal sulphates,  $\text{Li}_2\text{SO}_4$  (Kvist and Lunden 1965),  $\text{Na}_2\text{SO}_4$  (Jacob and Rao 1979) and  $\text{K}_2\text{SO}_4$  (Natarajan and Secco 1975) revealed that they are good ionic conductors with negligible electronic transference number in their high temperature form. Other than alkali metal sulphates, only  $\text{Ag}_2\text{SO}_4$  is a better cationic conductor which is used in  $\text{SO}_2$  sensor (Liu *et al* 1990). Silver sulphate is comparatively a less studied sulphate. The high temperature hexagonal phase is isomorphic with that of the high temperature phase of  $\text{K}_2\text{SO}_4$ . These sulphates have been used in the sulphur dioxide gas sensors (Gauthier and Chamberland 1977). For low temperature electrochemical applications, high ionic conductivity near ambient temperature is a prime requisite. In this regard binary sulphates are known to be more conducting than the mono components. Hence,  $\text{Ag}_2\text{SO}_4\text{--K}_2\text{SO}_4$  binary system is selected to develop from low temperature electrochemical applications, in general, and particularly  $\text{SO}_x$  gas sensor point of view. Kumari and Secco (1983) reported the conductivity only for 25 and 60 mole%  $\text{K}_2\text{SO}_4$  added to  $\text{Ag}_2\text{SO}_4$ . As a continuous effort for the development of sulphate based electrolytes for low temperature electrochemical applications, an investigation on the electrical conductivity over entire range of compositions belonging to  $\text{Ag}_2\text{SO}_4\text{--K}_2\text{SO}_4$  system is reported in this paper.

## 2. Experimental

The initial ingredients  $\text{Ag}_2\text{SO}_4$  and  $\text{K}_2\text{SO}_4$  with purity greater than 99.99% were procured from E Merck, India. An appropriate mole fraction of the well dried chemicals in  $(x) \text{Ag}_2\text{SO}_4\text{--}(1-x)\text{K}_2\text{SO}_4$  (where  $x = 0.1, 0.2, 0.3, \dots, 1$ ) were prepared by melting the mixture in a silica crucible followed by twin roller quenching technique at room temperature (Singh *et al* 1988, 1992). The samples were characterized by X-ray powder diffraction (XRD) and differential thermal analysis (DTA) using Philips PW1700, X-ray powder diffractometer and Perkin Elmer TADS 1700, thermal



### 3. Results and discussion

The XRD patterns of all compositions showed an increase in half width of full height of characteristic peaks (slight potential line broadening) in general; particularly for those samples which are biphasic mixtures. The potential line broadening is also seen for pure quenched samples. Such a line broadening is due to: (i) reduction of grain size resulting from quenching of melt and (ii) the composite nature of the samples under study. These results are in good agreement with the earlier reports (Singh and Bhoga 1990). A comparison of XRD data (a few lines as indicative) with JCPDS values are given in table 1. It is apparent that in case of 10 and 20 mole%  $K_2SO_4$  into  $Ag_2SO_4$ , all the diffracted lines closely match with those due to  $Ag_2SO_4$ . Absence of diffraction lines of  $K_2SO_4$  in these compositions rules out the possibility of  $K_2SO_4$  precipitation into  $Ag_2SO_4$  matrix. A small deviation in the values of  $d$  is, however, due to lattice distortion as a result of the formation of solid solution. Similarly, the solid solubility up to 20 mole% of  $Ag_2SO_4$  into  $K_2SO_4$  is determined. At higher concentrations the diffraction lines due to both the phases are identified whereby we conclude that the intermediate compositions are biphasic mixtures.

The transition temperatures for all samples obtained from onset of endothermic peaks in the thermogram are compared with the earlier reports (Nacken 1907; Kumari and Secco 1983) in table 2. The observed results are in close agreement with those of Nacken (1907). A careful study of phase diagram reported by Kumari and Secco

**Table 1.** Comparison of experimental  $d$  and relative intensity values of AK9, AK8, AK7 and AK6 with JCPDS\* data of pure  $Ag_2SO_4$  and  $K_2SO_4$ .

AK9		AK8		AK7		AK6		JCPDS			
$d$	$I/I_0$	$d$	$I/I_0$	$d$	$I/I_0$	$d$	$I/I_0$	$d$	$I_0I_0$	Phase	$hkl$
4.72	6.3	4.71	6.2	4.72	7.4	4.71	8.7	4.69	10	Ag	111
—	—	—	—	4.19	3.2	4.19	5.4	4.17	28	K	021
4.24	21	4.02	22	4.00	25	4.04	28	3.99	25	Ag	022
—	—	—	—	3.77	4.2	3.75	6.1	3.74	18	K	002
3.19	75	3.18	81	3.18	74	3.18	74	3.17	77	Ag	040
—	—	—	—	3.00	8.4	3.01	14	3.00	77	K	022
2.88	100	2.88	100	2.88	100	2.88	100	2.87	100	Ag	311
2.66	71	2.66	96	2.65	72	2.66	68	2.64	100	Ag	002
2.28	12	2.27	8.3	2.27	9.5	2.27	8	2.27	8	Ag	151
1.92	33	1.92	29	1.92	32	1.93	28	1.92	30	Ag	351
1.71	17	1.71	18	1.71	15	1.72	14	1.71	17	Ag	062
1.59	4.2	1.60	4.8	1.59	6.3	1.59	3.6	1.58	3	Ag	080

AK9—90  $Ag_2SO_4$ :10  $K_2SO_4$ , AK8—80  $Ag_2SO_4$ :20  $K_2SO_4$ , Ag— $Ag_2SO_4$ , AK7—70  $Ag_2SO_4$ :30  $K_2SO_4$ , AK6—60  $Ag_2SO_4$ :40  $K_2SO_4$ , K— $K_2SO_4$

\*JCPDS nos. 27-1403 ( $Ag_2SO_4$ ) and 5-613 ( $K_2SO_4$ ).

**Table 2.** Comparison of solid-solid phase transition temperatures for  $\text{Ag}_2\text{SO}_4\text{-K}_2\text{SO}_4$  binary system with the reports of Nacken (1907) and Kumari and Secco (1983).

Composition	Observed	Nacken (1907)	Kumari and Secco (1983)
$\text{Ag}_2\text{SO}_4\text{:K}_2\text{SO}_4$			
100:00	415	416	416
90:10	—	300	284
80:20	—	300	284
70:30	302	300	284
60:40	302	300	276
50:50	302	300	283
40:60	301	300	280
30:70	301	300	261
20:80	—	294	261
10:90	—	304	261
00:100	—	555	554

(temperature in  $^{\circ}\text{C}$ )

(1983) and Nacken (1907) reveals two phase mixtures in entire binary system below  $300^{\circ}\text{C}$ . Above  $300^{\circ}\text{C}$ , they form a complete solid solution. Furthermore, the XRD results discussed above also predicted that the compositions in the range 30 to 70 mole%  $\text{K}_2\text{SO}_4$  are two-phase mixtures of  $\text{Ag}_2\text{SO}_4$  and  $\text{K}_2\text{SO}_4$ . Hence, the observed endothermic peak in thermogram is due to formation of a solid solution at that temperature. The absence of endothermic peak around  $300^{\circ}\text{C}$  in cases of 10, 20, 80 and 90 mole% of  $\text{K}_2\text{SO}_4$  confirms the solid solubility. These results indicate that, during cooling of the melt of intermediate compositions, two phases ( $\text{Ag}_2\text{SO}_4$  and  $\text{K}_2\text{SO}_4$ ) separate out at  $302^{\circ}\text{C}$  and forms the biphasic mixtures at room temperature. Figures 1a and 1b display the microphotographs of 80:20 and 50:50 ( $\text{Ag}_2\text{SO}_4\text{:K}_2\text{SO}_4$ ) samples respectively. 80  $\text{Ag}_2\text{SO}_4\text{:}20 \text{K}_2\text{SO}_4$  (figure 1a) shows a uniform grain morphology indicating a single phase compound. Similar microstructures are also observed for 10, 80 and 90 mole%  $\text{K}_2\text{SO}_4$  incorporated  $\text{Ag}_2\text{SO}_4$  and of pure components. On the other hand, 50  $\text{K}_2\text{SO}_4\text{:}50 \text{Ag}_2\text{SO}_4$  (figure 1b) shows the presence of two distinguishable phases. The microstructures of other remaining compositions also indicated the formation of biphasic mixtures.

The increased solid solubility limit (up to 20 mole%) obtained from XRD, DTA and SEM data is due to rapid quenching of the melt. The increased solid solubility limit as a result of quenching has also been observed in the case of a number of divalent sulphate doped lithium sulphates (Singh and Bhoga 1990).

The bulk conductivity, obtained from complex impedance analysis as discussed earlier (Singh *et al* 1992) is plotted as a function of  $\text{K}_2\text{SO}_4$  concentration at two different temperatures in figure 2. Three conductivity maxima at 20, 70 and 90 mole% of  $\text{K}_2\text{SO}_4$  are clearly seen. In order to discuss the concentration and temperature dependent conductivity behaviour of the system, entire investigated compositional range is divided into two groups: (i) group I includes the results of solid solutions 0 to 20 and 80 to 100 mole%  $\text{K}_2\text{SO}_4$  and (ii) group II covers the compositions ranging from 30 to 70 mole%  $\text{K}_2\text{SO}_4$  which are biphasic mixtures. Figure 3 illustrates the Arrhenius plots for the first group. Over the entire temperature range of investigation,

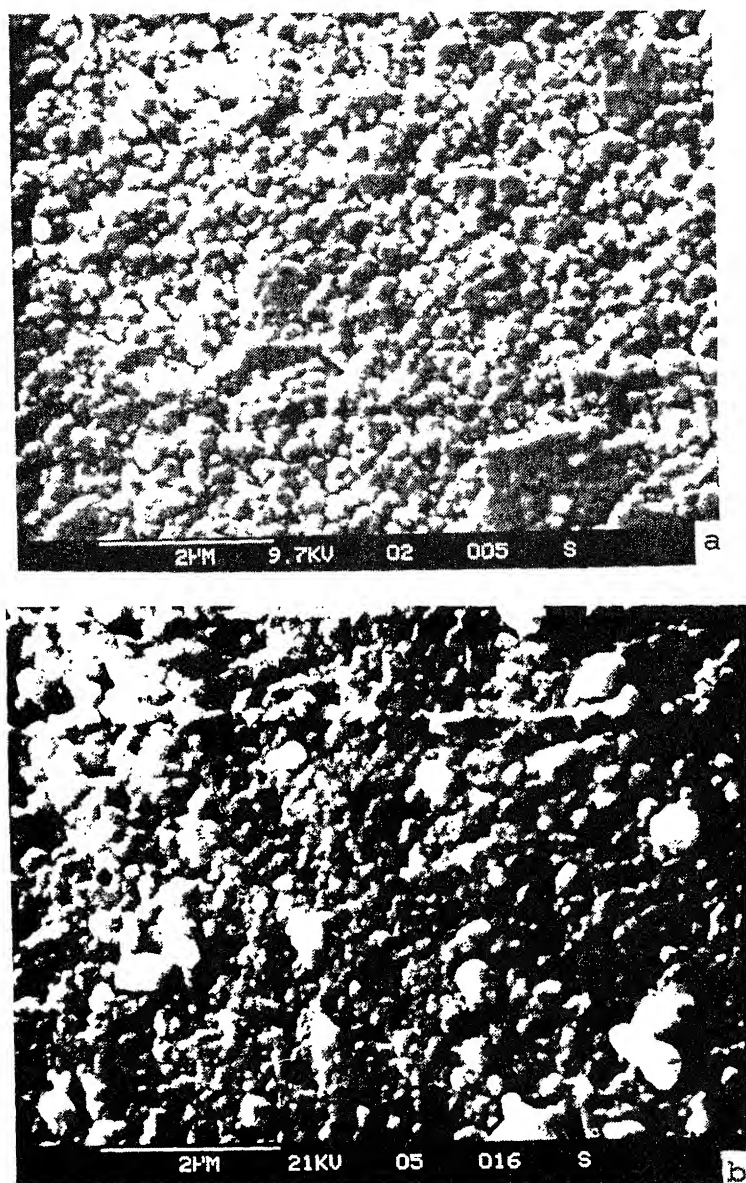


Figure 1. Microphotographs of a.  $80\text{Ag}_2\text{SO}_4:20\text{K}_2\text{SO}_4$  and b.  $50\text{Ag}_2\text{SO}_4:50\text{K}_2\text{SO}_4$ .

all compositions obey the Arrhenius law:

$$\sigma T = (\sigma T)_0 \exp(-E_a/kT), \quad (1)$$

where  $(\sigma T)_0$  and  $E_a$  are respectively the pre-exponential factor and the activation enthalpy. The values of  $\sigma$ ,  $(\sigma T)_0$  and  $E_a$  obtained using (1) are presented in table 3. The absence of expected change in slope at  $302^\circ\text{C}$  (due to formation of solid solution)

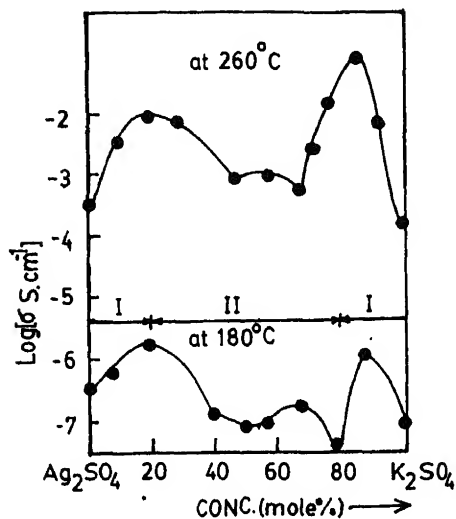


Figure 2. Functional dependence of conductivity on  $\text{K}_2\text{SO}_4$  concentration.

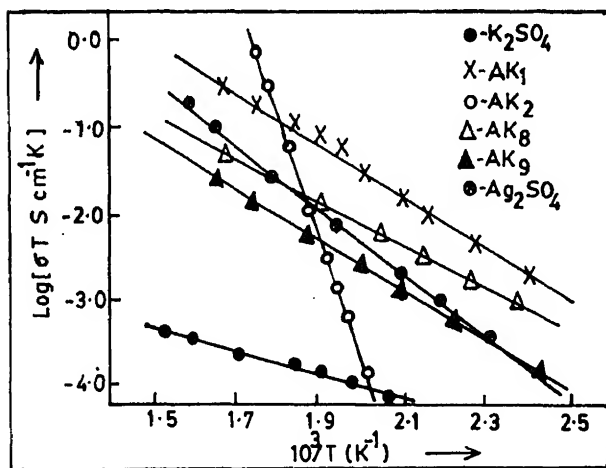
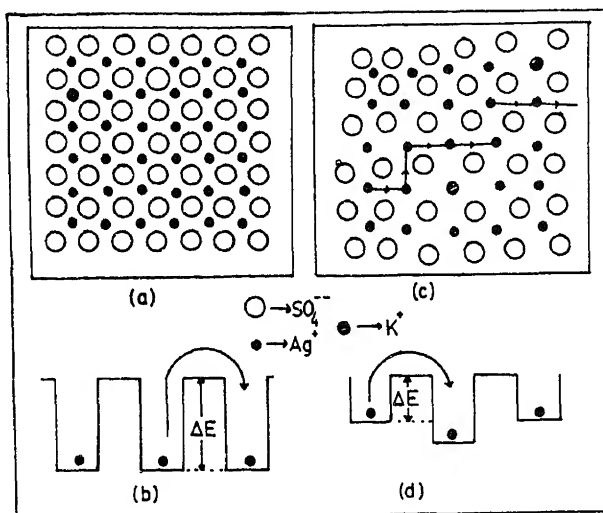


Figure 3. Arrhenius plots for region I.

Table 3. The values of conductivity  $\sigma$ , pre-exponential factor  $(\sigma T)_0$  and activation energy  $E_a$  for the pure, 10 and 20 mole% of  $\text{K}_2\text{SO}_4$  doped  $\text{Ag}_2\text{SO}_4$ .

Sample	$\log(\sigma)$ (S/cm)	$\log(\sigma T)_0$ (SK/cm)	$E_a$ (eV)
$\text{Ag}_2\text{SO}_4\text{:K}_2\text{SO}_4$			
00:00	-1.899	-4.626	0.71
90:10	-2.465	-5.192	0.54
80:20	-2.046	-4.772	0.47



**Figure 4.** (a) Schematic representation of a plane through the host  $\text{Ag}_2\text{SO}_4$  lattice, (b) potential well of host lattice, (c) host lattice in which  $\text{Ag}^+$  sites are randomly occupied by relatively larger size  $\text{K}^+$  resulting into local distortion and (d) potential after partial substitution.

Since anions and cations of the  $\text{Ag}_2\text{SO}_4$  and  $\text{K}_2\text{SO}_4$  are of same valency, an increased conductivity in  $\text{Ag}_2\text{SO}_4$  rich region cannot be explained by classical theory of aliovalent doping (Hoffer *et al* 1981). Obviously, the main factor responsible for an enhancement in conductivity is considered to be solely due to lattice distortion caused by the incorporation of the bigger guest  $\text{K}^+$  into the  $\text{Ag}_2\text{SO}_4$  host lattice. A model based on the mobility of ions as a function of lattice distortion was proposed recently (Singh and Bhoga 1992). According to this model although,  $\text{Ag}^+$  and  $\text{K}^+$  possess the same charge, there is a difference in their ionic sizes ( $r_{\text{Ag}} < r_{\text{K}}$ ). Therefore, the partial replacement of former by latter produces local lattice expansion in the host  $\text{Ag}_2\text{SO}_4$ . A simplest pictorial representation of the model is depicted in figures 4a and c. Such a lattice distortion widens the inter connecting windows and subsequently reduces the height of potential well (figure 4d). Hence, the energy required for surmounting the energy barrier so as to realize a net ion migration from one shallow potential well to nearby one, decreases. This is supplemented by the experimental results presented in table 3, wherein a decrease in activation energy  $E_a$  with the partial substitution of  $\text{K}^+$  for  $\text{Ag}^+$  is seen. Thus a lattice expansion not only opens up the lattice but also reduces the activation energy which, in turn, gives rise to a number of interconnecting percolating pathways between the adjacent interstitial sites. Such percolating pathways increase with increased dopant concentration leading to a rise in conductivity. The maximum conductivity at 20 mole% of  $\text{K}_2\text{SO}_4$  is due to percolation threshold concentration.

Interestingly, the conductivity enhances in spite of the contraction of  $\text{K}_2\text{SO}_4$  lattice due to the partial substitution of smaller  $\text{Ag}^+$  in place of  $\text{K}^+$  (figure 2). This enhancement is attributed to the strong preference for the mobility of  $\text{Ag}^+$  relative to  $\text{K}^+$ , because  $\text{Ag}^+$  needs relatively smaller lattice opening compared to  $\text{K}^+$ . Thus the addition of  $\text{Ag}_2\text{SO}_4$  enhances the mobile ion concentration, in turn, the conductivity.

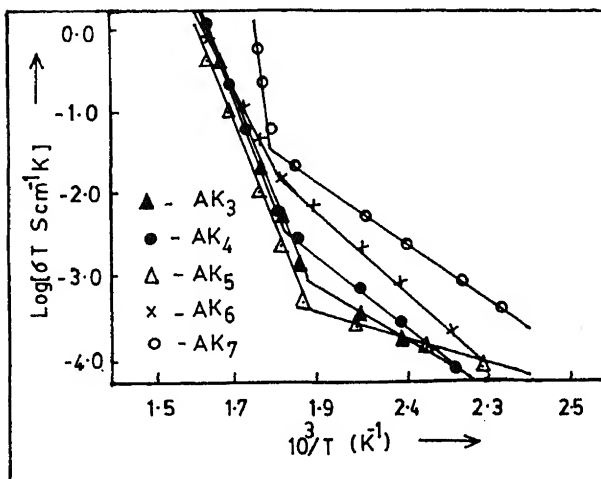


Figure 5. Arrhenius plots for region II.

Arrhenius plots of group II depicted in figure 5 show a change in slope at around  $300^\circ\text{C}$  corresponding to the formation of solid solution. In this group 70 mole% of  $\text{K}_2\text{SO}_4$  added into  $\text{Ag}_2\text{SO}_4$  shows maximum conductivity. The conductivity enhancement in binary system, in general, could be caused by the presence of highly conducting intermediate phase. For the present system, however, this is not true as XRD, DTA and SEM results show the presence of only  $\text{K}_2\text{SO}_4$  and  $\text{Ag}_2\text{SO}_4$  phases. Amongst the existing theories of composite solid electrolytes, the theory proposed recently (Singh 1993) explains an increase in the conductivity in this region. The total ionic conductivity of the specimen of this group is due to the contributions made by: (a) the grains of  $\text{Ag}_2\text{SO}_4$  solid solution, (b) grains of  $\text{K}_2\text{SO}_4$  solid solution and (c) interfacial space charge region between the  $\text{Ag}_2\text{SO}_4/\text{Ag}_2\text{SO}_4$ ,  $\text{K}_2\text{SO}_4/\text{K}_2\text{SO}_4$  and  $\text{Ag}_2\text{SO}_4/\text{K}_2\text{SO}_4$  grains. Interfacial space charge region ( $\text{Ag}_2\text{SO}_4/\text{K}_2\text{SO}_4$ ) formed due to the net transfer of surface cations from  $\text{Ag}_2\text{SO}_4$  to  $\text{K}_2\text{SO}_4$  and *vice versa*. The ion transport parallel to the interface (in the space charge region) is called surface percolation. This surface percolation is of great importance from mass transport view point and provides an increase in overall conductivity of the sample. The maximum conductivity at 30 mole%  $\text{Ag}_2\text{SO}_4$  is due to its optimum dispersion or percolation threshold (Bunde *et al* 1985).

#### 4. Conclusions

An investigation of electrical conductivity of the  $\text{Ag}_2\text{SO}_4\text{-K}_2\text{SO}_4$  system—supported by XRD, DTA and SEM—have shown maxima in conductivity at 20, 70 and 90 mol%  $\text{K}_2\text{SO}_4$ . Intragrain percolation (20, 90 mol%) due to lattice distortion, and, surface percolation (70%) account for these maxima. Rapid quenching has enhanced the limit of solid solubility of  $\text{K}_2\text{SO}_4$  to 20 mol%. The 90–10  $\text{Ag}_2\text{SO}_4\text{-K}_2\text{SO}_4$  composition with highest conductivity is proposed as a candidate for  $\text{SO}_2/\text{SO}_3$  gas sensor.

### Acknowledgement

Authors are thankful to the Department of Environment, New Delhi, for providing financial assistance to carry out this work.

### References

- Bunde A, Dieterich W and Roman H E 1985 *Phys. Rev. Lett.* **55** 5  
Gauthier M and Chamberland A 1977 *J. Electrochem. Soc.* **124** 1579  
Hoffer H H, Eysel W and Alpen U V 1981 *J. Solid State Chem.* **36** 365  
Jacob K T and Rao D U 1979 *J. Electrochem. Soc.* **128** 1842  
Kumari M S and Secco E A 1983 *Canadian J. Chem.* **61** 2804  
Kvist A and Lunden A 1965 *Z. Naturforsch.* **20a** 235  
Liu Q, Xi S and Wu W 1990 *Solid State Ionics* **41** 456  
Nacken R N 1907 *Jahrb. Mineral Geol.* **24** 65  
Natarajan M and Secco E A 1975 *Canadian J. Chem.* **53** 1542  
Singh K, Chandrayan V R and Deshpande V K 1988 *Solid State Ionics* **27** 57  
Singh K and Bhoga S S 1990 *Solid State Ionics* **39** 205  
Singh K, Bhoga S S and Wachasundar S D 1992 *Appl. Phys.* **A55** 493  
Singh K and Bhoga S S 1992 *J. Solid State Chem.* **97** 141  
Singh K 1993 *Solid State Ionics* **66** 5

## Resistivity studies of melt spun and annealed Al–Mn–Fe–Si multiply twinned samples

KULVIR SINGH, D BAHADUR and G V S SASTRY\*

Department of Metallurgical Engineering and Materials Science, Indian Institute of Technology, Powai, Bombay 400 076, India

\*Department of Metallurgical Engineering, Institute of Technology, Banaras Hindu University, Varanasi 221 005, India

MS received 11 January 1995

**Abstract.** The quaternary  $\text{Al}_{75}\text{Mn}_{10}\text{Fe}_5\text{Si}_{10}$  alloy was synthesized by induction melting, melt spinning and subsequent annealing. The melt spun sample shows the multiply twinned nodular-type microstructure. These plates surround an icosahedral seed of the nodule. Annealing induces relaxation/transformation of the seeds due to diffusion process. We studied the electrical properties of all the three states (as-cast, quenched and annealed) of  $\text{Al}_{75}\text{Mn}_{10}\text{Fe}_5\text{Si}_{10}$  alloy. The results are discussed in the framework of Ziman–Faber theory.

**Keywords.** Melt spinning; multiply twinned structure; icosahedral; microstructure; electrical resistivity.

### 1. Introduction

The remarkable discovery of icosahedral phase in rapidly solidified  $\text{Al}_6\text{Mn}$  alloys (Shechtman *et al* 1984) has generated enough interest in looking for newer systems and their physical properties (Kimura *et al* 1986; Wong and Poon 1986; Mizutani *et al* 1991). Similarly, the discovery of twinning by rotation around irrational axes in the cubic  $\alpha\text{-Al}_9(\text{Mn Fe})_2\text{Si}_2$  phase (Bendersky *et al* 1989; Mandal *et al* 1991) marks another milestone in the field of quasicrystallography. By rapid solidification from the melt, the twin is grown in such a fashion that it retains the icosahedral motifs present in the unit cells in the same orientation across the interface, while the lattice itself undergoes a five-fold rotation around  $[1, \tau, 0]$  axes. The icosahedral motif plays an important role in the growth of the twinned crystals (Goldman and Widom 1991). These irrational twins have five variants. These variants together give rise to forbidden point group symmetry which gives rise to pseudoicosahedral in multiply twinned structures. Such irrational twinning had also been observed in Al–Fe–V–Si (Srivastava and Ranganathan 1992), Al–Mn–Ge (Lalla *et al* 1992) and Al–Mn–Cr–Si (Singh *et al* 1992) systems. Field and Fraser (1985) suggested that icosahedral symmetry patterns likely arose from the microtwinning among twenty twin variants of distorted diamond cubic lattice. Their twinning model is different from the present one.

It is known that all quasicrystals have complex crystalline counterparts, which are closely related to the quasicrystals in composition and local atomic structure. These are known as rational approximant structures (RAS). They have played an important role in describing the atomic-scale structure of quasicrystals, their formation, stability and physical properties (Goldman and Kelton 1993).

Usually the resistivity of quasicrystalline alloys is quite high compared to conventional crystalline alloys. But the temperature dependence of resistivity in approximant crystalline phases is similar to that in the quasicrystalline phases with a few exceptions such as



Al-Cu-Li. Al-Cu-Li quasicrystal has the negative temperature coefficient of resistance (TCR), while the RAS of Al-Cu-Li has a positive TCR (Poon 1992; Fujiwara 1993).

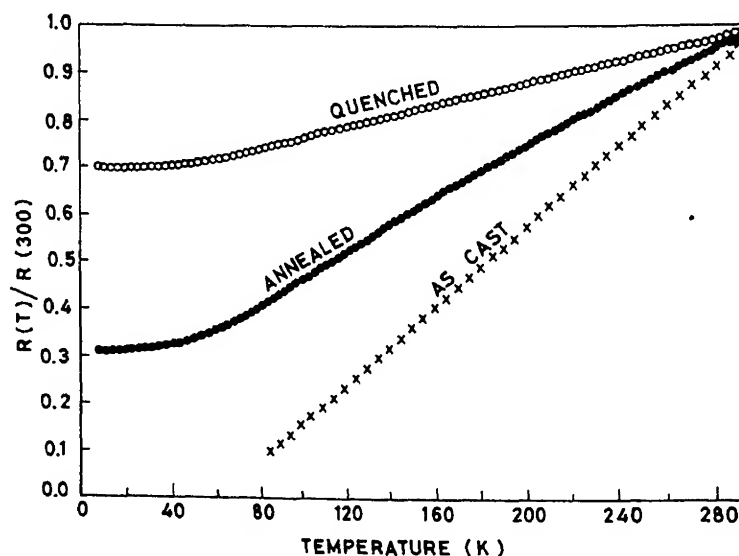
In this paper we report studies on the electrical resistivity of nominal composition  $\text{Al}_{75}\text{Mn}_{10}\text{Fe}_5\text{Si}_{10}$  for the as-cast, rapidly quenched and annealed samples.

## 2. Experimental

The quaternary alloy of nominal composition  $\text{Al}_{75}\text{Mn}_{10}\text{Fe}_5\text{Si}_{10}$  was induction melted in argon atmosphere. Small quantities of the as-cast alloy were subsequently spun using a copper wheel. More details of sample preparation are given elsewhere (Mandal *et al* 1991). Standard four-probe DC electrical resistivity measurements with 10 mA current were carried out using a DRC-82C (CTI and cryosystems) closed-cycle helium refrigerator in the range 8 to 300 K. The temperature was controlled with a Lakeshore DRC-82C temperature controller to a stability of  $\pm 0.1$  K. The resistance was measured with a Datron 1071 Autocal digital multimeter. The resolution in resistance was about 1 part in  $10^5$ . Low-thermal, low-melting-point nonsuperconducting solder was used for the contacts. Transmission electron microscopy was also done for microstructural characterization. A JEOL 1000 transmission electron microscope with  $\pm 45^\circ$  tilt facility and a heating holder for *in situ* heating up to  $1000^\circ\text{C}$  was used for this purpose.

## 3. Results and discussion

The temperature dependence curves of normalized resistance of the as-cast, quenched and annealed samples of  $\text{Al}_{75}\text{Mn}_{10}\text{Fe}_5\text{Si}_{10}$  are shown in figure 1. From this figure



can readily make the following observations: (i) The general nature of temperature dependence of resistance  $R(T)$  and the magnitude of the resistivity for the as-cast alloys are almost similar to those of pure Al metal. The resistance of the as-cast alloy increases monotonically, with a resistance ratio  $R(300\text{ K})/R(80\text{ K}) = 11$ . (ii) The melt spun (quenched) sample shows a minimum at low temperature ( $\sim 20\text{ K}$ ), while after annealing at  $400^\circ\text{C}$  for 2 h it does not exhibit any minima throughout the temperature range. A saturation effect, however, is observed below  $20\text{ K}$ . The possibility of minima below  $10\text{ K}$  cannot be ruled out. The temperature dependence of resistivity of Al-Mn-based quasicrystals commonly shows a minimum at low temperatures (Macko *et al* 1989). Similar resistivity behaviour was observed in  $\text{Al}_{86}\text{Co}_{14}$  quasicrystal (Dunlap *et al* 1986). Data below the minimum are well described by root  $T$  temperature behaviour predicted by the electron-electron interaction effect. Data above the minimum are usually well described by Ziman-Faber theory (Macko *et al* 1989). According to the generalized Ziman-Faber theory (Howson 1984) the temperature dependence of the resistivity comes from the temperature dependence of the structure factor and the Debye-Waller factor. Within this model, there can be two competing mechanisms which can in principle give rise to a resistivity minimum.

After annealing of the melt spun sample different features are observed in the  $R(T)$  plot. The negative TCR which is shown by melt spun sample is not seen for annealed sample and the resistance ratio  $R(300\text{ K})/R(8\text{ K})$  also increases about two times more compared to the quenched sample. Unfortunately, we could not estimate the resistivity before and after the annealing on the same sample because of the brittle and wavy nature of samples. However, the effect on the temperature coefficient of resistivity is obvious. The above described effect in annealed sample might occur due to changes in microstructure during annealing. The multiply twinned crystals have a typical nodular microstructure as shown in figure 2. These multiply twinned plates surround a central icosahedral seed of the nodule. After annealing, the icosahedral seeds might get transformed and relaxed due to diffusion process occurring around icosahedral seed and act as glue regions around the multiply twinned nodules. These may influence the dominant preferred electrical paths for electron transport. This effect may be greatest when such regions exist along the boundaries of the twinned nodules (Takeuchi *et al* 1993). In the quenched Al-Mn-Fe-Si sample annealed *in situ* in the microscope by R K Mandal and G V S Sastry (unpublished work), the twinned plates did not show any morphological transformation up to  $600^\circ\text{C}$ . The icosahedral seed too did not show appreciable changes, though any minute changes in the icosahedral seed cannot be ruled out. Detection of such changes in the maze of the seed structure (figure 2) is difficult. Also, the relaxation of phason strains which cannot be seen as microstructural changes may be reflected in electronic properties.

The temperature dependence of resistance  $R(T)$  shown in figure 1 cannot be explained by a single functional form. Hence, we have attempted here to fit the data over the limited ranges of temperature to the conventional theories applicable for the amorphous materials for want of a comprehensive model suitable for this class of materials. The obtained values for different functions are given in table 1. The quenched sample shows positive TCR in the temperature range 22 to  $300\text{ K}$ . We have fitted the resistivity data between 50 and  $300\text{ K}$  to the relation

$$r_n(T) = \frac{R(T) - R(T_{\min})}{R(T_{\min})} = a + bT. \quad (1)$$

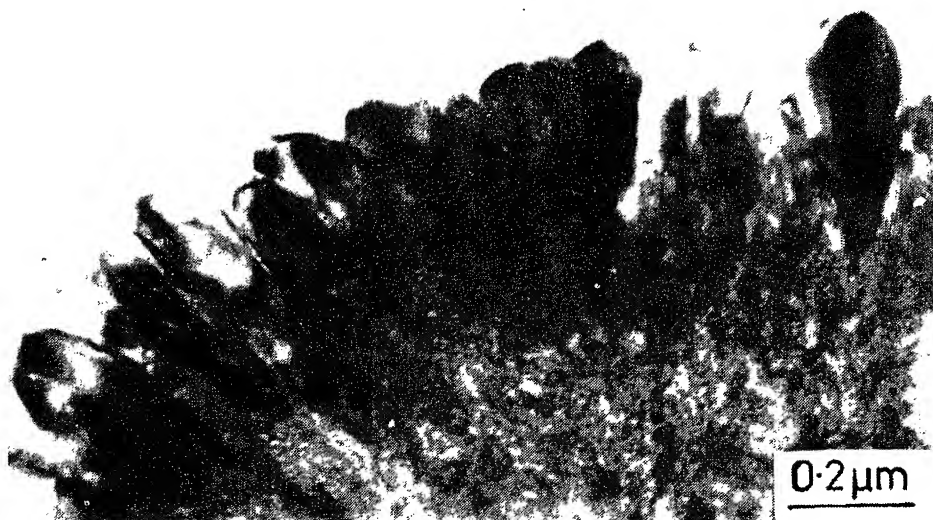


Figure 2. Transmission electron micrograph of a portion of nodule showing twin plates at the periphery and speckled contrast corresponding to the icosahedral seed at the centre.

Table 1. Fits to the normalized resistance  $r_n(T)$ : compositions, various parameters, equations and temperature ranges of fits for quenched and annealed  $\text{Al}_{75}\text{Mn}_{10}\text{Fe}_5\text{Si}_{10}$  are given.

Sample	$R_{RT}/R(8\text{ K})$	Functions	Ranges of temp.(K)	Parameters	
				$b(\text{K}^{-1} \text{ or } \text{K}^{-2})$	$c(\text{K}^{-2})$
$\text{Al}_{75}\text{Mn}_{10}\text{Fe}_5\text{Si}_{10}$ (quenched)	1.5	$a - b\sqrt{T}$	8–20	$6.6 \times 10^{-4}$	—
		$-a + bT^2$	35–120	$9.4 \times 10^{-6}$	—
		$a + bT$	50–300	$1.7 \times 10^{-3}$	—
$\text{Al}_{75}\text{Mn}_{10}\text{Fe}_5\text{Si}_{10}$ (annealed)	3.1	$-a + bT^2$	25–60	$4.6 \times 10^{-5}$	—
		$a + bT$	50–225	$9.2 \times 10^{-3}$	—
		$a + bT - cT^2$	225–300	$1.1 \times 10^{-2}$	$6.3 \times 10^{-6}$

In the low-temperature range 35 to 120 K the data are well fitted to the relation

$$r_n(T) = a + bT^2. \quad (2)$$

Below 22 K it has a negative TCR and fits to root  $T$  dependence. The electron-electron interaction is considered to be responsible for this temperature dependence at low temperature. Following Meisel and Cote (1977), the  $T^2$  dependence arises from the temperature dependence of the structure factor using diffraction model. The high-temperature region where  $T$  dependence is prevalent may be interpreted as due

to electron-phonon interaction in the diffraction model (Altshuler and Aronov 1985; Kimura *et al* 1989).

In the higher temperature region between 225 and 300 K the annealed sample does not fit the expected relation (1). Instead, the data are fitted to an empirical relation of the form

$$r(T) = a + bT - cT^2, \quad (3)$$

where the  $T$  dependence arises from the electron-phonon interaction in the diffraction model. However, the origin of the  $-T^2$  term is not well understood. Similar observation has been reported in case of Ti-Ni-Fe-Si (Bahadur *et al* 1991) and in Al-Cu-Fe (Srinivas and Dunlap 1991). The data between 25 and 60 K fit equation (2).

Phillips (1993) has suggested that, in a two-component system consisting of icosahedral regions and non-icosahedral twinning regions, the twinning region provides the dominant electrical paths for transport. The twinning region, which is highly defective, may still be locally periodic. Almost all the background density of states  $N_b(E_F)$  at  $E = E_F$  is associated with the twin regions in such a case and can be associated with a pseudogap which is responsible for stabilization of the structure. Following discussion on the density of states by Phillips (1993) annealing may produce an interesting feature in  $N_b(E_F)$ . For example, a minigap could develop due to relaxation through diffusion phenomena of the icosahedral seed. These minigaps in the density of states may be largely responsible for the anomalous behaviour of electrical resistivity. The  $-T^2$  term in the high-temperature regime for the annealed sample could be due to the presence of such minigaps. Such  $-T^2$  dependence has recently been reported in many quasicrystalline systems (Srinivas and Dunlap 1991; Singh *et al* 1994).

It may be concluded that multiply twinned structures not only mimic 5-3-2 symmetry but also exhibit electronic properties similar to those of the icosahedral quasicrystals. The icosahedral seeds which are randomly present presumably do not interfere with the conduction path in the as-quenched sample. However, when annealed at 400°C, some transformation relaxation of the icosahedral seeds occurs which results in the modified resistivity behaviour explained on the basis of Phillips's (1993) hypothesis of minigaps and pseudogaps.

### Acknowledgements

We are thankful to Dr Alok Banerjee for help in electrical resistivity measurements, and to Dr R K Mandal for helpful discussions. Financial support by DST, Government of India, is gratefully acknowledged.

### References

- Altshuler B L and Aronov A G 1985 in *Electron-electron interaction in disordered systems* (eds) A L Efrov and M Pollak (Amsterdam: North Holland) p. 1
- Bahadur D, Das A, Singh K and Majumdar A K 1991 *J. Phys. Cond. Matter* **3** 4125
- Bendersky L A, Cahn J W and Gratias G 1989 *Philos. Mag.* **B60** 685

- Field R D and Fraser H I 1985 *Mater. Sci. Eng.* **68** 117
- Fujiwara T 1993 *J. Non-Cryst. Solids* **153-154** 390
- Goldman A I and Kelton R F 1993 *Rev. Mod. Phys.* **65** 1
- Goldman A I and Widom M 1991 *Annu. Rev. Phys. Chem.* **42** 685
- Howson M A 1984 *J. Phys.* **F14** L25
- Kimura K, Hasimoto T and Takeuchi S 1986 *J. Phys. Soc. Jpn.* **55** 2472
- Kimura K, Iwahashi H, Hasimoto T, Takeuchi S, Mizutani U, Ohashi S and Itoh G 1989 *J. Phys. Soc. Jpn.* **58** 2472
- Lalla N P, Tiwari R S and Srivastava O N 1992 *J. Mater. Res.* **7** 53
- Macko D, Hudak O and Hajko V Jr 1989 *Phys. Lett.* **A136** 327
- Mandal R K, Sastry G V S, Lele S and Ranganathan S 1991 *Scr. Metall. Mater.* **25** 1477
- Meisel L V and Cote P J 1977 *Phys. Rev.* **B16** 2978
- Mizutani U, Kaniya A, Matsuda T and Takeuchi S 1991 *Mater. Sci. Eng.* **A133** 111
- Phillips J C 1993 *Phys. Rev.* **B47** 2522
- Poon S J 1992 *Adv. Phys.* **41** 303
- Shechtman D, Blech I, Gratias G and Cahn J W 1984 *Phys. Rev. Lett.* **53** 1951
- Singh Alok, Srivastava A K and Ranganathan S 1992 *Proc. Symp. on Microstructure of Materials* Berkeley, USA
- Singh K, Bahadur D, Nigam A K, Shiv Prasad and Girish Chandra 1994 MRSI conference, Hyderabad, India
- Srivastava A K and Ranganathan S 1992 *Scr. Metall. Mater.* **27** 53
- Srinivas V and Dunlap R A 1991 *Philos. Mag.* **B64** 475
- Takeuchi S, Akiyama H, Naito N, Shibuya T, Hasimoto H, Kadagawa K and Kimura K 1993 *J. Non-Cryst. Solids* **153-154** 353
- Wong K M and Poon S J 1986 *Phys. Rev.* **B34** 7371

## Room-temperature low-cycle fatigue behaviour of Ti–27Al–15Nb alloy

P N SINGH, C RAMACHANDRA, B K SINGH and V SINGH

Department of Metallurgical Engineering, Banaras Hindu University, Varanasi 221 005, India

MS received 4 May 1994; revised 25 January 1995

**Abstract.** Low-cycle fatigue (LCF) behaviour of the alloy Ti–27Al–15Nb, in ( $\alpha_2 + B2$ ) heat-treated condition was studied in total axial strain control mode at different total strain amplitudes ( $\Delta\epsilon_t/2$ ) from  $\pm 0.65$  to  $\pm 1.0\%$  and room temperature. While there was little hardening of the material at the lowest strain amplitude ( $\Delta\epsilon_t/2: \pm 0.65\%$ ), pronounced hardening was observed at the higher strain amplitudes ( $\Delta\epsilon_t/2 \geq 0.83\%$ ). The cyclic stress, at high strain amplitudes, continuously increased from the beginning till fracture of the specimens. The LCF resistance of the material was found to be low and this was due to its poor ductility at room temperature. Dual slope was observed in the Coffin–Manson plot, with less slope of the upper segment than that of the lower one, as observed in several alloys. The fracture behaviour pointed to brittleness and faceted features were observed.

**Keywords.** Titanium aluminide; low-cycle fatigue; cyclic hardening; fatigue life; dual slope; C–M plot.

### 1. Introduction

Titanium aluminides possess attractive properties like high creep resistance (MacAndrew and Kessler 1956; Blackburn and Smith 1981), high temperature-specific strength and sufficient oxidation resistance (MacAndrew and Kessler 1956) and retain high static strength and stiffness at elevated temperatures (Lipsitt *et al* 1975). These characteristics make them potential candidate materials for applications in gas turbine engines and airframe structures in advanced aircraft. The use of stoichiometric Ti<sub>3</sub>Al and TiAl alloys is limited due to their poor ductility at ambient temperature (Sastry and Lipsitt 1977a, 1980; Lipsitt *et al* 1980; Baker and George 1992). However, the addition of Nb to Ti<sub>3</sub>Al has been found to improve its ductility through stabilization of another phase, B2 (based on the high-temperature bcc allotrope of Ti), and thus rendering the single phase Ti<sub>3</sub>Al to a dual phase ( $\alpha_2 + B2$ ) system. Investigations have been carried out on the influence of morphology of the constituent phases  $\alpha_2$  and B2 on tensile properties and fracture behaviour of Ti<sub>3</sub>Al–Nb alloys (Gogia *et al* 1992; Kim *et al* 1993). Reports are also available on creep behaviour (Mediratta and Lipsitt 1980; Hayes 1989; Mishra and Banerjee 1990), fracture toughness and fatigue crack growth (Soboyejo 1992) of the titanium aluminides. Sastry and Lipsitt (1977b) studied the cyclic deformation behaviour of Ti<sub>3</sub>Al over a range of temperature and analysed the process of cyclic hardening. However, little work has been carried out on low-cycle fatigue (LCF) behaviour of Ti<sub>3</sub>Al–Nb alloys. The present work is concerned with characterization of LCF behaviour of the Ti–27Al–15Nb alloy in the  $\alpha_2 + B2$  heat-treated condition at room temperature.

### 2. Experimental

Hot rolled rods of 15 mm dia of the alloy Ti–27Al–15Nb were procured from the Defence Metallurgical Research Laboratory (DMRL), Hyderabad. Blanks of 12 mm dia were

vacuum-encapsulated in silica tubes with titanium getter and solution-treated in the  $\alpha_2 + \text{B2}$  phase field at  $1060 \pm 5^\circ\text{C}$  for 4 h and cooled at a rate of  $\approx 288^\circ\text{C/h}$ . The specimen for optical microscopy was prepared by mechanical polishing and etching with a solution of 10% HF + 5%  $\text{HNO}_3$  + 85%  $\text{H}_2\text{O}$  (by volume). Tensile specimens with double shoulder having gauge length and gauge diameter 11 and 3.25 mm respectively were machined from the heat-treated blanks and tested using Instron universal testing machine. LCF specimens with threaded ends, having gauge length and gauge diameter 15 and 5.5 mm respectively and shoulder radii of 20 mm, were machined from the heat-treated blanks. The gauge section was mechanically polished up to 4/0 grade of emery paper. LCF tests were conducted in tension-compression ( $R = -1$ ), under total axial strain control, in the range of total strain amplitude ( $\Delta\epsilon_t/2$ ) from  $\pm 0.65\%$  to  $\pm 1.0\%$  at constant frequency of 0.2 Hz, using a computer-controlled servohydraulic MTS test facility. The variation of stress amplitude ( $\Delta\sigma/2$ ) and inelastic strain amplitude ( $\Delta\epsilon_p/2$ ) in tension and compression with number of cycles was recorded. Fracture characteristics were examined using a JEOL 840A scanning electron microscope.

### 3. Results and discussion

The optical microstructure of the alloy in the  $\alpha_2 + \text{B2}$  heat-treated condition shows primary  $\alpha_2$  phase isolated in the B2 matrix (figure 1). The microstructure is seen more clearly at higher magnification obtainable in the scanning electron micrograph shown in figure 2. The material in the  $\alpha_2 + \text{B2}$  treated condition was found to have yield strength 609 MPa, fracture strength 759 MPa and elongation 3.1%. The LCF data at different total strain amplitudes ( $\Delta\epsilon_t/2$ ) in terms of the plastic strain amplitude ( $\Delta\epsilon_p/2$ ), elastic strain amplitude ( $\Delta\epsilon_e/2$ ) and cyclic stress amplitude ( $\Delta\sigma/2$ ) at first cycle ( $N_1$ ), half life ( $N_f/2$ ) and the last cycle to failure ( $N_f$ ) along with the

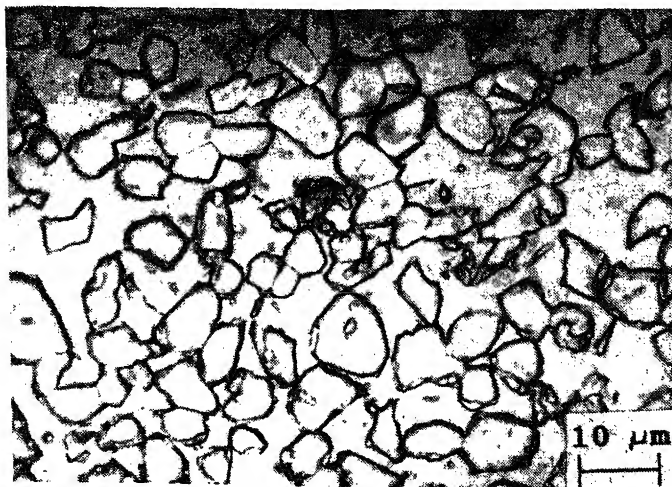


Figure 1. Optical micrograph showing the microstructure, consisting of isolated  $\alpha_2$  and transformed B2 phases.

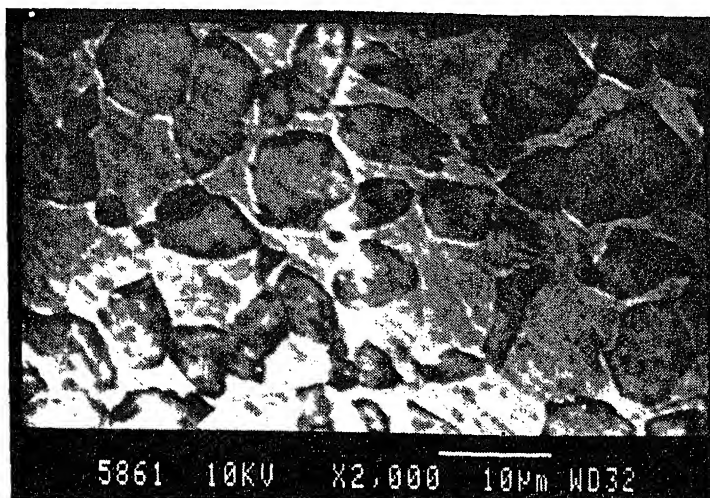


Figure 2. Scanning electron micrograph showing  $\alpha_2$  and transformed B2 phases.

Table 1. Low-cycle fatigue data for the alloy Ti-27Al-15Nb at room temperature.

$\Delta\epsilon_i/2$ (%)	$\Delta\epsilon_o/2$ (%) at			$\Delta\epsilon_e/2$ (%) at			$\Delta\sigma/2$ (MPa) at			Cycles to failure
	$N_i$	$N_f/2$	$N_f$	$N_i$	$N_f/2$	$N_f$	$N_i$	$N_f/2$	$N_f$	$N_f$
0.83	0.242	0.106	0.100	0.588	0.724	0.730	640.2	771.6	777.8	1724
0.84	0.250	0.175	0.160	0.590	0.665	0.680	643.9	746.9	766.6	268
0.85	0.258	0.200	0.201	0.592	0.645	0.649	646.8	739.0	762.6	54
0.88	0.280	0.250	0.216	0.600	0.630	0.664	650.0	731.7	760.1	32
1.00	0.347	0.330	0.321	0.653	0.670	0.679	653.5	664.5	675.1	4

number of cycles to failure ( $N_f$ ) are presented in table 1. It may be seen from table 1 that while  $\Delta\epsilon_p/2$  continuously decreases, ( $\Delta\epsilon_e/2$ ) and ( $\Delta\sigma/2$ ) steadily increase from  $N_i$  to  $N_f$  and thus there is continuous hardening of the material during cyclic loading. It may, however, be noted that changes in these parameters ( $\Delta\epsilon_p/2$ ,  $\Delta\epsilon_e/2$  and  $\Delta\sigma/2$ ) are relatively more during the first half of the life than those in the later half. The cyclic hardening behaviour at different strain amplitudes may be seen from the stress response curves shown in figure 3. There is little hardening at the lowest strain amplitude ( $\Delta\epsilon_i/2: \pm 0.65\%$ ). However, it is relevant to mention that this test was not continued till fracture but was interrupted after 10632 cycles. On the other hand there is pronounced hardening at the higher strain amplitudes ( $\Delta\epsilon_i/2 \geq 0.83\%$ ). The cyclic hardening at higher strain amplitudes shown in figure 3 is similar to that observed by Sastry and Lipsitt (1977b) in  $Ti_3Al$  below  $700^\circ C$ . They have analysed the process of cyclic hardening in  $Ti_3Al$  and related the observed behaviour to



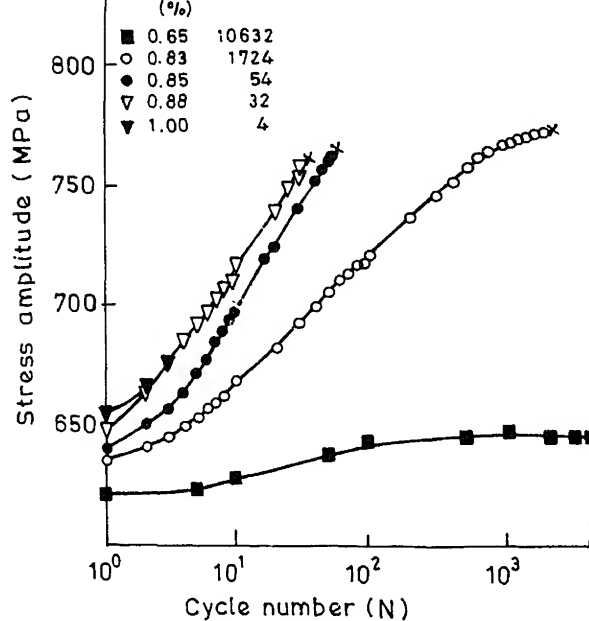


Figure 3. Cyclic stress response curves showing variation of stress amplitude with of cycles.

debris of  $\frac{1}{3}\langle 11\bar{2}3 \rangle$  Burgers vector. The extent and, in particular, the rate of hardening in the alloy Ti-27Al-15Nb (figure 3) is relatively lower than that in (Sastry and Lipsitt 1977b) and may perhaps be related to different dislocation behaviour in the  $\alpha_2$  and B2 phases of the alloy Ti-27Al-15Nb in contrast to the single phase  $\alpha_2$  in  $\text{Ti}_3\text{Al}$ .

Cyclic hardening in the alloy Ti-27Al-15Nb in the present investigation is evident from the cyclic and monotonic stress-strain curves (figure 4). Stress amplitude values of the cyclic curve correspond to the cycle close to the half life ( $N_f/2$ ). The increase in the cyclic stress at the highest strain amplitude ( $\Delta\epsilon_t/2: \pm 1.0\%$ ) may be due to crack initiation in the specimen tested at the highest strain amplitude to failure in four cycles.

The variation of fatigue life with different components of the strain amplitude is shown in figure 5. It may be noted that the values of  $\Delta\epsilon_p/2$  and  $\Delta\epsilon_e/2$  used in the plot correspond to the cycle close to  $N_f/2$ . The variation of reversals to failure ( $2N_f$ ) with  $\Delta\epsilon_t/2$  is linear. However, there is mild tendency for dual slope in the elastic strain region. While the slope of the segment corresponding to high-strain region is negative, the slope of the segment corresponding to low-strain region is positive (figure 5, table 2). A very weak tendency of bilinearity in the elastic strain plot has earlier been reported in a high-temperature ( $\alpha + \beta$ ) titanium alloy Ti-6.6Al-3.3Mo-1.9Zr-0.3Si (Varma *et al* 1993); however, the slopes of the segments, corresponding to high- as well as low-strain region, were negative. Bilinearity in the elastic strain plot in the present investigation may be related to the

differences in cyclic work hardening behaviour of the material at low- and high-strain amplitudes. The Coffin–Manson (C–M) plot ( $\Delta\epsilon_p/2$  vs  $2N_f$ ) displays a distinct bilinear behaviour (figure 5). The slopes of the segments I and II are  $-0.132$  and  $-0.219$  respectively. These slopes are quite different from the usual slope of  $\approx -0.5$  observed

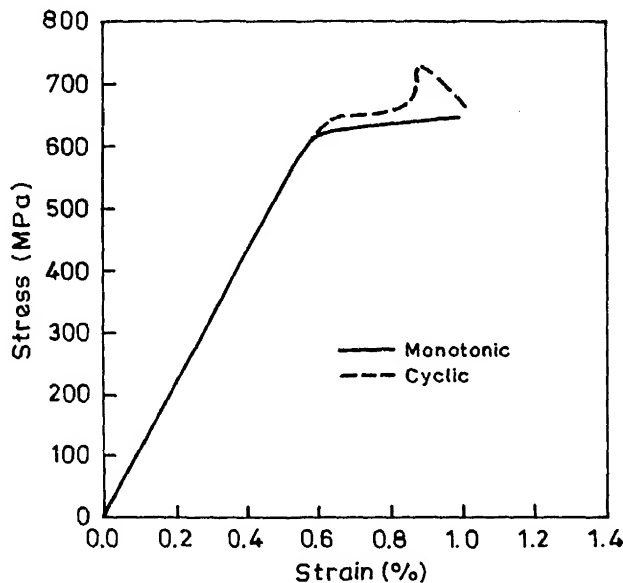


Figure 4. Cyclic and monotonic stress-strain curves.

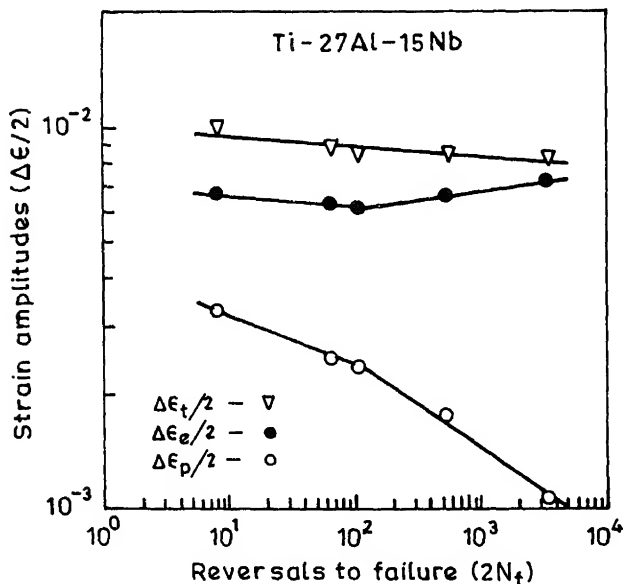


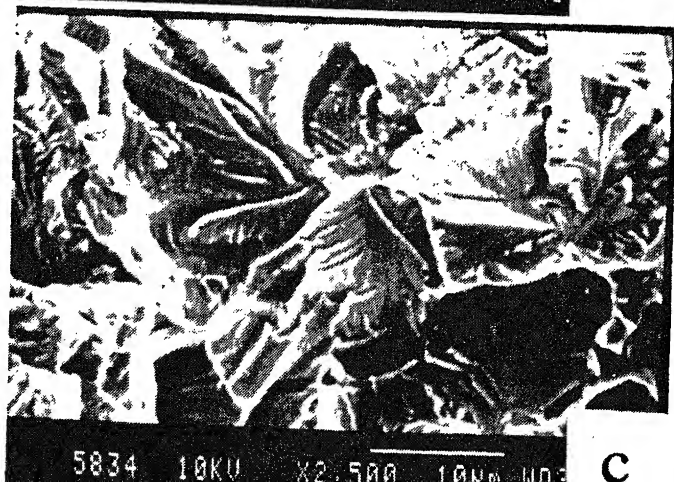
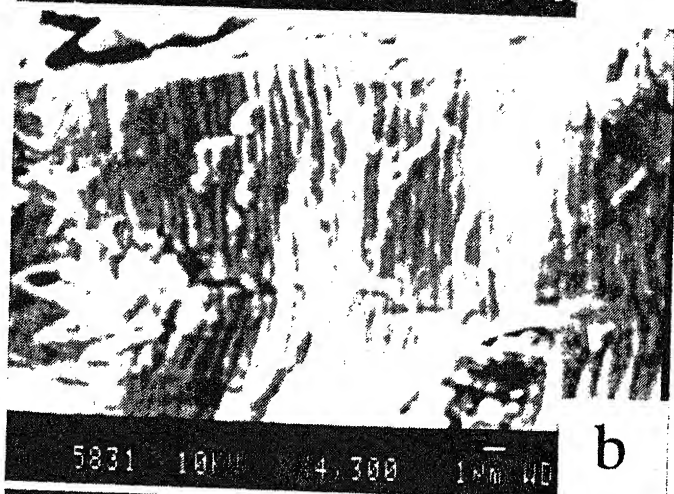
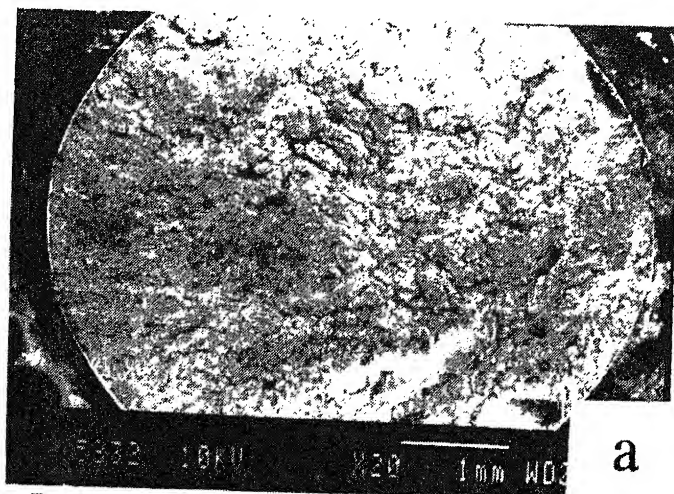
Figure 5. Variation of number of reversals to failure ( $2N_f$ ) with elastic, plastic and total strain amplitudes.

**Table 2.** Low-cycle fatigue parameters for alloy Ti-27Al-15Nb at room temperature.

LCF parameters	Segment I	Segment II
$\epsilon'_f$	0.00434	0.00664
$c$	-0.132	-0.219
$\sigma'_f$	766.7	528.58
$b$	-0.0319	0.047

in many alloys. Bilinearity in C-M plot is reported in a number of alloys such as dual-phase steel (Mediratta *et al* 1986), Al-Li alloy (Eswara Prasad *et al* 1989), Nimonic PE16 (Singh *et al* 1991) and VT9 (Singh *et al* 1994). The occurrence of bilinearity in the C-M plot has been attributed to different factors like change in the deformation behaviour through work hardening characteristics (Mediratta *et al* 1986), variations in the fracture morphology with increasing strain amplitude (Coffin 1971; Eswara Prasad *et al* 1989), environmentally assisted fatigue degradation (Coffin 1972; Sanders and Starke 1976), and change in the microstructural characteristics of deformation from low to high strain amplitude (Singh *et al* 1991; Singh *et al* 1994). Recently Radhakrishnan (1992), has analysed the bilinear behaviour in the C-M plot in many ferrous and non-ferrous alloys and rationalized that the materials, with cyclic stress range corresponding to one million cycles below the cyclic yield strength range of the material, are likely to exhibit a bilinear relationship. However, the prediction of dual slope in aluminide in the present investigation cannot be made on the above lines in view of the fatigue life of specimens being far less than one million cycles. As seen from figure 5, the slope of segment I is less steeper than segment II, hence estimation of fatigue life from extrapolation of either of the segments would lead to overestimation of fatigue life. Thus, it is essential to evaluate fatigue life of such materials, exhibiting dual slope in the C-M plot of the type shown in figure 5, over a wide range of strain amplitudes. It can be seen from figure 5 that the level of the plastic strain amplitude plot is much lower than that of the elastic one even in the region of high strain amplitude and hence the LCF resistance of this material appears to be quite low. The poor LCF resistance could also be visualized in terms of extremely low value of the fatigue ductility coefficient ( $\epsilon'_f$ ) (table 2). The transition fatigue life, estimated from extrapolation of even the segment II of the elastic and plastic (C-M) plots is quite low ( $< 2 \times 10^4$ ) (figure 5). The poor LCF resistance of this material may thus be attributed to its extremely low ductility at room temperature. On the other hand the high-cycle fatigue resistance appears to be high, as reflected by high value of the fatigue strength coefficient ( $\sigma'_f$ ) and low value of fatigue strength exponent ( $b$ ) (table 2). The fracture characteristics of this material, tested in fatigue, are observed to be considerably different.

**Figure 6.** Scanning electron micrographs showing fracture characteristics of the LCF sample ( $\Delta\epsilon_f/2 = 0.83\%$ ,  $N_f = 1724$  cycles). (a) Fracture surface at low magnification, showing striations in peripheral region and (c) cleavage-type fracture in central region of the surface.



those of the ductile alloys. The fracture surface does not show flat region, typical of fatigue failure, at low magnification (figure 6a). Fatigue striations are observed at higher magnification in some circumferential regions, to a very limited extent from the surface (figure 6b). The fracture surface in general shows cleavage type failure (figure 6c).

#### 4. Conclusions

The alloy Ti-27Al-15Nb in  $\alpha_2$  + B2 heat-treated condition exhibits little hardening at low strain amplitude ( $\Delta\epsilon_f/2$ :  $\pm 0.65\%$ ), but pronounced hardening at high-strain amplitudes ( $\Delta\epsilon_f/2 \geq \pm 0.83\%$ ), starting from the first cycle till the failure, during strain cycling ( $R = -1$ ), at room temperature. The C-M plot shows a distinct bi-linear behaviour. The LCF resistance of this material is very low and it is due to its low ductility at RT. However, fatigue life in the region of low total strain amplitude where there is dominance of the elastic strain component appears to be highly promising.

#### Acknowledgements

The authors are grateful to Dr D Banerjee, Associate Director, and Dr A K Chakrabarty, Deputy Director, Defence Metallurgical Research Laboratory (DMRL), Hyderabad, for supply of the material and keen interest in the work. Financial assistance from ARDB (Project 642), Government of India, is gratefully acknowledged.

#### References

- Blackburn M J and Smith M P 1981 US Patent No. 4 294 615
- Baker I and George E P 1992 *Metals and Materials* June 318
- Coffin L F 1971 *J. Mater. Sci.* **6** 388
- Coffin L F 1972 *Metall. Trans. A* **3A** 1777
- Eswara Prasad N, Malakondaiah G, Raju K N and Rama Rao P 1989 *Proc. Advances in Fracture Mechanics* IC77 Houston, USA 21103
- Gogia A K, Nandy T K and Banerjee D 1992 *Mater. Sci. Eng.* **A159** 73
- Hayes R W 1989 *Scr. Metall.* **23** 1931<sup>2</sup>
- Kim J Nack, Kim J Y and Cho W S 1993 *Metall. Trans. A* **24A** 1785
- Lipsitt H A, Schechtman D and Schafrik R E 1975 *Metall. Trans. A* **8A** 1991
- Lipsitt H A, Schechtman D and Schafrik R E 1980 *Metall. Trans. A* **11A** 1369
- MacAndrew J B and Kessler H D 1956 *J. Metals* **8** 1348
- Mediratta M G and Lipsitt H A 1980 *J. Mater. Sci.* **15** 2985
- Mediratta S R, Ramaswamy V and Rama Rao P 1986 *Scr. Metall.* **20** 555
- Mishra R S and Banerjee D 1990 *Mater. Sci. Eng.* **A130** 151
- Radhakrishnan V M 1992 *Int. J. Fatigue* **14** 305
- Sanders T H and Starke E A 1976 *Metall. Trans. A* **7A** 1407
- Sastry S M L and Lipsitt H A 1977a *Metall. Trans. A* **8A** 1543
- Sastry S M L and Lipsitt H A 1977b *Acta Metall.* **25** 1279
- Sastry S M L and Lipsitt H A 1980 in *Titanium 80 Science and Technology* (eds) H Kimura and J W Warrendale, PA: TMS AIME) p. 1231
- Singh P N, Ramachandra C and Singh V 1994 *Low Cycle Fatigue Behaviour of Ti-6.5Al-3.3Mo-0.3Si at RT*. Presented at 5th Annual General Meeting Feb. 1994 MRSI Hyderabad (to be published)
- Singh V, Sundararaman M, Chen W and Wahi R P 1991 *Metall. Trans. A* **22A** 499
- Soboyejo W O 1992 *Metall. Trans. A* **23A** 1737
- Varma Vijay Kumar, Saxena Vikas Kumar and Srinivas M 1993 *Scr. Metall. Mater.* **29** 673

## Oxidation and corrosion behaviour of laser-alloyed mild steel with chromium

A K PATTANAIK, A S KHANNA, C S HARANDRANATH\*,  
K WISSENBACH† and G L GOSWAMI††

Corrosion Science and Engineering Programme, \*RSIC, Indian Institute of Technology,  
Bombay 400 076, India

†Fraunhofer Institute for Lasertechnik, Aachen, Germany

††Bhabha Atomic Research Centre, Bombay 400 085, India

MS received 20 October 1994; revised 22 February 1995

**Abstract.** The oxidation and corrosion of mild steel coated with chromium powder followed by laser treatment has been investigated. Chromium powder was deposited on mild steel surface using atmospheric plasma spraying. The chromium-coated surface was irradiated separately using a pulsed Nd:YAG laser and a continuous CO<sub>2</sub> laser. The oxidation tests were carried out in air at 700°C and anodic polarization tests in 1N H<sub>2</sub>SO<sub>4</sub> solution. There was significant difference in the morphologies of the surface alloys formed using CO<sub>2</sub> laser and Nd:YAG laser. Samples treated with CO<sub>2</sub> laser showed better oxidation resistance whereas the surface alloys formed using Nd:YAG laser showed poor oxidation resistance. Anodic polarization tests carried out on samples laser-treated with CO<sub>2</sub> laser showed improved corrosion resistance.

**Keywords.** Oxidation; corrosion; laser treatment; surface alloying; plasma coating; chromium coating.

### 1. Introduction

Mild steel is generally used for many low- and moderate-temperature applications. However, its applications are restricted because of its inherently poor resistance to moisture, oxygen and other gases present in the atmosphere. It reacts quickly and accumulates heavy corrosion products when exposed to atmosphere. Protective coatings, inorganic or organic, and paints are generally employed when such steels are used in aggressive environments such as marine, acidic or strong basic (Macdowell 1992). These methods are, however, temporary and need replenishment of paint coatings quite often. Thus, an alternative method of improving mild steel and other low-alloy steels is by forming a corrosion-resistant surface alloy, which permanently protects the steel from corrosion not only at ambient temperatures but also at higher temperatures. This can be achieved by altering the surface composition, favouring the formation of passive film at ambient temperatures or protective oxide layer at higher temperatures.

Methods such as electroplating (Honey *et al* 1986), spray coatings (Parks 1985; Arvidsson 1992) and plasma coatings (Lugscheider *et al* 1985; Fairbanks and Hecht 1987) have been in use for a long time to deposit protective materials on the surface of mild steels or other less-corrosion-resistant materials. Plasma spray techniques have inherent advantages over other spray techniques because of their higher density, homogeneity, etc. However, the main limitations of these techniques are their rough and porous surface and poor bonding to the substrate. Such overlay coatings can be improved further if they are remelted.

The use of lasers for surface modification such as surface melting/alloying, surface hardening, and surface cladding of metals has now become a well-accepted material processing technique (Gasser *et al* 1988; Steen and Watkins 1993). A number of studies have been carried out which highlight the use of laser to improve the oxidation and corrosion behaviour of metals and alloys (Chiba *et al* 1984; Stott *et al* 1987; Roy *et al* 1993). Laser surface alloying provides a unique facility where surface alloys can be made with ease, cleanliness and at a much faster rate. This is achieved because of high delivery rate of energy and localized surface melting of the pre-deposited alloying elements (or a simultaneous feed of powder of desired element) and a portion of the substrate, without affecting the bulk properties of the materials.

In the present work, an attempt has been made to study the influence of laser treatment on the oxidation and corrosion behaviour of chromium-coated mild steel. Similar work on stainless steel, plasma coated on mild steel, followed by laser treatment, showed considerable improvement in oxidation behaviour (Khanna *et al* 1992). Improved corrosion resistance of electrodeposited chromium on 9Cr-1Mo steel followed by laser treatment has been observed (Pujar *et al* 1993).

## 2. Experimental

### 2.1 Plasma coating of chromium on mild steel

Mild steel samples (100 mm × 50 mm × 2 mm) were degreased and then sand-blasted (surface finish of SA 2½ as per Swedish specification) before plasma coating. A 60 µm thick coating of chromium was obtained using atmospheric plasma technique, at Laser and Plasma Division, BARC, Bombay. The following plasma parameters were used for this purpose:

Plasma torch power: 20 kW

Plasma gas: 20 l/min argon + 1 l/min N<sub>2</sub>

Current: 350 amp

Voltage: 25 V

Powder feed rate: 15 g/min

Power carrier gas: 8 l/min argon

Specimen to torch distance: 125 mm.

### 2.2 Laser irradiation

Laser irradiation was carried out on the coated specimens. A 300 W Nd:YAG pulse laser and a 3 kW continuous CO<sub>2</sub> laser were used for this purpose. Laser irradiation using a 300 W Nd:YAG laser was carried out at BARC. A focused laser beam of energy 4 to 8 J with pulse width varying from 8 to 12 ms was used for laser alloying with power frequency of 8 Hz, under argon flow, at the rate of 0.5 kg/cm<sup>2</sup>. The sweep speed was maintained at 2 mm/sec. Six different tracks were obtained by varying the laser processing parameters, shown in table 1. Samples treated using Nd:YAG laser with different pulse energies and pulse width are designated LT1 to LT6 as given in table 1.

Laser treatment using a 5 kW continuous CO<sub>2</sub> laser was carried out at Fraunhofer Institute for Laser Technique, Aachen, Germany. A 3 kW laser beam in line focus

Table 1. Nd:YAG laser parameters.

Track no.	Laser energy (J)	Parameters pulse width (ms)	Depth of penetration ( $\mu\text{m}$ )	Cross-sectional area ( $\mu\text{m}^2$ )	Zone 1* composition (% wt)			Zone 2 composition (% wt)		
					Fe	Cr	Si	Fe	Cr	Si
LT1	4	8	170	45124.7	83.27	13.24	3.49	30.74	62.89	6.37
LT2	4	12	110	36231.2	73.67	16.12	10.20	27.99	68.84	3.17
LT3	6	8	162	79878.9	86.38	10.36	3.26	25.74	69.52	4.74
LT4	6	12	157	66484.5	85.15	11.48	3.37	31.79	61.54	6.67
LT5	8	8	195	105662.0	89.66	7.92	2.42	33.83	49.19	16.98
LT6	8	12	193	104378.0	87.94	7.68	4.38	55.15	39.05	5.77

\*See figure 3a.



**Table 2.** CO<sub>2</sub> laser parameters.

Sample no.	Sweep speed (mm/min)	Interaction time (ms)	Thickness of laser-melted zone ( $\mu\text{m}$ )
LT9	500	60	275
LT8	625	48	250
LT7	750	40	200

mode (spot size 0.5 mm  $\times$  6 mm) was used for irradiation, which gave an energy density of 105 watts/cm<sup>2</sup>. Irradiation was carried out under a continuous Ar flow at the rate of 20 l/min. The sweep speed was varied from 750 to 500 mm/min, which gave an interaction time of 40 to 60 ms. Samples treated using CO<sub>2</sub> laser with three sweep speeds are designated LT7 to LT9 (table 2).

### 2.3 Microstructural analysis

The coated and laser-treated samples were mounted in epoxy for the cross-sectional analysis. The mounted specimens were polished to fine diamond finish, cleaned in acetone and chemically etched in 3% nital solution to reveal the microstructure. Concentration of the alloying elements in the melted zone was determined by the line scan mode using electron probe microanalysis. The surface morphologies of the plasma-coated and the laser alloyed specimens were observed in a scanning electron microscope.

### 2.4 Oxidation studies

The oxidation tests were carried out in air at 700°C for 100 h by exposing the uncoated, plasma-coated and laser-treated specimens. The change in weight was measured after a definite interval of time by interrupting the experiment.

### 2.5 Corrosion studies

The corrosion behaviour of the samples laser-treated using CO<sub>2</sub> laser was investigated in 1N H<sub>2</sub>SO<sub>4</sub> solution using potentiodynamic polarization technique. The laser-alloyed specimen of size 1 cm<sup>2</sup> was used for this purpose. The sample was mounted in epoxy resin with an electric contact on the reverse side using a copper wire. Anodic polarization experiments were carried out by measuring the electrode potentials with respect to a saturated calomel electrode (SCE) and were started from a cathodic potential of -700 mV (SCE) and continued until transpassivity was obtained, with a scan rate of 1 mV/sec. Subsequent polarization tests were carried out on the same sample after repolishing the sample approximately up to 40  $\mu\text{m}$  each time with a 600 grit SiC paper until the mild steel reappeared. Anodic polarization curves thus obtained were analysed for corrosion potential, corrosion current density, critical current density, passive current density and passive potential range.

### 3.1 Characterization of plasma and laser treated samples

3.1a *Plasma-coated specimen*: The surface morphology of the plasma-coated sample is shown in figures 1a and 1b. It is clear from these figures that the coating is uneven and has many pores. The cross-section of the coated sample, observed using an optical

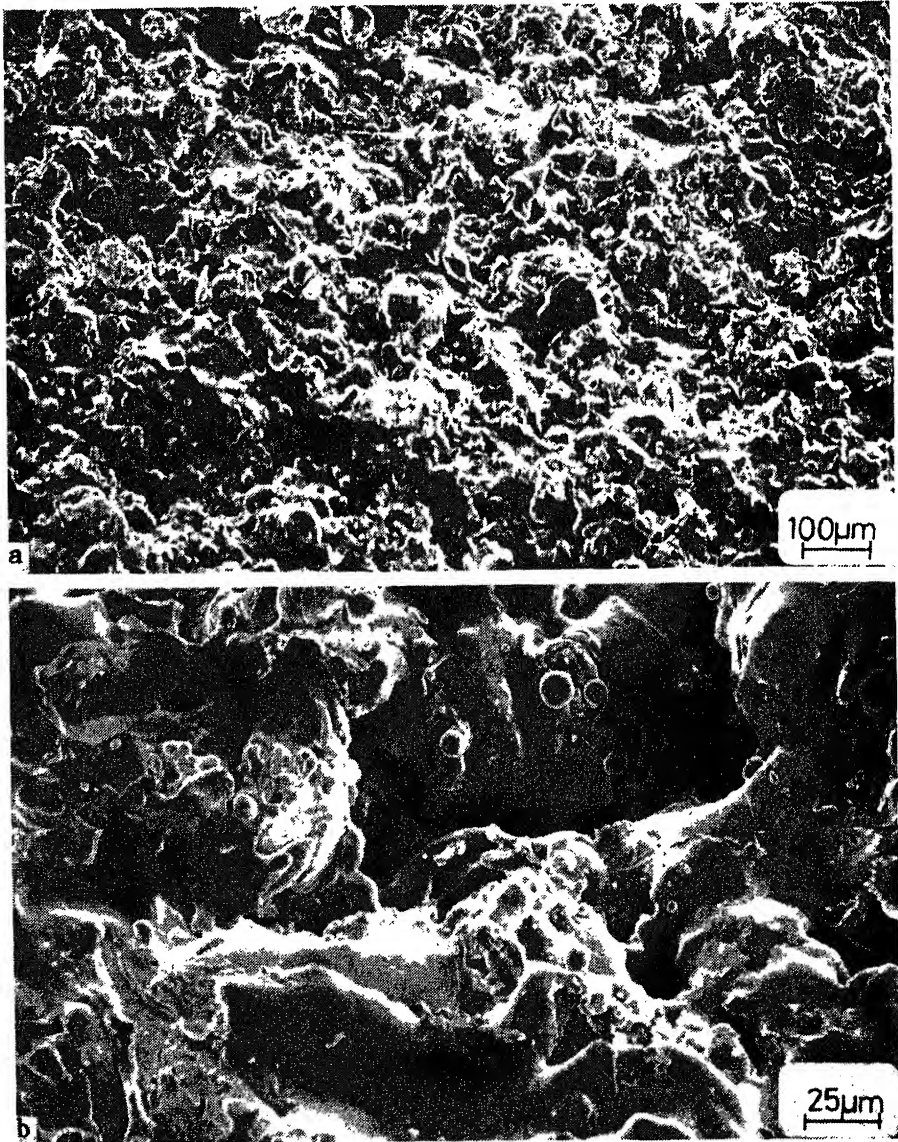
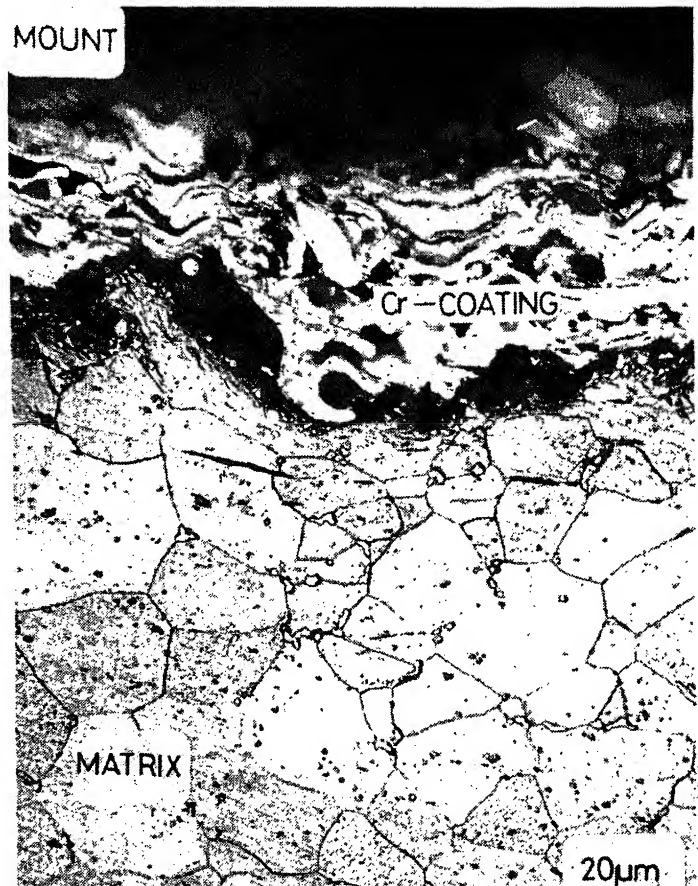


Figure 1. SEM micrographs showing (a) the surface morphology of the chromium plasma-coated on mild steel and (b) the same at higher magnification showing pores.

microscope, also reveals the porous and uneven nature of the coating, as shown in figure 2. The thickness of the Cr coating is found to be  $60\text{ }\mu\text{m}$ .

**3.1b Nd:YAG laser-treated specimen:** Figure 3a shows the surface morphology of the Nd:YAG laser-treated specimen. Each track shows two different zones (with 60% overlapping), which are magnified and shown in figures 3b, 3c and 3d. Figure 3b reveals zone-1 (Z-1) as a dense and uniform coating whereas figures 3c and 3d, of zone-2 (Z-2), show chromium oxide particles, which might have formed as a result of the oxidation of chromium during laser treatment. Figure 3c also shows a crack in Z-2 along with chromium oxide particles. The compositions of the two zones, analysed by EDAX, are summarized in table 1. The weight percentage of chromium was found to be more in Z-2 than in Z-1. The effect of laser energy and pulse width on the chromium in the laser-alloyed zone for various tracks is illustrated in figure 4. It shows that at constant energy and with varying pulse width the chromium concentration in the two zones increases. But with varying



energy and at constant pulse width the chromium concentration decreases as shown in figure 5.

Typical optical micrographs of the cross-section of the samples made using laser parameters LT2 and LT5 along with X-ray line scan analysis are shown in figure 6. The depth of penetration and the area of laser-alloyed zones calculated for each track with different laser parameters, viz. pulse energy and width, using an image analyser, are listed in table 1.

**3.1c  $\text{CO}_2$  laser-treated specimen:** The surface morphology of the  $\text{CO}_2$  laser-treated specimen is given in figures 7a and 7b. A uniform and dense surface is clearly evident from figure 7a. Analysis of the surface indicated that a large triangular phase rich in chromium, probably chromium oxide, and a round iron-rich phase (figure 7b) formed during laser processing. There was not much difference in the surface

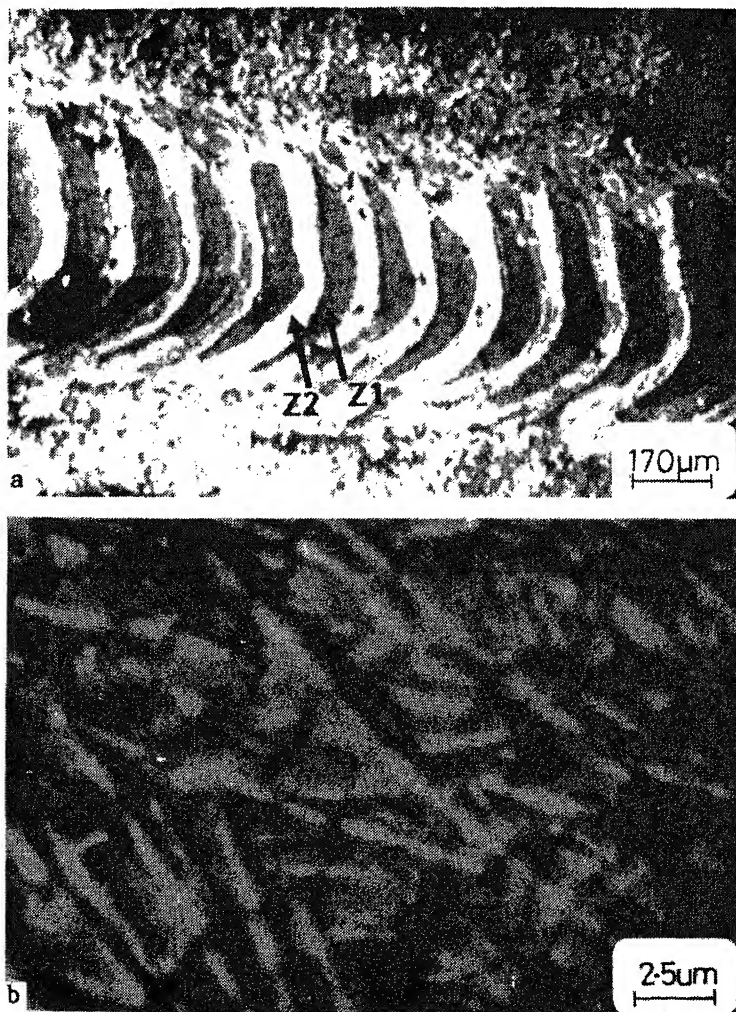
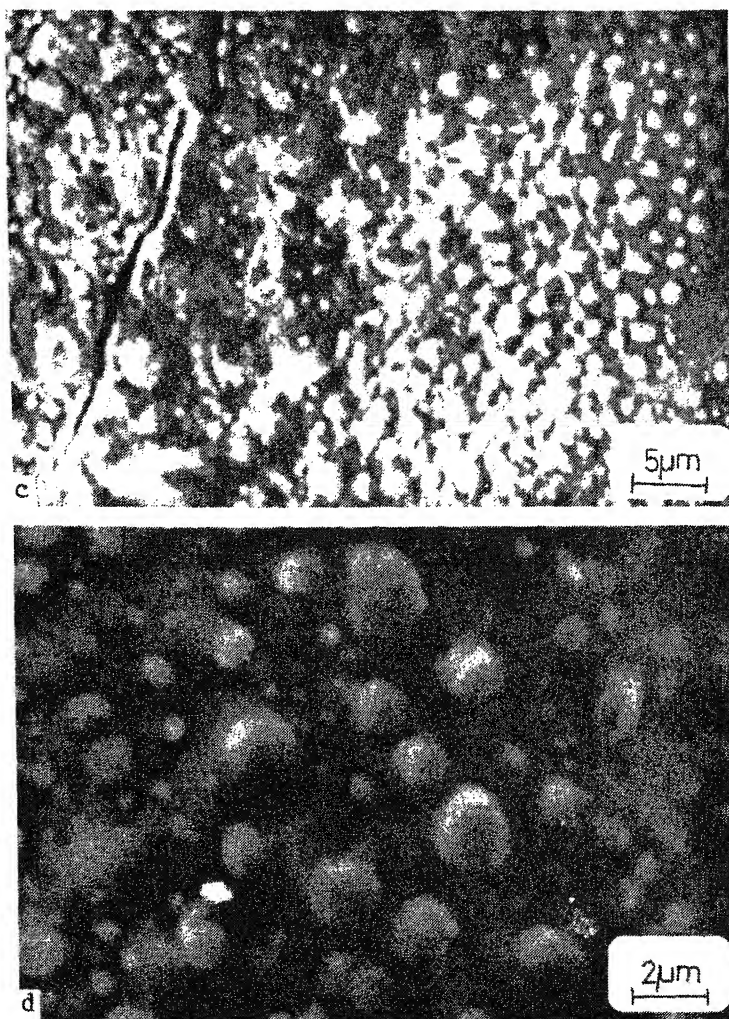


Figure 3. a-b.



**Figure 3.** SEM micrographs showing the surface morphologies of the chromium-coated specimen laser-treated using Nd:YAG laser; (a) showing different tracks after laser treatment, (b) showing zone 1 with uniform Fe and Cr distribution, (c) and (d) showing zone 2 with chromia particles.

morphologies of the alloys formed with other sweep velocities. The optical micrographs of the cross-sections of the specimens for three different sweep velocities are shown in figure 8. It shows that the laser-alloyed zone is very smooth, uniform and pore-free, compared to the as-coated specimens which were quite non-uniform and porous (figure 1).

The distribution of the alloying element in the laser alloying zone depends very much on the laser parameters and these are summarized in figure 9. It shows that the concentration of the chromium in the alloying zone decreases from about

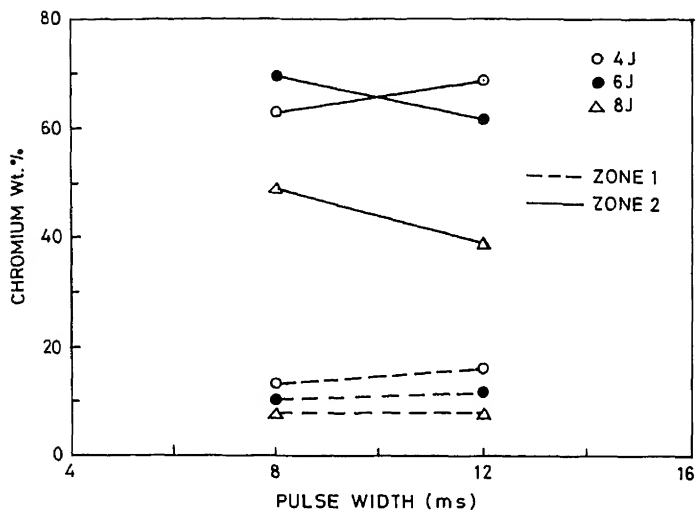


Figure 4. Effect of pulse width on the chromium distribution in two zones.

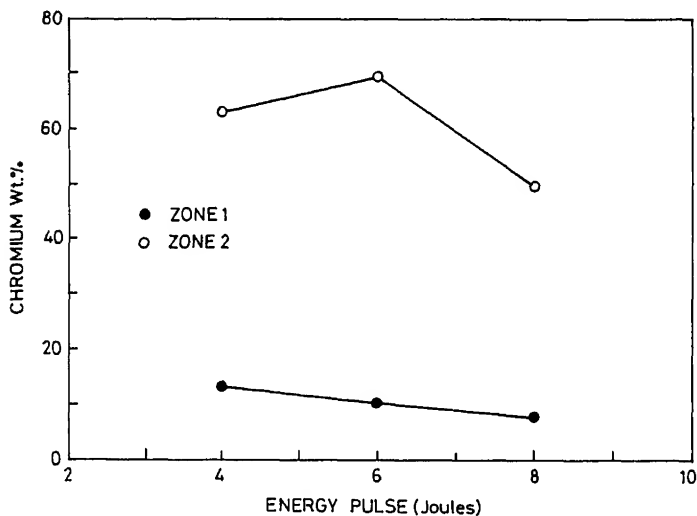


Figure 5. Effect of pulse energy on the distribution of chromium in two zones.

22 wt% for LT7 to about 8 wt% for LT9. It therefore implies that with increasing interaction time, i.e. with decreasing sweep velocity, the alloying element has enough time to diffuse into the matrix and therefore results in a thicker laser alloying zone as shown in figure 8. The thickness of the alloy zone with laser parameters are given in table 2. The X-ray maps and X-ray line profiles through the cross-sections of the laser-alloyed zone (LT9, LT8 and LT7), measured using an inclined WDS, are shown in figures 10, 11 and 12 respectively. It appears that the distribution of chromium

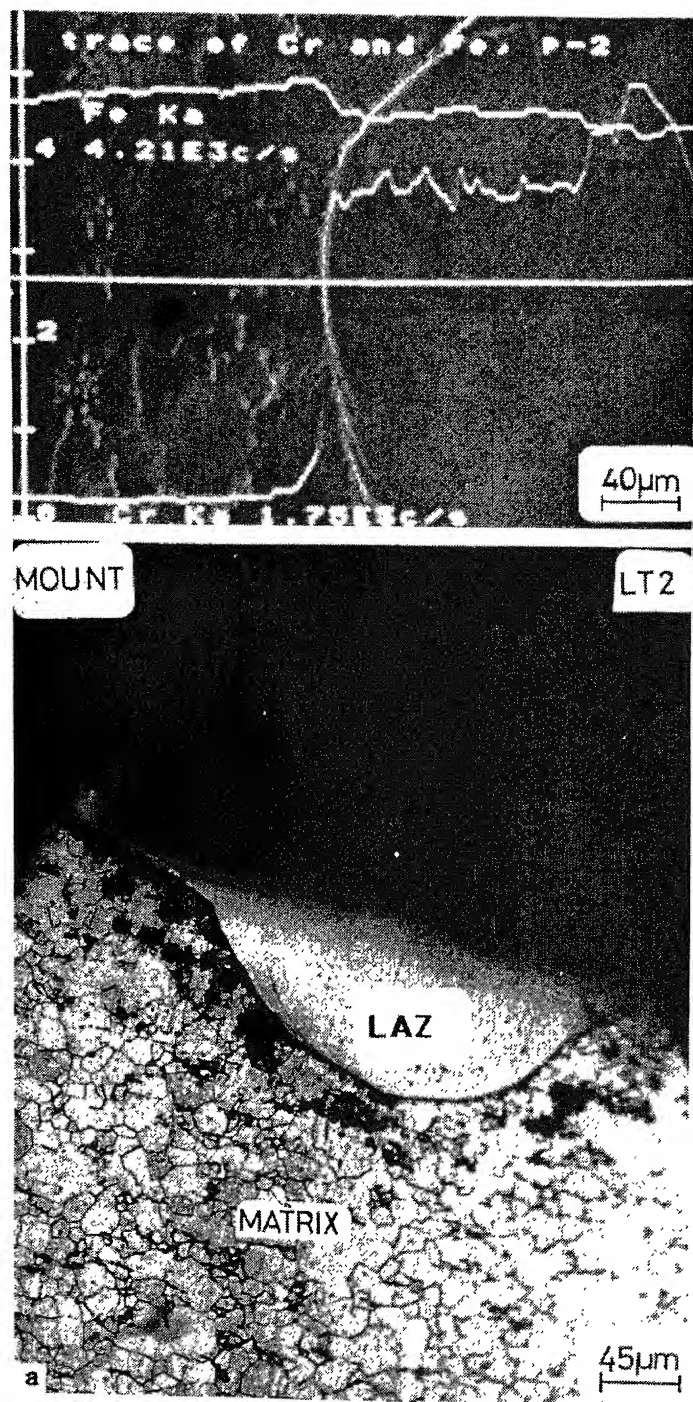


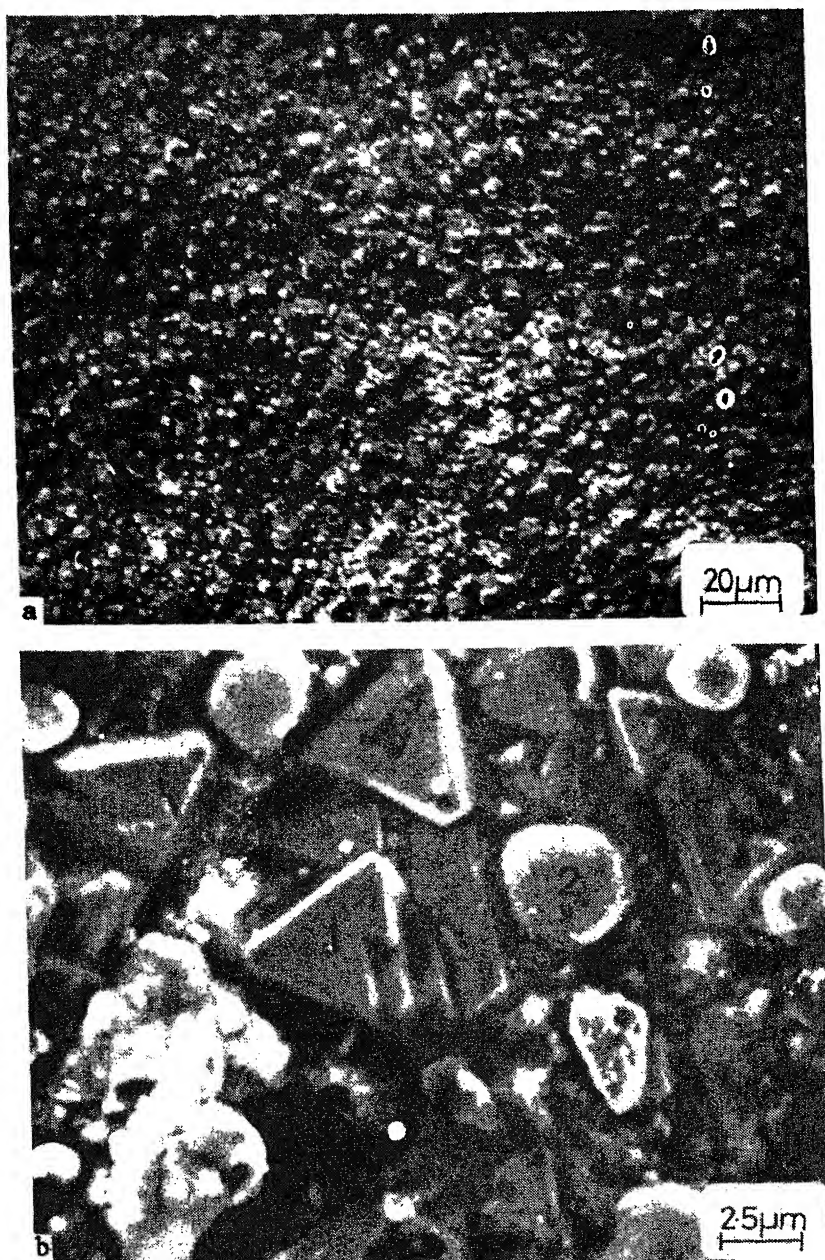
Figure 6a.





Figure 6. Optical micrographs showing the cross-sections of coated sample laser-treated using Nd:YAG laser with parameters (a) LT2 and (b) LT5, along with the SEM showing the chromium distribution using X-ray line scan mode.





**Figure 7.** SEM micrographs showing (a) the morphology of the laser-treated specimen using CO<sub>2</sub> laser and (b) showing fine structure at higher magnification.

in the laser alloying zone depends very much on the laser sweep velocity. This is clearly observed in the X-ray maps, which show the increases in the chromium distribution in the alloy zone when the laser sweep velocity increases, i.e. interaction time decreases.

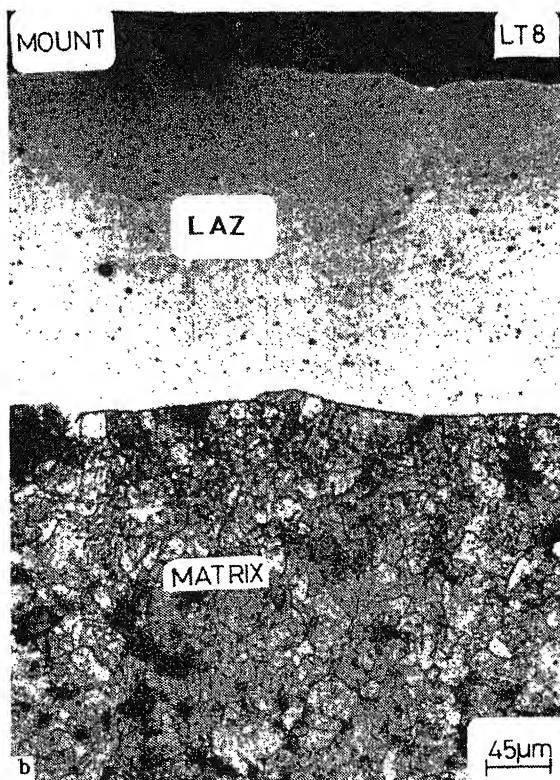
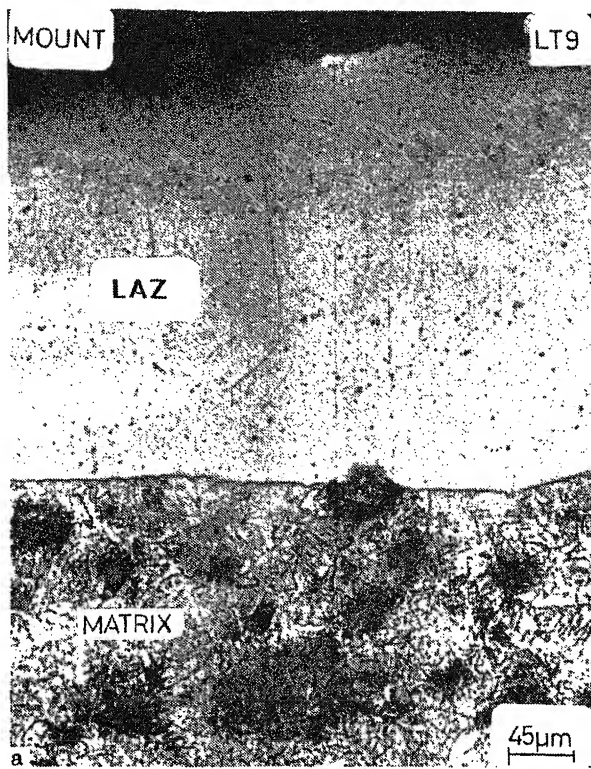


Figure 8 a b

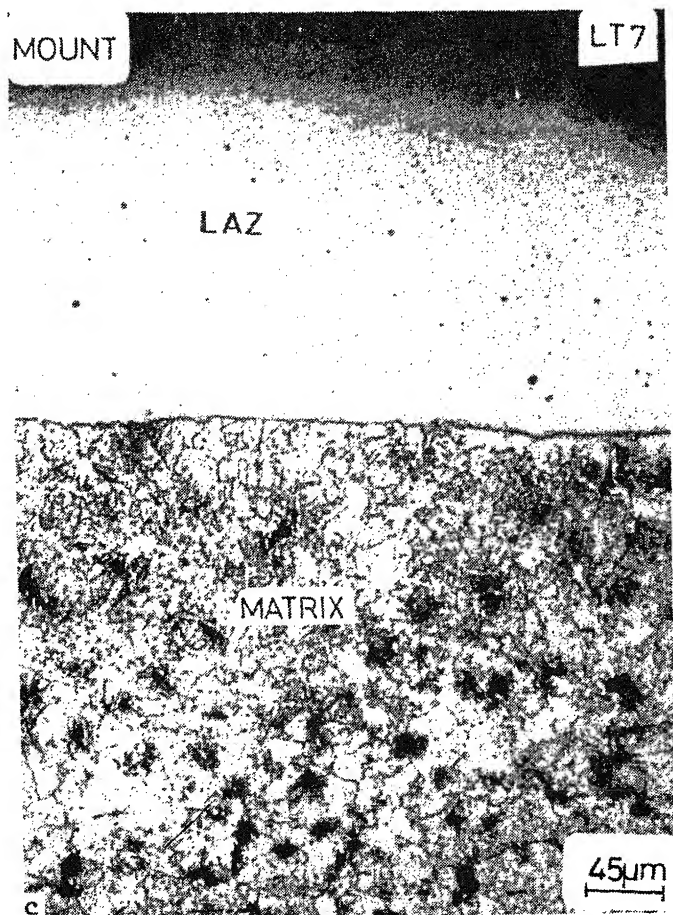


Figure 8. Optical micrographs showing the coating cross-section after laser treatment using  $\text{CO}_2$  laser with parameters (a) LT9, (b) LT8 and (c) LT7.

### 3.2 Oxidation tests

3.2a *Nd:YAG laser-treated specimens:* Oxidation results for the uncoated, plasma-coated and the Nd:YAG laser-treated specimens, with laser parameters LT2 and LT3 are shown in figure 13. It shows that the plasma-coated specimen has lower oxidation rate than the laser-treated specimens. This, though unexpected, can perhaps be attributed to the formation of an inhomogeneous laser-alloyed surface of chromium content much lower than that of the corresponding plasma-coated surface. Furthermore, the laser-treated specimen also cracked, especially in zone 2, as shown in figure 13c.

3.2b  *$\text{CO}_2$  laser-treated specimens:* Figure 14 shows the oxidation result for uncoated, plasma-coated and  $\text{CO}_2$  laser-treated specimens. It is clearly evident from the figure that there is a considerable drop in the oxidation rate when mild steel is plasma-coated with chromium. The oxidation rate further drops after treatment with  $\text{CO}_2$  laser. However, there is little difference in the oxidation behaviour of the specimens treated with the

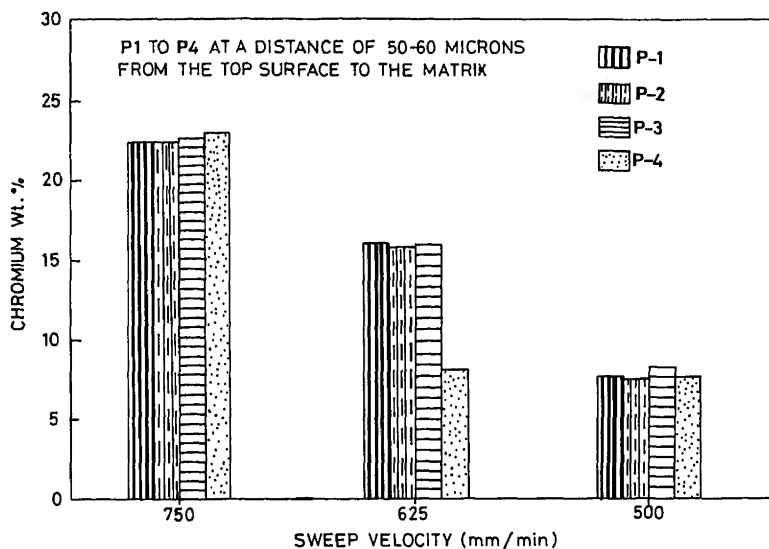


Figure 9. Concentration of chromium distributed in the coating after laser treatment with  $\text{CO}_2$  laser as a function of sweep velocity.

different laser parameters in spite of the fact that chromium level in the laser-alloyed zone varies from 22 wt% to about 8 wt%. The main reason for improvement in oxidation resistance is therefore the formation of a uniform, pore-free surface alloy with better bonding.

### 3.3 Corrosion tests

Anodic polarization tests were carried out only on the samples treated with  $\text{CO}_2$  laser. Figure 15 shows the results for specimen LT9 in 1N  $\text{H}_2\text{SO}_4$  solution. The polarization curves shown in the figure were obtained on the same sample after polishing about 40  $\mu\text{m}$  each time till the base metal was reached. As can be seen from the four curves a, b, c and d, all show passive behaviour with marginal change in the critical current density ( $I_{\text{crit}}$ ), increasing with depth, and also critical passive potential ( $E_{\text{pass}}$ ), increasing with depth, indicating that the corrosion behaviour deteriorates with subsequent removal of the laser-alloyed zone, perhaps due to continuous but slow

Table 3. Anodic polarization values for  $\text{CO}_2$  laser-treated specimen (sweep velocity of 500 mm/min).

Curve	$E_{\text{Corr}}$ (mV)	$I_{\text{Corr}}$ ( $\mu\text{A}/\text{cm}^2$ )	$I_{\text{Critical}}$ ( $\text{mA}/\text{cm}^2$ )	$E_{\text{Passive range}}$ (mV)	$I_{\text{p}}$ ( $\mu\text{A}/\text{cm}^2$ )
a	-482.00	1700.00	40.5	528-934	134.9
b	-508.84	1692.72	61.9	526-932	272.0
c	-526.20	1504.30	73.3	536-940	170.2
d	-517.46	1781.36	106.0	528-952	348.0

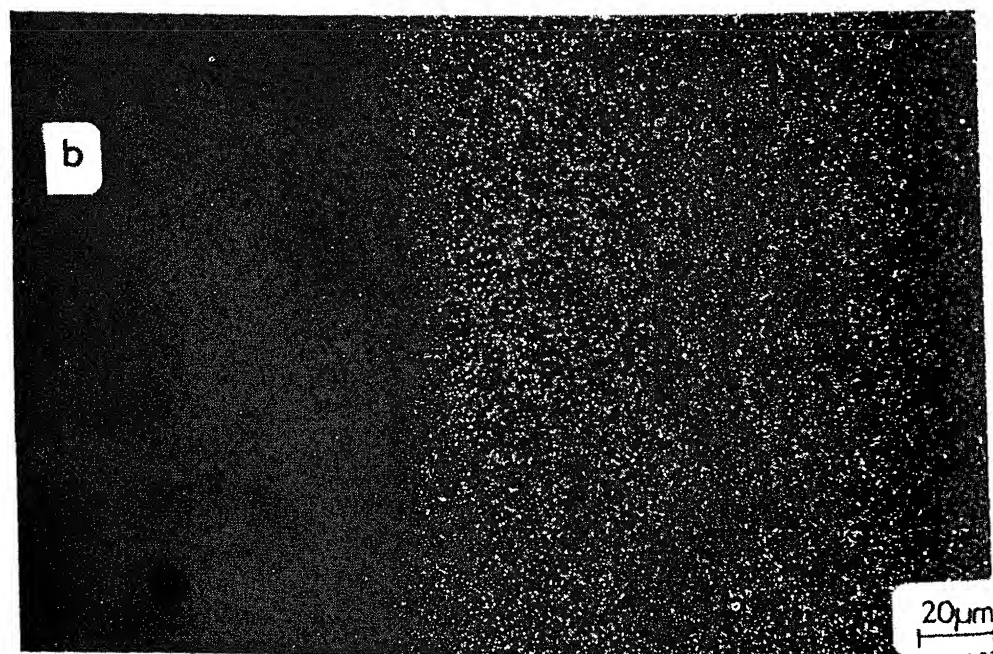
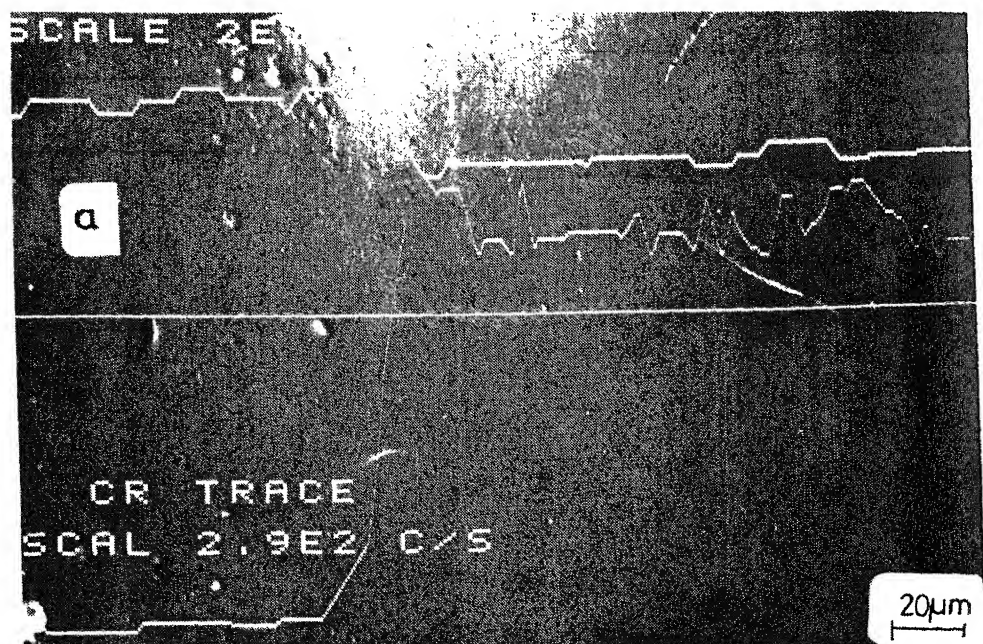


**Figure 10.** (a) SEM micrograph of the coating cross-section with X-ray profile of Cr and (b) the X-ray point map showing Cr distribution in the LAZ for sample LT9.



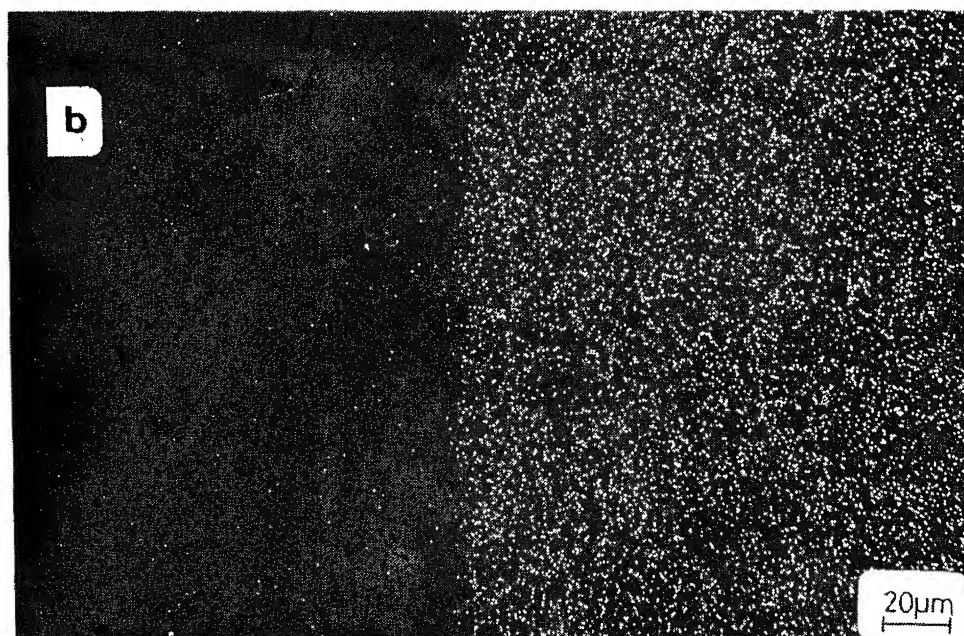
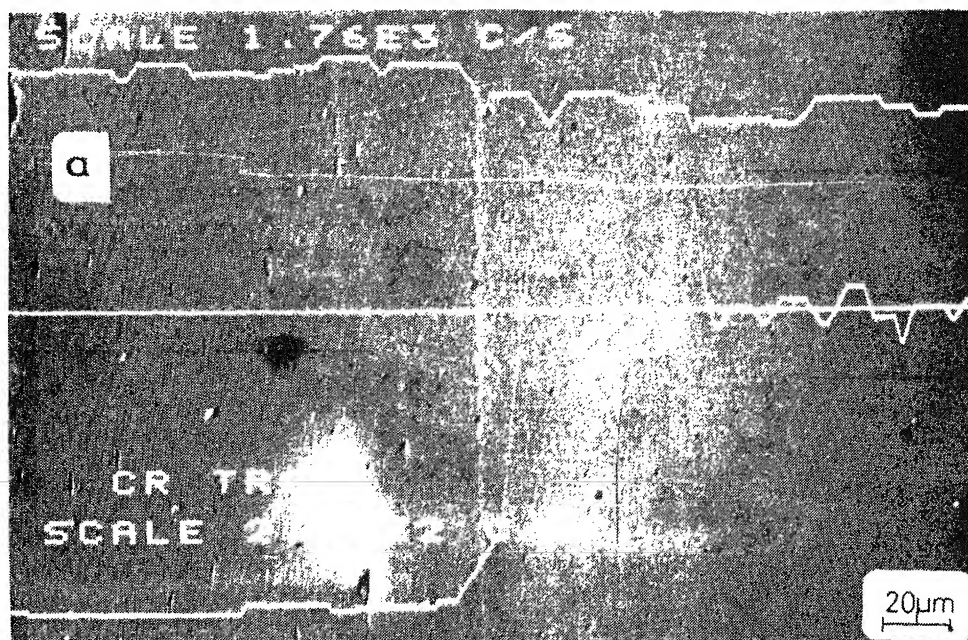


**Figure 11.** (a) SEM micrograph of the coating cross-section with X-ray profile of Cr and (b) the X-ray point map showing Cr distribution in the LAZ for sample LT8.

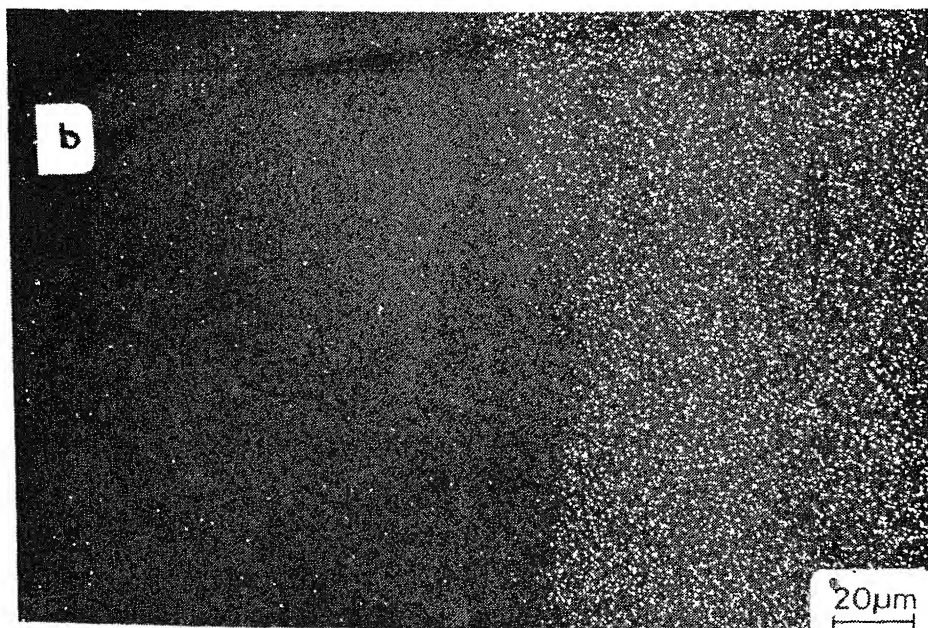


**Figure 12.** (a) SEM micrograph of the coating cross-section with X-ray profile of Cr and (b) the X-ray point map showing Cr distribution in the LAZ for sample LT7.

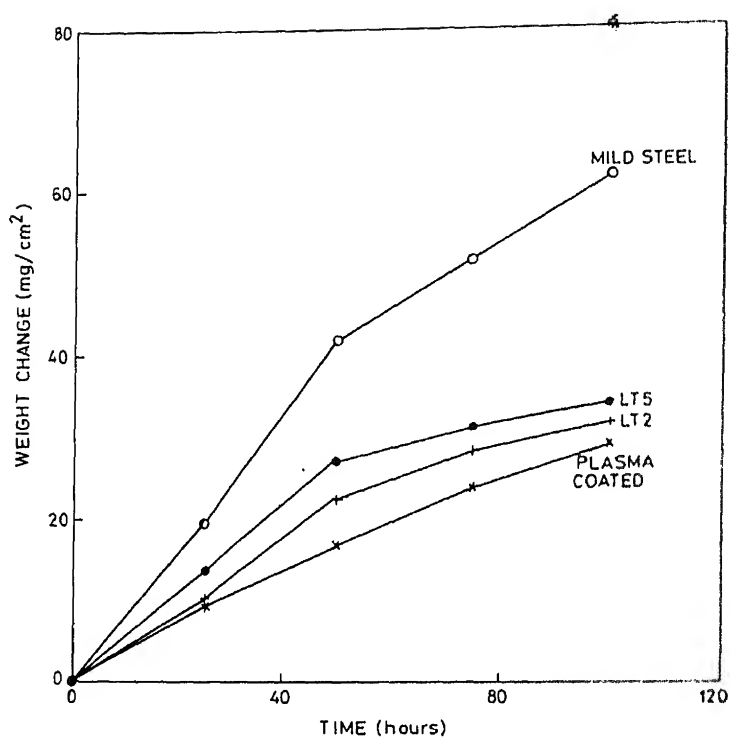


Figure 13. Linear plots of weight gain vs time for the oxidation of uncoated, plasma-coated and laser-treated (using ND:YAG laser) samples in air at 700°C.

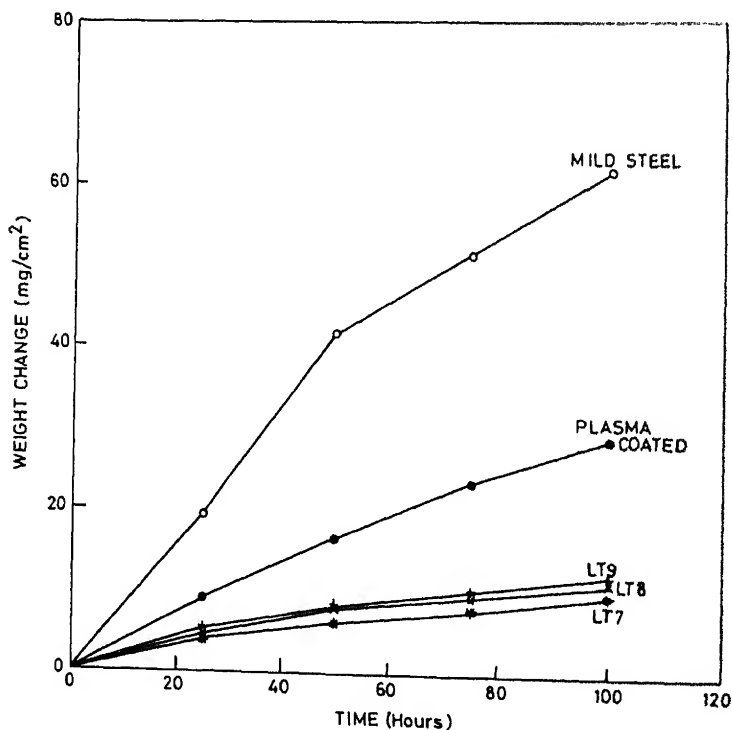


Figure 14. Linear plots of weight gain vs time for the oxidation of uncoated, plasma-coated and laser-treated (using CO<sub>2</sub> laser) samples in air at 700°C.



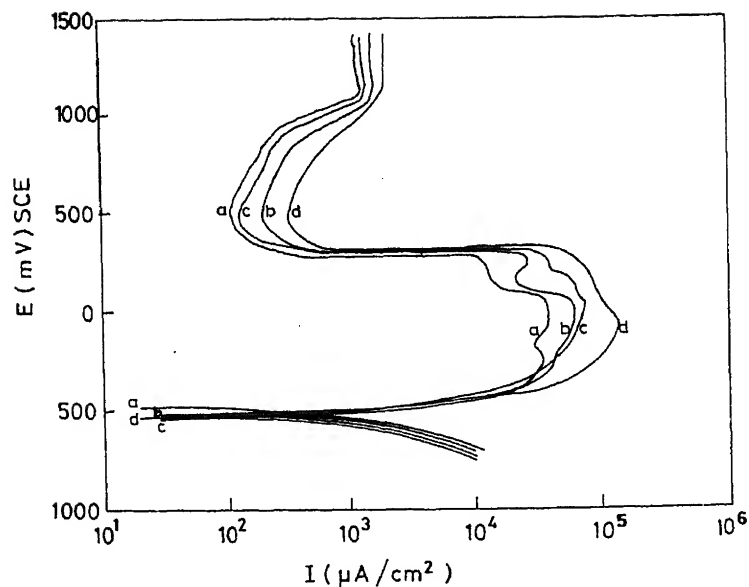


Figure 15. Anodic polarization curves for the sample LT9 in 1N H<sub>2</sub>SO<sub>4</sub> at various depths from the coated surface.

decrease in the chromium concentration with depth. Table 3 lists variation of various corrosion parameters measured during the polarization test.

#### 4. Discussion

The present results emphasize the characterization of the surface alloys formed as a result of laser treatment more than their oxidation or corrosion behaviour. Two different lasers were employed for laser treatment. A 300 W Nd:YAG pulse laser is actually not a suitable tool for laser surface alloying. It is basically used for laser cutting and laser drilling. The two main limitations of this laser are: (i) it is a pulse laser as a result of which the power terminates after a fixed duration interrupting the melting process, (ii) its optics are not very good. It gives only a spot of size 1 to 2 mm. This poses a great difficulty in getting a uniform laser surface-alloyed area. To get a minimum area of 10 mm<sup>2</sup>, for a reasonable corrosion and oxidation test, one has to use at least 60% overlapping from one track to the other. Thus there are more than 10,000 spots per cm<sup>2</sup> with different history of cooling and heating. This results in two or more zones on the surface with heterogeneous composition and often intermediate cracks. Such a surface is not good for corrosion protection. That is why the oxidation results obtained on samples laser-alloyed using Nd:YAG laser show a bit higher oxidation rate in comparison to the corresponding plasma-coated surface, in spite of improvement in the surface roughness, density and bond strength. Nevertheless, detailed characterization of the surface-alloyed zone as a function of pulse width and pulse energy has shown how the composition of the laser-alloyed zone varies with these parameters. Lower pulse width w

intermediate pulse energy of 6 J gives maximum concentration of chromium in the alloyed zone.

The results obtained with continuous CO<sub>2</sub> laser are quite interesting and show that concentration of chromium in the laser-alloyed zone depends upon the chosen laser parameters. Because of the better optics, using a line focus mode, a uniform surface area with homogeneous composition was obtained with no cracks in the laser-alloyed zone. As confirmed in an earlier work by Khanna *et al* (1992), low interaction time retains maximum alloying element, lowest thickness of laser-alloyed zone, and hence better oxidation resistance. The observation of little difference in the oxidation rates of the three samples with different laser parameters (LT7, LT8 and LT9), having Cr concentration varying from 22 wt% to about 8 wt%, is a bit surprising. However, considering 700°C a bit lower temperature and 100 h a bit short duration for oxidation test, the full beneficial effect of high Cr level cannot be fully judged. At this temperature, perhaps the three alloys have no significant difference in their oxide forming capability. Lower chromium in the alloyed zone for specimen treated for longer interaction time LT9 could be due to dilution in the larger alloyed zone and also some loss due to the evaporation of chromium during laser processing. These results are in conformity with those reported by Khanna *et al* (1992), in which they alloyed mild steel with stainless steel rather than pure chromium.

As far as aqueous corrosion results are concerned, the results are encouraging. Mild steel, which does not show any passivity in any acidic solution, is found to exhibit a good and stable passive zone after laser alloying. Although the values of  $I_{crit}$  and  $I_{pass}$  are far from those of 304 stainless steel, a stable passivity on mild steel confirms the surface having reasonable chromium level to achieve passivity and lower the corrosion rate.

## 5. Conclusions

From the present results, it can be concluded that for improving the corrosion and oxidation behaviour of a low-corrosion-resistant surface such as mild steel, laser surface alloying may be carried out using laser parameters which provide uniform, homogeneous laser-alloyed surface, with no cracks in the coating as well as in the underlying matrix. A continuous laser with high power and better optics such as line focus mode are required to achieve a homogeneous surface. Further, laser parameters which retain maximum concentration of the alloying components of the pre-coating should be chosen to enhance the protective properties of the alloyed zone. Corrosion and oxidation behaviour would therefore be enhanced as a result of higher concentration of these elements, for example Cr in the present case. Better coating methods, and perhaps a base with higher initial concentration of chromium, may also help to achieve higher Cr concentration on the New York.

## Acknowledgements

The authors are grateful to Ms K. Anuja, RSIC, IIT, Bombay, for helping in carrying out SEM/EDAX and WDS analysis and Mr Shreekumar, BARC, Bombay, for plasma spraying. This work is part of the sponsored project from the Department of Science and Technology, New Delhi.

## References

- Arvidsson P E 1992 in *Thermal spray coatings: Properties, processes and applications* (ed.) Frank N Longo (Ohio: ASM International) p. 295
- Chiba A Sato, Kawashima T, Asami K and Hashimoto K 1984 *Corrosion Sci.* **26** 311
- Fairbanks J W and Hecht R J 1987 *Mater. Sci. Eng.* **88** 321
- Gasser A, Kreutz E W, Leibrandt S and Wissenbach K 1988 *Proc. 2nd European Conference on Thermal Spray Coatings, Treatment of Materials, Bad Nauheim, Germany*, (Dusseldorf: German Welding Society) p. 81
- Honey F J, Kedward E C and Wride V 1986 *J. Vac. Sci. Technol.* **A4** 2593
- Khanna A S, Singh Raman R K, Kreutz E W and Terrance A L E 1992 *Corrosion Sci.* **33** 949
- Lugscheider E, Eschnauer H and Gruner H 1985 in *Thermal spray coatings, New materials processing and application* (ed.) Frank N Longo (USA: ASM) p. 77
- MacDowell L G 1992 *Mater. Performance* **31** 30
- Parks Albert R 1985 in *Thermal spray coatings: New materials, processing and application* (ed.) Frank N Longo (USA: ASM) p. 65
- Pujar M G, Dayal R K, Khanna A S and Kreutz E W 1993 *J. Mater. Sci.* **28** 3089
- Roy S K, Fasasi A, Pons M, Gallerie A and Caillet M 1993 *J. Physique IV* **3** 625
- Steen W M and Watkins K G 1993 *J. Physique IV* **3** 581
- Stott F H, Bartlett P K N and Wood G C 1987 *Mater. Sci. Eng.* **88** 163

## Structure of vacuum deposited SnSe films

T SUBBARAO<sup>†</sup>, B K SAMANTARAY and A K CHAUDHARI

Department of Physics, Indian Institute of Technology, Kharagpur 721 302, India

<sup>†</sup>Department of Physics, S.K.U.P.G. Centre, Kurnool 518 001, India

MS received 15 July 1994; revised 30 October 1994

**Abstract.** Tin selenide (SnSe) thin films prepared on mica and glass substrates by vacuum sublimation technique and examined by scanning electron microscopy and transmission electron diffraction techniques showed epitaxial and polycrystalline nature respectively irrespective of substrate temperature. Grain size of the films deposited on glass substrate increased with increase in substrate temperature.

**Keywords.** Electron microscopy; tin selenide films; semiconductors.

### 1. Introduction

SnSe thin films are of great importance because of their use in memory switching devices (Baxter and McLennan 1975). SnSe has a highly anisotropic structure with the tin selenide layers stacked along the b-axis with strong intralayer bonding giving rise to many lattice defects. Using X-ray line profile analysis techniques, Subba Rao *et al* (1985) studied the different microstructural parameters like crystallite size, rms strain, dislocation density, faulting probability and extent of faults arising due to variability of interlayer spacings in the case of SnSe films deposited on glass substrates. Subba Rao *et al* (1986) also observed the formation of the high temperature phase (which occurs in bulk SnSe above 807°K) when deposited on glass substrates kept at 473°K and above. However, no such X-ray line profile analysis study was undertaken in the case of SnSe films deposited on mica substrates because of overlapping of mica and SnSe reflections. Hence, an electron microscopic investigation has been undertaken for SnSe thin films vacuum deposited on mica and glass substrates.

### 2. Experimental

Thin films of SnSe were deposited on properly cleaned glass substrates and freshly cleaved (001) planes of mica in a vacuum of  $6.67 \times 10^{-3}$  Pa with the help of a Hind High vacuum coating unit model 12-A4. During deposition, a substrate temperature of 473°K was maintained constant for all the films. The rate of deposition was maintained constant at 30 nm/min and for the present investigation, films of thickness 200 nm have been used. Scanning electron micrographs were obtained by using a Philips model 500 electron microscope at 25 kV. Gold films were deposited on the SnSe films by sputtering for improving the contrast. Electron diffraction patterns have been recorded using AEI EM6 transmission electron microscope at 100 kV. Samples were prepared following the carbon replica techniques. However the carbon-coated specimens had to be made thinner by dissolving the film material in dilute (10–15%) nitric acid. Photographs were taken on dia positive plates ( $0.095 \times 0.08$  m<sup>2</sup>), the exposure time being about 10–20 sec.

### 3. Results and discussions

Two representative scanning electron micrographs for the films deposited on mica and glass substrates are shown in figures 1a and c respectively. Figures 1b and d show the electron diffraction patterns from films deposited on mica and glass respectively.

Electron diffraction patterns of films deposited on glass substrates are in the form of continuous rings. This shows that the films are polycrystalline in nature. With increase in the substrate temperature, the rings become more sharp showing the growth of the crystallites and removal of defects. In the case of films deposited on mica substrates the diffraction patterns consist of spots reflecting an epitaxial nature. Higher order of (111) reflections are observed in diffraction patterns from films deposited on mica showing that the films have grown with (111) planes parallel to the substrate. Also the spots became sharper with increase in substrate temperature.



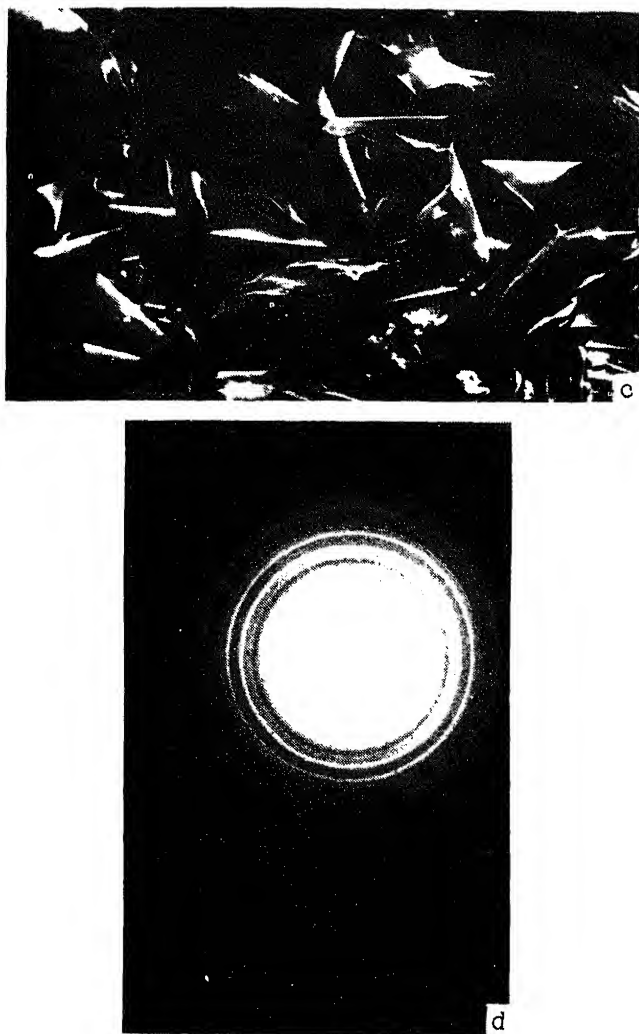


**Figure 1.** Secondary electron micrographs and electron diffraction pattern, respectively of SnSe films deposited on (a) and (b) mica and (c) and (d) glass substrates at 473°K.

The SEM patterns from the films deposited on glass substrates show the actual mono crystalline structure clearly. The average size (at 473°K substrate temperature) being 80  $\mu\text{m}$  along the length and 30  $\mu\text{m}$  along the breadth. With increase in substrate temperature there is a slight increase in the crystallite size. The observed size values are much greater than the X-ray crystallite size values reported earlier. This is expected because size values obtained from the X-ray line profile analysis studies correspond to the size of the coherently diffracting domain, whereas the SEM gives the size of the crystallites. One such crystallite may consist of many tiny crystals which are linked by dislocation networks. In SEM patterns of thin films deposited on mica substrates an array of dislocation patterns is observed. This is similar to the observations reported by Amelinck (1964) for  $\text{SnS}_2$  films in which an extensive network of screw dislocations separated by areas of stacking fault contrast were observed.

#### 4. Conclusions

It was concluded that the SnSe films vacuum-deposited on glass substrates are polycrystalline in nature. Films deposited on mica substrate show epitaxial type spotty patterns with (111) planes parallel to the substrate surface.

#### References

- Amelinck S 1964 *Direct observation of dislocations* (New York: Academic Press) p. 271  
Baxter C R and McLennan W D 1975 *J. Vac. Sci. Technol.* **12** 110  
Subba Rao T, Samantaray B K and Chaudhari A K 1985 *J. Mater. Sci. Lett.* **4** 743  
Subba Rao T, Samantaray B K and Chaudhari A K 1986 *Z. Kristallogr.* **175** 37

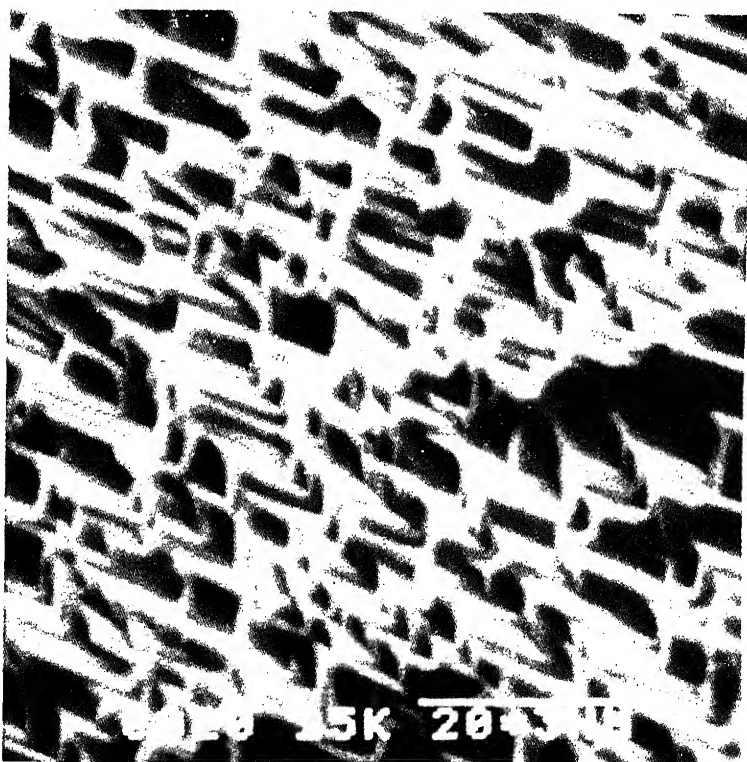
Journal of

# Materials Science

Volume 18

Number 3

June 1995



Published by  
**INDIAN ACADEMY OF SCIENCES**  
in collaboration with  
**MATERIALS RESEARCH SOCIETY OF INDIA and**





# Bulletin of Materials Science

## Editor

K J Rao

*Indian Institute of Science, Bangalore*

## Editorial Board

D C Agrawal, *Indian Institute of Technology, Kanpur*  
M F Ashby, *University of Cambridge, Cambridge, UK*  
S Banerjee, *Bhabha Atomic Research Centre, Bombay*  
D Chakravorty, *Indian Association for the Cultivation of Science, Calcutta*  
A K Chatterjee, *The Associated Cement Companies Limited, Thane*  
K L Chopra, *Indian Institute of Technology, Kharagpur*  
A D Damodaran, *Regional Research Laboratory, Trivandrum*  
B K Das, *National Physical Laboratory, New Delhi*  
H Herman, *State University of New York, Stony Brook, USA*  
B Ilschner, *Ecole Polytechnique Federale de Lausanne, Lausanne, Switzerland*  
Indira Rajagopal, *National Aerospace Laboratories, Bangalore*  
K T Jacob, *Indian Institute of Science, Bangalore*  
S K Joshi, *Council of Scientific and Industrial Research, New Delhi*  
S Mahajan, *Carnegie Mellon University, Pittsburgh, USA*  
R A Mashelkar, *National Chemical Laboratory, Pune*  
S B Ogale, *University of Poona, Pune*  
Pradip, *Tata Research Development and Design Centre, Pune*  
P Ramachandra Rao, *National Metallurgical Laboratory, Jamshedpur*  
S Ranganathan, *Indian Institute of Science, Bangalore*  
C N R Rao, *Indian Institute of Science, Bangalore*  
B B Rath, *Naval Research Laboratory, Washington, USA*  
R W Siegel, *Argonne National Laboratory, Argonne, USA*  
R Srinivasan, *Inter-University Consortium for DAE Facilities, Indore*  
G V Subba Rao, *Central Electrochemical Res. Inst., Karaikudi*  
G Sundararajan, *Defence Metallurgical Research Laboratory, Hyderabad*  
M S Valiathan, *Manipal Academy of Higher Education, Manipal*  
I K Varma, *Indian Institute of Technology, New Delhi*  
Vikram Kumar, *Solid State Physics Laboratory, Delhi*

## Editor of Publications of the Academy

V K Gaur

*C-MMACS, NAL, Bangalore*

### Subscription Rates

(Effective from 1989)

All countries except India  
(Price includes AIR MAIL charges)

1 year	3 years	5 years
US\$ 100	\$ 270	\$ 400

India.....

1 year	10 years
Rs. 75	Rs. 400

All correspondence regarding subscription should be addressed to **The Circulation Department**  
Academy.

### Editorial Office

Indian Academy of Sciences, C V Raman Avenue,  
P. B. No. 8005, Bangalore 560 080, India

Telephone: 334 2546  
Telex: 845-2178 AC  
Telefax: 9180-334 60

© 1995 by the Indian Academy of Sciences. All rights reserved.

Cover : SEM of Ag surface bombarded by 30 keV  $^{40}\text{Ar}^+$  ions at an oblique incidence of  $58^\circ$  with a dose of  $10^{18}$  ions/cm $^2$  : corrugated faceted structure at the central part of the bombarded spot. For details, see p. 201.

## Bulk high- $T_c$ magnetometer

NEERAJ KHARE\*, J R BUCKLEY<sup>†</sup> and G B DONALDSON<sup>†</sup>

Superconductivity Group, National Physical Laboratory, New Delhi 110012, India

<sup>†</sup>Department of Physics and Applied Physics, University of Strathclyde, Glasgow G4 0NG, Scotland, UK

MS received 18 February 1995

**Abstract.** We report a study of a bulk YBCO magnetometer based on the detection of harmonics during nonlinear magnetization. For a low-DC field, the amplitude of the even harmonic appearing at the pickup coil depends linearly on the DC field intensity. The performance of the magnetometer depends on the quality of the sample, and the intensity and frequency of the AC field excitation. At higher  $H_{ac}$ , the fourth harmonic becomes more sensitive than the second harmonic. The hysteresis in the magnetometer for DC field measurement has been reported.

**Keywords.** Harmonic generation; YBCO; magnetometer.

### 1. Introduction

A bulk YBCO magnetometer based on the RF SQUID effect, with noise sensitivity  $\approx 10^{-10} \text{ T}/(\text{Hz})^{1/2}$ , was reported earlier (Pegrum *et al* 1987). It utilizes the internal superconducting loops connecting internal weak links. However, the presence of many loops of varying area and critical current introduces an ambiguity in flux locking and thus limits the applicability of the bulk magnetometer. Eventually more controllable two-hole devices were constructed which showed more sensitive performance (Harrop *et al* 1988; Poulshkin and Vaisiliev 1989; Khare *et al* 1991). Recently observations of harmonic generation in bulk YBCO have been reported by many workers (Ji *et al* 1989; Muller 1989; Ishida and Goldfarb 1990; Buckley *et al* 1991; Kumar *et al* 1993; Gilbricht and Domre 1994; Karthikeyan *et al* 1994; Revenaz and Dumas 1994). This is an outcome of the nonlinear magnetization behaviour of the material. A bulk high- $T_c$  magnetometer based on this nonlinear phenomenon was demonstrated by Gallop *et al* (1988) and had noise sensitivity  $\approx 10^{-10} \text{ T}/(\text{Hz})^{1/2}$ . Such a device is sometimes called a 'superconducting flux gate magnetometer' because of its mode of operation. Buckley *et al* (1991) have demonstrated the applicability of this magnetometer to nondestructive evaluation of steel plates.

In this paper we report on a detailed study of the dependence of the sensitivity factor of the bulk YBCO magnetometer on operating conditions and on the quality of sample. A comparison of the sensitivity of the magnetometer using second and fourth harmonics has been made.

### 2. Background to the experiment

Consider a specimen on which a uniform AC magnetic field ( $H(t) = H_{ac} \sin \omega t$ ) is applied.

---

\*To whom correspondence should be addressed

The magnetization  $M(t)$  as a function of  $t$  is given by

$$M(t) = H_{ac} \sum_{n=1}^{\infty} [\chi'_n \sin(n\omega t) - \chi''_n \cos(n\omega t)],$$

where  $\chi_n = \chi'_n - i\chi''_n$  ( $n = 1, 2, 3, \dots$ ). The quantities  $\chi'_n$  and  $\chi''_n$  can be calculated by

$$\chi'_n = 1/\pi H_{ac} \int_0^{2\pi} M(t) \sin(n\omega t) d(\omega t),$$

and

$$\chi''_n = -1/\pi H_{ac} \int_0^{2\pi} M(t) \cos(n\omega t) d(\omega t).$$

When a pickup coil is wound over the specimen, the voltage induced in it is proportional to the time derivative of  $M(t)$ ,

$$V(t) = dM(t)/dt = H_{ac} \sum_{n=1}^{\infty} n\omega [\chi'_n \cos(n\omega t) + \chi''_n \sin(n\omega t)].$$

It is usual to use a spectrum analyser to display the Fourier transform of  $V(t)$  directly, so that the amplitudes,  $V_n$ , of higher-harmonic terms can be directly served. Here  $V_n$  is directly proportional to  $\omega H_{ac} \chi_n$ . When the DC field is also present then  $H(t) = H_{ac} \sin(\omega t) + H_{dc}$ , while the form of (1) remains the same.

Measurements of the AC susceptibility of YBCO superconducting materials have shown that the materials have a highly nonlinear magnetization which is strongly dependent on both  $H_{dc}$  and  $H_{ac}$  even at low fields (Buckley 1991). The application of the critical state model, in which the critical current density  $J_c$  flowing at any point in the sample is solely a function of the local field intensity  $H_l$  at that point, has been used by many workers (Ji *et al* 1989; Ishida and Goldfarb 1990; Buckley *et al* 1991) to explain the nonlinear magnetization and the appearance of even and odd harmonics. Even harmonics are found to be odd functions and odd harmonics to be even functions of DC field.

### 3. Experimental

Three types of bulk samples were used in the present study: dense, less dense and porous types, which had 34%, 64% and 88% porosity respectively. In each case a bulk sample of YBCO was cut into rectangular blocks of dimensions 10 mm  $\times$  4 mm  $\times$  2 mm. A 100 turn copper coil wound on the YBCO rectangular block formed the pickup coil. The block was mounted on the axis of a solenoid. A signal generator (HP 3325A) provided the excitation and the spectrum of the signal in the pickup coil was measured using a spectrum analyser (HP 3561A at low frequencies and HP 8590 for excitation frequencies above 25 kHz).

To determine the sensitivity of the device as a magnetometer a second solenoid coaxial with the first, was used to apply DC fields on the specimen. The size of the harmonics was measured by the spectrum analyser.

### 4. Results and discussion

The presence of a DC field causes the appearance of even harmonics in the Fourier

are linear. Thus measuring the voltage corresponding to even harmonics can give an estimate of the DC field. The magnitude of this voltage has been found to depend on the quality of the sample, on the intensity and frequency of the AC drive, and also on which even harmonics was considered. For comparing various results a sensitivity figure  $\alpha_n$ , indicating the smallest field change which could be detected using the  $n$ th harmonic, was defined as

$$\alpha_n = \delta V / (\delta V_n / \delta H_{dc}), \quad (5)$$

where  $\delta V_n / \delta H_{dc}$  is the rate of change of voltage corresponding to even harmonic with DC field for linear region of  $V_n - H_{dc}$  characteristic.  $\delta V$  is the uncertainty in measurement for a particular operating condition at a fixed DC field ( $H_0$ ), and is due to the combined noise present in the sample and measuring system.

#### 4.1 Dependence of DC field sensitivity on $H_{ac}$

Figure 1 shows the variation of the sensitivity,  $\alpha_2$ , with  $H_{ac}$  for three YBCO samples of varying porosities (sample A 34%, sample B 64%, sample C 88% 'foam type'). For samples B and C,  $\alpha_2$  increases as  $H_{ac}$  increases, whereas for sample A  $\alpha_2$  decreases at first before increasing at  $H_{ac} \sim 3.4$  mT. The second-harmonic amplitude depends upon the pinning force density of the material, which in turn depends upon the number of pinning sites per unit volume ( $n_p$ ) and the pinning force of the sites. The critical current of the sample governs the depth to which magnetic field penetrates. In samples B and C,  $n_p$  was less than in sample A and furthermore because of weak flux pinning, the field penetrated the sample fully even at  $H_{ac} \sim 0.9$  mT. As  $H_{ac}$  was increased the intergranular critical current decreased according to the Kim model, and hence  $\delta V_n / \delta H_{dc}$  decreases leading to an increase in  $\alpha_2$ . In sample A, the stronger pinning and larger value of  $n_p$  caused the increase in  $\delta V_n / \delta H_{dc}$  ( $\alpha_2$  decreases) with increase in  $H_{ac}$ . As the flux penetration increased, more and more pinning sites

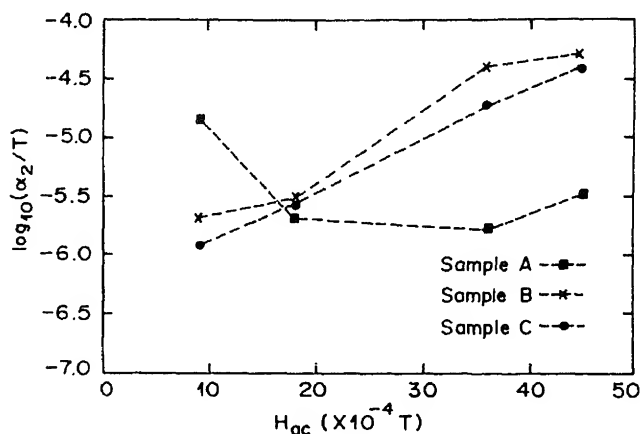
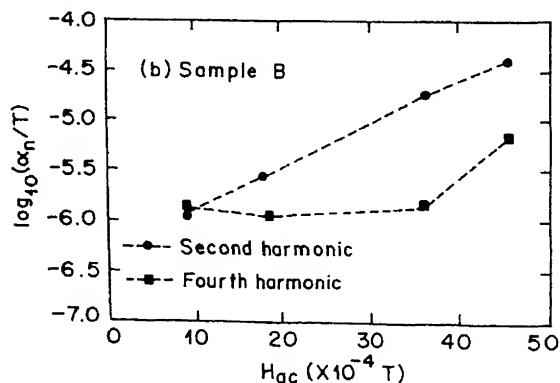
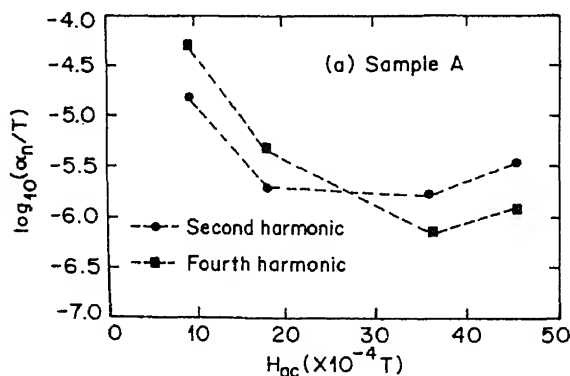


Figure 1. Variation of  $\alpha_2$  (for second harmonic) with  $H_{ac}$  for three samples of YBCO of varying porosities (sample A 34%, sample B 64%, sample C 88%).

contributed to magnetization.  $\alpha_2$  reached a minimum when AC field fully penetrated the sample. As AC field was increased to 3.4 mT,  $\alpha_2$  started increasing in a manner similar to samples B and C.

#### 4.2 Second versus fourth harmonic

Measurements of  $\alpha_n$  for second ( $\alpha_2$ ) and fourth ( $\alpha_4$ ) harmonics revealed an interesting result. Figures 2a and 2b show the variation of  $\alpha_n$  for second and fourth harmonics with  $H_{ac}$  for samples A and B. For the dense sample,  $\alpha_2$  was greater than  $\alpha_4$  at small values of  $H_{ac}$ . However for  $H_{ac} > 28$  Oe the fourth harmonic became smaller. For the less dense sample B, this crossover point was observed to occur at low  $H_{ac} \approx 10$  Oe. This feature is predicted in Kim's critical state model. The crossover point depends on the critical current density of the sample. If  $J_c$  is small (for less dense sample) then the crossover point is expected to occur at a lower value of AC field.



#### 4.3 Dependence of DC field sensitivity on frequency of AC drive field

Figure 3 shows the variation of  $\alpha_n$  with the frequency of AC drive field. The AC field intensity was kept constant to  $3.6 \text{ mT } p^k - p^k$  during the whole measurement.  $\alpha_n$  was found to decrease with the frequency. The signal at the pickup coil is the time derivative of the magnetization,  $M$ . Thus it is expected to be proportional to  $f$ . The inset in figure 3 shows a plot of  $(V_2/f)_n$  against  $f$  which is proportional to  $\alpha_2$ .  $(V_2/f)_n$  represents the normalized value of  $V_2/f$  at 1 kHz. It shows a decrease with an increase in frequency. The critical state model for granular high- $T_c$  superconductors does not predict the frequency dependence of the intergranular and intragranular critical state profiles (Muller 1989). However, the addition of thermally activated flux creep to the current density term in the critical state equation can explain the frequency dependence behaviour (Muller 1990). With the increase in frequency due to flux creep effect, the effective penetration decreases and hence  $\chi_2$  is expected to decrease as observed experimentally. Thus the operation of the magnetometer at very high frequencies will not yield any improvement in its performance.

#### 4.4 Hysteresis in bulk YBCO magnetometer

An essential criterion for a practical magnetometer is that it should show negligible hysteresis in its output between increasing and decreasing fields. To investigate this we measured a hysteresis parameter  $h$  which was defined as:

$$h = (V_1 - V_2)/(\delta V_n/\delta H),$$

where  $V_1$  was the magnetometer output voltage at a field  $H_0 (= 10^{-5} \text{ T})$  when the field was increasing to  $H_{\max}$  and  $V_2$  was the output voltage at  $H_0$  when the field was decreasing from  $H_{\max}$ . These measurements were taken by ramping the field from zero to  $H_{\max}$  and then back to zero.  $\delta V_n/\delta H$  was the slope of  $V_n-H$  characteristic corresponding

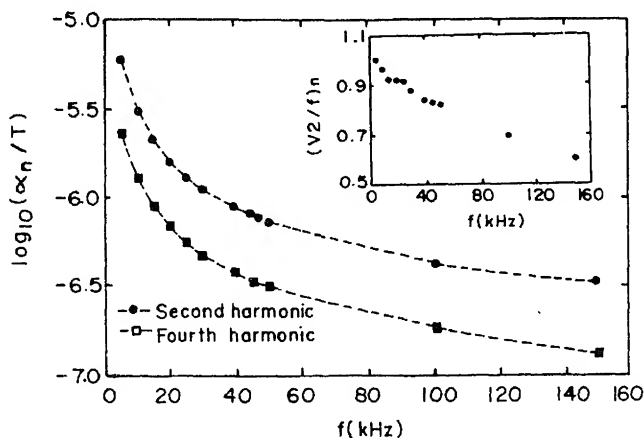


Figure 3. Variation of  $\alpha_n$  with frequency of AC drive field. Inset shows variation of  $(V_2/f)_n$  with  $f$ .  $V_n$  being normalized value of the output voltage.

to second harmonic. For DC field measurement, when  $H_{\max}$  was less than  $0.2 \text{ mT h}$  was equal to  $\alpha_2$ , but when  $H_{\max} > 0.2 \text{ mT h}$  increased. This measurement indicates the limitation of the present bulk YBCO magnetometer for DC field measurement when the variation in the field is large.

## 5. Conclusion

The performance of the bulk YBCO magnetometer has been found to depend on the quality of YBCO sensor, intensity and frequency of the exciting AC field. At higher AC fields, the fourth harmonic was more sensitive than the second harmonic. Use of the dense sample as a sensor gave a better performance. Increasing the operating frequency improves magnetometer sensitivity but due to flux creep effect  $\chi_2$  decreases, and so there is no improvement if the magnetometer is operated above  $150 \text{ kHz}$ .

Hysteresis measurements revealed that the magnetometer for DC field measurement could work well if the variation in the DC field is less than  $0.2 \text{ mT}$ . Field sensitivities of  $\sim 10^{-7} \text{ T}$  were achieved in the present experiment by optimizing the operating conditions. However, no averaging of the observations and no optimization in pickup coil designing and sample size was done. Inclusion of these will improve the sensitivity further.

## References

- Buckley J R, Khare N, Donaldson G B, Cochran A and Hui Z 1991 *IEEE Trans. Mag.* **27** 3051
- Gallop J C, Lilleyman S, Longham C D, Radcliff W J, Gee M and Stewart M 1988 *Cryogenics* **28** 691
- Gilbricht J and Dotre T 1994 *Phys. Rev.* **B49** 1466
- Harrop S, Grough C E, Keene M and Muirhead C M 1988 *Supercond. Sci. Technol.* **1** 168
- Ishida T and Goldfarb R B 1990 *Phys. Rev.* **B41** 8937
- Ji L, Sohn R H, Spalding G C, Lobb C I and Tinkham M 1989 *Phys. Rev.* **B39** 4772
- Karthikeyan J, Paithankar A S, Prasad R and Soni N C 1994 *Supercond. Sci. Technol.* **7** 949
- Khare N, Gupta A K, Chaudhry S, Arora S K, Tomar V S and Ojha V N 1991 *IEEE Trans. Mag.* **27** 3029
- Kumar S, Pradhan S B, Chadda P, Prasad R and Soni N C 1993 *J. Appl. Phys.* **77** 1539
- Muller K H 1989 *Physica* **C159** 717
- Muller K H 1990 *Physica* **C168** 585
- Pegrum C M, Donaldson G B, Carr A H and Hendry A 1987 *Appl. Phys. Lett.* **51** 1364
- Poulshkin V N and Vaisiliev B V 1989 *Physica* **C162** 397
- Revenaz S and Dumas J 1994 *Physica* **C219** 450

# Cone formation on Ag surface bombarded by Ar at oblique incidence

S R BHATTACHARYYA, T K CHINI<sup>†</sup> and D BASU

Saha Institute of Nuclear Physics, Block-AF, Sector 1, Bidhan Nagar, Calcutta 700064, India

<sup>†</sup>Present address: Department of System Engineering, Nagoya Institute of Technology, Gokiso-cho, Showa-ku, Nagoya 466, Japan

MS received 13 January 1995; revised 4 April 1995

**Abstract.** Sputter-induced topographical modifications of a silver surface bombarded by mass-analysed ions of 30 keV  $^{40}\text{Ar}^+$  obtained from an electromagnetic isotope separator incident at an angle of  $58^\circ$  was studied. Analysis of the silver surface by scanning electron microscopy showed that most of the bombarded area was covered with features similar to corrugated terrace steps, sharp and fine cones, and pyramids. The underlying mechanism for formation of such features is discussed. The method of formation of such sharp cones produced by ion bombardment will increasingly find applications in the formation of fine tips required in scanning probe and field emission microscopy.

**Keywords.** Sputter-erosion; sputter-induced cones; topography; oblique cone formation.

## 1. Introduction

An interesting aspect of heavy-ion irradiation of the surfaces of solids at relatively high doses ( $> 10^{17}$  ions/cm<sup>2</sup>) is the development of well-defined topography which has been the subject of experimental and theoretical investigations in view of both the fundamental physical concept and substantial technological interest. These features due to sputtering often resemble cones, pyramids, steps, ripples, etc. As far as applications are concerned (Auciello 1982), a textured surface due to sputtering can be used as cathode for better field emission or explosion emission, in experiments requiring low electron or ion reflectance, to increase optical absorption important in solar cell technology, and to increase secondary emission. It is also established that textured surface made by sputtering could be beneficial in lowering the surface erosion by energetic ions striking the first walls of controlled fusion reactors. These applications show that studies of surface topography of ion-bombarded solids are important for better understanding of the physical processes in the evolution of such features. With the advent of scanning electron microscopy it has been possible to investigate solid surfaces in greater detail and precision. It has been found that the nature and form of surface features are related to the ion species, the material under study and the environment in the collision chamber. Therefore the mass, energy, dose and current density of the projectile ion and the mass, orientation and environmental conditions of the target material are crucial in determining the nature and form of topographical features developed (Carter *et al* 1983). Sputtered erosion by ion bombardment is the most effective and controlled way of processing sharp and fine tips which are essential in scanning probe and field emission microscopy. Quite recently, computer simulation studies have been started (Wege *et al* 1993) to see how ion-beam sputtering can be used to construct fine tips with small apex angle and radius as applied to the above mentioned microscopy.



In this report we show evidence of topography consisting mostly of cones on mirror-polished silver samples bombarded by 30 keV mass-analysed  $^{40}\text{Ar}^+$  ions at an oblique incidence of  $58^\circ$  with the normal to the surface. Silver was chosen as target because of its large secondary electron emission under SEM and therefore reveals greater details of the features developed on the surface. Preliminary results on the development of fine and sharp cones or tips by ion-induced sputter erosion at oblique incidence are also reported.

## 2. Experimental

Samples of polycrystalline Ag were bombarded at oblique incidence of  $58^\circ$  with the surface normal by 30 keV mass-analysed ions of  $^{40}\text{Ar}^+$  obtained from an electromagnetic isotope separator. The residual gas pressure in the target chamber was around  $2 \times 10^{-5}$  torr. Beam current density was around  $200 \mu\text{A}/\text{cm}^2$ . Bombardment doses were measured by integrating the current on the target by a current integrator (Danfysik 554). To suppress secondary electrons, the collector cups were biased at a negative potential with respect to the target. The surfaces were bombarded with a dose of  $1 \times 10^{19}$  ions/ $\text{cm}^2$  and were examined by a Hitachi S-415S scanning electron microscope.

## 3. Results and discussion

### 3.1 Observation of surface under SEM

The micrographs (figure 1) of Ag surface bombarded by 30 keV  $\text{Ar}^+$  projectile ions at an oblique incidence of  $58^\circ$  with the surface normal show interesting features. Most of the bombarded areas are covered with features similar to corrugated terraces (figure 1a) and sharp cones (figures 1b–d). These terrace planes are always aligned parallel to the ion beam. Faceted cones or pyramids developed are also aligned with their axes parallel to the ion beam direction as seen in figures 1b and 1c. Some of the cones are very sharp; the apex angles of these cones range from  $11^\circ$  to  $17^\circ$ . An important observation in the present case is that some of the oblique cones form a bent at their stems or tips. A typical case is shown in figure 1d.

### 3.2 Possible mechanism of cone formation on the sample

According to first-order erosion theory, the dependence of sputtering yield on the angle of incidence of the ion beam plays a major role in formation of sputtered cones, as suggested by different authors (Carter *et al* 1983; Ghose and Karmohapatro 1990). If  $\theta$  be the angle between the direction of the incident ion beam and the normal to the surface, then the sputtering yield  $Y(\theta)$  follows a  $\sec \theta$  dependence when  $\theta$  is low. However,  $Y(\theta)$  deviates from  $\sec \theta$  dependence for large values of  $\theta$ , reaches a maximum at  $\hat{\theta}$  between  $60^\circ$  and  $80^\circ$  and then falls to zero at  $\theta = 90^\circ$ . This variation of  $Y(\theta)$  with  $\theta$  is shown in figure 2. A number of authors have discussed the mechanism of cone formation as summarized by Ghose and Karmohapatro in their recent review of the subject. The following mechanism for the nucleation of cones can be regarded as responsible in our present investigation.

(ii) The surface impurity seems to be the initiator and results in the formation of cones by a combination of erosion and surface migration.

### 3.3 Mechanism of oblique cone formation

The underlying mechanism for oblique cone or pyramid formation is found to be similar to that responsible for the formation of normal cones or pyramids. However, Auciello and Kelly (1982) identified five sources of perturbation to the first-order erosion theory to account for the evolution of oblique cones. These are the growth of topography relative to the instantaneous surface, asymmetrical flux enhancement originating

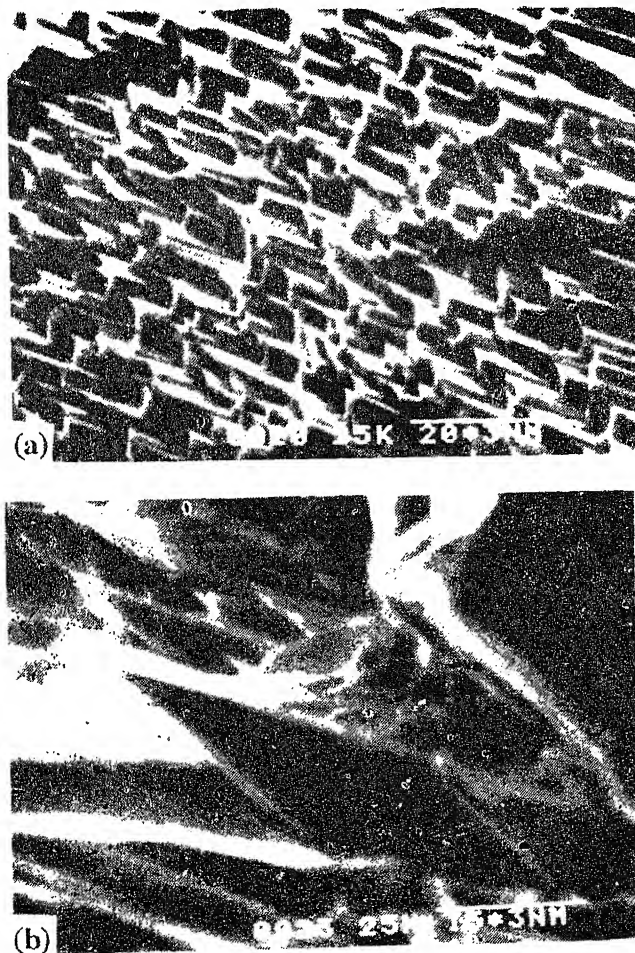
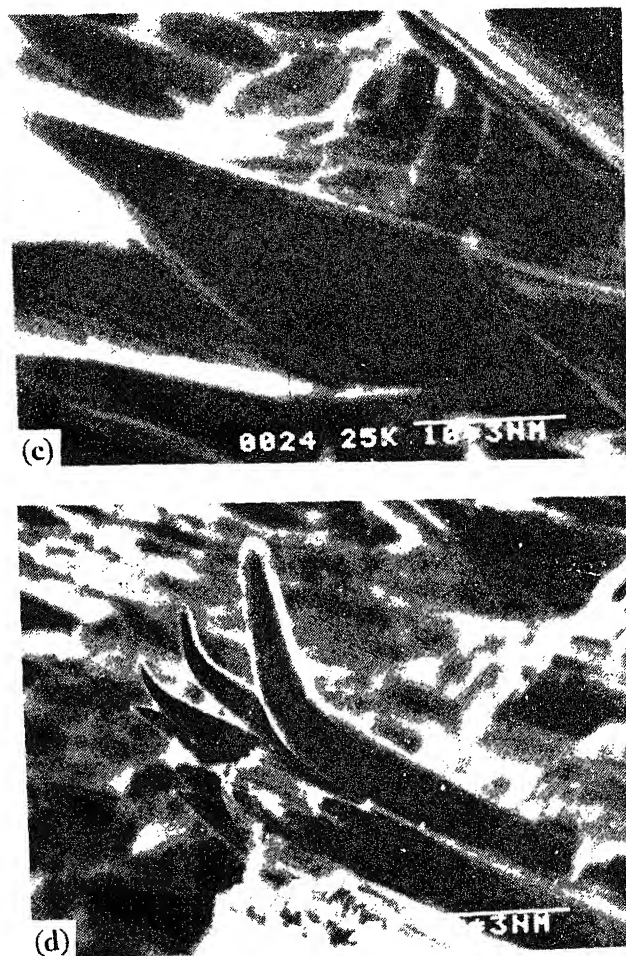


Figure 1. a-b.



**Figure 1.** Scanning electron micrographs of Ag surface bombarded by 30 keV  $^{40}\text{Ar}^+$  at an oblique incidence of  $58^\circ$  with a dose of  $1 \times 10^{19}$  ions/cm $^2$ . (a) Corrugated faceted structure at the central part of the bombarded spot. (b and c) Oblique cones along the ion direction are seen. (d) Sharp cones bent at their stems are seen. Tilt angle of the micrograph was  $30^\circ$  in a and  $60^\circ$  in b, c and d.

from the high-angle surface, redeposition of sputtered material, effects due to divergence, and the role of latent planes. Among these sources, the effects of divergence, redeposition and latent plane have important contributions to structure development. At lower doses of oblique incidence or at early stages of evolution, a rippled or corrugated structure may form. Quasiperiodic structures like that in figure 1a have been observed on Ge (Chini *et al* 1992) and Si (Chini *et al* 1991). In the present studies, however, no ridge or web-like structures were found. Careful observation also shows that the oblique and bent cones in figure 1d have their diameters almost uniform along the length and they are somewhat sharper in appearance in contrast to other oblique cones (figures 1b, c).

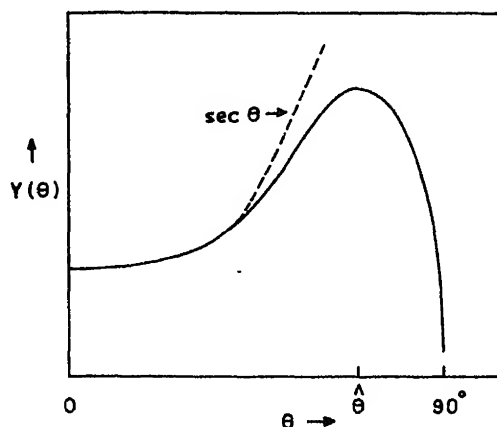


Figure 2. Variation of sputtering yield  $Y(\theta)$  as a function of ion incident angle  $\theta$ .

### 3.4 Bent cones

Some cones developed on silver in the present studies are found bent at their tips or stems. Such spontaneous bending of cones is rare in cone evolution on polycrystalline metal targets. The mechanism of bending of the oblique cones in the present case may be conceived of as due to stresses developed on these cones in the process of beam divergence or fluctuation away from the cone axes. According to Wilson (1989), around the tip of a typical  $\hat{\theta}$  cone, the surface stress exceeds the critical shear stress of a metal and, therefore, if the orientation is such that there is an asymmetry in resolved shear stresses along low index planes, plastic deformation can occur resulting in the bending of some cones in a direction where yield strength is minimum.

## 4. Conclusion

Preliminary studies of topography of Ag surface were carried out with  $^{40}\text{Ar}^+$  ions incident at an oblique angle. The modified topography shows sharp oblique cones and corrugated features. The formation of oblique cones seems not to be the consequence of the first-order erosion theory alone. Therefore the angle-dependent topographical evolution and thereby various conditions for fine cone formation as feeding data are essential to optimize the required results. Studies on the same aspect may be pursued both theoretically and experimentally at different angles of ion incidence for better understanding of oblique cone formation, and the results can be used to process fine and sharp tips as used in scanning probe or field emission microscopes.

## Acknowledgement

The authors thank Electron Microscope Facility of the Indian Association for the

## References

- Auciello O 1982 *J. Vac. Sci. & Technol.* **19** 841  
Auciello O and Kelly R 1982 *Radiat. Eff.* **66** 195  
Carter G, Navinsky B and Whitton J L 1983 in *Sputtering by particle bombardment II* (ed.) R Behrisch (Berlin: Springer) p. 231  
Chini T K, Bhattacharyya S R, Ghose D and Basu D 1991 *Jpn. J. Appl. Phys.* **30** 2895  
Chini T K, Bhattacharyya S R, Ghose D and Basu D 1992 *Vacuum* **43** 219  
Ghose D and Karmohapatro S B 1990 *Adv. Electron. Electron Phys.* **79** 73  
Wege S, Bautsch M, Rübesame D, Niedrig H and Wittich T 1993 *Nucl. Instrum. Methods* **B80** 94  
Wilson I H 1989 *Surface Topography* **2** 289

## The role of active elements in Fe–Cr–Al alloys for heating element applications

D V V SATYANARAYANA and M C PANDEY

Defence Metallurgical Research Laboratory, Kanchanbagh, Hyderabad 500 258, India

MS received 12 August 1994; revised 10 April 1995

**Abstract.** The role of active elements (zirconium, cerium and yttrium) in grain growth and its subsequent effect on room-temperature tensile fracture behaviour of Fe–Cr–Al alloys has been investigated. The alloys containing active elements exhibited improved resistance to grain growth. Yttrium-containing alloy retained higher room-temperature tensile ductility even after heating at higher temperatures because of its superior resistance to grain coarsening. All the alloys, with and without active elements, exhibited a sudden drop in room-temperature tensile ductility, with concomitant change in fracture mode from dimple rupture to cleavage, in a narrow band of 39–44  $\mu\text{m}$  grain size. The ductile–brittle transition temperatures (DBTT) of these alloys were found to be 150°C and 215°C for grain sizes 25  $\mu\text{m}$  and 100  $\mu\text{m}$  respectively. The accelerated life test showed that the alloys containing active elements exhibited longer lives.

**Keywords.** Ferritic stainless steel; heating element; active element; ductile brittle transition temperature; grain growth; fracture mode.

### 1. Introduction

Iron–chromium–aluminium alloys are essentially ferritic stainless steels and are extensively used for heating element and other applications where high-temperature oxidation resistance is the most important requirement. These alloys are available in the market with trade names Kanthal (Sweden), Gilphal (France), Fecralloy (UK). A variety of heating element materials are available; however, bulk of the requirement is met by Ni–Cr, Ni–Fe–Cr and Fe–Cr–Al alloys because of their easy processing coupled with good performance over a wide range of temperatures in varied environments. Of these, Ni–20Cr and Ni–Fe–Cr alloys are being produced at MIDHANI, Hyderabad. However, technology for indigenous production of Fe–Cr–Al alloys is not available and these are being imported. In view of this, a developmental programme was initiated at DMRL and the production technology has been established on a laboratory scale.

Fe–Cr–Al alloys have been in use for heating element applications for a fairly long time. However, there is little information published on the physical metallurgy of these alloys because of its technological significance (Keown 1987). These alloys have outstanding oxidation resistance due to the formation of a very compact, adherent and stable  $\text{Al}_2\text{O}_3$  layer at the surface. The details concerning the oxidation behaviour of these alloys with and without addition of rare earth elements such as Ce, La, Y, Er, etc are well documented (Tien and Pettit 1972; Golightly *et al* 1976; Amano *et al* 1979, 1983; Ramanarayan *et al* 1984; Beranger *et al* 1989). This paper presents the effect of active elements in Fe–Cr–Al alloys on their grain growth and its subsequent effect on their tensile fracture behaviour (at room temperature) and impact properties. Also, the role of active elements in the performance of Fe–Cr–Al alloys during accelerated life test is presented.

## 2. Experimental

The chemical composition of three alloys melted at DMRL and designated K-1, K-7 and K-8 is given in table 1. Of these, alloys K-1 and K-8 were melted in an induction furnace and alloy K-7 in a vacuum induction furnace and cast into ingots. All the ingots were hot-transferred to a furnace and homogenized at 1100°C for 8 h. The ingots were subsequently processed according to the details given in the flow chart (figure 1). In order to evaluate the role of active elements on the grain growth behaviour, samples of all the three alloys with initial grain size of 15  $\mu\text{m}$  were heated at 1050 and 1200°C for 100 and 25 h respectively. Test bars of alloys K-1, K-7 and K-8 were heated at 750, 850, 950, 1050 and 1150°C for 2 h to determine the effect of temperature on grain growth and its subsequent effect on their tensile fracture behaviour at room temperature. Heat-treated test bars were machined to the dimensions of 4 mm gauge diameter and 25 mm gauge length and tensile tests were carried out on an Instron machine. Impact properties of alloys K-7 and K-8 were determined as a function of temperature using 6-mm-thick substandard charpy specimens. Metallographic samples of heat-treated and tensile tested specimens were prepared. Grain size was measured by the linear intercept method. A scanning electron microscope energy dispersive X-ray microanalysis facility was used to detect and identify the boundary particles and also to examine the microcracks in the tensile tested specimens.

### 2.1 Accelerated life test

Accelerated life test was carried out according to ASTM specification No. B78 (1982) to determine the resistance to oxidation of heating element materials under cyclic heating and cooling conditions. In this test, a 0.6 mm diameter wire of 250 mm length was bent to a U-shape and was intermittently heated by resistance heating (by passing current through the wire) between room temperature and 1200°C with a hold time of 2 min. Temperature of the wire was measured using an optical pyrometer once in a while and adjusted, if necessary. Time elapsed for first appearance of the hot spot was considered to be life of the wire.

## 3. Results and discussion

### 3.1 Grain growth behaviour

Figure 2 shows the microstructures of the three alloys K-1, K-7 and K-8 obtained after heating at 1050°C for 100 h. Grain size of the three alloys after heating at

Table 1. Chemical composition of the three alloys (wt%).

Identification	Cr	Al	Co	Zr	Si	Mn	C	Ce	Y
K-1	21.8	5.1	0.98	—	0.4	0.3	0.06	—	—
K-7	22.0	4.98	1.0	0.15	0.4	0.3	0.014	—	0.47
K-8	21.6	5.0	1.0	0.15	0.5	0.3	0.08	0.03	—

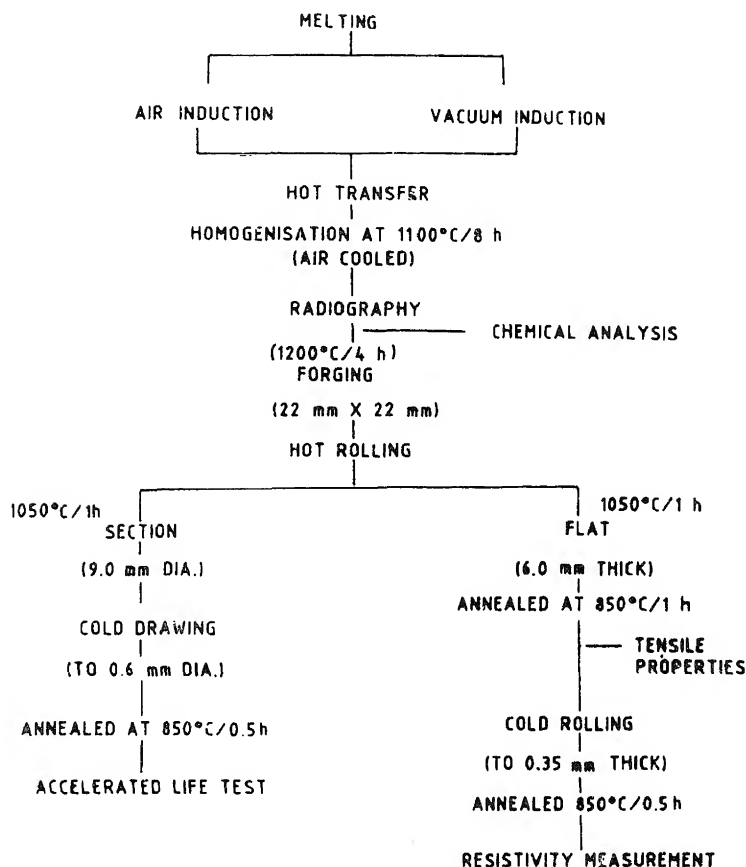


Figure 1. Process flow chart of iron-chromium-aluminium alloys.

and 1200°C for 100 and 25 h respectively is recorded in table 2. Considerable grain coarsening can be noted in the alloy which did not contain any active element (K-1). In contrast, grain coarsening was restricted in the alloy which contained about 0.5% yttrium (K-7). Figure 3a shows the presence of yttrium-rich particles both at the grain boundaries and within grains of alloy K-7 (figure 3b). A number of yttrium-rich phases have been reported in Fe-Cr-Al alloys containing yttrium (Keown 1987), but the major phases identified are  $\text{YFe}_9$  and  $\text{Y}_2\text{O}_3$ . Both the phases are extremely stable up to very high temperatures and they are considered to be responsible for the remarkable grain growth resistance of yttrium-containing Fe-Cr-Al alloys. Grain coarsening was also restricted to some extent in the alloy which contained Zr and Ce (K-8). Precipitates of chromium carbide were formed in both K-8 and K-1 (figure 4). In addition, there were a few alumina inclusions as melting of K-1 and K-8 was carried out in an air induction furnace. Although these carbide particles were present in both the alloys, grain coarsening was restricted only in alloy K-8. Considerable grain growth in alloy K-1 indicates that chromium-rich carbide was not effective in inhibiting grain coarsening, because of its instability at temperatures greater than 1000°C (Satyanarayana and Pandey 1993). It appears therefore that grain coarsening in alloy K-8 was restricted due to the presence of



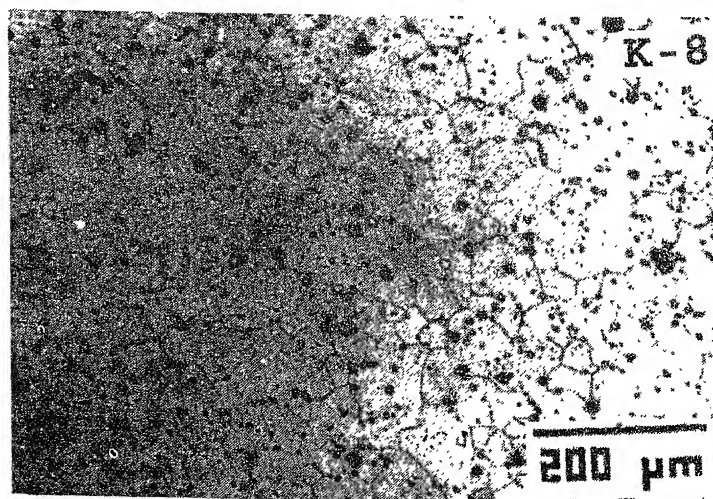
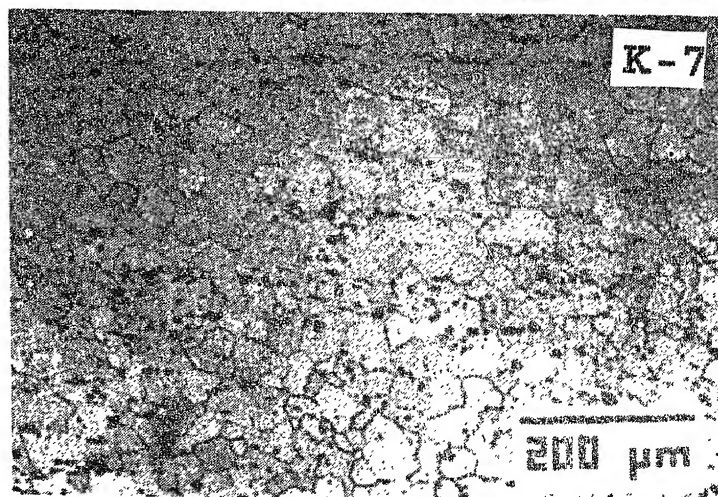
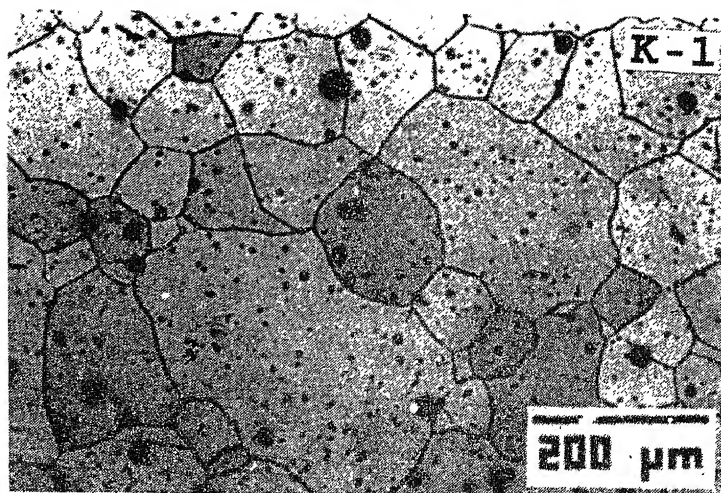


Figure 2. Microstructures of the alloys K-1, K-7 and K-8 after heating at 1050°C for 100 h.

zirconium and/or cerium, in the form of some intermetallic compound. Figure 5 shows the variation of grain size in all the three alloys as a function of temperature. It can be seen that grain coarsening, above 1000°C, is very rapid for alloys K-1 and K-8 compared to alloy K-7. This clearly demonstrates that addition of yttrium to Fe-Cr-Al alloy is very effective in inhibiting grain growth up to very high temperatures.

### 3.2 Tensile fracture behaviour

Figure 6 shows the effect of exposure temperature on the room-temperature ductility of alloys K-1, K-7 and K-8. It can be seen that ductility is reduced quite steeply for

**Table 2.** Grain size of alloys K-1, K-7 and K-8 obtained after heating at 1050°C and 1200°C (initial grain size 15  $\mu\text{m}$ ).

Identification	Exposure temperature (°C)	Duration (h)	Grain size ( $\mu\text{m}$ )
K-1	1050	100	100
K-7	1050	100	30
K-8	1050	100	50
K-1	1200	25	370
K-7	1200	25	90
K-8	1200	25	140

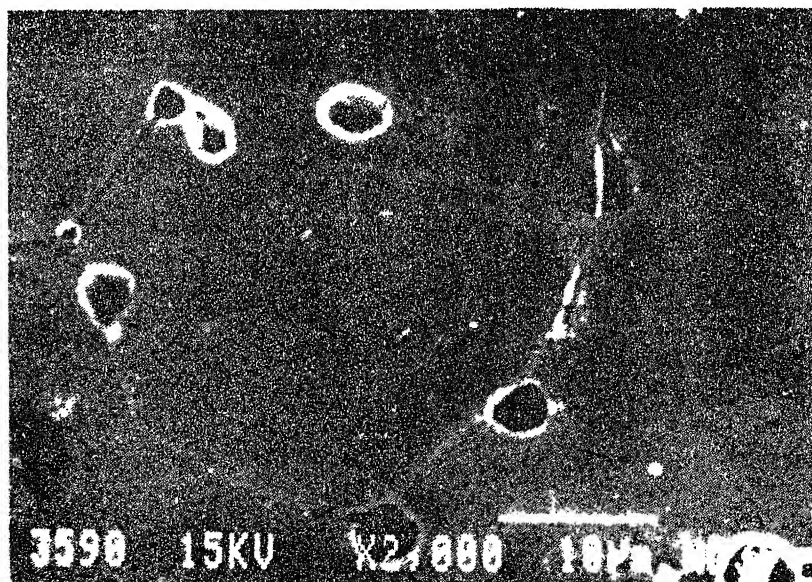
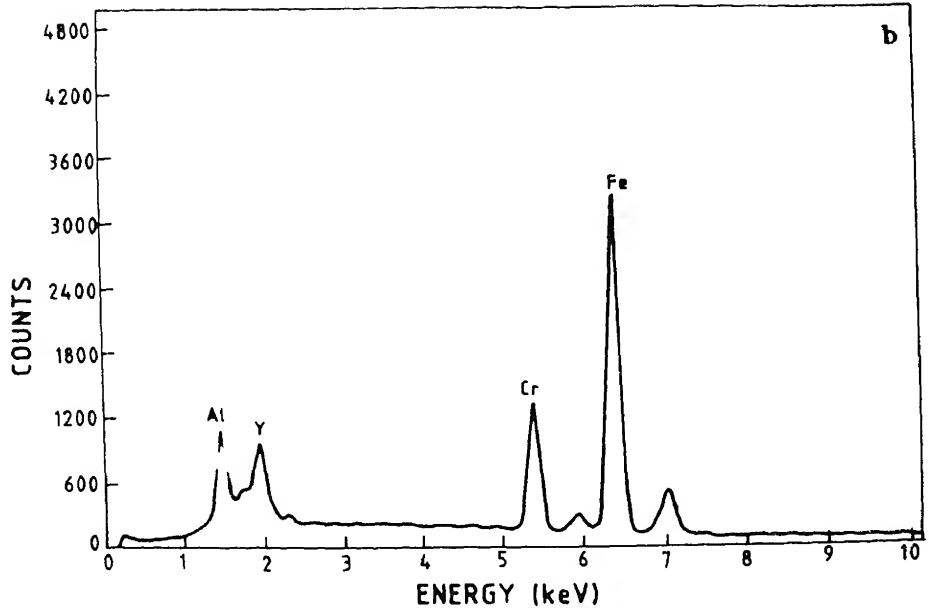
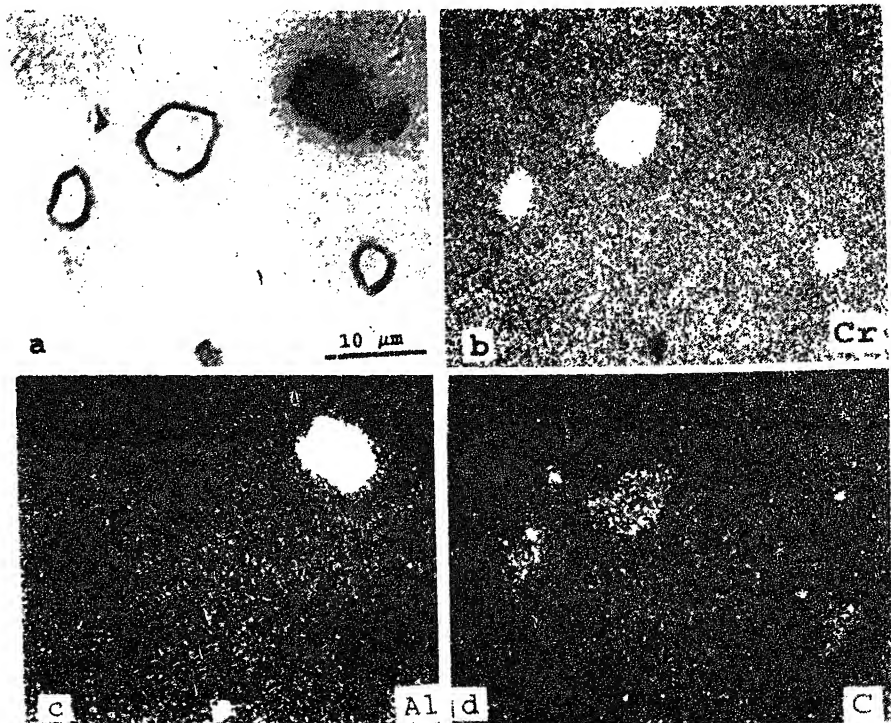


Figure 3. a.



**Figure 3.** a. Scanning electron micrograph showing the presence of yttrium-rich particles, both at the grain boundaries and within the grains in alloy K-7 and b. EDAX spectrum showing presence of yttrium in the grain boundary particles.



**Figure 4.** a. Backscattered electron image showing the presence of chromium carbide and alumina particles both at grain boundary and within the grains; X-ray images of b. chromium, c. aluminium and d. carbon.

exposure temperature of 950°C and above for alloys K-1 and K-8, and for 1050°C and above for alloy K-7. Also, ductility values are quite high for alloy K-7 for all exposure temperatures above 900°C. This indicates that alloy K-7 has ability to retain a good amount of ductility after exposure to higher temperatures in contrast to alloys K-1 and K-8. This can be attributed to its better resistance to grain coarsening (figures 2 and 5). Figure 7 shows the effect of grain size on tensile ductility of alloys K-1, K-7 and K-8. A sudden drop in ductility, with concomitant change in the fracture mode from

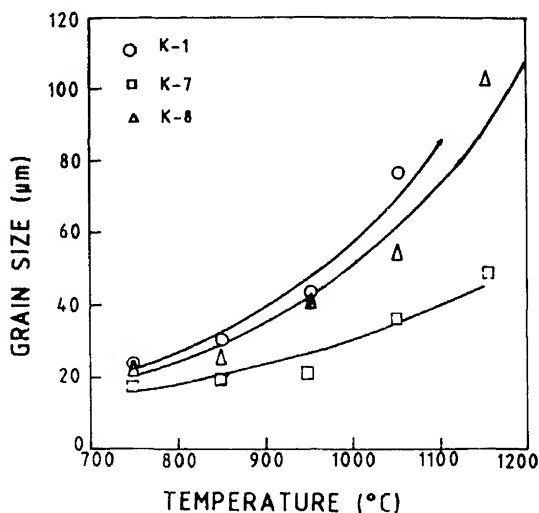
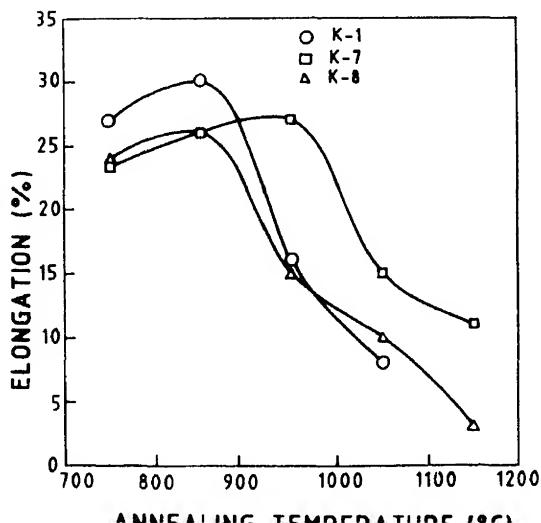


Figure 5. Variation of grain size for alloys K-1, K-7 and K-8 as a function of temperature.



dimple rupture to cleavage, can be noted for all the three alloys in a narrow band 39–44  $\mu\text{m}$  grain size. This shows that there is a ductile-to-brittle transition at room temperature in these alloys at grain size close to 40  $\mu\text{m}$ . Embrittlement of Fe–Cr–Ni alloys following high-temperature exposure has also been reported (Dubey *et al* 1988). Fractographic studies revealed that the fracture surface of tested specimens of all the three alloys exhibited dimples when grain size was below about 40  $\mu\text{m}$  (figure 8a) and cleavage when grain size was above about 40  $\mu\text{m}$  (figure 8b). Figures 9a and 9b show nucleation of microvoids at the particle–matrix interface near the fracture end of specimens with fine grain size below 40  $\mu\text{m}$  of alloys K-7 and K-8. Nucleation of microvoids occurred either by decohesion of smaller particles or cracking of coarser particles. Final fracture occurred by subsequent growth and coalescence of these microvoids resulting in dimple rupture. Figures 10a and 10b show cleavage microcracks in the tensile tested specimens of alloys K-7 and K-8 with coarse grain structure ( $> 40 \mu\text{m}$ ). Microscopic examination of tensile tested specimens revealed that all the cleavage microcracks were not associated with particles, indicating that the presence of particles is not mandatory for nucleation of microcracks. It has been shown in some bcc metals (Zener 1948) that nucleation of cleavage cracks occurs due to stress concentration ahead of slip band blocked either by particles or by grain boundaries. The stress concentration at the tip of the slip band depends on slip distance which increases with grain size. This indicates that once grain size reaches a critical value, sufficient stress concentration is built up to cause nucleation of cleavage cracks. In the present alloys the critical grain size was found to be about 40  $\mu\text{m}$ .

### 3.3 Impact properties

Figure 11 shows variation of impact energy of alloy K-8 as a function of temperature for 25 and 100  $\mu\text{m}$  grain sizes. It can be seen that ductile–brittle transition temperature

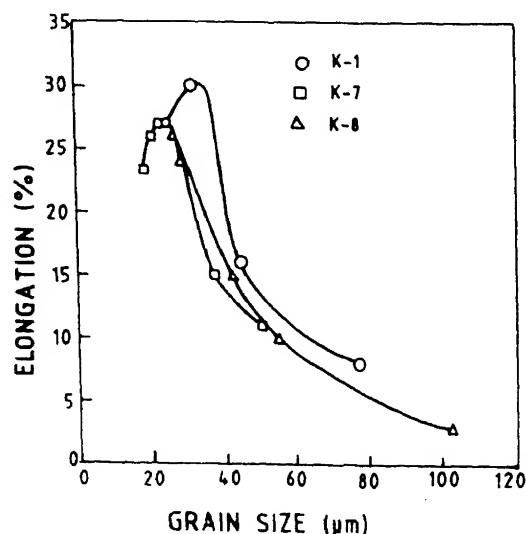
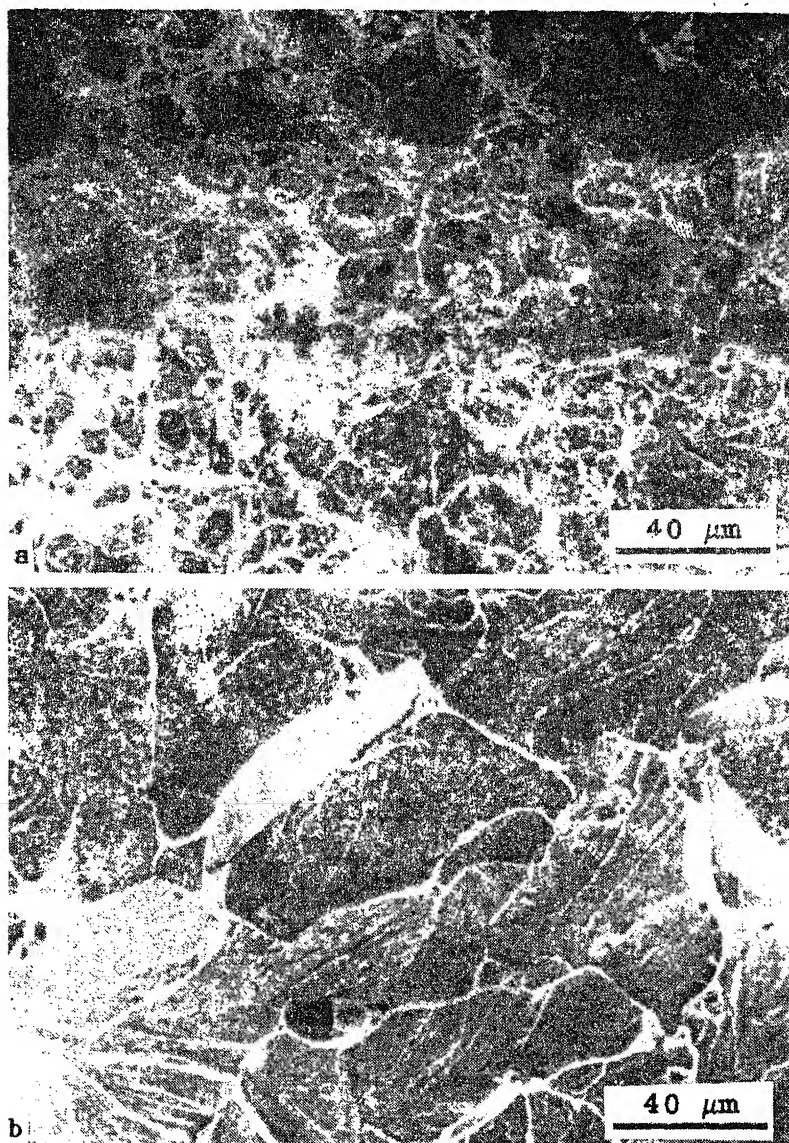


Figure 7. Effect of grain size on the tensile ductility of the alloys K-1, K-7 and K-8.



**Figure 8.** Fractographs of Fe-Cr-Al alloys showing **a.** dimple rupture for specimens with grain sizes below about  $40\text{ }\mu\text{m}$  and **b.** cleavage mode of fracture for specimens with grain sizes above about  $40\text{ }\mu\text{m}$ .

(DBTT) is about  $150^{\circ}\text{C}$  for grain size of  $25\text{ }\mu\text{m}$  and about  $215^{\circ}\text{C}$  for  $100\text{ }\mu\text{m}$ . DBTT was also determined for alloy K-7 at a grain size of about  $100\text{ }\mu\text{m}$  and was found to be about the same as that for alloy K-8, indicating that addition of yttrium and the vacuum melting route had no effect on DBTT of these alloys. The high DBTT of this family of alloys indicates that these alloys are very notch-sensitive at room temperature and therefore appropriate care needs to be taken while handling (shifting from





Figure 9. Scanning electron micrographs showing nucleation of microvoids at particle-matrix interface in tensile tested specimens of a. alloy K-7 and b. alloy K-8.

one place to other), conditioning (grinding and/or machining to remove surface defects) and room-temperature processing of large sections of these alloys.

#### 3.4 Accelerated life test

The life test was carried out to evaluate the ability of the heating element material to form and retain a protective oxide film under severe cyclic heating and cooling.

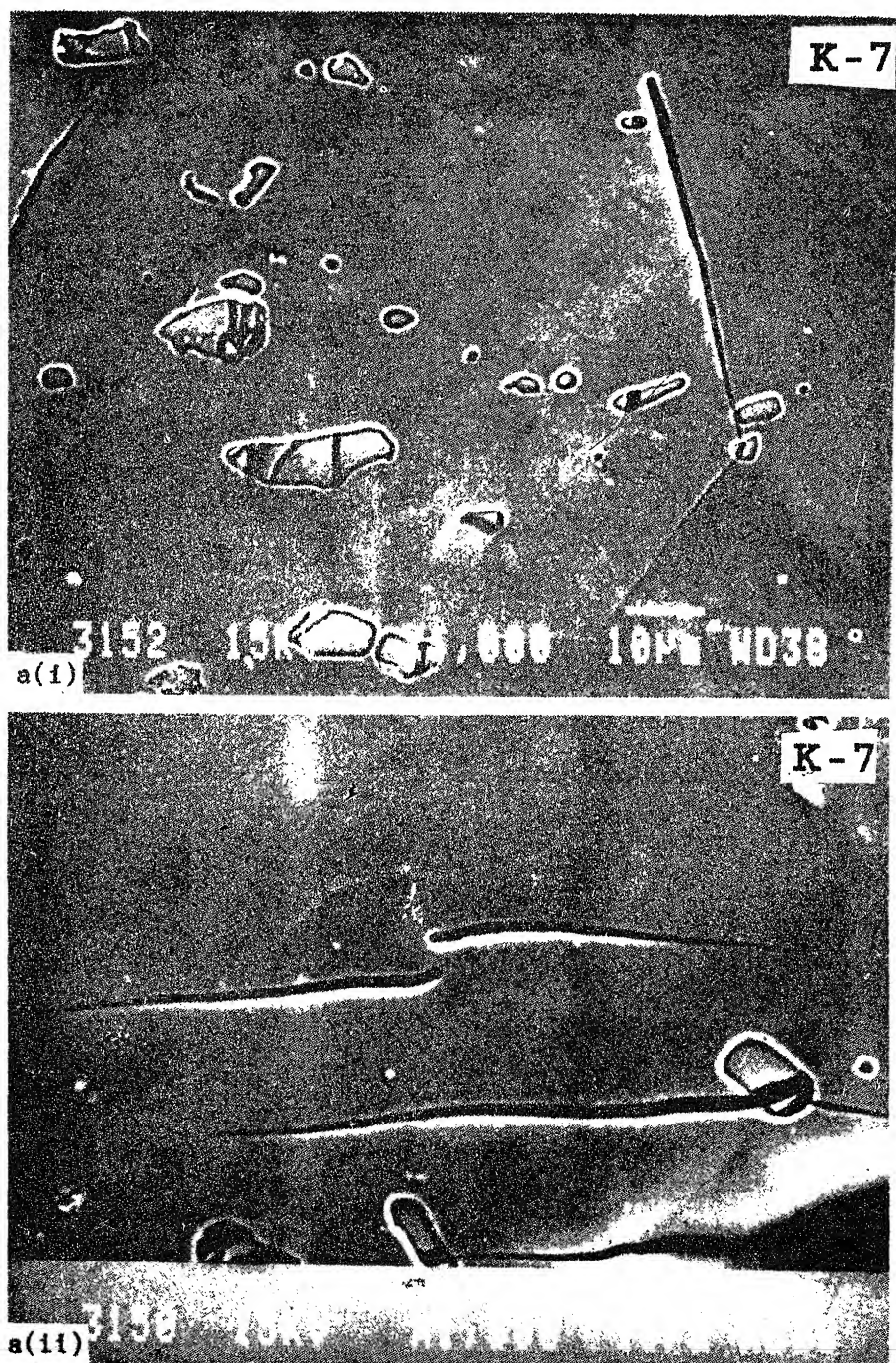


Figure 10a.



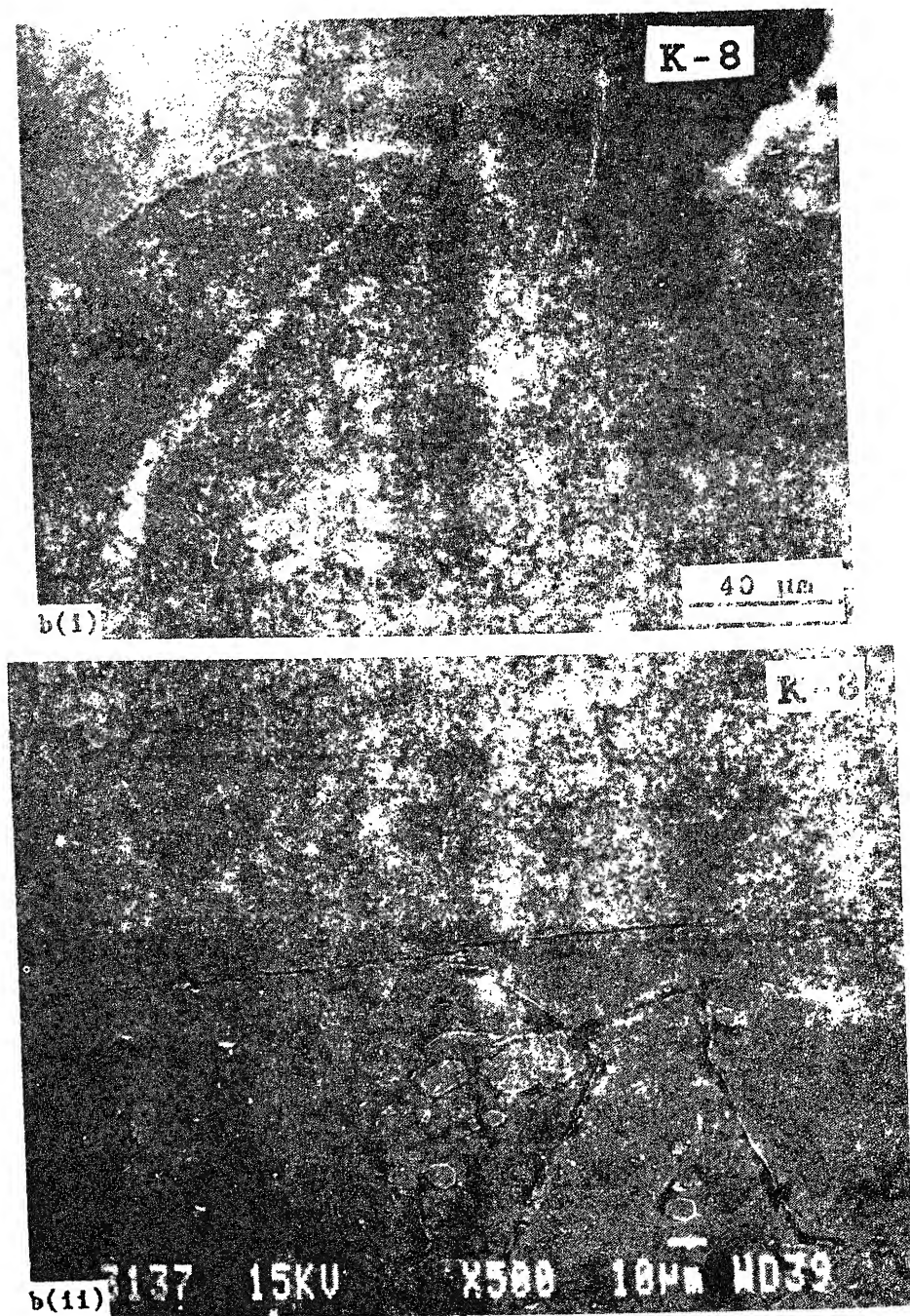


Figure 10. Scanning electron micrographs showing nucleation of cleavage microcracks in tensile tested specimens of a. alloy K-7 and b. alloy K-8.

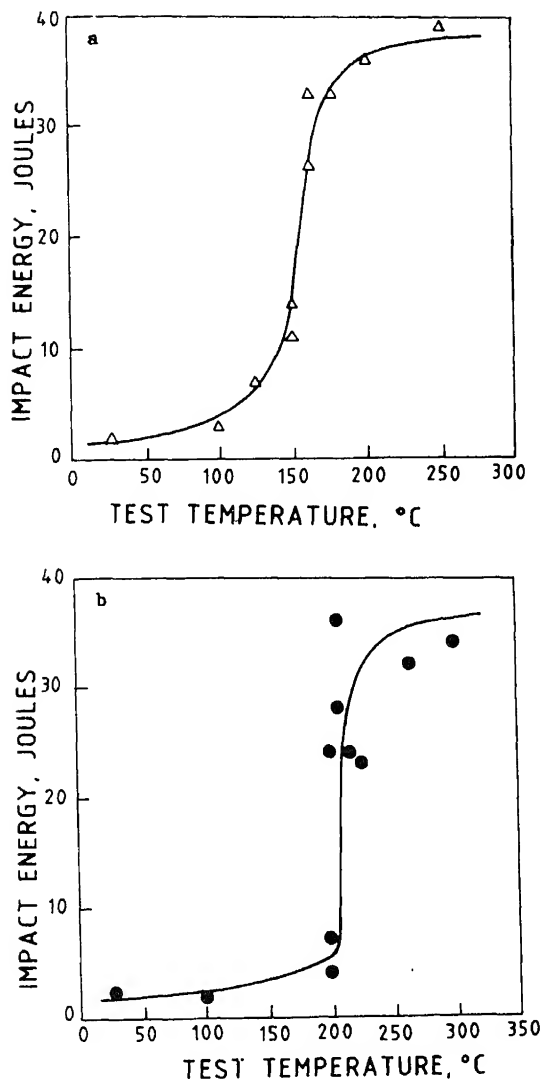
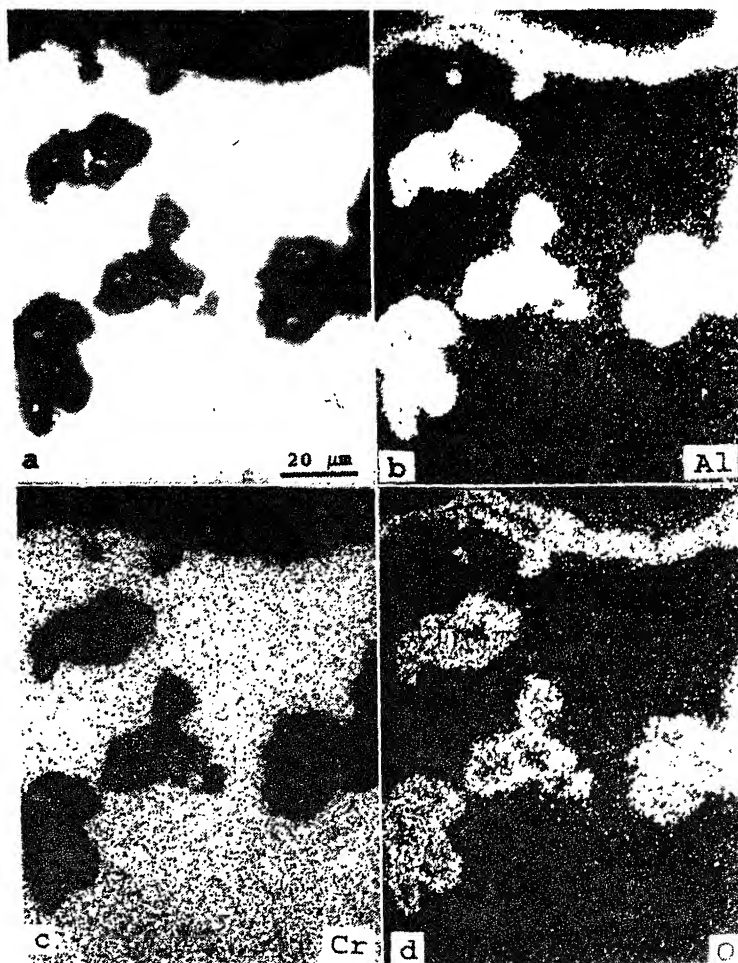


Figure 11. Variation of impact energy as a function of temperature for alloy K-8 for grain sizes a. 25  $\mu\text{m}$  and b. 100  $\mu\text{m}$ .

conditions. The life and performance of a heating element, therefore, depends on the nature of oxide film formed under these conditions. Table 3 shows the life of heating elements of the three alloys obtained from the accelerated life test. Alloy K-1 showed very poor life compared to alloys K-7 and K-8. Protective film formed in all three alloys was  $\text{Al}_2\text{O}_3$  (figure 12). However, adherence of the oxide film formed on the heating element of alloy K-1 was very poor and it spalled off over almost the whole length of the wire after a few cycles. In case of alloys K-7 and K-8 the film was very compact and strongly adherent over the whole length of the heating element wire and appearance of bright spot occurred in localized

**Table 3.** Accelerated life test data.

Identification	Life (h)
K-1	50
K-7	300
K-8	220



**Figure 12.** a. Backscattered electron image showing aluminium oxide film formed on surface of heating element during accelerated life test of Fe–Cr–Al alloys; X-ray images of b. aluminium, c. chromium and d. oxygen.

regions where oxide film spalled off after large number of cycles. It appears that the better performance of alloys containing active elements is due to the improved adherence of the oxide film formed at the heating element surface. Active elements improve the adherence of  $\text{Al}_2\text{O}_3$  film in Fe–Cr–Al alloys either by preventing

the formation of voids at oxide-alloy interface (vacancy-sink mechanism, Tien and Pettit 1972) or by changing growth mechanism and morphology of oxide scale (Golightly *et al* 1976) or by forming oxide pegs along the grain boundaries (Amano *et al* 1979).

#### 4. Conclusions

- (i) Fe-Cr-Al alloys containing active elements exhibited better resistance to grain coarsening. The effect was more pronounced in the case of alloy containing yttrium.
- (ii) The alloy with yttrium was able to retain higher room-temperature tensile ductility even after heating at higher temperatures due to its better resistance to grain coarsening.
- (iii) A sudden drop in ductility, with concomitant change in fracture mode from dimple rupture to cleavage, was observed in all the three alloys in a narrow band of 39–44  $\mu\text{m}$  grain size.
- (iv) The ductile-brittle transition temperatures of these alloys were found to be 150 and 215°C for 25 and 100  $\mu\text{m}$  grain sizes respectively.
- (v) Alloys containing active elements exhibited longer lives in accelerated life test.

#### Acknowledgements

We would like to express our gratitude to Dr P Rama Rao, Secretary, Department of Science and Technology, New Delhi (former Director of DMRL), for his encouragement in initiation of the developmental work on Fe-Cr-Al alloys. We are thankful to Dr K K Sharma for his guidance and enthusiastic help in melting of various compositions of these alloys. Our thanks are due to Shri R K Mahapatra, Chairman-cum-Managing Director, MIDHANI, Hyderabad for many useful discussions and providing facilities for processing of the alloys. Assistance of Melting, Forging, Rolling Groups and Workshop is acknowledged with pleasure. We are grateful to Shri S L N Acharyulu, Director, DMRL, for his constant encouragement.

#### References

- Amano T, Yajima S and Saito Y 1983 *Proceedings JIMIS-3: High Temperature Corrosion* (Japan: Trans. JIM supplement) p. 247
- Amano T, Yajima S and Saito Y 1979 *Trans. JIM* **20** 431
- Beranger G, Armanet F and Lambertin M 1989 *Conf. Proc. on the role of active elements on the oxidation behaviour of high temperature metals and alloys*, 33, Patten, The Netherlands, (eds) E Lang (England: Elsevier Science Publishers Ltd.)
- Cottrell A H 1958 *Trans. Am. Inst. Min. (Metall.) Engres* **212** 192
- Dubey R K, Basak P and Chaudhury S K 1982 *Tool & Alloy Steels* **16** 51
- Golightly F A, Scott F H and Wood G C 1976 *Oxidation of Metals* **10** 163
- Keown S R 1987 *Stainless Steel '87*, (London: Institute of Metals) pp. 345
- Ramanarayan T A, Raghavan M and Petkovic-Luton R 1984 *J. Electrochem. Soc.* **131** 923
- Satyanarayana D V V and Pandey M C 1993 Unpublished research
- Tien J K and Pettit F S 1972 *Metall. Trans.* **3** 1587
- Zener C 1948 *Fracturing of metals* (Ohio: Amer. Soc. Metals) p. 3



# Influence of ion-induced interfacial chemical reactivity on contact resistance

S T LAKSHMIKUMAR

National Physical Laboratory, Dr K S Krishnan Road, New Delhi 110012, India

MS received 5 December 1994; revised 29 March 1995

**Abstract.** Contact resistance measurements of chromium contacts deposited by partially ionized beam deposition on transparent conducting indium tin oxide (ITO) were performed. These provide a direct experimental evidence of the influence of interfacial chemical interaction on the contact resistance. The interfacial reactivity is controlled by modifying the energy and flux of ionized chromium atoms deposited on ITO employing a specially designed partially ionized deposition system with very high ionization efficiency. The true contact resistivity  $\rho_c$  is obtained by iteratively correcting the experimentally measured values for the finite sheet resistance of the ITO layer.  $\rho_c$  decreases linearly with the energy of the ionized chromium. Auger sputter profiling shows no structural modifications at the interface due to a change in the energy of the chromium atoms, confirming that the observed change in the contact resistivity is directly related to interfacial chemical bonding of the atoms with the oxygen atoms in the ITO leading to a local increase of carrier concentration and lower interfacial resistance.

**Keywords.** Chromium contacts; beam deposition.

## 1. Introduction

Contact resistance, the resistance to flow of electric current at the interface between two materials, is a major technological problem, particularly when large current densities are encountered. In microelectronic devices with very small contact areas, the crowding of current lines and the electronic band structure of the ohmic contact contribute to the contact resistance (Cohen and Gildenblat 1986). Contact resistance is also an important technological problem in solar cells (Hovel 1975; Kanicki 1988; Rastogi and Lakshmikumar 1989). In addition, our work on metal oxide conductor contacts, where oxygen has a direct role to play in the generation of the conducting species, has shown that the physicochemical interactions at the interface directly control the contact resistance. Two distinct processes with different physical origins contribute to the contact resistance (Lakshmikumar and Rastogi 1989). One relates to the modification in the detailed charge balance and carrier concentration at the interface induced by the proximal contact metal. The second is due to the nature of carrier injection at the free surface of the oxide conductor. This was confirmed by the observed scaling of  $\rho_c$  with the strength of metal-oxygen interaction represented by the heat of formation of the oxide. The interaction between oxygen and metal leads to the modification of the availability of conducting species at the interface.

Partially ionized deposition is a powerful technique for the controlled variation of the reactivity of adatoms. Ion bombardment is known to influence adhesion, stress, impurity content and packing density (McNiel *et al* 1984). Low-energy ion bombardment (energy  $\leq 200$  eV) has the capacity to provide activation energy for the growth of epitaxial films (Takagi *et al* 1975; Itoh *et al* 1977; Appleton *et al* 1986), to significantly affect the growth process in thin films (Harper *et al* 1983), to modify the interfacial

electronic properties of Schottky barriers (Wong *et al* 1986) and to enhance surface reconstruction and reaction leading to the formation of compounds at very low temperatures (Li and Lu 1990; Liu *et al* 1993). At the same time, the total ionic energy is small and there is no structural damage to the interface between the substrate and the film (Greene *et al* 1986).

The present work is an attempt to directly modify the reactivity of a depositing species and study the resultant changes in contact resistivity. The special design of the electron bombardment heater provides high concentrations, up to 5%, of ions (Mei and Lu 1988). By biasing the substrate, the energy and flux of the ions impinging on the substrate can be directly modified, thereby controlling the interfacial reactivity. Chromium was selected as the contact metal because Cr/ITO contacts show the lowest resistivities. The contact resistance on ITO was measured by depositing chromium contacts with various fluxes of the ionized species in a 4-terminal contact resistivity test structure configuration (Chern and Oldhiem 1984). The true contact resistivity,  $\rho_c$  was iteratively calculated from the experimentally measured resistance. Auger sputter profiling has been employed to determine the width of the interface and the bonding state of the chromium atoms.

## 2. Experimental

Chromium films were deposited using partially ionized beam (PIB) deposition procedure described earlier (Mei and Lu 1988). Cr metal is evaporated from a graphite crucible by heating with an electron beam accelerated to a high positive potential ( $\approx 1$  kV) applied to the crucible. A tantalum filament is used to produce a high ( $\approx 1$  A) electron current by thermionic emission. The unique filament design results in 2–5% ionization as determined from the ion current measurements. This high level of ionization for an indirect ionization procedure is primarily due to the extremely high electron density in the vicinity of the mouth of the graphite crucible which enhances the probability of atom–electron collisions. The system has a base pressure of  $10^{-5}$  Pa. An external retarding bias is applied to the substrate to control the energy of the ionized beam, as required. The ITO substrates were initially cleaned in alkaline detergent and then washed in hot running water. They were then degreased in boiling trichloroethylene before loading into the system through a load-lock arrangement. The Cr metal (4N purity) was evaporated at a rate of  $\approx 1$  Å/s at a background pressure of  $\approx 3 \times 10^{-5}$  Pa, to a final thickness of 1000 Å. Depositions were performed at various bias voltages from 0 V (ion energy  $\approx 1$  keV) to 1 kV (ion energy  $\approx 0$  eV). The substrates were not heated and the temperature rise due to incidental heating from the source was measured to be less than 20°C. For contact resistance measurements, the contacts were formed on the freshly cleaned ITO of sheet resistance 20–30  $\Omega/\square$  by evaporating the metal through lithographically delineated masks. The wide contact test structure (Chern and Oldhiem 1984) which is most appropriate for large-area contacts was employed for the contact resistivity measurements. Typical contact area was  $\approx 0.01$  cm<sup>2</sup>. The schematic view of the wide contact test structure employed is shown in figure 1. The experimental contact resistance  $R_{\text{exp}}$  was determined by four-probe measurement using the  $I$ – $V$  leads as shown in figure 1. The contribution from the ITO layer under the contact can be evaluated by measuring the transmission

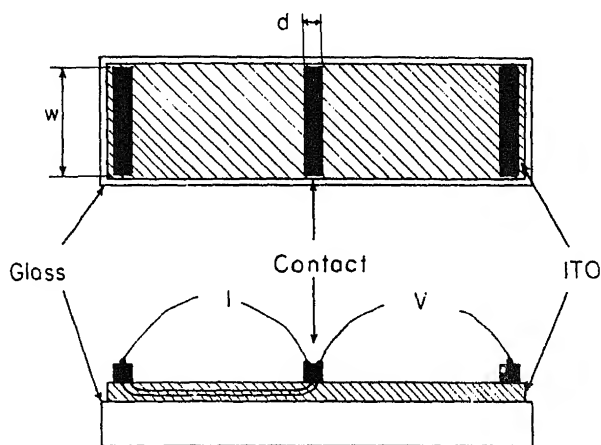


Figure 1. Schematic of the wide contact test structure.

iteratively using the equation

$$R_{\text{exp}} = (R_s \rho_c)^{1/2} / \{w \sinh [(R_s / \rho_c)^{1/2} \cdot d]\}.$$

Here  $R_s$  is the sheet resistance of ITO, measured individually for each test structure, and  $w$  and  $d$  are the dimensions of the contact determined by optical microscopy for each contact. In view of the low temperatures involved in the preparation of the contact, it was assumed that  $R_s$  is not altered during the process of deposition of the metal layer. AES was performed on samples for evaluating the quality of the films and the interface. For depth profile studies, the film was sputtered away using 3 kV Ar ions. The composition was evaluated using the height of the 532 eV peaks for Cr since the main peak overlaps with the oxygen peak at 515 eV. The composition of the ITO was evaluated by monitoring the lines of In(400 eV), Sn(428 eV) and  $O_2$  (515 eV) respectively.

### 3. Results and discussion

The variation of the contact resistivity with the applied bias voltage is shown in figure 2. The experimentally measured contact resistance  $R_{\text{exp}}$  and the true contact resistance (the product of the iterated contact resistivity  $\rho_c$  and the experimental contact area  $w \cdot d$ ) are shown. Both decrease as the ion energy increases. The values of  $R_{\text{exp}}$  and  $R_c$  shown are averaged over several samples. The scatter in data is  $\approx 10\%$ . The parasitic contribution, the difference between the measured contact resistance  $R_{\text{exp}}$  and the true contact resistance ( $\rho_c \cdot w \cdot d$ ) is small for the low-sheet-resistance ITO employed in this study. All the contacts were completely ohmic over a current range of  $10^{-6}$ – $2 \times 10^{-1}$  A, ruling out the presence of interfacial insulating layers. The values of  $R_c$  obtained are similar to earlier measurements on thermally deposited Cr films. The lowest value obtained is  $1.51 \times 10^{-2} \Omega \text{cm}^2$ , less than the lowest value previously reported for Cr



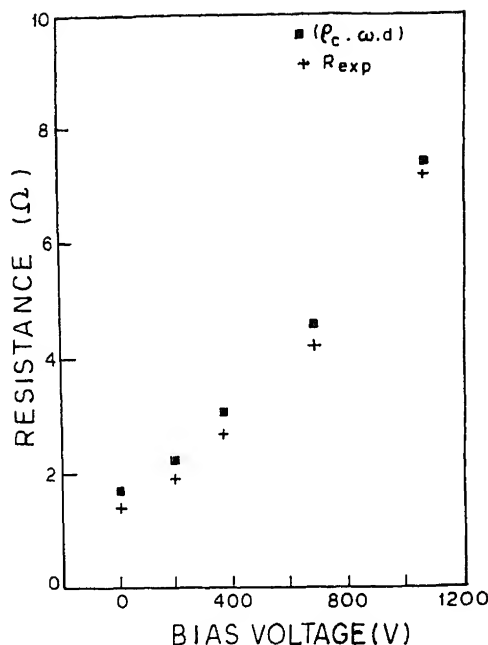


Figure 2. Variation of the contact resistance with the ion energy.

ensure that no ionized species are being deposited, the  $\rho_c$  value is  $6.4 \times 10^{-2} \Omega \text{cm}^2$ , which is comparable to the earlier values obtained for thermally deposited contacts.

The contact resistivity in these conducting oxides is not determined by the semiconductor contact theory (Chang *et al* 1971), which predicts

$$\rho_c \approx \exp(V_{bo}/E_{oo}).$$

Here,  $V_{bo}$  is the barrier height between ITO and the metal and  $E_{oo}$  is an energy term which depends on the effective mass,  $m^*$  and density  $N$  of the carriers and the effective permittivity of the semiconductor,  $\epsilon$ , as

$$1/E_{oo} = (h/2)(N/m^*\epsilon)^{1/2}.$$

It is difficult to estimate the theoretical value of  $\rho_c$ , since the constants are unknown. However, ITO has an effective carrier concentration of  $\approx 10^{21}$ , and at these densities, calculations on Si show that the value is very low ( $\approx 10^{-7}$ ) and is generally insensitive to other parameters.

It is clear that the variation of  $R_c$  with the effective ion energy is only explained in terms of the model developed earlier (Lakshmikumar and Rastogi 1989) based on the physicochemical interactions at the interface. In terms of this model, the effective ion energy of the Cr atoms increases the binding between the Cr and O atoms at the interface and this interaction directly controls the interfacial resistance. Since the oxygen vacancies act as double donors in ITO, the freezing of the oxygen atoms at the interface would effectively alter the carrier density and hence the  $\rho_c$ . Unlike earlier

work, the present studies involve a single metal and the reactivity has been experimentally modified.

In order to rule out the possibility of structural modification of the interface due to the penetration of ionized Cr atoms, Auger sputter studies were performed on some samples. The typical compositional profile at the interface is shown in figure 3. The width of the interface, estimated from the time taken to sputter known thicknesses of Cr and ITO, is  $\approx 100 \text{ \AA}$ . The shape of the Cr Auger line at 530 eV at various depths in the interface region is shown as an inset in figure 3. This line shows a distortion as the interface is traversed. The Cr line observed at the Cr side of the interface, at points A and B in figure 3, shows free Cr. The Cr in intimate contact with the ITO appears to be bonded. This is clear from the line shape of the 530 eV line at position C in figure 3.

The shape of the sputter profile, width of the interface region, and the lineshape of the Cr Auger line do not change with the energy of the ions. The variation in the experimentally determined width of the interface with ion energy is not significant. The bonded Cr is located only after the interfacial region is sputtered away. The width of the region showing bonded Cr (the region beyond the position C in figure 3) is  $\approx 100 \text{ \AA}$  at all ion energies. These results suggest that there is no systematic increase of the penetration of the adatoms into ITO as the ion energy increases from zero to  $\approx 1 \text{ keV}$ . This confirms that the observed variation of contact resistivity with the ion energy is not related to structural changes involving the penetration of ions into ITO. The observed local bonding of Cr supports our model of interfacial resistance being controlled by physicochemical interactions at the contact.

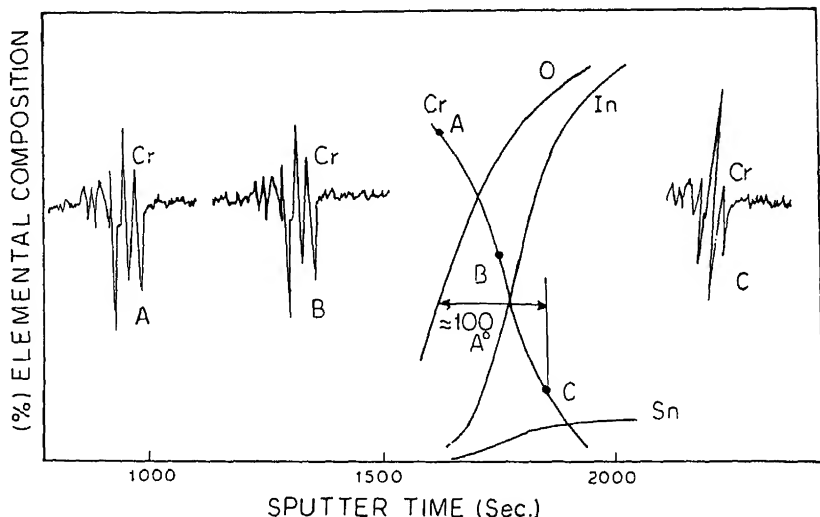


**Figure 3.** Auger sputter profile of the Cr/ITO interface. The inset shows the change in the lineshape of the Cr Auger line at 530 eV at the interface.

#### 4. Conclusions

The interfacial resistivity of Cr/ITO contacts formed by partially ionized deposition of the metal have been measured. The resistivity decreases with the increase in the effective ion energy. All the contacts were completely ohmic over a current range of  $10^{-6}$ – $2 \times 10^{-1}$  A. The lowest value obtained is  $1.51 \times 10^{-2} \Omega\text{cm}^2$ , less than the lowest values reported in earlier measurements on thermally deposited Cr films on  $10 \Omega/\square$  ITO. Auger studies show no systematic variation of the interfacial depth or structural changes at the interface as the ion energy is varied. Lineshape analysis of the 530 eV Auger line of Cr shows that the Cr atom becomes bonded at the interface. These results show that the observed variation of interfacial resistivity is not due to structural modifications at the interface and provide a direct evidence for the influence of chemical interactions at the interface on contact resistivity.

#### Acknowledgements

The author thanks Prof. T M Lu, Centre for Integrated Electronics, Rensselaer Polytechnic Institute, New York, where the depositions were performed during his stay there as a Raman Fellow. Thanks are due to Dr S M Shivaprasad for the Auger measurements.

#### References

- Appleton B R, Zuhr R A, Noggle T S, Herbots N and Pennycook S J 1986 *MRS Sym. Proc. Photon, beam and plasma stimulated chemical processes at surfaces* (eds) V M Donnelly, I P Hermann and M Hirose (New York: MRS) p 319
- Chern J G J and Oldhiem W G 1984 *IEEE Electron Dev. Lett.* **5** 178
- Cohen S S and Gildenblat G S 1986 *VLSI Science and Technology* (ed.) N G Einspruch **13** p. 87
- Greene J E, Rockett A and Sundgren J E 1986 *MRS Sym. Proc. Photon, beam and plasma stimulated chemical processes at surfaces* (eds) V M Donnelly, I P Hermann and M Hirose (New York: MRS) p. 39
- Harper J M E, Cumo V J and Kaufmann H R 1983 *Ann. Reviews of Mater. Sci.* (eds) R A Huggins, R H Bube and D A Vermilea **13** 413
- Hovel H J 1975 *Semiconductors and semi-metals* (eds) R K Willardson and A C Beer **11** p. 1
- Itoh T, Nakamura T, Utomachi M and Sugiyama T 1977 *Jap. J. Appl. Phys.* **16** 553
- Kanicki J 1988 *Appl. Phys. Lett.* **53** 1943
- Lakshmikumar S T and Rastogi A C 1989 *Appl. Phys.* **A48** 325
- Li P and Lu T M 1990 *Appl. Phys. Lett.* **57** 2336
- Liu W T, Lakshmikumar S T, Knorr D B, Lu T M and van der Leeden Ir G A 1993 *Appl. Phys. Lett.* **64** 573
- McNiel J R, Barron A C, Wilson S R and Hermann W C Jr. 1984 *Appl. Opt.* **23** 552
- Mei S N and Lu T M 1988 *J. Vac. Sci. Technol.* **A6** 9
- Rastogi A C and Lakshmikumar S T 1989 *Solar Cells* **26** 323
- Takagi T, Tamada I and Sasaki A 1975 *Thin Solid Films* **45** 569
- Wong J, Mei S N and Lu T M 1986 in *MRS Sym. Proc. Interfaces, superlattices and thin films* (eds) J D Dow and I K Schuller (New York: MRS) p. 211

# Electrical and magnetic studies of iron(III) vanadate

N SURESH RAO and O G PALANNA\*

\* Materials Science Research Laboratory, Department of Chemistry, St. Philomena College, Puttur 574 202, India

MS received 15 February 1993; revised 13 March 1995

**Abstract.** Iron(III) vanadate ( $\text{FeVO}_4$ ) is an n-type semiconductor between 300 and 800 K. Electrical conduction in this phase occurs due to small deviation from oxygen stoichiometric composition. The mechanism of electrical transport is of a thermally activated hopping of charge carriers (electrons) on equivalent iron lattice sites. The  $\text{FeVO}_4$  obeys Curie-Weiss law between 80 and 300 K. The measured magnetic moment ( $\mu_{\text{eff}}$ ) of  $\text{Fe}^{3+}$  ion in  $\text{FeVO}_4$  is 5.270 BM at 298 K, which is lower than the  $\mu_{\text{spin}}$  only value. The predominant exchange interactions are the weak  $90^\circ$  M-O-M superexchange and M-O-O-M super-superexchange. The negative Weiss constant  $\theta = -30$  K of the phase indicated the possibility of an antiferromagnetic ordering of the iron(III) vanadate lattice. The IR absorption spectrum of  $\text{FeVO}_4$  gave bands at 990, 900, 825 and  $725\text{ cm}^{-1}$  due to the presence of distorted  $\text{VO}_4$  polyhedra of the lattice.

**Keywords.** Conduction; stoichiometric composition; superexchange; antiferromagnetic ordering.

## 1. Introduction

Phase studies of the binary oxides  $\text{Fe}_2\text{O}_3$ - $\text{V}_2\text{O}_5$  (Milligan *et al* 1949; Burdese 1957; Schwartz and Young 1962) have established the formation of only iron(III) vanadate of composition  $\text{FeVO}_4$ . Its occurrence as an incongruently melting compound in the  $\text{Fe}_2\text{O}_3$ - $\text{V}_2\text{O}_5$  system has been reported (Burdese 1957) along with the fact that it transforms under high pressures to an orthorhombic disordered wolframite structure type (Schwartz and Young 1962; Schwartz *et al* 1964). Levinson and Wanklyn (1970) reported crystal growth and magnetic behaviour of  $\text{FeVO}_4$  indicating antiferromagnetic ordering with Neel temperature of  $22 \pm 1$  K. Investigation of the crystal structure and Mössbauer effect was done by Robertson and Kostiner (1972). The crystal structure and symmetry of  $\text{FeVO}_4$  is triclinic,  $\text{P}\bar{1}$ . Their Mössbauer spectroscopy result indicated iron in trivalent oxidation state ( $\text{Fe}^{3+}$ ). In the crystal of  $\text{FeVO}_4$ , they noticed that three independent iron atoms (two in distorted octahedral and one in a distorted trigonal bipyramidal environment) are joined to create a doubly bent chain of six edge shared polyhedra. No other information is available in the literature. As a part of investigation on  $\text{MO-V}_2\text{O}_5$  (where M = 3d cation), we have undertaken a systematic study of the electrical, thermal and magnetic properties of iron(III) vanadate. The results are described in the present paper.

## 2. Experimental

$\text{FeVO}_4$  phase was obtained by heating an intimate mixture of  $\text{Fe}_2\text{O}_3$  and  $\text{V}_2\text{O}_5$  (both pure AR grade) in 1:1 molar ratio at  $800^\circ\text{C}$  for 4–5 days by conventional solid state

reaction technique. The DC electrical conductivity ( $\sigma$ ) was measured by two-probe method and Seebeck coefficient ( $\alpha$ ) by the integral method between 300 and 800 K. The samples were in the form of sintered (high density) pellets, 18 mm in diameter and 2 mm thick. The magnetic susceptibility ( $\chi$ ) was measured in the temperature range 80–300 K by the Gouy technique using  $\text{HgCo(CNS)}_4$  as calibrant. The change in the weight of the sample was noted at magnetic field  $H = 0, 2140, 4400$  and  $6150$  oersted on a single-pan sensitive balance ( $15 \times 10^{-5}$  g, Praha, Czech make). For low-temperature measurements, a sample heater sensor (SHS) assembly coupled with automatic temperature controller ( $\pm 0.2^\circ\text{C}$ ) was used. The sample was maintained at each temperature for about 15 min and the change in weight was recorded for  $H = 0, 2140, 4400$  and  $6140$  oersted at temperatures between 80 and 300 K.

The electron spin resonance (ESR) spectrum of the sample was recorded on a Varian V4502 x-band spectrometer operating at 8.62–9.5 GHz with DPPH as reference marker.

The IR spectrum of  $\text{FeVO}_4$  phase was taken in nujol mull in the range 1200–600  $\text{cm}^{-1}$  using a Perkin-Elmer spectrophotometer (237B). Differential thermal analysis (DTA) of  $\text{FeVO}_4$  was done in a fabricated DTA unit using a sensitive strip chart recorder in static air.

### 3. Results and discussion

The X-ray diffraction (XRD) pattern of  $\text{FeVO}_4$  phase agrees with one reported earlier (ASTM card No 15-294, Burdese 1957). DTA of the sample did not show any indication of phase transition in  $\text{FeVO}_4$  upon increasing the temperature. However, it melts incongruently at  $870 \pm 2^\circ\text{C}$ .

Electrical conductivity ( $\sigma$ ), Seebeck coefficient ( $\alpha$ ) and magnetic susceptibility ( $\chi$ ) data are shown in figures 1a, 1b and 2. The relationship between  $\sigma$  and  $T$  may be expressed as

$$\sigma = \frac{\sigma_0}{T} \exp(-\Delta G^*/KT),$$

where  $\sigma_0$  is a constant and  $\Delta G^*$  is the free energy of activation for electrical conduction process.

$$\log_{10} \sigma T = \log_{10} \sigma_0 - \Delta G^*/2.303K.$$

From figure 1a it can be seen that a plot of  $\log_{10} \sigma T$  versus  $1/T$  should be linear with a slope of  $\Delta G^*/2.303K$ , provided (1) is obeyed. Figure 1a confirmed the validity of the expression in the case of  $\text{FeVO}_4$ . It is observed that  $\log_{10} \sigma T$  versus  $1/T$  is linear for the sample between 300 K and 550 K with free energy of activation ( $\Delta G^*$ ) of 0.70 eV. However, it could be seen that there is a linear plot with deviation in the slope above 550 K.

Seebeck coefficient ( $\alpha$ ) is constant and temperature-independent for localized electrons (charge carriers) if the density of charge carriers are independent of temperature in the lattice of the sample. The Seebeck coefficient,  $\alpha$  ( $\mu\text{V}/^\circ\text{C}$ ) for the sample showed a linear plot (figure 1b) typical of localized electrons; but  $\alpha$  value increased slightly with temperature and indicated a dependence of density

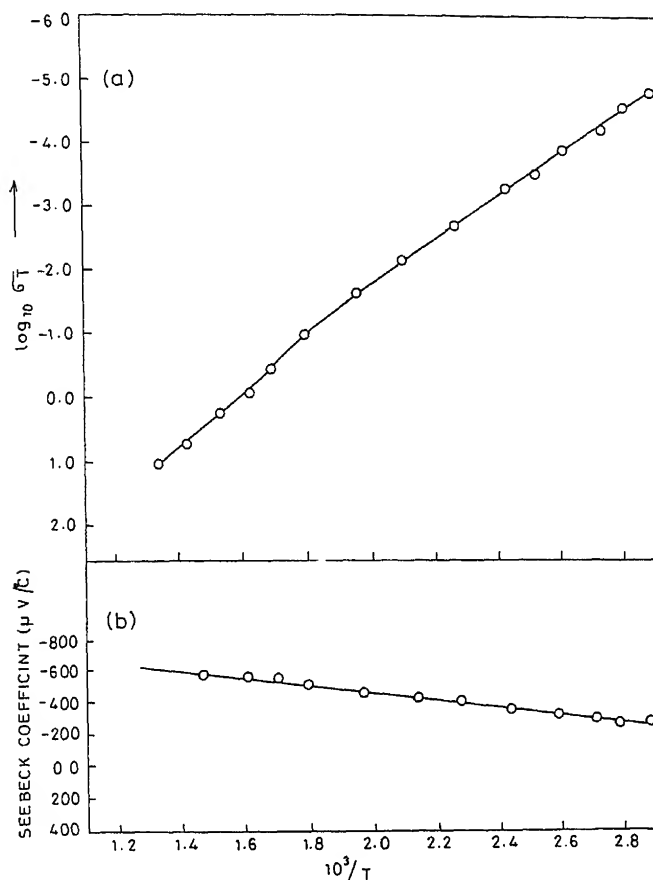


Figure 1. (a) Plot of  $\log_{10} \sigma T$  versus  $10^3/T$  and (b) Seebeck coefficient versus  $10^3/T$ .

charge carriers (electrons) on temperature. It could be shown in the lattice of  $\text{Fe}^{3+}$  (and or  $\text{V}^{5+}$ ) in  $\text{FeVO}_4$  that the Seebeck coefficient depends on the second term of (3) and (4):

$$\alpha = \frac{A}{eT} - K/e \ln \frac{(\text{Fe}^{3+})}{(\text{Fe}^{2+})}, \quad (3)$$

$$\alpha = \frac{A}{eT} - K/e \ln \frac{(\text{V}^{5+})}{(\text{V}^{4+})}, \quad (4)$$

where the terms have the usual significance. The term  $A$  represents the kinetic energy transported by the migrating electrons. The  $A/eT$  term is negligibly small ( $> 10 \mu\text{V}/\text{degree}$ ) for ionic oxides. The second term predominates and determines the sign of  $\alpha$ . In (3),  $(\text{Fe}^{3+})$  is the density of states available to mobile electrons in the lattice and

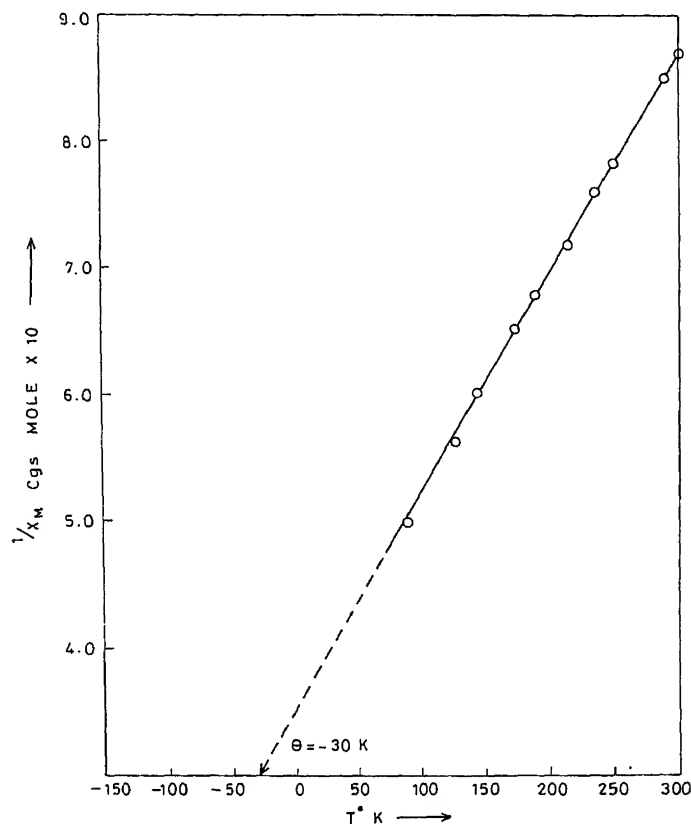
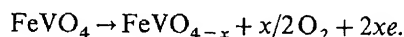


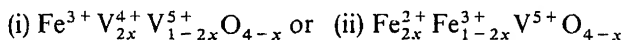
Figure 2. Plot of  $1/X_M$  versus  $T^\circ$  for iron(III) vanadate.

( $\text{Fe}^{2+}$ ) is the density of mobile electrons (cations in lower valency state) created due to a very small deviation from oxygen stoichiometry.

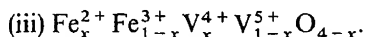
The above results indicated that  $\text{FeVO}_4$  is an n-type semiconductor where electrical conduction is due to the thermally activated mobility of electrons. This is quite expected because the phase is predominantly ionic so that the charge carriers (electrons) are localized. Therefore the only mode of charge transport is via thermally activated jumps on equivalent cationic sites. The sign of  $\alpha$  is negative which indicates that it is an n-type semiconductor between 300 and 800 K. One can expect  $\text{FeVO}_4$  to be a good insulator in pure and stoichiometric compositions. Semiconduction observed in  $\text{FeVO}_4$  phase is due to deviation from stoichiometric composition of the phase. The Seebeck coefficient is negative which could be due to oxygen vacant structure of the lattice. Thus one can attribute n-type semiconduction of the sample to the following reason: Under normal conditions of temperature and pressures, oxygen vacancies (defect structure) occur in  $\text{FeVO}_4$  lattice, leaving behind two electrons per half molecule of oxygen leaving the lattice:



In other words, iron(III) vanadate can be represented as



and/or



The following results confirm the above. (i) Mössbauer spectroscopy (Robertson and Kostiner 1972) identified the iron in  $\text{FeVO}_4$  lattice as  $\text{Fe}^{3+}$  (trivalent). (ii) ESR spectrum of the sample consisted of a small signal at  $g = 1.96$ , which is typical of a localized electron ( $\text{V}^{4+}$ ) in the lattice. (iii)  $\text{FeVO}_4$  phase exhibited n-type semiconduction and the Seebeck coefficient is negative between 300 and 800 K. (iv) The observed magnetic moment ( $\mu_{\text{eff}}$ ) of  $\text{Fe}^{3+}$  in  $\text{FeVO}_4$  lattice is 5.270 BM from the magnetic susceptibility measurements, which is slightly lower than the  $\mu_{\text{spin}}$  only value for  $\text{Fe}^{3+}$  ion.

In the crystal structure of  $\text{FeVO}_4$ , Robertson and Kostiner (1972) found three independent iron atoms (two in distorted octahedral and one in a distorted trigonal bipyramidal environment) in polyhedra which are joined to create a doubly bent chain of six edge shared polyhedra as shown in figure 3. The bond lengths ( $\text{Fe}^{3+}-\text{O}^{2-}$ ) range from 1.8690 to 2.114 Å. The chains are linked by  $\text{VO}_4$  tetrahedra. The  $\text{VO}_4$  tetrahedra share corners with up to four polyhedra within a single chain, but none of them share an edge with an individual polyhedron in a chain. The three independent vanadium atoms are each in a slightly distorted tetrahedral environment of oxygen atoms. The bond lengths ( $\text{V}^{5+}-\text{O}^{2-}$ ) range from 1.666 to 1.806 Å, depending on the environment of oxygen atoms. The  $\text{Fe}^{3+}-\text{Fe}^{3+}$  interatomic distance (figure 3) within the chain ( $\text{Fe}(1)-\text{Fe}(2) = 3.073$  Å,  $\text{Fe}(2)-\text{Fe}(3) = 3.048$  Å, and  $\text{Fe}(3)-\text{Fe}(3) = 3.119$  Å) showed

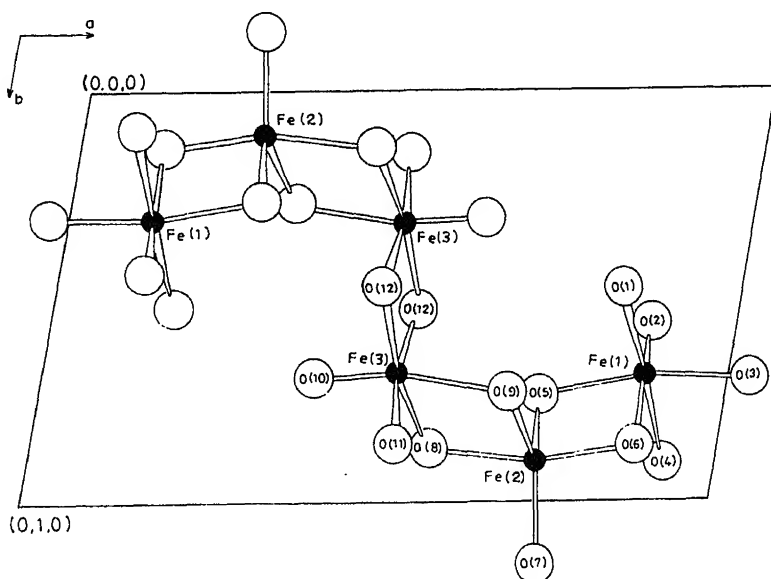


Figure 3. The doubly bent chain of six iron atoms in  $\text{FeVO}_4$ , projected onto the  $a$ - $b$  plane.



the largest separation between the two octahedrally coordinated iron atoms at centre of the chain.

n-Type semiconduction observed in  $\text{FeVO}_4$  can be explained as follows:  $\text{Fe}^{3+}(\text{d}^5)$  and  $\text{V}^{5+}(\text{d}^0)$  are in their highest oxidation state in  $\text{FeVO}_4$  and thus formation  $\text{V}^{6+}$  and  $\text{O}^-$  ions is not energetically favourable in the iron vanadate lattice.  $\text{FeVO}_4$  phase has oxygen-deficient lattice structure due to deviation from oxygen stoichiometry (5). The  $2x$  electrons released per  $\frac{1}{2}\text{O}_2$  are trapped on either (a)  $\text{Fe}^{3+}$  or (b)  $\text{V}^{5+}$  and or (c) both the lattice sites as localized electrons for conduction which results in the formation of  $\text{Fe}^{2+}(\text{d}^6)$  or  $\text{V}^{4+}(\text{d}^1)$  sites in the lattice of  $\text{FeVO}_4$ . Therefore the only mode of charge transport in  $\text{FeVO}_4$  is via thermally activated hopping of electrons on equivalent ( $\text{Fe}^{2+}-\text{O}-\text{Fe}^{3+}$ ) lattice sites (type ii) of the double bent chain of edge shared polyhedra (figure 3) or the corner shared  $\text{VO}_4$  polyhedra within a single chain. It can be remarked from the perspective view of the crystal structure of  $\text{FeVO}_4$  projected on to  $b$ - $c$  plane (Robertson and Kostiner 1972) that the most favoured path for activated electrons to jump is the continuous chains of  $\text{Fe}^{2+}$  sites of the lattice rather than the  $\text{V}^{5+}$  sites. However, thermally activated hopping of an electron on equivalent  $\text{V}^{5+}$  sites also cannot be overlooked for electrical conduction in the lattice. It is clear from DTA and other available data that there is neither structural transformation nor electronic transition in  $\text{FeVO}_4$  lattice upon increasing temperature, though figure 1a indicated a deviation in slope at about 550 K. The observed behaviour could possibly be due to the additional path available for thermally activated hopping of electrons at the vanadium sites (type iii) of a corner shared  $\text{VO}_4$  tetrahedron within a single chain in the lattice. The presence of such localized ( $\text{V}^{4+}$ ) centres in the lattice of the sample is confirmed by the observed ESR signal at  $g = 1.9$ .

Figure 1b shows a linear plot, but the Seebeck coefficient increased slightly with increasing temperature, as against an expected constant value of  $\alpha$  for localized electrons with constant density of charge carriers in the lattice. This behaviour of the sample could be accounted for by a decrease in the density of  $\text{Fe}^{2+}$  sites in the lattice (3) upon increasing the temperature. It is well established that generally the  $\text{Fe}^{2+}$  state in oxides is not stable at higher temperatures, and it gradually changes to the  $\text{Fe}^{3+}$  state. Therefore one can remark that as the density of  $\text{Fe}^{2+}$  state decreases due to the above reason the Seebeck coefficient value would be expected to increase proportionately with increase in temperature as observed in the present work. However, increase in electrical conduction of the sample is due to thermally activated mobility of electrons, which increased exponentially with temperature. Moreover, one would expect a very small increase in deviation from oxygen stoichiometry of the lattice upon increasing the temperature, which would increase the density of charge carriers (electrons) in the lattice. These electrons may not be located at  $\text{Fe}^{3+}$  sites in the temperature range of the investigation as localized electrons but would be trapped on  $\text{V}^{5+}$  sites of the lattice as typical localized electrons ( $\text{V}^{4+}$  centres) for conduction and would hop on to equivalent sites with little higher free energy of activation at about 550 K, as is evident from figure 1a.

The magnetic susceptibility of  $\text{FeVO}_4$  measured between 80 and 300 K is shown in figure 2. It may be observed that (a)  $\text{FeVO}_4$  is paramagnetic down to 80 K and obeys the Curie-Weiss law, (b) the Weiss constant ( $\theta$ ) is negative and (c) the  $\mu_{\text{eff}}$  observed is slightly lower than  $\mu_{\text{spin}}$  only value for  $\text{Fe}^{3+}$  ions.

The magnetic susceptibility of  $\text{FeVO}_4$  sample at 300 K is  $6.73 \times 10^{-5}$  cgs/rmole. Figure 2 shows a linear plot of  $1/\chi_{\text{M}}$  versus temperature. It is evident that the V

constant of  $\text{FeVO}_4$  is  $-30$  K, which indicates, possibly, an antiferromagnetic ordering of the  $\text{FeVO}_4$  lattice. The observed magnetic moment ( $\mu_{\text{eff}}$ ) value of  $\text{Fe}^{3+}$  ion is  $5.270$  BM which is lower than  $5.92$  BM for  $\mu_{\text{spin}}$  only value of  $\text{Fe}^{3+}$  ( $t_{2g}^3 e_g^2$ ). It is clear from the crystal structure of  $\text{FeVO}_4$  (Robertson and Kostiner 1972) that the predominant exchange interactions are  $\text{M}^{3+}-\text{O}-\text{M}^{3+}$  (superexchange) and  $\text{M}^{3+}-\text{O}-\text{O}-\text{M}^{3+}$  (super-superexchange). Direct cation-cation magnetic exchange interactions and cation-anion-cation superexchange interactions between adjacent iron atoms of  $\text{FeVO}_4$  (figure 3) with  $d^5$  configuration give antiferromagnetic coupling (Goodenough 1963). The cation-anion-cation superexchange energy term allows antiferromagnetic coupling over the full range of  $\text{Fe}^{3+}-\text{O}-\text{Fe}^{3+}$  angles from  $90^\circ$  to  $180^\circ$  with maximum energy expected at  $180^\circ$ . Because of sharing of  $\text{FeO}_6$  polyhedral edges in  $\text{FeVO}_4$  structure, the  $\text{Fe}^{3+}-\text{O}-\text{Fe}^{3+}$  angles are limited to  $100^\circ$  and therefore indicate small superexchange interaction, which resulted in a value ( $5.270$  BM) lower than  $\mu_{\text{spin}}$  only value ( $5.92$  BM) for  $\text{Fe}^{3+}$  ion. Interestingly, it can be observed that the presence of certain number of  $\text{Fe}^{2+}(d^6)$  ( $t_{2g}^4 e_g^2$ ) ions in the lattice of  $\text{Fe}^{3+}(t_{2g}^3 e_g^2)$  ions of  $\text{FeVO}_4$

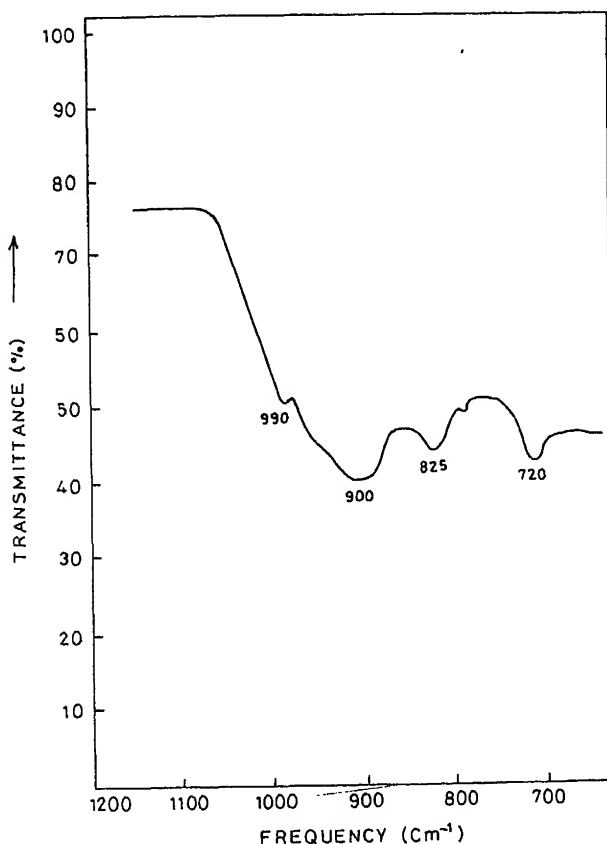


Figure 4. IR spectrum of iron(III) vanadate.

could contribute less to the effective magnetic moment ( $\mu_{\text{eff}}$ ) of the cation, depending on the concentration of  $\text{Fe}^{2+}$  ions in the lattice.

The IR spectrum of  $\text{FeVO}_4$  (figure 4) indicates bands at 990, 900, 825 and  $720\text{ cm}^{-1}$ . Siebert (1954) and Ayamonino *et al* (1978) have obtained the IR spectra of  $\text{VO}_4^{3-}$  group of many divalent cations, while Fotiev *et al* (1971) obtained IR spectra of  $\text{VO}_4^{3-}$  group with cations in the trivalent oxidation state. It can be seen from figure 4 that the IR spectrum of  $\text{VO}_4^{3-}$  group in  $\text{FeVO}_4$  lattice is different from the spectra obtained for  $\text{VO}_4^{3-}$  group of  $T_d$  symmetry (Siebert 1954) in orthovanadates. In the crystal structure of  $\text{FeVO}_4$ , Robertson and Kostiner (1972) found that the iron is in the trivalent oxidation state and the three  $\text{V}^{5+}$  ions are each distorted in distorted tetrahedral environment of oxygen atoms, whose V–O bond lengths ranged from 1.660 to 1.806 Å; the average V–O bond length in many orthovanadates is 1.720 Å. Thus one can expect that these three distorted  $\text{VO}_4^{3-}$  polyhedra of  $\text{FeVO}_4$  would give bands (990, 900, 825,  $725\text{ cm}^{-1}$ ) different from the ones observed for orthovanadate lattice having one kind of  $\text{VO}_4^{3-}$  polyhedra (Siebert 1954; Ayamonino *et al* 1978).

### Acknowledgements

The authors sincerely thank UGC for providing a research grant for this investigation and also express their gratitude to Head, Chemical Division, BARC, Bombay, for the ESR and XRD of the sample.

### References

- Ayamonino P J *et al* 1978 *Monatsh. Chem.* **109** 1139
- Burdese A 1957 *Ann. Chim. (Rome)* **47** 797
- Goodenough J B 1963 *Magnetism and the chemical bond* (New York: Wiley)
- Levinson L M and Wanklyn B M 1970 *J. Solid State Chem.* **3** 131
- Milligan W O, Watt L M and Rachford H H 1949 *J. Phys. Colloid Chem.* **53** 227
- Robertson B and Kostiner E 1972 *J. Solid State Chem.* **4** 29
- Schwartz C M and Young A P 1962 *Acta Crystallogr.* **15** 1305
- Schwartz C M, Laves F and Young A P 1964 *Acta Crystallogr.* **17** 1476
- Siebert H 1954 *Z. Anorg. Allg. Chem.* **275** 225

## An analysis of the electrical conductivity in BaSO<sub>4</sub>-added Ag<sub>2</sub>SO<sub>4</sub> solid electrolyte system

K SINGH, S M PANDE\* and S S BHOGA<sup>†</sup>

Department of Physics, Nagpur University, Nagpur 440010, India

\*Department of Applied Physics, Ramdeobaba Kamala Nehru College of Engineering, Nagpur 440013, India

<sup>†</sup> Department of Physics, Hislop College, Nagpur 440001, India

MS received 22 December 1994; revised 20 April 1995

**Abstract.** The compositions  $(1-x)\text{Ag}_2\text{SO}_4-(x)\text{BaSO}_4$ , where  $x = 0.01$  to  $0.6$ , were prepared by slow cooling of the melt. The extent of the solid solubility of  $\text{Ba}^{2+}$  in  $\text{Ag}_2\text{SO}_4$  was determined by X-ray powder diffraction and scanning electron microscopy. The bulk conductivity of each sample was obtained using a detailed impedance analysis. The partial substitution of  $\text{Ba}^{2+}$  results in the enhancement of conductivity in compliance with the classical aliovalent doping theory. A simplistic model based on lattice distortion (expansion) due to partial substitution of  $\text{Ag}^+$  by the bigger  $\text{Ba}^{2+}$  has been considered to explain enhanced conductivity. Beyond solid-solubility limit (5.27 mole%) the  $\text{BaSO}_4$ -dispersed  $\text{Ag}_2\text{SO}_4$  conductivity follows the usual trend seen in binary systems. An increase in conductivity in this case is discussed in the light of interfacial reactions and surface defect chemistry. The maximum conductivity in 20 mole%  $\text{BaSO}_4$  dispersed  $\text{Ag}_2\text{SO}_4$  is due to percolation threshold.

**Keywords.** Solid solubility; ionic radius; lattice distortion; space charge; ionic conductivity.

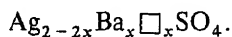
### 1. Introduction

The sulphate-based solid electrolytes differ in some respect from other solid electrolyte materials in the sense that they are thermodynamically more stable, less expensive and easy to handle. An advantage is that many monovalent and divalent cations have high mobility in their high-temperature phases and the choice of electrode materials is greater in electrochemical applications in general (Heed *et al* 1975). Particularly, they have potential applications in  $\text{SO}_x$  galvanic gas sensors (Gauthier and Chamberland 1977; Liu *et al* 1990).

Among others, silver sulphate has received little attention. It is a polymorphic compound with two different modifications which are  $\beta$ -phase (orthorhombic) below  $416^\circ\text{C}$  and  $\alpha$ -phase (hexagonal) above this temperature. The low- and high-temperature phases of  $\text{Ag}_2\text{SO}_4$  are isomorphous to those of  $\text{BaSO}_4$ .

Several attempts have been made to enhance the ionic conductivity in polycrystalline solids. In this direction essentially the following approaches have been adopted: (i) aliovalent substitution of conducting cations (Hofer *et al* 1981), (ii) opening of the lattice structure by substitution with wrong size ion (Singh and Bhoga 1992), (iii) optimization of the preparative parameters (Singh and Deshpande 1982), (iv) trapping of high-temperature highly conducting phases at room temperature (Singh *et al* 1988), (v) stabilization of open-channel structure (Rodger *et al* 1985), and (vi) dispersion of insoluble second phase (Liang 1973). The first two approaches have

The conductivity is strongly correlated to the vacancy concentration regardless of the size and the electronic configuration of the substituting ions (Hofer *et al* 1981). However, dependence of conductivity on aliovalent ionic size and charge has been reported (Singh 1988; Singh and Bhoga 1992). A decrease in conductivity due to partial substitution as well as dispersion of  $\text{CaSO}_4$  has been reported earlier (Singh *et al* 1995). We have introduced the concept of lattice contraction (due to the partial replacement of host by smaller-size guest cation) to understand the fall in conductivity. The present investigation has been undertaken to probe further into the role of ionic size of aliovalent cation on the ionic conductivity. A partial substitution of  $\text{Ag}^+$  by  $\text{Ba}^{2+}$  has been made with a view to distort the lattice while creating extrinsic vacancies on the basis of the following formula:



A few biphasic mixtures of  $\text{Ag}_2\text{SO}_4$  with  $\text{BaSO}_4$  have also been investigated with a view to seeing the effect of valency and ionic size in space charge region.

## 2. Experimental

The initial ingredients  $\text{Ag}_2\text{SO}_4$  and  $\text{BaSO}_4$  with purity greater than 99% were procured from E Merck, India. Appropriate mole fractions of the above chemicals in  $(1-x)\text{Ag}_2\text{SO}_4-(x)\text{BaSO}_4$  ( $x = 0.01$  to  $0.6$ ) were prepared by slow-cooling the melt in silica ampoules at a predetermined cooling rate of  $1.5^\circ\text{C}/\text{min}$ . The prepared samples were characterized by X-ray powder diffraction and scanning electron microscopy as discussed elsewhere (Singh *et al* 1995).

For electrical conductivity measurements, the samples were obtained in the form of circular discs of 9 mm dia and 2 mm thickness by pressing the powder in a Specac (US) stainless steel die-punch and hydraulic press. A good ohmic contact was ensured by using quality graphite paint (Eleteck, India) followed by baking at  $200^\circ\text{C}$  for 1 h. The above process was carried out in a dark room. The pellets were sintered at  $450^\circ\text{C}$  for 24 h before spring-loading them between silver electrodes of a sample holder. Prior to impedance measurements, the spring-loaded sample was again heated to  $360^\circ\text{C}$  for 2 h in order to homogenize the charge carriers in the sample and simultaneously to remove the moisture content therein. The AC electrical conductivity was measured as a function of frequency in the range 5 Hz to 13 MHz and temperature in the range  $450$  to  $250^\circ\text{C}$  using a HP 4192A LF impedance analyser. HP 16048 test leads were used for electrical connections from sample to analyser to avoid any otherwise parasitic impedance due to improper connecting cables. The temperature of the furnace was controlled to  $\pm 1^\circ\text{C}$  using a Eurotherm 810 PID temperature controller. The entire measurement system was properly shielded. The reproducibility of impedance data was confirmed by repeating the measurement on freshly prepared samples.

## 3. Results and discussion

Table 1 shows the experimental  $d$  and relative intensity  $I/I_0$  values for  $(1-x)\text{Ag}_2\text{SO}_4-(x)\text{BaSO}_4$  (where  $x = 0.000$ ,  $0.0527$  and  $0.0757$ ) along with the JCPDS data of parent phases. It is worth noting that in the X-ray diffraction pattern

**Table 1.** A comparison of  $d$  and  $I/I_0$  with JCPDS data for  $(1-x)\text{Ag}_2\text{SO}_4\text{-(}x\text{)BaSO}_4$  ( $x = 0.00, 0.0527$  and  $0.0757$ ).

$\text{Ag}_2\text{SO}_4$ ( $x = 0.00$ )		$x = 0.0527$		$x = 0.0757$		*JCPDS		Phase (hkl)
$d$	$I/I_0$	$d$	$I/I_0$	$d$	$I/I_0$	$d$	$I/I_0$	
4.670	5	4.711	9	4.709	10	4.699	10	Ag(111)
—	—	—	—	4.361	2	4.334	30	Ba(101)
3.969	18	4.018	23	3.999	26	3.994	25	Ag(220)
—	—	—	—	3.444	5	3.445	100	Ba(021)
—	—	—	—	3.318	4	3.319	70	Ba(210)
3.164	92	3.179	50	3.177	93	3.177	70	Ag(040)
2.866	100	2.879	100	2.876	100	2.873	100	Ag(311)
—	—	—	—	2.731	2	2.735	45	Ba(002)
2.636	87	2.652	43	2.645	87	2.644	90	Ag(022)
2.521	19	2.535	16	2.531	18	2.530	17	Ag(202)
2.410	30	2.428	20	2.425	24	2.421	30	Ag(331)
—	—	—	—	2.355	4	2.325	14	Ba(022)
—	—	—	—	2.104	4	2.106	75	Ba(212, 231)
1.973	11	1.978	12	1.979	11	1.980	11	Ag(242)
1.918	35	1.929	21	1.924	29	1.926	30	Ag(351)
—	—	—	—	1.759	3	1.762	8	Ba(103)
—	—	—	—	1.647	3	1.644	3	Ba(151)
—	—	—	—	1.587	5	1.587	4	Ba(421)
1.542	10	1.549	10	1.545	8	1.546	8	Ag(371)
—	—	—	—	1.363	2	1.363	18	Ba(004, 520)

Ag-Ag<sub>2</sub>SO<sub>4</sub> (orthorhombic) JCPDS card numbers 27-1403Ba-BaSO<sub>4</sub> (orthorhombic) JCPDS card numbers 24-1035

of sample with  $x = 0.0527$ , not a single line corresponding to BaSO<sub>4</sub> is observed, whereas all the experimental lines are found to be in good agreement with the JCPDS data for Ag<sub>2</sub>SO<sub>4</sub>. The absence of lines corresponding to BaSO<sub>4</sub> for this composition indicates the formation of a solid solution. From table 1 it is also evident that when the dopant concentration ( $x$ ) is increased to 0.0757, a few weak lines corresponding to BaSO<sub>4</sub> are observed. The samples with ( $x > 0.0757$ ) in general show strong lines corresponding to Ag<sub>2</sub>SO<sub>4</sub> and very weak ones for BaSO<sub>4</sub>. The small deviation in the  $d$  values for Ag<sub>2</sub>SO<sub>4</sub> can be due to the partial replacement of Ag<sup>+</sup> by the bigger Ba<sup>2+</sup>, since such a replacement results in local lattice distortions. The lattice cell constants presented in table 2 show that the host Ag<sub>2</sub>SO<sub>4</sub> lattice undergoes an expansion upon Ba<sup>2+</sup> addition within the solid solubility limit. From this study the solid-solubility limit of BaSO<sub>4</sub> in Ag<sub>2</sub>SO<sub>4</sub> is set up to be 5.27 mole%.

The variations of  $\log(\sigma)$  as a parametric function of BaSO<sub>4</sub> concentration in high- and low-temperature modifications are shown in figures 1 and 2 respectively. In general, it can be seen that as impurity concentration increases the conductivity also increases and exhibits a maximum within solid-solubility limit in both the phases. Furthermore, in low-temperature modification one more conductivity maximum (figure 2) is observed at 20 mole% BaSO<sub>4</sub>. The results of low temperature modification are similar to those of earlier reported results in case of Li<sub>2</sub>SO<sub>4</sub>:CaSO<sub>4</sub>, AgBr:AgI and Na<sub>2</sub>SO<sub>4</sub>:Na<sub>2</sub>WO<sub>4</sub> (Singh and Bhoga 1990; Dekker

1990; Rao *et al* 1992). In order to discuss the conductivity behaviour of the  $\text{Ag}_2\text{SO}_4\text{:BaSO}_4$  system, the investigated compositional range is divided into two regions: region I:  $0 \leq x \leq 0.0527$ , and region II:  $0.0527 < x \leq 0.6$ .

### 3.1 Region I

The bulk conductivity of each composition is obtained using a computerized impedance analysis. Figure 3 illustrates the variation of  $\log(\sigma T)$  with  $10^3/T$  within the solid-solubility range. The break-over in the conductivity indicates the occurrence of transition from orthorhombic to hexagonal phase.

**Table 2.** A comparison of lattice cell constants of doped and undoped  $\text{Ag}_2\text{SO}_4$  as calculated from table 1.

Cell constant	$x = 0.0$	$x = 0.0527$
$a(\text{\AA})$	10.247	10.287
$b(\text{\AA})$	12.688	12.764
$c(\text{\AA})$	05.748	05.765
Cell volume $\text{\AA}^3$	747.32	756.96

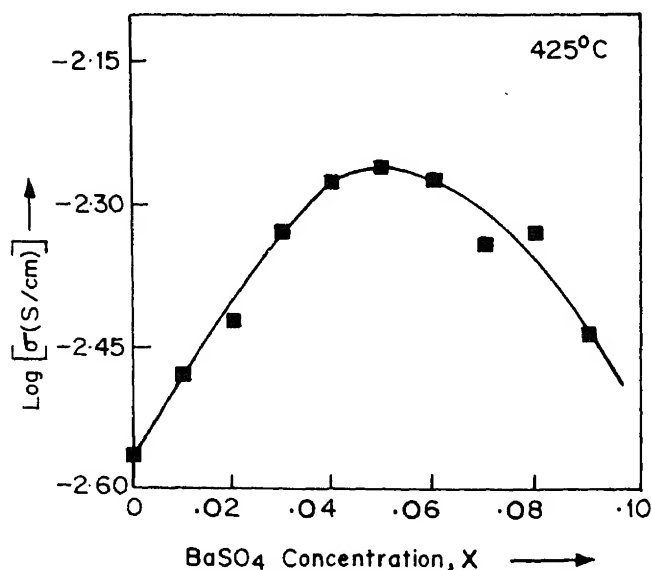


**Figure 1.** Variation of  $\log(\sigma)$  with  $x$  in  $(1-x)\text{Ag}_2\text{SO}_4-(x)\text{BaSO}_4$  in high-temperature phase (at  $425^\circ\text{C}$ ).

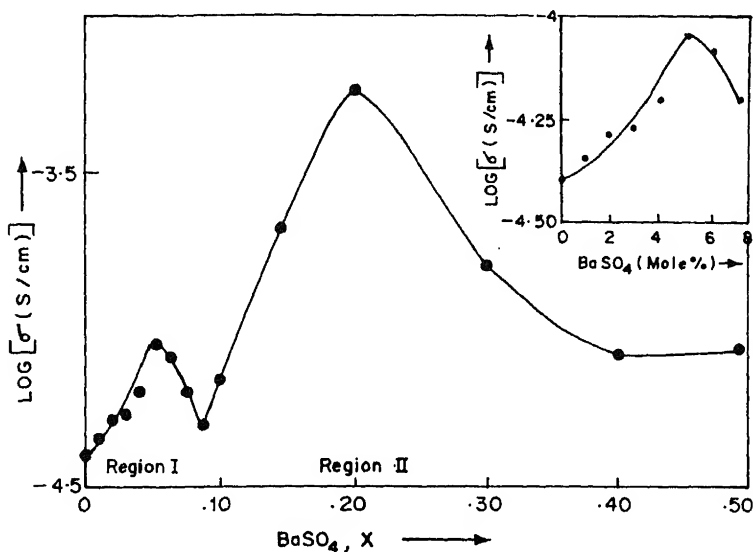


Figure 2. Variation of  $\log(\sigma)$  with  $x$  in  $(1-x)\text{Ag}_2\text{SO}_4-(x)\text{BaSO}_4$  in low-temperature phase (at  $300^\circ\text{C}$ ).

In both ranges of modification of  $\text{Ag}_2\text{SO}_4$ , upon  $\text{Ba}^{2+}$  addition the conductivity, as expected, increases initially and falls off after attaining a maximum at 5% vacancy (5.27 mole%). The initial rise in conductivity could be understood by considering that the dopant  $\text{Ba}^{2+}$  occupies an  $\text{Ag}^+$  site in the  $\text{Ag}_2\text{SO}_4$  lattice to produce one  $\text{Ba}_{\text{Ag}}$  and one extrinsic  $\text{Ag}$  ion vacancy  $V'_{\text{Ag}}$  in order to maintain the charge neutrality. At low doping levels with increase in  $\text{Ba}^{2+}$  concentration the conductivity increases as number of vacancies ( $V'_{\text{Ag}}$ ) increases. At higher  $\text{Ba}^{2+}$  concentration the extrinsic  $\text{Ag}^+$  vacancies interact with the dopant ions to form an associate, termed cluster. Such extended clustering of defects hinders the  $\text{Ag}^+$  mobility and hence the fall in conductivity. The doping amount of  $\text{BaSO}_4$  for which defect-defect interactions predominate is greater than 5% vacancy. The results are in excellent agreement with conductivity behaviour vis-a-vis aliovalent doping (Hofer *et al* 1981; Singh and Bhoga 1990; Dekker 1990; Rao *et al* 1992). It is worth noting here that the magnitude of conductivity enhancement in low-temperature modification is more pronounced compared to that in high-temperature hexagonal phase. Obviously, the structure of hexagonal phase is more open, thus the effect of ionic size of the guest cation on the lattice structure is expected to be negligible (Hofer *et al* 1981). In contrast, in low-temperature orthorhombic phase, the ionic size has a predominant role to play from ion mobility point of view which can be understood as follows:

The ionic conductivity in solid electrolytes is often interpreted in terms of hopping of mobile charge carriers from site to site (Kimball and Adams 1978; Dieterich 1988). For this not only is nearby vacancy needed but also the lattice should be sufficiently open so that the ion can jump from the filled site to the available nearby vacant site



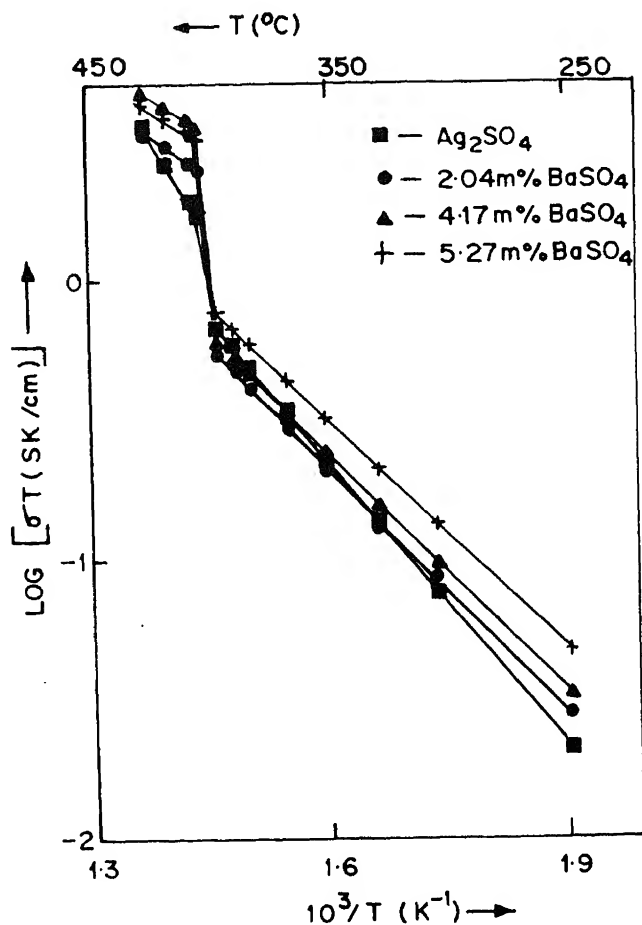


Figure 3. Variation of  $\log(\sigma T)$  with  $10^3/T$  in  $(1-x)\text{Ag}_2\text{SO}_4-(x)\text{BaSO}_4$  ( $0 \leq x \leq 0.05$ , Region I).

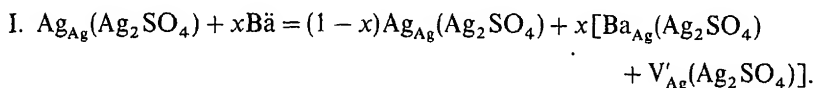
generally expressed as

$$\sigma T = (\sigma T)_0 \exp(-E_a/kT),$$

where  $E_a = E_f + E_m$ ,  $E_f$  and  $E_m$  are the energy of defect formation and migration respectively, and  $(\sigma T)_0$  is a pre-exponential factor. Evidently, the activation energy is then indeed a better criterion for characterization of ionic conductors than conductivity itself.

The activation energy,  $E_a$ , obtained using (1) is found to decrease initially with increase in  $\text{BaSO}_4$ , indicating reduction in  $E_m$ . Owing to increase in vacancies along with lattice expansion caused, a large number of ion-percolative pathways are created thereby enhancing the  $\text{Ag}^+$  hopping probability from a filled site to the next available vacant site leading to a net ionic transport.

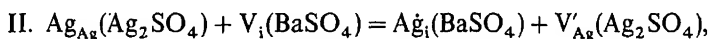
In the simplest case, the above process can also be visualized by considering the host matrix of pure  $\text{Ag}_2\text{SO}_4$  (figure 4a) and the modified lattice when the guest  $\text{Ba}^{2+}$  is partially substituted randomly for  $\text{Ag}^+$  (figure 4c). In order to attain the thermodynamical equilibria (constancy of electrochemical potential, constancy of activity and hence a constancy of electric potential) in the vicinity of  $\text{Ba}^{2+}$ , (i) additional vacancy is created and (ii) expansion of the host lattice takes place, since  $\text{Ag}^+$  ( $1.26 \text{ \AA}$ ) has a much smaller ionic radius than  $\text{Ba}^{2+}$  ( $1.38 \text{ \AA}$ ). The disorder reaction using Kröger–Vink notations can be written as



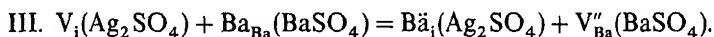
The lattice expansion in the vicinity of  $\text{Ba}^{2+}$  reduces the potential barrier height for nearby mobile  $\text{Ag}^+$  ions (figure 4d). Such an additional vacancy with a shallow potential well offers a lower activation energy of migration ( $E_m$ ) for mobile  $\text{Ag}^+$  which in turn increases the conductivity. The dependence of ionic conductivity on the ionic size of divalent dopant (at fixed vacancy concentration) in  $\text{Li}_2\text{SO}_4$  reported earlier supports the above discussed model (Singh and Bhoga 1990).

### 3.2 Region II

The variation of  $\log(\sigma T)$  with  $10^3/T$  for  $\text{BaSO}_4$  added  $\text{Ag}_2\text{SO}_4$  samples (biphase) for compositional range region II is shown in figure 5. The conductivity in this region is seen to be optimized at 20 mole%  $\text{BaSO}_4$  addition, as seen in figure 2. This enhancement in conductivity could be understood in light of the following: According to dispersed-phase theory for  $\text{MX}/\text{M}'\text{X}$ , there is a net transfer of cations from either phase across the interface (Maier 1985; Singh 1993). Two probable Frenkel analogue interface reactions are



and



The corresponding mass action law takes the form

$$C_v C_i = C_0 \exp[-(\Delta G^0)], \quad (2)$$

where  $C_v$  and  $C_i$  are the vacancy concentration in one phase and interstitial concentration in the other in contact respectively,  $\Delta G^0$  is free enthalpy for reaction, and  $C_0$  is the pre-exponential factor.

If the free energy of reaction II exceeds that of reaction III, it gives rise to additional interstitial  $\text{Ba}^{2+}$  in  $\text{Ag}_2\text{SO}_4$  leaving behind equivalent vacancies in the  $\text{BaSO}_4$  lattice; otherwise the converse is true. Since  $\text{Ba}^{2+}$  is more electropositive than  $\text{Ag}^+$ , reaction III is thermodynamically favoured. In addition, as a result of repulsive interaction,  $\text{Ba}^{2+}$  pushes back the surface  $\text{Ag}^+$  into the  $\text{Ag}_2\text{SO}_4$ , thus forbidding reaction II. These two factors enrich the interstitial ion and vacancy concentration forming space charge layers close to the  $\text{Ag}_2\text{SO}_4$  and  $\text{BaSO}_4$  surface respectively. The presence of foreign  $\text{Ba}^{2+}$  in space charge region at  $\text{Ag}_2\text{SO}_4$  surface also leads to the lattice

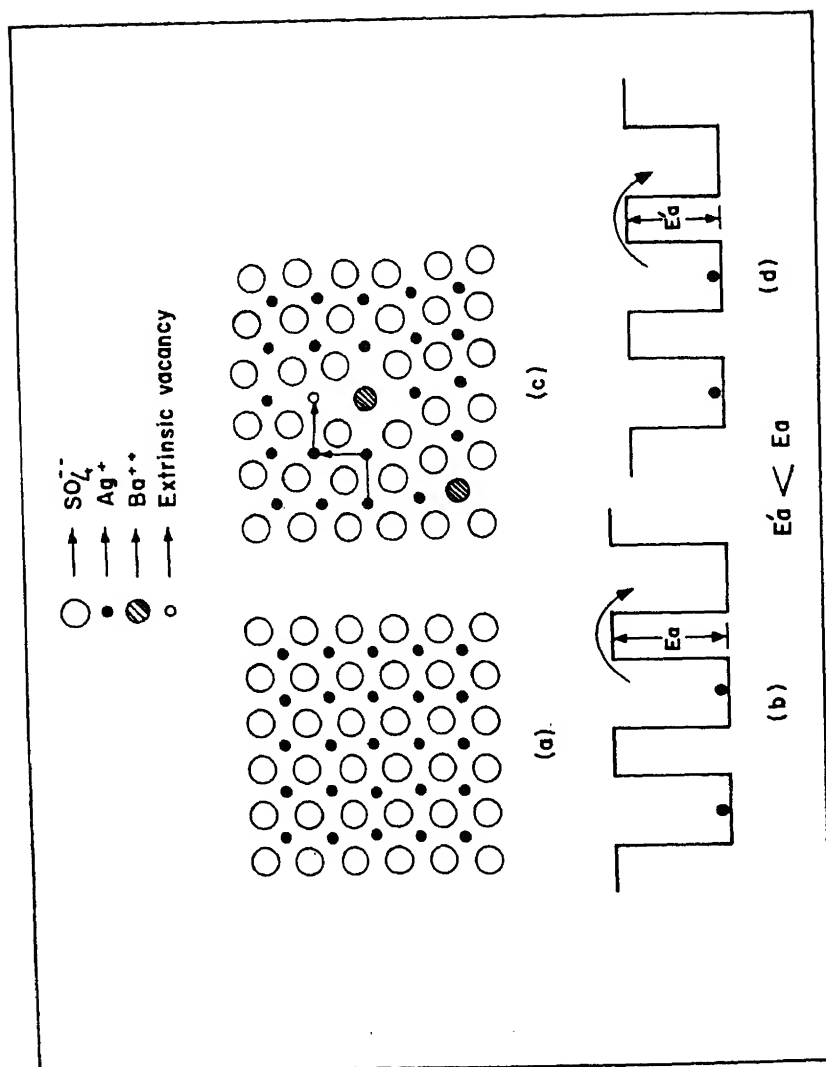


**Figure 4.** Schematic representation of a  $\text{Ag}_2\text{SO}_4$  lattice plane through: (a) the regular host lattice, (b) an ideal potential well, (c) the host lattice with some of the  $\text{Ag}^+$  partially replaced by  $\text{Ba}^{++}$ , and (d) the host lattice with some of the  $\text{Ag}^+$  partially replaced by  $\text{Ba}^{++}$ .

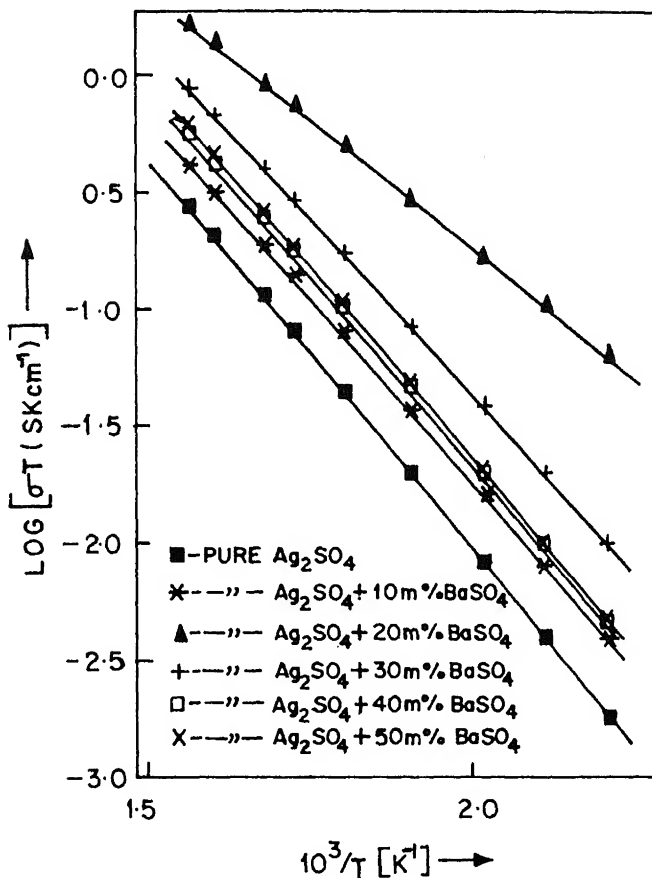


Figure 5. Variation of  $\log(\sigma T)$  with  $10^3/T$  in  $(1-x)\text{Ag}_2\text{SO}_4-(x)\text{BaSO}_4$  ( $0.1 \leq x \leq 0.6$ ) in low-temperature phase (Region II).

expansion thus favouring the  $\text{Ag}^+$  mobility parallel to the interface which is considered as an ion-percolating path in the space charge region (Bunde *et al* 1985). The maximum conductivity at 20 mole%  $\text{BaSO}_4$  is due to optimum percolating paths in the sample.

#### 4. Conclusion

Electrical conductivity in  $(1-x)\text{Ag}_2\text{SO}_4-(x)\text{BaSO}_4$  ( $0.0 \leq x \leq 0.6$ ), characterized by XRD and SEM, has been investigated using complex impedance technique. Partial substitution within the solubility limit (5.27 mole%) of  $\text{Ag}^+$  by the bigger  $\text{Ba}^{2+}$  enhances conductivity in compliance with the classical aliovalent doping theory. A simplistic model based on lattice expansion upon substitution qualitatively accounts for conductivity enhancement. Beyond the solid solubility limit the system behaves as a typical binary composite, with  $\text{BaSO}_4$  dispersed in  $\text{Ag}_2\text{SO}_4$ . The

enhancement of conductivity upon introduction of excessive  $\text{BaSO}_4$  into  $\text{Ag}_2\text{SO}_4$  reasonably discussed in terms of interfacial reactions and surface-defect chemistry. The percolation threshold seems to occur at 20 mole%  $\text{BaSO}_4$  resulting in maximum conductivity. Thus both homogeneous and heterogeneous doping of an aliovalent  $\text{Ba}^{2+}$  ion optimize conductivity in certain compositions which could be considered for electrochemical device applications.

## Acknowledgement

Authors are thankful to UGC, New Delhi, for providing financial assistance to carry out this work.

## References

- Bunde A, Dieterich W and Roman H E 1985 *Phys. Rev. Lett.* **55** 5
- Dekker M 1990 *Electrical properties of gas sensor materials*, Ph D thesis, Delft University of Technology, Delft, The Netherlands
- Dieterich W 1988 *High conductivity solid ionic conductors* (ed.) T Takahashi (Singapore: World Sc.) p. 1
- Gauthier M and Chamberland A 1977 *J. Electrochem. Soc.* **124** 1579
- Heed B, Lunden A and Schroeder K 1975 10th Intersoc. Energy Conv. Eng. Conf. IECEC75 Record p. 6
- Hofer H H, Eysel W and Alpen U V 1981 *J. Solid State Chem.* **36** 365
- Kimball J C and Adams L W Jr. 1978 *Phys. Rev.* **B18** 5851
- Liang C C 1973 *J. Electrochem. Soc.* **120** 1289
- Linford R G and Hackwood S 1981 *Chem. Rev.* **81** 327
- Liu Q, Sun X and Wu W 1990 *Solid State Ionics* **40/41** 456
- Maier J 1985 *Ber. Bunsenges. Physik. Chem.* **89** 355
- Rodger A R, Kuwand I and West A R 1985 *Solid State Ionics* **15** 185
- Rao N, Schoonman J and Sorensen O T 1992 *Solid State Ionics* **57** 159
- Singh K and Deshpande V K 1982 *Solid State Ionics* **7** 295
- Singh K 1988 *Solid State Ionics* **28-30** 1371
- Singh K, Chandrayan V R and Deshpande V K 1988 *Solid State Ionics* **27** 57
- Singh K and Bhoga S S 1990 *Solid State Ionics* **39** 205
- Singh K and Bhoga S S 1992 *J. Solid State Chem.* **97** 141
- Singh K 1993 *Solid State Ionics* **66** 5-14
- Singh K, Pande S M and Bhoga S S 1995 *J. Solid State Chem.* **116** 232

## Acoustical parameters of polyethylene glycol/water mixtures

A VARADA RAJULU and P MABU SAB

Department of Polymer Science and Technology, Sri Krishnadevaraya University, Anantapur 515 003, India

MS received 12 September 1994; revised 17 February 1995

**Abstract.** Ultrasonic velocity ( $v$ ) and density ( $d$ ) have been measured for polyethylene glycol/water mixtures at 30°C. The adiabatic compressibility ( $\beta_{ad}$ ), molar compressibility ( $\beta$ ), specific acoustic impedance ( $Z$ ), Rao number ( $R$ ) and van der Waals constant ( $b$ ) have been computed. The variations of  $v$ ,  $d$ ,  $\beta_{ad}$ ,  $\beta$ ,  $Z$ ,  $R$  and  $b$  with mole ratio of water/ether group oxygen have been studied. The association between the components and the formation of tetrahydrate have been reported.

**Keywords.** Polyethylene glycol; acoustical parameters; van der Waals constant; molecular association; liquid mixtures.

### 1. Introduction

The variation of ultrasonic velocity and adiabatic compressibility of dilute aqueous solutions of solid polyethylene glycol (PEG) with concentration was studied by Gerecze (1977) who concluded that there was no solute–solvent interaction. Recently Graham and Chen (1993) studied the interaction of liquid and solid PEG (PEG-300, 400, 1000 and 3330) with water and revealed the formation of tetrahydrate in low molecular weight PEG (MW < 600) and tri- and hexahydrate formation for higher molecular weight PEGs using density data. In the present work we have measured the ultrasonic velocity and density of PEG-200 (MW ~ 200) at 30°C. The acoustical parameters molar compressibility  $\beta$ , specific acoustic impedance  $Z$  and Rao number  $R$  have been computed. The van der Waals constant  $b$  has also been determined by ultrasonic method. The variation of these parameters with the ratio of moles of water per ether oxygen in the PEG has been studied. We selected PEG as it has applications as hydrogel and PEG-200 was not covered in the interaction studies of Graham and Chen (1993).

### 2. Experimental

PEG-200 (S D Chemicals) was dried under vacuum at 65°C for 24 h before use. To known weight of the dry PEG in 50 ml standard flasks the appropriate amounts of double distilled water was added to give the desired ratio of moles of water per ether oxygen in the PEG and test samples with  $H_2O/CH_2-CH_2-O$  of 1.5, 2.0, 2.5, ..., 7.0 were prepared. These mixtures were maintained in the oven for 6 h at 65°C to obtain thorough mixing, cooled to room temperature, and allowed to attain equilibrium for several days in sealed containers. The ultrasonic velocities of these mixtures were measured with a 2 MHz variable path interferometer at 30°C as described by Varada Rajulu *et al* (1990). The densities were measured with a precalibrated density bottle using a water bath thermostated at 30°C.

**Table 1.** Ultrasonic velocity ( $v$ ), density ( $d$ ), adiabatic compressibility ( $\beta_{ad}$ ), molar compressibility ( $\beta$ ), van der Waals constant ( $b$ ), Rao number ( $R$ ) and acoustic impedance ( $Z$ ) of polyethylene glycol/water mixtures at 30°C.

Mole ratio (H <sub>2</sub> O/ether group)	$v$ (m/sec)	$d$ (g/cm <sup>3</sup> )	$\beta_{ad}$ (cm. sec <sup>2</sup> /g)	$R$ (cm <sup>10/3</sup> /mol/sec <sup>1/3</sup> )	$\beta$ (cm <sup>20/7</sup> . sec <sup>-2/7</sup> /mol g <sup>-1/7</sup> )	$Z$ (g/cm <sup>2</sup> /sec)	$b$ (cm <sup>3</sup> /mol)
1.5	1722.2	1.0881	30.986	4643	2646.5	187392	83.45
2.0	1716.1	1.0855	30.281	4023	2293.0	186282	72.40
2.5	1709.9	1.0831	31.578	3586	2043.9	185199	64.62
3.0	1705.3	1.0806	31.822	3258	1856.6	184274	58.75
3.5	1699.2	1.0777	32.138	3001	1709.7	183122	54.18
4.0	1692.7	1.0769	32.409	2794	1591.8	182286	50.14
4.5	1685.3	1.0733	32.804	2629	1497.1	180883	47.59
5.0	1677.1	1.0693	33.249	2492	1419.1	179332	45.20
5.5	1670.8	1.0641	33.664	2380	1354.6	177789	43.22
6.0	1663.2	1.0610	34.072	2280	1297.2	176465	41.46
6.5	1652.9	1.0545	34.710	2199	1250.6	174298	40.08
7.0	1646.1	1.0518	35.088	2123	1207.1	173136	38.74

### 3. Results and discussion

The measured values of ultrasonic velocity ( $v$ ) and density ( $d$ ) are presented in table 1. The adiabatic compressibility ( $\beta_{ad}$ ) was calculated using the relation (Varada Rajulu *et al* 1990)

$$\beta_{ad} = (dv^2)^{-1}. \quad (1)$$

The Rao number ( $R$ ) was calculated using the relation (Rao *et al* 1989)

$$R = (M/d)v^{1/3}, \quad (2)$$

where  $M$  is the molecular weight of the liquid mixture given by

$$M = (n_1 M_1 + n_2 M_2)/(n_1 + n_2), \quad (3)$$

where  $M_1$  and  $M_2$  are the molecular weights and  $n_1$  and  $n_2$  are the moles of the components comprising the mixture. The molar compressibility ( $\beta$ ) was calculated using Wada's (1949) relation

$$\beta = (M/d)(\beta_{ad})^{-1/7}. \quad (4)$$

The specific acoustic impedance ( $Z$ ) was calculated using the relation

$$Z = (dv). \quad (5)$$

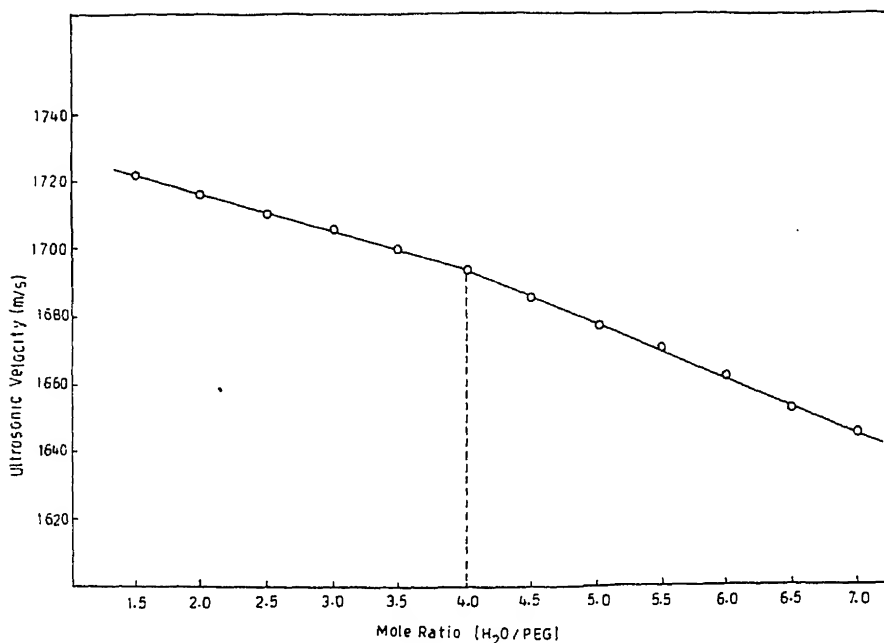


**Figure 1.** Variation of ultrasonic velocity ( $v$ ) with moles of water per ether group in PEG-200/water mixtures at 30°C.



$$b = (M/d)[1 - (RT/Mv^2)\sqrt{1 + (Mv^2/3RT)} - 1].$$

Though (2) and (4) are empirical and additive in nature, (1) which has a semiempirical origin soon found theoretical support (Blitz 1967). Similarly (5) is written considering its analogy to the mechanical and electrical impedance without reactive components (Blitz 1967). Equation (6) is semiempirical in nature (Flugge 1961).

The measured values of  $v$  and  $d$  and the computed values of  $\beta_{ad}$ ,  $R$ ,  $Z$ ,  $\beta$  and  $b$  are given in table 1. The variation of  $v$ ,  $d$ ,  $\beta_{ad}$ ,  $\beta$ ,  $R$ ,  $Z$  and  $b$  with mole ratio of  $H_2O$ /ether group is shown in figures 1, 2, 3, 4, 5, 6 and 7 respectively. From figures 1–3 and 6 it is evident that the variation of  $v$ ,  $d$ ,  $\beta_{ad}$  and  $Z$  show two linear portions with different slopes with a break at a mole ratio of 4. A similar observation was made by Grah and Chen (1993) in the case of PEG (MW < 600) by density measurements and this was attributed to the formation of tetrahydrate.

Nomoto (1953) established the validity of (2), (4) and (6) in a large number of liquid mixtures and stated that for unassociated components in the liquid mixtures the variation of  $R$ ,  $\beta$  and  $b$  with mole ratio will be linear. In the present study a smooth nonlinear relation is observed indicating that association exists between PEG and water. The nonlinear behaviour is probably due to the fact that there will be a change in molecular weight due to the association and the weight of the associated group

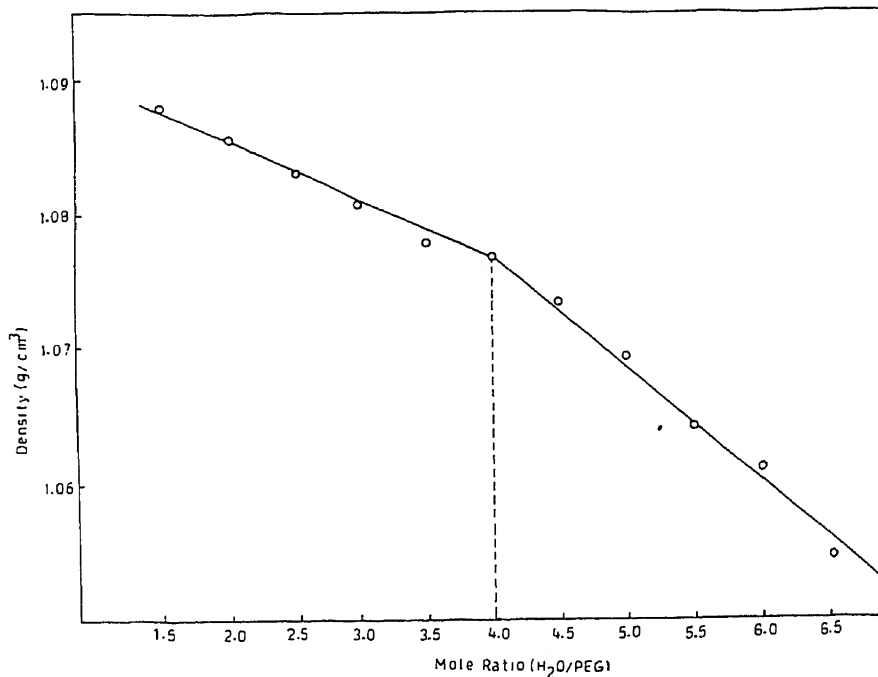


**Figure 2.** Variation of density ( $d$ ) with moles of water per ether group in PEG-200 mixtures at 30°C.

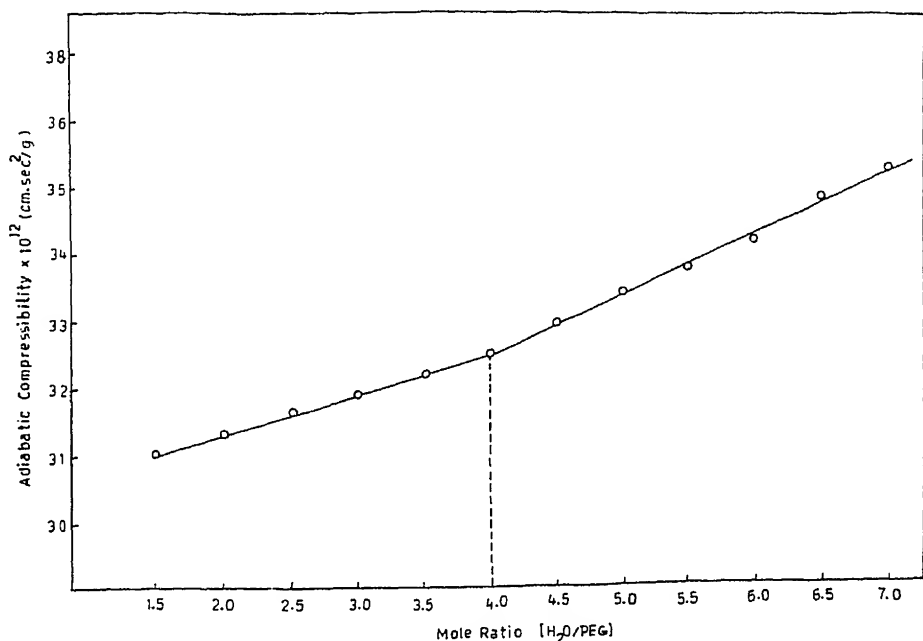


Figure 3. Variation of adiabatic compressibility ( $\beta_{ad}$ ) with moles of water per ether group in PEG-200/water mixtures at 30°C.

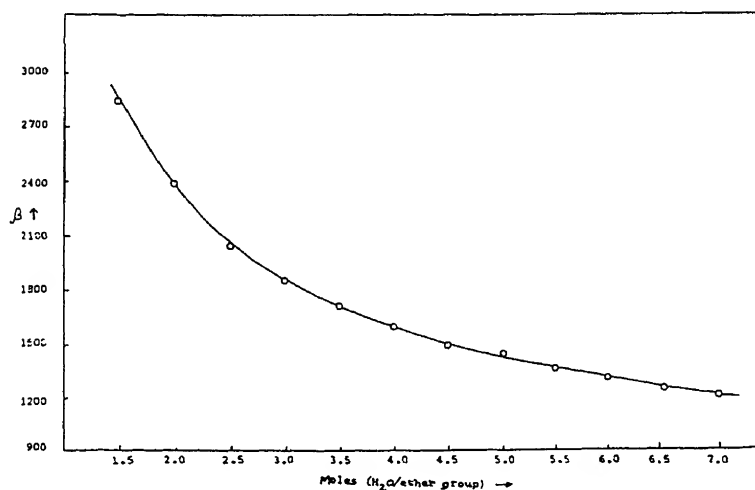


Figure 4. Variation of molar compressibility ( $\beta$ ) with moles of water per ether group in PEG-200/water mixtures at 30°C.

different from that of the components (Nomoto 1953). Further the smooth nonlinear behaviour is observed only in the case of the variation of parameters  $\beta$ ,  $R$  and  $b$  which is not the case of adiabatic compressibility. Similar observations have been made by Choudhary

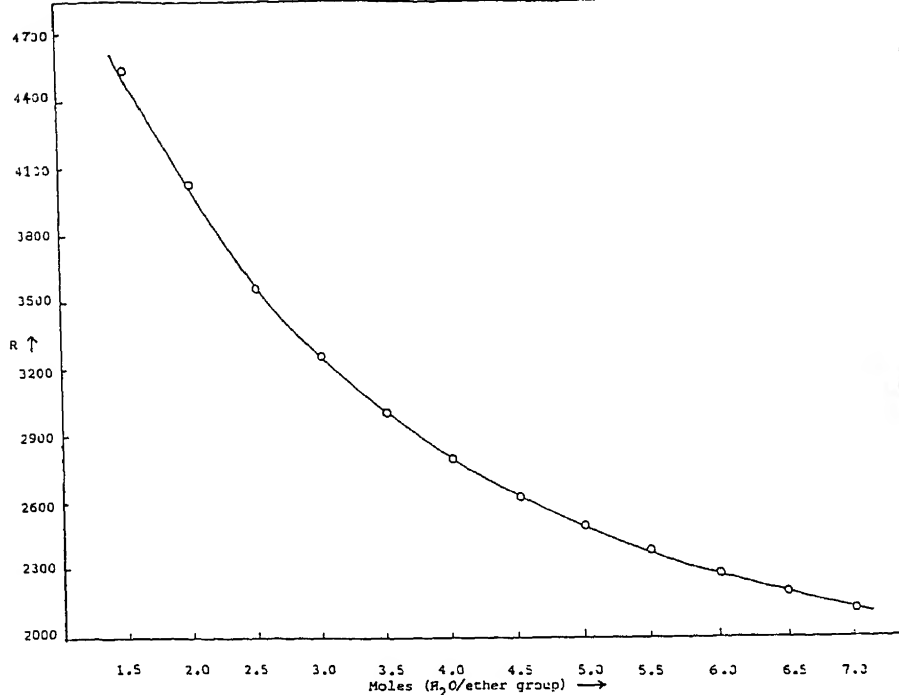


Figure 5. Variation of Rao constant ( $R$ ) with moles of water per ether group in PEG-200/water mixtures at 30°C.

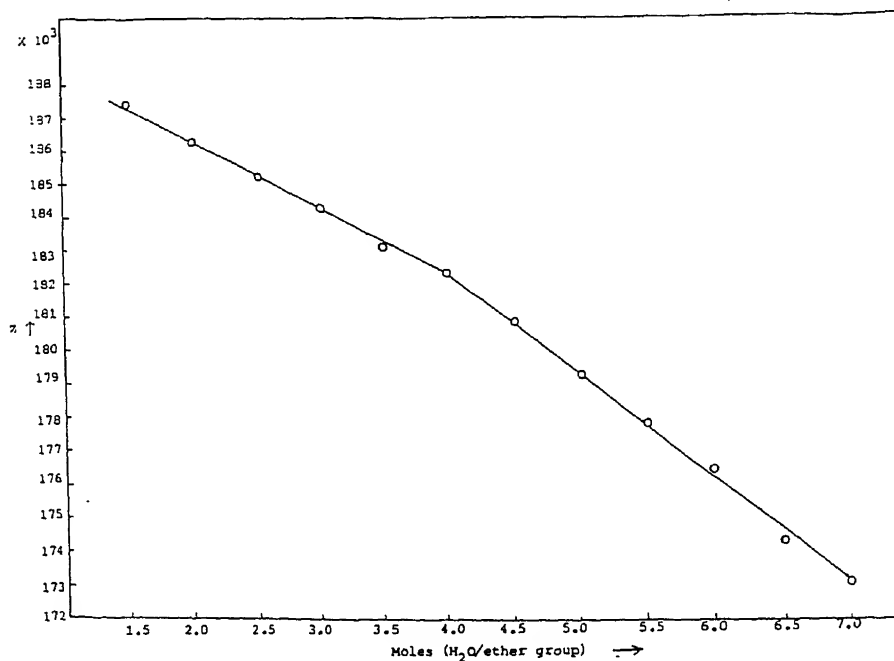
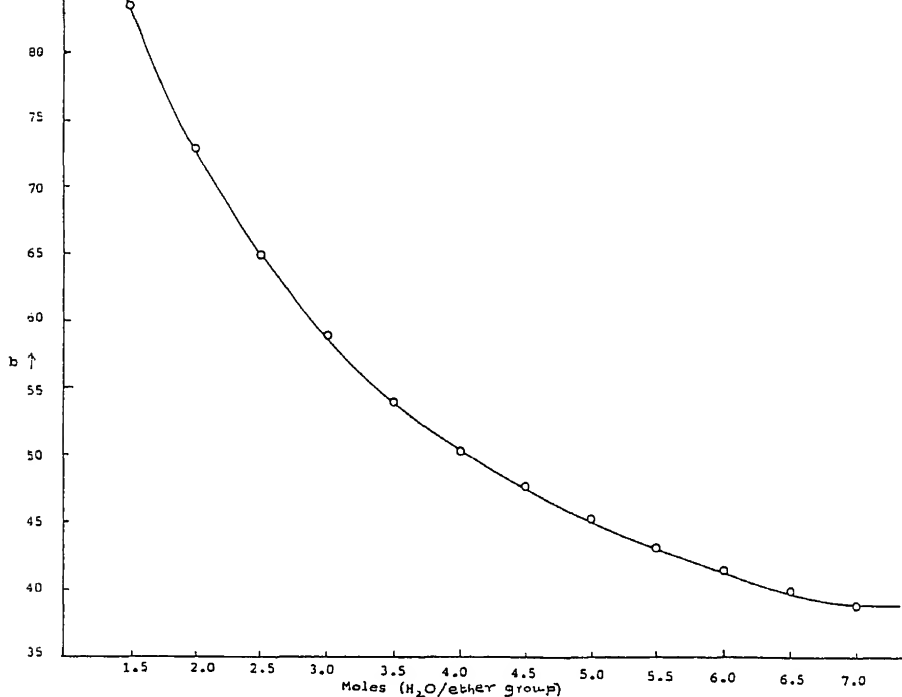


Figure 6. Variation of acoustic impedance ( $Z$ ) with moles of water per ether group in PEG-200/water mixtures at 30°C.



**Figure 7.** Variation of van der Waals constant ( $b$ ) with moles of water per ether group in PEG-200/water mixtures at 30°C.

solutions. These observations help us to confirm the association. Thus the association between PEG-200 and water and the tetrahydrate formation can be confirmed using ultrasonic velocity data in the present case. The interaction of PEG (MW > 1000) with water was not observed by Gerecze (1977) as the solution concentration was maintained very low.

## References

- Blitz J 1967 in *Fundamentals of ultrasonics* (London: Butterworth Publishing Co. Ltd.)  
 Chowdoji Rao K, Venkata Naidu S and Varada Rajulu A 1990 *Eur. Polym. J.* **26** 657  
 Flugge S 1961 in *Encyclopedia of physics* (Berlin: Springer Verlag) Vol. X1/1  
 Gerecze N G 1977 *Acustica* **38** 51  
 Graham N B and Chen C F 1993 *Eur. Polym. J.* **29** 149  
 Nomoto O 1953 *J. Chem. Phys.* **21** 950  
 Rao K Ch, Rajulu A V and Naidu S V 1989 *Acta Polymerica* **40** 743  
 Varada Rajulu A, Chowdoji Rao K and Venkata Naidu S 1990 *J. Pure Appl. Ultrason.* **12** 115  
 Vigoureux P 1952 in *Ultrasonics* (London: Chapman and Hall)  
 Wada Y 1949 *J. Phys. Soc. Jpn.* **4** 280



# Thermal stability of electrochemically prepared polythiophene and polypyrrole

F MOHAMMAD\*, P D CALVERT and N C BILLINGHAM

School of Chemistry and Molecular Sciences, University of Sussex, Brighton BN1 9QJ, UK

\*Department of Applied Chemistry, Z. H. College of Engineering and Technology, Aligarh Muslim University, Aligarh 202 002, India

MS received 30 November 1993; revised 25 January 1995

**Abstract.** The degradation behaviour of electrochemically prepared polythiophene and polypyrrole has been studied by thermal gravimetric analysis technique. Studies on both the polymers show that they are more stable than polyacetylene but still undergo degradation reactions which involve two steps, viz. loss of dopant and then degradation of polymer backbone. The general features of degradation mechanisms are discussed.

**Keywords.** Conducting polymers; polythiophene; polypyrrole; TGA studies; degradation.

## 1. Introduction

Polymers undergo chemical reactions just like any typical low molecular weight compound, provided the reactants are made available at the reaction site. The process of deterioration of the useful polymer properties involving chemical reactions is defined as degradation. There are many external causes of degradation of polymeric materials such as heat, light, mechanical stress, oxygen, ozone, moisture, atmospheric pollutants, etc along with the factors effective at the time of processing. Also, the presence of reactive sites in the polymers such as peroxides, defects, chemically reactive groups, etc may degrade the polymer properties with or without the combination of external factors.

The emergence of direct and precursor route to polyacetylene films (Shirakawa and Ikeda 1971; Shirakawa *et al* 1977) and electrochemical polymerization of heterocyclics into polymer films such as polythiophene (Tourillon and Garnier 1982; Kaneto *et al* 1983) and polypyrrole (Dall'olio *et al* 1968; Diaz *et al* 1979; Street *et al* 1982) has triggered the investigation of these materials due to somewhat easier fabrication of experimental samples.

Knowledge of environmental stability and degradation behaviour is a prequalification for use of polymer films in many practical applications. This has led us to try to develop some chemical understanding of their stability and degradation behaviour in different environmental conditions.

## 2. Experimental

An evacuable electrochemical cell, assembled with platinum or indium–tin oxide conducting glass working electrode and aluminium counter electrode, was used for the preparation of oxidized polythiophene and polypyrrole films (Dall'olio *et al* 1968; Diaz *et al* 1979; Street *et al* 1982; Tourillon and Garnier 1982; Kaneto *et al* 1983). A current density of 9–12 mA/cm<sup>2</sup> was applied. Washing was done by extremely dry acetonitrile stored over

\*For correspondence

freshly dried molecular sieves. Polymer films were further dried by pumping on vacuum line for about an hour prior to use. The thickness was estimated to be around 5 to 10 microns from the area and the weight of the polymer film. The TGA studies were performed on samples of as-prepared polythiophene and polypyrrole films in dry air as well as in nitrogen. Typically 5 to 8 mg samples were used and heated up to 700°C at a rate 30°C per min for the samples containing  $\text{BF}_4^-$  counterion and at a rate of 10°C per min in case of polythiophene containing  $\text{ClO}_4^-$  counterion. Isothermal TGA studies were carried out on as-prepared polythiophene ( $\text{BF}_4^-$ ) and polythiophene ( $\text{ClO}_4^-$ ) and their ammonia compensated counterparts in dry air. Typically 3 to 5 mg samples were heated at a rate of 100°C per min and then maintained at a desired temperature ranging from 372°C to 484°C. A Stanton Redcroft TGA instrument was used in these studies.

### 3. Results and discussion

Samples of polythiophene and polypyrrole containing various counterions and their ammonia compensated counterparts were examined in air and in nitrogen atmospheres both isothermally and with programmed temperature increase.

Thermogravimetric analysis of polythiophene ( $\text{BF}_4^-$ ) and polypyrrole ( $\text{BF}_4^-$ ) with programmed temperature increase reveals that polythiophene ( $\text{BF}_4^-$ ) lost weight in two distinct steps. Step-1 is identical in nitrogen atmosphere and in air with a similar weight loss of 18% in the temperature range 70°C to 260°C. In step-2, the additional weight losses of 7% in nitrogen by 700°C and of 77% in air by 600°C were observed.

Polypyrrole ( $\text{BF}_4^-$ ) lost weight in three rather indistinct steps in nitrogen as well as in air. Step-0 and step-1 are identical in nitrogen and air. Step-0 is very mild with a weight loss of 3% in the temperature range 45°C to 125°C in nitrogen and similar in air. Step-1 ranges from 125°C to 285°C with an additional weight loss of 19.5% in nitrogen and the same in air. Step-2 was monitored up to 700°C and found to be incomplete with further weight losses of 29% in nitrogen and 55% in air. The thermograms are shown in figure 1 and the results are given in table 1.

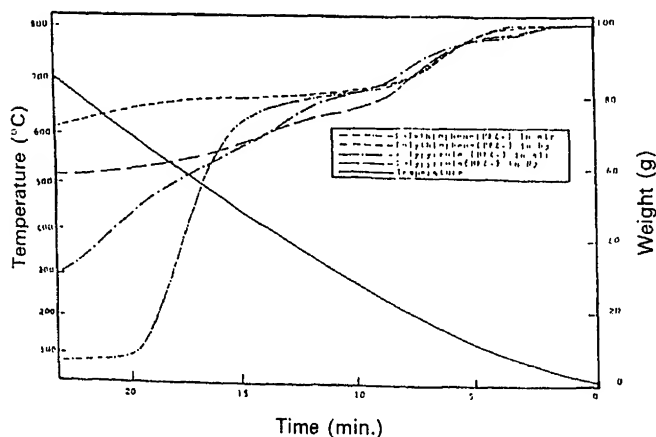


Figure 1. Thermograms of polythiophene and polypyrrole containing  $\text{BF}_4^-$  counterion in air and nitrogen.

Isothermal TGA studies of as-prepared polythiophene ( $\text{BF}_4^-$ ) and polythiophene ( $\text{ClO}_4^-$ ) and their ammonia compensated counterparts in air were carried out in the temperature range 372°C to 484°C. Plots of  $\log W/W_0$  against time followed straight line characteristic of a first-order weight loss as shown in figure 2. Table 2 gives the rate constants of first order weight loss as estimated from  $\log W/W_0$  versus time plots at various temperatures from different thiophene samples. The activation energy was calculated to be 94.5 kJ/mol from the slope of the Arrhenius plot shown in figure 3.

Table 1. Observed weight loss for 5–10  $\mu\text{m}$  thick films of as-prepared PTh- $\text{BF}_4$  and PPy- $\text{BF}_4$  in various steps during programmed heating.

Step	PTh- $\text{BF}_4$		PPy- $\text{BF}_4$	
	Air	$\text{N}_2$	Air	$\text{N}_2$
Step-0				
Temp. range(°C)			45–125	45–125
Weight loss(%)			3.0	3.0
Step-1				
Temp. range(°C)	70–260	70–260	125–285	125–285
Weight loss(%)	18	18	19.5	19.5
Step-2				
Temp. range(°C)	260–600	260–700	285–700	285–700
Weight loss(%)	77	7	22.5	48.5
Residue(%)	5	75	55	29
Total	100	100	100	100

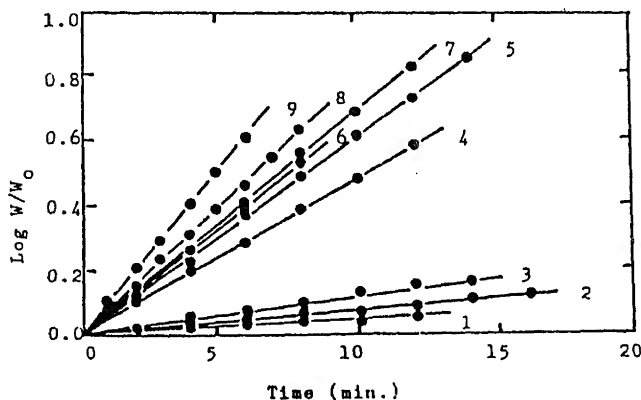


Figure 2. First-order weight loss of polythiophene on isothermal heat treatment. 1,  $\text{NH}_4\text{OH}$  compensated polythiophene with  $\text{BF}_4^-$  at 377°C; 2, as-prepared polythiophene with  $\text{BF}_4^-$  at 372°C; 3,  $\text{NH}_4\text{OH}$  compensated polythiophene with  $\text{ClO}_4^-$  at 400°C; 4,  $\text{NH}_4\text{OH}$  compensated polythiophene with  $\text{BF}_4^-$  at 462°C; 5, as-prepared polythiophene with  $\text{ClO}_4^-$  at 475°C; 6, as-prepared polythiophene with  $\text{BF}_4^-$  at 464°C; 7,  $\text{NH}_4\text{OH}$  compensated polythiophene with  $\text{ClO}_4^-$  at 475°C; 8, as-prepared polythiophene with  $\text{ClO}_4^-$  at 475°C; and 9,  $\text{NH}_4\text{OH}$  compensated polythiophene with  $\text{BF}_4^-$  at 483°C.



**Table 2.** First-order rate constants estimated from the logarithmic plots of the weight loss for as-prepared and ammonia compensated polythiophene containing various counterions during isothermal heating in a TGA instrument in the temperature range 372–483°C.

Counterion	Temperature (°C)	$k_1$ (s <sup>-1</sup> )
BF <sub>4</sub> <sup>-b</sup>	377	$2.50 \times 10^{-4}$
BF <sub>4</sub> <sup>-a</sup>	372	$2.66 \times 10^{-4}$
ClO <sub>4</sub> <sup>-b</sup>	400	$4.83 \times 10^{-4}$
BF <sub>4</sub> <sup>-b</sup>	462	$1.84 \times 10^{-3}$
ClO <sub>4</sub> <sup>-a</sup>	475	$2.12 \times 10^{-3}$
BF <sub>4</sub> <sup>-a</sup>	464	$2.44 \times 10^{-3}$
ClO <sub>4</sub> <sup>-b</sup>	475	$2.64 \times 10^{-3}$
ClO <sub>4</sub> <sup>-a</sup>	475	$2.94 \times 10^{-3}$
BF <sub>4</sub> <sup>-b</sup>	483	$3.97 \times 10^{-3}$

<sup>a</sup>As-prepared

<sup>b</sup>Aqueous ammonia compensated.

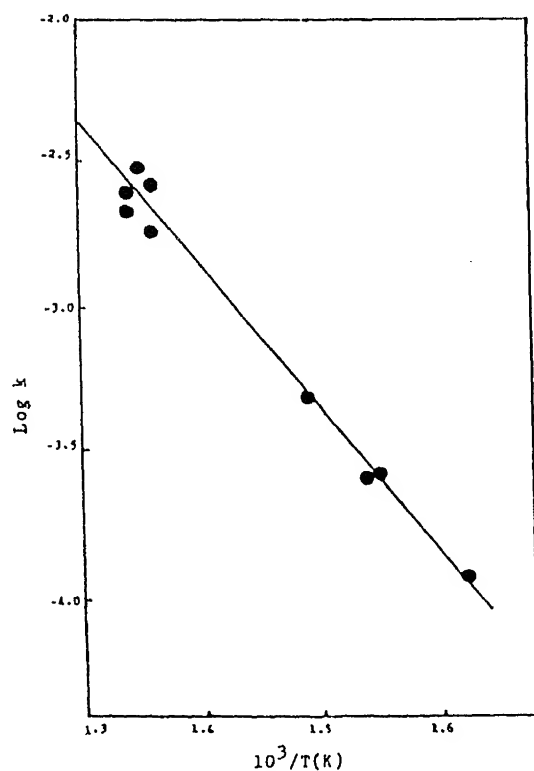
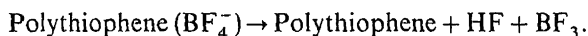


**Figure 3.** Arrhenius plot of first-order rate constants of isothermal weight loss of polythiophene.

It is evident from TGA studies that degradation of polythiophene involves two steps depending upon the experimental temperature. In step-1, a similar weight loss of 18% in air as well as in nitrogen with programmed temperature increase is observed whereas a massive weight loss is the main characteristic of step-2. Step-0 with a 3% weight loss in polypyrrole ( $\text{BF}_4^-$ ) seems to be due to the removal of trapped moisture which is also supported by our electrical conductivity loss studies (Mohammad 1988) by the consistency of the temperature range from 45°C to 125°C and also by the work of Wynne and Street (1985). The presence of moisture could not be confirmed in our FTIR studies (Mohammad *et al* 1994) due to the presence of a strong and broad band in the -OH absorption region.

Step-1 seems to correspond to the loss of the counterion by some complex chemical reaction but without any loss of conjugation as reported in our UV-VIS studies with a corresponding change in the colour to red and green in polythiophene and polypyrrole respectively (Mohammad *et al* 1989, 1993). The dopant concentrations (mol ratio) of 0.21 and 0.19 [excluding 3% moisture in case of polypyrrole ( $\text{BF}_4^-$ )] for polythiophene ( $\text{BF}_4^-$ ) and polypyrrole ( $\text{BF}_4^-$ ) respectively as estimated from weight loss studies are in agreement with the reported  $y$  values (Diaz 1981; Cao *et al* 1985), but are greater than our electrochemically estimated  $y$  values (Mohammad *et al* 1990). Erlandsson *et al* (1985) proposed the formation of OH-counterion in polypyrrole and also observed the formation of  $\text{BF}_3$  and HF by mass spectrometry. In our opinion, the formation of  $\text{HBF}_4$  with or without carboxylate as an end group is most consistent with the FTIR spectra of aged polythiophene ( $\text{BF}_4^-$ ) at 80°C as shown in figure 4 (Mohammad *et al* 1994). This process of counterion loss may be given by the following total chemical reaction, analogous to what we have observed in our compensation studies (Mohammad *et al* 1989):



Step-2 corresponds to the oxidative degradation reactions of polymer backbone producing segments of various conjugation lengths (Mohammad *et al* 1993) and may

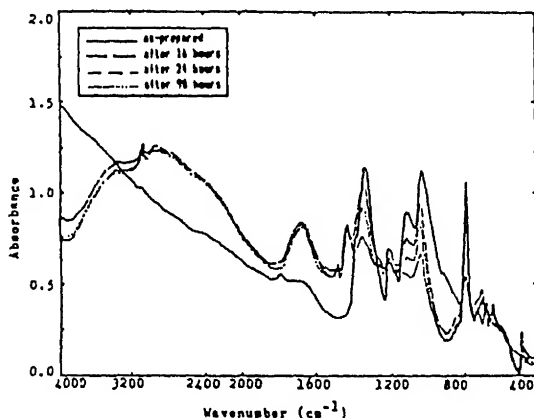
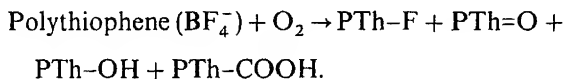


Figure 4. Effect of aging on FTIR spectra of  $\text{BF}_4^-$  containing polythiophene at 80°C in air.

involve substitution, addition and chain scission. The presence of resonances due to broad H-bonded -OH and C=O groups in the FTIR spectra of degraded polythiophene ( $\text{BF}_4^-$ ) (Mohammad 1988) are further supported by the work of Hahn *et al* (1986) on polypyrrole. An overall chemical reaction for the oxidative degradation of polythiophene ( $\text{BF}_4^-$ ) may be given by the following equation:



Oxidative degradation of most polymers proceeds via chemical reactions of peroxy radicals. Yang and Chien (1985) reported autooxidation of polyacetylene, a typical unsaturated polymer with a long conjugated system, and a value of  $9 \times 10^{-7} \text{ mol(g)s}^{-1}$  for the rate constant at  $70^\circ\text{C}$  and 760 torr  $\text{O}_2$ . By analogy with polyacetylene, we expect to find that polythiophene and polypyrrole will also be rather oxygen-sensitive and will degrade with or without loss of conjugation involving addition to  $\text{C}=\text{C}$  bonds, substitution and chain scission. Figure 5 shows the proposed mechanism for the various competing degradation reactions which is supported by our FTIR (Mohammad 1988; Mohammad *et al* 1994) and UV-VIS studies (Mohammad *et al* 1993).

#### 4. Conclusion

The degradation of polythiophene and polypyrrole occurs in two steps: step-1 corresponds to decomposition of dopant counterion and step-2 corresponds to oxidative degradation of polymer backbone. However, polypyrrole seems to contain about 3% moisture as evident from step-0. Oxidative degradation seems to follow first-order kinetics of weight loss with an activation energy of  $94.5 \text{ kJ/mol}$  in isothermal TGA experiments. There is no doubt that polythiophene and polypyrrole are much more stable than polyacetylene and may be capable of retaining their initial electrical

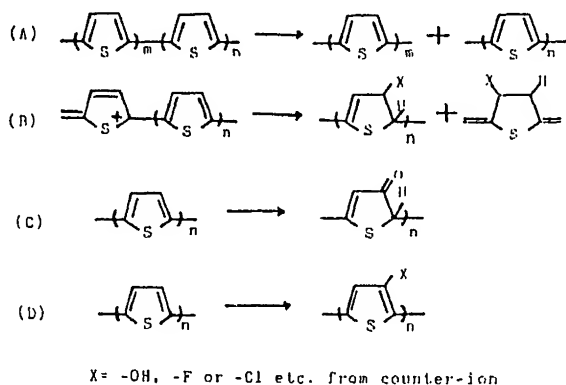


**Figure 5.** Oxidative degradation of polythiophene. (A) Random chain scission accompanied with loss of conjugation, (B) random chain scission with addition on  $\text{C}=\text{C}$  bond leading to loss of conjugation, (C) addition on  $\text{C}=\text{C}$  bond without chain scission leading to loss of conjugation and (D) substitution on  $\text{C}=\text{C}$  bond without chain scission leading to the retention of conjugation.

properties for long periods (months or years) in ambient atmosphere but there are evidences of chemical reactions in both the polymers. Although the study of degradation has barely begun, we can identify several processes which can contribute to the instability and degradation of conducting polymers such as (i) reaction of main chain with oxygen leading to irreversible loss of conjugation and conductivity, (ii) reaction of the main chain with its counterion again leading to irreversible loss of conjugation and conductivity, (iii) reaction with oxygen or counterions at hetero-atoms without loss of conjugation but with modification of the electronic structure of the polymer and (iv) reversible or partly reversible undoping reactions of the conjugated system by moisture.

## Acknowledgements

One of us (FM) thankfully acknowledges the financial assistance provided by the Ministry of Education and Culture (Government of India) to carry out this work. Thanks are also due to Dr P J S Foot, Kingston University, UK, for his suggestions.

## References

- Cao Y, Wang P and Qian R 1985 *Macromol. Chem.* **186** 1093  
 Chien J C W 1986 *Proc. PDDG Meeting* Univ. Manchester, UK  
 Dall'olio A, Dascola Y, Varacca V and Bocchi V 1968 *Acad. Sci. Ser. C* **267** 433  
 Diaz A F 1981 *Chim. Scripta* **17** 145  
 Diaz A F, Kanazawa K K and Gardini G P 1979 *J. Chem. Soc., Chem. Commun.* 635  
 Erlandsson R, Inganas O, Lundstorm I and Salaneck W R 1985 *Synth. Metals* **10** 303  
 Hahn S J, Gajda W J, Vogellhut P O and Zeller M V 1986 *Synth. Metals* **14** 89  
 Kaneto K, Kohno Y, Yoshino K and Inuishi Y 1983 *J. Chem. Soc., Chem. Commun.* 382  
 Mohammad F 1988 D. Phil. thesis, University of Sussex, UK  
 Mohammad F, Calvert P D and Billingham N C 1989 *Proc. 2nd CECRI's Res Conf. on Electroactive Polymers, Karaikudi, India*  
 Mohammad F, Calvert P D and Billingham N C 1990 *Bull. Electrochem.* **6** 194  
 Mohammad F, Calvert P D and Billingham N C 1993 *Bull. Electrochem.* **9** 109  
 Mohammad F, Calvert P D and Billingham N C 1994 *Synth. Metals* **66** 33  
 Shirakawa H and Ikeda S 1971 *Polymer J.* **2** 231  
 Shirakawa H, Louis E J, MacDiarmid A G, Chiang C K and Heeger A J 1977 *J. Chem. Soc., Chem. Commun.* 578  
 Street G B, Clark T C, Croumbi M, Kanazawa K K, Lee V, Fluger P, Scott J and Weiser G 1982 *Mol. Cryst. Liq. Cryst.* **83** 253  
 Tourillon G and Garnier F 1982 *J. Electroanal. Chem.* **135** 173  
 Wynne K J and Street G B 1985 *Macromolecules* **18** 2361  
 Yang X Z and Chien J C W 1985 *J. Polym. Sci. Polym. Chem. Ed.* **23** 859



## Study of the effect of chopping on the adhesion of codeposited mixed thin films

VIJAYA PURI and R K PURI\*

Department of Physics, \*Department of USIC, Shivaji University, Kolhapur 416 004, India

MS received 1 July 1994; revised 16 January 1995

**Abstract.** This paper reports adhesion of codeposited mixed films of Cu–Ag, Cu–Al,  $\text{MgF}_2$ –ZnS and  $\text{MgF}_2$ –cryolite and enhancement of adhesion by chopping technique. Results indicate that codeposited mixed films show higher adhesion than single films and chopping improves the adhesion further. The quenching of crystal growth seems to be more effective if two materials are codeposited and chopped. Chopping along with mixing increases the number of nucleation sites and decreases defects in the film. Decreasing defects and modifying the microstructure increases the adhesion of the films. Chopping also seems to increase oxygen affinity of both metallic and dielectric films for growth of interfacial bonding layer.

**Keywords.** Chopping; codeposition; mixed films; adhesion; non-chopped.

### 1. Introduction

Metallic and dielectric films are widely used in microelectronics and optical thin film systems. The designers of these systems have a very limited selection of materials. Mixed films offer a wider choice of materials. The most direct method is to prepare a mixture of the materials and deposit from a single source (Hiradayanath *et al* 1979; Vankar *et al* 1979; Ganner 1986). Simultaneous evaporation using several sources (Jacobson 1966) is a very flexible method. Our work (Vijaya *et al* 1980, 1987; Puri *et al* 1983) on codeposited mixed  $\text{MgF}_2$ –cryolite films has shown the superiority of chopped mixed films over single films.

In order to be functional the thin film has to be adherent to the substrate. Various methods like deposition on hot substrate (Pulkar 1982; Martin *et al* 1983; Pierce and Vaughan 1983), deposition in presence of plasma or glow discharge cleaning (Stoddart *et al* 1970; Fancey and Mathews 1990; Pulkar *et al* 1990), deposition of bonding layer (Mattox 1973), etc have been reported to increase the adhesion of the films.

This paper reports the adhesion of codeposited mixed films of Cu–Ag, Cu–Al,  $\text{MgF}_2$ –ZnS and  $\text{MgF}_2$ –cryolite and the effect of chopping (Vijaya *et al* 1980) on the adhesion of these films.

### 2. Experimental

Both metallic and dielectric films were deposited on glass by thermal evaporation ( $\sim 7 \text{ \AA/s}$ ) in a vacuum of better than  $8 \times 10^{-6}$  torr using two tungsten filaments for codeposited mixed films. Figure 1 gives the schematic diagram of the arrangement for deposition of mixed films and single films in the same vacuum cycle. The two materials were in the ratio 1:1 by weight. The two sources were kept opposite to each other at a distance of 10 cm. A metal partition was kept between the two sources to avoid

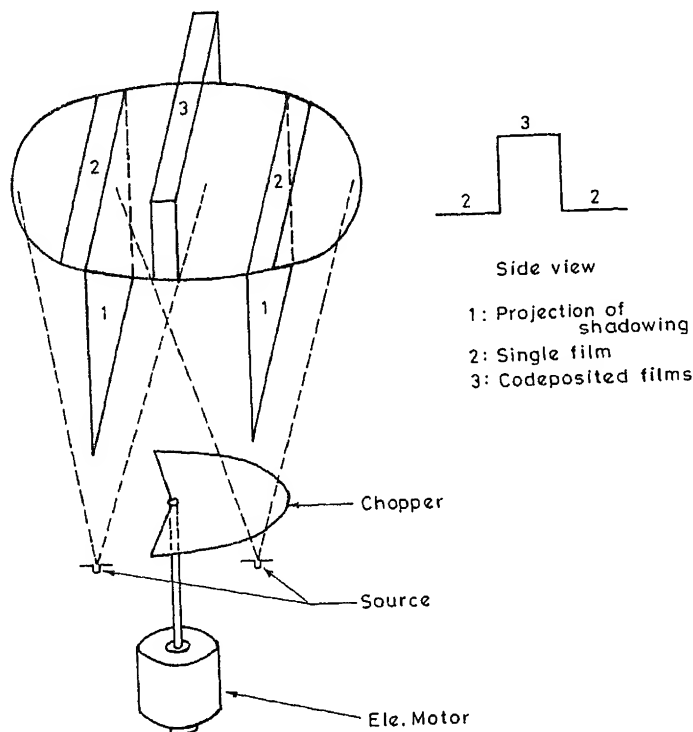


Figure 1. Schematic diagram of substrate holder along with chopper.

contamination of source. The height of the substrate holder was adjusted such that both codeposited mixed and single films had the same thickness. The substrates were glass slides maintained at room temperature during deposition. The thickness of the films was in the range 500–2500 Å. The chopper was a circular metallic vane with a V-shaped cutout kept above the evaporation source (figure 1) giving a chopping rate of 5–6 rot/sec. The adhesion was measured by direct pulloff (DPO) method by sticking aluminium studs of 0.5 cm diameter to the film surface and back of substrate and pulling by tensile testing machine until fracture occurred at the interface. The error in the measurement using the adhesion testing machine (Puri *et al* 1991) was  $\pm 9.81 \text{ kgF/cm}^2$ .

### 3. Results and discussion

The typical values of adhesion of codeposited mixed metallic and dielectric films as a function of thickness are shown in figures 2 and 3 respectively. Table 1 gives the average values of adhesion of codeposited mixed and single films. From the graphs and table it is seen that there is an appreciable increase in adhesion of the codeposited mixed films due to chopping. An interesting result is that non-chopped mixed films show higher adhesion than non-chopped single films, the exception being: Al. Both metallic and dielectric films of thickness  $> 1000 \text{ Å}$  show near-saturation effect as

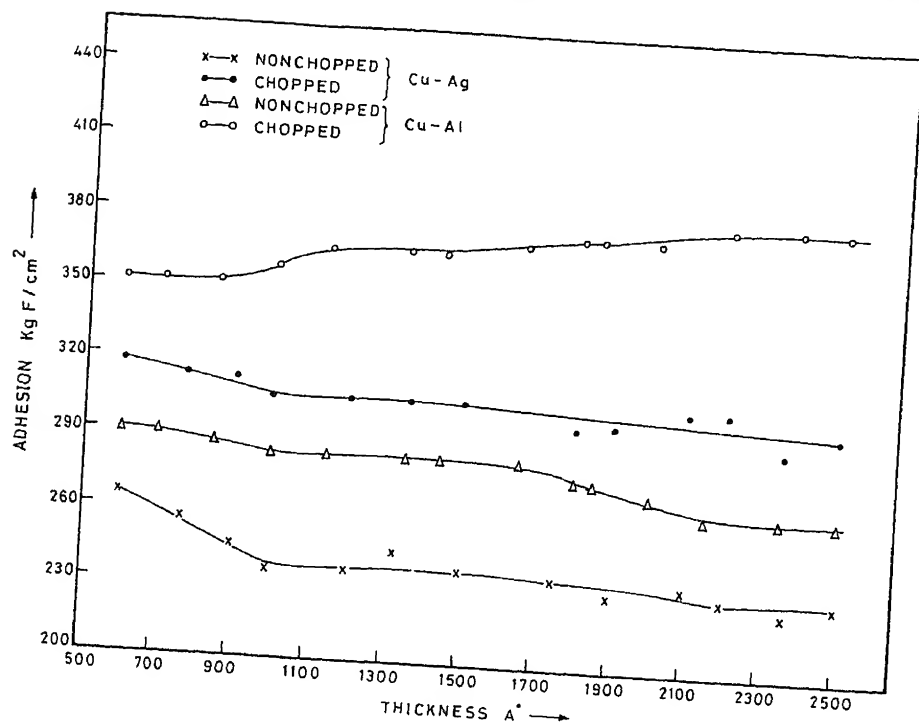


Figure 2. Typical values of adhesion vs thickness of codeposited mixed metallic films.

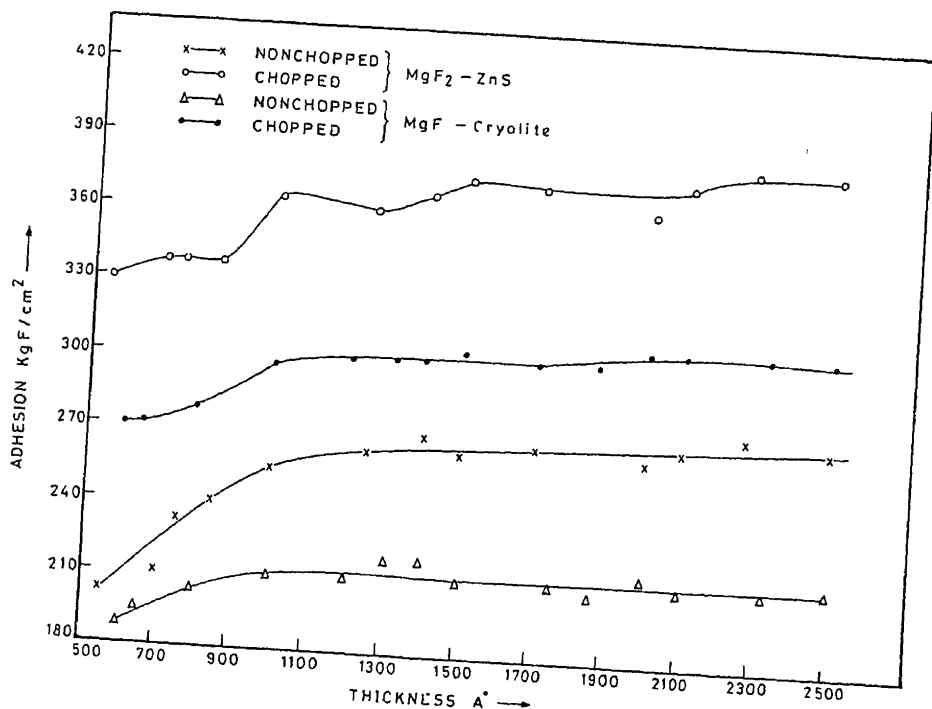


Figure 3. Typical values of adhesion vs thickness of codeposited mixed metallic films.



**Table 1.** Average values of adhesion of codeposited mixed and single films.

Type of film		Adhesion (kgF/cm <sup>2</sup> ) Thickness range (Å)					
		500-1000		1000-1500		1500-2500	
		c	nc	c	nc	c	nc
Codeposited mixed	Cu-Ag	310	250	305	238	300	238
	Cu-Al	350	285	365	280	370	270
	MgF <sub>2</sub> -ZnS	338	225	370	260	375	270
	MgF <sub>2</sub> -cryolite	280	198	300	210	310	210
	Cu	280	145	210	105	208	105
Single film	Ag	289	153	228	100	228	100
	Al	353	314	280	275	280	275
	MgF <sub>2</sub>	185	110	206	125	206	127
	ZnS	298	220	314	255	333	255
	Cryolite	162	98	193	110	193	110

C, Chopped; nc, non-chopped.

adhesion does not change appreciably with thickness. From figure 3 it is seen that thinner dielectric films have lesser adhesion than thicker films.

During codeposition a pseudodiffusion type of interface might be formed (Mattox and Rigney 1986) which might be the cause of enhanced adhesion of codeposited mixed films. It has been reported (Jacobson 1966) that evaporated mixtures have a finer structure than that of the individual materials. The films of Ag, Al, MgF<sub>2</sub>, ZnS and cryolite have been observed to have columnar microstructures (Guenther and Jung 1976; Pulkar 1982).

During the process of chopping there is a continuous growth flux interruption. Due to this interruption there is a quenching of the columnar crystal growth. It has been reported (Ogura 1975) that pseudoboundaries are formed when there is a discontinuity in the rate of deposition. Formation of pseudoboundaries leading to pseudodiffusion becomes more prominent if two materials are codeposited and chopped giving more adherent films.

The chopping process also enhances surface mobility of adatoms whereby the defects are not frozen at the site of impingement. Due to the arrival of two adatoms of different species during codeposition the number of nucleation sites increases and constant flux interruptions prevent growth of large crystallites. Also due to the presence of different species there are chances of recrystallization thereby ordering the film microstructure. The net effect of these processes is to decrease the voids in the film due to lateral surface diffusion and change in the columnar morphology of the films. Since defects are not frozen and there is a decrease in grain size due to chopping, fractures do not propagate for large distances in the film. These contribute to the increase in adhesion of the film. Enhanced adhesion due to increased mobility, decreased void density and lateral surface diffusion has been reported (Martin *et al* 1983) for deposition on heated substrate. Our values of adhesion of chopped single films compare very well with those of deposition on heated substrate (Vijaya *et al* 1993).

Another process dominant while chopping is to assist the affinity of adatoms to oxygen. Our electron diffraction (Puri *et al* 1983) data for  $\text{MgF}_2$  and cryolite show the presence of oxide in a complex form in the chopped films. The ESCA of  $\text{MgF}_2$  and  $\text{CeO}_2$  (unpublished work) also show excess oxygen in chopped films. Excess oxygen has been reported (Laugier 1981) to decrease stress in films. Decrease of stress increases the adhesion (Jacobs *et al* 1986). This oxygen incorporation mechanism is more dominant in chopped metallic films, except single aluminium films. Aluminium being an oxygen active metal, during deposition oxygen migration takes place in the Al-glass interface forming a bonding layer (Laugier 1981). The chopping process does not seem to enhance this effect in Al, since single chopped Al films do not show appreciable increase in adhesion compared to non-chopped films. Chopped Cu-Ag films show an appreciable increase in adhesion indicating the presence of interfacial bonding layer. The presence of excess oxide is also shown in DC resistivity data of these films (Vijaya *et al* 1993). The DC resistivity of chopped copper is  $3.97 \mu\text{ohm cm}$  and that of non-chopped copper  $1.89 \mu\text{ohm cm}$ , whereas for non-chopped and chopped aluminium the values are 5.2 and  $5.6 \mu\text{ohm cm}$  respectively. It has been reported (Sun 1973; Nagano 1980; Craig and Harding 1981) that there is a reduction in grain size and change in morphology due to increase in DC resistivity. These facts give validity to the argument that due to chopping there is change in morphology of the films, a decrease in grain size and enhancement of oxygen affinity. The refractive index and packing density of chopped films are higher than those of non-chopped films (Puri *et al* 1983) indicating a close packed structure formation due to chopping.

A combination of all the above processes seems to be operating in chopped films which is more effective when mixed films are codeposited, the net effect being increase in adhesion of the film.

#### 4. Conclusions

Our studies indicate that mixing by codeposition gives films with better adhesion than single films, the process of chopping enhancing this. The chopping process seems to increase surface mobility, reduces defects and decreases grain size, whereby quenching of crystal growth takes place due to which a more compact film structure is obtained which increases the adhesion of the films. The presence of two different adatom species during codeposition enhances the above effect. Increase in oxygen affinity also seems to be a very dominant effect of chopping.

Chopping along with mixing by codeposition might give wide scope for tailoring of film properties both for microelectronics and optical purposes. The fact that chopped codeposited mixed films age the least (Vijaya *et al* 1987) and that chopped mixed films have higher adhesion indicate the use of chopping technique as a technologically useful process for functional coatings. Non-destructive analysis of the interface may give better insight into the adhesion process due to chopping.

#### Acknowledgement

One of the authors (VP), gratefully acknowledges the award of Research Scientist by the University Grants Commission, New Delhi.

## References

- Craig S and Harding G L 1981 *J. Vac. Sci. Technol.* **19** 205
- Fancey K S and Mathews A 1990 *IEEE Trans. Plasma Sci.* **18** 869
- Ganner P 1986 *Proc. SPIE.* **652** 69
- Guenther H K and Jung E 1976 *Thin Solid Films* **4** 219
- Hiradayanath R, Chopra K N and Grover O P 1979 *Appl. Opt.* **18** 3328
- Jacobs S D, Hrycin A L, Cerqua K A, Kennemore C M and Gibson U J 1986 *Thin Solid Films* **144** 69
- Jacobsson R 1966, 1975 *Physics of thin films* (Academic Press) Vol. 3, Vol. 8 pp. 2 and 53
- Laugier M 1981 *Thin Solid Films* **79** 15
- Martin P J, Macleod H A, Netterfield R P, Pacey C G and Sainty W G 1983 *Appl. Opt.* **22** 178
- Mattox D M 1973 *Thin Solid Films* **18** 173
- Mattox D M and Rigney D A 1986 *Mater. Sci. Eng.* **83** 189
- Nagono J 1980 *Thin Solid Films* **67** 1
- Ogura S 1975 Ph. D. Thesis, New Castle upon Tyne Polytechnic, UK
- Pierce R W and Vaughan J G 1983 *IEEE CHMT.* **6** 202
- Pulkar H K 1982 *Thin Solid Films* **89** 191
- Pulkar H M, Reinhold M and Esposito R 1990 *Laser Optron.* **9** 51
- Puri R K, Vijaya K and Karekar R N 1983 *Pramana - J. Phys.* **21** 311
- Puri R K, Puri Vijaya and Mali S A 1991 *Proc. IVSNS.* 354
- Stoddart C T H, Clarke D R and Robbie C J 1970 *J. Adhesion* **2** 270
- Sun R C 1973 *J. Appl. Phys.* **44** 1099
- Vankar V D, Pandya D K and Chopra K L 1979 *Thin Solid Films* **59** 43
- Vijaya Puri and Puri R K 1993 *Jpn. J. Appl. Phys.* **32**, **10** 4699
- Vijaya K, Puri R K and Karekar R N 1980 *Thin Solid Films* **70** 105
- Vijaya K, Puri R K and Karekar R N 1987 *Pramana - J. Phys.* **28** 277

## Photoconductivity in crystalline phthalocyanines

FRANCIS P XAVIER\* and GEORGE J GOLDSMITH

Physics Department, Boston College, Chestnut Hill, MA 02167, USA

\*Present Address: Physics Department, Loyola College, Madras 600 034, India

MS received 23 September 1994; revised 6 May 1995

**Abstract.** The wavelength, temperature, time and intensity dependence of photocurrent of metal-free phthalocyanine ( $H_2Pc$ ) and copper phthalocyanine ( $CuPc$ ) single crystals were investigated. The thermal activation energies in the dark are 0.5 and 0.6 eV for  $H_2Pc$  and  $CuPc$  respectively and the corresponding photo-thermal activation energies are 0.3 and 0.2 eV. An energy level scheme for single crystals of  $H_2Pc$  and  $CuPc$  is proposed which consists of two trapping levels and five narrow optically active valence bands. In  $H_2Pc$  ( $CuPc$ ), one trapping level at 0.5 eV (0.6 eV) above the valence band edge to which the charge carriers are thermally excited in the dark; and the other trapping level is at 0.3 eV (0.2 eV) below the conduction band edge where all the optical transitions terminate. In  $H_2Pc$  ( $CuPc$ ), the forbidden gap is 1.44 eV (1.34 eV) wide; the five valence bands are at the band edge, and 0.09 (0.22), 0.42 (0.63), 0.69 (0.90), 1.32 (2.17) eV below the band edge.

**Keywords.** Organic semiconductor; photoconductivity.

### 1. Introduction

Phthalocyanines (Pc's) are semiconductors (Inokuchi 1989) that exhibit significant photoconductivity. The most common polymorphic forms of Pc's are designated  $\alpha$ -form and  $\beta$ -form (Moser and Thomas 1963; Gutmann and Lyons 1981; Simon and Andre 1985). The  $\alpha$ -form occurs as polycrystalline films formed by sublimation onto cold substrates, in vacuum, while the  $\beta$ -form, which is the subject of this study, occurs when single crystals are produced by vacuum sublimation at a temperature around 460°C. The crystals are needle-shaped, typically 2 to 3 cm long, 0.03 cm wide and 0.013 cm thick.

### 2. Experimental

Crystals were grown from 99.9% pure phthalocyanine by slow sublimation in vacuum at 460°C, and prepared for measurement by applying silver conducting paint electrodes across the short dimension, separated by between 1 and 2 mm.

The experimental arrangements were as shown in figure 1. Light from a 100 watt quartz-halogen lamp was incident on the sample through a monochromator (Instruments SA, H20 800VIR). The sample, kept enclosed inside a quartz cylindrical tube connected to a vacuum system, was electrically connected in series with a DC power supply and an electrometer (Keithley 614). A potential of 500 V was applied across the electrodes. For the temperature dependence of photoconductivity measurements a heater-coil arrangement and a thermocouple (Constantin-Copper) were used. The readings were registered using a X-Y plotter (YEW 3022 A4).

In  $H_2Pc$  the photoconductivity spectrum over the range 1.00 to 3.50 eV exhibits one large maximum at 1.56 eV with a width at half maximum of 0.17 eV, and a broader large maximum at 2.46 eV with about half the amplitude of the first peak and

half-width of 0.41 eV. There are three additional smaller peaks at 1.14, 1.23 and 1.83 eV (figure 2). In CuPc, the two major peaks appear to have coalesced into a broad feature lying between around 1.59 eV and 2.75 eV with maxima at 1.77 and 2.04 eV (figure 3). The three smaller peaks appear at 1.14, 1.36 and 3.31 eV.

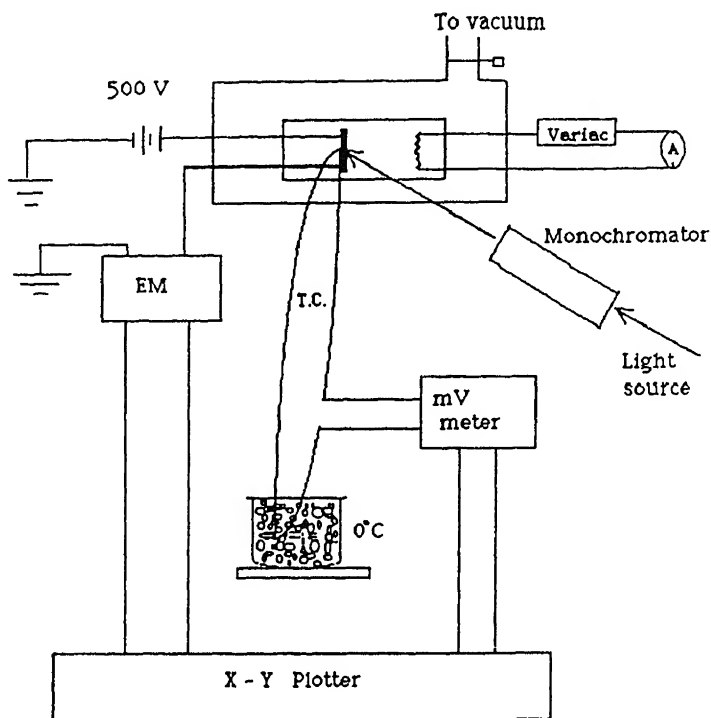


Figure 1. Apparatus for photoconductivity measurement.

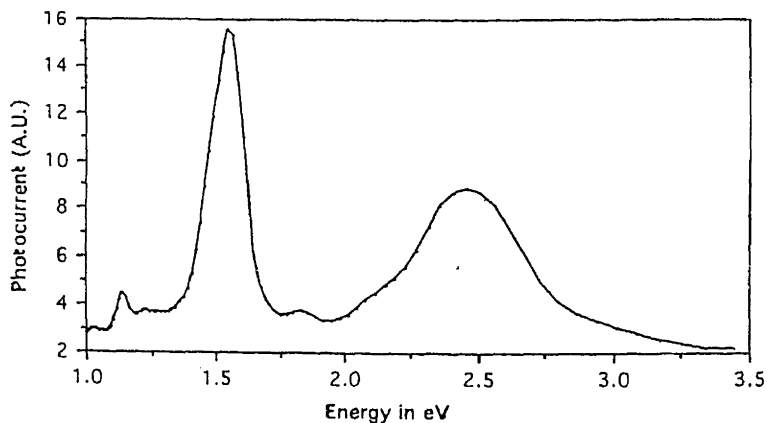


Figure 2. Photoconductivity spectrum of  $H_2Pc$  crystal.

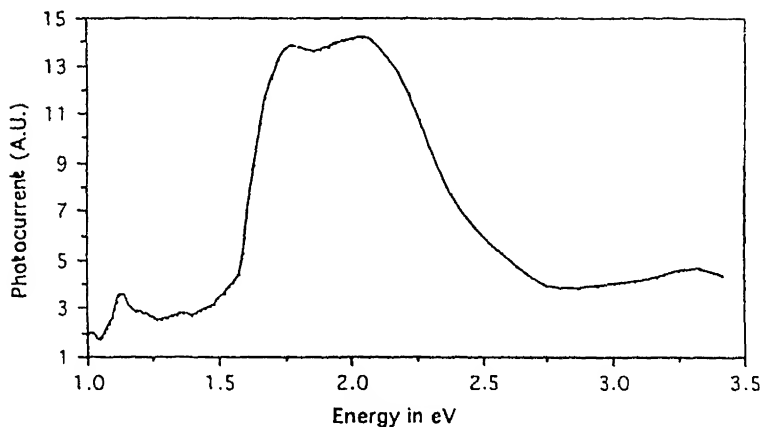


Figure 3. Photoconductivity spectrum of CuPc crystal.

The photocurrent is dependent on the square root of the intensity in both modifications:

$$I_{ph} = (\text{const}) L_{int}^{0.5}. \quad (1)$$

Over the temperature range 100–300 K, the photoconductivity follows the relation

$$\sigma = \sigma_0 e^{-E_i/kT} + C, \quad (2)$$

where  $T$  is the temperature,  $E_i$  the activation energy, and  $C$  represents dark current plus leakage current. Under excitation at wavelengths corresponding to the major peaks the activation energy,  $E_i$ , is 0.3 eV for  $H_2Pc$  (figure 4) and 0.2 eV for CuPc. In the dark, over a similar temperature range, the thermal activation energy for  $H_2Pc$  is 0.5 eV, and for CuPc it is 0.6 eV.

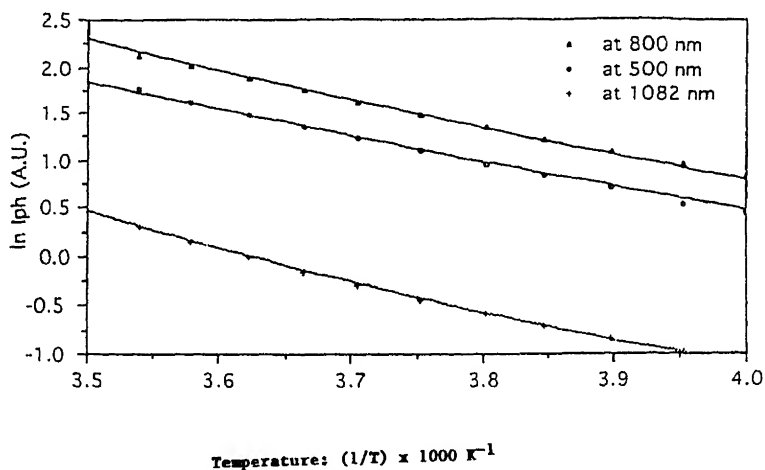


Figure 4.  $\ln I_{ph}$  vs  $(1/T)$  of  $H_2Pc$  crystal.

The time dependences of the photoconductivity at the onset and removal of excitation are exponential with long time constants. A representative plot of the time dependence of photocurrent,  $I_t$ , in  $\text{H}_2\text{Pc}$  illuminated at 800 nm is shown in figure 5a. The rising portion corresponds to the relation

$$I_t = I_0(1 - e^{-t/\tau_r}), \quad (3)$$

where  $t$  is the time and  $\tau_r$  is a characteristic time constant. The resulting value of  $\tau_r$  is 1.55 sec (figure 5b).

The decaying portion corresponds to the relation

$$I_t = I_0(e^{-t/\tau_1} + e^{-t/\tau_2}). \quad (4)$$

The shorter time constant,  $\tau_1$ , is 1.33 sec. The longer time constant,  $\tau_2$ , is 11.4 sec (figure 5c). Simultaneous illumination of the crystal with IR light ( $\lambda > 1100$  nm) results in an approximate doubling of the photocurrent and no change in the rise time but a 30% reduction in the decay time.

### 3. Discussion

We consider first the steady-state characteristic.

With regard to the intensity dependence, it has been suggested (see, e.g. Bube 1960, Rose 1963, Böer 1990) that carrier traffic among multiple trapping levels with the associated shift in the "quasi-Fermi levels" does, under these conditions, yield, in the steady state as found here, a dependence on intensity of the form  $n_i = (g_0/C)^{1/2}$ .

The thermal activation energy in the dark is 0.5 eV for  $\text{H}_2\text{Pc}$  and 0.6 eV for  $\text{CuPc}$ . Under constant illumination it is, respectively, 0.3 and 0.2 eV independent of the exciting wavelength. This behaviour suggests that the effective phototransitions lead to a common terminal state which becomes the source of the thermally excited carriers. On this basis and considering the p-type behaviour of both modifications, the following energy level schemes (figures 6 and 7) emerge.

In  $\text{H}_2\text{Pc}$  there are two electron trapping levels, one 0.5 eV (F) above the valence band edge and a second 0.3 eV (G) below the conduction band edge. Level F serves as a trap for electrons thermally excited in the dark. The common thermal activation for equilibrium photoconductivity at all excitation wavelengths corresponds to a common trapping level 0.3 eV below the conduction band. Electrons trapped into these levels subsequently are either thermally excited into the conduction band, recombine with holes in the valence bands, or are trapped in a trapping level at a lower energy. With the lowest energy valence band at 1.14 eV (E) below the common trapping centre, the two trapping levels are separated by 0.64 eV (G–F) and the entire forbidden gap is 1.44 eV (E–H) wide. The five narrow valence bands are therefore located at the band edge (E) and at 0.09 eV (D), 0.42 eV (C), 0.69 eV (B), and 1.32 eV (A) below the band edge (see figure 6).

In the copper-substituted modification, thermal activation of the photoexcited states places the upper trapping level 0.2 eV (G) below the first conduction band. The dark activation energy places the lower trapping level at 0.6 eV (F) above the first valence band. The five optically active valence bands are at the band edge (E) and at 0.22 eV (D), 0.63 eV (C), 0.90 eV (B), and 2.17 eV (A) below the band edge (see figure 7).

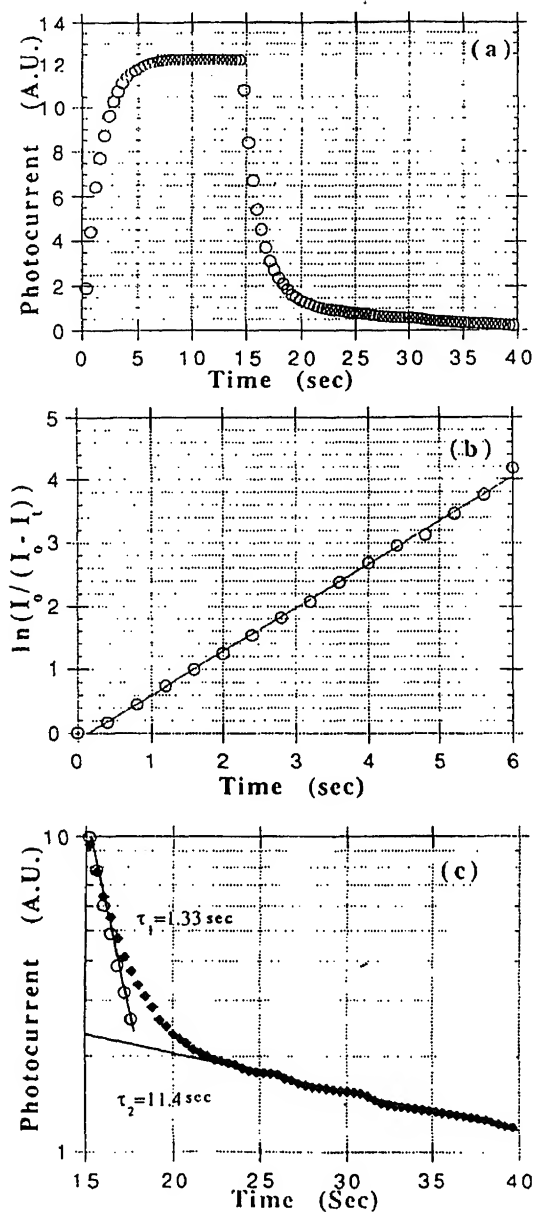


Figure 5. a. Response curve for  $H_2Pc$  crystal, b. rise of photocurrent in  $H_2Pc$  crystal ( $\tau_r = 1.55$  sec) and c. two-step decay curve for  $H_2Pc$  crystal: the shorter time constant  $\tau_1 = 1.33$  sec and the longer time constant  $\tau_2 = 11.4$  sec.

Thus, according to this model, in the dark electrons are excited thermally from band E into trapping level F leaving behind free holes in band E. This would account for the observed thermal dark activation energy. Similarly, electrons optically excited into level G are raised thermally into the lowest conduction band, H, giving rise to the



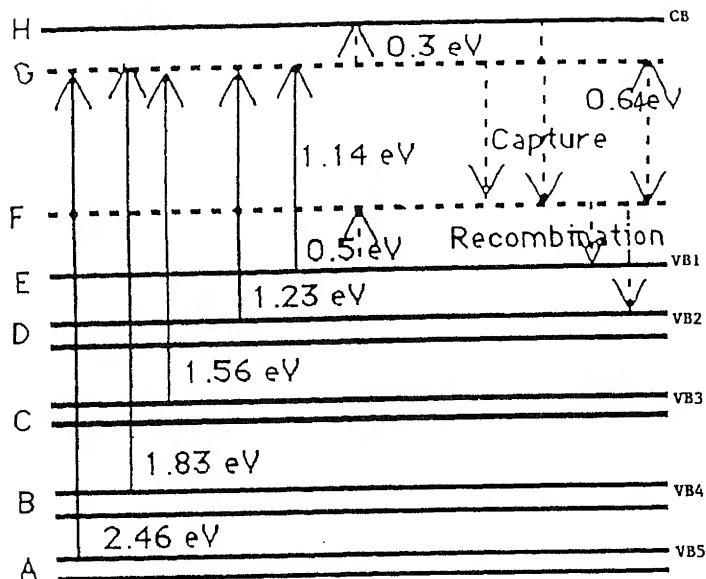


Figure 6. Energy level scheme for  $H_2Pc$  crystal.

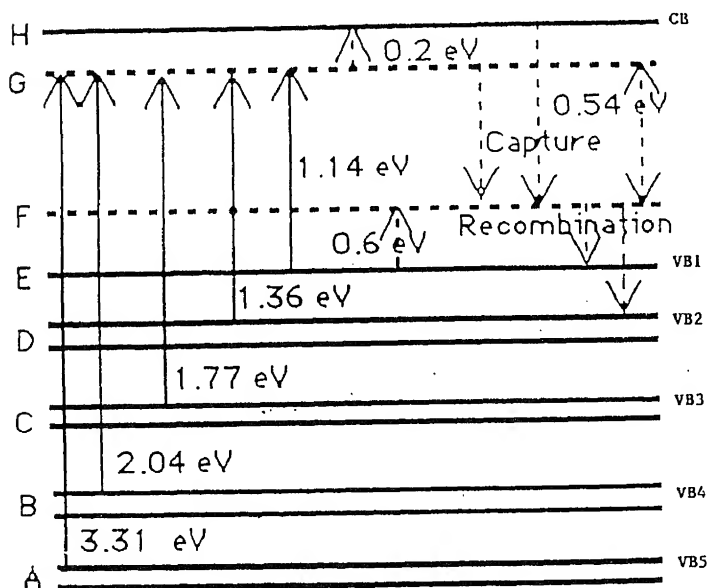


Figure 7. Energy level scheme for  $CuPc$  crystal.

0.3 eV and 0.2 eV activation energy observed respectively for the optically excited states in  $H_2Pc$  and  $CuPc$ .

We consider next the temporal behaviour of the photocurrent (figure 5). Optical excitation raises the electrons to trapping level, G, leaving free holes in the relevant

valence band. Electrons in level G may then either be thermally excited into the conduction band, H, or captured in level F. The capture cross-section to level F both from the lowest conduction band and from level G is evidently sufficiently large to dominate. Level G continues to fill until its rate of decay to the "capture" level, F, equals the optical excitation rate. We assume, also, that electrons promoted thermally to the lowest conduction band are very quickly captured in level F (H to F). Electrons in level F are recaptured by recombining with holes in the valence band.

The two-step decay from equilibrium photocurrent after removal of illumination (figure 5c) results from the sequential electron decay G to F (shorter decay constant), followed by F to the valence bands (longer decay constant).

Infrared stimulation of photocurrent occurs because the magnitude of the photocurrent is limited by the equilibrium populations in the two trapping levels, since the electron holdup in these two levels establishes the concentration of free holes. The effect of the infrared is to excite electrons from the upper valence band into level F and from level G into H. The net effect is to increase the population of free holes in the valence bands, and simultaneously to increase the number of extra electrons in the lower conduction bands. The decrease in the decay time is a consequence of an increase in the population of photoexcited electrons in level F.

## References

- Böer K W 1990 *Survey of semiconductor physics* (New York: Van Nostrand Reinhold)  
Bube R H 1960 *Photoconductivity of solids* (New York: John Wiley)  
Gutmann F and Lyons L E 1981 *Organic semiconductors (Part A)* (Malabar: Krieger)  
Inokuchi H 1989 *Mol. Cryst. Liq. Cryst.* **171** 23  
Moser F H and Thomas A L 1963 *Phthalocyanine compounds* (New York: Reinhold)  
Rose A 1963 *Concepts in photoconductivity and allied problems* (New York: Interscience)  
Simon J and Andre J J 1985 *Molecular semiconductors* (Berlin: Springer)



## Photoconductivity in thin films of phthalocyanine

FRANCIS P XAVIER\* and GEORGE J GOLDSMITH

Physics Department, Boston College, Chestnut Hill, MA 02167, USA

\* Present Address: Physics Department, Loyola College, Madras 600 034, India

MS received 23 September 1994; revised 6 May 1995

**Abstract.** The photocurrent and electrolyte electromodulation (EEM) spectra of thin films of metal-free phthalocyanine ( $H_2Pc$ ) and of copper phthalocyanine ( $CuPc$ ) were investigated. The modulation spectra yielded three distinct features around 1.61, 2.30 and 2.93 eV for  $H_2Pc$  and around 1.63, 2.04 and 3.20 eV for  $CuPc$ . The spectral dependence maxima of photoconductivity correspond to the modulation spectra. These features are interpreted to indicate transitions at critical points, i.e. the existence of transitions between three valence bands, since  $Pc$ 's are p-type, and the lowest conduction band in  $Pc$ 's.

**Keywords.** Organic semiconductors; films; polymer.

### 1. Introduction

Some organic compounds having single-double bond structure, such as anthracene and phthalocyanine ( $Pc$ ), were found to possess semiconducting properties (Inokuchi 1989). The  $Pc$ 's exist in at least three different (polymorphic) modifications (Gutmann and Lyons 1981), the most common of these are designated  $\alpha$ -form and  $\beta$ -form (Kanemitsu *et al* 1991; Qian 1989), and differ slightly in structure and electrical properties. The  $\alpha$ -form is tetragonal, while the  $\beta$ -form is monoclinic (Schoch *et al* 1988). The  $\alpha$ -form has six molecules per unit cell but the  $\beta$ -form has only two molecules per unit cell (Moser and Thomas 1963; Aoyagi *et al* 1971; Robertson 1935, 1936). The  $\alpha$ -form, which is the subject of this investigation, occurs as polycrystalline films when sublimed under vacuum onto cool (room temperature) substrates, while the  $\beta$ -form is crystallized into single crystals by vacuum sublimation at a temperature around 460°C.

Modulation technique is used to obtain sharp, well-resolved spectra that can be analysed to yield directly the properties of the material under study (Aspnes 1973), for example the band structure. In electromodulation the applied electric field on the material under study produces changes in the dielectric function associated primarily with interband transitions at the critical points (Bordas 1976). Thus the electromodulation is of greatest importance in studying the band structure of a semiconductor. This technique provides optimum sensitivity for the detection of weak or closely spaced critical points. Electrolyte electromodulation techniques on thin films could be used to gain further insight into details of the band structure of the material under study.

Under the influence of an electric field the energy bands of the semiconductors are tilted and an electron, in order to tunnel from the valence band to the conduction band, meets with a triangular barrier. Further, as the electron tunnels through the barrier if it interacts with a photon the effective width of the barrier becomes smaller

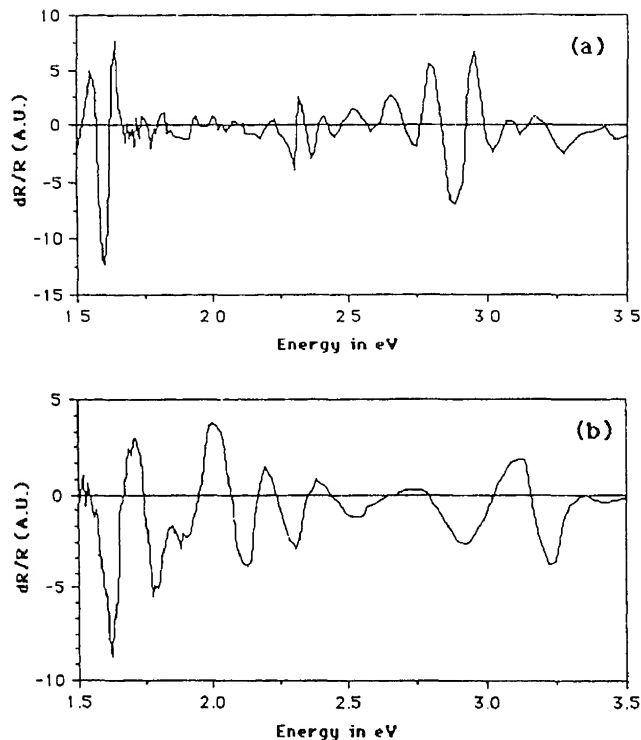


Figure 1. Electromodulation spectrum of (a)  $H_2Pc$  film and (b)  $CuPc$  film.

## 2. Experimental

Films of metal-free phthalocyanine ( $H_2Pc$ ) and of copper phthalocyanine ( $CuPc$ ) were prepared (for room-temperature electrolyte electromodulation studies) by vacuum sublimation (at  $10^{-6}$  torr) atop an aluminium electrode which had been deposited onto pre-cleaned glass microscope slides. Electrical connections were made to the aluminium electrode by means of thin copper wire (0.08 mm) fixed by air-dried silver conducting paint. The electrode was isolated from coming into contact with the electrolyte by spreading a thin layer of paraffin exposing only the  $Pc$  thin film to the electrolyte. The sample thus prepared was inserted into an electrolyte consisting of ethylene glycol containing a trace of dry  $KOH$ . A platinum electrode was inserted into the solution to complete the electrical circuit.

The electromodulation (EM) measurements were carried out at room temperature using modulation spectroscopy. Modulation spectroscopy involves the application of a periodic perturbation (here electrical field, i.e. square waves of p-p amplitude between 2 and 16 V at a frequency of 235 Hz) to the material under study. By separating the effect of the perturbation from the reflection or absorption background using lock-in phase-sensitive detection, the periodic modulation of the optical properties of the material (Aspnes *et al* 1968) is recorded by scanning over a wavelength range. The measured output was proportional to  $dR/R$ , with  $R$ , the reflectance.

The EM spectra were characterized by three spectral regions where there were prominent features. In  $H_2Pc$  the first extends between 1.5 and 1.7 eV, the second between 2.3 and 2.4 eV and the third between 2.8 and 3 eV as shown in figure 1a. In the case of  $CuPc$  the regions were broader, the first extending from 1.5 to 1.7 eV, the second from 1.9 to 2.1 eV and the third from 2.9 to 3.3 eV as shown in figure 1b (Tokura *et al* 1983). The oscillatory structures after the second and third prominent features on the higher energy side are Franz-Keldysh oscillations.

The spectral dependence of the photoconductivity was measured in the range between 1.5 and 3.5 eV at room temperature. The resulting spectra are illustrated in figures 2a and 2b. In both  $H_2Pc$  and  $CuPc$ , the spectra are characterized by an initial peak at about 1.60 eV followed by broad, shallow maxima. The maxima occur around 1.64, 1.84, 2.29 and 2.93 eV for  $H_2Pc$  and around 1.59, 1.85, 2.39 and 2.92 eV for  $CuPc$ .

### 3. Discussion

The first of the prominent features in the EM spectra (figures 1a and 1b) are third-derivative-like. Features such as these are interpreted to indicate transitions between critical points. On the assumption that electroreflection/absorption spectra in these materials are analogous to those from inorganic semiconductors, the Aspnes three-point method (Aspnes 1973) was applied to compute the transition energies at the critical point. These are at 1.61 eV for  $H_2Pc$  and at 1.63 eV for  $CuPc$ .

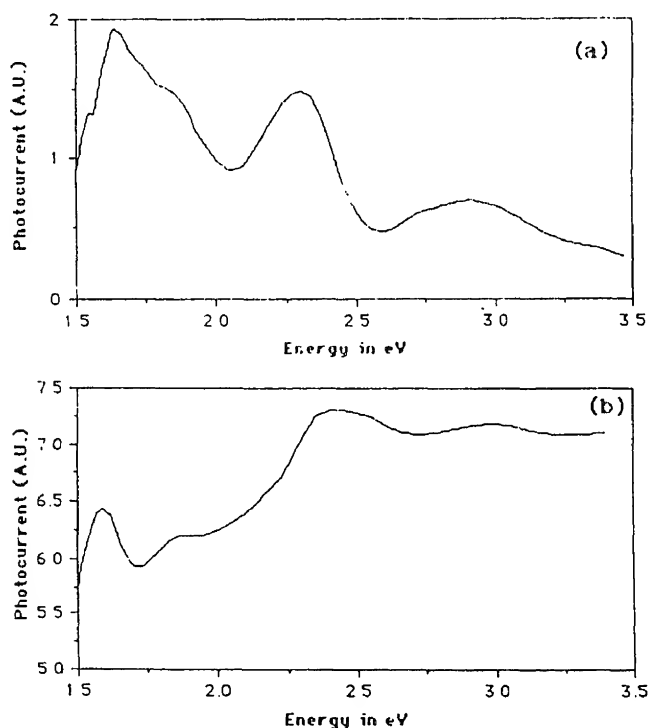


Figure 2. Photoconductivity spectrum of (a)  $H_2Pc$  film and (b)  $CuPc$  film.

The oscillatory features (the second and third prominent features) in the EM spectra (figures 1a and 1b) are interpreted as photon energies above the absorption edge (Pollak *et al* 1993) corresponding to the transition energies at the critical points. These energies are calculated using the Aspnes three-point method to be 2.30 and 2.93 eV for H<sub>2</sub>Pc and 2.04 and 3.20 eV for CuPc.

Even poorly conducting molecular materials exhibit photoconduction (Wright 1989). When the material is subjected to exciting radiation many electron and hole pairs are created. These will drift, under the influence of the applied field, giving rise to photocurrent. The threshold of light absorption normally corresponds to excitation of an electron from the valence band to the conduction band, which in turn corresponds to the maxima in the photoconductivity spectrum.

The photoconductivity maxima of H<sub>2</sub>Pc and CuPc are indicated in figures 2a and 2b which correspond to the maxima of EM spectra as shown in table 1. The maxima of the photoconductivity spectra are interpreted as the many possible electronic transitions. These photoactive transitions are assumed to take place within the  $\pi$ -electron system of the phthalocyanine molecule. Since the material under study is p-type (Epstein 1960; Eley 1962; Heilmeyer 1962; Gutmann and Lyons 1981), its transport characteristics involve electron traps. So it is assumed that the net effect of photoconduction is to increase the population of free holes in the valence bands and each of the prominent maxima corresponds to an energy level in the valence band.

**Table 1.** Comparison of maxima of electromodulation and photoconductivity spectra of H<sub>2</sub>Pc and CuPc thin films.

Metal-free phthalocyanine		Copper phthalocyanine	
Electroreflectance	Photoconductivity	Electroreflectance	Photoconductivity
1.5–1.7 eV	1.64 eV 1.84 eV	1.5–1.7 eV	1.59 eV 1.85 eV
2.3–2.4 eV	2.29 eV	1.9–2.1 eV	2.39 eV
2.8–3.0 eV	2.93 eV	2.9–3.3 eV	2.92 eV

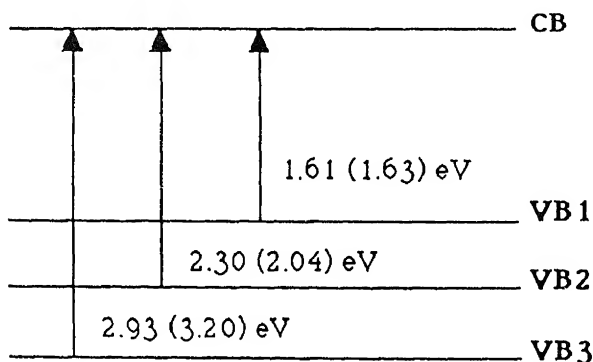


**Figure 3.** Proposed band diagram of H<sub>2</sub>Pc (CuPc) film.

Thus these observations indicate that the maxima in the ER spectra corresponding to those in the photoconductivity spectra are transitions at critical points which most likely occur between three narrow valence bands and the lowest conduction band. Figure 3 illustrates the band structure model for thin films of phthalocyanine where transitions at critical points for  $H_2Pc$  (CuPc) are indicated. In the case of  $H_2Pc$  there are three distinct third-derivative-like features at 1.61, 2.30 and 2.93 eV which are transition energies at the critical points and in the case of CuPc the transition energies at the critical points are 1.63, 2.04 and 3.20 eV. The maximum seen in the photoconductivity spectrum (figures 2a and b) around 1.84 (1.85) eV for  $H_2Pc$  (CuPc) is ascribed to excitonic level.

## References

- Aoyagi Y *et al* 1971 *J. Phys. Soc. Jap.* **31** 164  
 Aspnes D E 1973 *Surf. Sci.* **37** 418  
 Aspnes D E *et al* 1968 *Phys. Rev.* **166** 921  
 Bordas J 1976 Some aspects of modulation spectroscopy in layer materials, in *Optical and electrical properties* (ed.) P A Lee (Dordrecht-Holland: Reidel)  
 Eley D D 1962 *Mol. Cryst. Liq. Cryst.* **171** 1  
 Epstein A *et al* 1960 *J. Chem. Phys.* **32** 324  
 Gutmann F and Lyons L E 1981 *Organic semiconductors (Part A)* (Malabar: Krieger)  
 Heilmeyer G H *et al* 1962 *Phys. Rev. Letts.* **8** 309  
 Inokuchi H 1989 *Mol. Cryst. Liq. Cryst.* **171** 23—The term "Organic Semiconductors" is applied to the group of conjugated single/double bond compounds such as polycyclic aromatics and Pc's  
 Kanemitsu Y *et al* 1991 *J. Appl. Phys.* **69** 7333—In the case of  $H_2Pc$  the other polymorphs are called as  $\chi$ - and  $\tau$ -forms  
 Moser F H and Thomas A L 1963 *Phthalocyanine compounds* (New York: Reinhold)  
 Pollak F H *et al* 1993 *Mater. Sci. Eng.* **R10** 275  
 Qian R 1989 *Mol. Cryst. Liq. Cryst.* **171** 117—The other polymorphs forms in the case of CuPc are known as  $\delta$ -,  $\epsilon$ -,  $\chi$ - and  $\pi$ -forms  
 Robertson M 1935 *J. Chem. Soc.* 615  
 Robertson M 1936 *J. Chem. Soc.* 1195  
 Schoch K F *et al* 1988 *J. Vac. Sci. Technol.* **A6** 155  
 Tokura Y *et al* 1983 *Chem. Phys. Letts.* **102** 174—Our room temperature EM spectrum of CuPc film is the same as that measured by Tokura *et al* on CuPc single crystals at 77°K with a phase shift of 180°  
 Wright J D 1989 *Molecular crystals* (Cambridge: Cambridge University Press)





# Photoconductivity of iodine-doped single crystals of phthalocyanine

FRANCIS P XAVIER\* and GEORGE J GOLDSMITH

Physics Department, Boston College, Chestnut Hill, MA 02167, USA

\* Present Address: Department of Physics, Loyola College, Madras 600 034, India

MS received 23 September 1994; revised 6 May 1995

**Abstract.** Single crystals of metal-free phthalocyanine ( $H_2Pc$ ) and of copper phthalocyanine ( $CuPc$ ) were grown in the presence of iodine vapour. The presence of iodine enhances the spectral dependence of photoconductivity of  $H_2Pc$  in the visible region but of  $CuPc$  in the near-IR region. The dark current is decreased but the photocurrent is increased by one order of magnitude in iodine-doped  $H_2Pc$  but in the case of iodine-doped  $CuPc$  both currents are increased by nearly three orders of magnitude. Introduction of iodine results in about one order of magnitude decrease in response time for both modifications. Thus the introduction of iodine into  $Pc$  crystals decreases the energy barrier for conduction and increases the drift mobility of charge carriers thereby enhancing the conductivity of the material.

**Keywords.** Photoconductivity; doping; organic semiconductor.

## 1. Introduction

Study of doped semiconductors has proven useful in the area of electronic technology today. Some organic materials which have a structure of conjugated single/double bond chain possess photoconductivity (Inokuchi 1989). Doping of photoconductors by suitable dopants has been shown to increase the conductivity of materials (Schramm *et al* 1980; Hoffman *et al* 1983; Barbaszweski *et al* 1986; Zabkowska-Waclawek *et al* 1987; Orihashi *et al* 1988; Harikumar *et al* 1989) by several orders of magnitude (Waclawek *et al* 1987). The doping is, in general, done by diffusion, i.e. exposing the crystals to iodine vapour for a few hours. But in this investigation single crystals of metal-free phthalocyanine ( $H_2Pc$ ) and copper phthalocyanine ( $CuPc$ ) were grown in the presence of iodine vapour.

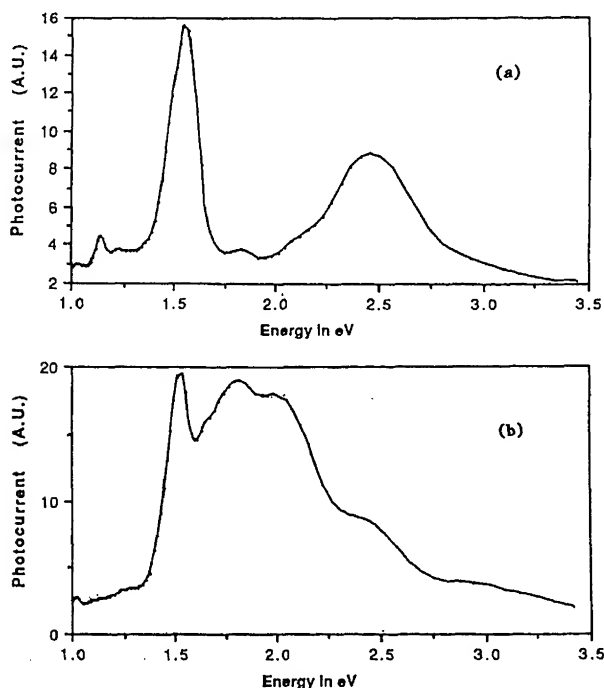
## 2. Experimental

In a Pyrex tube 20 cm long and 3.5 cm in diameter fitted with a side arm, phthalocyanine powder (about 5 g) was placed. A few iodine crystals were placed in the side arm. The Pyrex tube was then evacuated. Because of the high vapour pressure of iodine the pressure could not be brought below about 40 millitorr but with the use of a liquid nitrogen trap to lower the iodine vapour pressure, the pressure was brought down to a few millitorr before sealing off the tube. The main tube was inserted into a temperature-controlled oven leaving the side arm outside the oven near room temperature. Crystal growth was then allowed to proceed. For iodine-doped metal-free phthalocyanine ( $HPcI$ ) single crystal growth the temperature at the point where  $Pc$  powder was placed was maintained at  $460^\circ\text{C}$ , whereas the iodine-doped copper phthalocyanine ( $CuPcI$ ) single crystals started growing only when the temperature was raised to  $500^\circ\text{C}$ . The crystals appeared in the form of clusters of hundreds of whiskers with dimensions of about  $15\text{ mm} \times 0.3\text{ mm} \times 0.13\text{ mm}$ . The colour of the

crystals was dark red. The crystals were tested for the presence of free iodine by rinsing them with trichloroethylene. In no case was the characteristic purple colour of free iodine observed. Further the doped crystals were heated up to 100°C and it was established, from the study of the photoconductivity spectra, that the iodine was stable in the doped crystals.

For the study of the spectral behaviour of the photoconductivity, the samples were mounted on a glass substrate. Electrode contacts, spaced 1 to 2 mm along the crystal growth axis (*b* axis), were attached to the crystals using silver paint and thin copper wires. The sample thus prepared was connected in series with an electrometer (Keithley 614) and a DC power supply. A potential of 500 V DC was applied across the sample. The photoconductivity was measured as a function of wavelength by use of a monochromator. In the case of undoped  $H_2Pc$  the photoconductivity spectrum exhibits maxima at about 1.14, 1.23, 1.56, 1.83 and 2.46 eV (figure 1a). The spectrum of iodine-doped crystal (HPcI) retains the same maxima as in the undoped material. There is, however, an additional broad maximum at about 2.1 eV (figure 1b). In the case of CuPc undoped crystal the photoconductivity spectrum exhibits maxima at about 1.14, 1.36, 1.77, 2.04 and 3.31 eV (figure 2a). But the photoconductivity spectrum of CuPcI differs markedly from that of the undoped form. The major response is shifted entirely toward the red end of the spectrum (figure 2b) with maxima at about 1.05, 1.19, 1.26, 1.49 and 2.44 eV.

Comparison of the doped-during-growth crystals with the undoped crystals reveals that the dark current in the unsubstituted modification is decreased by one order of



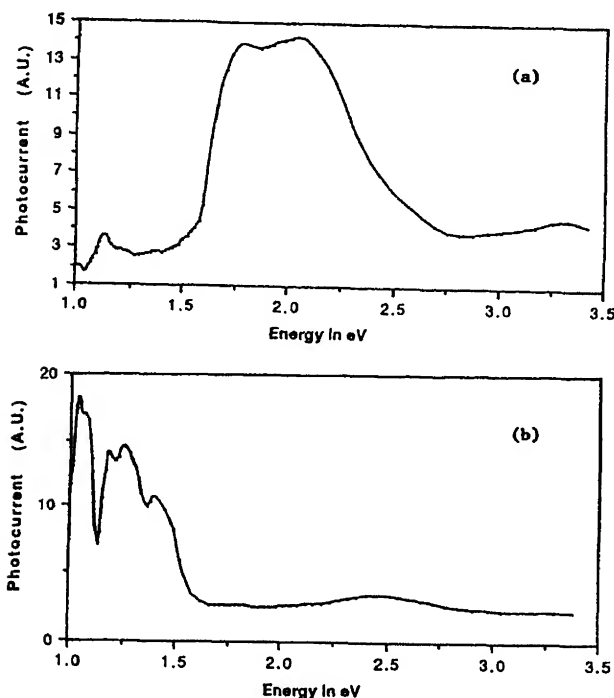


Figure 2. Spectral dependence of photoconductivity of (a) single crystal of CuPc and (b) iodine-doped single crystal of CuPc.

Table 1. Comparison of iodine-doped crystals with undoped crystals.

	H <sub>2</sub> Pc	HPcI	CuPc	CuPcI
Dark current (amp)	$4.45 \times 10^{-11}$	$3.15 \times 10^{-12}$	$1.82 \times 10^{-13}$	$1.13 \times 10^{-10}$
Photocurrent (amp)	$1.86 \times 10^{-9}$	$1.12 \times 10^{-8}$	$2.53 \times 10^{-12}$	$2.76 \times 10^{-9}$
Rise time (sec)	1.37	0.10	1.97	0.28
Decay time (sec)	2.20	0.09	2.68	0.18

magnitude upon doping while in CuPcI it is increased by nearly three orders of magnitude upon doping as shown in table 1. The discrepancy in the case of the copper-substituted Pc may be due to the leakage current in the circuit. For the purpose of measuring the photocurrent, light from a quartz-halogen lamp (through the monochromator at zero order) was incident on the sample and the corresponding current in the circuit noted using an electrometer (Keithley 614). The photocurrent at similar conditions of incident intensity is greater in HPcI than in H<sub>2</sub>Pc by one order of magnitude and it is three orders of magnitude greater in CuPcI than in CuPc (Grigoryan *et al* 1984; Wacławek *et al* 1987) as shown in table 1. All the samples

investigated—both undoped and iodine-doped—exhibited pronounced photoconductivity along the *b*-axis, while no photoconductive response was observed perpendicular to this direction.

The illumination was modulated by means of a standard camera leaf shutter capable of opening and shutting within 0.01 sec or faster. From the current measuring circuit the output of the electrometer was led to a strip chart recorder ( $t_r = 0.1$  sec; maximum chart speed 30 cm/min). Light from the source was incident on the crystal through the monochromator set at zero order and fitted with the camera shutter. The measurements were carried out at room temperature. The procedure was first to illuminate the sample for a few seconds and then close the shutter while recording the decay of the photocurrent. After the current reached its minimum value, the shutter was opened and the steady-state current was allowed to rise till it attained a constant value once more. The rise and decay times were measured between 10% and 90% points using an oscilloscope (Hitachi V-222). In the iodine-doped crystals the response time were lower by one order of magnitude for both modifications (table 1).

### 3. Discussion

The introduction of iodine into a Pc results in a new material where the dopant iodine is stable since heating of the iodine-doped material up to 100°C does not alter the characteristics of the doped crystal. In the case of HPcI, the introduction of iodine seems to populate all the energy levels between 1.56 and 1.83 eV and also those between 1.83 and 2.4 eV (figures 1a and 1b). The level corresponding to the energy level at 1.83 eV which is seen in the undoped  $H_2$ Pc is still seen in the iodine-doped crystal. Due to the population increase in this level also, the photocurrent seen at 1.83 eV in the doped crystal is higher than that seen for the undoped crystal. In the case of CuPcI, the material becomes photoactive in the near-infrared range of the spectrum on doping with iodine, in lieu of its activity between 1.6 to 2.5 eV in the undoped crystal (figures 2a and 2b). The valence band in the CuPcI crystal is therefore continuous for energies higher than about 1.6 eV. The increase of photocurrent in iodine-doped crystal indicates that the iodine makes the crystal more photosensitive. Since the Pc's are p-type material and iodine is an electron acceptor, introduction of iodine probably enhances the mobility of holes acting as a trap for electrons. The shorter rise and decay times in the iodine-doped crystals probably indicate that the drift mobility of charge carriers is greater since the lifetime of charge carriers in the traps is shorter. Based on this experimental evidence we could conclude that the introduction of iodine into Pc crystals decreases the energy barrier for conduction and increases the drift mobility of charge carriers thereby enhancing the conductivity of the material.

### References

- Barbaszweski T *et al* 1986 *Phys. Status Solidi* **a94** 419
- Grigoryan L S *et al* 1984 *Phys. Status Solidi* **a84** 597—Grigoryan *et al* found no marked difference in the case of iodine doped CuPc crystals (iodine was doped by diffusion)
- Harikumar P S *et al* 1989 *J. Mater. Sci. Letts.* **8** 969
- Hoffman B M *et al* 1983 *Acc. Chem. Res.* **16** 15
- Inokuchi H 1989 *Mol. Cryst. Liq. Cryst.* **171** 23

Orihashi Y *et al* 1988 *Mol. Cryst. Liq. Cryst.* **160** 139

Schramm C J *et al* 1980 *J. Am. Chem. Soc.* **102** 6702

Waclawek W *et al* 1987 *Thin Solid Films* **146** 1—Waclawek *et al* reported seven to nine orders of magnitude increase in photocurrent for PbPc (iodine was doped by diffusion)

Zabkowska-Waclawek M *et al* 1987 *Mater. Sci.* **13** 315



## Growth mechanism of $\text{NaBrO}_3$ crystals from aqueous solutions

V SURENDER and K KISHAN RAO\*

Department of Physics, Kakatiya University, Warangal 506 009, India

MS received 27 March 1995; revised 15 May 1995

**Abstract.** To study the growth mechanism of  $\{111\}$  faces of  $\text{NaBrO}_3$ , crystals were grown at different supersaturations ranging from 2% to 8%. The growth mechanisms were investigated based on the growth rate versus supersaturation relation and from the surface features observed on  $\{111\}$  faces. The growth mechanism of these crystals appear to be due to 2D nucleation. The growth rate curve has been further investigated using Ohara and Reid equations. Polynucleation model in two-dimensional nucleation growth theory is suggested as the most possible growth mechanism for these crystals in the present supersaturation range.

**Keywords.**  $\text{NaBrO}_3$ ; supersaturation; growth rate.

### 1. Introduction

To understand the mechanism of growth of crystals from solution, several investigators have focused attention on growth kinetics. Among the crystals grown from solution, extensive studies have been made on K-alum (Bennema 1965), KCl (Klein-Haneveld 1971), ADP (Mullin and Gaska 1969), and KDP (Mullin and Amatavivadhana 1967). Kitamura *et al* (1982) carried out simultaneous growth and dissolution studies on  $\text{NaClO}_3$  crystals.

Sodium bromate ( $\text{NaBrO}_3$ ) belongs to the cubic tetrahedral class with point group 23.  $\text{NaBrO}_3$  is isomorphous with  $\text{NaClO}_3$  and exhibits properties like optical activity (Chandrasekharan and Madhava 1967) and piezoelectricity (Mason 1946). Although considerable information is available on the growth of  $\text{NaClO}_3$ , there is no report on the growth of  $\text{NaBrO}_3$ . Hence we planned to study the growth of  $\text{NaBrO}_3$  crystals systematically. Preliminary results of these studies are reported in this paper.

### 2. Experimental

#### 2.1 Solubility and supersaturation of sodium bromate

Solubility data on sodium bromate at various temperatures are not available. Hence solubility measurements were made at temperatures ranging between 25°C and 60°C. For this purpose approximate saturated solutions were prepared at the required temperatures by adding a known amount of solute to 100 ml of double distilled water. Sufficient care was taken to see that the solution was always slightly undersaturated. Then a crystal of known size and mass was introduced into the solution and held in the middle of the solution with the help of a holder. In most of the experiments, initially the crystal dissolved slightly and then it stabilized with the solution. The



crystal was allowed to remain in this condition for about 6–8 h. When the crystal appeared to start growing, it was removed from the solution and its size and mass were again measured. During the whole process the solution in the jar was stirred and the process observed using a cathetometer. All these experiments were conducted in a constant temperature bath. The mass of the solute plus the loss of mass of crystal gives the solubility at that temperature. For each temperature, the solubility measurements were made at least 4 to 5 times and the average value taken as the solubility at that temperature. The variation of solubility with temperature is shown in figure 1.

Supersaturation of the solution is expressed as

$$S = \frac{C}{C_s} - 1, \quad (1)$$

where  $C$  is the concentration of the dissolved substance at a given moment,  $C_s$  the saturation concentration, and  $S$  the supersaturation.

## 2.2 Crystallization

All the crystals were grown from aqueous solutions at a constant temperature of 30°C at different supersaturations between 2% and 8%. A water circulation thermostat obtained from INSREF was employed which provides  $\pm 0.05^\circ\text{C}$  constancy of temperature. The thermostat was initially adjusted to a temperature of 30°C.

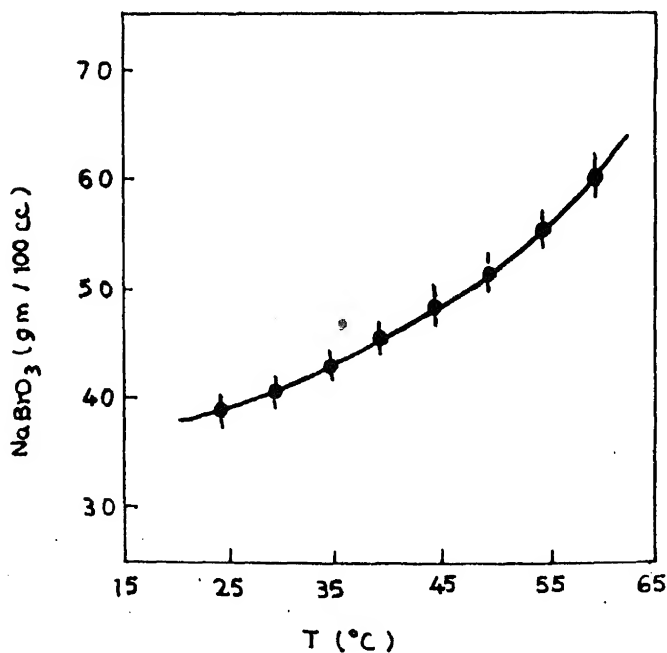


Figure 1. Solubility data of sodium bromate.

Supersaturated solutions were prepared at temperature  $2-3^\circ\text{C}$  above  $30^\circ\text{C}$  and transferred into the crystallization jar (250 ml) until two thirds of it was filled with the solution. The jar was then closed with a rubber cork fitted with a thermometer. When the temperature reached  $30^\circ\text{C}$ , a seed crystal was introduced into the supersaturated solution. Seed crystals were grown in another beaker at  $30^\circ\text{C}$  by slow evaporation. The seed crystals were mounted on a plastic platform with the help of an adhesive. For growth rate measurements, initial and final dimensions of the crystal were measured using a travelling microscope. From these values and time of growth, the growth rates were estimated. The time of crystallization was not constant for all the crystals but varied from 10 to 36 h depending upon the supersaturation of the solution. In the present work all the crystals were allowed to grow in a static system.

### 3. Results and discussion

#### 3.1 Growth rate versus supersaturation

Sodium bromate crystals grow in tetrahedral form bounded by two sets of  $\{111\}$  faces as shown in figure 2a. Figure 2b shows the line diagram of the crystal faces. One set of  $\{111\}$  faces grows to a larger size than the other. The larger faces are called major  $(111)$  faces and the other faces minor  $(111)$  faces. The present studies are confined to the major  $(111)$  faces which are more stable.

As the crystals are bounded by triangular  $\{111\}$  faces, the edges of each face are along  $\langle 110 \rangle$  direction. Hence, for the rate-of-growth experiments the initial and final dimensions of the crystals before and after the growth were measured along the three



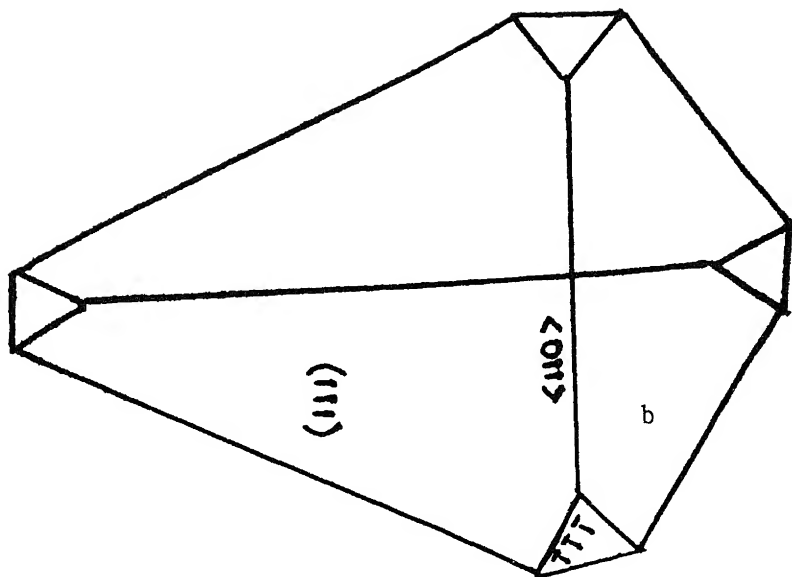


Figure 2. a. Sodium bromate crystals grown at different supersaturations ( $\times 3$ ) and b. line diagram of sodium bromate crystal faces.

$\langle 110 \rangle$  directions. The average of these was taken as the size of the crystal. Figure 2a shows some of the crystals grown at various supersaturations. It can be seen from the photograph that all the crystals grown under these supersaturations are bounded by two sets of  $\{111\}$  faces as mentioned above with no change in morphology.

Growth rates of  $(111)$  faces of sodium bromate crystals were measured in about 50 different runs in a relative supersaturation range 2% to 8%. The measured growth rates were in the range  $8 \times 10^{-6}$  to  $40 \times 10^{-6}$  cm/sec. The rate-of-growth data for different supersaturations is given in tables 1 and 2.

Figure 3a shows the plot of rate of growth versus supersaturation. Each point is the average of at least six measurements. Figure 3b shows the same plot with all the data points. It is clearly seen that the rate of growth increases parabolically with supersaturation with some scattering of data points at higher supersaturations. A similar observation was made in growth rate studies on sodium chlorate (Hosoya and Kitamura 1978) and barium nitrate crystals (Tsukamoto *et al* 1983). Tsukamoto *et al* (1983) attributed the scattering of data points at higher supersaturation in barium nitrate crystals to rapid nucleation of material on the walls of the vessel. In the present study no such nucleation was observed. But small tiny crystals were found on the base of the jar at higher supersaturation. This could be the reason for the scattering of data points at higher supersaturations. The variation of growth rate at the same supersaturation (figure 3b) could be due to differences in external and internal conditions in each growth experiment, such as turbulence, mass transfer caused by convection, temperature distribution in the crystallization chamber, or defect densities already

**Table 1.** Summary of the experimental data.

S (%)	$R(10^{-6})$ (cm/sec)
2.0	6.10
2.0	6.81
2.2	8.30
2.3	11.40
2.4	9.75
2.4	9.75
2.4	11.30
2.4	14.20
2.4	10.60
2.8	14.00
2.8	13.70
2.8	16.60
2.8	17.00
2.8	10.00
2.8	13.00
2.8	18.00
4.0	18.60
4.1	24.40
4.2	24.40
4.2	18.60
4.3	19.40
4.3	21.00
5.0	29.40
5.0	30.00
5.3	27.00
5.6	22.00
6.0	28.40
6.8	24.00
6.8	40.00
6.8	40.30
7.0	51.00
7.8	45.00
8.2	40.00

**Table 2.** Values (with standard errors) of slope and intercept in equations for 2D growth mechanism, which are calculated from curve fitting.

Parameter	Growth models		
	Mononuclear	Polynuclear	Birth and spread
Intercept	-8.49 ( $\pm 0.18$ )	-1.56 ( $\pm 0.22$ )	-7.77 ( $\pm 0.18$ )
Slope	-0.0078 ( $\pm 0.0025$ )	-0.029 ( $\pm 0.003$ )	-0.012 ( $\pm 0.002$ )
Regression coefficient	0.73	0.96	0.42

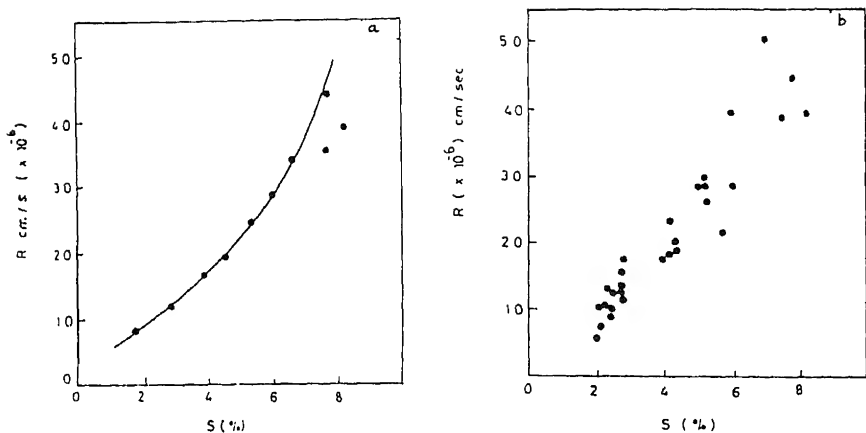


Figure 3. a. Plot of growth rate ( $R$ ) versus supersaturation ( $S$ ) for sodium bromate crystals and b. shows all the data points.

In growth rate studies on  $\text{NaClO}_3$  crystals Hosoya *et al* (1978) obtained a parabolic curve at higher supersaturation, but the data of Bennema (1965) gave a linear growth rate plot at lower supersaturation. They concluded that the linear plot indicates growth due to screw dislocation mechanism and the parabolic curve points to growth due to two-dimensional mechanism. In the present work, the supersaturation range is higher than 2%. Hence it appears that the parabolic plot obtained in sodium bromate could be due to two-dimensional growth mechanism.

In two-dimensional nucleation growth theory three models have been put forward by Ohara and Reid (1973). The normal growth rates are expressed by the following equations:

(i) Mononuclear (mono-) model,

$$R = A_{\text{mono}} [\ln(1 + S_B)]^{1/2} \exp[-3B/T_g^2 \ln(1 + S_B)]; \quad (2)$$

(ii) Polynuclear (poly-) model,

$$R = [A_{\text{poly}}/T_g^2 (\ln(1 + S_B))^{3/2}] \exp[-3B/T_g^2 \ln(1 + S_B)]; \quad (3)$$

(iii) Birth and spread (B and S) model,

$$R = [A_{\text{B\&S}} S_B^{2/3} / \ln(1 + S_B)]^{1/6} \exp[-B/T_g^2 \ln(1 + S_B)]; \quad (4)$$

where the constants are given as

$$A_{\text{mono}} = \left(\frac{2}{\pi}\right) n_1^2 \bar{V} \left(\frac{V_m}{h}\right)^{1/2} S, \quad (5)$$

$$A_{\text{poly}} = 2\bar{V} \left(\frac{\sigma n_1}{k}\right)^2 h^{1/2} V_m^{5/2}, \quad (6)$$

$$A_{\text{B\&S}} = 2h^{1/6} V_m^{5/6} \left(\frac{\bar{V}}{\pi}\right)^{1/3} \left(\frac{n_1 D_S C_{\text{SE}}}{X_S}\right)^{2/3}, \quad (7)$$

where  $n_1$  is the equilibrium number of mono-molecules on the surface,  $\bar{V}$  the average speed of surface adsorbed molecule,  $V_m$  the volume of a molecule,  $h$  the step height as lattice constant,  $D_s$  the solution diffusion coefficient on the surface,  $C_{SE}$  the equilibrium surface concentration,  $X_s$  the mean diffusion distance in mean lifetime of adsorbed molecule on the surface,  $S_B$  the solution supersaturation,  $T_g$  the growth temperature and  $\sigma$  the interfacial free energy.

$$B = \frac{\pi h \sigma^2 V_m}{3 K^2}. \quad (8)$$

The three equations can be rewritten as follows:

$$\ln \left[ \frac{R}{[\ln(1 + S_B)]^{1/2}} \right] = - \frac{3B}{T_g^2 \ln(1 + S_B)} + \ln A_{\text{mono}}, \quad (9)$$

$$\ln [R \cdot T_g^2 (\ln(1 + S_B))^{3/2}] = - \frac{3B}{T_g^2 \ln(1 + S_B)} + \ln A_{\text{poly}}, \quad (10)$$

$$\ln \left[ \frac{R}{S_B^{2/3} [\ln(1 + S_B)]^{1/6}} \right] = - \frac{B}{T_g^2 \ln(1 + S_B)} + \ln A_{B\&S}. \quad (11)$$

In the present work, an attempt has been made to assess the applicability of (9), (10) and (11). It can be seen from these equations that a linear plot should be obtained by plotting left hand side versus  $1/[\ln(1 + S_B)]$  for all the three equations. The three-plots are shown in figures 4a, 4b and 4c. The solid lines are obtained by least-squares fit. All the three plots are roughly linear with some scattering of data points. It can be seen from these plots that the data points fit best with (10) (figure 4b); next comes (9); the fit with (11) is clearly the poorest. The values of slopes, intercepts and regression coefficients were obtained by computation and are given in table 2 along with their standard errors. From an observation of the values of regression coefficient in the three models, relation (10) for the poly-model fits best with the present experimental data.

However, it is not possible to draw conclusions about the relative merits of the three equations very forcefully because of the limitations in the experimental facilities. Under the present conditions it appears reasonable to attribute the growth mechanism of sodium bromate to polynuclear model in two-dimensional nucleation theories.

### 3.2 Surface studies

It is known that when well-developed crystal faces are observed under the microscope, they sometimes reveal typical growth features, from which the growth mechanism can be understood. To probe the growth mechanism of  $\text{NaBrO}_3$  crystal further, surface studies were carried out on these crystals. The crystals grown were gently dried with tissue paper and immediately transferred to a Meopta reflection microscope to study the surface. Figure 5a shows a photomicrograph of typical growth steps observed on (111) faces of  $\text{NaBrO}_3$ . These steps are triangular with curved edges, the edges are parallel to  $\langle 110 \rangle$  direction, and the steps are distributed randomly on the surface. The shape of the spiral steps or hillocks is controlled by the roughness of the steps. If

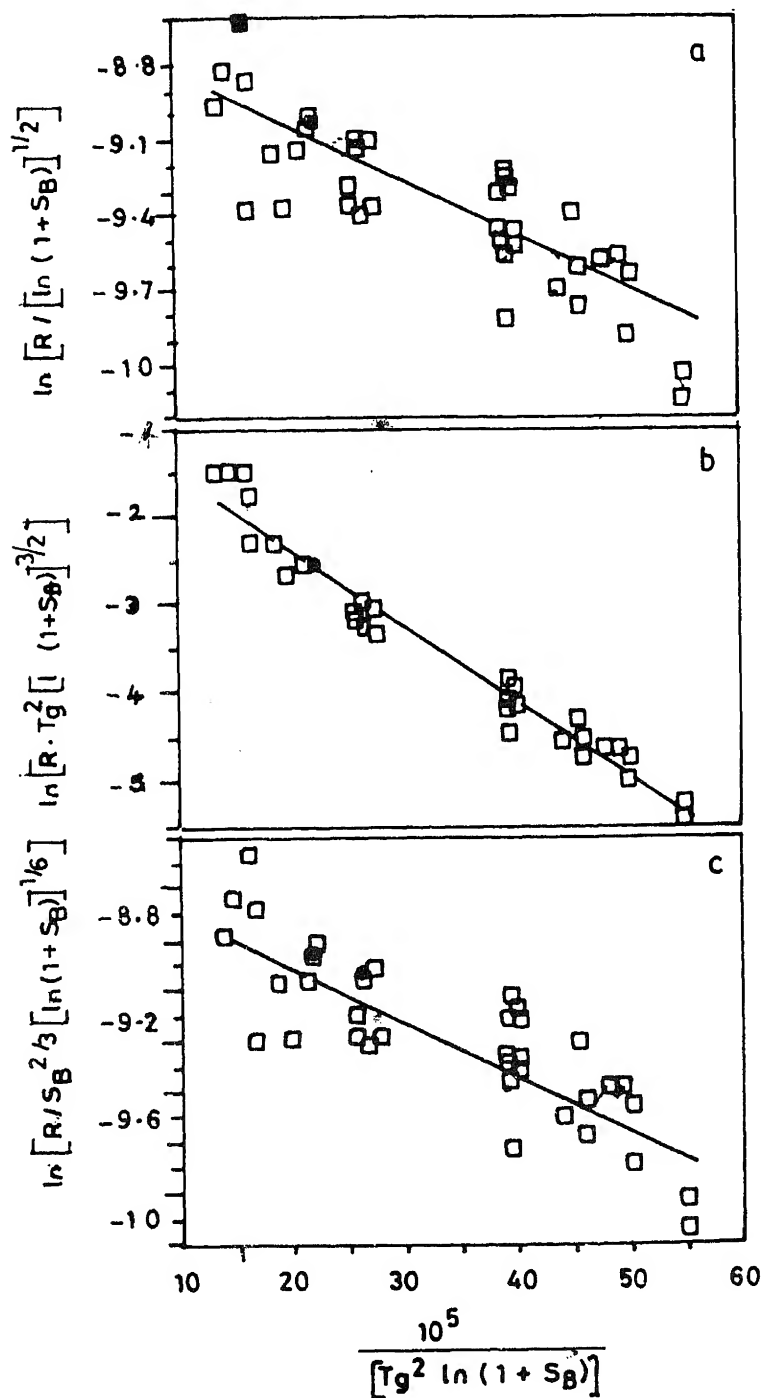


Figure 4. Plots of the data for examination of a. mononuclear model, b. polynuclear model and c. birth and spread model for sodium bromate crystals.

the step is rough, i.e. kink density is high, the step can advance independently of crystallographic direction, which leads to a circular step. If the step is smooth it becomes more polygonalized. Perhaps higher kink density is responsible for the formation of the present steps.



Figure 5. a-b.



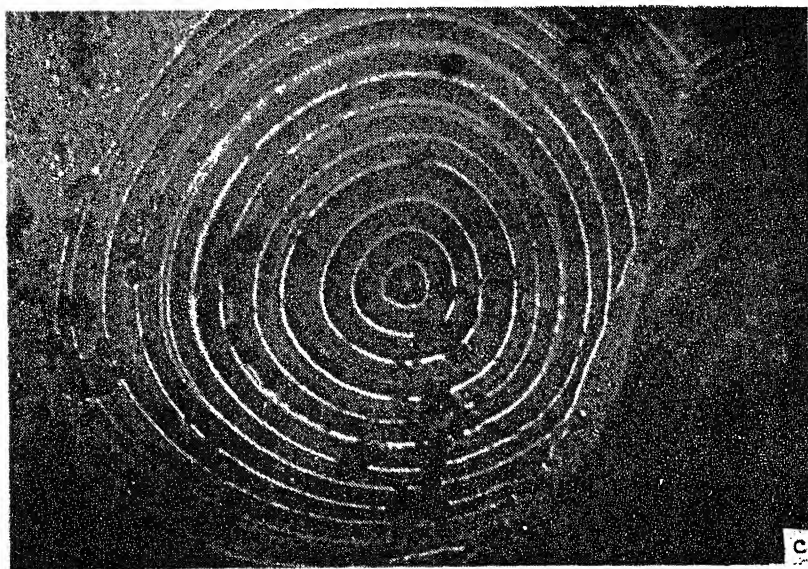


**Figure 5.** a. Independent macroconcentric steps on (111) faces of sodium bromate crystals ( $\times 120$ ); b. and c. interlaced pattern on (111) faces of sodium bromate crystals ( $\times 300$ ).

Figures 5b and 5c show an interlacing pattern of the steps of neighbouring sources. Different types of cooperation or interaction among the steps may take place depending on the mutual separation, step height, etc. Figure 5b shows smooth interlacing of the steps of two neighbouring sources, whereas a line is observed along the boundary at the intersection of the steps from the two neighbouring sources shown in figure 5c. This could be due to the interaction of steps of different heights which appear similar to a fault line. In the present study no growth spirals were recorded on these crystals.

These surface features together with the growth rate studies show that the growth mechanism of  $\text{NaBrO}_3$  crystal in the present supersaturation range could not be due to screw dislocation mechanism but appears to be due to two-dimensional growth mechanism.

### Acknowledgements

The authors are grateful to the referees for a careful scrutiny of the paper and for some useful suggestions. The authors thank Prof. D B Sirdeshmukh for his interest in the work and for valuable suggestions.

### References

- Bennema P 1965 *The rate of growth of crystals from slightly supersaturated solutions*, Ph D Thesis, Technical University of Delft, Delft
- Chandrasekharan S and Madhava M S 1967 *Acta Crystallogr.* **23** 911
- Hosoya S and Kitamura M 1978 *Miner. J.* **9** 73

- Hosoya S, Kitamura M and Miyata T 1978 *Miner. J.* **9** 147  
Kitamura M, Kouchi A, Hosoya S and Sunagawa T 1982 *Miner. J.* **11** 119  
Klein-Haneveld H B 1971 *J. Crystal Growth* **10** 111  
Mason W P 1946 *Phys. Rev.* **70** 529  
Mullin J W and Gaska G 1969 *Canadian J. Chem. Eng.* **47** 483  
Mullin J W and Amatavivadhana A 1967 *J. Appl. Chem.* **20** 153  
Ohara M and Reid R C 1973 in *Modelling crystal growth rates from solutions* (New Jersey: Prentice-Hall, Inc.)  
Tsukamoto K, Ohba H and Sunagawa T 1983 *J. Crystal Growth* **63** 18



## Near ideal electrical switching in fast ion conducting glasses: Evidence for an electronic process with chemical origin

B VAIDHYANATHAN, S ASOKAN<sup>†</sup> and K J RAO\*

Solid State and Structural Chemistry Unit, <sup>†</sup>Instrumentation and Services Unit, Indian Institute of Science, Bangalore 560 012, India

MS received 25 May 1995

**Abstract.** Bulk AgI based fast ion conducting (FIC) glasses have been prepared by a novel microwave technique. Electrical switching characteristics of these glasses have been investigated for the first time. It has been found that AgI based FIC glasses exhibit a current-controlled high speed memory electrical switching behaviour. SEM, EDAX and ESR investigations have been performed on the virgin and switched samples to understand the nature of the conducting state. A chemical model is proposed to explain the switching behaviour of these glasses, which is consistent with the observed results.

**Keywords.** Electrical switching; fast ion conducting glasses.

There has been a tremendous interest in silver ion conducting glasses because of their ability to show relatively high ionic conductivities at room temperature. These glasses also have other merits such as homogeneity, absence of grain boundaries, ease of preparation, diversity of composition and transparency. The earlier investigations on silver ion conducting glasses, are focussed mainly on the ionic transport and structure (Minami *et al* 1977; Kawamura and Shimoji 1986; Tatsumisago *et al* 1991). Also, the reported applications of these materials are mostly directed towards their use as electrolytes in solid state batteries of low energy density. Recently, the possibility of applications of AgI based fast ion conducting glasses as ambient temperature oxygen sensors, electron beam recording materials, etc has been explored (Kuwano 1990). In the present work, AgI–Ag<sub>2</sub>O–MoO<sub>3</sub> (WO<sub>3</sub>) glasses have been prepared by a simple and fast microwave irradiation method. Electrical switching studies have been carried out, to find out the possibility of using these glasses in memory devices.

Bulk AgI–Ag<sub>2</sub>O–MoO<sub>3</sub> (WO<sub>3</sub>) (50:25:25) glasses have been prepared using a domestic microwave oven, operating at 2450 MHz with a continuous power level of 980 W maximum. Appropriate amounts of analar grade reagents (in powder form), having a batch weight of 6 g, were mixed thoroughly and placed inside the oven in a silica crucible. A homogeneous melt of the material, obtained in just about 5 min, was quenched (quenching rate  $\approx 10^3$  K/sec) between polished quartz plates. The rapid time scales involved in this preparation avoids the reduction of Ag<sup>+</sup> to Ag<sup>0</sup>, encountered normally in conventional methods. Since the melt do not couple to microwave field as effectively as the initial charge containing AgI, the temperature of the melt does not raise further as rapidly as that of the initial mixture (Vaidhyathan *et al* 1994). Yellow, transparent glasses obtained in the above manner were confirmed to be amorphous by X-ray diffraction (no sharp diffraction peaks) and glassy by differential scanning calorimetry (the glass transition temperature ( $T_g$ ) is 348 K for molybdate glass and 419 K for tungstate glass).

\*Corresponding author

The electrical switching behaviour of  $\text{AgI-Ag}_2\text{O-MoO}_3 (\text{WO}_3)$  (50:25:25) glass was studied in a custom built PC based system (Chatterjee *et al* 1994a). Samples mechanically polished to different thicknesses, were mounted in a spring loaded cell between a point contact top electrode (cathode) and a flat plate bottom electrode made of brass. A programmable, constant direct current (0–50 mA) was passed through the sample and the voltage developed across was measured.

The current–voltage characteristic of  $\text{AgI-Ag}_2\text{O-MoO}_3 (\text{WO}_3)$  (50:25:25) glass is shown in figure 1. It is seen from figure 1 that with the increasing current, there is an initial ohmic increase in the voltage across the sample. At a threshold voltage, the sample suddenly switches to a low resistance state. Though the switching behaviour of  $\text{AgI-Ag}_2\text{O-MoO}_3 (\text{WO}_3)$  (50:25:25) glasses is similar to that of chalcogenide glasses, it should be noted that the switching characteristic of AgI based samples is near ideal. Firstly,  $\text{AgI-Ag}_2\text{O-MoO}_3 (\text{WO}_3)$  glasses do not show any significant non-linearity

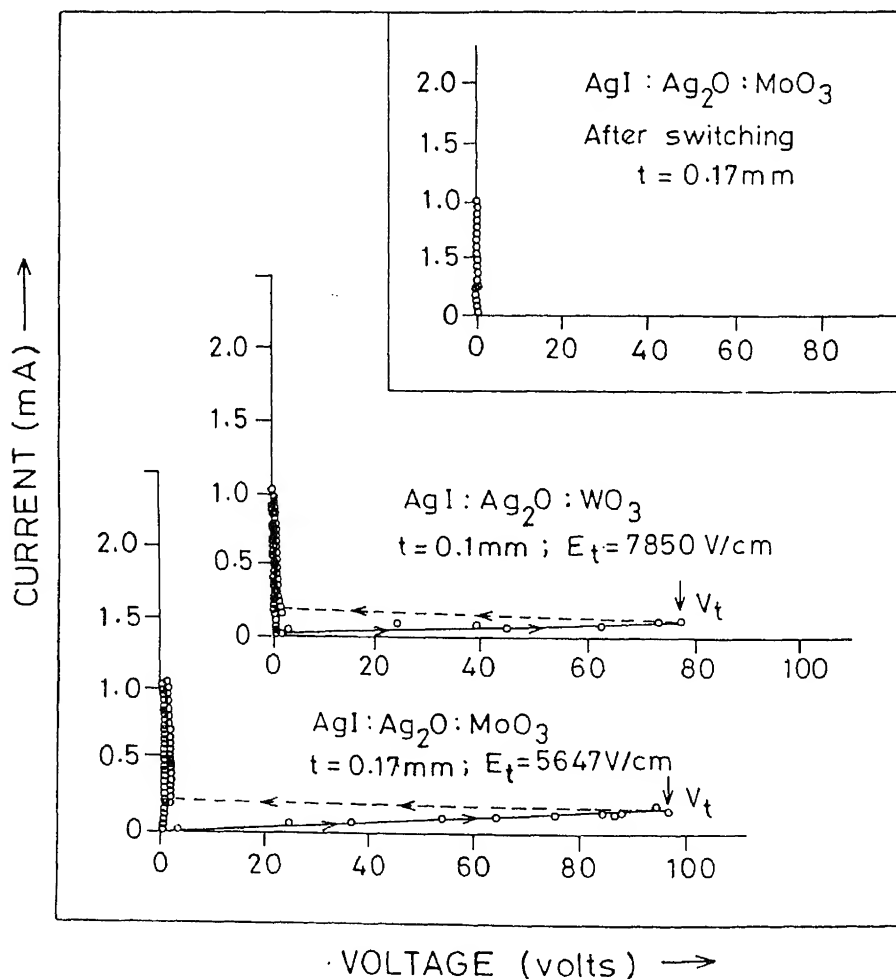


**Figure 1.** Electrical switching characteristics of  $\text{AgI-Ag}_2\text{O-MoO}_3$  and  $\text{AgI-Ag}_2\text{O-WO}_3$  glasses. The inset shows the  $I-V$  behaviour of  $\text{AgI-Ag}_2\text{O-MoO}_3$  glass after switching.

near the switching threshold. Secondly, the samples switch very fast without exhibiting a stable negative resistance zone. Thirdly, the characteristic after switching is vertical indicating that the dynamic resistance is almost zero. Also the switching characteristics are found to be independent of the polarity. It is interesting to note that the switching in these samples can also be effected by a current sweep (0–30 mA) of 50  $\mu$ sec duration.

Due to experimental limitations it has not been possible to exactly determine the switching times of the samples studied. However, it is found with the available facilities that the switching time involved is around a  $\mu$ sec.

The inset in figure 1 shows the  $I$ - $V$  characteristic of AgI-Ag<sub>2</sub>O-MoO<sub>3</sub> sample, after the first switching cycle, indicating that the material is permanently latched in its low resistance state. Unlike many chalcogenide glasses (Chatterjee *et al* 1994b), the AgI based fast ion conducting glasses once switched are not brought back to the initial high resistance state by the application of resetting (large) current pulse. The switching experiments undertaken on different samples of the same thickness and composition reveal that the threshold voltage is highly reproducible within  $\pm 2$  V. Figure 2 shows the variation of the threshold fields ( $E_t$ ) of AgI-Ag<sub>2</sub>O-MoO<sub>3</sub> (WO<sub>3</sub>) glasses as a function of sample thickness. It can be seen that  $E_t$  increases linearly with the decrease in thickness, as in the case of many chalcogenide glasses (Adler 1971). It has also been found that for a given thickness AgI-Ag<sub>2</sub>O-WO<sub>3</sub> samples have a slightly higher switching field compared to AgI-Ag<sub>2</sub>O-MoO<sub>3</sub> samples.

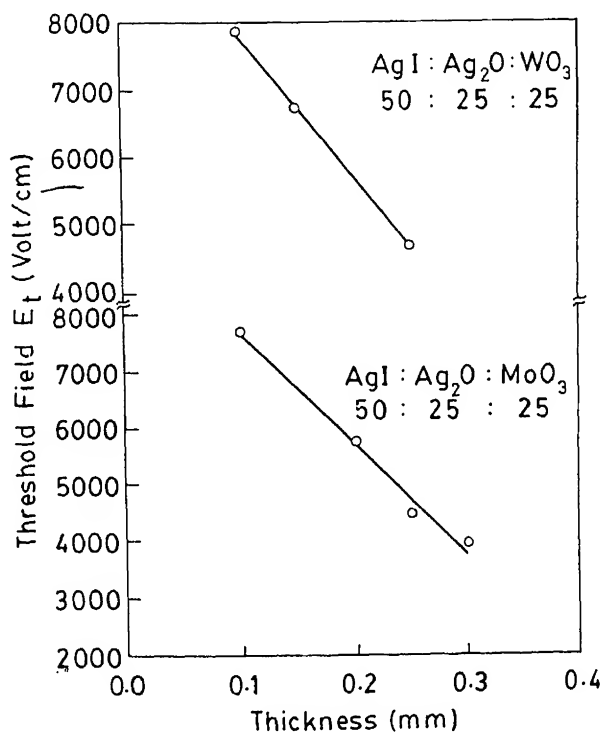
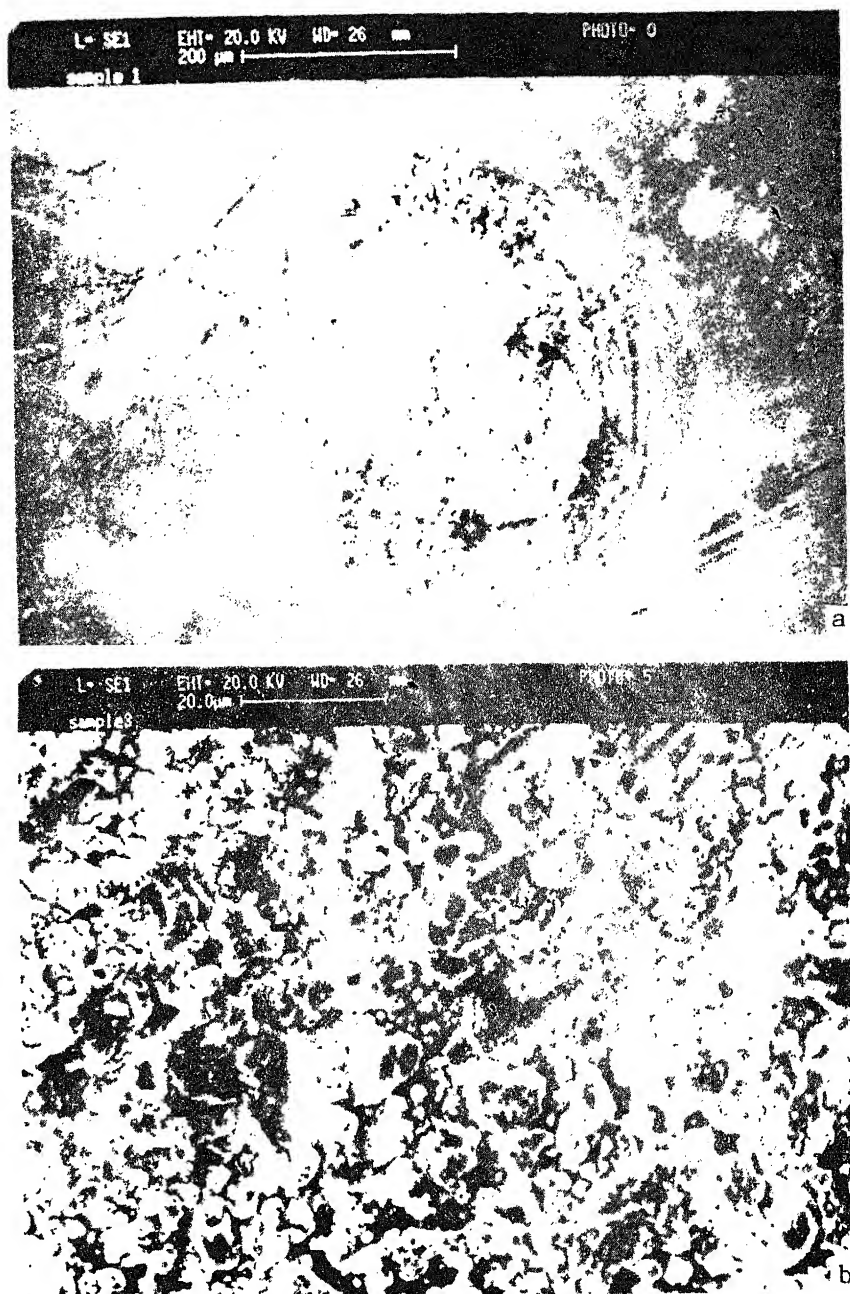


Figure 2. Thickness dependence of the threshold field of AgI-Ag<sub>2</sub>O-MoO<sub>3</sub> and AgI-Ag<sub>2</sub>O-WO<sub>3</sub> glasses.



**Figure 3.** a. SEM photograph of AgI-Ag<sub>2</sub>O-MoO<sub>3</sub> sample after switching, showing the switched (central region) and the unswitched portions and b. SEM photograph of the switched zone of AgI-Ag<sub>2</sub>O-MoO<sub>3</sub> sample.

Electron microscopic and EDAX investigations have been carried out on the switched AgI-Ag<sub>2</sub>O-MoO<sub>3</sub> samples. Figures 3(a) and 3(b) show the SEM pictures of AgI-Ag<sub>2</sub>O-MoO<sub>3</sub> sample taken after switching. These electron micrographs reveal that the switched region between the top electrode and the bottom plate differ markedly from the bulk of the material. Composition analysis (EDAX) of the switched portion and the surrounding bulk indicates that there is a depletion of silver concentration and an enhancement of molybdenum in the switched zone (see table 1). The switched region also appears darker in colour compared to the unswitched surroundings. There was no detectable crystallization observed in the X-ray diffractogram of the switched sample.

Electron spin resonance (ESR) spectra of the two regions of AgI-Ag<sub>2</sub>O-MoO<sub>3</sub> samples were examined. Interestingly it was found that the ESR trace of molybdenum in the virgin and the switched samples differed markedly (figure 4). The splitting reveals that Mo<sup>5+</sup> is present in different structural configurations (Mo<sup>5+</sup> is always present in very low amounts—a few ppm—in molybdate glasses and give rise to ESR spectrum). There is also an enhancement of the ESR signal although we could not quantify the extent of enhanced reduction of Mo<sup>6+</sup> → Mo<sup>5+</sup>.

The switching seems to be associated with (i) depletion of Ag and a corresponding increase in Mo in the switched region, (ii) reduction of Mo<sup>6+</sup> to Mo<sup>5+</sup> in addition to the reduction of Ag<sup>+</sup> to Ag<sup>0</sup> at the electrode. The electrolyzed silver possibly gets deposited on the cathode as indicated by the tarnishing of the cathode. While the reduction of Ag<sup>+</sup> to Ag<sup>0</sup> occurs at the cathode, Mo<sup>6+</sup> to Mo<sup>5+</sup> appears to be a chemical response to the anodic process, where it is easy to visualize loss of oxygen. In this connection we note that Mo<sup>5+</sup> itself is more stable in an octahedral environment than in tetrahedral environment as shown elsewhere (Selvaraj and Rao 1985). Considering together the above observations we tentatively favour the following as the most probable mechanism: (i) at the cathode Ag<sup>+</sup> → Ag<sup>0</sup> and (ii) at the anode successive reactions take place as follows: (a) [MoO<sub>4</sub>]<sup>2-</sup> → [MoO<sub>4</sub>]<sup>0</sup> + 2e<sup>-</sup>, (b) [MoO<sub>4</sub>]<sup>0</sup> → MoO<sub>3</sub> + 1/2 O<sub>2</sub>, (c) MoO<sub>3</sub> + [MoO<sub>4</sub>]<sup>2-</sup> → 2[MoO<sub>5/2</sub>O]<sup>1-</sup> and (d) 2[Mo<sup>6+</sup>O<sub>5/2</sub>O]<sup>1-</sup> → 2[Mo<sup>5+</sup>O<sub>6/2</sub>]<sup>1-</sup> + 1/2 O<sub>2</sub>.

Thus the net process involves transport of two electrons in the external circuit and transfer of two electrons (2Mo<sup>6+</sup> → 2Mo<sup>5+</sup>) in the chemistry driven reduction of Mo<sup>6+</sup> to Mo<sup>5+</sup>. The *d* orbitals of Mo<sup>5+</sup> in an octahedral field are split into *t*<sub>2g</sub> and *e*<sub>g</sub> set and the *t*<sub>2g</sub> (4d) with the 5s and 5p orbitals constitute the six bonding orbitals overlapping with the *p* (or *sp*<sup>*n*</sup>) orbitals of the oxygen. The *e*<sub>g</sub> orbitals (*d*<sub>z<sup>2</sup></sub> and *d*<sub>x<sup>2</sup>-y<sup>2</sup></sub>) of Mo now possess one electron (the degeneracy is lifted by Jahn-Teller distortion in

**Table 1.** Compositional analysis of the switched and the unswitched regions of the AgI-Ag<sub>2</sub>O-MoO<sub>3</sub> sample.

Element	Atomic (%)	
	Unswitched zone	Switched zone
Ag	56	38
Mo	18	28
I	26	34



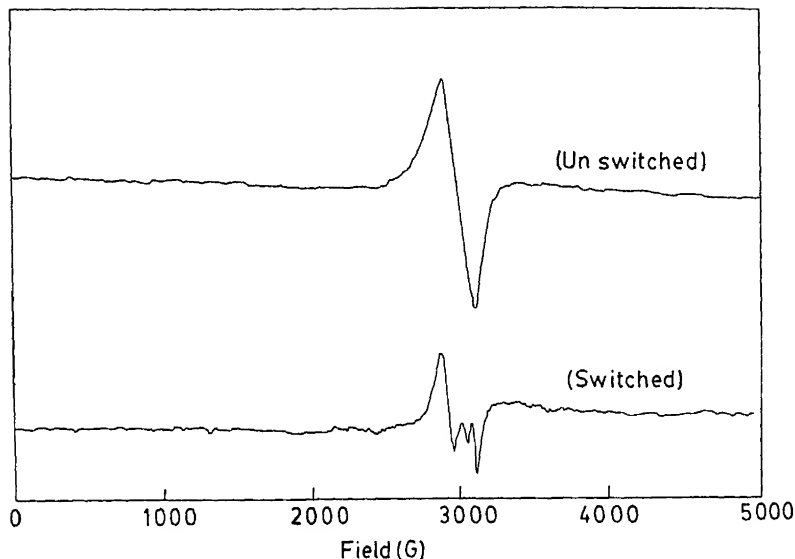


**Figure 4.** The ESR spectra of the virgin and switched AgI-Ag<sub>2</sub>O-MoO<sub>3</sub> samples taken at 300 K.

isolated  $[\text{Mo}^{5+}\text{O}_{6/2}]^{1-}$  units). When an extensive chain of these units is formed between the electrodes it results in the formation of an  $e_g$  band and can easily provide a 'metallic' path (partially filled band) for electron transport. The observed switching is likely to be a consequence of this. It is emphasized that the initial reduction of  $\text{Ag}^+$  to  $\text{Ag}^0$  at the electrode triggers the reduction of  $\text{Mo}^{6+}$  to  $\text{Mo}^{5+}$  in the glass. The change is irreversible in the experiment since both Ag and O are lost. The anodic reduction can proceed either with a single electron transfer or two-electron transfer and the stages of anodic processes cannot be established without that knowledge. However  $\text{Mo}^{6+}$  to  $\text{Mo}^{5+}$  reduction is ultimately driven by chemical and stability considerations.

Structural change of tetrahedrally coordinated  $\text{Mo}^{6+}$  to octahedrally coordinated  $\text{Mo}^{5+}$  is only incidental. Because, we should expect reduction of  $\text{Ag}^+$  to drive a reduction of anionic species and if there is an energetically accessible empty orbital which can form a partially filled band, a similar switching should be expected to occur. In borates and germanates we expect the empty  $p$  (or  $sp^3$ ) orbital of boron or the antibonding  $d^2sp^3$  orbitals of Ge to constitute conduction bands which host the electron added during reduction. Indeed we observed sudden switching in these glasses also.

There is a difference in the switching voltages of molybdate and tungstate glasses; the latter switches at higher voltages. It may be due to the higher enthalpy of reduction for  $\text{W}^{6+} \rightarrow \text{W}^{5+}$  (in oxides) than  $\text{Mo}^{6+} \rightarrow \text{Mo}^{5+}$ .

Interestingly it is found that the electrical switching fields of the samples studied are almost independent of temperature (ambient to  $T_g$ ) (Vaidhyanathan *et al* 1995). This observation confirms that the sharp permanent switching in AgI based fast ion conducting glasses is electronic, non-thermal in nature, corroborating the proposed chemical model.

The thickness dependence of the switching voltage is however unclear at this stage. We tentatively attribute it to the facility of oxygen transport away from the region of electrical field between electrodes, in the case of thick samples. Thus the threshold field drops in thicker samples.

It will be interesting to study the effect of electrode material and geometry on the switching characteristics, the conductance ratio of the switched and unswitched regions of the material, etc. These investigations form the basis for future work.

We conclude that this novel electronic switching mode which leaves behind a permanent change in the glasses provides a new approach to designing memory switching materials.

## Acknowledgement

The authors thank Mr S Prakash, Mr S Murugavel, Instrumentation and Services Unit and Mr A R Raju, Materials Research Centre for their help.

## References

- Adler D 1971 *Amorphous semiconductors* (London: CRC, Butterworths)
- Chatterjee R, Acharya K V, Asokan S and Titus S S K 1994a *Rev. Sci. Instrum.* **65** 2382
- Chatterjee R, Asokan S and Titus S S K 1994b *J. Phys. D: Appl. Phys.* **27** 2624
- Kawamura J and Shimoji M 1986 *J. Non-cryst. Solids* **88** 281
- Kuwano J 1990 *Solid State Ion.* **40/41** 696
- Minami T, Nambu H and Tanaka M 1977 *J. Am. Ceram. Soc.* **60** 467
- Selvaraj U and Rao K J 1985 *J. Non-cryst. Solids* **72** 315
- Tatsumisago M, Shinkuma Y and Minami T 1991 *Nature* **354** 217
- Vaidhyanathan B, Munia Ganguli and Rao K J 1994 *J. Solid State Chem.* **113** 448
- Vaidhyanathan B, Rao K J, Prakash S, Murugavel S and Asokan S 1995 *J. Appl. Phys.* (in press)

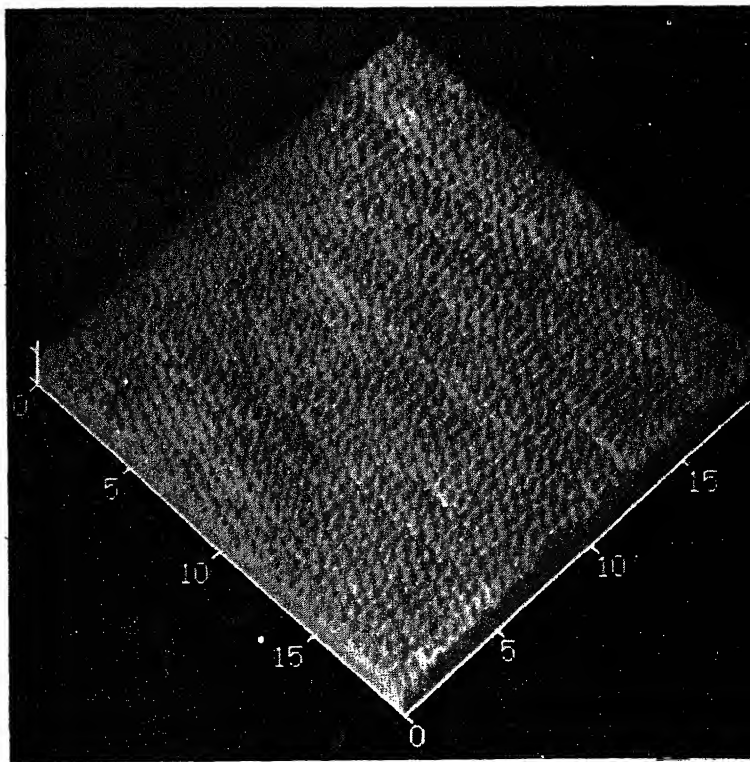


# Materials Science

Volume 18

Number 4

August 1995



Published by  
**INDIAN ACADEMY OF SCIENCES**  
in collaboration with  
**MATERIALS RESEARCH SOCIETY OF INDIA and**  
**INDIAN NATIONAL SCIENCE ACADEMY**



# Bulletin of Materials Science

## Editor

K J Rao

*Indian Institute of Science, Bangalore*

## Editorial Board

D C Agrawal, *Indian Institute of Technology, Kanpur*  
M F Ashby, *University of Cambridge, Cambridge, UK*  
S Banerjee, *Bhabha Atomic Research Centre, Bombay*  
D Chakravorty, *Indian Association for the Cultivation of Science, Calcutta*  
A K Chatterjee, *The Associated Cement Companies Limited, Thane*  
K L Chopra, *Indian Institute of Technology, Kharagpur*  
A D Damodaran, *Regional Research Laboratory, Trivandrum*  
B K Das, *National Physical Laboratory, New Delhi*  
H Herman, *State University of New York, Stony Brook, USA*  
B Ilschner, *Ecole Polytechnique Federale de Lausanne, Lausanne, Switzerland*  
Indira Rajagopal, *National Aerospace Laboratories, Bangalore*  
K T Jacob, *Indian Institute of Science, Bangalore*  
S K Joshi, *Council of Scientific and Industrial Research, New Delhi*  
S Mahajan, *Carnegie Mellon University, Pittsburgh, USA*  
R A Mashelkar, *National Chemical Laboratory, Pune*  
S B Ogale, *University of Poona, Pune*  
Pradip, *Tata Research Development and Design Centre, Pune*  
P Ramachandra Rao, *National Metallurgical Laboratory, Jamshedpur*  
S Ranganathan, *Indian Institute of Science, Bangalore*  
C N R Rao, *Indian Institute of Science, Bangalore*  
B B Rath, *Naval Research Laboratory, Washington, USA*  
R W Siegel, *Argonne National Laboratory, Argonne, USA*  
R Srinivasan, *Inter-University Consortium for DAE Facilities, Indore*  
G V Subba Rao, *Central Electrochemical Res. Inst., Karaikudi*  
G Sundararajan, *Defence Metallurgical Research Laboratory, Hyderabad*  
M S Valiathan, *Manipal Academy of Higher Education, Manipal*  
I K Varma, *Indian Institute of Technology, New Delhi*  
Vikram Kumar, *Solid State Physics Laboratory, Delhi*

## Editor of Publications of the Academy

V K Gaur

*C-MMACS, NAL, Bangalore*

---

### Subscription Rates (Effective from 1989)

<b>All countries except India</b> (Price includes AIR MAIL charges)	1 year US\$ 100	3 years \$ 270	5 years \$ 400
<b>India.....</b>	1 year Rs. 75	10 years Rs. 400	

All correspondence regarding subscription should be addressed to **The Circulation Department** of the Academy.

---

### Editorial Office

Indian Academy of Sciences, C V Raman Avenue,  
P. B. No. 8005, Bangalore 560 080, India

Telephone: 334 2546  
Telex: 845-2178 ACAD IN  
Telefax: 9180-334 6094

© 1995 by the Indian Academy of Sciences. All rights reserved.

Cover : A filtered AFM image of a stearic acid monolayer. For details, see p. 375.

**FOREWORD**

The India-Japan Seminar on New Materials was held in Tokyo, on October 16 and 17, 1994, under the sponsorship of Department of Science and Technology in Indian side and Japan Society for the Promotion of Science in Japanese side. This was one of the activities in the area of new materials supported by the India-Japan Cooperative Science Programme which started in August 1993.

The main aim of the Seminar was to promote the India-Japan scientific cooperation in material science and technology by deepening mutual understanding of the present research situation of the partner countries. Eleven lectures were delivered at the Seminar by distinguished scientists from India and Japan. They covered various research frontiers in the area of new materials and provided the participants with comprehensive and valuable knowledge.

I had a strong feeling on the occasion of the Seminar that a publication based on the presented lectures would be significant. It is my great pleasure that the Special Issue on New Materials including ten of them can be published. I sincerely hope that the Issue will be found to be useful by researchers in material science and technology.

I am heartily grateful to Dr P Rama Rao and Professor K J Rao for their kind effort in publishing the Special Issue and to Professor T Tsuruta and Professor H Koinuma for their kind cooperation in organizing the Seminar and collecting the articles in Japanese side.

Saburo Nagakura  
*Guest Editor*



# Computer simulation of deformation and fracture of small crystals by molecular dynamics method

MASAO DOYAMA

The Nishi-Tokyo University, Uenohara, Yamanashi 409-01, Japan

**Abstract.** Body-centred cubic iron whiskers having  $[100]$  and  $[1\bar{1}0]$  axes were pulled in a molecular dynamics simulation using a supercomputer. The upper yield stress close to the theoretical strength was found. Above the upper yield stress, phase transformation was observed; at the same time the stress was greatly reduced. A new possible mechanism of twinning is proposed. The whiskers were pulled until they had broken into two pieces. Copper small crystals with and without a notch were sheared. It was observed that the edge dislocations were created at the surface and moved through and escaped from the crystals. Copper small single crystals with a notch were pulled. A half-dislocation was created near the tip of the notch. Sharp yield stress was observed. In medium deformation dislocations on different slip planes were created. Due to the cutting of dislocations the tensile stress increased.

**Keywords.** Computer simulation; deformation; fracture; small crystals; molecular dynamics method.

## 1. Introduction

Plastic deformation of metals is caused by the creation and motion of dislocations. Fracture is a very important problem in engineering and science but atomistic explanations of it have not been verified. Molecular dynamics has found much application in materials science and engineering. It is quite useful for simulating the creation and motion of dislocations during plastic deformation in metals. It is also useful for simulating deformation until the specimen is fractured.

## 2. Interatomic potentials

The interaction potentials between the  $i$ th and  $j$ th atoms are often represented by a pairwise potential. The simplest pair potential is only a function of the distance between two atoms. In this paper, the two-body interaction between two atoms in body-centred iron is represented by

$$\Phi(r_{ij}) = a_1(r_{ij} - a_2)^4 + a_3(r_{ij} - a_4)^2 + a_5, \quad (1)$$

where  $a_1 = -0.188917 \text{ eV/\AA}^4$ ,  $a_2 = 1.82709 \text{ \AA}$ ,  $a_3 = 1.70192 \text{ eV/\AA}^2$ ,  $a_4 = 2.50849 \text{ \AA}$ ,  $a_5 = 0.198294 \text{ eV}$ , and  $r_{ij}$  is the distance between the  $i$ th and  $j$ th atoms. This potential was determined by Pak and Doyama (1969). It has been used for calculating point defects in iron, the structure of amorphous iron, etc. It is smoothly truncated at  $3.44 \text{ \AA}$  between the second nearest neighbour and the third nearest neighbour. By this potential body-centred cubic lattice is the most stable configuration. This potential is called Fe-1 potential hereafter. In figure 1 Fe-1 is plotted against the distance.

The two-body potential in copper used here (Doyama and Yamamoto 1986) is

$$\Phi(r_{ij}) = -2.093936(r_{ij} - 3.139365)^2(r_{ij} - 2.251664) \text{ (eV)}. \quad (2)$$



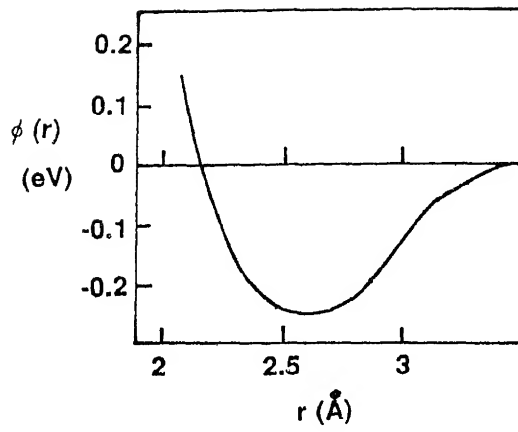


Figure 1. The effective interaction potential between atoms in iron.

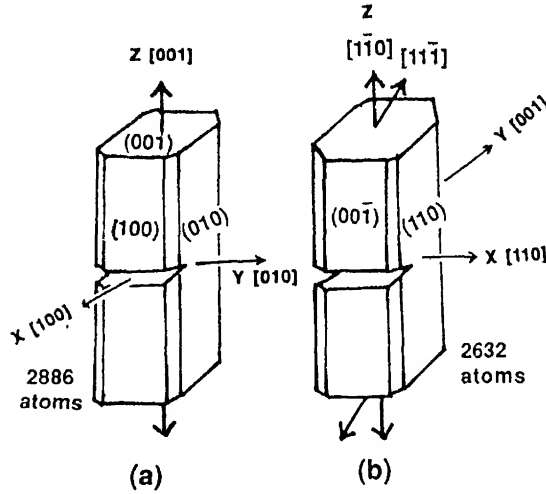


Figure 2. Iron specimens (a) Fe-1 and (b) Fe-2.

This potential is spherically symmetric and smoothly truncated. It is called potential Cu-1 hereafter.  $r_{ij}$  is represented in Å.

The interatomic potentials in metals, however, cannot be expressed by two-body interaction.  $N$ -body embedded function determined by Oh and Johnson (1988, 1989) is used for copper. This is called potential Cu-2 hereafter.

$$E_{\text{total}} = \sum E_i$$

$$r_{ij} = |r_i - r_j|$$

$$E_i = F(\rho_i) + (1/2) \sum \Phi(r_{ij})$$

$$F(\rho) = a(\rho/\rho_e)^n + b(\rho/\rho_e)$$

$$\rho_i = \sum f(r_{ij}).$$

Here  $E_{\text{total}}$  is the total internal energy,  $E_i$  the internal energy associated with atom  $i$ ,  $\rho_i$  the electron density at atom  $i$  due to all other atoms,  $F(\rho_i)$  the embedding energy of the atom into the electron density,  $\rho_i$ ,  $\Phi(r_{ij})$  the two-body central potential between atoms  $i$  and  $j$  separated by  $r_{ij}$  and  $f(r_{ij})$  the contribution to the electron density at atom  $i$  due to atom  $j$  at the distance  $r_{ij}$  from atom  $i$ .

$$f(r) = f_{\text{old}}(r) - f_c(r)$$

$$f_{\text{old}} = f_c \exp\{-\beta(r/r_c) - 1\}$$

$$f_c(r) = f_{\text{old}}(r_c) + g(r)f'_{\text{old}}(r_c)/g'(r_c)$$

$$\Phi(r) = \Phi_{\text{old}}(r) - \Phi_c(r)$$

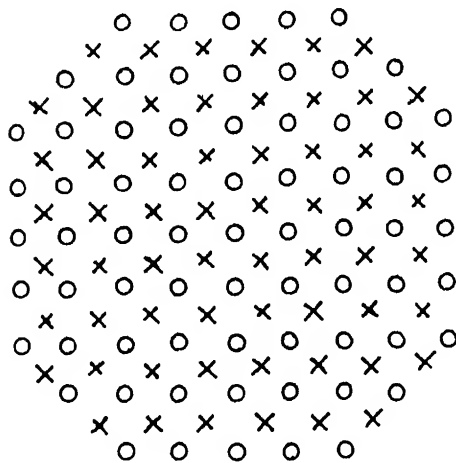


Figure 3. Cross-section of specimen Fe-1.

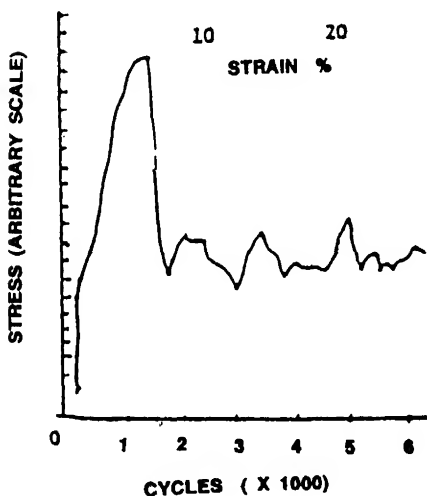


Figure 4. Stress-strain curve of specimen Fe-1.

$$\Phi_{\text{old}}(r) = \Phi_e \exp\{-\gamma(r/r_e - 1)\}$$

$$\Phi_c(r) = \Phi_{\text{old}}(r_e) + g(r)\Phi'_{\text{old}}(r_e)/g'(r_e)$$

$$g(r) = 1 - \exp\{\delta(r/r_e) - r_e/r_e\}$$

For copper Oh and Johnson (1988, 1989) give  $\beta = 5$ ,  $\gamma = 8.5$ ,  $\delta = 20$ ,  $r_e = 1.9 r_c$ ,  $\Phi_c(r) = 0.36952 \text{ eV}$ ,  $a = -4.0956$ ,  $b = -1.6979$ ,  $n = 0.44217$  and  $\rho_e = 12.793$ .

### 3. Iron whiskers

#### 3.1 Tensile deformation of iron whiskers

Needle-shaped iron whiskers were pulled in a molecular dynamics simulation in a Hitachi S-810 supercomputer. Two body centred cubic iron specimens were created. Specimen Fe-1 contains 2886 atoms. The axis was [001] direction. The specimen size is  $8a \times 8a \times 14a$ , where  $a$  is the lattice parameter, and is truncated at the edges

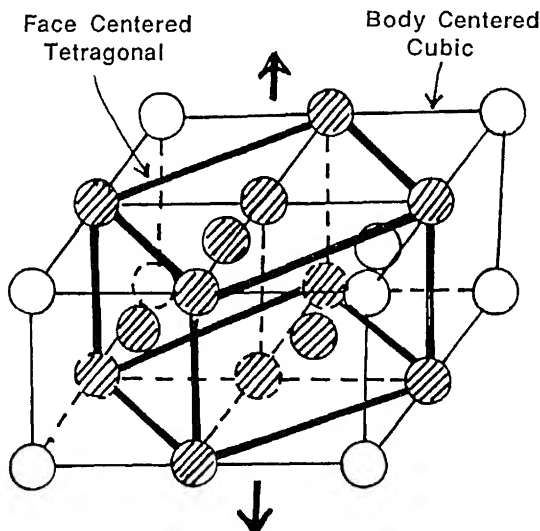


Figure 5. Face-centred tetragonal lattice in a body-centred cubic lattice.

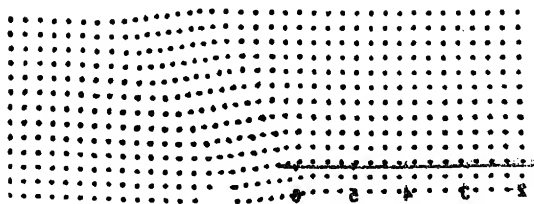
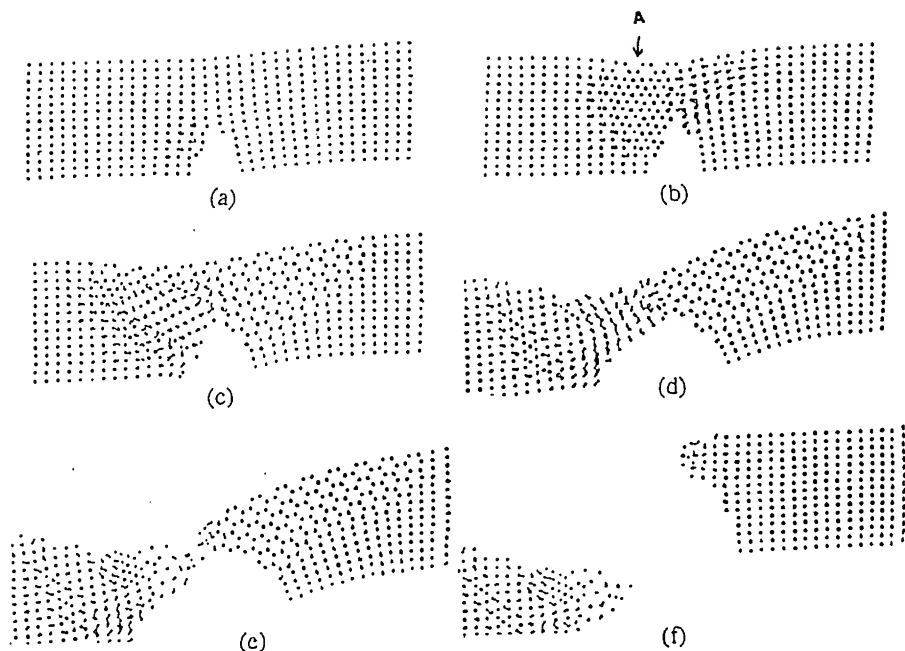
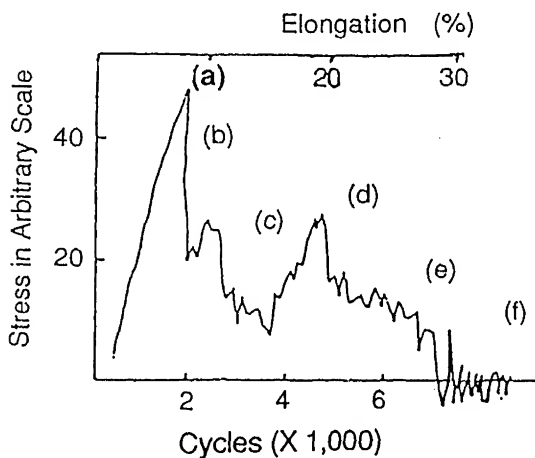


Figure 6. Atomic positions, projected to (010) in specimen Fe-1 at 24.4% elongation (6200 cycles).



**Figure 7.** (a) Atomic positions of specimen Fe-2 at 6.8% elongation, pulled in  $[111]$  direction; (b) in region A twin was initiated; (c) necking was observed at 22% elongation; (d-f) Fe-2 was completely broken into two pieces.



**Figure 8.** Stress-strain curve for specimen Fe-2 pulled in  $[111]$  direction. The letters represent figures of atomic configuration in figure 7.

(figure 2a). The surfaces are  $(100)$ ,  $(\bar{1}00)$ ,  $(010)$ ,  $(0\bar{1}0)$ ,  $(001)$  and  $(00\bar{1})$ .  $x$ ,  $y$  and  $z$  axes are taken in  $[100]$ ,  $[010]$  and  $[001]$  directions, respectively. The cross-section is plotted in figure 3. Specimen Fe-2 contains 2632 atoms having faces of  $(1\bar{1}0)$ ,  $(\bar{1}10)$ ,  $(110)$ ,  $(\bar{1}\bar{1}0)$ ,  $(001)$  and  $(00\bar{1})$  (figure 2b).

The iron specimens were first relaxed for 100 cycles by the molecular dynamics method. In each cycle all the atoms in the specimen are moved toward the resultant forces by neighbouring atoms proportional to the forces. The atoms in two atomic layers at both ends, "holder" regions, were specially treated, extended and held  $z$  coordinates. The  $z$  direction was taken to be the direction of the whisker axes. Uniform tensile deformation of 0.004 (0.4%) was given in a tensile direction (nominal elongation), then all atoms other than holder regions were relaxed. After each uniform tension was given, atoms were relaxed for 100 cycles, then uniform tension was again given. One hundred cycles of relaxation were performed. This procedure was repeated. The amount of tension each time was 0.004 (0.4%). The atoms in the holder were relaxed in the  $x$  and  $y$  directions only, not in  $z$  direction.

The total force in the  $z$  direction of all the atoms in the "holder" region was calculated. This can be taken as the tensile stress. The tensile stress-strain curve is plotted in figure 4. As seen from the stress-strain curve, very sharp yield stress was observed. Up to the yield stress, the specimen was almost uniformly deformed. Above the yield stress, stress was greatly reduced. At the same time, a face-centred tetragonal lattice was formed. The relationship between the tetragonal face-centred lattice and the body-centred lattice is as follows:  $(001)_{\text{bcc}} // (001)_{\text{fcc}}$ ,  $[110]_{\text{fcc}} // [100]_{\text{bcc}}$  and  $[110]_{\text{fcc}} // [010]_{\text{bcc}}$ . A face-centred tetragonal structure can be considered in a body-centred cubic lattice as shown in figure 5. Applying a tension in the  $c$  direction, the  $c$  axis is expanded and the  $a$  axes are shrunk, then finally face centred cubic structure is obtained. Figure 6 is the projection of atom positions to  $xz$  direction at 24.4% elongation.

Specimen Fe-2 was pulled in  $[11\bar{1}]$  direction. In this specimen, the resolved shear stress to  $[11\bar{1}]$  on  $(111)$  plane is the highest for one of the slip systems. An easier glide is expected. The slip started at the corner of the tip of the crack, i.e. the place where the crack ends at the surface. Slip started from the tip of the notch. Up to 6.8% elongation, the specimen was very uniformly extended except very near the crack (figure 7a). Above 6.8%,

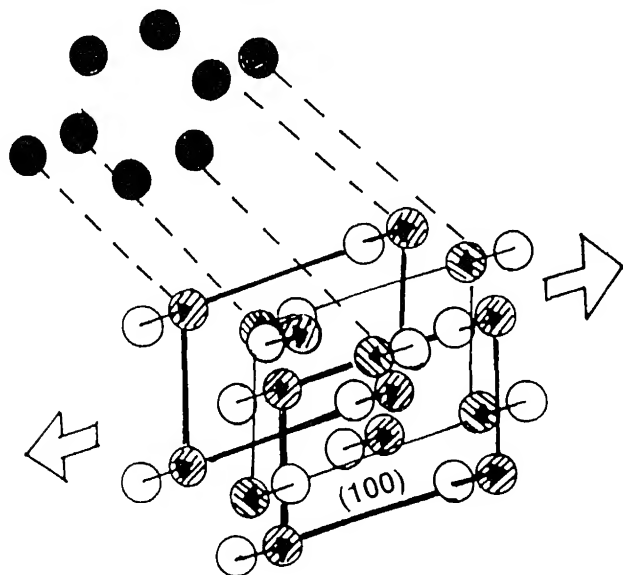
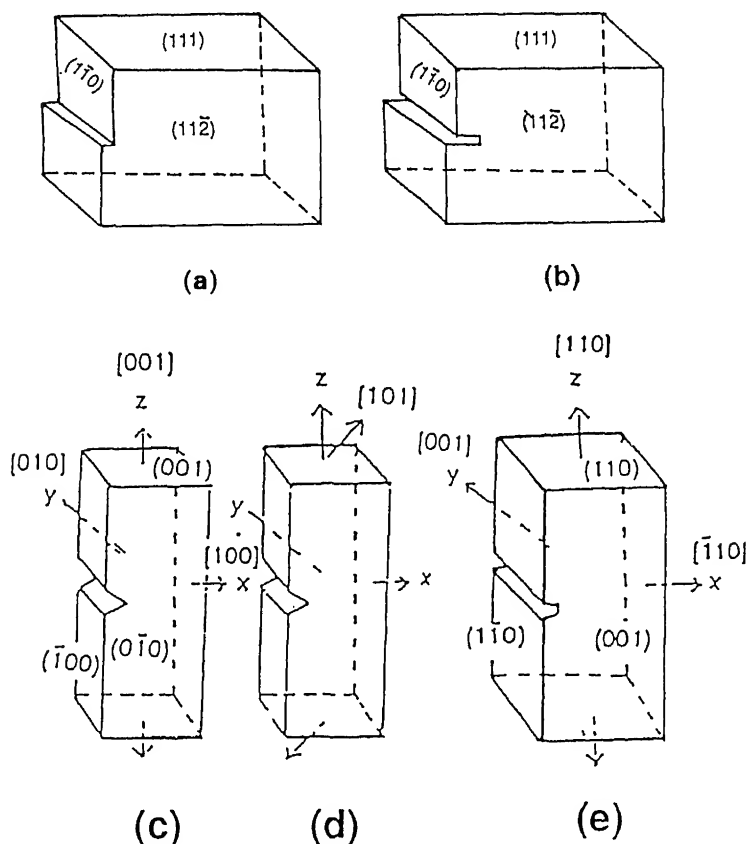


Figure 9. Formation of six-fold symmetry by shuffling (100) planes.



**Figure 10.** Copper specimens (a) Cu-1, (b) Cu-2, (c) Cu-3, (d) Cu-4 and (e) Cu-5.

the specimen was suddenly transformed. Inside the crystal six-fold symmetrical configuration was observed. This intermediate six-fold symmetry configuration suddenly changed to a twin at about 10% elongation. Twin was formed in region A shown in figure 7b. The twin region expanded as the deformation progressed. The six-fold symmetry region also expanded. At about 17% elongation, very severe deformation was observed.

The "necking" started above 22% elongation (figure 7c). At 28% elongation, the specimen was broken into two pieces (figure 7d). After fracture, the region of the six-fold symmetry configuration decreased under no stress and the original body-centred cubic lattice of alpha-iron was obtained (figure 7d).

For specimen Fe-2, the stress-strain curve is shown in figure 8. After the yield point, a phase transition was again observed. This time, however, the body-centred iron transformed into six-fold symmetry. A possible shear mechanism is shown in figure 9. Six-fold symmetry can be obtained by shuffling every other (100) plane.

#### 4. Shear deformation of copper small crystals

The deformation mechanism is much simpler in face-centred cubic lattice than that in

body-centred cubic lattice. As an example a face-centred metal, copper, was chosen. *N*-body embedded function (potential Cu-2) was used. A small crystal of rectangular parallelepiped having the faces (111), (11 $\bar{2}$ ), (1 $\bar{1}$ 0), ( $\bar{1}\bar{1}\bar{1}$ ), ( $\bar{1}\bar{1}$ 2) and (1 $\bar{1}$ 0) was created in the computer. The specimen contains 1890 atoms. The periodic boundary condition in [11 $\bar{2}$ ] was used. The specimen is called specimen Cu-1 hereafter (figure 10a).

On (1 $\bar{1}$ 0) plane, stepwise displacement of  $0.08d$ , where  $d$  is the nearest-neighbour distance, was given, then relaxation for 100 cycles, again  $0.08d$  displacement, and relaxation for 100 cycles. The process was repeated. The projections of atomic positions on (11 $\bar{2}$ ) are given in figures 11a to 11c. The projections of atoms on (111) are given in figures 12a to 12c. Dislocations were created on the (111) and moved through and ejected from the crystal. The first dislocation created was a half

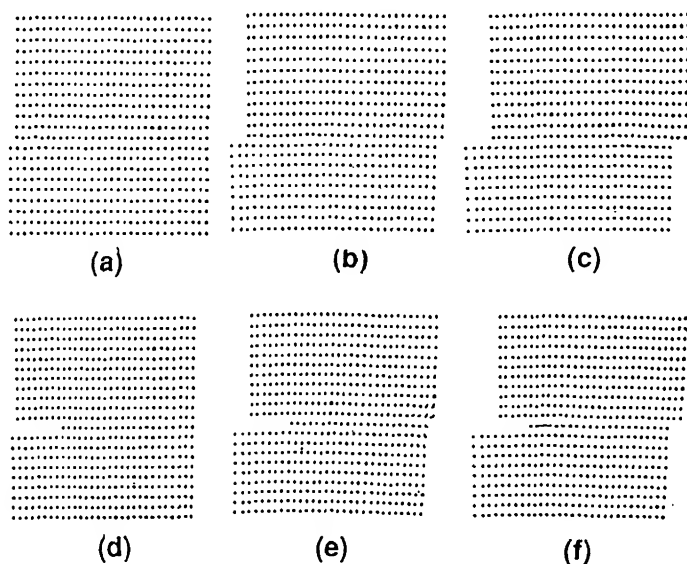


**Figure 11.** Projection of atom positions of copper specimen Cu-1 on (112). Creation of dislocations. Step heights are (a)  $0.4d$ , (b)  $1.2d$  and (c)  $2d$ . With a notch, specimen Cu-2, (d)  $0.4d$ , (e)  $1.2d$  and (f)  $2d$ .

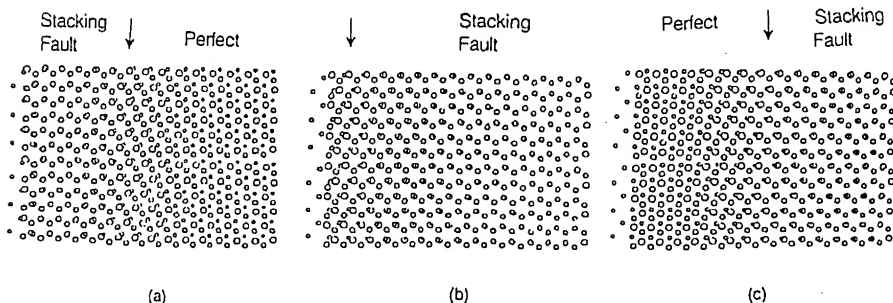


**Figure 12.** Projection of copper atoms on (111). Two half-dislocations are connected with a stacking fault. (a) At 3500 time cycles ( $0.7d$  step height), (b) at 5000 time cycles ( $1.0d$  step

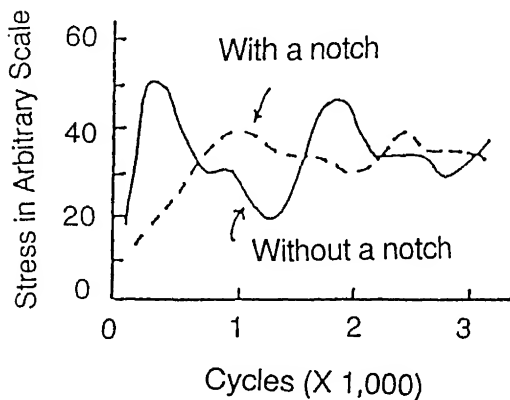


**Figure 13.** Stress-strain curves of specimen Cu-1 (without a notch) and Cu-2 (with a notch).

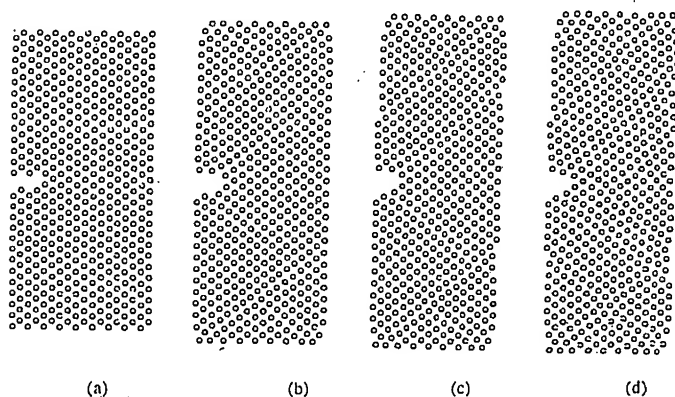


**Figure 14.** Specimen Cu-3 (Al deformation), projection on  $xz$  plane: (a) at 300 time cycles (6% elongation), (b) at 375 cycles (7.5% elongation), (c) at 500 cycles (10% elongation), and (d) at 675 cycles (13.5% elongation).

Heidenreich–Shockley dislocation and the second dislocation was the other half of the Heidenreich–Shockley dislocation and these half-dislocations were connected by the stacking fault. The stress on the surface of  $(1\bar{1}0)$  was calculated by the sum of the force in the  $[101]$  direction on the atom in the two atomic layers on  $(1\bar{1}0)$ .

For a crystal with a notch, similar deformation was applied. A crack was made by taking out one atomic layer on  $(111)$ . This specimen is called Cu-2 (figure 10b). Dislocations were created from the tip of the notch, slid on  $(111)$ , and ejected. The projection of atomic positions on  $(11\bar{2})$  are given in figures 11d to 11f. The stress-strain curves are shown in figure 13. It was found that the stress to create the first half-dislocation into the crystal was the highest and the stress to create the second half-dislocation was lower, and that the stress to create the second dislocation is a little lower than that for the first one. The stress to create dislocations in the crystal with a notch (specimen Cu-2) was lower than that in the crystal without a notch (specimen Cu-1). The projection of atomic positions on  $(11\bar{2})$  are similar to figures 11a to 11c. Edge dislocations were created on  $(1\bar{1}0)$ . The edge dislocations were split into



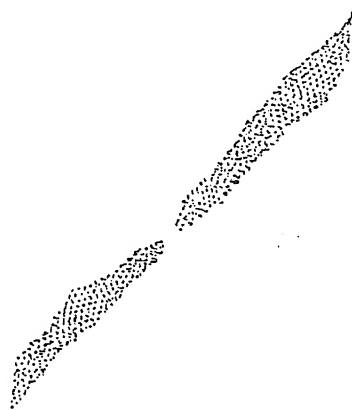


Figure 18. Specimen Cu-3 just after break into two pieces.

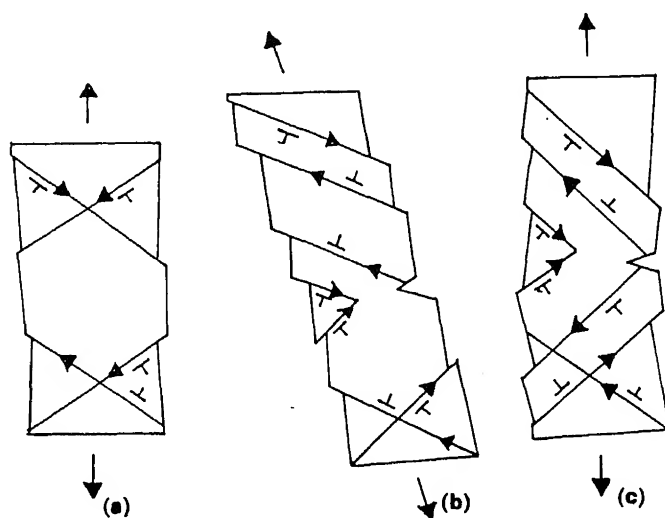


Figure 19. Schematic diagrams of the creation and motion of half-dislocations in specimen Cu-3 (A1 deformation), (b) specimen Cu-2 (A2 deformation), and (c) specimen Cu-1 (A3 deformation).

direction, all the atoms except one layer of both ends relaxed for 25 cycles, pulled 0.7% in  $[101]$  direction and all atoms relaxed for 25 cycles.

Specimen Cu-4 was pulled in  $[110]$  direction (G1 deformation). All atoms were moved  $0.005 \times (x_i^2 + z_i^2)^{1/2}$  in  $[101]$  direction, then all the atoms except one layer of both ends were relaxed for 25 cycles, pulled 0.5% and all atoms relaxed for 25 cycles. The atoms in one layer of the both ends were relaxed in  $x$  and  $y$  directions. This was repeated. The time step of the molecular dynamics was  $5 \times 10^{-15}$  sec.

Atomic positions near the centre in the  $y$  direction of specimen Cu-3 (A1 deformation) projected on  $xz$  plane (010) are plotted in figures 14(a), (b), (c) and (d), figure 14(a) is the initial configuration. In figure 14b, near the tip of the notch, a half-dislocation was created. In figure 14c, the half-dislocation moved to the right. In figure 14d, the half-dislocation moved to the left. These can be clearly seen from the figure.

the centre of Cu-3 (A2 deformation) projected on  $xz$  plane (010) are plotted in figure 15. A half-dislocation was created near the tip of the crack, and two half-dislocations were created near the grip. This is more clearly seen in figure 15c. In figure 16 the stress-strain curve of specimen Cu-3 (A2 deformation) is plotted. A very sharp yield point was found. Atomic positions near the centre of specimen Cu-4 projected to  $xz$  plane are plotted in figure 17. In figure 17a a half-dislocation is seen near the grip. More dislocations are seen in figures 16c and 16d. The projection on  $xz$  plane just after fracture is plotted in figure 18.

It was found that a notch is normally a source of dislocations due to stress concentration. When the notch thickness was small however, (in the case of figure 17), the effect of the notch was not large. The interaction across the notch still existed.  $[211]$   $(111)$  and  $[112]$   $(111)$  half-dislocations were created leaving stacking faults. Schematic diagrams are given in figures 19(a), (b) and (c) for specimen Cu-3 (A1 deformation), specimen Cu-2 (A2 deformation) and specimen Cu-4, respectively. The initial stage of deformation was surely caused by the creation and motion of dislocations. In the middle stage, dislocations on different slip planes cross each other. The work hardening occurs due to the cutting of dislocations. In the final stage, in the case of copper, crystalline state with many dislocations and the inhomogeneous is normal.

## Acknowledgement

The research was supported by a Grant-in-Aid by the Ministry of Education, Science and Culture under Priority Area "Crystal Growth Mechanism in Atomic Scale".

## References

- Doyama M 1993 *Computer aided innovation of new materials II* (eds) M Doyama, J Kihara, M Tanaka and R Yamamoto (Amsterdam: North-Holland) pp 587–590
- Doyama M and Yamamoto R 1986 *Computational mechanics 86* (Springer Verlag) part III, pp 203–208
- Oh D J and Johnson R A 1988 *J. Mater. Res.* **3** 471
- Oh D J and Johnson R A 1989 *Atomistic simulation of materials* (eds) V Vitek and D J Srolovitz (New York: Plenum Press) pp 233–238
- Pak H M and Doyama M 1969 *J. Fac. Engg.* **B30** 111



## Basic studies leading to the development of an ultrahigh strength, high fracture toughness low-alloy steel

G MALAKONDAIAH, M SRINIVAS and P RAMA RAO\*

Defence Metallurgical Research Laboratory, Kanchanbagh P O, Hyderabad 500 258, India

\*Jawaharlal Nehru Centre for Advanced Scientific Research, IISc Campus, Bangalore 560 012, India

**Abstract.** Ultrahigh strength steels have been used increasingly in recent years for critical aircraft and aerospace structural applications. In such applications, though materials performance is of prime consideration, cost and availability makes the low-alloy steels an attractive option. This paper describes the development of an ultrahigh strength NiSiCrCoMo low-alloy steel, supported by significant findings obtained from the basic studies that were aimed at understanding how solute additions influence fracture resistance of iron, with and without the presence of carbon. The results of the basic studies, in combination with the work of Garrison (1986) on a NiSiCr steel, have profitably been employed in the development of a NiSiCrCoMo low-alloy steel possessing a strength–toughness combination quite comparable to the highly alloyed 250-grade maraging steel. Reproducibility of attractive strength and toughness properties has been established in tonnage scale melts. This steel, in the softened condition, has good formability and machinability. Weld parameters have also been established. The NiSiCrCoMo low-alloy steel thus meets the requirements of performance and cost rendering it an attractive option for advanced structural applications.

**Keywords.** Ultrahigh strength low-alloy steel; fracture toughness; alloy softening; tempered martensite embrittlement.

### 1. Introduction

Steels for several high-technology applications, such as aircraft and aerospace, need to possess ultrahigh strength coupled with high fracture toughness in order to meet the requirement of minimum weight while ensuring high reliability. In such applications, though materials performance is of prime consideration, cost and availability makes the low-alloy steels an attractive option. The commercial use of low-alloy steels for such applications has often been limited by their low fracture toughness. It is well-known that increase in strength is generally accompanied by a decrease in toughness. Considerable research effort has been directed over the past two decades or so towards improving fracture toughness of low-alloy steels at yield strengths  $\geq 1400$  MPa. As recently reviewed by Tomita (1991), these efforts can broadly be classified into three methods, namely (i) thermal and thermomechanical treatments, (ii) control of sulphide inclusions and (iii) design of new alloys. Here we present the work carried out by us aimed at development of a low-alloy NiSiCrCoMo steel possessing strength–toughness combination quite comparable to highly alloyed 250-grade maraging steel.

We embarked upon a research programme with the aim of understanding the fracture toughness behaviour of iron and its alloys, which constitute the basis for widebanded engineering steels. Evaluation of fracture behaviour of iron based solid

the work of Garrison (1986) on a NiSiCr steel, has been profitably employed for the development of a NiSiCrCoMo low-alloy steel.

## 2. Basic studies

Solute additions to metals to form solid solutions invariably results in improvement in strength with a concomitant decrease in fracture resistance. There exists a fair amount of understanding as to how solutes influence strength of the alloys (Leslie 1972; Pickering 1978). However, understanding in regard to resistance to fracture, in comparable depth, is yet to evolve. To-date studies pertaining to the fracture resistance of iron and its solid solutions are limited and have been carried out in terms of either tensile ductility or impact transition temperature, which parameters do not always correlate well with the fracture toughness. In our work, the  $J$ -integral method was used for the measurement of ductile fracture toughness  $J_{IC}$  of eight solid solution alloys of Armco iron containing cobalt, molybdenum, nickel or silicon at two levels of concentration. The studies were then extended to Fe-C based alloys.

### 2.1 Solid solution alloys of iron

Solid solution alloys of iron with Co, Mo or Ni at 0.5 and 5.0 wt.% and Si at 0.5 and 3.5 wt.% concentrations were processed, the details of which are given elsewhere (Srinivas 1991). Armco iron, Fe-0.5 Co, Fe-5 Co and Fe-0.5 Mo exhibited stable crack extension while Fe-0.5 Ni, Fe-5 Ni, Fe-0.5 Si, Fe-3.5 Si and Fe-5 Mo showed cleavage instability during loading of precracked fracture toughness specimens (Srinivas *et al* 1994a).  $J$ - $R$  curve technique as well as critical stretch zone width were employed to derive  $J_{IC}$  in the former case while in the latter case the value of  $J$  at the onset of cleavage instability was taken as  $J_Q$  and subjected to validity checks. Fracture toughness  $J_{IC}$  data for the four binary alloys are presented in table 1 and plotted as a function of alloying content in

**Table 1.** Tensile, impact and fracture toughness properties for Armco iron and its binary alloys.

Material	Grain size ( $\bar{L}/\mu\text{m}$ )	Yield stress (MPa)	UTS (MPa)	$n$	CVN impact		$J_{IC}$ ( $\text{kJ/m}^{-2}$ )	Notch yield ratio**
					energy at RT (J)	DBTT* (K)		
Armco iron	78	189	296	0.29	250	243	170	—
Armco iron	118	180	296	0.28	260	251	140	2.5
Fe-0.5 Si	125	225	385	0.21	8	330	97	—
Fe-3.5 Si	140	423	541	0.15	6	405	42	1.5
Fe-0.5 Mo	125	187	359	0.27	52	276	112	—
Fe-5.0 Mo	120	212	385	0.22	40	285	102	—
Fe-0.5 Ni	125	195	335	0.25	8	353	59	—
Fe-5.0 Ni	80	257	386	0.21	15	423	80	—
Fe-0.5 Co	130	110	290	0.30	210	253	162	—
Fe-5.0 Co	125	130	293	0.35	270	263	187	3.7

\*20 J (15 ft. lb) criterion

\*\*Ratio of notch tensile strength and yield strength

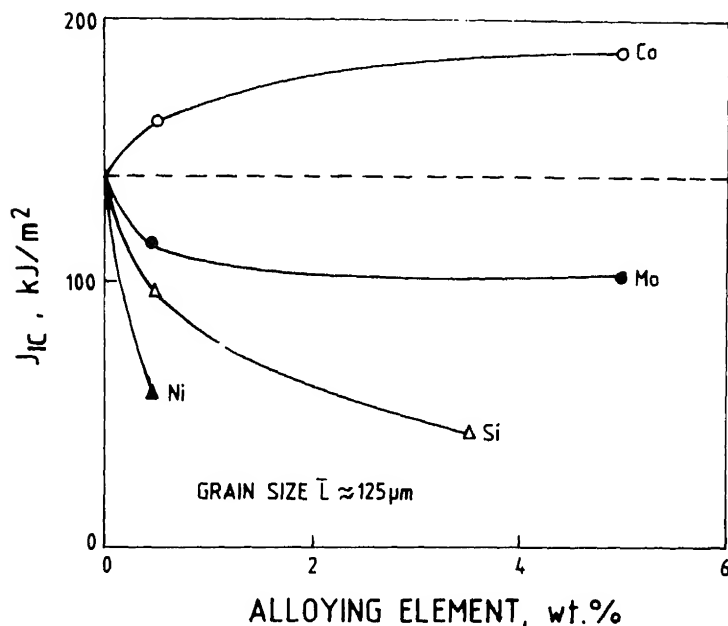


Figure 1. Influence of solute additions on fracture toughness of Armco iron at a constant grain size of 125  $\mu\text{m}$ .

figure 1. The notable observation is that cobalt imparts to Armco iron significant improvement in fracture toughness. On the other hand, Si and Ni have an increasing degree of deleterious effect on Armco iron in that order, with the least effect being noticed with Mo (Srinivas *et al* 1991a, 1994a).

The large decrease in  $J_{IC}$  with silicon and higher molybdenum concentration is explained on the basis of a change in fracture mode from ductile to cleavage as a result of stress concentration ahead of the crack tip reaching the cleavage fracture stress. On the other hand, the loss in fracture toughness with nickel addition is attributed to sulphur segregation at grain boundaries which results in pockets of intergranular fracture.

Mo, Ni or Si increases the yield strength (YS) of iron. On the other hand, cobalt lowers the yield strength of iron, with no observable effect on ultimate tensile strength (UTS) (table 1). The extent of reduction in yield strength (alloy softening) was seen to decrease with increasing cobalt content. Through secondary ion mass spectroscopy (SIMS), experimental evidence has been obtained, for the first time, for the suggestion that the 'scavenging' of interstitials (Rees *et al* 1951; Stoloff *et al* 1965; Ravi and Gibala 1969; Smialek *et al* 1970; Pink *et al* 1980; Ishii *et al* 1984) leads to alloy softening. Ion images for Armco iron, figures 2a and 2b, clearly indicate that the interstitial carbon is homogeneously distributed in the solution. On the other hand,  $C^-$  and  $CN^-$  ion images for Fe-5 Co alloy, figures 2c and 2d, clearly reveal segregation of carbon and nitrogen at the grain boundaries. It was also observed through yield stress dependence on grain size that the Hall-Petch constants  $\sigma_0$  and  $k_y$  substantiate SIMS observations (Srinivas *et al* 1994a).

The increase in  $J_{IC}$  of Armco iron due to cobalt addition is primarily attributable to the increase in the strain hardening exponent  $n$ . The critical plastic zone size increases with increasing  $n$ . Furthermore, increase in  $n$  results in slip dispersal and reduces the void growth rate. Increased  $n$  as a result of cobalt addition is therefore expected to delay void nucleation and decrease the void growth rate. It thus appears that cobalt addition toughens iron by influencing the energy spent in the plastic zone formation as well as in the subsequent stages of the ductile fracture process, namely void nucleation, growth and coalescence of ductile fracture. If the lowering of yield strength

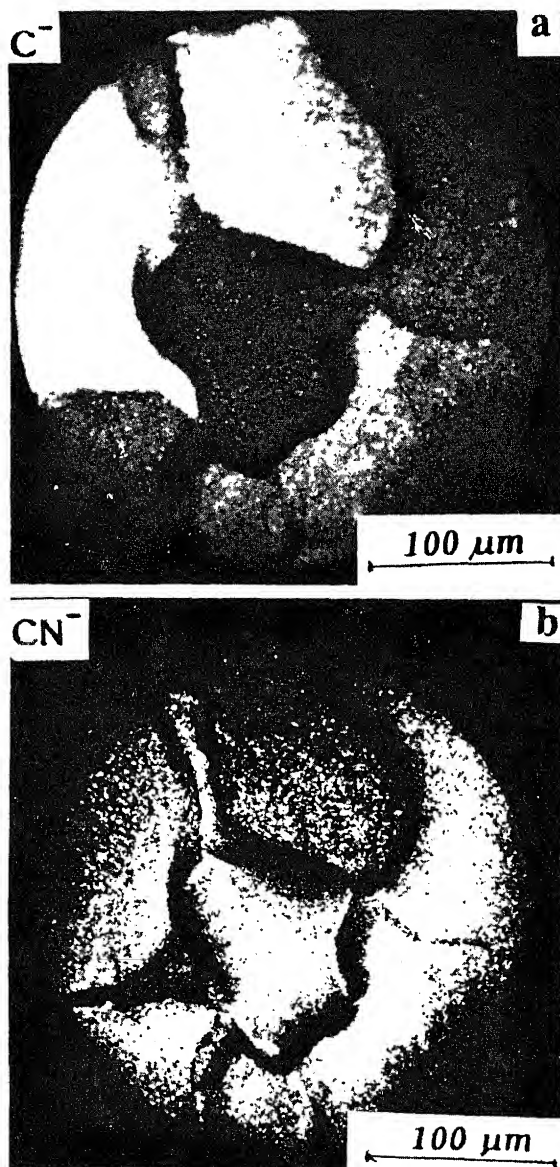
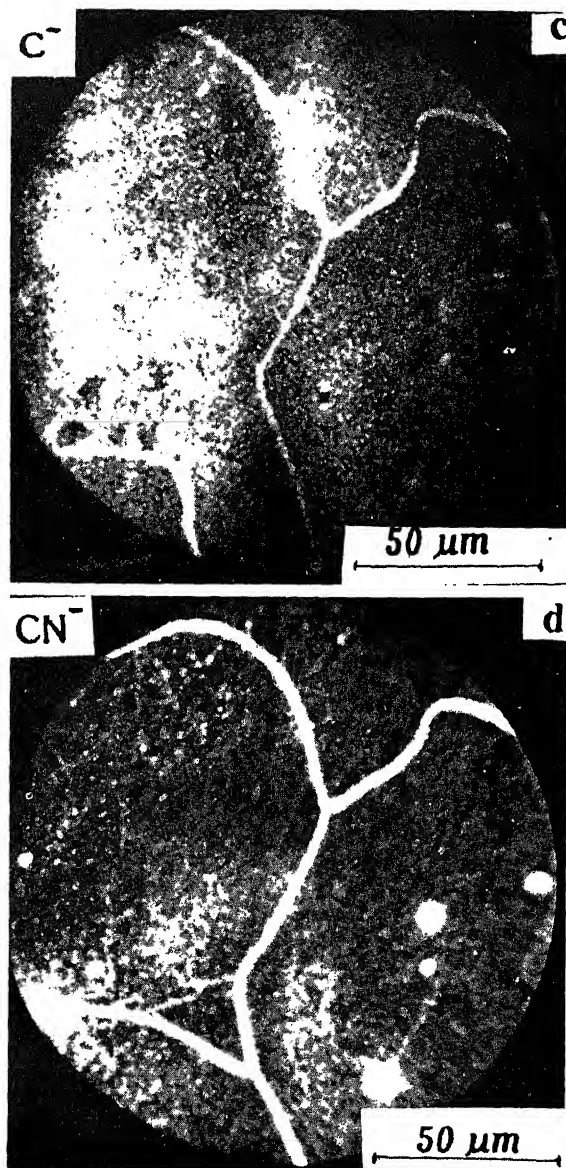


Figure 2a-b.



**Figure 2.** SIMS ion images showing (a, b) uniform distribution of interstitials in Armco iron, and (c, d) scavenging of interstitials to grain boundaries in Fe-5Co alloy.

by cobalt addition to iron were to be the prime reason for the enhancement of  $J_{IC}$ , addition of 0.5% Co, which reduced the yield strength by 40% as compared with a 25% decrease with 5% Co addition, should have resulted in a larger increase in  $J_{IC}$ . Contrary to these expectations, a 5% cobalt addition caused a higher increase in  $J_{IC}$  of iron (35%). Although Fe-Co alloys have lower yield strengths than Armco iron, the flow stress builds up rapidly as a result of higher strain hardening rate at the early stages of plastic deformation.



A new approach has been proposed (Srinivas *et al* 1994b) to the calculation of  $J_{IC}$  in terms of the critical strain criterion model, originally developed by Rice and Johnson (1970) and Ritchie and Thompson (1985), for engineering alloys having a substantial volume fraction of second phase particles. The sequence of events leading to crack initiation is assumed to be as follows. As soon as the pre-cracked sample is loaded in tension under a monotonically increasing load, extensive blunting of the crack tip occurs. The crack blunting process is completed, leading to a constant stretch zone width (SZW), before the void nucleation and growth occur at a characteristic distance  $l_c$  from the blunted crack tip. The mechanism of void nucleation ahead of the blunted crack and also the characteristic distance  $l_c$  of the void from the crack tip have been determined for a single phase material, for the first time, through a careful examination of the interrupted fracture toughness test specimens (Srinivas 1991; Srinivas *et al* 1994b). The proposed approach not only incorporates the experimentally measured  $l_c$  values but also the plastic flow related energy dissipation in the Hutchinson–Rice–Rosengren zone beyond the process zone. Theoretically predicted  $J_{IC}$  values are compared in figure 3 with those derived experimentally. Figure 3 also includes data on Armco iron and nickel derived over the temperature range 298–673 K (Srinivas *et al* 1991a). It is clear

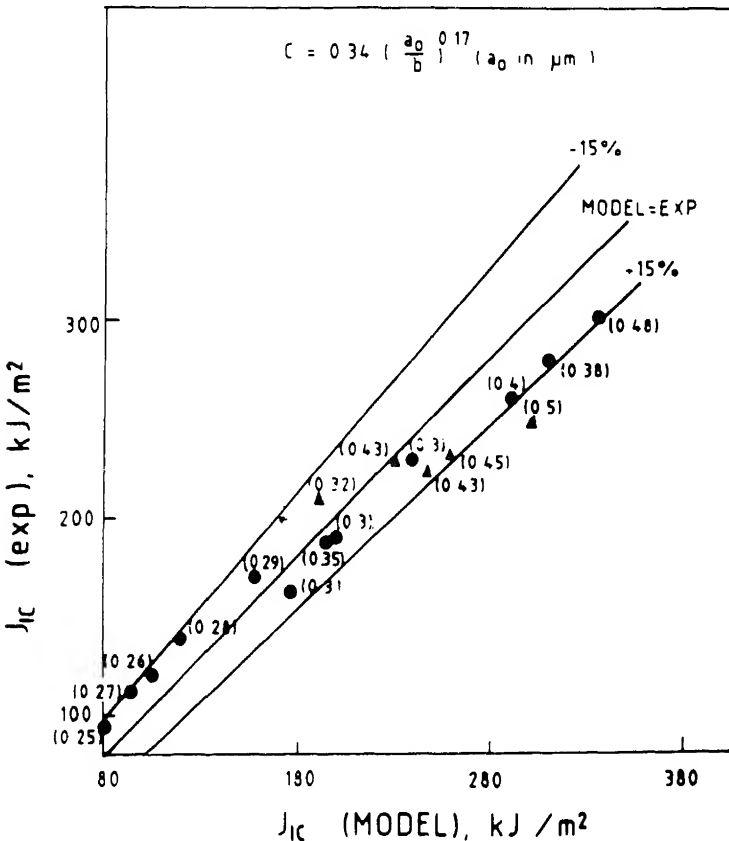


Figure 3. A comparison between experimentally measured and model predicted  $J_{IC}$  values.

from figure 3 that the proposed method estimates reasonably well (to within  $\pm 15\%$ ) the ductile initiation fracture toughness  $J_{IC}$  of single phase materials exhibiting a wide range of values (100–300 kJ/m<sup>2</sup>).

## 2.2 Fe–C–X alloys

The studies on Fe–C–X alloys have significantly revealed that the beneficial effect of cobalt on  $J_{IC}$  of iron is even more pronounced in the presence of carbon (Srinivas *et al* 1991b). The strength and toughness properties of Fe–0.2 C, Fe–0.2 C–5 Co and Fe–0.2 C–5 Ni alloys are compared in table 2. A 5% cobalt addition does not influence significantly the strength behaviour of Fe–0.2 C alloy. On the other hand, a 5% nickel addition appreciably increases the strength and reduces ductility and work hardening exponent. The addition of 5% cobalt significantly enhances (80%)  $J_{IC}$  of Fe–0.2 C alloy, while the addition of 5% nickel increases the same marginally (18%). Nickel, generally considered to be a beneficial element in the presence of carbon is seen to influence dramatically the impact toughness with only a marginal effect on  $J_{IC}$ . On the other hand, cobalt addition, with no observable effect on impact toughness, causes significant improvement in  $J_{IC}$ . These results further suggest that there is no one-to-one correlation between impact toughness and static fracture toughness for this class of alloys.

Similar findings have been reported in recent years (Ritchie *et al* 1976; Lin *et al* 1986) although, on the other hand, there is a fairly widespread use of correlations between impact toughness and fracture toughness. High temperature austenitizing treatment at 1473 K results in a two-fold increase in fracture toughness  $K_{IC}$  of AISI 4340 steel but gives rise to inferior charpy impact energy as compared to conventional 1143 K austenitizing treatment (Ritchie *et al* 1976). This behaviour was shown to be independent of shear lip energy and the variation in strain rate imposed by  $K_{IC}$  and impact tests. Such an effect was found to result from the differing response of each microstructure in regard to the influence of notch root radius on toughness. Ritchie *et al* (1976) proposed that failure occurs when the maximum tensile stress exceeds the critical fracture stress  $\sigma_F$  over a characteristic distance ahead of a sharp crack ( $K_{IC}$ ) or at the elastic-plastic interface ahead of a rounded notch (impact). Fracture toughness of 1473 K structure is higher because the characteristic distance (associated with coarser grain size) is larger while the higher impact toughness of 1143 K structure is a result of larger fracture stress. On the other hand, the reasons for the dramatic effect of nickel on impact toughness observed in the present study could be traced to alloy softening at high strain rates prevailing under impact conditions (Srinivas *et al* 1991c),

**Table 2.** Tensile, impact and fracture toughness properties of Fe–C–X alloys.

Material	YS (MPa)	UTS (MPa)	El. (25 mm GL) (%)	CVN impact energy (J)	$J_{IC}$ (kJ/m <sup>2</sup> )
Fe–0.2 C	244	370	44	16	130
Fe–0.2 C–5 Co	242	409	47	15	232
Fe–0.2 C–5 Ni	297	467	37	120	153

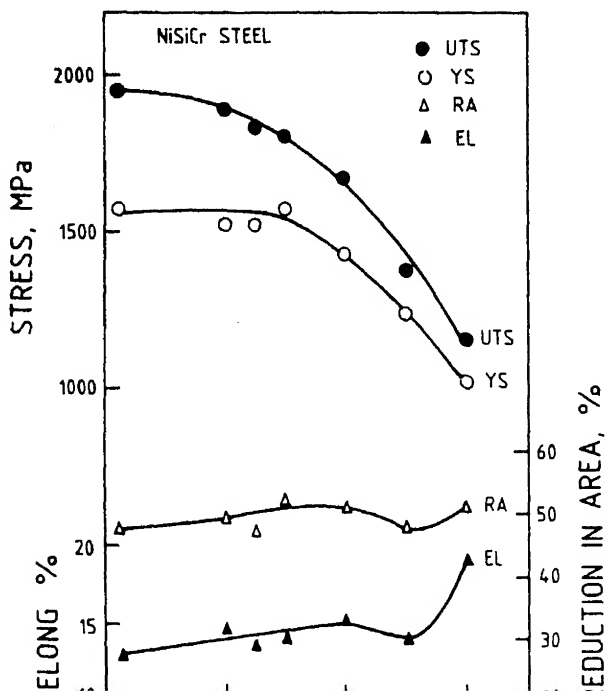
as also suggested by Jolley (1968) and Petch (1987). The microstructural features, namely ferrite grain size and the volume fraction of pearlite were maintained nearly the same in all the three Fe-C based alloys under consideration.

### 3. Development of NiSiCrCoMo steel

It is evident from the foregoing that cobalt toughens iron, and even more positively in the presence of carbon. In our efforts to arrive at a new alloy chemistry that possesses improved fracture toughness at ultrahigh strength levels, cobalt addition was made to Garrison NiSiCr steel.

#### 3.1 Cobalt modified NiSiCr steels

Silicon is a solid solution strengthening element. It is known to delay tempering and shift tempered martensite embrittlement to higher temperatures, which features enable retention of ultrahigh strength levels even after tempering at relatively higher temperatures. Silicon is also known to influence sulphide distribution in the presence of nickel (Garrison 1986). Silicon refines sulphide particle size and increases sulphide spacing and thereby causes an increase in fracture toughness by rendering the fracture



process that involves void nucleation, growth and linkage more difficult. In view of these observations, Garrison (1986) NiSiCr steel containing high silicon has been chosen as the base material.

The variation of strength with tempering temperature (figure 4) shows that the NiSiCr steel retains high strength up to 250°C. Beyond about 300°C, there occurs a steep fall in strength, which is also accompanied by a loss in ductility. A trough in ductility variation with tempering temperature occurs in the temperature range 400 to 600°C. The impact energy at room temperature increases with tempering temperature up to around 300°C, beyond which a steep fall occurs, with a minimum at 500°C (figure 5). It is evident from the data presented in figures 4 and 5 that the steel develops an optimum combination of strength and impact toughness in the 250°C tempered condition. Accordingly, fracture toughness and ductile-to-brittle transition temperature (DBTT) were evaluated for the steel in the 250°C tempered condition. Fracture toughness tests conducted according to ASTM standard E399 yielded  $K_{IC}$  of 103 MPa√m. The impact toughness in the 250°C tempered condition is plotted against test temperature in figure 6. The 20 J criterion yields a DBTT of -100°C. Mechanical properties of the base Garrison NiSiCr steel subjected to an optimum treatment of 250°C tempering are summarized in table 3.

Transmission electron microscopy (TEM) and Auger electron spectroscopy (AES) studies have revealed (Malakondaiah *et al* 1994) that the loss in ductility and impact toughness of NiSiCr steel in the tempering temperature range 350 to 600°C is due to the simultaneous occurrence of tempered martensite embrittlement (TME) and tempered embrittlement (TE). It is now well established that TME occurs in low-alloy

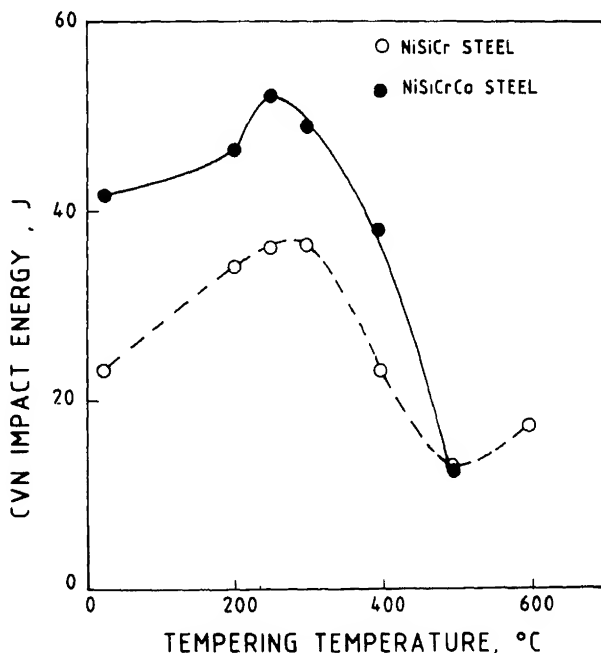


Figure 5. Charpy V-notch impact energy as a function of tempering temperature for NiSiCr and NiSiCrCo steels.

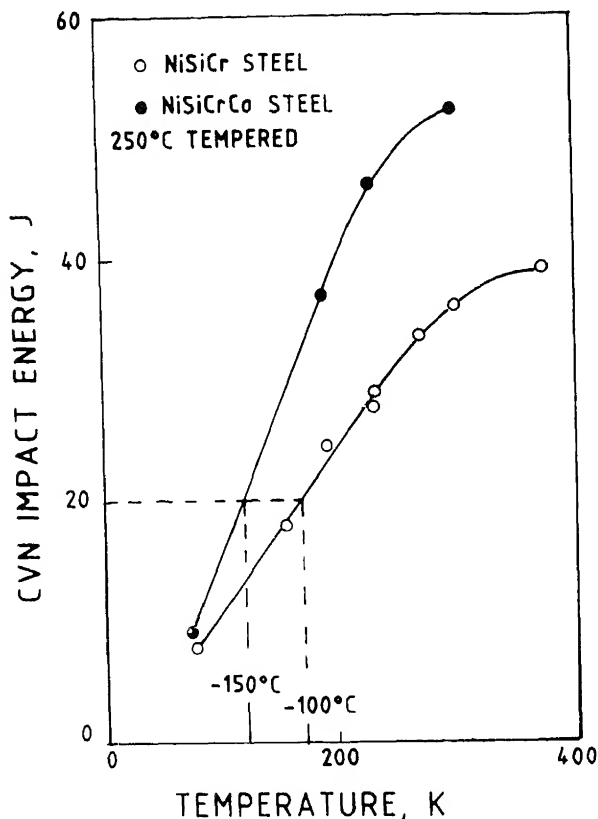


Figure 6. Variation of Charpy V-notch impact energy with test temperature for NiSiCr and NiSiCrCo steels in 250°C tempered condition.

Table 3. Mechanical properties of steels developed in the present study in the optimum heat treated condition.

Material	YS (MPa)	UTS (MPa)	RA (%)	CVN impact energy at RT (J)	$K_{IC}$ (MPa $\sqrt{m}$ )
NiSiCr	1550	1825	47	36	103
NiSiCrCo	1360	1670	50	52	140
NiSiCrMo	1648	1904	48	35	102
NiSiCrCoMo	1530	1890	48	34	120

steels when tempered in the temperature range 250 to 400°C. A higher temperature range of 350 to 600°C for NiSiCr steel is understandable as silicon is known to shift TME to higher temperatures. TEM carried out on 250, 500 and 600°C tempered specimens revealed the presence of interlath-retained austenite in the 250°C tempered condition, transformation of retained austenite to carbides in the 500°C tempered condition and coarse interlath carbides in the 600°C tempered condition (figure 7).

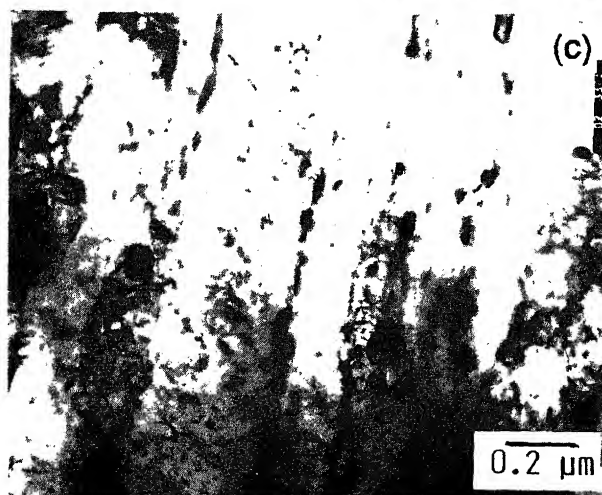
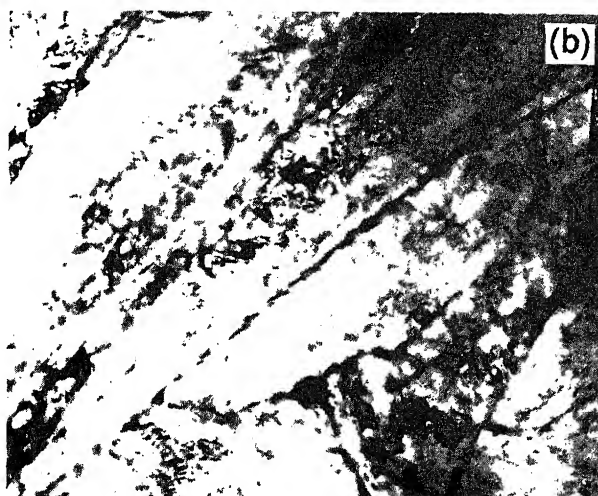
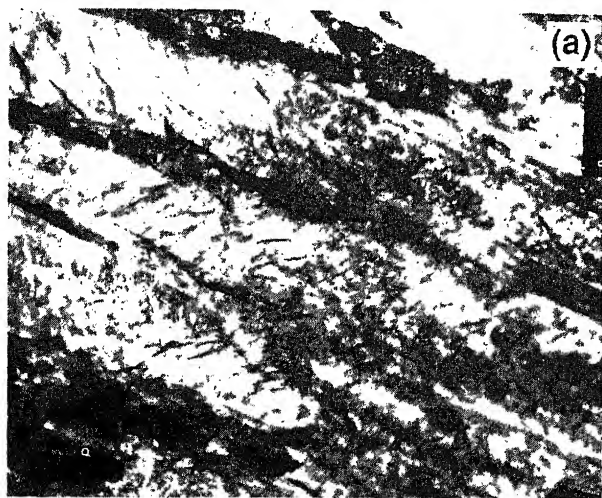


Figure 7. TEM micrographs of NiSiCr steel tempered at (a) 250°C and (b) 500°C showing

Further, AES carried out on 500°C tempered condition revealed segregation of phosphorous, which was absent in the as-quenched condition, suggesting occurrence of temper embrittlement.

Cobalt addition was made to the base NiSiCr steel to achieve further improvements in fracture toughness. The tempering behaviour of NiSiCrCo steel, shown in figure 8, reveals that the steel retains higher strength up to 300°C, as against 250°C observed with NiSiCr steel. Ductility shows a trough in the tempering temperature range 400 to 600°C. The impact energy data included in figure 5 reveals that the impact toughness increases with tempering temperature up to 250°C, beyond which a steep fall occurs. It is evident from figures 5 and 8 that NiSiCrCo steel, in a manner similar to that observed with the base NiSiCr steel, develops an optimum combination of strength and impact toughness in the 250°C tempered condition. Fracture toughness tests carried out in this optimum condition yielded a  $K_{IC}$  of 140 MPa√m. The 20 J criterion yields a DBTT of -150°C (figure 6). Mechanical properties of NiSiCrCo steel in 250°C tempered condition are included in table 3. A significant increase in fracture toughness is seen with accompanying loss in strength. However, the loss in strength is not in proportion to the increase in fracture toughness. A 40% increase in fracture toughness is seen while the loss in strength is around 10%. More than 40% increase in impact toughness is also evident (table 3).

The increase in fracture toughness with an accompanying decrement in strength with cobalt addition to base steel is in line with the observations made on cobalt

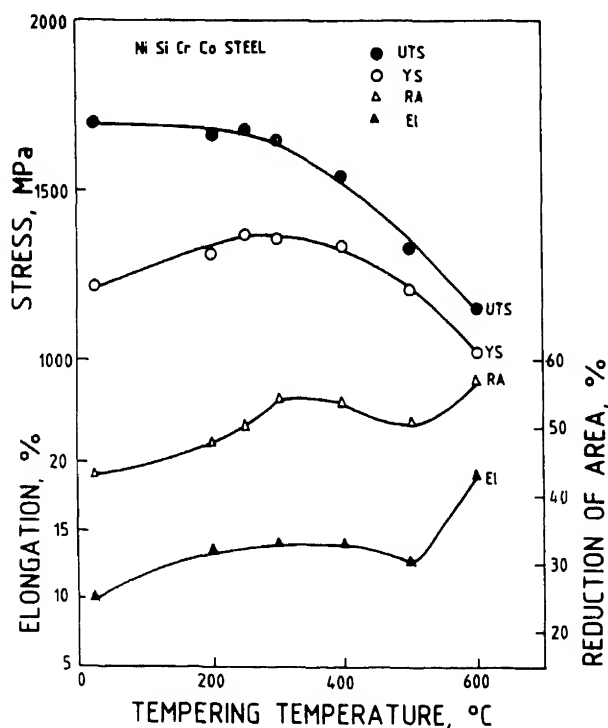
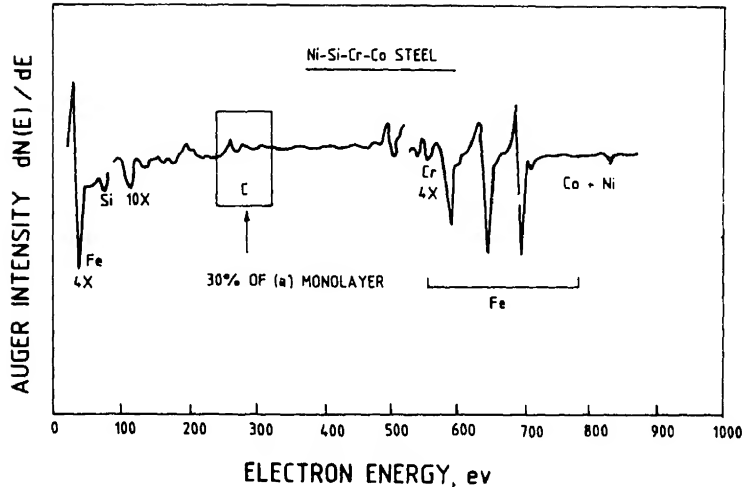


Figure 8. Tensile properties of NiSiCrCo steel as a function of tempering temperature.



**Figure 9.** Scanning Auger spectrum showing carbon segregation at grain boundaries in NiSiCrCo steel.

additions to Armco iron (Srinivas *et al* 1994a). Microsegregation studies carried out on NiSiCrCo steel using a scanning auger microscope show segregation of carbon to the grain boundaries (figure 9). The increase in fracture toughness with cobalt addition is attributable to the segregation of carbon to the grain boundaries, thus increasing the cohesive strength of the grain boundary and rendering the crack initiation process much more difficult (Olson 1990; Misra and Rama Rao 1993).

To build up strength in the presence of cobalt in the base NiSiCr steel, molybdenum addition was resorted to. The studies on iron based solid solutions have shown that, while molybdenum is a solid solution strengthener, the fracture toughness of Armco iron is only marginally lowered as a result of molybdenum addition, below a certain level of concentration. The influence of molybdenum on the base NiSiCr steel was therefore studied. The study has interestingly revealed that the addition of molybdenum to the base NiSiCr steel leads to an increase in yield and ultimate tensile strength with negligible reduction in fracture toughness (table 3). The increase in yield strength is as much as 7% while the increase in UTS is around 5%.

As a follow-up, molybdenum addition was made to the cobalt containing steel. To optimize the composition further, melts with varying content of Co and Mo were taken and processed. The tempering behaviour of each steel was studied and the optimum property combination was established. The fracture toughness of the optimized NiSiCrCoMo steel is nearly 15% higher than that of the base Garrison NiSiCr steel at a matching strength level (table 3). The transmission electron micrograph corresponding to the optimum condition, shown in figure 10, shows lightly tempered lath martensitic structure. SIMS studies carried out on NiSiCrCoMo steel in the optimized condition pointed to carbon segregation to grain boundaries (figure 11) reinforcing the suggestion that grain boundary carbon contributes to enhanced fracture toughness, observed in the results on binary Fe-Co alloys, even when the steel is a complex composition of six alloying elements.



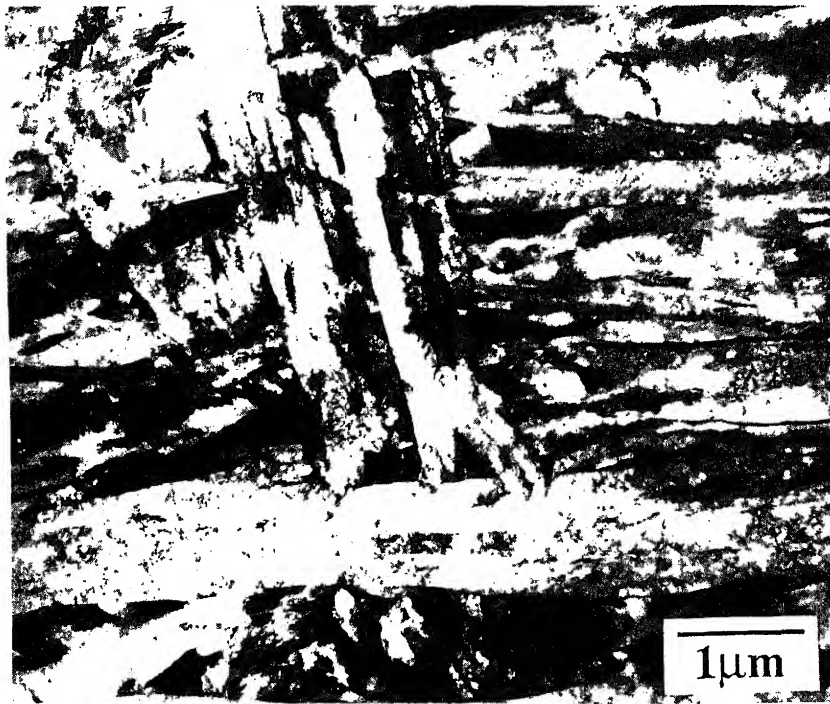


**Figure 10.** TEM micrograph of NiSiCrCoMo steel showing lightly tempered lath martensitic structure in the optimum heat treated condition.

## 2 Comparison with other ultrahigh strength steels

The properties of NiSiCr, NiSiCrCo, NiSiCrMo and NiSiCrCoMo steels are compared in figure 12 with those of the low-alloy steels AISI 4340, 15CDV6 and D6ac, and highly alloyed HP 9-4-30 and maraging steels. Figure 12 shows the range of properties attainable with low-alloy quenched and tempered steels and 18 Ni maraging steels as two separate bands. Among the three low-alloy steels under consideration, namely 15CDV6, AISI 4340 and D6ac, the properties of D6ac steel that was developed for aircraft and missile structural applications fall in the maraging steel regime. While the strength-toughness combination of the base Garrison NiSiCr steel is quite comparable to that of D6ac steel, the cobalt and molybdenum containing NiSiCrCoMo steel possesses properties superior to those of D6ac steel. The NiSiCrCoMo steel is also superior to HP 9-4-30 in terms of strength. The strength-toughness data for NiSiCrCo and NiSiCrCoMo steels fall in the upper bound range for 250-grade maraging steel, with a total alloying content in excess of 30%.

## 2.3 Reproducibility of properties of NiSiCrCoMo steel on tonnage scale

Two 5 ton capacity melts of NiSiCrCoMo steel were taken and processed by Mishra Dhatu Nigam Limited (MIDHANI), a special alloy undertaking. Electric arc melting, followed by vacuum arc refining process, was employed. The mechanical properties of



**Figure 11.** SIMS ion image showing carbon segregation to grain boundaries in NiSiCrCoMo steel.

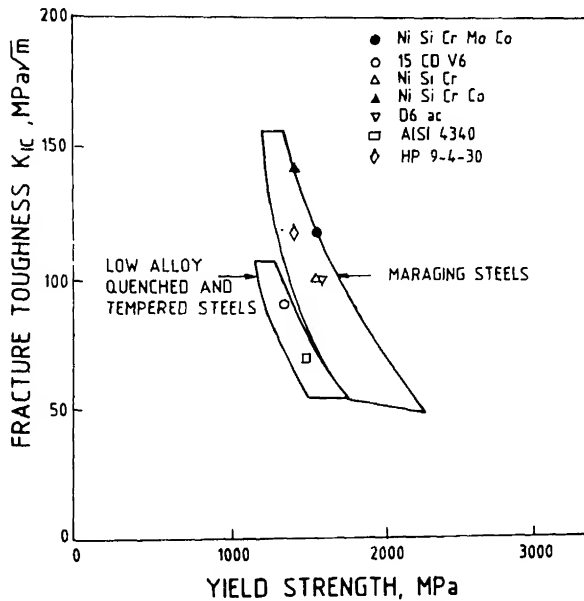


**Figure 12.** Fracture toughness vs yield strength for various ultrahigh strength steels.

**Table 4.** Mechanical properties of NiSiCrCoMo steel.

Property	Lab-scale melt	Industrial-scale melt
YS (MPa)	1530	1610
UTS (MPa)	1890	1970
El. (25 mm GL) (%)	14	13.6
CVN impact energy at RT (J)	34	28–32*
$K_{IC}$ (MPa $\sqrt{m}$ )	120	90–110*

\*The property range is due to the properties obtained at various stages of processing of the ingot to hot-formed products.

**Table 5.** A comparison of mechanical properties in the softened condition.

Steel	YS (MPa)	UTS (MPa)	El. (%) (25 mm GL)
NiSiCrCoMo (740° C/4h, Furnace cooled)	652	853	19.4
250-grade Maraging (Solution treated)	725	1000	18.0

NiSiCrCoMo steel processed on this scale are compared in table 4 with those derived from a laboratory-scale melt. The attractive combination of strength and toughness observed in the laboratory melt is seen to have been reproduced in the industrial-scale melt.

### 3.4 Machinability and formability

Spheroidise-annealing (740° C) softens the NiSiCrCoMo steel considerably. The properties of the steel in the spheroidise-annealed condition are, again, quite comparable to those of the 250-grade maraging steel in the solutionized condition (table 5). NiSiCrCoMo steel in the softened condition can easily be rough machined before finally subjecting to hardening and tempering treatment in order to develop an optimum combination of strength and fracture toughness.

The steel in the softened condition also possesses good formability. Erichsen cupping test yielded a cup depth of 10.8 mm for 2.3 mm sheet. In conformity with these observations, industrial trials of cold forming revealed that a 7 mm thick blank of 570 mm diameter could be formed, without intermediate annealing, to a shell of 350 mm inner radius.

### 3.5 Weldability

Gas tungsten-arc (GTA) process, generally recommended for low-alloy steels, has been chosen. Detailed studies were undertaken to arrive at a suitable filler material. Tension test results of butt-welded and heat-treated 2.3 mm thick sheet specimens revealed that the W2 filler (trade name of MIDHANI for the filler developed for

250-grade maraging steel) yields 96% weld efficiency in terms of yield strength. Experiments have shown that the base metal strength could be realized in the butt-welded and heat-treated condition with base steel as filler. Efforts are now underway to process the base steel in the form of wires for use as filler.

The NiSiCrCoMo steel discussed in this presentation promises to be an inexpensive, and therefore attractive, substitute for expensive, high alloy steel like the well-known maraging steel for light-weight, high performance structural applications.

## Acknowledgements

The authors thank Mr S L N Acharyulu, Director, DMRL for encouragement. Thanks are due to Dr R D K Misra and Mr T V Balasubramanian for their help in conducting Auger studies and Dr K Muraleedharan for TEM studies. Dr R D K Misra helped in obtaining SIMS pictures. We are deeply grateful to Mr K K Sinha and Mr R K Mahapatra, former and present CMDs of MIDHANI, respectively, and their colleagues for their leadership in processing the tonnage-scale melts of the steel. We are grateful to Larsen and Toubro Limited, Bombay for weldability and formability studies.

## References

- Garrison W M Jr. 1986 *Metall. Trans.* **A17** 669
- Ishii H, Kawarazaki T and Fujimora Y 1984 *Metall. Trans.* **A15** 679
- Jolley W 1968 *Trans. Metall. Soc. AIME* **242** 306
- Leslie W C 1972 *Metall. Trans.* **3** 5
- Lin T, Evans A G and Ritchie R O 1986 *Acta Metall.* **34** 2205
- Malakondaiah G, Srinivas M, Marthanda Murthy J and Rama Rao P 1994 *Bull. Mater. Sci.* **17** 73
- Misra R D K and Rama Rao P 1993 *Scr. Metall. Mater.* **28** 513
- Olson G B 1990 in *Innovations in ultrahigh strength steel technology* (eds) G B Olson, M Azrin and E S Wright, *Proc. 34th Sagamore Army Materials Research Conference*, 30 August–3 September, 1987, Lake George, New York, p. 3
- Petch N J 1987 *Acta Metall.* **35** 2027
- Pickering F B 1978 in *Physical metallurgy and design of steels* (London: Applied Science Publishers Ltd)
- Pink E, Mugschl E and Ortner B 1980 *Proc. Fifth int. conf. strength metals and alloys* (eds) P Haasen, V Gerold and G Kosterz (Oxford: Pergamon Press) Vol. 2, p. 1019
- Ravi K V and Gibala R 1969 *Scr. Metall.* **3** 547
- Rees W P, Hopkins B E and Tipler H R 1951 *J. Iron Steel Inst.* **169** 157
- Rice J R and Johnson M A 1970 in *Inelastic behaviour of solids* (eds) M F Kanninen, W F Adler, A R Rosenfield and R I Jaffee (New York: McGraw Hill Book Co) p. 641
- Ritchie R O and Thompson A W 1985 *Metall. Trans.* **A16** 233
- Ritchie R O, Francis B and Server W L 1976 *Metall. Trans.* **A7** 831
- Smialek R L, Webb G L and Mitchell T E 1970 *Scr. Metall.* **4** 33
- Srinivas M 1991 *Fracture behaviour of iron, iron-based solid solutions and Fe–C–X alloys*, Ph D Thesis, Banaras Hindu University, Varanasi
- Srinivas M, Malakondaiah G and Rama Rao P 1991a *Acta Metall. Mater.* **39** 807
- Srinivas M, Malakondaiah G and Rama Rao P 1991b *Proc. 6th int. conf. mech. behav. mater. (ICM6)* Kyoto, Japan
- Srinivas M, Malakondaiah G and Rama Rao P 1991c *Proc. Joint FFG/ICF int. conf. on fracture of engineering materials and structures*, National University of Singapore, Singapore, 6–8 August 1991
- Srinivas M, Malakondaiah G and Rama Rao P 1994a *Proc. R. Soc. London* **447** 223
- Srinivas M, Sundararajan G, Malakondaiah G and Rama Rao P 1994b *Proc. R. Soc. London* **447** 237
- Stoloff N S, Davies R G and Ku R C 1965 *Trans. Metall. Soc. AIME* **233** 1500
- Tomita Y 1991 *Mater. Sci. Tech.* **7** 481



## MOVPE growth and characterization of ZnSe–GaAs heterovalent heterostructures

MITSURU FUNATO, SHIZUO FUJITA and SHIGEO FUJITA

Department of Electrical Engineering, Kyoto University, Kyoto 606-01, Japan

- **Abstract.** ZnSe–GaAs heterovalent heterostructures were fabricated by metalorganic vapour phase epitaxy and characterized structurally and electrically. A study on growth behaviour of GaAs on ZnSe revealed that either the 2-dimensional or the 3-dimensional growth mode may occur depending on the growth conditions. This growth behaviour is applied to the construction of low-dimensional structures. Successful fabrication of quantum well structures and GaAs islands buried into ZnSe is demonstrated by means of X-ray diffraction and transmission electron microscopy. The electrical properties of the heterostructures are also described.

**Keywords.** ZnSe; GaAs; heterovalent heterostructure; X-ray diffraction; TEM; DLTS.

### 1. Introduction

The concept of integrating compound semiconductors seems attractive in the field of optoelectronic devices. For example, laser diodes and light emitting diodes cannot be realized without the integration of different materials such as GaAs and AlGaAs. So far, in order to avoid electron-excess or electron-deficient chemical bonds at the interfaces, devices have generally consisted of homovalent materials. On the other hand, recent considerable progress of growth techniques such as metalorganic vapour phase epitaxy (MOVPE) and molecular beam epitaxy (MBE) is making it possible to integrate heterovalent materials. This may allow a wider range of applicable thin-film materials and heterostructures. Compared with homovalent systems, heterovalent systems may have larger band-gap discontinuities and larger differences in the dielectric constant, which would enhance device performance. Furthermore, heterovalent systems may lead to new functions which cannot be predicted by the conventional idea of the compositional average (Greene 1983).

ZnSe–GaAs is one of the most promising heterovalent material combinations, because the lattice mismatch between ZnSe and GaAs is relatively small (0.27% at room temperature) and optoelectronic devices composed of this combination may cover the entire visible spectrum. Recently some theoretical analyses have shown interesting properties of ZnSe–GaAs quantum wells (QW) (Ihm and Cohen 1979; Khurgin 1988; Kumagai and Takagahara 1988; Shen *et al* 1988; Eppenga 1989). Kumagai and Takagahara (1988) proposed a dielectric QW in which the large difference in dielectric constants between well and barrier layers was positively utilized, and introduced a ZnSe–GaAs QW as a realistic example. Khurgin (1988) showed that the nonlinear and electrooptic coefficients of ZnSe–GaAs heterostructures are substantially larger than those of conventional materials, such as AlGaAs–GaAs heterostructures. However, there are few reports on the fabrication of ZnSe–GaAs QWs (Kobayashi and Horikoshi 1990; Funato *et al* 1992, 1993; Zhang and Kobayashi 1992), because growth of GaAs on ZnSe is considerably more difficult than

optimum growth temperatures for the two materials: high-quality ZnSe on GaAs is grown at temperatures below 500°C, whereas GaAs with superior properties is grown at temperatures above 600°C by MOVPE.

Kobayashi and Horikoshi (1990) investigated GaAs MBE on ZnSe. To avoid the problem of the low  $\text{As}_4$  sticking coefficient on the ZnSe surface, the combination of solid-phase epitaxy (SPE) and migration-enhanced epitaxy (MEE) was employed. The best quality of GaAs was obtained by initiating the growth on ZnSe with  $\text{As}_4$  exposure and deposition of two monolayers (ML) of Ga at room temperature followed by SPE. Farrell *et al* (1991) examined the correlation between interface structures and the growth behaviour of GaAs MBE onto ZnSe. They pointed out that a ZnSe(100) $c(2 \times 2)$ -Zn surface, which is terminated with 1/2 ML of Zn, is optimized by a sequence of steps involving a predeposition of excess Se and a low-temperature deposition of 1/2 ML of Ga prior to GaAs epitaxy. This would provide equal numbers of Ga-Se and As-Zn bonds, resulting in charge neutrality at the interface.

On the other hand, MOVPE has an advantage over MBE that GaAs can be grown on ZnSe at constant growth temperature (Funato *et al* 1992, 1993). In the work described in this paper, the effect of growth conditions, especially growth temperature and V/III ratio, on the growth behaviour in GaAs MOVPE onto ZnSe (001) was studied by means of transmission electron microscopy (TEM). The growth was carried out without changing the growth temperature, unlike GaAs MBE on ZnSe mentioned above. We show that either the 2-dimensional or 3-dimensional growth mode occurs depending on the growth conditions. This growth behaviour is applied to the fabrication of low-dimensional structures and then structural properties characterized in detail by means of double-crystal X-ray diffraction (XRD) and TEM. Finally we refer to electrical properties of Zn(S)Se-GaAs heterostructures.

## 2. Experimental

Samples were grown on [001]-oriented GaAs substrates by an atmospheric-pressure MOVPE system with a cold-wall vertical reactor. Both ZnSe and GaAs layers were grown in the same reactor. Prior to the growth, GaAs substrates were cleaned by degreasing in solvents followed by chemical etching in acidic solution. Etched substrates were loaded into the reactor and were heated to thermally desorb the surface oxide layer at a temperature of 580°C for 10 min in an As ambient. The growth temperature ( $T_g$ ) was varied between 450°C and 550°C. Source materials used were diethylzinc (DEZn) and dimethylselenium (DMSe) for ZnSe, and triethylgallium (TEGa) and tertiary butylarsine (TBAs) for GaAs. Typical flow rates of DEZn, DMSe and TEGa were 6, 48 and 10  $\mu\text{mol}/\text{min}$ , respectively, and the TBAs flow rate ([TBAs]) ranged from 20 to 100  $\mu\text{mol}/\text{min}$ . It should be pointed out that in the case of homoepitaxy, the growth rates of GaAs did not depend on the growth conditions employed here.

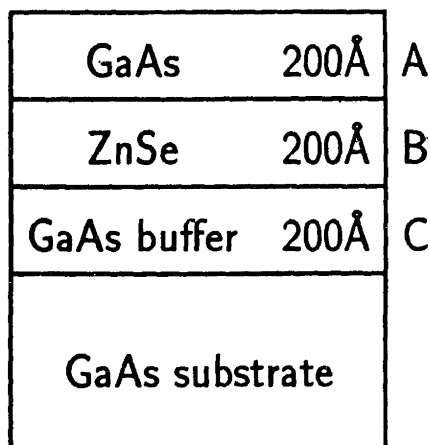
Double-crystal XRD patterns were obtained in the vicinity of the symmetric 004 GaAs Bragg angle, utilizing a  $\text{CuK}\alpha_1$  line ( $\lambda = 1.5405 \text{ \AA}$ ). Theoretical calculation of the X-ray rocking curve is based on the step model (Segmüller and Blakeslee 1973). In the calculation, it was assumed that only ZnSe layers were distorted tetragonally (coherent growth) and that GaAs layers were not distorted. Validity of this assumption was confirmed structurally by comparison of the experimental diffraction pattern with the theoretical calculation and optically by the reflection measurement.

TEM is a powerful technique which provides direct visualization of the interfaces in cross-sectional images, and allows accurate thickness measurements. A [110] cross-section was prepared by ion milling (3 keV Ar<sup>+</sup>). The image was obtained in the bright field.

### 3. Growth of GaAs on ZnSe

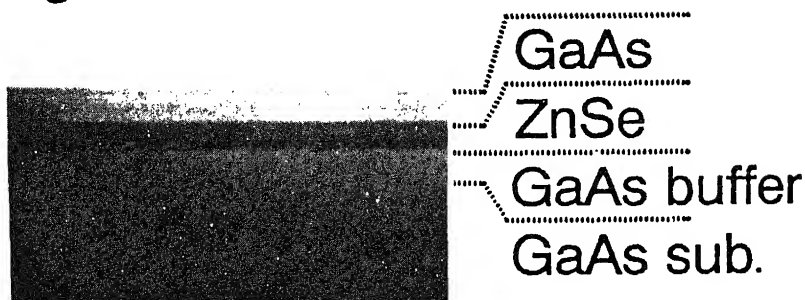
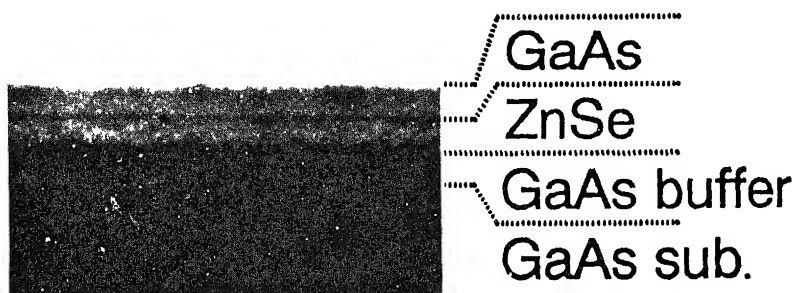
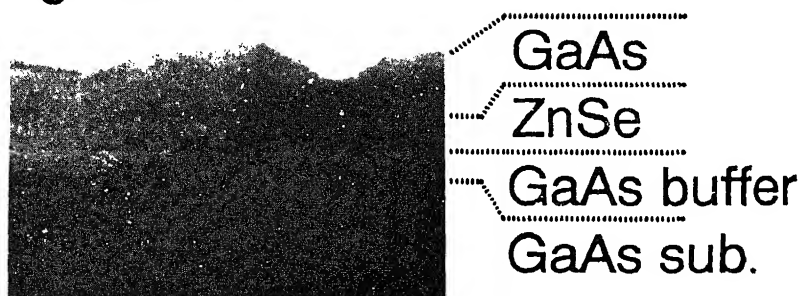
An effort was made to grow the double-layered structure designed as in figure 1, wherein we investigated the growth behaviour of GaAs heteroepitaxy on ZnSe, ZnSe heteroepitaxy on GaAs, and GaAs homoepitaxy through observation of cross-sectional views of layers A, B and C, respectively. A series of samples were grown at the same gas flow rates of VI/II = 8 and V/III = 5 at the different growth temperatures of  $T_g = 450\text{--}550^\circ\text{C}$ . The surface morphology observed by a Nomarski microscope revealed that the double layers grown at high temperature ( $550^\circ\text{C}$ ) have rough surfaces, while those grown at low temperatures ( $\leq 550^\circ\text{C}$ ) have mirror-like surfaces, consistent with the previous report on thicker double layers (Funato *et al* 1992). Figure 2 shows cross-sectional [110] TEM bright-field images of the samples. These images clearly indicate that the growth mode of GaAs buffer layers on GaAs substrates (homoepitaxy) is 2-dimensional at any growth temperature examined here. ZnSe layers grown on GaAs are also uniform in thickness at all temperatures. In contrast, although GaAs growth on ZnSe below  $500^\circ\text{C}$  is 2-dimensional, as easily predicted by the Nomarski microscope observation, GaAs grown at  $550^\circ\text{C}$  is highly 3-dimensional. These findings indicate that the growth behaviour of GaAs on ZnSe is quite different from that of the reverse sequence of ZnSe on GaAs and that of GaAs homoepitaxy.

To elucidate the reason for this growth behaviour, we attempted to grow the same structures as shown in figure 1 at  $550^\circ\text{C}$ , varying the V/III ratio from 2 to 10. Since the flow rate of TEGa is unchanged, a variation of the V/III ratio means flow rate variation of TBAs. Cross-sectional [110] TEM bright-field images are shown in figure 3. They reveal that as the V/III ratio increases i.e. as [TBAs] increases, GaAs



**Figure 1.** Schematic diagram of the designed GaAs on ZnSe double-layered structure. The expected dimensions are GaAs (200 Å), ZnSe (200 Å) and GaAs buffer layer (200 Å).



$T_g = 450^\circ\text{C}$  $T_g = 500^\circ\text{C}$  $T_g = 550^\circ\text{C}$ 

—  
500Å

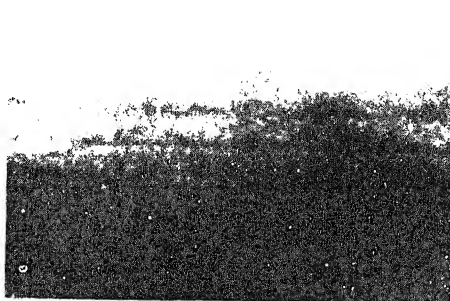
**Figure 2.** Cross-sectional  $[110]$  TEM bright-field images of GaAs (200 Å)/ZnSe (200 Å) double-layered structures grown at various temperatures. V/III ratio is fixed at 5.0.

$V/III=2$



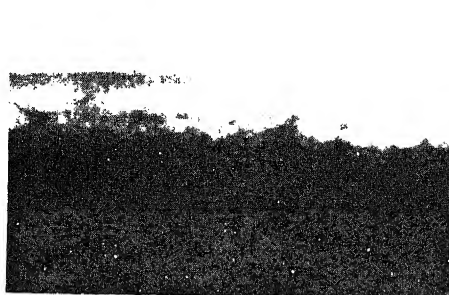
GaAs  
ZnSe  
GaAs buffer  
GaAs sub.

$V/III=5$



GaAs  
ZnSe  
GaAs buffer  
GaAs sub.

$V/III=10$



GaAs  
ZnSe  
GaAs buffer  
GaAs sub.

—  
500Å

becomes flat, whereas as the V/III ratio decreases, GaAs exhibits island-type 3-dimensional growth in which the islands tend to separate from each other.

Figure 4 shows the variation of GaAs island height as a function of the V/III ratio. Island height was measured from cross-sectional TEM images at several different positions on the samples, and is equivalent to layer thickness for the flat layers grown at 450°C or 500°C. For GaAs grown at 550°C, as the V/III ratio increases GaAs shows a stronger tendency for 2-dimensional growth, as seen in figure 3, and the island height decreases. At high V/III ratios, the island height approaches the thickness of the flat layers. This figure suggests that the mechanism behind the formation of GaAs islands on ZnSe is mainly related not to desorption but to migration, because if desorption were the main cause of island formation, the island height would decrease with decrease of the V/III ratio.

For confirmation of this hypothesis, ZnSe–GaAs multilayered structures were grown at 500°C and 550°C without changing the duration of supply of source precursors; hence, unless desorption occurs, the nominal mean thickness of 3-dimensional GaAs growth at 550°C must be equal to the thickness of 2-dimensional GaAs grown at 500°C. This is because GaAs growth rate is constant through the growth conditions employed here, as mentioned in §2. XRD analysis of multilayered structures was applied for the evaluation of the mean thickness. The XRD pattern has satellite peaks and a fundamental peak. The satellite peaks reflect the periodicity and the fundamental peak is located at the angular position determined by the thickness ratio of a set of alternating layers, from which the mean thickness can be estimated. Figure 5 shows double-crystal XRD patterns of the multilayered structures grown at 500°C and 550°C. The structure intended is two cycles of GaAs (200 Å)/ZnSe (250 Å). The XRD profile of the multilayer grown at 500°C has satellite peaks (denoted by open arrows in the figure), indicating good periodicity. On the other hand, satellite peaks are absent in the profile of the multilayer grown at 550°C. This is due to degradation of the periodicity by 3-dimensional growth of GaAs at 550°C.

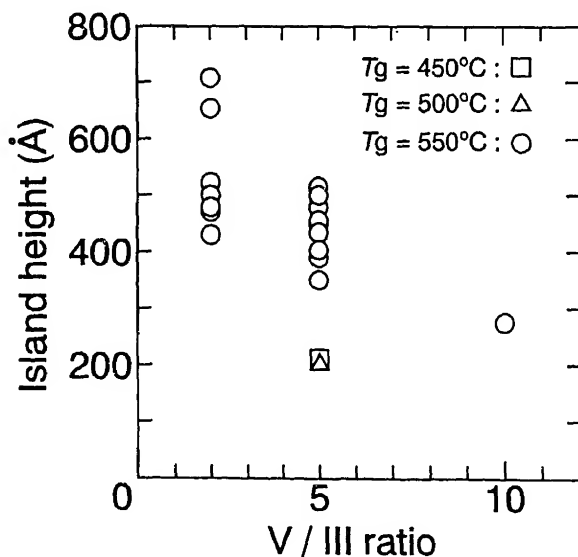
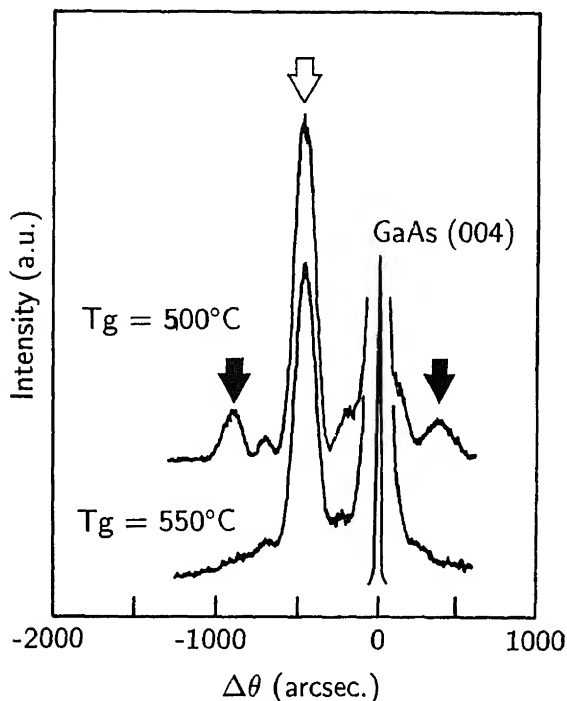


Figure 4. Dependence of GaAs island height on V/III ratio.



**Figure 5.** Double-crystal XRD patterns of GaAs (200 Å)/ZnSe (250 Å)  $\times$  2 multilayered structures grown at 500°C and 550°C. The open arrow designates the fundamental peak and the closed arrows the satellite peaks.

However, since the fundamental peaks of both multilayers are at the same angle, we can conclude that the mean thickness of GaAs grown 3-dimensionally is equal to the layer thickness of GaAs grown 2-dimensionally. This finding provides the evidence for the above hypothesis that migration, not desorption, causes the 3-dimensional GaAs island formation.

In heteroepitaxy of dissimilar materials, migration length of adspecies is crucial to determine the growth mode. Lower growth temperatures will mean lower, or perhaps even negligible, migration lengths, and will therefore promote 2-dimensional growth (Bean *et al* 1984). A high density of adspecies may also bring about the 2-dimensional growth mode, because it inhibits migration and reduces epilayer surface roughness. These tendencies agree well with our results shown in figures 2 and 3. The problem is what the migrating species are. We investigated the effects of TEGa and TBAs on the ZnSe surface (Funato *et al* 1995). When ZnSe was annealed at 550°C in a TBAs ambient, ZnSe was drastically etched at the rate of 150 Å/min under  $[TBAs] = 20 \mu\text{mol/min}$ , whereas it was not appreciably etched thermally. Therefore As-containing molecules, which are generated through decomposition of TBAs, are not the cause of island formation, because an As-related process includes a desorption process. On the other hand, when ZnSe was exposed to TEGa at 550°C, the ZnSe surface became rough due to the nucleation of adsorbed Ga, indicating that metallic Ga may easily migrate on ZnSe. These results indicate that Ga-related clusters are the migrating species and cause GaAs island formation on ZnSe.

#### 4. Fabrication of ZnSe–GaAs low dimensional structures

The growth behaviour discussed above suggests that QWs or quantum dots (QD), where GaAs dots are buried in ZnSe, can be fabricated by controlling the TBAs flow rate and the growth temperature so that GaAs may be grown 2-dimensionally or 3-dimensionally, respectively. We describe the fabrication and structural properties of those low-dimensional structures.

##### 4.1 Multiple quantum well structures

A multiple QW (MQW) whose structure is 10 cycles of ZnSe (200 Å)/GaAs (100 Å), inset of figure 6b, was fabricated under the growth conditions of  $T_g = 500^\circ\text{C}$  and  $V/\text{III} = 5$ , which bring about 2-dimensional GaAs growth on ZnSe.

Figure 6 shows (a) the  $[110]$  cross-sectional TEM bright-field image and (b) the XRD pattern. TEM reveals the successful alternating deposition of 2-dimensional ZnSe and GaAs. The thicknesses of ZnSe and GaAs layers extracted from the photograph turned out to be about 200 Å and 100 Å, respectively, and these values are consistent with the expected dimensions. Fluctuation of the layer thicknesses from period to period seems quite small; we give detailed discussion on this on the basis of XRD. Neither threading dislocations nor stacking faults were observed over the whole area, implying that the lattice mismatch strain is accommodated elastically. Despite some possible intermixing of the layers, the evidence of abrupt compositional modulation is given by the marked contrast between dark ZnSe and bright GaAs.

The XRD pattern shown in figure 6b exhibits intense and well-defined satellite peaks. For comparison, the result of theoretical calculation is also indicated. Supposing

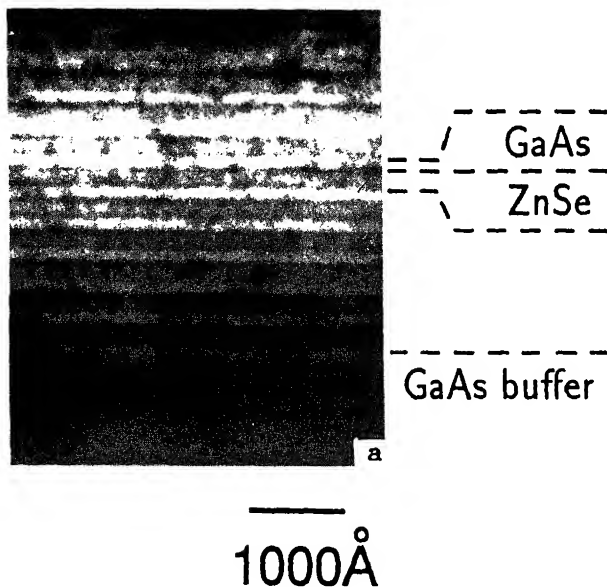


Figure 6a.

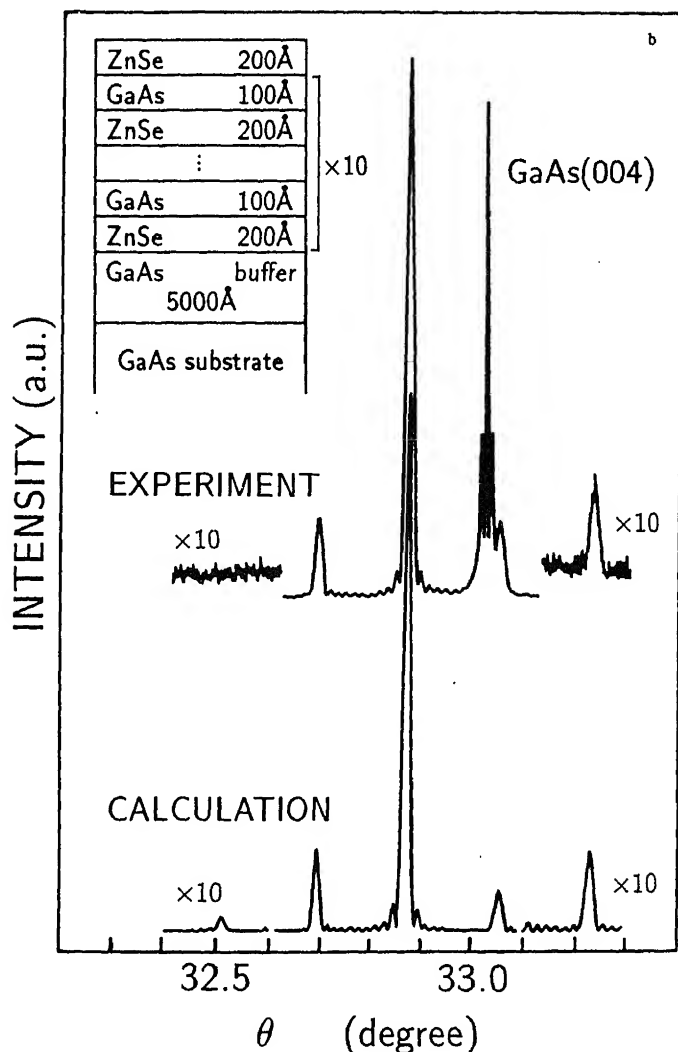


Figure 6. a. Cross-sectional [110] TEM bright-field image and b. double-crystal XRD patterns of GaAs (200 Å)/ZnSe (100 Å)  $\times 10$  MQW. The growth conditions are  $T_g = 500^\circ\text{C}$  and  $V/\text{III} = 5$ .

that the thicknesses of ZnSe and GaAs are 206 and 88 Å, respectively, the calculated peak positions agree well with those of the measured one, indicating the achievement of the designed structure. The full width at half maximum (FWHM) of 53 arcsec and relative intensity of satellite peaks against the fundamental peak are almost equal to the theoretical values; hence the sample may have a high crystalline quality, a high degree of lateral uniformity, and well-defined interfaces. These findings validate the conclusions derived from TEM.

Interference fringes which appear between Bragg peaks are quite sensitive to the small thickness fluctuation (Funato *et al* 1993). The thickness fluctuation in the same

MQW was investigated by examining the profile of interference fringe. The layer thickness with small fluctuation of  $\Delta$  was assumed as  $L(1 + \Delta)$  in the theoretical calculation, where  $L$  is the designed layer thickness.  $\Delta$  will probably follow a Gaussian distribution. We can therefore define the thickness fluctuation using only one parameter, i.e. dispersion ( $\delta$ ) of the Gaussian distribution. Since the fluctuation is considered to be proportional to the thickness, the same dispersion can be used for both GaAs and ZnSe layers.

The profile of interference fringes between 0th and 1st satellite peaks is shown in figure 7, with results calculated by changing the degree of fluctuation from  $\delta = 0\%$  to  $7\%$ . With increasing dispersion, i.e. increasing fluctuation, the profile becomes more irregular. Even when  $\delta = 3\%$ , a distinct deviation from the ideal diffraction pattern is already observed, whereas such deviation is not detectable in the theoretically calculated intensity and FWHM of the fundamental and  $\pm 1$ st satellite peaks. Of course, higher-order satellite peaks will be more sensitive probe to degradation of structural properties, but we believe that interference fringes provide another sensitive approach to evaluating a very small fluctuation. Comparing the experimental result with the calculations (a)–(d) in figure 7, it is found that the experimental profile shows relatively

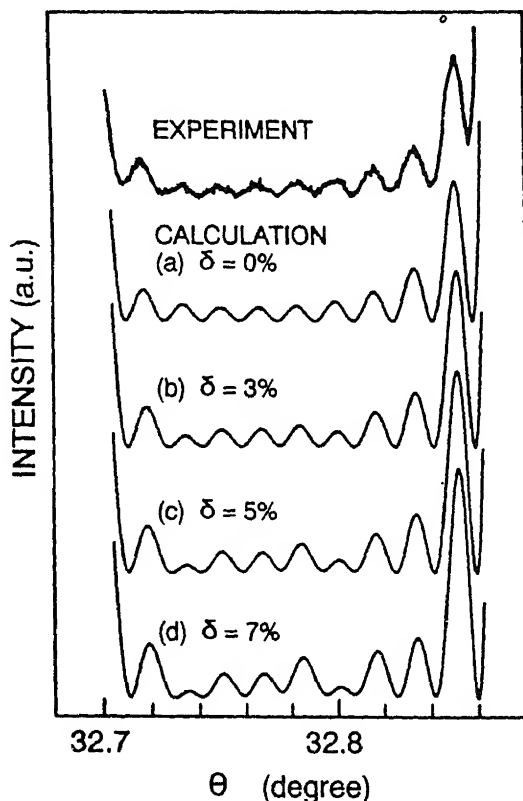


**Figure 7.** Profile of interference fringe between 0th and  $-1$ st satellite peaks of the MQW described in figure 6. The results calculated by assuming various degrees of thickness fluctuation of each individual layer are shown together with the experimental result.

regular oscillation and the structure has fairly complete periodicity, such that the dispersion of fluctuation is within a few per cent.

To investigate the fluctuation in the fabricated structure in detail, the difference between the profile with fluctuation and that without fluctuation ( $\delta = 0$ ) was evaluated in terms of the  $R$  factor defined by (1) below. The profiles of interference fringes between 0th and  $-1$ st satellite peaks were used again.

$$R = \frac{\sum(|I_f| - |I_i|)}{\sum|I_f|}, \quad (1)$$

where  $I_f$  is observed scattering intensity or calculated one under the assumption of some fluctuation, and  $I_i$  the calculated ideal scattering intensity ( $\delta = 0$ ). Scattering amplitude would be used in the conventional  $R$  factor. However, since what is observable is intensity, we use scattering intensity directly instead of scattering amplitude modulus. The result is shown in figure 8. The dashed line indicates the experimental  $R$  factor and the solid line is the  $R$  factor theoretically calculated under the assumption of some fluctuation. In the calculation, random numbers were used in order to express fluctuation, therefore the calculated  $R$  factor would change with every series of random numbers. Hence the calculation was done with 15 different series of random numbers and the theoretical curve in figure 8 represents its average. The calculation shows the best agreement with the experiment under around  $\delta = 3\%$ , which corresponds to the fluctuations of one ( $2.8 \text{ \AA}$ ) and two ( $5.6 \text{ \AA}$ ) monomolecular layers for GaAs and ZnSe, respectively. Therefore the fluctuation, if it exists, seems to be very small in the fabricated structure.

It is important to investigate to what extent constituent layers can be made thinner, especially in the case of multilayered structures constructed from heterovalent

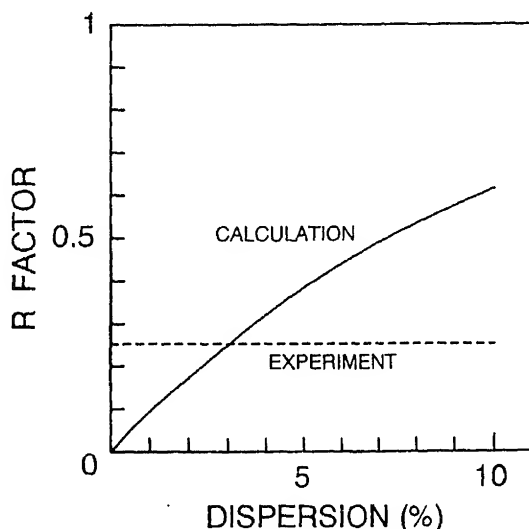


**Figure 8.** Evaluation of fluctuation in terms of the  $R$  factor, using  $\delta = 0\%$  as a standard. The dashed line indicates the experimental value and the solid line represents result of theoretical calculation.



semiconductors such as ZnSe–GaAs QWs. Another MQW, 100 cycles of ZnSe (33 Å)/GaAs (25 Å), which has much smaller layer thicknesses and larger number of cycles compared with the MQW mentioned above, was fabricated. To our knowledge, this is the first reported fabrication of MQW that consists of heterovalent materials with such thin constituent layers. Successful construction was confirmed by comparing the X-ray rocking curve with that calculated theoretically, as shown in figure 9. FWHM of the fundamental peak is 31 arcsec, which provides the evidence of its good crystalline quality. However, FWHM of two satellite peaks are broad and intensities are weak, compared with the theoretical calculation. The satellite peaks have the feature of tailing toward the fundamental peak. The thickness fluctuation is considered to be the origin of this tailing. However, if an accidental thickness fluctuation were the origin, the broadening would occur symmetrically. Therefore, either increase or decrease of period in the growth direction may be the origin of the tailing. Additionally, since the FWHM of the fundamental peak itself is very narrow, the average lattice spacing is unchanged even if there is the change in period; in other words, thickness ratio of constituent materials is constant. This also supports the assumption that the origin is not an accidental fluctuation but an increase or a decrease of period. The mechanism of this phenomenon is unknown yet and further investigation is required.

#### 4.2 GaAs island in ZnSe

In figure 5, FWHM of both profiles are comparable, indicating that crystalline quality of the multilayered structure with 3-dimensional GaAs ( $T_g = 550^\circ\text{C}$ ) is equivalent to that with 2-dimensional GaAs ( $T_g = 500^\circ\text{C}$ ). This high-quality 3-dimensional GaAs

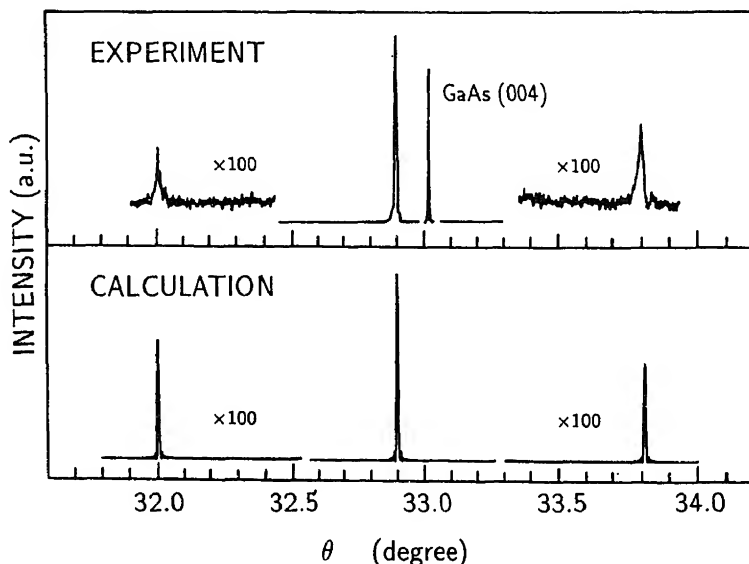
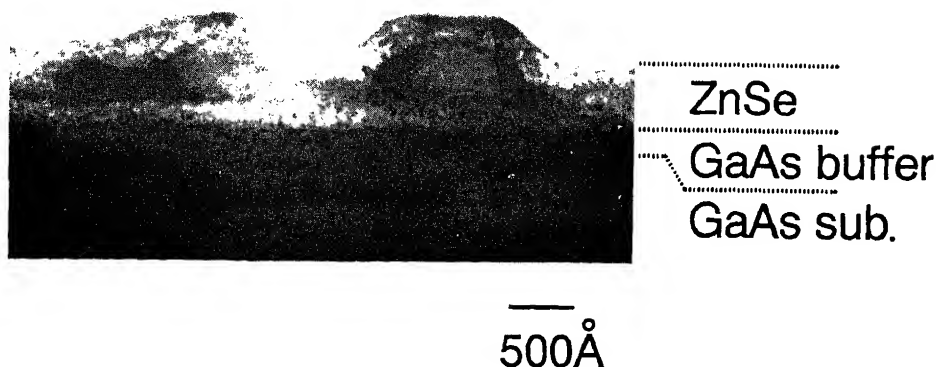


Figure 9. Double-crystal XRD pattern of GaAs (25 Å)/ZnSe (33 Å)  $\times 100$  short-period MQW.



**Figure 10.** Cross-sectional [110] TEM bright-field image of GaAs islands buried into ZnSe. The growth conditions are  $T_g = 550^\circ\text{C}$  and  $V/\text{III} = 2$ .

suggests the way to bury high-quality GaAs QDs into ZnSe. The TEM bright-field image of a [110] cross-section of GaAs islands surrounded by ZnSe is shown in figure 10. The growth conditions are  $T_g = 550^\circ\text{C}$  and  $V/\text{III} = 2$ . GaAs shows the Vollmer–Weber growth mode and is isolated completely by ZnSe layers. This preliminary experiment strongly suggests successful fabrication of GaAs QDs buried into ZnSe by reducing island size.

## 5. Electrical properties of Zn(S)Se–GaAs heterostructures

Heterojunction diodes (HD) which consist of n-Zn(S)Se and p-GaAs were used to characterize the electrical properties of the heterostructures. The impurity density of p-GaAs is  $1.0\text{--}2.0 \times 10^{19} \text{ cm}^{-3}$ . The electrodes used were AuZn for p-GaAs, Au/AuGeNi for n-GaAs and In for n-ZnSe through  $n^+$ -ZnSe ( $2 \times 10^{19} \text{ cm}^{-3}$ ) contact layer. Following evaporation of electrodes, mesa structure was fabricated by chemical etching procedure.

### 5.1 ZnSSe/GaAs HD

Since the dimension of ZnSe in HDs is usually much larger than its critical thickness (1500 Å), lattice-matched ZnSSe is adopted instead of ZnSe to keep full coherence. The impurity density of n-ZnSe is  $1.0\text{--}2.0 \times 10^{17} \text{ cm}^{-3}$ .

Figure 11 shows  $I$ – $V$  characteristics at various temperatures. In order to clarify carrier transport mechanism, dependence of  $I$  on temperature was investigated as a function of bias voltage. Consequently,  $I$  is proportional to  $\exp(1/T)$  below 0.7 V, and to  $\exp(T)$  above 0.7 V. This indicates that  $I$  is limited by injection and recombination below 0.7 V, and by tunnelling above 0.7 V (Ribben and Feucht 1966). The diode factor in the region of injection and recombination is 1.8.

Dependence of  $C$ – $V$  characteristics of the same sample on measurement frequency is shown in figure 12. The straight line obtained in the  $1/C^2$  versus  $V$  plot indicates

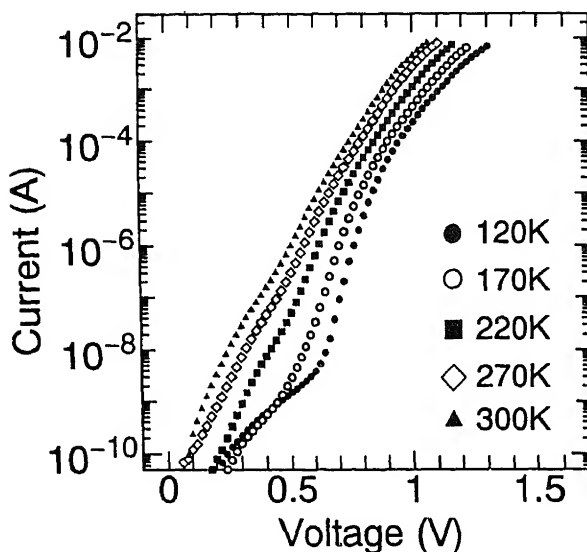


Figure 11.  $I$ - $V$  characteristics of ZnSSe/GaAs HD.

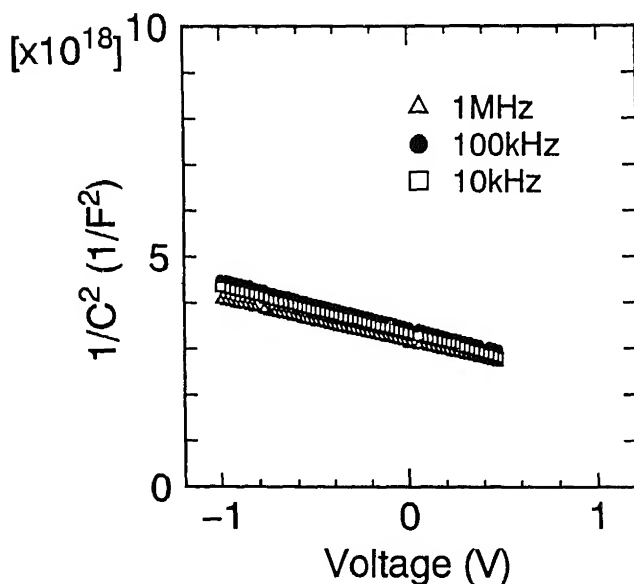


Figure 12.  $C$ - $V$  characteristics of ZnSSe/GaAs HD.

abrupt junction without serious interdiffusion, and the slope gives the effective impurity concentration of  $2.5 \times 10^{17} \text{ cm}^{-3}$ , which is very close to the expected value. If a heterojunction has a large interface state density, the  $C$ - $V$  curve shows frequency dispersion (Choi *et al* 1990). Since the frequency dispersion of the ZnSSe/GaAs HD is within the measurement error, the state density at the interface is below  $10^{10} \text{ cm}^{-2}/\text{eV}$ , which is the lowest detectable limit derived from the measurement error.

Deep levels in heterostructures often act as recombination and/or nonradiative centres and degrade their carrier transport and/or optical properties. We study the nature of deep traps in the HD by means of deep-level transient spectroscopy (DLTS), which provides a very sensitive method for identifying deep levels and for determining their parameters. A typical DLTS spectrum is shown in figure 13, where a majority-carrier pulse ( $V_p$ ) of 0.4 V is applied to the HD for 3 ms under a quiescent measurement bias ( $V_m$ ) of  $-3.6$  V. Although two deep electron trap levels peaking around 120 K (labelled A) and 150 K (labelled B) are observed, comparing with reported DLTS spectra of ZnSe/GaAs HDs (Shirakawa and Kukimoto 1981; Venkatesan *et al* 1989) it is easily found that the ZnSSe/GaAs HD fabricated in this study has fewer traps. Since the difference between the ZnSe/GaAs HDs and the ZnSSe/GaAs HD is lattice relaxation, reduction of traps in the ZnSSe/GaAs HD is due to lattice-matching effect. The Arrhenius plot of thermal emission rate times square of temperature gives the thermal activation energy of 220 meV for both traps. Although detailed discussion of the origins of these peaks will be shown elsewhere, trap A is attributed to the lattice mismatch-induced trap and we believe that the trap may be suppressed by further optimization of growth conditions. There are many reports on trap B (Shirakawa and Kukimoto 1981; Venkatesan *et al* 1989) and it is considered to arise from dopantsite ( $\text{Ga}_{\text{Zn}}$ ,  $\text{V}_{\text{Zn}}$ ) complexes. Relatively large capture cross-section of trap B ( $9 \times 10^{-15} \text{ cm}^2$ ), which is estimated from the Arrhenius plot, seems to cause recombination current and to make the diode factor large, to the value of 1.8.

## 5.2 GaAs/ZnSe HD

We refer to first investigation of electrical properties of GaAs on ZnSe HD, briefly. The thickness of underlying ZnSe is  $1.8 \mu\text{m}$ . Therefore, crystalline quality at ZnSe surface, i.e. at the interface of p-GaAs/n-ZnSe junction, recovers well from the damage caused by lattice relaxation. The GaAs layer thickness is as thin as  $1000 \text{ \AA}$  to keep

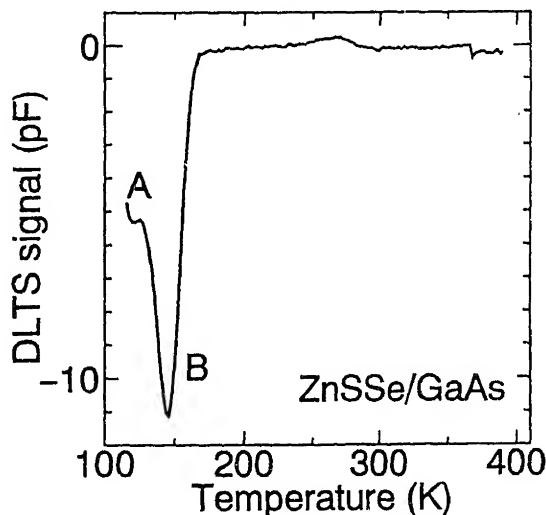


Figure 13. DLTS spectrum of ZnSSe/GaAs HD taken at a rate window of  $1.2 \times 10^3 \text{ s}^{-1}$ .

coherency of GaAs against ZnSe. Coherent growth of GaAs on ZnSe is confirmed by XRD. The impurity density of n-ZnSe is  $1.0 \times 10^{16} \text{ cm}^{-3}$ .

$I$ - $V$  measurement at various temperatures revealed that the current transport was limited by tunnelling and implied the existence of high density of interface state at a level near conduction band edge.  $C$ - $V$  curves showed frequency dispersion and the interface state density is estimated to be  $\sim 6 \times 10^{10} \text{ cm}^{-2}/\text{eV}$  by the similar procedure with Choi *et al* (1990). DLTS spectrum of the HD showed no peak, but the junction capacitance depended on temperature strongly. The analysis of the temperature dependence provided the deep-level parameters; thermal activation energy is 180 meV and trap density  $7.3 \times 10^{15} \text{ cm}^{-3}$ . It is worth noting that the trap density is comparable to the impurity density, which is consistent with the result derived from  $I$ - $V$  measurement.

Although further optimization should be directed to improve electrical properties, this preliminary experiment may open the way to the applications of ZnSe-GaAs multilayered structures for electronic devices.

## 6. Conclusions

We studied MOVPE growth and characterization of ZnSe-GaAs heterostructures.

Growth behaviour of GaAs grown on ZnSe by MOVPE was studied as a function of growth conditions. TEM observations revealed that GaAs growth at 550°C and low V/III ratio ( $\leq 5$ ) was highly 3-dimensional, whereas the growth at low temperatures ( $\leq 500^\circ\text{C}$ ) or high V/III ratios ( $\geq 10$ ) was 2-dimensional. The cause of 3-dimensional growth is considered to be migration of Ga-related clusters.

This variation of the growth mode was applied for the fabrication of ZnSe-GaAs low-dimensional structures; QW was fabricated and the possibility of burying GaAs QDs into ZnSe was indicated. The structural properties of QW were characterized mainly by XRD. Good correspondence of the experiments with the simulations indicates high crystalline quality, a high degree of lateral uniformity, and well-defined interfaces. Additionally, it was found by analysis of interference fringe that the dispersion of thickness fluctuation, if it existed, was about 3%, that is, one or two monomolecular layers in the fabricated structure. Further optimization in order to grow thinner layers successfully allowed fabrication of the MQW with  $\sim 30 \text{ \AA}$  layers.

Zn(S)Se-GaAs heterostructure was characterized electrically. The diode factor of ZnSSe/GaAs heterostructure obtained from  $I$ - $V$  curve is 1.8, which is attributed to the deep level related to Ga dopant. The transport mechanism in GaAs/ZnSe heterostructure is limited by tunnelling and the existence of high density of interface state at a level near conduction band edge was implied by both  $I$ - $V$  and DLTS measurements.

## Acknowledgements

TEM and X-ray diffraction were carried out at the experimental facilities of the Alloy Semiconductor Laboratory at Kyoto University. This work was supported in part by a Grant-in-Aid for Scientific Research from the Ministry of Education, Science and Culture.

## References

- Bean J C, Feldman L C, Fiory A T, Nakahara S and Robinson I K 1984 *J. Vac. Sci. & Technol.* **A2** 436
- Choi Y W, Wie C R, Evans K R and Stutz C E 1990 *J. Appl. Phys.* **68** 1303
- Eppenga R 1989 *Phys. Rev.* **B40** 10402
- Farrell H H, Tamargo M C, de Miguel J L, Turco F S, Hwang D M and Nahory R E 1991 *J. Appl. Phys.* **69** 7021
- Funato M, Ishii M, Murawala P A, Tsuji O, Fujita Sz and Fujita Sg 1992 *J. Cryst. Growth* **117** 543
- Funato M, Fujita Sz and Fujita Sg 1993 *Jpn. J. Appl. Phys.* **32** 3396
- Funato M, Fujita Sz and Fujita Sg 1995 *J. Cryst. Growth* **145** 616
- Greene J E 1983 *J. Vac. Sci. & Technol.* **B1** 229
- Ihm J and Cohen M L 1979 *Phys. Rev.* **B20** 729
- Khurgin J 1988 *Phys. Rev.* **B38** 4056
- Kobayashi N and Horikoshi Y 1990 *Jpn. J. Appl. Phys.* **29** L236
- Kumagai M and Takagahara T 1988 in *Extended abstracts of the 20th international conference on solid state devices and materials* p. 335
- Riben A R and Feucht D L 1966 *Solid State Electron.* **9** 1055
- Segmüller A and Blakeslee A E 1973 *J. Appl. Cryst.* **6** 19
- Shen D, Zhang K and Fu R F 1988 *Appl. Phys. Lett.* **53** 500
- Shirakawa Y and Kukimoto H 1981 *J. Appl. Phys.* **51** 5859
- Venkatesan S, Pierret R F, Qiu J, Kobayashi M, Gunshor R L and Kolodziejski L A 1989 *J. Appl. Phys.* **66** 3656
- Zhang S and Kobayashi N 1992 *Appl. Phys. Lett.* **60** 883



## On the stability of intermetallic phases

S LELE, B N SARMA, A GHOSAL and G V S SASTRY

Centre of Advanced Study, Department of Metallurgical Engineering, Banaras Hindu University, Varanasi 221 005, India

**Abstract.** A general methodology using atomic clusters is applied to three problems connected to the study of alloy phase stability. The cluster method proposed by Allen and Cahn is applied to non-ideal hcp structures under tetrahedral approximation using multiatom interactions. The possible ground-state structures which are stable at absolute zero temperature are obtained. A geometrical representation in 4D parameter space of the possible strengths of multiatom interactions permitted for these structures is illustrated in terms of a 2D analogue. Extending these ideas, the cluster variation method (CVM) proposed by Kikuchi is applied to fcc structures under tetrahedral approximation to find the effect of multiatom interactions on the topology of the coherent phase diagrams in which all the phases present are derivable by mere rearrangement of atoms on the parent disordered structure. In addition, the possible invariant reactions are identified in such coherent phase diagrams. Finally the CVM is applied for calculating a model incoherent phase diagram, that of Ti–Zr system, where disordered hcp and bcc phases are present. The free energies of hcp and bcc phases are formulated using CVM procedures respectively under tetrahedral–octahedral and tetrahedral approximations. The CVM is shown to be in better agreement with the thermodynamic data and to be able to reproduce the correct value of measured enthalpy of transformation compared to that given by the regular solution model, which significantly overestimates the same.

**Keywords.** Phase stability; cluster method; cluster variation method; ground-state structures; coherent phase diagrams; incoherent phase diagrams.

### 1. Introduction

The stability of intermetallic phases is a topic of long-standing and continuing interest. Recently developed first-principles calculations are still not generally capable of predicting stability to within the limits of experimental errors. One has therefore to resort to physically acceptable models which use suitable empirical inputs and are mathematically tractable. This is usually accomplished by a general methodology which uses atomic clusters of finite size. A complete configurational description of a system containing  $N$  atoms requires a representation in  $N$ -dimensional hyperspace, which is mathematically intractable. This problem can be simplified and the description can be made meaningful when atomic clusters are considered. The state of the order of the alloy can be accurately described (up to the size of the largest cluster considered) in terms of a much smaller number of variables: the probabilities of occurrence of each of the possible cluster configurations. As local order of the alloy can be described accurately in terms of the known atomic configurations of the clusters and their respective numbers, such descriptions can be made increasingly realistic by a hierarchy of cluster approximations. However, this has to be kept in balance with a very rapidly growing demand on computational resources as the cluster size increases. This is also a very realistic approach in the sense that frequently, the available experimental data are somewhat inaccurate and highly limited. Two promising methods which utilize the above ideas with remarkable success are the cluster method and the cluster variation method (CVM). Of these, the cluster method due to Allen and Cahn (1972) gives the so-called



ground-state structures. These structures are stable at absolute zero temperature and are characterized by minimum configurational energies. On the other hand, the method proposed by Kikuchi (1951) provides a systematic method of approximation of the configurational entropy of a structure so that its finite temperature phase stability can be studied. CVM has been applied for the calculation of several phase diagrams since van Baal (1973) demonstrated the procedure for calculation of coherent phase diagrams under tetrahedral approximation considering the effects of tetrahedral multiatom interactions. These methods together provide a consistent framework for studying the phase stability of alloys.

In this contribution, three applications which illustrate the versatility of this approach are presented. They are: (i) determination of hcp ground states using the cluster method under tetrahedral approximation considering 4-body interactions, (ii) calculation of global phase diagrams for fcc ordering systems (coherent phase diagrams) using cluster variation method (§ 3), and (iii) calculation of incoherent phase diagrams with coexisting disordered hcp and bcc phases respectively under tetrahedral-octahedral and tetrahedral approximations of CVM considering up to second-neighbour pair interactions (§ 4).

## 2. Ground-state structures

In the cluster method proposed by Allen and Cahn (1972), the configurational energy of mixing of the alloy is expressed as a bilinear function of the cluster probabilities (state variables) and their energy coefficients. This configurational energy is minimized in the presence of chosen clusters using the linear programming method subject to certain constraint conditions on the cluster variables. The minimum conditions thus obtained define the requirements for the occurrence of the relevant ground-state structures formed by the clusters chosen earlier. In this section, we obtain the ground-state structures of binary hcp alloys having non-ideal axial ratio using cluster method under tetrahedral approximation, considering 4-body tetrahedral multiatom interaction effects.

### 2.1 Cluster variables and correlation functions

In this method, at first a basic motif is chosen. The motif is a closed graph containing a set of atomic sites in the structure under consideration. The motif sites are then populated by the atomic species A and B to obtain all the possible configurations of atomic clusters and subclusters. The probabilities of occurrence of these configurations are the corresponding cluster variables. However, all these variables are not independent. A convenient way of obtaining the independent set of variables which governs the dimensionality of the ordering field, is through correlation functions. This is illustrated below.

Consider a crystal with  $N$  atomic sites. In a binary (A-B) alloy,  $A$  atoms occupy  $(1 - C)N$  of these  $N$  sites while the remaining  $CN$  sites are occupied by  $B$  atoms. Site occupation operators are defined (Flinn 1956; Clapp and Moss 1966) as  $p_A^i = 1$  ( $p_B^i = 1$ ) if an  $A$  ( $B$ ) atom occupies site  $i$  and  $p_A^i$  ( $p_B^i$ ) is zero otherwise. Vacancies are not considered,

$$p_A^i + p_B^i = 1.$$

$$\sigma_i = \tau_A p_A^i + \tau_B p_B^i,$$

where  $\tau_A$  and  $\tau_B$  ( $\neq \tau_A$ ) are arbitrary numbers. Averages of  $\sigma_i$  or its products over crystallographically equivalent sites or clusters of sites are defined as the corresponding correlation functions. We have chosen  $\tau_A = 0$  and  $\tau_B = 1$  so that  $\sigma_i = p_B^i$  and correlation functions take the form  $\langle p_B^i \rangle$ ,  $\langle p_B^i p_B^j \rangle$ , etc. The averages of the operators in (1) over all the sites are

$$\langle p_A^i \rangle = \langle 1 - p_B^i \rangle = 1 - \langle p_B^i \rangle = 1 - C \quad \text{and} \quad \langle p_B^i \rangle = C. \quad (2)$$

The pair cluster variables are defined by

$$y_0 = \langle p_A^i p_A^j \rangle; \quad y_1 = \langle p_A^i p_B^j \rangle + \langle p_B^i p_A^j \rangle \quad \text{and} \quad y_2 = \langle p_B^i p_B^j \rangle, \quad (3)$$

where  $y_0$ ,  $y_1$  and  $y_2$  represent the probabilities of occurrence of atom pairs AA, AB or BA, and BB respectively on the pair of sites  $i$  and  $j$ . In view of (1),  $y_0$  and  $y_1$  can be expressed in terms of  $C$  and  $y_2$  as follows:

$$y_0 = \langle (1 - p_B^i)(1 - p_B^j) \rangle = 1 - \langle p_B^i \rangle - \langle p_B^j \rangle + \langle p_B^i p_B^j \rangle = 1 - 2C + y_2, \quad (4a)$$

$$y_1 = \langle (1 - p_B^i)p_B^j \rangle + \langle p_B^i(1 - p_B^j) \rangle = 2\langle p_B^i \rangle - 2\langle p_B^i p_B^j \rangle = 2(C - y_2). \quad (4b)$$

Thus, in an alloy of fixed composition, only one pair variable remains independent. It follows from the above that the cluster variables can all be expressed as linear combinations of a set of independent correlation functions. This set contains one correlation function corresponding to each of the distinct subgraphs contained in the motif and the motif itself. (For the sake of convenience, we shall use  $\langle pij \rangle$  to represent the correlation function  $\langle p_B^i p_B^j \rangle$  in the following.)

## 2.2 Configurational energy

For the study of ground states in this section, we choose a distorted tetrahedron connecting four adjacent sites in a non-ideal hcp structure as shown by vertices 1-2-3-4 in figure 1. Eight distinct types of clusters can occur. The number of equivalent clusters of each type (statistical weights  $w_i$ ) are identified by rotational symmetry considerations. The details of these clusters are depicted in table 1. By extending the argument of correlation functions in §2.1 to the tetrahedral correlations, we find that only five correlation functions, namely  $\langle p12 \rangle$ ,  $\langle p14 \rangle$ ,  $\langle p123 \rangle$ ,  $\langle p124 \rangle$  and  $\langle p1234 \rangle$  are independent when the composition is fixed, suggesting that three constraint conditions should be operating on  $Z_i$ . They are obtained as explained in the following. We express  $Z_1$  in terms of the above five correlation functions by a procedure similar to that used for obtaining (4). Elimination of the correlation functions from this set of equations yields the following constraints:

$$Z_0 + Z_1 + Z_2 + Z_3 + Z_4 + Z_5 + Z_6 + Z_7 = 1, \quad (5)$$

$$Z_1 + Z_2 + 2Z_3 + 2Z_4 + 3Z_5 + 3Z_6 + 4Z_7 = 4C, \quad (6)$$

$$Z_1 - 3Z_2 + 2Z_3 - 2Z_4 + 3Z_5 - Z_6 = 0. \quad (7)$$

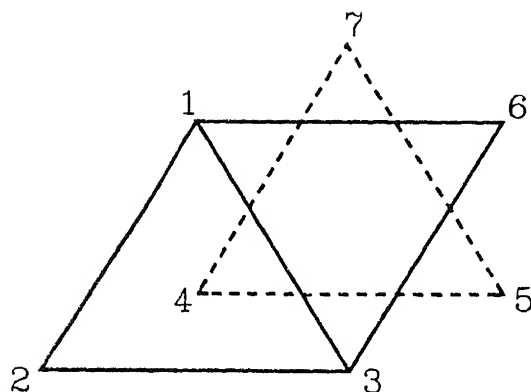


**Figure 1.** Projection of tetrahedral-octahedral motif on the close-packed plane in hcp or fcc structures. Sites 1-2-3-4 join to form a tetrahedron whereas sites 1-3-4-5-6-7 form the vertices of an octahedron. Continuous lines join sites on one layer and broken lines join sites on an adjacent one.

**Table 1.** Tetrahedral cluster configurations and their energies.

Cluster type $i$	Cluster probability $Z_i$	Cluster configuration (sites occupied by B atoms)	Weight of the cluster $w_i$	Concentration of the cluster $c_i$	Number of first and second neighbour unlike pairs $n_i^I + n_i^{II}$	Energy coefficient of cluster variable
0	$Z_0$	—	1	0	0	0
1	$Z_1$	1	3	1/4	3	$3/2 W(1 +$
2	$Z_2$	4	1	1/4	3	$3/2 W(1 +$
3	$Z_3$	1,2	3	1/2	4	$2W$
4	$Z_4$	1,4	3	1/2	4	$2W$
5	$Z_5$	1,2,3	1	3/4	3	$3/2 W(1 +$
6	$Z_6$	1,2,4	3	3/4	3	$3/2 W(1 +$
7	$Z_7$	1,2,3,4	1	1	0	0

The configurational energy  $E$  of the alloy can be expressed in terms of cluster variables and their corresponding energies as

$$E = 2N \sum_{i=0}^7 Z_i \varepsilon_i.$$

Here  $2N$  is the number of tetrahedra arising from  $N$  atomic sites. The configurational energy of mixing  $U$  can be found by subtracting from  $E$  the energy of a mechanical mixture of A and B having the same composition. By utilizing the constraint conditions (5)–(7),  $U$  can be expressed as follows:

$$\begin{aligned} U/N = & 2[Z_1(\varepsilon_1 - 1/2\varepsilon_0 - 1/4\varepsilon_3 + 1/4\varepsilon_4) + Z_2(\varepsilon_2 - 3/2\varepsilon_0 + 3/4\varepsilon_3 - 3/4\varepsilon_4 - \varepsilon_7) \\ & + Z_3(1/2\varepsilon_3 + 1/2\varepsilon_4 - 1/2\varepsilon_0 - 1/2\varepsilon_7) + Z_4(1/2\varepsilon_3 + 1/2\varepsilon_4 - 1/2\varepsilon_0 - 1/2\varepsilon_7) \\ & + Z_5(\varepsilon_5 + 1/2\varepsilon_0 - 3/4\varepsilon_3 + 3/4\varepsilon_4) + Z_6(\varepsilon_6 - 1/2\varepsilon_0 + 1/4\varepsilon_3 - 1/4\varepsilon_4 - \varepsilon_7) \end{aligned}$$

We note that only five independent combinations of the eight cluster energies,  $\epsilon_i$ , appear in  $U$ .

A convenient and physically meaningful abbreviated notation for these energy combinations can be chosen in terms of an effective pair interchange energy  $W$ , and four so-called multiatom interaction parameters  $\alpha$ ,  $\beta$ ,  $\gamma$  and  $\delta$  as given in table 1. These energies reduce to those given by the pairwise-interactions model when the axial ratio becomes ideal and multiatom interaction parameters vanish.

### 2.3 Linear programming method

To obtain ground state in the presence of a triplet of clusters, we solve for three corresponding cluster variables from (5)–(7) and eliminate them from the energy expression in (9). If the energy coefficients of  $Z_i$  present in this equation are all positive, then  $U$  will be minimum when the  $Z_i$  appearing in the equation themselves vanish. The requirement that the energy coefficients of  $Z_i$  should be positive defines the ranges of multiatom interaction parameters permissible for the occurrence of ground states. In the case of cluster triplet  $(Z_0, Z_1, Z_2)$ , when the ordering tendency is considered for which  $W < 0$ , if

$$\begin{aligned} -1 - 3\alpha < 0; \quad -2 - 3\alpha - 3\beta < 0; \quad -2 - 3\alpha + \gamma < 0; \\ -2 - 2\alpha - \beta + \delta < 0; \quad -4 - 3\alpha - \beta < 0, \end{aligned} \quad (10)$$

then the minimum in  $U$  occurs at

$$\begin{aligned} U/N &= 3CW(4 + 3\alpha + \beta), \\ Z_3 &= Z_4 = Z_5 = Z_6 = Z_7 = 0, \\ Z_0 &= 1 - 4C, Z_1 = 3C, Z_2 = C. \end{aligned} \quad (11)$$

As  $0 \leq Z_i \leq 1$ , we get  $0 \leq C \leq 0.25$ .

At  $C = 0$ , pure A is stable whereas at the other end of this composition range, at  $C = 0.25$ , two distinct degenerate superstructures  $A_3B^1$  (Strukturbericht type  $DO_{19}$ ) and  $A_3B^3$  are stabilized with equal but minimum energies. [Our nomenclature for superstructures follows that used by Singh *et al* (1991).] These structures which are stable at the ends of composition ranges are known as terminal superstructures. At all the intermediate values of the composition range, phase mixtures of these terminal superstructures are stable. In principle, an infinite number of degenerate intermediate superstructures are also possible. This procedure is repeated for all  $\binom{8}{3}$  possible cluster triplets to complete the search for ground-state structures.

The linear programming method ensures a minimum in energy whenever a solution can be found in terms of the cluster triplets from the conditions (5)–(7). In this case, for eight of the cluster triplets exemplified by  $(Z_0, Z_1, Z_3)$  there are no solutions in terms of other clusters. Similarly, for triplets of type  $(Z_0, Z_i, Z_7; i = 1-6)$ , it is not possible to make the cluster coefficients simultaneously positive when  $W < 0$ . Further, this method cannot decide whether the superstructures made up of more than three clusters belong to ground state.

## 2.4 Parameter space for ground-state structures

We shall illustrate the representation of permitted domain of the parameter space for the occurrence of ground state structures. The parameter space is a 4D hyperspace spanned by the multiatom interaction parameters  $\alpha$ ,  $\beta$ ,  $\gamma$  and  $\delta$ . For the cluster  $(Z_0, Z_1, Z_2)$  we have five inequalities in (10) each of which defines a half-space hyperspace bounded by an infinitely extended 3D hyperplane represented by the corresponding equality. The intersection of these half-spaces defines the permitted domain of parameter space. The procedure for obtaining the permitted domain is illustrated in the following for a 2D case. We begin with three inequalities defining three half-spaces in 2D where the corresponding straight lines are non-parallel. As shown in figure 2, the permitted domain can then be obtained in the following manner. Generally, the lines intersect in pairs giving rise to three vertices. Each of the vertices lies in the permitted domain only when it lies in the half-space on the permitted side of the third line; otherwise the vertex is in a non-permitted domain. Four cases can arise:

- (i) When all the three points are permitted, as can be seen from figure 2(a), the permitted domain  $P$  is a 2D simplex, the triangle.
- (ii) When two of the three points are permitted, the permitted domain is a union of the line segment joining the permitted points and an angle whose edge

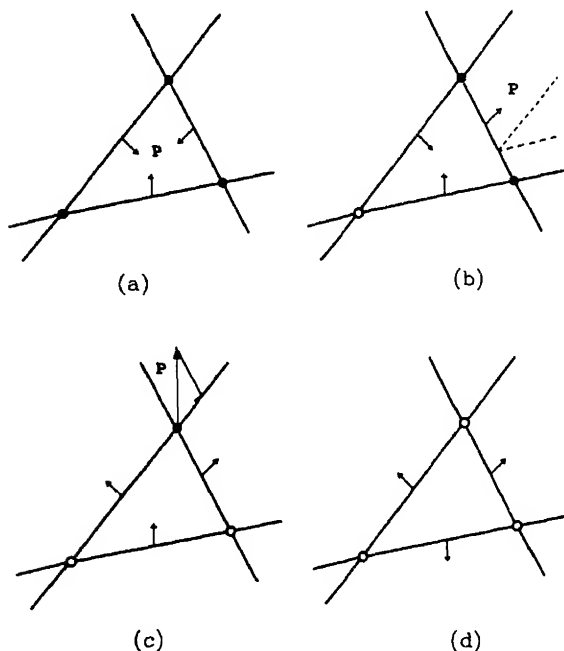


**Figure 2.** Graphical representation of the possible cases of permitted domains (P) when three inequalities are present, as explained in section 2.4. Arrows on one side of the lines indicate the half-space permitted. Filled (open) circles represent permitted (non-permitted) vertices.

parallel to the rays originating at the permitted vertices along the directed segments from the non-permitted vertex through permitted vertices.

- (iii) When only one of the three vertices is permitted, then  $P$  is an angle (pyramidal cone for higher-dimensional case) with its vertex at the permitted point and edges originating at the vertex along the directed segments from the nonpermitted points through the permitted vertex. Then any point in  $P$  can be spanned by moving appropriate lengths along the edges of the angle, as suggested in figure 2c.
- (iv) When none of the three points is permitted, there is no permitted domain (figure 2d).

An extension of this procedure was utilized for determining the permitted domains for each of the ground-state structures by Sarma *et al* (1994). This gives an idea of the possible strengths of the 4-body multiatom interaction effects in a binary alloy system depending on the actual structures present. The results of the ground-state analysis are presented in table 2.

### 3. Coherent fcc ordering phase diagrams

Coherent phase diagrams are those in which all the phases present are derivable from the disordered parent lattice by mere rearrangement of atomic species. CVM has been applied to fcc alloys undergoing order-disorder transformations under tetrahedral approximation to investigate the effects of 4-body tetrahedral interactions on the topology of the possible phase diagrams. Global behaviour of such systems has been investigated and the possible invariant reactions have been identified.

#### 3.1 Cluster variation and natural iteration methods

Due to the preferential occupancy of certain sets of sites by some atomic species during ordering reactions, one has to divide the atomic sites into a suitable number of sublattices for a complete description of the system. The fcc structure is here subdivided into four interpenetrating simple cubic sublattices, denoted by a, b, c and d to treat  $L1_2$  and  $L1_0$

**Table 2.** Summary of ground-state superstructures.

Superstructures	Cluster concentration	Prototypes
Terminal superstructures		
$A_3B^1(DO_{19})/A_3B^3$ (degenerate)	$Z_1 = 3Z_2 = 3/4$	$Ti_3Al, Ni_3Sn,$ $Mg_3Cd$ , etc.
$A_2B^2$	$Z_1 = 2Z_4 = 2/3$	$Pt_2Ta$
$AB^1(Bh)$	$Z_2 = Z_5 = 1/2$	$LiRh$
$AB^2(B19)/AB^4$ (degenerate)	$Z_3 = Z_4 = 1/2$	$MgCd$
$AB^3/AB^5$ (degenerate)	$Z_1 = Z_6 = 1/2$	...
Intermediate superstructures		
$A_5B$	$Z_0 = 1/3, Z_1 = 3Z_2 = 1/2$	$Al_5W$
$A_4B$	$Z_0 = 1/3, Z_1 = Z_2 = 1/5$	$Au_4Zr$
$A_{10}B_3$	$Z_0 = 1/13, Z_1 = 9/13, Z_2 = 3/13$	$Cu_{10}Sb_3$

types of ordering. Point variables and pair variables for each sublattice are defined according to equations similar to those in (1)–(4). Atoms are permuted on the sites of a regular tetrahedral motif so as to obtain the distinct tetrahedral cluster configurations and the corresponding variables. There are five tetrahedral cluster variables ( $i = 0$  to 4) in the case of a disordered alloy and the configurational energy of mixing in this case can be expressed as first shown by van Baal (1973) as follows:

$$U/N = 3W(1 + \alpha)Z_1 + 4WZ_2 + 3W(1 + \beta)Z_3, \quad (10)$$

where  $\alpha$  and  $\beta$  are the tetrahedral multiatom interaction parameters. Note the similarity with (9).

Then the configurational entropy of the alloy is calculated by CVM (Kikuchi 1974). In this method, the largest  $r$ -point clusters considered are assumed to be randomly distributed on the set of atomic sites and the Boltzmann statistical entropy summations are obtained. In doing so, it is required that all the cluster and subcluster configurations are counted only once. The configurational entropy in tetrahedral approximation is given by (van Baal 1973)

$$S = s_4 - s_2 + 5s_1, \quad (11)$$

where  $s_r$  is the Boltzmann statistical entropy summation for  $r$ -point clusters. As  $U$  and  $S$  are expressed as functions of  $Z_i$ , the equilibrium distribution of  $Z_i$  is found by minimizing the Helmholtz free energy

$$F = U - TS, \quad (12)$$

with respect to each of the independent cluster variables by keeping the composition fixed. Since for condensed phases the difference between  $F$  and the Gibbs free energy  $G$  is very small, we shall not distinguish the two. An alternative method of arriving at equilibrium is through minimization of grand potential  $\Omega$  defined through

$$\Omega = G - (1 - C)\mu_A - C\mu_B,$$

where  $\mu_A$  and  $\mu_B$  are chemical potentials of atomic species A and B. The conditions of equilibrium are a set of nonlinear equations, solvable for  $Z_i$  either by Newton-Raphson method or by so-called natural iteration method (NIM), especially developed for this purpose by Kikuchi (1974). In this part of the work NIM was used to obtain equilibrium values of  $Z_i$ . The conditions of equilibrium in this case are obtained as

$$Z_i = \exp \left[ \frac{\Omega}{2RT} - \frac{1}{RT} \left( \varepsilon_i - \frac{(\mu_m + \mu_n + \mu_p + \mu_q)}{8} \right) \right] Y^{1/2} X^{-5/8},$$

where  $\varepsilon_i$  are the energy coefficients of  $Z_i$  as appearing in  $U$  (12);  $\mu_m, \mu_n, \mu_p, \mu_q$  are equal to  $\mu_A$  or  $\mu_B$  depending on the occupancy of the sites  $m, n, p, q$  in the tetrahedral cluster by A or B atoms respectively; and  $X$  and  $Y$  are respectively the products of all point and pair variables.

The above equations are solved iteratively to yield values of  $\Omega$  and  $Z_i$  for selected values of  $\mu = (\mu_B - \mu_A)/2$  and  $T$ . Equilibrium between a pair of phases occurs when each of  $\Omega$  and  $\mu$  are equal for both the phases. The corresponding compositions are found from the  $Z_i$  evaluated earlier.

## 3.2 Effect of multiatom interactions on the topology of phase diagrams

An analysis of ground-state structures of fcc alloys under tetrahedral approximation of cluster method using multiatom interactions by Cahn and Kikuchi (1979) showed that for ordering systems where  $W < 0$ , the phases  $A_3B$ ,  $AB$  and  $AB_3$  are stable within a triangular domain (XYZ in figure 3) of the parameter space spanned by  $\alpha$  and  $\beta$ . In order to investigate the effects of multiatom interactions on the topology of typical fcc ordering phase diagrams involving three ordered phases, a symmetric half of the permitted domain (triangle PQR in figure 3) was chosen and phase diagrams were calculated using values of  $\alpha$  and  $\beta$  within this domain. The invariant reactions were identified in each case. Results are summarized in table 3. As can be seen from figure 3, equal values of  $\alpha$  and  $\beta$  gave rise to symmetric phase diagrams. At P,  $AB$  is stabilized compared to  $A_3B$  and  $AB_3$  with the presence of peritectoid reactions. At Q, there is an exactly opposite tendency and the reaction is eutectoid type I. At R,  $A_3B$  phase is very strongly stabilized and for compositions below 50%, eutectoid type II reaction takes place in which an ordered phase transforms to a disordered one together with another ordered phase. For a detailed analysis of the results, reference can be made to Ghosh-Moulic *et al* (1994). This investigation thus gives a clear idea of the various possible effects of the multiatom interactions on the phase stability of fcc alloys.

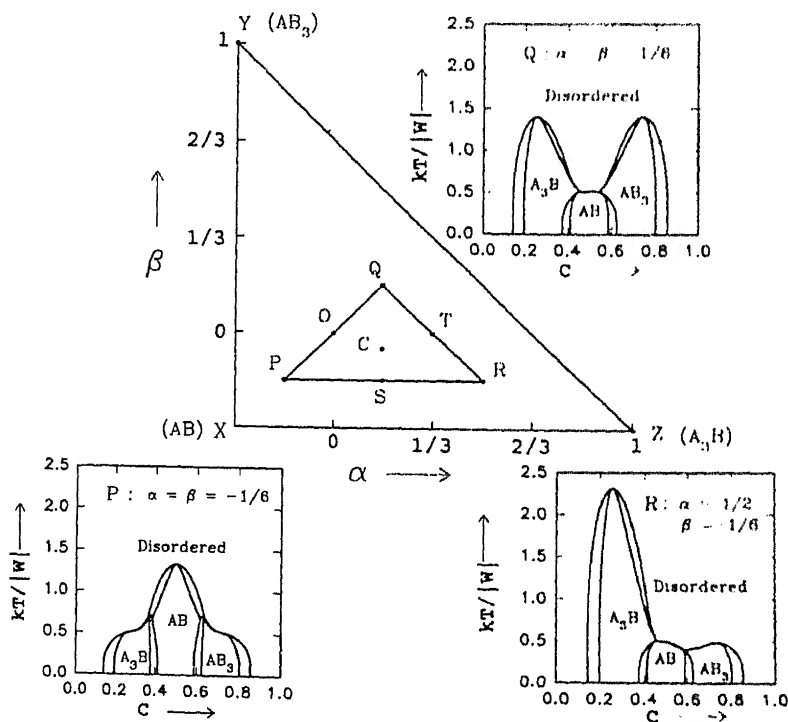


Figure 3. Permitted domain of the parameter space ( $\alpha, \beta$ ) for the stability of  $L1_2$  and  $L1_0$  structures. Typical phase diagrams obtainable for different choices of multiatom interaction parameters  $\alpha$  and  $\beta$  are also shown.



**Table 3.** Nature of invariant reactions for various values of multiautom interaction parameters  $\alpha$  and  $\beta$ .

Points in parameter space	$\alpha$	$\beta$	Invariant reaction	
			$C < 0.5$	$C > 0.5$
O	0	0	Eutectoid I	Eutectoid I
P	-1/6	-1/6	Peritectoid	Peritectoid
Q	1/6	1/6	Eutectoid I	Eutectoid I
R	1/2	-1/6	Eutectoid II	Peritectoid
S	1/6	-1/6	Eutectoid I	Peritectoid
T	1/3	0	Eutectoid II	Eutectoid I
C	1/6	-1/18	Eutectoid I	Peritectoid

Eutectoid I : Disordered  $\rightarrow$  AB +  $A_3B/AB_3$

Eutectoid II :  $A_3B \rightarrow$  Disordered + AB

Peritectoid : Disordered + AB  $\rightarrow$   $A_3B/AB_3$

#### 4. Calculation of incoherent phase diagrams: Ti-Zr system

Incoherent phase diagrams are those in which the phases present belong to more than one parent disordered structure. An example of such systems is the Ti-Zr system in which disordered hcp  $\alpha$  phase transforms to disordered bcc  $\beta$  phase. CVM has been applied for a calculation of phase diagram of Ti-Zr system in the following.

The free energy of hcp  $\alpha$  phase is calculated under tetrahedral-octahedral (TO) approximation of CVM. As shown in figure 1, a motif joining seven nearby sites in the disordered hcp structure is considered in which sites 1, 2, 3, 4 join a distorted tetrahedron (which is also used in §2), and sites 1, 3, 4, 5, 6, 7 join a distorted octahedron, the distortions being due to the nonideal axial ratio. There are a total of 13 correlation functions corresponding to this motif as governed by the space group symmetry of hcp structure. Among them,  $\langle p_{12} \rangle$ ,  $\langle p_{14} \rangle$ ,  $\langle p_{123} \rangle$ ,  $\langle p_{124} \rangle$  and  $\langle p_{1234} \rangle$  arise due to tetrahedral clusters and the additional ones, viz.  $\langle p_{15} \rangle$ ,  $\langle p_{136} \rangle$ ,  $\langle p_{135} \rangle$ ,  $\langle p_{1357} \rangle$ ,  $\langle p_{1346} \rangle$ ,  $\langle p_{1345} \rangle$ ,  $\langle p_{13456} \rangle$  and  $\langle p_{134567} \rangle$ , arise due to octahedral clusters.

The configurational energy of mixing  $U$  can be obtained by a procedure similar to that given in §2.

$$U/N = (\langle p_{12} \rangle - C^\alpha) 3e_{12}^\alpha + (\langle p_{14} \rangle - C^\alpha) 3e_{14}^\alpha + (\langle p_{15} \rangle - C^\alpha) 3e_{15}^\alpha. \quad (17)$$

By extending the CVM arguments as illustrated in §3 to the case of TO approximation, the configurational entropy  $S_{TO}$  can be calculated as follows:

$$S_{TO} = s_{1234} + s_{134567} - s_{123} - s_{136} - s_{124} + s_{12} + s_{14} - s_1, \quad (18)$$

where  $s_i$  represents the Boltzmann entropy summation for the cluster  $i$ .

Then  $G$  in (14) and the chemical potentials of  $\alpha$  phase can be calculated. This  $G$  can be minimized with respect to each of the  $\langle p_i \rangle$  in order to obtain the conditions for the internal equilibrium of  $\alpha$  phase. Similar procedures are adopted for the bcc  $\beta$  phase under tetrahedral approximation of CVM (Kikuchi and van Baal 1974; Kikuchi 1987) including interactions up to second-neighbour distances. If the hcp  $\alpha$  phase is taken as

the reference state, then the chemical potentials of the bcc  $\beta$  phase are obtained from

$$\mu_A^\beta = \Delta G_A^{\alpha \rightarrow \beta} + \left( G^\beta - C^\beta \frac{dG^\beta}{dC^\beta} \right),$$

$$\mu_B^\beta = \Delta G_B^{\alpha \rightarrow \beta} + \left( G^\beta + (1 - C^\beta) \frac{dG^\beta}{dC^\beta} \right).$$

Here,

$$\Delta G_A^{\alpha \rightarrow \beta} = \Delta H_A^{\alpha \rightarrow \beta} \left( 1 - \frac{T}{T_A^{\alpha \rightarrow \beta}} \right) \text{ and } \Delta G_B^{\alpha \rightarrow \beta} = \Delta H_B^{\alpha \rightarrow \beta} \left( 1 - \frac{T}{T_B^{\alpha \rightarrow \beta}} \right),$$

are the transformation free energies of A and B respectively,  $G^\beta$  the free energy, and  $C^\beta$  the composition of the  $\beta$  phase. For the case of Ti-Zr system, the necessary thermodynamic data are taken from Hultgren *et al* (1973).

Thermodynamic equilibrium between both the phases requires equality of chemical potentials of each component in both the phases. Modified Newton's method is used to arrive at the energy values corresponding to equilibrium.

In the present calculation, we have chosen a set of four energy parameters corresponding to isotropic first-neighbour ( $e_{12}^\alpha = e_{14}^\alpha$ ) and second-neighbour ( $e_{15}^\alpha$ ) pair interactions in the  $\alpha$  phase and first- ( $e_1^\beta$ ) and second- ( $e_{11}^\beta$ ) neighbour pair interactions in the  $\beta$  phase which can reproduce the observed value of  $\Delta H^{\alpha \rightarrow \beta} = 2460 \text{ J mol}^{-1}$  (Auffredic *et al* 1982) for the congruent transformation (temperature fixed at 878 K as suggested by Auffredic *et al* (1982) and Murray (1987)) and also give approximately the observed width of the two-phase field ( $\alpha + \beta$ ) at a temperature of 1013 K. The calculated phase diagram is given in figure 4.

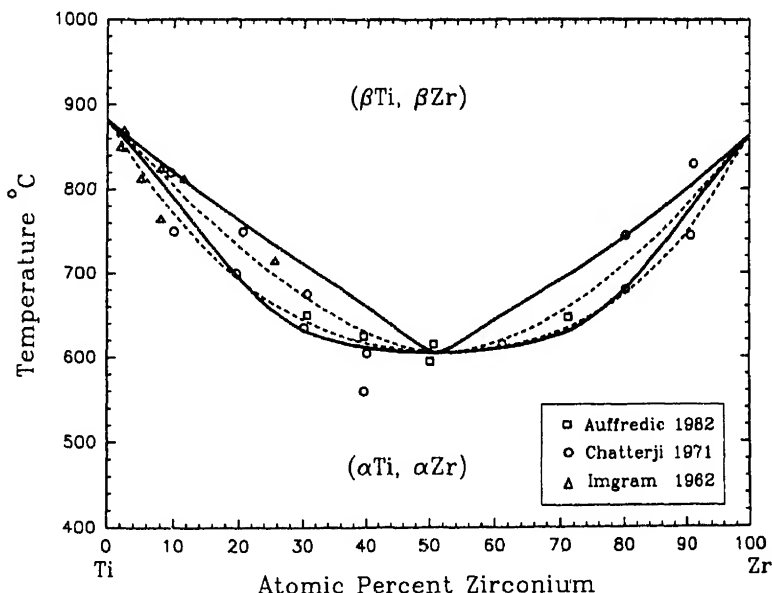


**Figure 4.** Phase diagram of Ti-Zr system showing selected experimental data. Continuous lines show phase diagram calculated in the present work using CVM whereas broken lines show that from Murray (1987) using regular solution model.

The set of energy parameters used for the calculation of this phase diagram are

$$e_{12}^{\alpha} = e_{14}^{\alpha} = -2300 \text{ J mol}^{-1},$$

$$e_{15}^{\alpha} = -500 \text{ J mol}^{-1},$$

$$e_1^{\beta} = -1038 \text{ J mol}^{-1},$$

$$e_{11}^{\beta} = -5623 \text{ J mol}^{-1}.$$

An earlier attempt by Murray (1987) using regular solution model does not reproduce the observed (Auffredic *et al* 1982) value of  $\Delta H^{\alpha-\beta}$  for equiatomic alloys. The regular solution model estimate for this is  $3197 \text{ J mol}^{-1}$  and the overestimation is well beyond experimental error.

The phase diagram obtained using regular solution model by Murray (1987) is also shown in figure 4 along with selected experimental data. The  $(\alpha + \beta)$  phase field found by Murray is much narrower than that suggested by the experimental data. The present calculations are in better agreement with the data in this respect. No attempt has been made, however, to optimize the energy parameters and the phase diagram. Also, multiautom interactions have been neglected. The main objective has been to demonstrate the capability of the CVM procedures to simultaneously represent thermodynamic and phase diagram data in an adequate manner. Availability of additional and more accurate data would make the modelling more realistic.

## 5. Conclusions

We have considered three applications of a general methodology using atomic clusters, each of which was designed to take us closer to solution of problems which are of much practical interest. These procedures can be extended to the study of phase stability in more complex systems such as Ti-Al-Nb. This involves all the three common metallic structures in disordered and/or ordered forms and presents great computational difficulties. In addition, interfacial energies for stacking faults and anti-phase boundaries can be obtained as part of the calculation.

## Acknowledgements

This paper is based on an invited talk by the first author in an Indo-Japan seminar on new materials which was supported by the Department of Science and Technology, India, and the Japan Society for Promotion of Science, Japan. This work was carried out as part of a research project funded by the Council of Scientific and Industrial Research, India.

## References

- Allen S M and Cahn J W 1972 *Acta Metall.* **20** 423
- Auffredic J P, Etchessahar E and Debuigne 1982 *J. Less-Common Metals* **84** 49
- Cahn J W and Kikuchi R 1979 *Acta Metall.* **27** 1329
- Clapp P C and Moss S C 1966 *Phys. Rev.* **142** 418
- Flinn P A 1956 *Phys. Rev.* **104** 350

- Ghosh-Moulic A, Sastry G V S and Lele S 1994 *Bull. Mater. Sci.* **17** 439
- Hultgren R, Desai P D, Hawkins D T, Gleiser M, Kelley K K and Wagman D D 1973 *Selected values of the thermodynamic properties of the elements* (Metals Park, OH: ASM) p. 516, p. 575
- Kikuchi R 1951 *Phys. Rev.* **81** 988
- Kikuchi R 1974 *J. Chem. Phys.* **60** 1071
- Kikuchi R 1987 *Physica A* **142** 321
- Kikuchi R and van Baal C M 1974 *Scr. Metall.* **8** 425
- Murray J L (ed.) 1987 in *Phase diagrams of binary titanium alloys* (Metals Park, OH.: ASM) p. 340
- Sarma B N, Ravisankar N, Gopal M, Singh A K, Prasad R and Lele S 1994 *Philos. Mag.* **B70** 1117
- Singh A K, Singh V and Lele S 1991 *Acta Metall. Mater.* **39** 2847
- van Baal C M 1973 *Physica* **64** 571



## Novel concept for the aggregation structure of fatty acid monolayers on the water surface and direct observation of molecular arrangements in their monolayers

TISATO KAJIYAMA and TAISHI KURI

Department of Chemical Science and Technology, Faculty of Engineering, Kyushu University, 6-10-1 Hakozaki, Higashi-ku, Fukuoka 812, Japan

**Abstract.** The aggregation structure of fatty acid monolayers on water subphases of different pH's was investigated by means of transmission electron microscopy. Fatty acid monolayers exhibited the phase transition from an amorphous state to a crystalline one by surface compression in the case of a highly dissociated state of hydrophilic groups, whereas they did not show the phase transition in the case of a slightly dissociated state. The aggregation structure of monolayers on the water surface was systematically classified into "the crystalline monolayer", "the amorphous monolayer" and "the compressing crystallized monolayer" with respect to thermal and chemical (intermolecular repulsive) factors.

Molecular-resolution images of fatty acid molecules in the monolayers on mica substrate were successfully observed with an atomic force microscope (AFM) for the first time. The AFM image of a lignoceric acid monolayer prepared at a surface pressure of  $5 \text{ mN m}^{-1}$  showed a two-dimensional periodic structure with locally disordered molecular arrangements. Also, the nondestructive AFM image observation was successful for a stearic acid monolayer which was prepared by a multistep creep method, indicating that a high mechanical stability of the monolayer is inevitably required for the nondestructive AFM observation.

**Keywords.** Aggregation structure of monolayer; thermal and chemical factors; molecular-resolution AFM image; nondestructive AFM observation.

### 1. Introduction

Great attention has been paid to Langmuir-Blodgett (LB) films because of their potential applications as electronic or electro-optical devices and as model biological membranes. The images of monolayers on water surface have been proposed on the basis of recent morphological and structural studies (Kjaer *et al* 1989; Kajiyama *et al* 1992). These images did not always agree with the general concept (see, for example, Gaines 1966) which was accepted only from surface pressure-area ( $\pi$ - $A$ ) isotherms and also did not come to universal understanding. Here we present a novel and systematic classification for the aggregation structure of monolayers on water surface.

Fatty acid monolayers on pure water surface have been classified into a crystalline monolayer and an amorphous one at the subphase temperature ( $T_{sp}$ ) below and above the melting temperature ( $T_m$ ) of the monolayer, respectively. These aggregation states are independent of the magnitude of the surface pressure. The  $\pi$ - $A$  isotherm for the fatty acid monolayer represents the aggregating process of isolated domains grown right after spreading a fatty acid solution on water surface. On the other hand, phosphatidylcholine, phosphatidic acid and anionic amphiphile formed a compressing crystallized monolayer which was crystallized by compression of the monolayer on water surface at  $T_{sp}$  below  $T_m$  (Kajiyama *et al* 1993). For these cases, a fairly high surface pressure was required to crystallize the amphiphilic molecules with ionic hydrophilic groups owing to strong repulsion among ionic charges of hydrophilic groups. In order to understand systematically the aggregation structure of monolayers,

it is necessary to investigate the effect of ionic repulsion among hydrophilic groups with respect to the aggregation structure of the monolayer on water surface.

An atomic force microscope (AFM) allows one to characterize the surface structure of organic materials on a molecular level. The molecular arrangements (Schwartz *et al* 1993) and structural defects (Peltonen *et al* 1992) of multilayered LB films have been observed by using an AFM. On the other hand, the molecular-resolution AFM images of monolayers was successfully taken by using only limited samples such as monolayers of merized amphiphilic monolayer, dialkyl amphiphilic monolayer and fatty acid monolayer which were formed owing to a relatively stronger aggregation force. However, there has been no observation of the molecular-resolution image of the fatty acid monolayer with a weaker aggregation force.

In this study, we investigate the effect of ionic repulsion among hydrophilic groups with respect to the aggregation structure of the monolayer on water surface. We will present the molecular-resolution AFM images of lignoceric and stearic acid monolayers on mica for the first time.

## 2. Experimental

### 2.1 Analyses of the aggregation structure of monolayer on water surface

Arachidic acid monolayers were prepared from a benzene solution on water surface at two phases of pH 5.8 (pure water) and 12.6 (adjusted by addition of NaOH) at  $T_{sp}$  below  $T_m$  ( $= 328$  K). The ionic dissociation state of the hydrophilic group was estimated on the basis of the stretching vibrations of carbonyl and carboxylate groups by Fourier transform infrared attenuated total reflection (FT-IR ATR) measurements (Kajiyama *et al* 1993). Seventy arachidic acid monolayers were transferred onto a germanium ATR prism, resulting in the formation of the multilayered film. The transfer of the prism was carried out at surface pressures of 25 or 28 mN m<sup>-1</sup>. For transmission electron microscopic observations, the monolayer was transferred on hydrophobic Formvar or SiO<sub>2</sub> substrates, on which the monolayer could be transferred without a change of the aggregation state, by the horizontal lifting or upward transfer methods. Electron microscopic observations were carried out at a temperature corresponding to  $T_{sp}$  at which the monolayer was prepared.

### 2.2 Observation of molecular arrangements in the monolayer with AFM

Benzene solutions of lignoceric (CH<sub>3</sub>(CH<sub>2</sub>)<sub>22</sub>COOH) and stearic (CH<sub>3</sub>(CH<sub>2</sub>)<sub>18</sub>COOH) acids with concentrations of  $1 \times 10^{-3}$  and  $3 \times 10^{-3}$  mol · L<sup>-1</sup>, respectively, were spread on pure water surface at  $T_{sp}$  of 293 K. Since  $T_{sp}$  is below the melting point of lignoceric acid ( $T_m = 347$  K) and the stearic acid ( $T_m = 317$  K) monolayers, the monolayers are in a crystalline state. The lignoceric acid monolayer was prepared at a surface pressure of 5 mN m<sup>-1</sup> by a continuous compression at a rate of  $1.7 \times 10^{-3}$  nm<sup>2</sup> molecule<sup>-1</sup> s<sup>-1</sup> (Kajiyama *et al* 1993). The stearic acid monolayer was prepared at 23 mN m<sup>-1</sup> by the continuous compression method or a multistep creep method (Kuri *et al* 1994). The multistep creep method is a monolayer preparation method for which the monolayer is compressed stepwise up to a high surface pressure by alternating the compression and area creep. This procedure

rearrangement of molecules in the crystalline monolayer and/or filling of the vacancies in the interfacial regions among crystalline monolayer domains, which releases the stress concentration in the monolayer. Therefore, the multistep creep method provides a mechanically stable and defect-diminished monolayer. Each monolayer was transferred onto freshly cleaved mica by a vertical dipping method. The transfer ratio for each monolayer was unity. The AFM images of the monolayers were obtained with a SFA300 (Seiko Instruments, Inc.) in air at room temperature, using a  $0.8\text{ }\mu\text{m}$  scanner and a silicone nitride tip on a cantilever with a small spring constant of  $0.027\text{ N m}^{-1}$  (Kajiyama *et al* 1994, 1995). Images were recorded within 20 s in the "constant-height" mode; that is, feedback electronics and software were used to keep the sample height constant and measure the cantilever deflection. The applied force on imaging was evaluated to be about  $10^{-10}\text{ N}$  in an attractive force region, from the magnitude of cantilever deflection. This attractive force may not be the actual applied force between the tip and sample but an apparent composite force (applied force between the tip and sample, adhesion force by the water molecule at sample surface, etc.).

### 3. Results and discussion

#### 3.1 Novel concept for the aggregation structure of monolayers on water surface

Infrared absorption measurements revealed that almost all the carboxylic groups of arachidic acid molecules did not dissociate on water subphase of pH 5.8, whereas all carboxylic groups dissociated as carboxylate ions on water subphase of pH 12.6.

Parts a and b of figure 1 show the  $\pi$ - $A$  isotherms for the arachidic acid monolayers on water surfaces of pH 5.8 (pure water) and pH 12.6 at  $T_{sp}$  of 303 K, respectively, as well as the electron diffraction (ED) patterns of the monolayers at several surface pressures. In the case of a neutral state of arachidic acid (pH 5.8), the  $\pi$ - $A$  isotherm showed a sharp rise of surface pressure with decreasing surface area without any appearance of a plateau region. The ED patterns at surface pressures of 0 and  $25\text{ mN m}^{-1}$  showed a crystalline arc and crystalline spot, respectively, indicating the formation of "the crystalline monolayer". Kjaer *et al* (1989) also reported from synchrotron X-ray diffraction studies that the arachidic acid monolayer on pure water surface revealed the crystalline phase of the monolayer at various surface pressures. The change of the ED pattern from the crystalline arc to the crystalline spot suggests that crystalline domains were fused or recrystallized at the monolayer domain interface owing to sintering behaviour caused by surface compression, resulting in the formation of larger two-dimensional crystalline domains (Tanizaki *et al* 1992).

In the case of a dissociated state of arachidic acid on water subphase of pH 12.6 at  $T_{sp}$  of 303 K, a plateau region of the  $\pi$ - $A$  isotherm was observed in the range  $0.3\text{--}0.5\text{ nm}^2\text{ molecule}^{-1}$ . The ED pattern at  $5\text{ mN m}^{-1}$  showed an amorphous halo, whereas those at 12 and  $28\text{ mN m}^{-1}$  exhibited a crystalline arc or spot. Therefore, figure 1b indicates that the arachidic acid monolayer is crystallized by compression on water surface of pH 12.6. This type of monolayer has been classified as "the compressing crystallized monolayer". It is clearly concluded from parts a and b of figure 1 that amphiphile molecules form the crystalline monolayer and the compressing crystallized



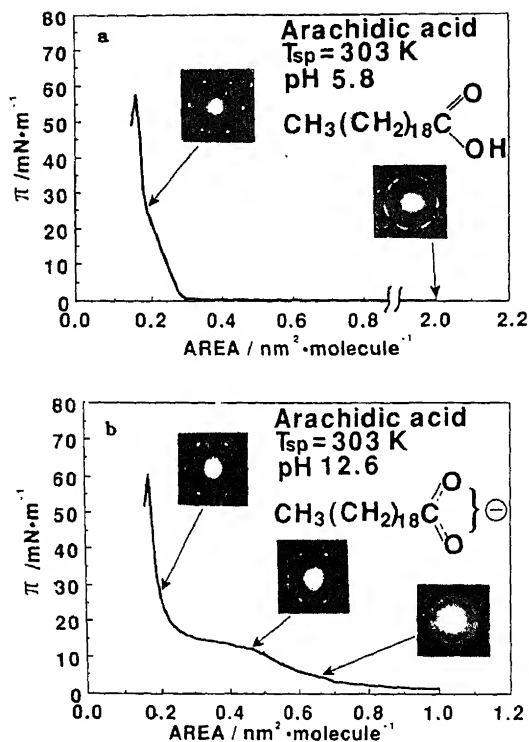


Figure 1.  $\pi$ -A isotherm and ED patterns of arachidic acid monolayers at a  $T_{sp}$  of 303 K in a water subphase of pH 5.8 (a) and pH 12.6 (b).

monolayer at  $T_{sp}$  below  $T_m$  in the case of a neutral state (may be the low degree of ionic dissociation) and a highly dissociated state of polar groups, respectively.

Figure 2 shows the classification based on the aggregation structure of monolayers with respect to thermal ( $T_{sp}$ ,  $T_{ac}$ ,  $T_m$ ) and chemical (the degree of ionic dissociation of the hydrophilic group) factors. This figure is divided into four quadrants by two axes:  $T_{sp}$  and the repulsive force among hydrophilic groups. In the case of amphiphiles with a nonionic hydrophilic group (corresponding to the third and fourth quadrants), isolated domains grown right after spreading a solution on the water surface are gathered to be a morphologically homogeneous monolayer by compression. This occurs at  $T_{sp}$  below  $T_m$  (the third quadrant), the monolayer is in a crystalline phase which is designated "the crystalline monolayer". The crystalline monolayer is further classified into two types: crystalline domains are assembled as a large homogeneous crystalline monolayer due to a surface compression-induced sintering at the interfacial contact among monolayer domains at  $T_{sp}$  below the crystalline relaxation temperature, and also crystalline domains are gathered without any special orientation at  $T_{sp}$  above  $T_{ac}$ . The crystalline relaxation phenomena correspond to a change from elastic to viscoelastic characteristics in a crystalline phase due to a remaining increase from anharmonic thermal vibration (Takayanagi and Matsuo, 1974; Kajiyama *et al.* 1974). At  $T_{sp}$  above  $T_m$  (the fourth quadrant), the monolayer is in an amorphous (noncrystalline) phase which is designated "the amorphous monolayer". In the case of amphiphiles with an ionic hydrophilic group (the first and second quadrants), the monolayer is in a liquid phase at  $T_{sp}$  below  $T_m$  (the first quadrant) and in a crystalline phase at  $T_{sp}$  above  $T_m$  (the second quadrant).

quadrants), a distinct domain structure is not formed at lower surface pressure owing to an electrostatic repulsion among polar head groups. At  $T_{sp}$  below  $T_m$  (the second quadrant), amphiphile molecules form a large homogeneous crystallized monolayer ( $T_{sp} < T_{ac}$ ) or an assembly of crystallized domains ( $T_{ac} < T_{sp} < T_m$ ) owing to the contribution of the van der Waals force with an increase of surface pressure. On the other hand, at  $T_{sp}$  above  $T_m$  (the first quadrant), the monolayer is not crystallized by compression owing to fairly active thermal molecular motion.

### 3.2 Direct observation of molecular arrangements in fatty acid monolayers with AFM

Figure 3a shows a nonfiltered AFM image of the lignoceric acid crystalline monolayer,

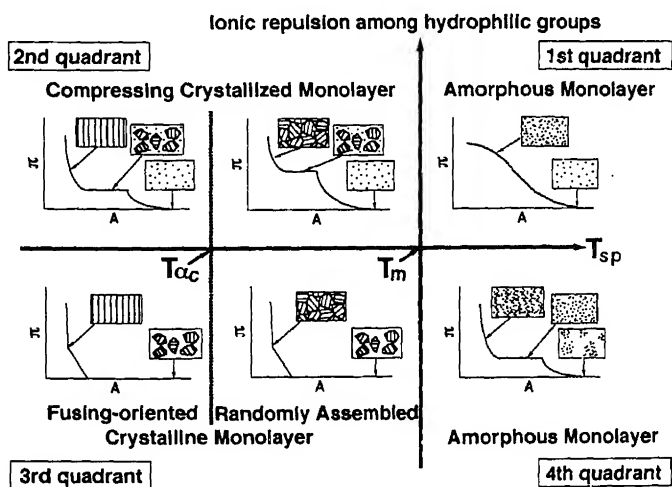


Figure 2. Classification of the aggregation structure of a monolayer on water surface.

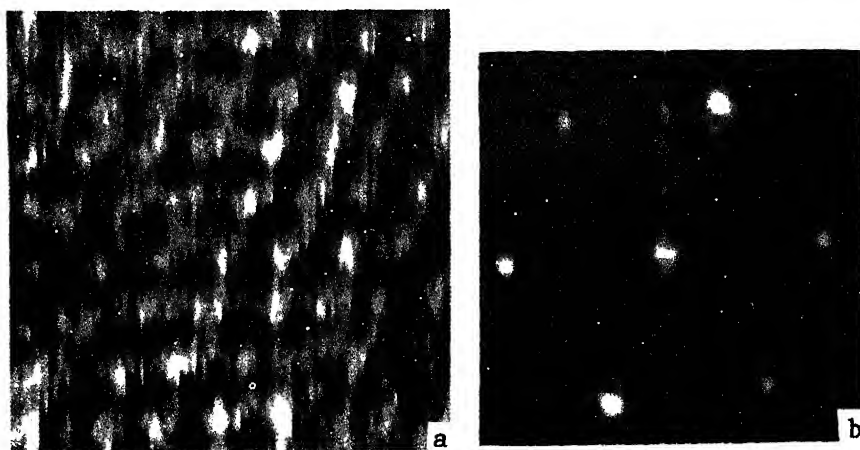


Figure 3. (a) Nonfiltered AFM image of a lignoceric acid monolayer on a scan area of  $4 \times 4 \text{ nm}^2$ . (b) 2D-FFT spectrum of (a).

which was prepared at  $5 \text{ mN m}^{-1}$  by the continuous compression method, on a scan area of  $4 \times 4 \text{ nm}^2$ . The AFM image is given in a top-view presentation in which the brighter and darker portions correspond to higher and lower regions of the monolayer surface, respectively. Though scanning was done repeatedly, the monolayer was not damaged by the tip. However, a hole could be artificially pierced through the monolayer with an applied force stronger than  $10^{-9} \text{ N}$ . The hole was about 3 nm deep, being comparable with the calculated molecular length based on the CPK model, in other words, the thickness of the lignoceric acid monolayer. It is reasonable to expect that the brighter portion in the AFM image represents the single methyl group of the lignoceric acid molecule, because the hydrophobic part of the lignoceric acid molecule was oriented toward air by the vertical dipping method. The AFM image exhibits that lignoceric acid molecules are regularly arranged with a hexagonal array. In order to clarify the molecular arrangement in the monolayer, a two-dimensional fast Fourier transform (2D-FFT) treatment was carried out.

Figure 3b shows the 2D-FFT spectrum of the image shown in figure 3a. The bright spots in the 2D-FFT spectrum exhibits a hexagonal pattern with the (10) spacing of 0.43 nm. (10) represents the two-dimensional lattice plane with Miller indices of  $h = 1$  and  $k = 0$ . The magnitude of (10) spacing which was evaluated from the 2D-FFT spectrum agrees well with the spacing of 0.43 nm which was estimated from the ED pattern of the lignoceric acid monolayer, and also this magnitude is quite different from the 0.46 nm spacing of a mica substrate calculated from the AFM image (figure 4). Moreover, the molecular occupied area of the lignoceric acid molecule in the monolayer which was evaluated from the AFM image and the ED pattern was  $0.21 \text{ nm}^2 \text{ molecule}^{-1}$ . This magnitude is close to  $0.25 \text{ nm}^2 \text{ molecule}^{-1}$  obtained on the basis of  $\pi$ -A isotherm measurements. Therefore, it is reasonable to conclude from figures 3 and 4 that the brighter portion in the AFM image of figure 3a represents the

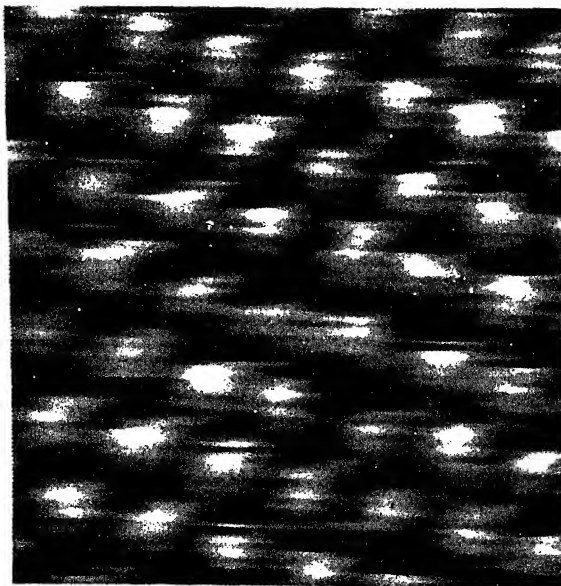
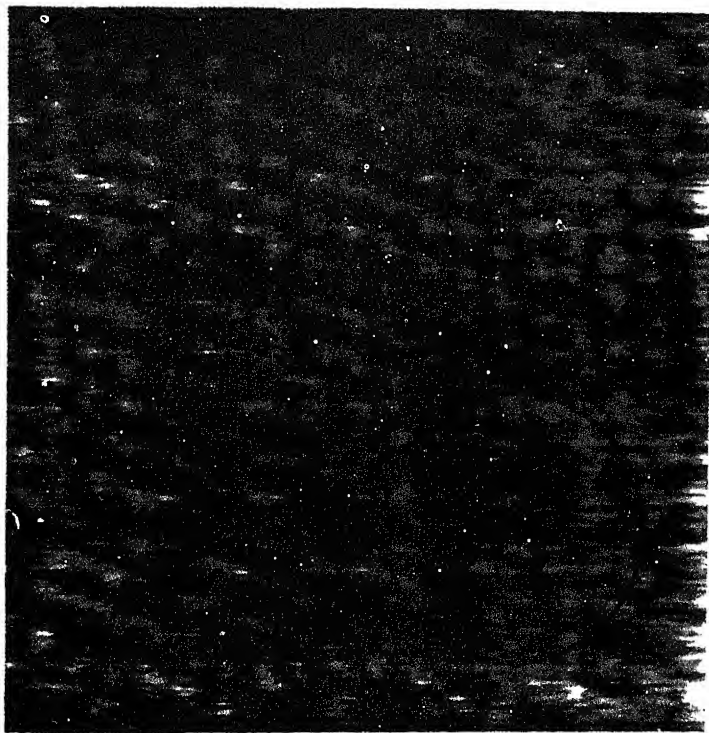


Figure 4. Nonfiltered AFM image of a mica substrate on a scan area of  $4 \times 4 \text{ nm}^2$ .



**Figure 5.** Nonfiltered AFM image of a lignoceric acid monolayer on a scan area of  $9 \times 9 \text{ nm}^2$ .

single methyl group of the lignoceric acid molecule in the monolayer and also that lignoceric acid molecules are regularly arranged in a hexagonal array.

Figure 5 shows a nonfiltered AFM image of the lignoceric acid monolayer on a larger area scan of  $9 \times 9 \text{ nm}^2$ . A regularly periodic hexagonal array in the AFM image was extended over about 10 nm. The range of the periodic hexagonal array was comparable to the magnitude of crystallographical continuity which was evaluated by a single line method (Hofmann and Walenta 1987; Oishi *et al* 1994) based on Fourier analysis of the ED profile of the lignoceric acid monolayer. As shown by the circle in figure 5, the hexagonal array of lignoceric acid molecules was locally disordered. Thus, the molecular-resolution AFM image of the lignoceric acid monolayer was nondestructively obtained and exhibited a two-dimensional periodic structure with locally disordered molecular arrangements.

The nondestructive AFM observation of the lignoceric acid monolayer was successful, as shown in figures 3 and 5. However, it was impossible to obtain a molecular-resolution AFM image of the lignoceric acid monolayer which was continuously compressed up to surface pressures higher than  $10 \text{ mN m}^{-1}$  because of monolayer destruction during the AFM scan. In the case of the crystalline monolayer, the crystalline domains grown right after spreading a solution are assembled into a morphologically homogeneous monolayer during compression. However, the vacancies at a molecular level may remain at the interfaces among the crystalline domains in the monolayer when the monolayer

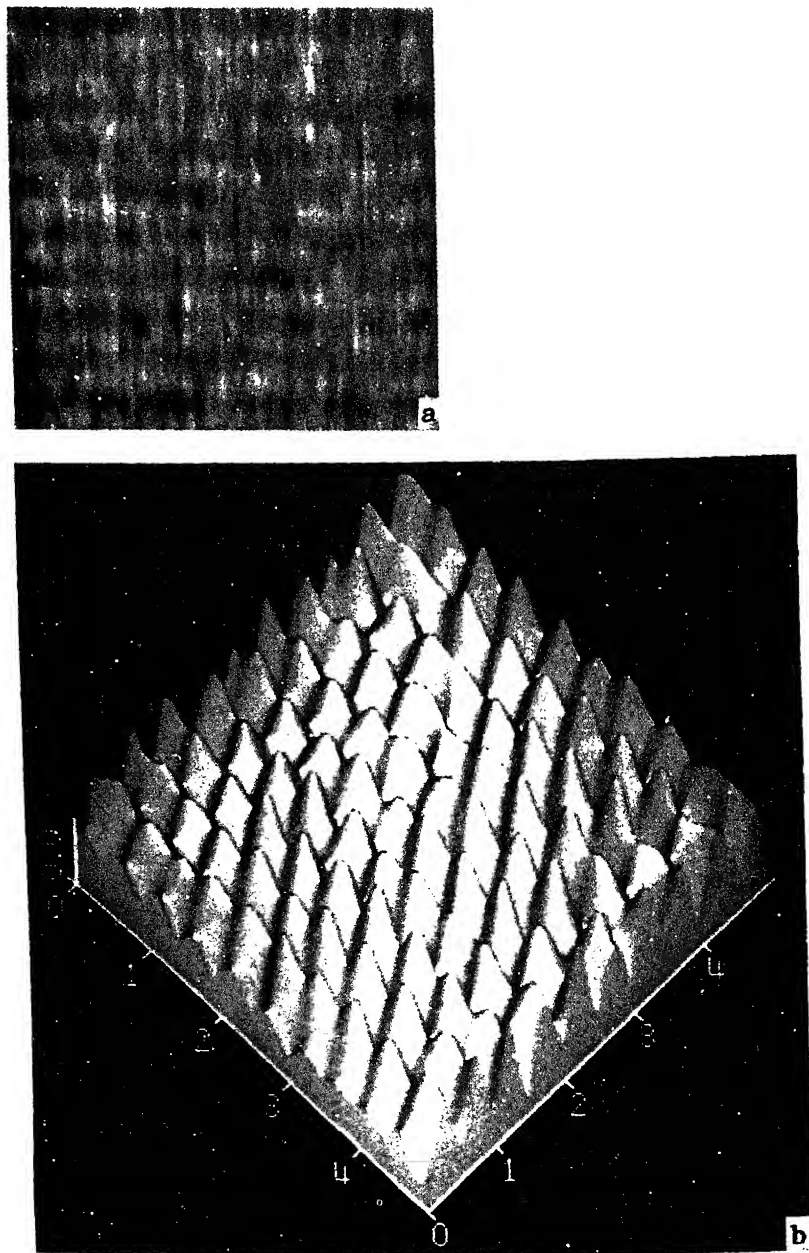


**Figure 6.** (a) Nonfiltered AFM image of a stearic acid monolayer on a scan area of  $5 \times 5 \text{ nm}^2$ . (b) A filtered AFM image of (a).

concentration in the monolayer under a continuous compression. Since large stress locally concentrates in the monolayer at higher surface pressures, such a monolayer is mechanically unstable. This mechanical instability may be the reason why the monolayer continuously compressed up to a high surface pressure, for example  $10 \text{ mN m}^{-1}$ ,

was easily collapsed by the applied force on the AFM scan. This argument was justified in the nondestructive AFM image of the monolayer prepared at a fairly higher surface pressure, for example  $23 \text{ mN m}^{-1}$ , by the multistep creep method, because stress concentration in the monolayer was almost completely released.

Figure 6a shows a nonfiltered AFM image of the stearic acid crystalline monolayer prepared by the multistep creep method with a scan area of  $5 \times 5 \text{ nm}^2$ . Though scanning was done repeatedly on the stearic acid monolayer prepared at the high surface pressure of  $23 \text{ mN m}^{-1}$  by the multistep creep method, the monolayer was not damaged by the tip. On the other hand, the monolayer prepared at the same surface pressure by the continuous compression method was easily collapsed by the tip on scanning. This collapse may be caused by stress concentration at vacancies among crystalline domains in the monolayer. In order to reduce the noise component in figure 6a, a digital filtering treatment was used to get the Fourier-transformed image. Figure 6b shows a filtered AFM image of the monolayer. A higher region in the AFM image represents the single methyl group of the stearic acid molecules, which are regularly arranged in a hexagonal array with a (10) spacing of  $0.42 \text{ nm}$ . This magnitude agrees with the spacing of  $0.42 \text{ nm}$  estimated from the ED pattern of the stearic acid monolayer. When the area scan was enlarged, the regularly periodic hexagonal array was extended over  $20 \times 20 \text{ nm}^2$  as shown in figure 7. This magnitude is comparable to the magnitude of crystallographical continuity evaluated on the basis of the single line method. Further, no distinct molecular disordered region was observed in

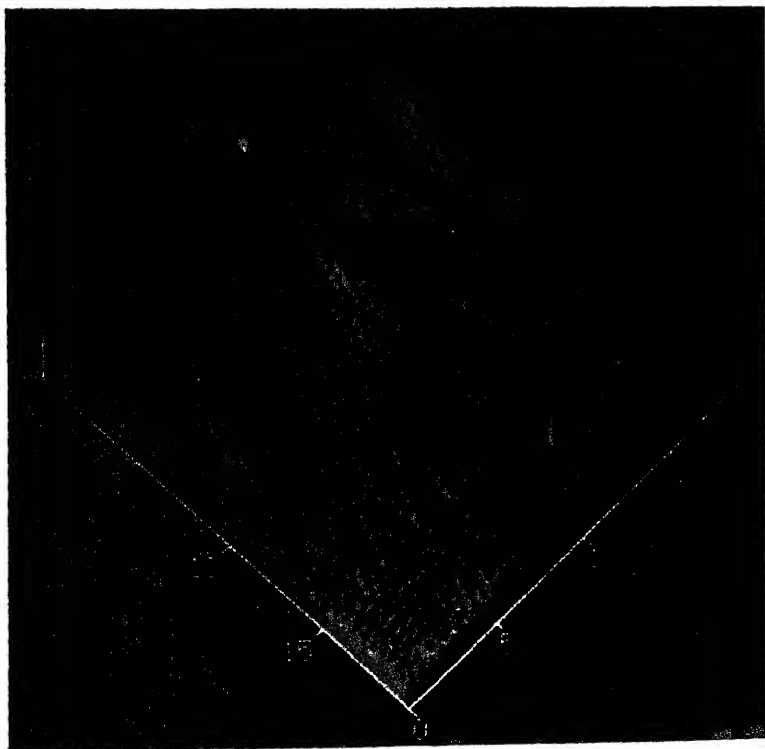


**Figure 7.** A filtered AFM image of a stearic acid monolayer on a scan area of  $20 \times 20 \text{ nm}^2$ .

the scan area of  $20 \times 20 \text{ nm}^2$  in the AFM image. The larger crystallographical continuity and extended regular molecular arrangement of the stearic acid monolayer are ascribed to effective sintering at interfaces among crystalline domains by the multistep creep method.

#### 4. Conclusion

The aggregation structure of fatty acid monolayers on water subphases of different pH's was investigated by TEM observations. The aggregation structure of monolayers on water surface was systematically classified into "the crystalline monolayer", "the amorphous monolayer" and "the compressing crystallized monolayer" with respect to thermal and chemical factors. The molecular-resolution AFM image of the fatty acid monolayer was successfully taken using a mechanically stable monolayer. The fatty acid monolayer with a remarkable mechanical stability for nondestructive AFM observations was prepared at a higher surface pressure by the multistep creep method and at a lower surface pressure by the continuous compression method.

#### References

- Gaines Jr G L 1966 *Insoluble monolayers at liquid-gas interface* (New York: Interscience) ch. 4  
Hofmann D and Walenta E 1987 *Polymer* **28** 1298  
Kajiyama T and Takayanagi M 1974 *J. Macromol. Sci. Phys.* **B10** 131  
Kajiyama T, Okada T and Takayanagi M 1974 *J. Macromol. Sci. Phys.* **B9** 35  
Kajiyama T, Oishi Y, Uchida M, Morotomi N, Ishikawa J and Tanimoto Y 1992a *Bull. Chem. Soc. Jpn.* **65** 864  
Kajiyama T, Oishi Y, Uchida M, Tanimoto Y and Kozuru H 1992b *Langmuir* **8** 1563  
Kajiyama T, Oishi Y, Hirose F, Shuto K and Kuri T 1993a *Chem. Lett.* 1121  
Kajiyama T, Oishi Y, Uchida M and Takashima Y 1993b *Langmuir* **9** 1978  
Kajiyama T, Zhang L, Uchida M, Oishi Y and Takahara A 1993c *Langmuir* **9** 760  
Kajiyama T, Oishi Y, Hirose F, Shuto K and Kuri T 1994 *Langmuir* **10** 1297  
Kajiyama T, Oishi Y, Suehiro K, Hirose F and Kuri T 1995 *Chem. Lett.* 241  
Kjaer K, Als-Nielsen J, Helm C A, Tippman-Krayer P and Möhwald H 1989 *J. Phys. Chem.* **93** 3200  
Kuri T, Oishi Y and Kajiyama T 1994 *Trans. Mater. Res. Soc. Jpn* **A15** 567  
Oishi Y, Hirose F, Kuri T and Kajiyama T 1994 *J. Vac. Sci. Technol.* **A12** 2971  
Peltonen J P K, He P and Rosenholm J B 1992 *J. Am. Chem. Soc.* **114** 7637  
Schwartz D K, Viswanathan R, Garnæs J and Zasadzinski J A 1993 *J. Am. Chem. Soc.* **115** 7374  
Takayanagi M and Matsuo M 1967 *J. Macromol. Sci. Phys.* **B1** 407  
Tanizaki T, Takahara A and Kajiyama T 1991 *J. Soc. Rheol. Jpn* **19** 208

## Some recent advances in bulk growth of mercury cadmium telluride crystals

R K SHARMA, R K BAGAI and VIKRAM KUMAR

Solid State Physics Laboratory, Lucknow Road, Delhi 110 054, India

**Abstract.** The inherent metallurgical problems associated with the HgTe/CdTe pseudobinary alloy system render the standard crystal growth processes inapplicable to the preparation of mercury cadmium telluride crystals for infrared detector applications. A variety of rather nonconventional techniques have been developed to overcome these problems. Two such techniques, viz. asymmetrical Bridgman and horizontal casting for solid-state recrystallization, developed at Solid State Physics Laboratory for the bulk growth of mercury cadmium telluride crystals are reviewed in this communication.

Due to the poor thermal conductivity of mercury cadmium telluride melts and solids, and the use of thick-walled quartz ampoules, it is extremely difficult to obtain a flat solid–liquid interface during Bridgman growth of this material. The technique of asymmetrical Bridgman has been successful in overcoming this problem to a great extent. Solid-state recrystallization has been widely accepted as one of the most successful techniques for obtaining large quantities of acceptable-quality mercury cadmium telluride crystals for infrared detector applications. This is a two-step process—the melt is first quenched to obtain a good cast, which is then subjected to a grain-growth annealing. The horizontal casting procedure developed for solid state recrystallization growth has been successful in improving the overall quality and yield of bulk mercury cadmium telluride crystals.

**Keywords.** Mercury cadmium telluride crystals; bulk growth.

### 1. Introduction

Solid-state electronic devices have played a vital role in the scientific and technological advancements of the later part of the current century. Particularly, the fields of electronics, optoelectronics and, lately, photonics were revolutionized with the development of some specific devices. Many of these devices could be realized, solely due to the invention of some specific materials. The discovery and development of new materials and devices has, in fact, been a regular feature of applied scientific research throughout these years. The materials of interest include semiconductors, insulators, ferrites, electrets, superconductors, etc which are used either as bulk crystals, or as epitaxial crystalline/strained-layered structures, quantum/nano-structures, etc for fabricating specific devices/device-structures. The stringent requirements of specific materials with desired characteristics for individual device fabrication make it imperative to have both material and device R&D works to be undertaken side by side. Major establishments engaged in device development work do, therefore, have material activities also going on concurrently. Solid State Physics Laboratory (SSPL) too is engaged in an extensive materials research activity to back up the widespread R&D work on advanced devices/device-structures. Figure 1 summarizes the materials activity at SSPL, which is supported by a range of material preparation and characterization facilities. The materials under study include semiconductors, oxide crystals and ferrites used for a variety of advanced electronic and optoelectronic devices. The material preparation techniques include bulk as well as epitaxial processes, including liquid-phase epitaxy (LPE), metal organic chemical vapour deposition (MOCVD),



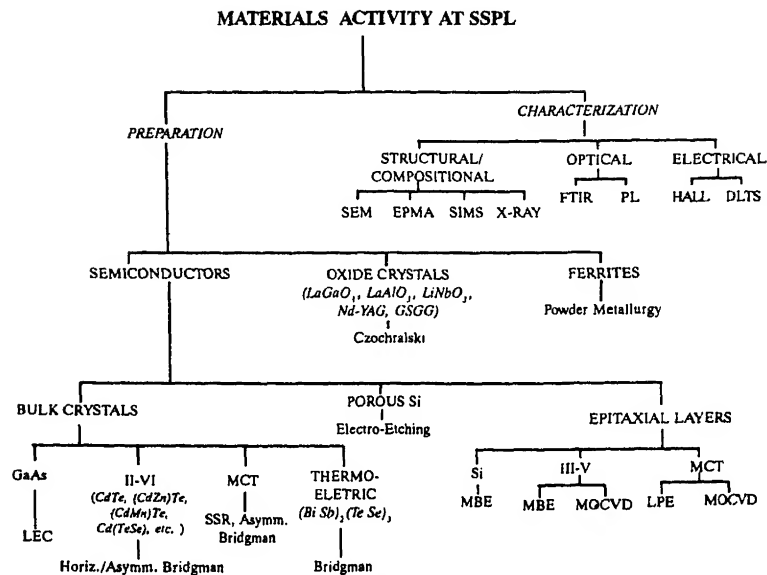


Figure 1. Materials activity at Solid State Physics Laboratory.

molecular beam epitaxy (MBE), etc. The characterization facilities include the optical and scanning electron microscopy (SEM), electron probe microanalysis (EPMA), secondary ion mass spectrometry (SIMS), X-ray diffraction/topography for structural/microstructural/compositional evaluation; Fourier-transform infrared (FTIR) and photoluminescence (PL) spectrometry for optical evaluation; and temperature Hall, deep-level transient spectrometry (DLTS), etc for electrical characterization. The prominent among the materials under study are various semiconductor materials including III-V, II-VI and other compounds/alloys, in addition to certain oxide crystals and ferrites.

Considerable progress in the preparation and characterization of these materials in the form of bulk crystals as well as epitaxial layers, including quantum well structures, etc has been made at SSPL as a result of consistent R&D work. However, the scope of this review is restricted to the preparation of bulk crystals of narrow-band gap semiconductor mercury cadmium telluride (MCT,  $\text{Hg}_{1-x}\text{Cd}_x\text{Te}$ ) (Cruse 1981) which is one of the most extensively studied materials here.

MCT is an alloy of two II-VI compounds,  $\text{HgTe}$  and  $\text{CdTe}$ , which are miscible in all proportions. Its band gap varies almost linearly with composition between the semimetallic  $\text{HgTe}$  ( $-0.3\text{ eV}$ ) and semiconducting  $\text{CdTe}$  ( $1.6\text{ eV}$ ). The  $\text{Hg}$ -rich compositions of this alloy are narrow-gap semiconductors for  $x > 0.16$ , and are, therefore, useful for IR detection over a wide wavelength range. However, the compositions with  $x \sim 0.2$  are of most significance, as they have a band gap  $\sim 0.1\text{ eV}$ , suitable for detecting IR radiation emitted by objects at around ambient temperature and transmitted through the strategically important  $8\text{--}14\text{ }\mu\text{m}$  atmospheric window (Ellis and Gordon 1993). Due to some unique intrinsic characteristics like high optical absorption due to a direct band gap, very low electron effective mass ( $\sim 0.005 m_0$ ), high electron mobility ( $\sim 2 \times 10^5\text{ cm}^2\text{ V}^{-1}\text{ s}^{-1}$ ), low dielectric constant ( $\epsilon_r \sim 16$ ), etc.

has proved to be the most successful material for fabricating IR detectors for strategic and commercial applications (Proc. SPIE 1979).

Although both bulk and epitaxial crystals of MCT are utilized for fabricating photoconductive (PC) and photovoltaic (PV) detectors, bulk-crystal-based linear PC and epitaxial-layer-based planar PV arrays are the most commonly used configurations. However, the preparation of device-quality bulk as well as epitaxial MCT crystals is a difficult task due to a large number of inherent metallurgical complexities associated with Hg–Cd–Te pseudobinary alloy system (Sharma and Sharma 1987), and some specific techniques are required to be evolved/perfected to overcome these problems. In the present paper we review the indigenously developed techniques of asymmetrical Bridgman and horizontal casting for solid state recrystallization (SSR) growth of bulk MCT crystals.

## 2. Bulk growth of MCT

The inherent metallurgical problems, mainly a wide phase diagram and very high Hg vapour pressures, associated with HgTe/CdTe pseudobinary alloy system render the conventional melt growth techniques inapplicable, as such, to MCT bulk growth. The Hg vapour pressure over the stoichiometric MCT melts at the liquidus point is  $\sim 35$  atm. Due to this, growth of MCT crystals from melts is required to be carried out in closed systems, such as sealed thick-walled ( $\sim 2.5$ – $3$  mm) quartz containers. The Czochralski growth process, which is currently the most successful one in case of Si and GaAs, cannot at all be applied to MCT. Moreover, the large CdTe segregation in the solid phase during freezing of melt ( $c_s/c_l \sim 3$ ), as a consequence of the broad pseudobinary phase diagram, requires the use of high temperature gradients to avoid constitutional supercooling across the solid liquid (s–l) interface during Bridgman growth of MCT crystals. The s–l interface normally remains quite curved due to the poor thermal conductivity of MCT melts and solids, in addition to the adverse effects of thick quartz walls. The heat is virtually extracted from the peripheral regions through radiation with negligible contribution from the solidified material and the melt. This results in marked compositional non-uniformity, both radial as well as axial, in MCT ingots grown conventionally using Bridgman method. The radial compositional variation due to peripheral segregation of CdTe also imposes a maximum limit to the ingot diameter (usually  $< 12$  mm). An improvement in compositional uniformity of such ingots can be obtained with the use of accelerated crucible rotation technique (ACRT) (Capper *et al* 1988). However, this involves the use of sophisticated instrumentation in addition to a sustained standardization schedule. An innovative modification of conventional Bridgman method, called asymmetrical Bridgman, was suggested by Bagai and Borle (1989) at SSPL, which resulted in marked improvement in the compositional uniformity by way of making s–l interface planar. This method is further discussed later in this section.

A variety of rather nonconventional techniques for bulk growth of MCT also emerged as a result of consistent efforts to circumvent the above problems. Solid-state recrystallization (SSR) (Micklethwaite 1981), variously called cast recrystallize anneal (CRA) or cast quench anneal (CQA), is one of the earliest, most successful and widely employed techniques among them. This process has little analogy with the SSR process

microstructure. Here a good cast is first obtained by quenching or by controlled cooling of MCT melt, which is then kept for a long-term (3–5 weeks) annealing near the solidus temperature (660–670°C) for the grain growth. Large-sized crystalline grains are normally obtained after the second step. The critical step in the process is the initial casting which controls the overall compositional uniformity of the ingot. With proper casting of ingots through appropriate quenching procedures and, finally, with selective slicing of grown ingots, large crystals, with much better compositional uniformity compared to conventional Bridgman ingots, can be obtained. However, the quenching efficiency of MCT ingots is normally poor due to the use of thick-walled quartz ampoules and poor thermal conductivity of the melt. This again puts a constraint on the maximum ingot diameter. The urge to improve ingot size led to the development of various variants of SSR by different growth workers. The most important of them are pressurized CRA (also called RSRE) (Vere *et al* 1982) and incremental quenching (Luigi Colombo *et al* 1985). However, both these methods involve much technical complexity. A relatively simple method of horizontal casting was invented by Sharma and co-workers (1993) at SSPL. This method not only resulted in a marked improvement in the compositional uniformity of SSR-grown MCT crystals but also crystalline perfection was improved to a great extent. These two techniques, asymmetrical Bridgman and horizontal casting, are quite successful in obtaining bulk MCT crystals for device fabrication, and are discussed in a little detail.

## 2.1 Asymmetrical Bridgman

Figure 2 schematically depicts the principle of asymmetrical Bridgman. The ampoule arrangement is similar to the conventional Bridgman except that the ampoule in this method is positioned asymmetrically instead of centrally aligned with the furnace/baffle axis. By suitably placing an appropriate baffle in the furnace, it is possible to achieve quite a high vertical (axial) temperature gradient ( $> 50^\circ\text{C}/\text{cm}$ ) along with a low horizontal (radial) gradient. The solid–liquid interface in the ampoule, though inclined, becomes quite flat. To facilitate proper nucleation of seed crystals, the ampoule design is also suitably modified (figure 2b). The technique allows the growth of larger ampoule diameters also (up to 21 mm dia crystals obtained).

The constant composition planes in Bridgman-grown crystals are expected to be parallel to the s–l interface. But generally the delineation of s–l interface in a grown ingot is an extremely cumbersome task, due to the variation in its inclination with the ingot axis. However, with judicious choice of furnace/ampoule design/positioning and growth parameters, it is possible to minimize the inclination/variation of the s–l interface to the ampoule axis without compromising on its flatness. Figure 3 compares the s–l interface shapes in two cases, where the ingots being grown by asymmetrical Bridgman method under different conditions/positioning are quenched at an intermediate stage during the run. It can be seen that excellent s–l interface flatness is achieved along with a low axial inclination.

Figures 4a and 4b compare the radial compositional profiles, as revealed by ICP-MS, across the asymmetrical Bridgman-grown crystals sliced parallel to the transverse s–l interface planes respectively. It can be seen that the crystal cut parallel to the s–l interface possesses fairly uniform composition. In the transversely cut crystals,

Symmetrical Bridgman

Asymmetrical Bridgman

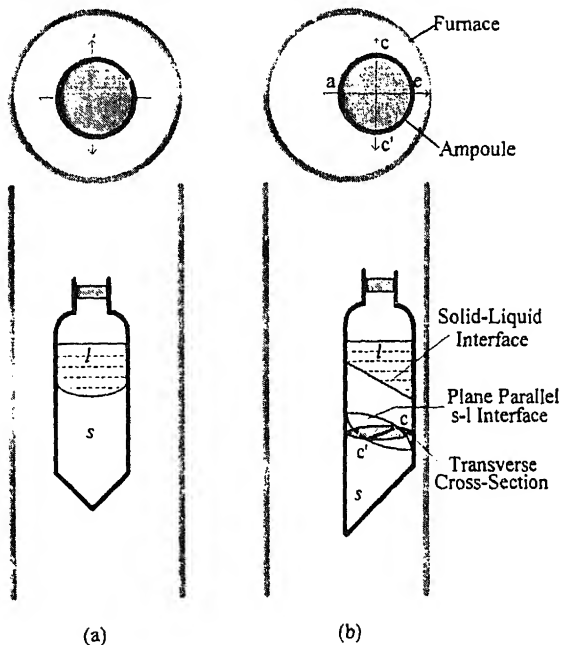


**Figure 2.** Schematic representation of ampoule position and shape of solid-liquid interface in (a) symmetrical and (b) asymmetrical Bridgman.

composition varies continuously from one end to the other along the line  $a-e$ , but in the perpendicular direction the same is nearly constant. These constant temperature lines are the intersections of  $s-l$  interface planes with the transverse cross-sections as schematically depicted in figure 2b. For linear array fabrication, normally narrow (1–2 mm wide) strips of material are utilized. Such strips cut along  $c-c'$  direction possess excellent compositional uniformity and, in turn, would result in fairly uniform detector characteristics.

The technique of asymmetrical Bridgman though basically developed for MCT could also be successfully applied for growing good-quality crystals of other low-thermal-conductivity materials like CdTe, CdZnTe, CdTeSe, etc. It is applicable in case of horizontal Bridgman as well, although for MCT, particularly, the horizontal Bridgman is inapplicable due to the extremely high Hg vapour pressures involved.

## 2.2 The horizontal casting of MCT for SSR growth

The cast obtained in the first step of the SSR process contains microscopic inhomogeneities due to the dendritic freezing—three-dimensional dendrite trees immersed in an interdendritic matrix having a comparatively lower CdTe content. However, it is removed through the process of Hg/Cd interdiffusion during the initial course of the second step of high-temperature long-term annealing. But the macroscopic compositional variations present in the cast as a result of non-uniform dendritic distributions etc are not affected appreciably. A very fine and fairly uniformly dendritic

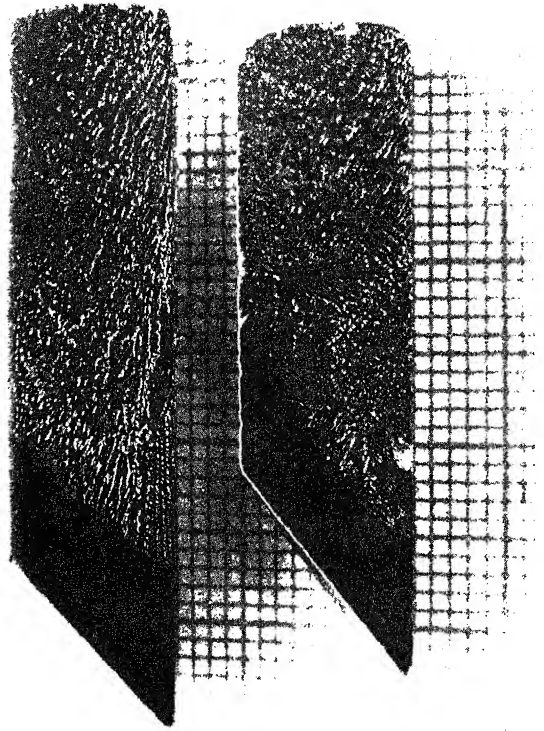


**Figure 3.** The shape of solid-liquid interface delineated in quenched ingots being asymmetrical Bridgman under different conditions. The dendritic structure represents the melt.

distribution is therefore desirable in the cast in order to attain a high degree of compositional uniformity in the SSR-grown ingots.

The quenching of the melts for obtaining good-quality cast is normally done by forcing compressed air/gas on the sealed quartz ampoules while keeping the space protected through thermal lagging to maintain the Hg vapour pressure, thereby avoiding melt eruption. Figure 5 compares the casting procedure in vertical (directional) and horizontal configurations. A vertically quenched cast normally consists of a core region where the density of dendritic matrix becomes low due to the depletion of CdTe in the first-to-freeze peripheral region. On the other hand, a horizontally cast ingot is expected to possess a fairly uniform dendritic distribution as depicted. A large s-l interface requires to move across the small thickness of the melt, thereby improving the quenching efficiency considerably, thereby resulting in a fair uniformity of composition compared to the conventionally obtained cast. Hence, obtaining a perfect cast free from pores/core/precipitates is technically a difficult task.

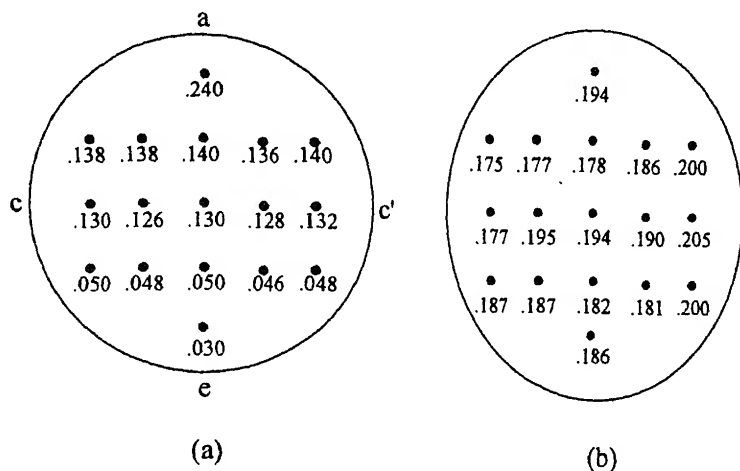


**Figure 4.** Compositional map ( $x$  value) of wafers cut parallel to (a) transverse cross-section and (b) solid-liquid interface.

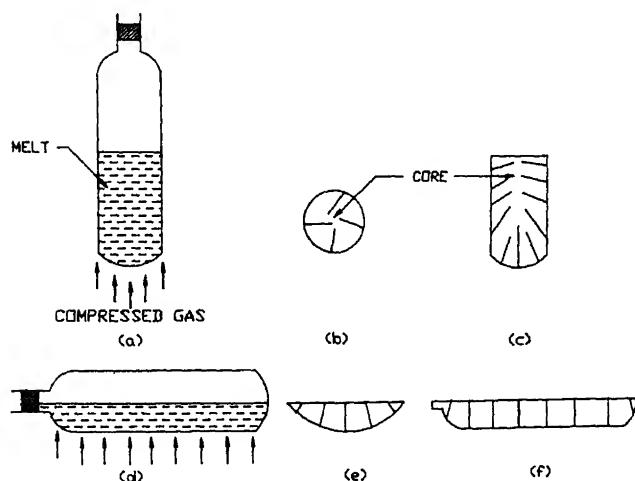


**Figure 5.** Schematic representation of (a) conventional and (d) horizontal casting configurations; (b), (e) and (c), (f) show expected dendritic distribution in transverse and longitudinal cross-sections for respective configurations.

After sustained experimentation the horizontal casting was first demonstrated with an arrangement in which the material-containing quartz ampoule was further sealed, under vacuum, in a thin-walled quartz ampoule with a definite amount of tin metal added to it. In horizontal configuration the molten tin partly filled the space between the two quartz tubes and provided a conducting path for the heat during the quenching, which was done by forcing compressed air on the lower part of the ampoule as schematically depicted in figure 5d. This resulted in excellent compositional uniformity in the grown ingots. As evident from the expected dendritic distribution the compositional uniformity was best in the longitudinal directions.

directions and  $\Delta x \sim \pm 0.002$  over the span of a  $30 \times 15 \text{ mm}^2$  area in longitudinally cut planks was achieved. These results compared well with those for even good-quality LPE layers. In addition to the excellent compositional uniformity, the crystalline perfection of these crystals was also found to be better. The core regions of the horizontally cast ingots are expected to be free of edge strains and, in fact, they were found to be free from subgrain structure. The dislocation (etch pit) densities in these regions were found to be about an order of magnitude lower compared to those normally obtained in conventionally cast SSR crystals.

Although the casting procedure described above was extremely effective and efficient it was technically a bit cumbersome due to the procedure of double wall sealing and determination of correct quantity of tin metal. A variation of this process was therefore evolved. The new experimental arrangement is schematically shown in figure 6. A semicircular stainless steel hollow jacket with end tubes for gas flow through it was designed for this purpose. The melt-containing ampoule rests horizontally on the matching internal groove of the jacket. The upper portion of the ampoule is carefully covered with thermal lagging. When compressed air is passed through the jacket, it quickly gets cooled and the heat is extracted through the lower peripheral region of

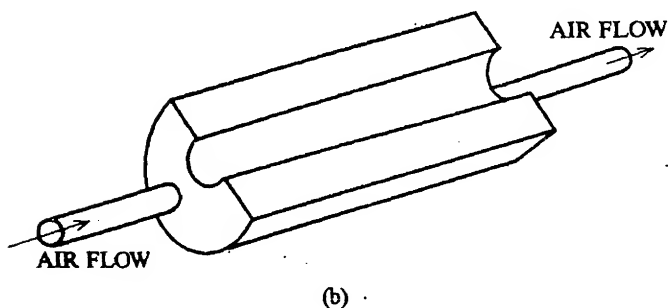
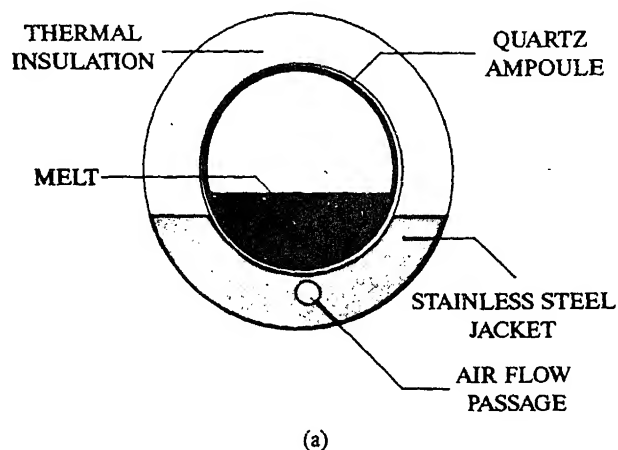


**Figure 6.** (a) Experimental arrangement for the horizontal casting and (b) schematic drawing of the casting apparatus.

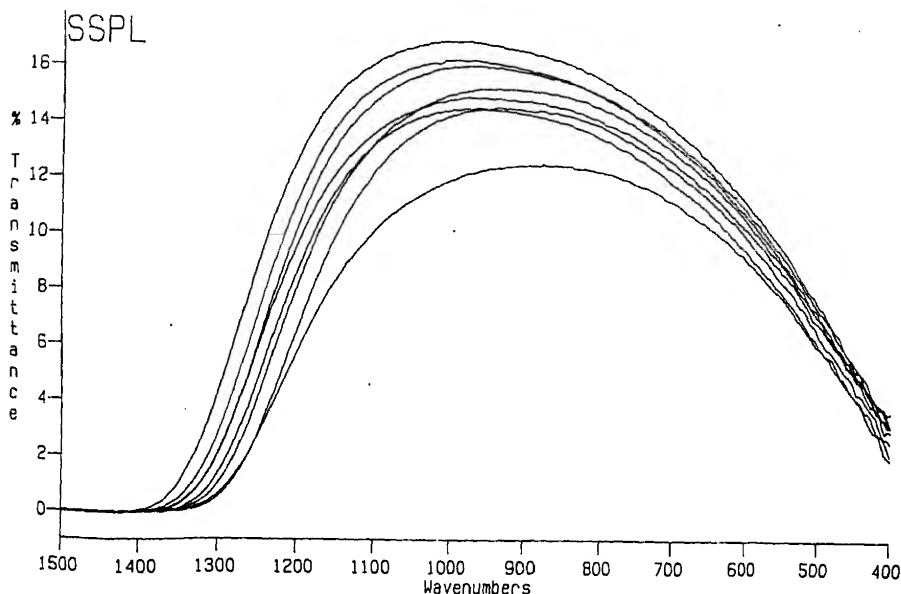


**Figure 7.** IR transmittance spectra of a  $20 \times 15 \text{ mm}^2$  longitudinally cut MCT plank, scanned across its area. The corresponding variation in composition,  $\Delta x$ , is of the order of  $\pm 0.0025$ .

the ampoule, thereby forcing a horizontal casting. By properly standardizing various associated parameters excellent casts could be obtained.

Figure 7 shows IR transmittance spectra across a  $20 \times 15 \text{ mm}^2$  plank, longitudinally cut from an SSR-grown crystal with the above arrangement. The compositional profile of this wafer deduced from the transmittance curves using the standard procedure (Micklethwaite 1988) reveals that the overall composition uniformity of this plank is almost of the same order as obtained in the initial experiment, the compositional variation being  $\Delta x \sim \pm 0.0025$ , and the linear variation along the longitudinal direction being  $\Delta x \sim \pm 0.0015$  over 20 mm. As described in case of asymmetrical Bridgman, excellent uniformity in spectral response could be achieved if the arrays are suitably aligned.

### 3. Conclusions

The asymmetrical Bridgman technique has been successfully applied to MCT bulk growth yielding crystals with fairly high compositional uniformity. The technique has the potential to solve the problem of acute curvature in solid-liquid interface in low-thermal-conductivity materials in general.

The horizontal casting procedure applied to the SSR growth of MCT improves the compositional uniformity, crystalline perfection and overall yield of crystals. Large-sized ( $\sim 20 \times 15 \text{ mm}^2$ ) wafers with compositional uniformity as good as  $\Delta x \sim \pm 0.0025$  could be readily obtained using this process.

The excellent uniformity of composition along the longitudinal direction in horizontally cast SSR crystals and in specific transverse directions in asymmetrical



Bridgman crystals could be utilized to fabricate linear IR detector arrays improved spectral response uniformity.

## References

- Bagai R K and Borle W N 1989 *J. Crystal Growth* **94** 561
- Capper P, Brice J C, Jones C L, Coates W G, Gosney J J G, Ard C and Kenworthy I 1988 *J. Growth* **89** 171
- Cruse P W 1981 in *Semiconductors and semimetals* (eds) R K Willardson and R K Beer (New Academic Press) Vol. 18, p. 1
- Elliot C T and Gordon N T 1993 in *Handbook on semiconductors* (eds) T S Moss and C (Amsterdam: North Holland) Vol. 4, p. 841
- Luigi Colombo, Syllaious A J, Perlakey R W and Brau M J 1985 *J. Vacuum Sci. & Technol.* **A3** 95
- Micklethwaite W F H 1981 in *Semiconductors and semimetals* (eds) R K Willardson and R (New York: Academic Press) Vol. 18, p. 48
- Micklethwaite W F H 1988 *J. Appl. Phys.* **63** 2382
- Proc. SPIE Meeting 1979 San Diego, California 197
- Sharma R K and Sharma B B 1987 *Indian J. Phys.* **A61** 350
- Sharma R K, Singh V K, Nayyar N K, Gupta S R and Sharma B B 1993 *J. Crystal Growth* **131** 563
- Vere A W, Straughan B W, Williams D J, Shaw N, Royale A, Gough J S and Mullin J B 1982 *J. Growth* **59** 121

# Recent studies on electrical and magnetic properties of molecular solids

YUSEI MARUYAMA

Department of Materials Chemistry, College of Engineering, Hosei University, Kajinocho, Koganei-shi, Tokyo 184, Japan

**Abstract.** Recent progress in studies on electrical and magnetic properties of some typical molecular solids is described, focussing on research in Japan. Especially we focus on two recent topics, organic semiconductor BTQBT and organic superconductors. Two types of compound are discussed, (BEDT-TTF)<sub>2</sub>Cu(NCS)<sub>2</sub> and M<sub>3</sub>C<sub>60</sub> (M = K or Rb). Finally, two kinds of molecular ferromagnet, nitronyl nitroxide radicals and C<sub>60</sub>(TDAE), are briefly introduced.

**Keywords.** Molecular solids; electrical conductivity; Molecular ferromagnetism; organic superconductors; fullerenes.

## 1. Electrical properties of organic molecular solids

### 1.1 Organic semiconductors and conductors

The first observation of electrical conduction in organic solids was most confidently presented as a concept of "organic semiconductors" by Akamatu and Inokuchi (1950). Typical organic semiconductors at that time were such polycyclic aromatic hydrocarbons as anthracene, perylene or violanthrone. The essentially important feature in these substances is that they consist of  $\pi$ -electron systems, and it has been known that a variety of functionalities of organic materials are caused by these  $\pi$ -electron systems.

A breakthrough from semiconductors to organic metallic conductors was also opened by Akamatu *et al* (1954) as the discovery of very high conductivity of perylene-bromine complexes. The first observation of metallic conductivity was reported by Coleman *et al* (1973) for tetrathiafulvalene-tetracyano-quinodimethane (TTF-TCNQ). The one-dimensional structure causes inherent instability in the electronic band structure and makes an energy gap at the Fermi-energy level. This electronic phase transition is accompanied by a lattice distortion through an electron-phonon coupling which stabilizes a charge-density-wave (CDW) insulating state. This type of metal-insulator transition usually occurs at a finite temperature, e.g. 53 K for TTF-TCNQ.

In order to stabilize metallic phases at low temperatures, the increase of dimensionality has been pursued by introducing intercolumnar interactions or heteroatom-heteroatom interactions in plane-parallel directions between TTF-type molecules. Replacement of sulphur atoms in TTF moiety with selenium atoms which have larger interaction radius and smaller ionization potential is effective in increasing dimensionality. High-pressure application is physically effective in increasing dimensionality and in suppressing the metal-insulator transition.

Electron-electron repulsive correlation is another crucial factor in realization of a metallic state in narrow electron energy band systems. Especially, the on-site (on-one-molecule) Coulomb repulsive energy ( $U$ ) relative to the bandwidth ( $W$ ) is a very important measure in determining if the material will be metallic or insulating. If the ratio  $U/W$  is much greater than unity, the material is a Mott-type insulator. If

order to reduce  $U$ , various strategies have been attempted, such as to use larger-size, twin-type or multi-valency molecules. The former approach was very successful, that is, to use (*bis*)ethylenedithio-tetrathiafulvalene (BEDT-TTF) as an electron donor (Saito *et al* 1982).

**1.1a BTQBT:** Relatively highly conductive single-component organic semiconductors were recently realized by Yamashita *et al* (1991). A typical example is *bis*[1, 2, 5]thiadiazolo-*p*-quinobis(1,3-dithiole) (BTQBT), which was synthesized with the strategy to realize much stronger intermolecular interactions in single-component molecular crystals. This novel molecule has electron-withdrawing heterocycles which are fused to the skeleton of a very strong electron donor, 2,2'-*p*-quinobis(1,3-dithiole) (QBT) (figure 1). In addition to the advantage of the strong intermolecular interactions (heteroatom-heteroatom contacts), relatively extending  $\pi$ -conjugation on the molecular plane of BTQBT may reduce the on-site Coulomb repulsion. Furthermore, this molecule is highly polarized because of intramolecular charge transfer, and accordingly it is expected to have a relatively small HOMO-LUMO gap. All these features may contribute to high electrical conductivity of this material.

BTQBT single crystals actually exhibited an unusually high conductivity of  $1 \times 10^{-3} \text{ Scm}^{-1}$  at room temperature with a thermal activation energy of 0.21 eV. Hall effect and its temperature dependence were successfully observed by Imaeda *et al* (1992). The Hall mobility with positive sign is  $2.4 \text{ cm}^2 \text{ V}^{-1} \text{ s}^{-1}$  at 330 K and  $6.3 \text{ cm}^2 \text{ V}^{-1} \text{ s}^{-1}$  at 175 K, and it changes with temperature  $T^{-1.6}$ .

**1.1b (DMe-DCNQI)<sub>2</sub>Cu complex:** The molecular structure of this compound is shown in figure 2. DMe-DCNQI is an electron-accepting molecule. The coordination to Cu ion is at the nitrogen atoms of cyanide groups. The DMe-DCNQI molecular planes overlap each other to form one-dimensional column structure in the crystal and copper ions connect these one-dimensional columns to form three-dimensional networks as shown in figure 3. The copper ions are in mixed valence state of  $4/3 +$  average valence charge, which indicates that the copper *d*-orbitals are interacting with the  $\pi$ -orbitals (LUMO) of DMe-DCNQI molecules.

The three-dimensional electronic structure stabilizes the metallic state down to low temperatures without metal-insulator transition. However, the metallic state is transformed to insulating state under relatively low pressure ( $> 100 \text{ bar}$ ), and around the critical pressure region the "metal-insulator-metal" reentrant behaviour was observed with decreasing temperature (Tomic *et al* 1988). Similar metal-insulator transition

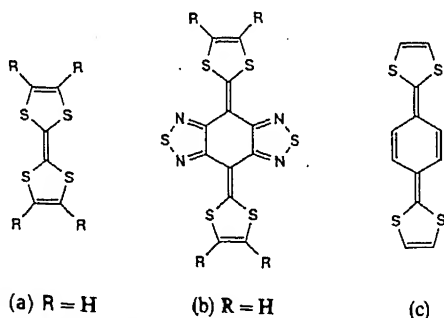


**Figure 1.** Molecular structures of some derivatives of TTF (a), BTQBT (b), and QBT (c).

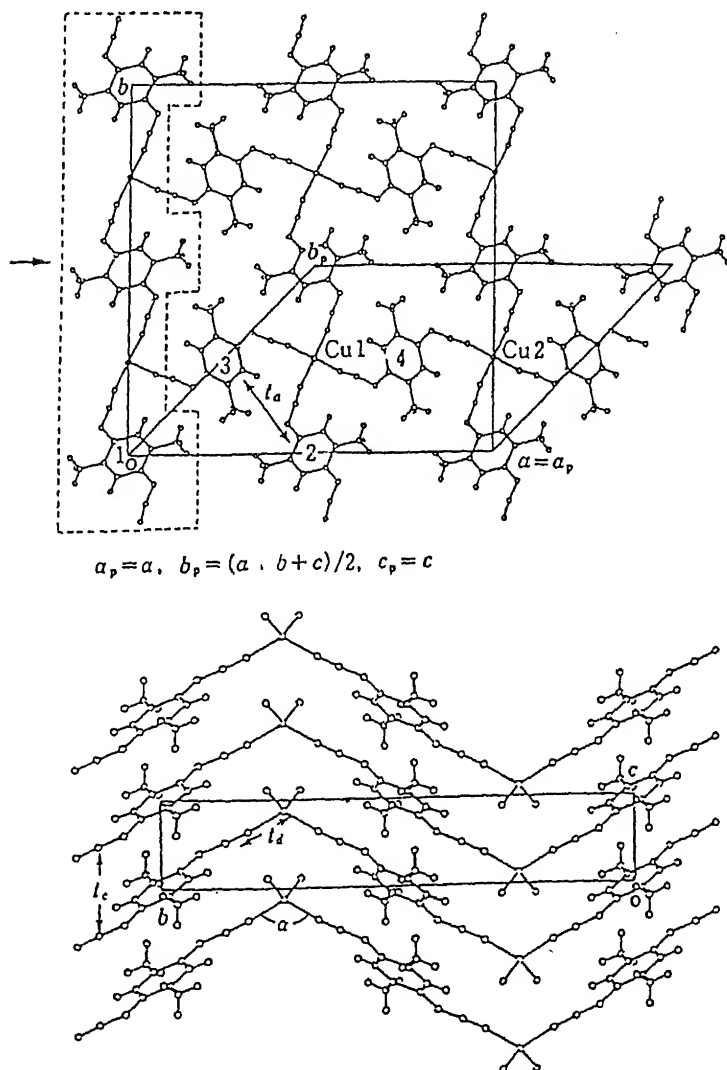


Figure 2. Crystal structure of  $(\text{DMe-DCNQI})_2\text{Cu}$ .

and also reentrant behaviour were discovered with the substitution of hydrogen atoms in DMe-DCNQI with deuteriums or  $^{12}\text{C}$  of cyanide groups with  $^{13}\text{C}$  (figure 4). The isotope exchange may cause qualitatively similar effect to the pressure effect, i.e. chemical pressure effect.

The theoretical details of the strongly correlated electron systems of  $(\text{DMe-DCNQI})_2\text{Cu}$  crystal have been studied by Fukuyama (1993).

## 1.2 Organic superconductors

In order to stabilize metallic states at low temperatures, enhancement of low dimen-

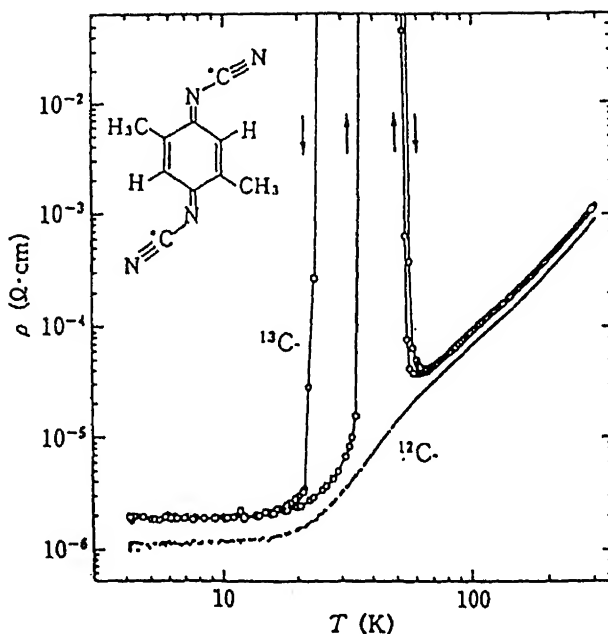


Figure 3. Reentrant metal-insulator transition by isotope substitution in  $\text{DCNQI}_2\text{Cu}$ .

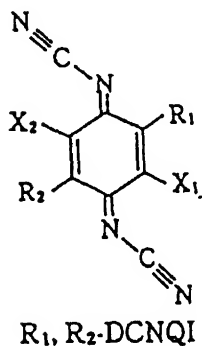


Figure 4. Molecular structure of  $R_1, R_2\text{-DCNQI}$ .

sionality and reduction of on-site Coulomb repulsion energies have been pursued. The first organic superconductor discovered by Jerome *et al* (1980) is  $\text{TMTSF-X}$  ( $X = \text{PF}_6$ ,  $T_c = 0.9 \text{ K}$  at 12 kbar) (figure 5). TMTSF complex forms quasi-one-dimensional columnar structure and the intercolumnar Se-Se interaction is essential to stabilize the metallic state. Although in the case of  $X = \text{PF}_6$  compound some pressure is necessary to suppress the metal-insulator transition,  $X = \text{ClO}_4$  compound is found to be superconducting at 1.4 K under ambient pressure due to the strong intercolumnar interactions in this case.

1.2a (BEDT-TTF)<sub>2</sub>X: (BEDT-TTF)<sub>2</sub>X compounds (figure 5) investigated by Saito *et al* (1982) have given much more successful results. The larger size of  $\pi$ -electron conjugation of BEDT-TTF may reduce the on-site Coulomb repulsion and the two-dimensional (not quasi-one-dimensional) crystal structure (figure 6) is advantageous for metallic phase.

The structure and function of the insulating layer X in (BEDT-TTF)<sub>2</sub>X are also important for two-dimensional metallic character of these compounds. In the cases of X = Cu(NCS)<sub>2</sub>, Cu(CN)[N(CN)<sub>2</sub>], Cu[N(CN)<sub>2</sub>]Br and Cu[N(CN)<sub>2</sub>]Cl the superconducting critical temperatures  $T_c$  are relatively high, 10.4, 12.3, 11.2 and 12.5 K, respectively. The highest  $T_c$  is 13.1 K under 0.3 kbar for X = Cu[N(CN)<sub>2</sub>]Br. The pressure dependence of  $T_c$  for X = Cu(NCS)<sub>2</sub> is, however, rather negative. The isotope

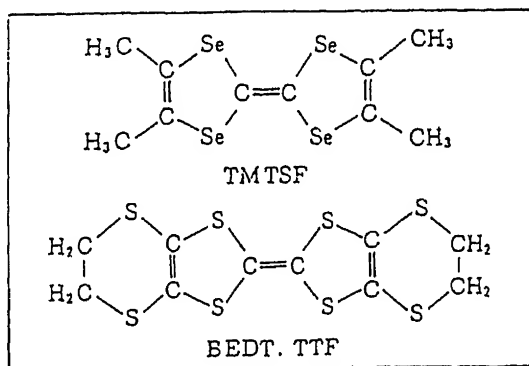


Figure 5. Molecular structures of the components of typical organic superconductors.

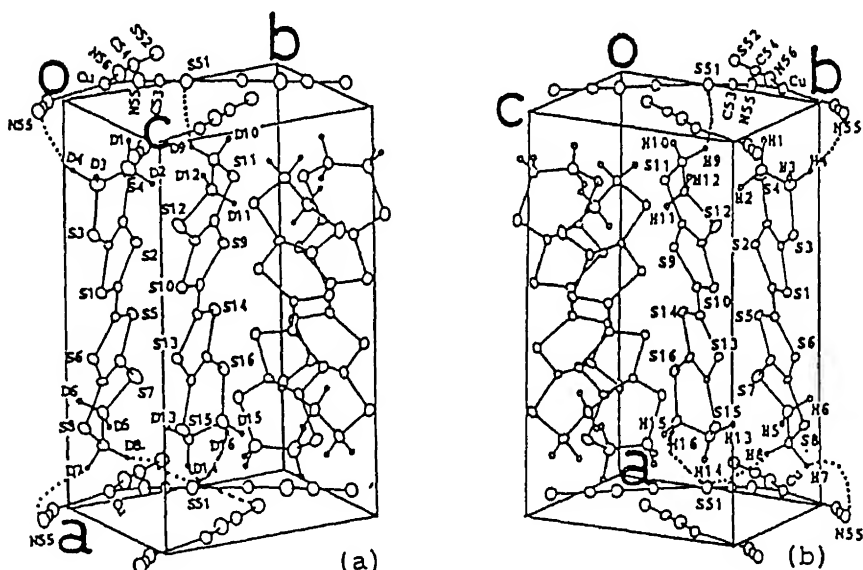


Figure 6. Crystal structure of (BEDT-TTF)<sub>2</sub>Cu(NCS)<sub>2</sub>.

effect for  $T_c$  is also negative for  $(\text{BEDT-TTF})_2\text{Cu}(\text{NCS})_2$  when the peripheral hydrogen atoms are substituted by deuterium atoms. On the contrary, substitution of atoms in inner TTF core with  $^{13}\text{C}$  exhibited almost no isotope shift in  $T_c$ . Magnetic field effects for metallic states have been very extensively studied to reveal the two-dimensional nature and Fermi-surface structures of these materials.  $(\text{BEDT-TTF})_2\text{X}$  compounds may be classified to type II superconductors, and the magnetic behaviours below  $T_c$  are not sufficiently clarified yet.

**1.2b Fullerenes:** The discovery of such new cage-type carbon-atom clusters or fullerenes has opened a new horizon in the field of molecular materials (Kroto 1985). After the development of mass-production method for fullerenes by contact arc discharge (Kratschmer *et al* 1990), the discovery of superconductivity at 18 K in  $\text{K}_3\text{C}_{60}$  (Hebard *et al* 1991) has strongly accelerated the study of fullerene compounds.

The electrical conductivity of  $\text{C}_{60}$  single crystal is strongly and negatively dependent on the ambient oxygen pressure, and it is believed to be around  $10^{-5}\text{ Scm}^{-1}$  at 295 K in the most oxygen-free pure  $\text{C}_{60}$  single crystals. The thermal activation energy of conductivity is 0.26 eV, which indicates that pure  $\text{C}_{60}$  crystal is a molecular semiconductor. The charge-carrier mobility in pure  $\text{C}_{60}$  single crystals was measured by two methods, time-of-flight (Frankevich *et al* 1993) and Hall effect (Arai 1994). The drift mobilities obtained by the former method were  $1.7\text{ cm}^2\text{ V}^{-1}\text{ s}^{-1}$  for holes and  $0.5\text{ cm}^2\text{ V}^{-1}\text{ s}^{-1}$  for electrons which are temperature-independent below (50–200 K) and above (260–300 K) the phase transition point, around 260 K. At this temperature, the mobility increased stepwise by 1.7 times with decreasing temperature. It is known that the changes in the molecular rotational freedom and accordingly in the crystal structure take place at this temperature, which suggests that transporting electrons or holes may couple with molecular rotations. The Hall mobility with positive sign was reported to be  $0.15\text{ cm}^2\text{ V}^{-1}\text{ s}^{-1}$  and it is again almost temperature-independent between 290 K and 570 K.

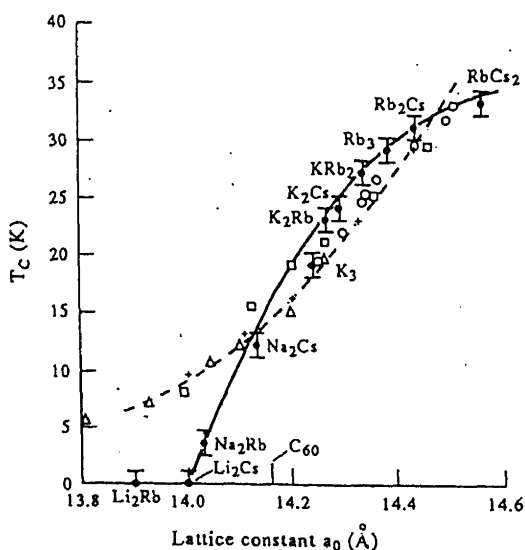


Figure 7. Correlation between  $T_c$  and  $a_0$  in alkali metal- $\text{C}_{60}$  superconductors.

$C_{60}$  crystals doped with alkali metals or alkaline-earth metals,  $M_xC_{60}$ , have realized a new family of molecular metals and superconductors which have much higher  $T_c$  than organic superconductors known so far. The dominant stoichiometry which yields metallic state is  $x = 3$  and the corresponding ones for alkali metal-doped complexes, fullerides, make a systematic family of molecular superconductors (figure 7). The highest  $T_c$  in this family is 33 K for  $Cs_2RbC_{60}$ . However, it was very recently reported that  $Cs_3C_{60}$  stabilized under pressure may have  $\sim 40$  K for  $T_c$ . The intrinsic nature of the metallic state and the mechanism of superconductivity in fullerides are not yet clarified. In the BCS regime a probable theoretical approach based on intramolecular-vibration-mediated Cooper pairing was proposed taking into account a strongly correlated electron system and relevant phonons and Coulomb energy windows (Ivanov and Maruyama 1995). However, such different approaches as charge-transfer pairing could be more general and relevant to molecular superconductors.

## 2. Magnetic properties of organic molecular solids

A very important subject in this field is to create or synthesize molecular ferromagnets. We focus on this subject in this section.

### 2.1 Molecular ferromagnetism

As radical molecules—neutral or charged—have unpaired electrons and show paramagnetism, they could be candidates for ferromagnetic materials. However, once these paramagnetic species are in the solid state, as a rule they are Curie–Weiss paramagnets. If the interactions between spins in different molecules are strong enough to order at some temperatures, the anti-ferromagnetically ordered states usually overcome the ferromagnetic states, since the bonding states between molecules are usually more stable than the antibonding states. Therefore the next strategy is how to make the bonding states unstable, or to make two unpaired spin states orthogonal.

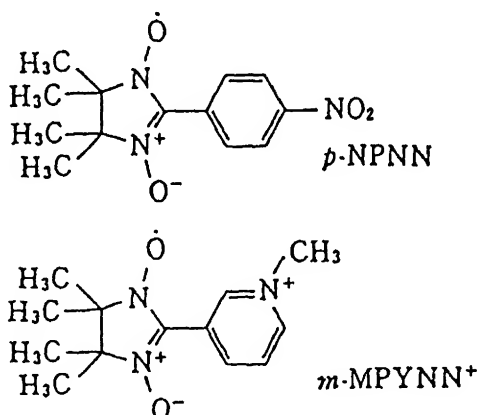


Figure 8. Molecular structures of nitronyl nitroxide radicals.



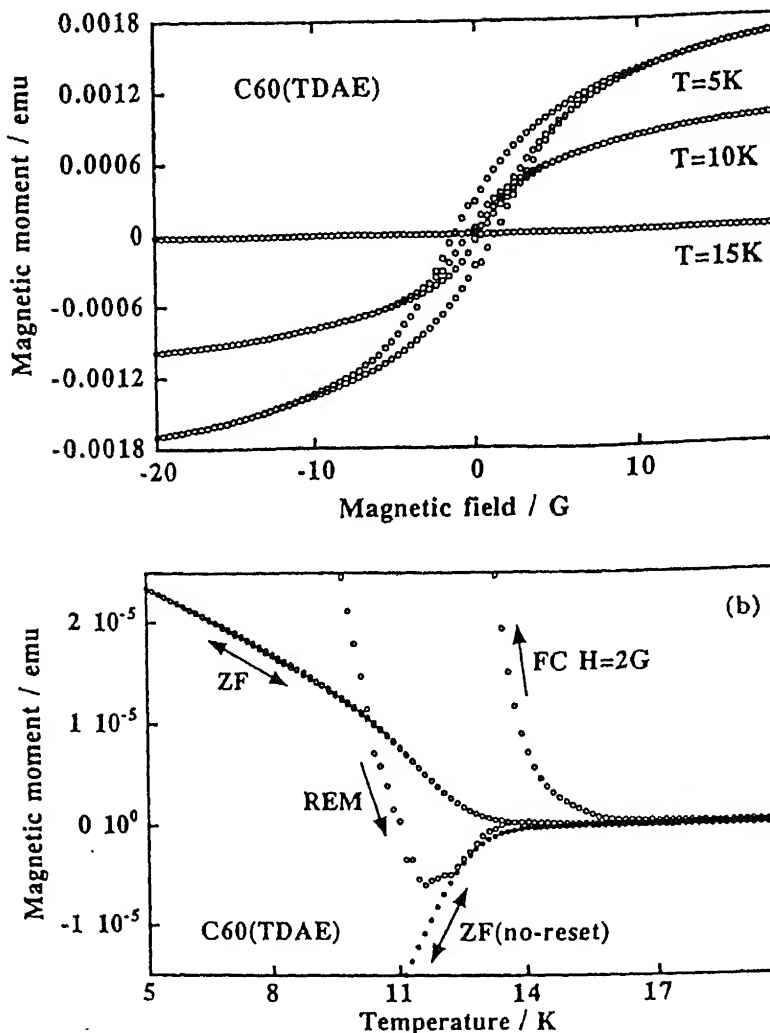


Figure 9. Spontaneous magnetization in  $C_{60}(TDAE)$ .

**2.1a Nitronyl nitroxide radicals:** Nitronyl nitroxide radicals are the simplest examples in this line (figure 8) (Kinoshita *et al* 1991). In the crystal unpaired states on  $-NO$  groups are rather localized and located very far from each other, so that a nearly orthogonal relation between two unpaired spin states of neighbouring molecules is fulfilled in this case. Further, large on-site Coulomb repulsion may contribute to stabilize the triplet or ferromagnetic states in this system. This compound shows ferromagnetic ordering below 0.65 K.

**2.1b  $C_{60}(TDAE)$  ferromagnet:**  $C_{60}(TDAE)$  complex, where TDAE means tetrakis(diamino-ethylene), could be a different approach for a molecular ferromagnet based on the charge transfer mechanism (Allemand *et al* 1991). Although extensive studies of this system have revealed aspects of its magnetic behaviour, such as the spontaneous magnetization, the mechanism of the ferromagnetic ordering is still unclear.

magnetization below 13 K or the hysteresis curve in the isothermal magnetization (figure 9) (Suzuki *et al* 1994), the nature of the magnetism, whether really ferromagnetic or spin-glass-like, is still unclear. The quest for itinerancy of ferromagnetic spins is almost known to be negative through the recent experiments by two groups (Maruyama and Blinc).

## References

- Akamatsu H and Inokuchi H 1950 *J. Chem. Phys.* **18** 810  
Akamatsu H, Inokuchi H and Matsunaga Y 1954 *Nature* **173** 168  
Allemand P M, Khemani K C, Koch A, Wudl F and Thompson J D 1991 *Science* **253** 301  
Arai T 1994 *Electrical properties of C<sub>60</sub> single crystals*, Doctor Thesis, University of Tokyo, Tokyo  
Coleman L B, Cohen M N, Sandman D J, Yamagishi F F, Garito A F and Heeger A J 1973 *Solid State Commun.* **12** 1125  
Frankevich E, Maruyama Y and Ogata H 1993 *Chem. Phys. Lett.* **214** 39  
Fukuyama H 1993 *J. Phys. Soc. Jpn* **62** 1436  
Hebard A F *et al* 1991 *Nature* **350** 600  
Imaeda K, Yamashita Y, Li Y, Mori T, Inokuchi H and Sano M 1992 *J. Mater. Chem.* **2** 115  
Ivanov V and Maruyama Y 1995 *Physica C* (in press)  
Jerome D, Mazaud A, Ribault M and Bechgaard K 1980 *J. Phys. Lett.* **41** L95  
Kinoshita M *et al* 1991 *Chem. Lett.* 1225  
Kratschmer W, Lamb L D, Fostiropoulos K and Huffman D R 1990 *Nature* **347** 354  
Kroto H W, Heath J R, O'Brien S C, Curl R F and Smalley R E 1985 *Nature* **318** 162  
Maruyama Y and Blinc R (Two groups)  
Saito G, Enoki T and Inokuchi H 1982 *Chem. Lett.* 1345  
Suzuki A, Suzuki T, Whitehead R J and Maruyama Y 1994 *Chem. Phys. Lett.* **223** 517  
Tomic S, Jerome D, Aumuller A, Erk P, Hunig S and von Schulz J U 1988 *Synth. Met.* **27** B281  
Wudl F and Thompson J D 1992 *J. Phys. Chem. Solids* **53** 1499  
Yamashita Y, Tanaka S, Imaeda K and Inokuchi H 1991 *Chem. Lett.* 1213



# Interfaces in discontinuously reinforced metal matrix composites: An overview

R MITRA and Y R MAHAJAN

Defence Metallurgical Research Laboratory, Hyderabad 500 258, India

**Abstract.** The fundamental and engineering aspects pertaining to the matrix-reinforcement interfaces in discontinuously reinforced metal matrix composites are presented in this overview. The interfaces play a key role in determining mechanical properties, namely Young's modulus, yield strength, elongation, creep and fracture behaviour, as well as physical properties like coefficient of thermal expansion, thermal conductivity and damping characteristics of metal matrix composites; these are discussed in detail. The ratio of the experimental value of the Young's modulus to that predicted from the rule of mixtures has been used as a measure of interfacial bond strength. Various issues such as the nature of the interfacial bond, chemical reaction at the interfaces, and effect of alloying and processing on the structure of the interfaces and the properties of the composite are examined. In order to exploit the full potential of reinforcing the metallic matrix, the suggested strategies include creation of metallic bonding at the interface, use of *in situ* processing, choice of right type of alloying elements, and heat treatments and engineering of interfaces.

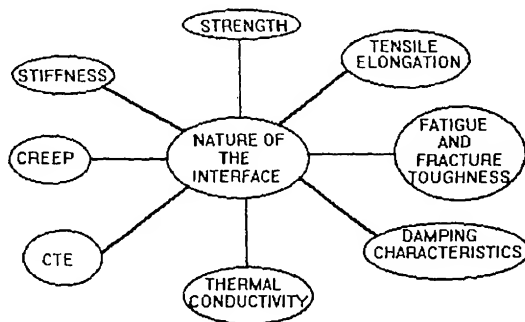
**Keywords.** Interfaces; bonding; wetting; coherency; Young's modulus; physical and mechanical properties; *in situ* composites; orientation relationship; interfacial energy.

## 1. Introduction

In recent years, the development of metal matrix composites (MMCs) has been receiving worldwide attention on account of their superior strength and stiffness, wear resistance, corrosion fatigue behaviour and creep resistance in comparison to the corresponding wrought alloys. The idea involved in the design of a composite material is to combine the good attributes of metals with ceramics. Metals have low stiffness values, and are ductile. Ceramics are stiff and strong, but are brittle and fail catastrophically. In MMCs, we exploit the strength of the ceramic while avoiding brittle failure. The performance of the composite depends, besides the matrix microstructure and the nature of the ceramic reinforcement, very critically on the matrix-reinforcement interface. This is schematically illustrated in figure 1. The interface plays a crucial role in the load transfer between the matrix and the reinforcement as well as in dislocation-particle interactions, which is significant in strengthening and stiffening of the composite. Moreover, physical properties such as thermal conductivity, coefficient of thermal expansion (CTE), dimensional stability, etc are also closely related to the nature of the interface. Thus it is desirable to have a clear understanding of the interfacial characteristics of specific metal matrix composites and to tailor them to achieve optimum performance in applications. In particular, the present paper addresses the issues pertaining to the interfaces in discontinuously reinforced MMCs.

## 2. Matrix-reinforcement bonding

In metal matrix composites, strengthening by the reinforcing phase is critical dependent on the strength of the bond between matrix and reinforcement. Interfaci



#### IMPORTANCE OF THE INTERFACE

**Figure 1.** Schematic diagram showing relationship of interface characteristics to physical and mechanical properties.

bonding can be categorized as mechanical and chemical (Chawla 1987). Mechanical bonding is significant only in the case of fibre-reinforced composites, when fibres have rough or faceted surfaces. Chemical bonding is important for all kinds of reinforcements: fibres, whiskers and particulates. A chemical bond is possible only if the matrix and reinforcement are in direct contact and is accomplished by the exchange of electrons, and the type of exchange determines the character of the bond. It can be metallic, which is non-directional, or ionic or covalent, which are directional. An interface with a metallic bond is thus more ductile than that with ionic or covalent bonds. For example, Fe-Fe<sub>3</sub>C interfaces in steel do not show fatigue crack initiation (Sunwoo *et al* 1982) as found in Fe-Al<sub>2</sub>O<sub>3</sub> interfaces (Eid and Thomas 1982). Interface segregants and chemical reaction can also affect the strength of the bond. The strength of the dual atomic bonds at the interface, which ultimately reflects on the macroscopic strength.

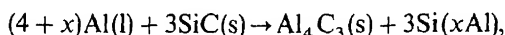
### 3. Reactive interfaces

A chemical reaction at the interface may lead to a strong bond between the matrix and the reinforcement, but a brittle reaction product can be highly detrimental to the performance of the composite. Table 1 gives matrices and reinforcements with reaction products seen at the interfaces. A ceramic-ceramic bond (reaction product of ceramic reinforcement) is weaker and more brittle than metal-ceramic or metal-metal intermetallic bond. Hence cracks initiate by cracking of the reaction product at the reaction product-matrix interface. For example, Al<sub>4</sub>C<sub>3</sub> which forms as a reaction product at Al matrix-SiC fibre interface during processing by melting and casting is a site for crack initiation (Clough *et al* 1990). Figure 2 shows an Al/TiC interface with reaction products comprising Al<sub>3</sub>Ti and Al<sub>4</sub>C<sub>3</sub>; sharp cracks can be observed to have occurred during cold rolling (Mitra *et al* 1993a). Thus, it is essential that the matrix and reinforcement coexist in thermodynamic equilibrium under processing conditions. This is the first criterion in choice of ceramic reinforcements for a metal matrix. Alloying can be used to prevent progress of chemical reactions. Ad-

**Table 1.** Reaction products at some of the matrix/reinforcement interfaces.

Matrix	Reinforcement	Reaction products and precipitates	References
<i>Aluminium</i>			
Al	SiC	$Al_4C_3$ , Al(Si)	Iseki <i>et al</i> (1984); Lec <i>et al</i> (1988)
Al-Mg	SiC	$Mg_2Si$ , $Al_4C_3$ , MgO	Rack (1988)
Al-Cu-Mg	SiC	$CuMgAl_2$ , MgO	Nutt (1986); Nutt and Carpenter (1985)
Al	$B_4C$	$AlB_2$ , $Al_4C_3$	Lucas <i>et al</i> (1992)
Al-Mg	$B_4C$	$AlB_2$ , $MgB_2$ , $Al_xMg_{(1-x)}B_2$ , $Al_4C_3$ , $Al_x(B-C-O)_{1-x}$ , $MgB_6$	Lucas <i>et al</i> (1992)
Al	TiC	$Al_4C_3$ , $Al_3Ti$	Yokokawa <i>et al</i> (1991); Satyaprasad <i>et al</i> (1992); Mitra <i>et al</i> (1993a)
Al	$TiB_2$	No reaction	Mitra <i>et al</i> (1993); Mitra (1993)
Al-Mg	$Al_2O_3$	$MgAl_2O_4$	Levi <i>et al</i> (1978)
Al-Cu	$Al_2O_3$	$CuAl_2O_4$	Sritharan <i>et al</i> (1990)
Al-Li	$Al_2O_3$	$\alpha$ - $LiAlO_2$ , $LiAl_5O_8$ , $Li_2O$	Chawla (1987); Sritharan <i>et al</i> (1990)
<i>Titanium</i>			
Ti	SiC	TiC, $Ti_5Si_3$ , $Ti_xSi_y$	Jones <i>et al</i> (1989); Reeves <i>et al</i> (1991)
Ti	TiC	$Ti_2C$	Konitzer and Loretto (1989a)
Ti-Al-V-Nb	TiC	$Ti_2(Al, Nb)C$	Konitzer and Loretto (1989b)
Ti	$TiB_2$	TiB	Reeves <i>et al</i> (1991)
<i>Magnesium</i>			
Mg	SiC	$Mg_2Si$ , C	Brown (1993)
Mg-Li	SiC	$Mg_2Si$ , $Li_2C_2$	Warwick and Clyne (1989)
Mg-Li	SiC with $SiO_2$ coating	$Mg_2Si$ , $Li_2O$	Warwick and Clyne (1989)
Mg	$Al_2O_3$	$MgAl_2O_4$	Chawla (1987)
<i>Intermetallics</i>			
NiAl	SiC	$Ni_xSi_y$ , $Al_4C_3$	Chawla (1987)
NiAl	$TiB_2$	No reaction	Wang and Arsenault (1991)
NiAl	TiC	No reaction	Fuchs (1990)
Ni-Al-Cr-Zr-B	$TiB_2$	$(Ti, Zr)B_2$	Fuchs (1990)
$Al_3Ti$	TiC	No reaction	Norman (1990)
$TiAl/Ti_3Al$	$TiB_2$	No reaction	Feng <i>et al</i> (1991)
$MoSi_2$	SiC	No reaction	Meschter and Schwartz (1989)
$MoSi_2$	TiC	No reaction	Meschter and Schwartz (1989)
$MoSi_2$	$Al_2O_3$	$SiO(g)$ , Al(g)	Meschter and Schwartz (1989)
$Ti_5Si_3$	SiC	TiSi, TiC	Meschter and Schwartz (1989)

3% Si, which raises significantly the activity of Si in Al, completely stops the reaction (Sritharan *et al* 1990)



from progressing in the forward direction according to the law of mass action.

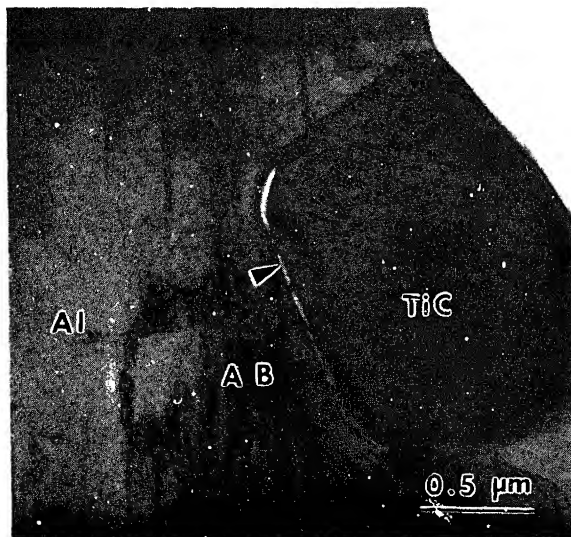


Figure 2. TEM micrograph showing interfacial cracking due to cold rolling of XD Al/TiC composite heat-treated for 24 h at 640°C. Heat treatment leads to formation of reaction product  $\text{Al}_3\text{Ti}$  (A) and  $\text{Al}_4\text{C}_3$  (B) at interfaces (Mitra *et al* 1993a).

#### 4. Type of reinforcement and electronic bonding

Even if the reinforcement is chemically compatible with the matrix, the strength and nature of the electronic interaction between matrix and reinforcement and structure and chemistry of interface are important for efficient load transfer. Thus it has been observed that for similar process variables, and in the absence of any chemical reaction product at the interface, the increase in Young's modulus by incorporation of the reinforcement in a metallic matrix provides a measure of the interfacial bond integrity between the matrix and the reinforcement. Two ways of averaging have been proposed: (i) Voight (1928) assumes uniform strain in both the constituent phases and (ii) Reuss (1929) assumes uniform stress in both the phases. The Voight averaging, also known as "rule of mixtures" (ROM) leads to

$$E_v = V_m E_m + V_p E_p, \quad (1)$$

where  $E_c$ ,  $E_m$  and  $E_p$  are Young's modulus values of the composite, matrix and reinforcement particles respectively and  $V_m$  and  $V_p$  are volume fractions of matrix and reinforcement phases.

The Ruess averaging gives

$$E_r = 1 / \{ (V_m / E_m) + (V_p / E_p) \}. \quad (2)$$

Figure 3 consists of bar diagrams for pure Al matrix P/M composites with 20 vol% SiC, TiC,  $\text{TiB}_2$  and  $\text{B}_4\text{C}$  particulate reinforcements showing the ratios of experimental Young's modulus (Kuruvilla *et al* 1989; Mahajan and Rama Rao 1992) values to those predicted by the rule of mixtures. TEM study did not reveal the presence of any reaction products at the matrix/reinforcement interface in these composites in the hot

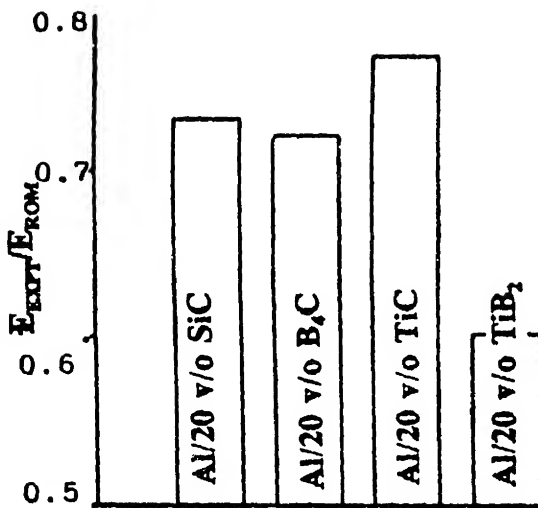


Figure 3.  $E(\text{expt})/E(\text{ROM})$  for Al matrix composites with different reinforcements (Kuruvilla *et al* 1989). Al/TiC shows the highest ratio.

rolled condition (Kuruvilla *et al* 1989). The process details have been published elsewhere (Kuruvilla *et al* 1989; Jain *et al* 1993). It is clear from figure 3 that Al/TiC shows the best correlation between theoretical and experimental values and Al/TiB<sub>2</sub> composite shows the worst, suggesting that the former has the strongest interfacial bond and the latter has the weakest among the four systems studied. In another investigation with P/M Al–Ti alloy containing Al<sub>3</sub>Ti, Al<sub>4</sub>C<sub>3</sub> and Al<sub>2</sub>O<sub>3</sub> as dispersoids (Hawk *et al* 1988), only changes in the volume fraction of the intermetallic compound Al<sub>3</sub>Ti could be correlated with change in Young's modulus, whereas those of Al<sub>4</sub>C<sub>3</sub> and Al<sub>2</sub>O<sub>3</sub> had a negligible effect. It is also interesting to note that rule of mixtures (Voigt law of averaging) was closely followed. Observations of Zedalias *et al* (1985) with Al<sub>3</sub>Zr dispersoids and Skinner (1988) with Al<sub>13</sub>(FeV)<sub>3</sub>Si dispersoids in pure Al also show excellent correlation between experimental values of Young's modulus and those predicted by rule of mixtures in the case of intermetallic dispersoids. Fine (1981) has shown that changes in Young's modulus values with volume fraction of MnAl<sub>6</sub> and Al<sub>2</sub>O<sub>3</sub> dispersoids in pure Al follow the Voigt and Ruess laws of averaging, respectively. A well-bonded interface would allow the maximum transfer of load from the matrix to the reinforcement and is expected to exhibit a high value of  $E(\text{expt})/E(\text{ROM})$  ratio, whereas a weakly bonded interface will result in lower  $E(\text{expt})/E(\text{ROM})$  ratio. In the case of the latter, values predicted by Ruess law of averaging will be closer to experimental values. Figure 4 shows bar diagrams of  $E(\text{expt})/E(\text{ROM})$  for four systems, namely Al/Al<sub>3</sub>Zr (Zedalias *et al* 1985), Cu/Fe (Krock 1966), Al/SiC (Bonollo *et al* 1991) and Al/Al<sub>2</sub>O<sub>3</sub> (Lyle 1967). It is seen that metal–intermetallic and metal–metal systems show  $E(\text{expt})/E(\text{ROM})$  values close to 1. Also,  $E(\text{expt})/E(\text{ROM})$  for Al/TiC was higher than those of Al/SiC, Al/TiB<sub>2</sub> and Al/B<sub>4</sub>C (figure 3). In case of TiC and intermetallic compounds as dispersoids, it is obvious that the matrix–reinforcement bond is stronger. Of course, the bonds between Al and the intermetallic compounds are metallic. At a metal–ceramic interface, there is a sharp discontinuity in the electronic structure due to delocalized nature of



## CHEMICAL NATURE OF DISPERSOID

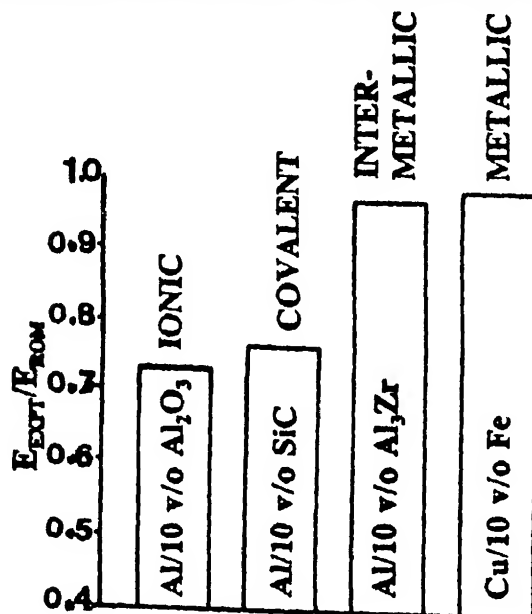


Figure 4.  $E(\text{expt})/E(\text{ROM})$  for Cu/Fe (Krock 1966), Al/ $\text{Al}_3\text{Zr}$  (Zedalia *et al* 1985), Al/SiC (Bonollo *et al* 1991) and Al/ $\text{Al}_2\text{O}_3$  (Lyle 1967) systems.

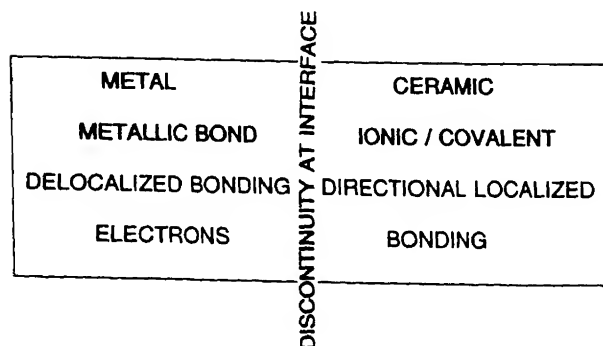


Figure 5. Schematic representation of discontinuity in the electronic structure at a metal-ceramic interface.

electrons in the metal and highly localized electrons in the covalently or ionically bonded ceramic reinforcement. Figure 5 shows a schematic diagram. This affects the wetting behaviour, and degree of interaction at the interface increases with lowering of this discontinuity. This agrees well with observations of Nicholas (1987), in which the degree of wetting of carbides and oxides by Cu decreased with increase in ionicity. Thus a weakly ionic or covalent ceramic will have a stronger bond with a metal compared to those which are strongly ionic or covalent. In metal-ceramic bonding, transition metal carbides like TiC which have partial metallic nature (Rhee 1970) thus

show stronger bond with Al, a reactive metal, than more covalent bonded ceramics (Delannay *et al* 1987) like  $\text{TiB}_2$  (table 2). Rhee (1970) observed that wetting increased in the order  $\text{AlN} < \text{TiB}_2 < \text{TiN} < \text{TiC}$ , and suggested the metallic character of TiC to be the reason for excellent wetting characteristics. Goretzki *et al* (1971) suggested a higher degree of overlapping of the electronic state wave functions in cases where both the components are metallic. For metal-like transition carbides, the density of states and work of adhesion vary with valence electron concentration in the same manner.

Comparing TiC and  $\text{TiB}_2$ , it is also clear that the latter has a higher heat of formation and is more stable. It has also been reported by Ramqvist (1965) that carbides with lower heat of formation are wetted better by metals than those with higher heat of formation. Also, from table 1, it is clear that TiC reacts with Al under certain conditions, whereas  $\text{TiB}_2$  does not. Thus higher stability of  $\text{TiB}_2$  in Al compared to that of TiC is another reason why the latter is wetted better.

Ni-16Al-8Cr-1Zr-0.1B matrix with TiC,  $\text{Al}_2\text{O}_3$  and  $\text{TiB}_2$  reinforcement prepared by P/M route has also been investigated (Fuchs 1990). While  $\text{TiB}_2$  was not chemically compatible with the matrix, both TiC and  $\text{Al}_2\text{O}_3$  were stable in the matrix. Interestingly, reinforcing with TiC has shown excellent bond integrity leading to much higher modulus and yield strength compared to those with  $\text{Al}_2\text{O}_3$ . This again can be explained by the metallic nature of TiC and strong interaction of Ti with both Ni and Al.

The above observations can be better appreciated with an understanding of wetting mechanisms. Wetting defines the extent of interaction between a liquid and a solid during fabrication of a composite and determines the bond strength. The mechanisms include, other than chemical reaction, Van der Waals and image forces, adsorption and electronic bonding (Oh *et al* 1989). It makes sense to believe that the adhesive force between a reactive metal and a reinforcement is dependent on the electronic properties of the latter, as the former will always have free electrons in the conduction band. Thus a ceramic reinforcement with more metallic nature is wetted better than those which are more covalent or ionic. Thus TiC and  $\text{Al}_3\text{Ti}$  act as effective nucleants during solidification of Al as has been reported by Cisse *et al* (1972). The fact that Al solidified with an epitaxial orientation relationship with respect to Al, that is,  $(001)\text{Al} // (001)\text{TiC}$  and  $[001]\text{Al} // [001]\text{TiC}$ , of course suggests that under equilibrium conditions interfaces of low energy form between Al and TiC. A similar phenomenon was observed for  $\text{Al}_3\text{Ti}$  too, and it has been seen from the data reported earlier that bond integrity between Al and these reinforcements are excellent. Thus good wetting

**Table 2.** A comparison of bonding, reactivity with Al and wetting characteristics of TiC and  $\text{TiB}_2$ .

Compound	$H_f$ (kJ/mol)	% Covalent bond	Reactivity with reaction $G_r$ product (kJ)	Contact angle with Al(l) at 1080 K (cos $\theta$ )

of TiC by Al occurs as has been reported in the literature (Samsonov *et al* 1968; Manning and Gurganus 1969; Rhee 1970).

Chemistry and crystallography of surfaces, which play a significant role in determining electronic density of states of surface atoms, also affect the wetting behaviour. For example, photoemission spectra from TiC  $\{111\}$  surfaces have shown high density of states near the Fermi level similar to Ti  $\{0001\}$  surfaces (Bradshaw *et al* 1980) and hence their behaviour with respect to wetting by Al is similar. An interesting observation in XD Al/TiC composite was that the interface plane of TiC was mostly  $\{111\}$  (figure 6) (Mitra *et al* 1993b). Besides its metallic nature which improves bonding, these planes are densely packed and result in maximization of number of bonds with matrix and lowering the interfacial energy. Similar observations were also made by Gao and Merkle (1992) for equilibrium and nonequilibrium metal-metal oxide interfaces.

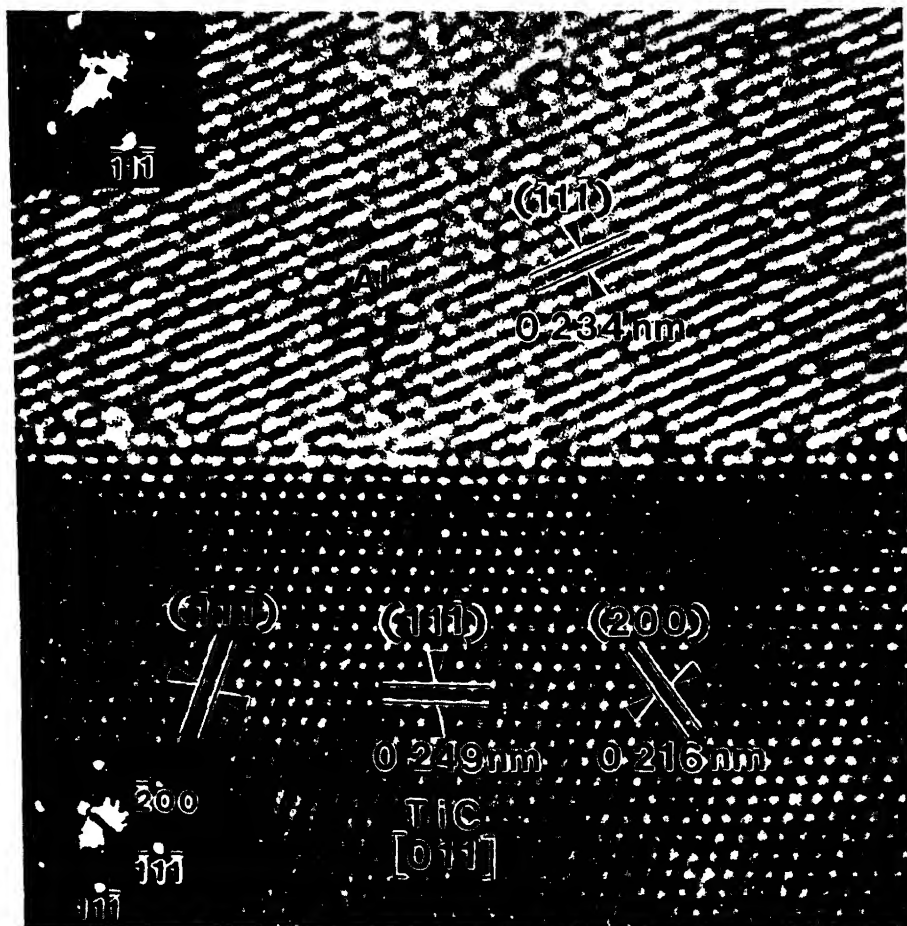


Figure 6. High-resolution TEM micrograph showing the particle/matrix interface in Al/TiC composite prepared by XD process. The interface is abrupt on an atomic scale and is parallel to TiC(111) plane, which is densely packed (Mitra *et al* 1993b).

In another experiment, Ohuchi (1987) observed that Cu adhered more strongly to AlN {0001} surfaces compared to AlN {1012} or AlN {1011} surfaces. The reason for this was the fact that Cu bonds to Al atoms during interaction and hence AlN {0001} surfaces containing only Al atoms were more favourable.

The differences in dielectric constants of the metal and the ceramic reinforcements (mainly oxide and carbide) also play a leading role in chemical bonding as this gives rise to image forces at the interface (Stoneham and Tasker 1985; Finnis *et al* 1990). The effect is strengthened if there are charged defects on the surfaces of the ceramic as these will have lower energy of formation at the interface than at a free surface. Thus an oxide or carbide which tends to lose stoichiometry more easily or have lower binding energy will be wetted better compared to one that is more stable. In a study of wetting characteristics of MgO single crystal by Pb, Sn and Bi liquid metals by Nogi *et al* (1992), it was observed that degree of polarization, type of charge distribution and atomic arrangements on the surface controlled the degree of wetting by the liquid metal.

TiC also is an excellent example. Atom fraction of carbon in TiC varies from 33% to 48% without any change in its crystal structure (Goretzki 1967). Nicholas (1987) has reported the wetting behaviour of TiC by Cu for different atom fractions of C in TiC, and the contact angle decreased with decrease in atom fraction of C, proving the better wettability of nonstoichiometric carbides. Stacking faults and dislocations have been seen close to Al–TiC interface using high-resolution transmission electron microscopy (HRTEM), and figure 7 shows an example. The fact that charged defects at the surface of ceramic reinforcement improves wetting suggests that irradiation of ceramic substrates or fibres will lead to better bonding with metal and this has been observed by Tombrello (1984). Fuchs *et al* (1989) observed significant improvement in Cu–Al<sub>2</sub>O<sub>3</sub> bonding due to ion-beam mixing of interface. After irradiation with 1.5 MeV Xe<sup>+</sup> ions of an Al<sub>2</sub>O<sub>3</sub> substrate, the surface roughness increased and the 6-nm-thick interface region was modified.

## 5. Work of adhesion and bonding: Effect of alloying elements and coherency

Work of adhesion  $W_{ad}$  of a particle–matrix interface is strongly affected by alloying element additions. Work of adhesion is defined as the energy of creation of free surfaces of particle and matrix by rupturing of the interfacial bond. Work of adhesion for solid/solid interface is given by

$$W_{ad} = \tau_{mv} + \tau_{pv} - \tau_{mp}, \quad (3)$$

where  $\tau_{mv}$  and  $\tau_{pv}$  are the surface energies of matrix and particle and  $\tau_{mp}$  is the particle–matrix interfacial energy. Figure 8 is a schematic diagram of a void formed at a particle–matrix interface. The void is created during deformation, and annealing treatment is conducted to reach equilibrium. If  $\theta$  is the contact angle between a particle facet and a spherical cap-shaped void, the force equilibrium in the horizontal direction gives

$$\tau_{mp} = \tau_{mv} \cos \theta + \tau_{pv}. \quad (4)$$

This is Young's equation (1805). Substituting (4) in (3), we get

$$W_{ad} = \tau_{mv}(1 - \cos \theta). \quad (5)$$

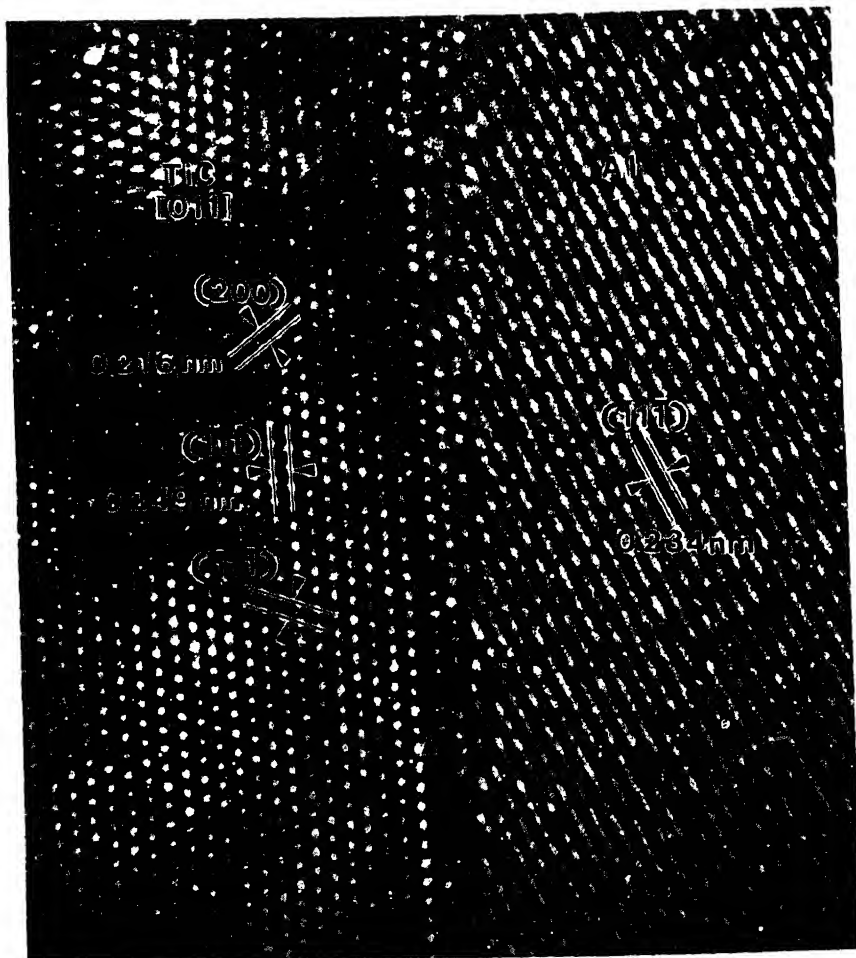


**Figure 7.** High-resolution TEM micrograph showing the particle/matrix interface in Al/TiC composite prepared by XD process. The first three atomic layers inside TiC near the interface appear distorted due to a stacking fault (arrowed) on the (111) TiC planes (shown with an arrow-head). Position of an extra half plane of an edge dislocation is shown with an arrow (Mitra *et al* 1993b).

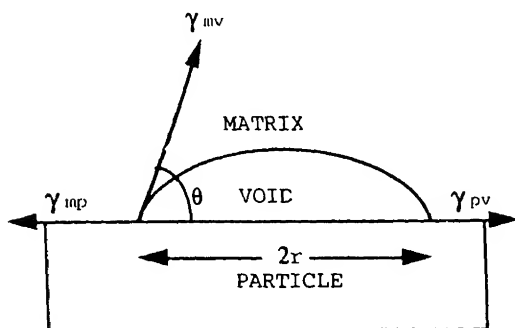


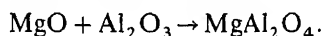
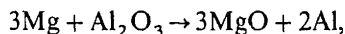
**Figure 8.** A spherical cap-shaped void formed at the interface a TiC particle facet and matrix (Mitra 1993).

Contact angle and interfacial energies were measured for XD Al/TiC composite from voids created by deformation followed by annealing at 500°C for 2 h. There was a variation in the interfacial energy from 200 to 850 mJ m<sup>-2</sup>. It is believed that for partially coherent interfaces, interfacial energy varies based on the orientation relationships and degree of coherency. Particles occurring at grain boundaries are expected to have much higher interfacial energies.

Easterling *et al* (1973) used (5) for determining the  $W_{ad}$  between the particle and the matrix in the Fe-Ni/Al<sub>2</sub>O<sub>3</sub> composite. Contact angle was seen to change very sharply with changes in atomic fraction of alloying elements in the matrix and so did the work of adhesion as shown in table 3. It was also observed that the flow stress was directly related to the work of adhesion.

Segregation of alloying elements to the interface reduces interfacial energy due to the Gibbs adsorption phenomenon. However, this may be detrimental to interface toughness if the alloying elements lead to an increase in the ionic or covalent character of the interface bonding (Fine *et al* 1988). Alloying elements play a significant role in coarsening behaviour of precipitates in metal-intermetallic composites (Calderon *et al* 1988). For example, in Fe-Ni-Al alloys containing a few per cent of Mo, the NiAl particles remain spherical upon ageing even though the particle-matrix lattice misfit is considerable. This is in contrast to that in absence of Mo, when the precipitates turn cuboidal. It has been suggested that Mo segregation at the interface relaxes the elastic misfit strains or changes the interfacial energy such that even large precipitates remain spherical.

Nature of the chemical bond also depends on alloying elements. For example, addition of Mg to Al-Al<sub>2</sub>O<sub>3</sub> composites leads to the formation of MgO and MgAl<sub>2</sub>O<sub>4</sub> at the interface (Levi *et al* 1978; Chawla 1987; Sritharan *et al* 1990) and this enhances the wettability which is otherwise poor. The reactions are:



Mg also improves the wetting between Al and SiC particles by reducing the SiO<sub>2</sub> layer on the surface of SiC and aiding in removal of Al<sub>2</sub>O<sub>3</sub> film on Al melt. The reaction is (Quigley *et al* 1982):

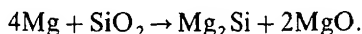


**Table 3.** Table showing variation in critical strain to interface cavity formation, contact angle and work of adhesion with alloying elements in a Fe-alloy/Al<sub>2</sub>O<sub>3</sub> composite (Easterling *et al* 1973).

Matrix	$\epsilon_c$	$\theta$ (degrees)	$W$ (mJm <sup>-2</sup> )
Fe-40 Ni	0.05	< 10	44
Fe-40 Ni-5 Cr	0.05	16	112
Fe-40 Ni-5 Mn	0.10	15	99
Fe-40 Ni-5 Mo	0.15	65	1674
Fe-1 Ti		35	524
Fe-10 Co	0.08	60	1450
Fe-5 Cr	0.10	80	2397

It has been reported by Sritharan *et al* (1990) that ideal matrices for SiC reinforcement, which show the maximum strengthening effect, are high Mg-containing 5XXX and 6XXX alloys as more of  $\text{Mg}_2\text{Si}$  can be precipitated. On the other hand, reduction in strength has been reported in case of Al–Cu–Mg alloys (with respect to monolithic alloy) as Mg segregation at interfaces results in the depletion of Mg content in matrix. Similar lowering of strength is reported for 7XXX alloys as Mg content is depleted by formation of  $\text{MgZn}_2$  and  $\text{Mg}_2\text{Si}$  at the interfaces. In certain other studies, addition of Mg to Al–SiC composites has proved to be detrimental due to formation of Mg-rich amorphous region (Nutt and Carpenter 1985; Nutt 1986), or intermetallic precipitates like  $\text{CuMgAl}_2$  (Nutt and Carpenter 1985; Bhanuprasad 1991) at the interface. In cast alloy–matrix MMCs, coarse intermetallic particles are quite often seen at the interfaces because the residual melt enriched in solute solidifies near poor heat-conducting ceramic reinforcement.

Other than Mg, Li has been successfully used as an alloying element to enhance wetting between Al and  $\text{Al}_2\text{O}_3$  (Dhingra 1980) and SiC (Webster 1982) reinforcements. The mechanism is similar to that of Mg, that is reduction of oxide layers at the interface, which otherwise prevents direct contact between Al and the ceramic reinforcement. Webster (1982) has systematically investigated the effect of Li addition (3–5%) to Al on mechanical properties of Al/SiC<sub>w</sub> composites. Strengthening effect was significantly enhanced by additions of Li as shown in table 4 and this has been attributed to increase in the matrix–reinforcement bond strength. Li increases reactivity of Al and as a consequence promotes its interaction with SiC at the interface. Thus Young's modulus values were close to those predicted by the rule of mixtures. No chemical reaction product could be observed at the interface using TEM. Alloying with indium, lead and thallium has improved wetting between Al and carbon fibres by reducing the surface tension of liquid metal (Kimura *et al* 1990). However, to our knowledge these have not been studied for Al/SiC composites. McDonald and Ransley (1954) observed that addition of Ni or Co to Al improved wettability of Al/TiC system.

Effect of matrix on bond integrity can also be appreciated by analysing the modulus values of Mg/SiC and Al/SiC metal matrix composites. Figure 9 is a comparison between  $E(\text{expt})/E(\text{ROM})$  of P/M Mg/SiC (Skinner *et al* 1990) and that of P/M Al/SiC, where the matrices are commercially pure metals. It is evident that Mg/SiC composite has smaller value of the ratio compared to the Al/SiC composite, indicating that the interfacial bond is stronger in the latter. The possible reason for this is that matrix–reinforcement chemical interaction is stronger in the latter as Al forms a stable carbide as well as alloys with Si.

**Table 4.** Variation in Young's modulus with addition of Li to Al/SiC<sub>w</sub> composites based on Webster's data (Webster 1982).

Matrix	Modulus (GPa)	% Increase with respect to matrix
Al	70	
6061 – Al + 20% SiC <sub>w</sub>	100	43.0
Al + 3.5% Li	86	
Al + 3.5% Li + 20.9 SiC <sub>w</sub>	139	62.0

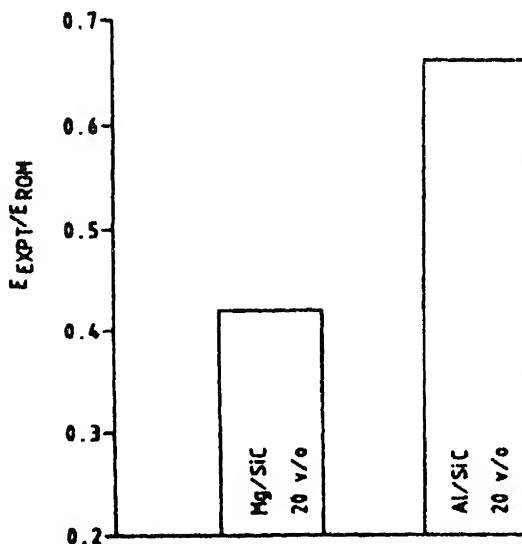


Figure 9. Comparison between  $E(\text{expt})/E(\text{ROM})$  ratios of Mg/20 v/o SiC and Al/20 v/o SiC (Schroder *et al* 1991) metal matrix composites.

## 6. Effect of processing: Conventional and *in situ* processing

Processing variables play a very significant role in control of interfacial characteristics. Based on processing, composites can be classified as 'conventional' or '*in situ*'. 'Conventional' composites are those which are prepared by powder metallurgy routes, which involves blending of matrix and reinforcement powders followed by cold compaction and hot pressing or casting routes. The flowchart in figure 10 shows the process developed and followed at DMRL. Hot pressing is carried out in two steps, the first being above solidus and for a short duration and the next for longer time below the solidus. Without a liquid phase formed during hot pressing or sintering, high modulus values are not achievable (McDonald and Ransley 1954). The mechanisms of bonding in absence of a liquid phase are mechanical interlocking of particles and solid-state diffusion leading to a chemical bond.

In casting route, conventional composites are fabricated by adding reinforcements to molten metal and distributing using a stirrer, or rheocasting or melt infiltration to ceramic preform or green compact by liquid metal. Higher processing temperature may promote wetting in many cases, but often leads to degradation of reinforcements by chemical reactions as is observed in Al-SiC system. Chiou and Chung (1990) prepared Al/SiC composite by infiltration of liquid Al into a porous preform of SiC whiskers in vacuum under inert gas pressure at 665°C, 690°C and 720°C and observed that tensile strength, Young's modulus, as well as the extent of elongation decreased with increase in processing temperature. Also, significant whisker pullout could be observed during tensile failure of the composites prepared at higher temperature. All this is attributed to formation of brittle reaction product  $\text{Al}_4\text{C}_3$  formed at the interface.

Sometimes processing in certain temperature ranges can only lead to chemical reactions between matrix and reinforcement. For example, Al and TiC react as



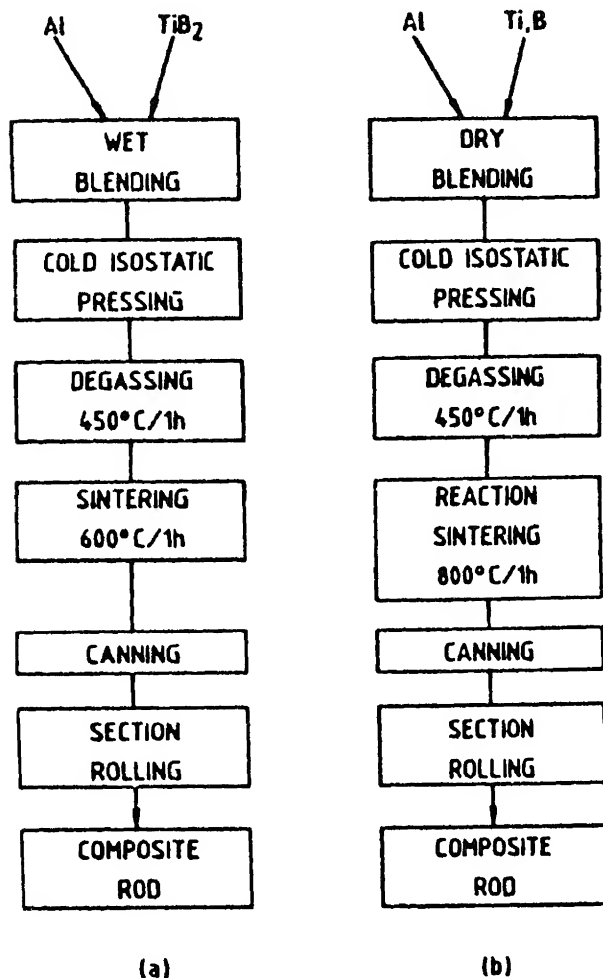
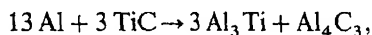


Figure 10. Flowchart showing conventional P/M and XD process developed at DMRL for preparing metal matrix composites.

(Satyaprasad *et al* 1992; Mitra *et al* 1992a, 1993a)



at temperatures below 752°C, above which the free energy of formation is positive and the chemical reaction is not feasible. Extent of chemical reaction also varies with time and a systematic study has been performed for Al–TiC (Mitra *et al* 1992b, 1993a) and Al–SiC (Lloyd and Jin 1988).

It has been discussed in the earlier section that coarse intermetallic particles precipitate at the matrix–reinforcement interface in MMCs prepared by casting as the solute-rich residual melt solidifies at the interface towards the end. However, in MMCs prepared by spray deposition (White *et al* 1983) TEM investigations have shown clean interfaces with negligible precipitation. This can obviously be explained

on the basis of the fact that contact time between liquid matrix phase and reinforcement is of the order of a few seconds in spray deposition processing and a few minutes in case of squeeze casting. Thus in Al-alloy composites prepared by spray deposition an attractive combination of strength and modulus could be achieved because of excellent bond integrity.

In the above processing techniques, reinforcement particles or whiskers are prepared in a separate process before processing of the composites. During this or subsequent handling, the surfaces of the particles pick up impurities or get oxidized, and continue as a third continuous or discontinuous phase at the interface. XPS studies on isolated  $\text{Si}_3\text{N}_4$  whiskers have shown  $\text{Si}_2\text{N}_2\text{O}$  and oxygen impurities (Homeny *et al* 1990).  $\text{SiO}_2$  has also been observed on the SiC whisker surfaces using XPS (Date 1994). These oxide layers participate in interfacial reactions during processing of MMCs and interface chemistry becomes complex. The interface in these cases fails to reach the state of thermodynamic equilibrium. Amorphous oxide layers are often found at interfaces (Nutt and Carpenter 1985; Nutt 1986; Ning *et al* 1992) and are responsible for interfacial void formation or cracking during external loading at room and elevated temperatures (Marcus and Rabenberg 1987; Ribes *et al* 1990; Xia *et al* 1990).

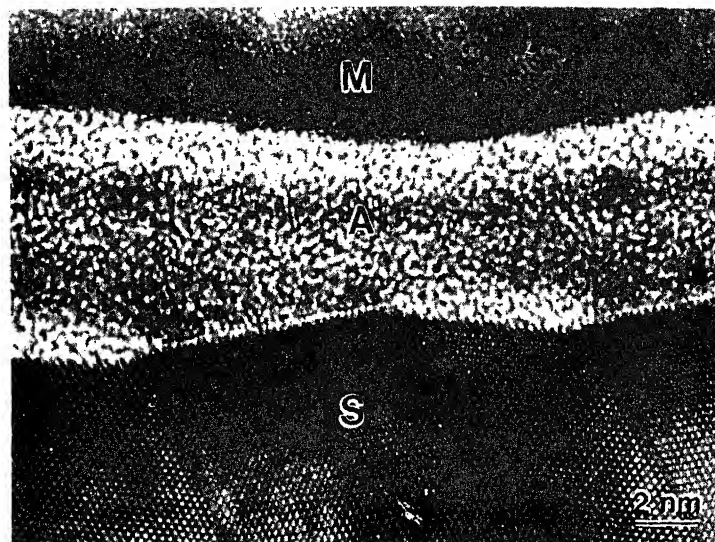
Amorphous phase (7–30 nm) has also been noticed at diffusion-bonded pure Al/SiC interface by Ratnaparkhi and Howe (1992). Auger studies have revealed that this region is enriched in Al, Si, C and O and there is diffusion of Al and O into the highly strained region of SiC, immediately adjacent to the interface. However, there is no evidence of C or Si diffusion into Al. This amorphous phase could have originated from solidification of Al–Si–C–O eutectic liquid at the interface. But *in situ* hot-stage microscopy, where specimen was reheated to 650°C, did not show any mechanical instability in the region, proving that a solid-state reaction was responsible for formation of amorphous region during processing.

Figure 11 shows a typical interface in  $\text{MoSi}_2/\text{SiC}$  composite containing an amorphous phase 5–8 nm thick. This composite was fabricated at DMRL, Hyderabad, by hot-pressing an intimate mixture of elemental Mo + Si (stoichiometric ratio) and SiC powders in vacuum, where Mo and Si react to form  $\text{MoSi}_2$  *in situ*. SiC was HF-treated to remove  $\text{SiO}_2$ . The composition of amorphous region is under investigation. Such amorphous regions at the matrix–reinforcement interfaces have also been noticed in KD  $\text{MoSi}_2/\text{SiC}$  composite (Suzuki *et al* 1993) as well as RBSC– $\text{MoSi}_2$  composites (Lim *et al* 1989).

In a recent review, Arsenault (1994) has reported the absence of orientation relationships in nonequilibrium interfaces or those with amorphous areas. This is common in composites fabricated by conventional P/M processes. For example, Radmilovic *et al* (1991) did not observe any preferred orientation relationship in 2014 Al/SiC composites fabricated by conventional P/M process. This is similar to the observations of Van Den Burg and De Hosson (1992). However in case of P/M 6061 Al/SiC composites, Van Den Burg and De Hosson noticed a preferred orientation relationship of  $(0001)_{\text{SiC}}//\{111\}_{\text{Al}}$  and  $\langle 2\bar{1}10 \rangle_{\text{SiC}}//\langle 110 \rangle_{\text{Al}}$ . In cast composites, a consistent orientation relationship could be seen (Arsenault 1994; Weimin *et al* 1991):

$$[11\bar{2}0]_{\text{SiC}}//[110]_{\text{Al}} \text{ and } (0001)_{\text{SiC}}//(\bar{1}12)_{\text{Al}}.$$

A variant relationship  $[11\bar{2}0]_{\text{SiC}}//[110]_{\text{Al}}, (01\bar{1}0)_{\text{SiC}}//(\bar{1}11)_{\text{Al}}$  has also been observed. In all cases (Arsenault 1994), (111) Al planes are aligned either perpendicular or at 70° to



**Figure 11.** An amorphous phase (A) observed at the interface between MoSi<sub>2</sub> (M) and SiC (S) in the MoSi<sub>2</sub>/20 v/o SiC composite (Mitra *et al* 1995).

the interfacial axis when the SiC basal planes are perpendicular to the interfacial axis. If SiC basal planes are parallel to the interfacial axis, the (111) Al planes are oriented at 20° to the interface. Again in contrast to observations in P/M 2014 Al/SiC composites, Carim could observe an orientation relationship of  $(1\bar{1}01)_{\text{SiC}}//(\bar{5}57)_{\text{Al}}$  in cast 2014 Al/SiC composites. In P/M processes, without a liquid phase, the particles bond together are randomly oriented leading to nonequilibrium and high-energy interfaces. In cast composites, there is a tendency for the liquid metal to solidify forming low-energy interfaces. This explains further the need for liquid phase in P/M processing, such as hot pressing.

Back in 1954, McDonald and Ransley (1954) through a series of investigations found that incorporation of high-modulus dispersoids in Al matrices resulted in modulus higher than that of the matrix by itself. It was obvious that increase of dispersoid content would affect the modulus. On the other hand, wetting took place automatically if the high-modulus phase was an 'intermetallic compound precipitated *in situ* by reaction between elements' and the same was difficult to induce by mechanical mixing of powders and purely solid-state processing. This is because the composites prepared by *in situ* processing have clean interfaces as the chemical reaction between elements to produce the dispersoid takes place inside the solid or liquid metal. Some of the *in situ* processing techniques involving molten metal and developed in recent years are hot-chamber casting (exothermic, dispersoid) developed at Martin Marietta Laboratory, Baltimore, USA (Westwood 1988) and gas injection process developed by Koczak at Drexel University, Philadelphia, USA (Koczak and Kumar 1989). Similarly, solid-state processing techniques like internal oxidation or reduction (Mader 1992) and displacement reactions (Henager *et al* 1992) have also been developed. Solid-state *in situ* processing normally lead to second-phase precipitates with an equilibrium low-energy orientation relationship with respect to the matrix and interfaces can show varying degrees of

coherency based on lattice misfit and strength of interaction between the matrix and the reinforcement (Mader 1992).

Atomic-resolution TEM studies of the interface between Al matrix and TiC particle in XD Al/TiC composite have proved that interface is abrupt on an atomic scale (figures 6 and 7) (Mitra *et al* 1993b). No impurities or sign of oxidation of particle surfaces could be seen by EDS and EELS at the interface. This is possible only because the particles were precipitated *in situ*, which prevents them from contamination.

EDS using a probe size of 3 nm (including effect of beam broadening) was used to investigate the interface in XD 2024 Al/TiB<sub>2</sub> composite in a field emission analytical TEM (Mitra *et al* 1993b). No segregation of Mg or Cu alloying elements could be found near the interface. This suggests that the interfaces formed are of sufficiently lower energy, and there is little driving force for interfacial segregation.

Apart from the fact that the interfaces are clean, some other interesting features are associated with the XD composites. Many of the Al/TiC interfaces in 0.7  $\mu\text{m}$  particle XD composite (cast and extruded at a ratio of 27:1 at 375°C) were semicoherent and showed localized strain contrast in the TEM (Mitra *et al* 1993b). Figure 12a is a bright-field TEM micrograph of a semicoherent Al/TiC interface, where interface dislocations and facets can be seen. Figure 12b is a weak-beam dark-field TEM image of an Al/TiC interface showing misfit strain localization. Normally, particles which were finer and located inside Al grains and surrounded by some Al subgrains had semicoherent interfaces. On cold rolling to 75% of its original thickness followed by annealing, the material recrystallized leading to a microstructure in which faces of the

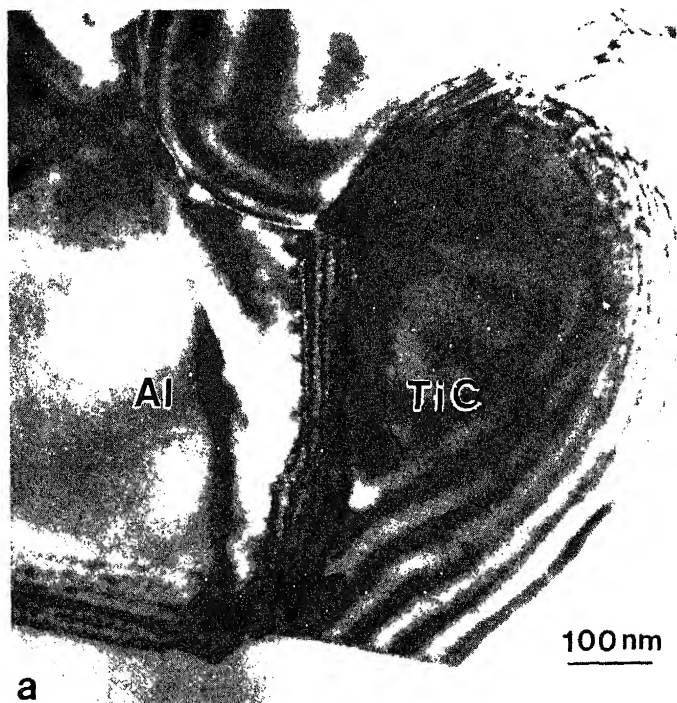


Figure 12a.

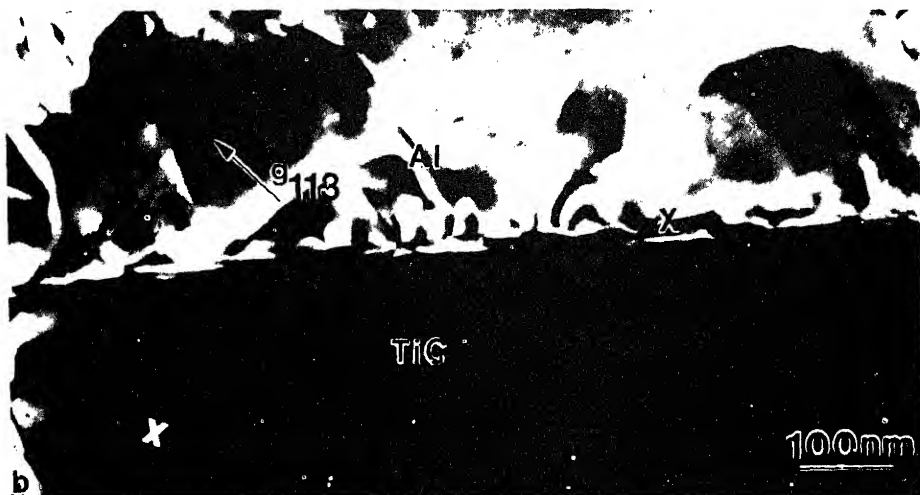


Figure 12. TEM micrographs of a semicoherent interface in cast and extruded XD Al/TiC composite (Mitra *et al* 1993b). (a) Bright-field image and (b) weak-beam dark-field image of a different particle/matrix interface 'X'. Misfit strain contrast can be distinguished.

TiC particles were surrounded by one or more subgrains (Mitra *et al* 1992a; Fine *et al* 1993). The interfaces between these and TiC particles were in most cases semicoherent with misfit strain localization (figure 13). As shown in figure 5, interfaces were always parallel to  $\{111\}$  TiC planes. In another investigation, Wang and Arsenault (1991) observed that the NiAl/ $\text{Al}_2\text{O}_3$  interfaces in XD NiAl/ $\text{Al}_2\text{O}_3$ /TiB<sub>2</sub> composites were semicoherent and showed misfit localization. Presence of semicoherency of course supports the idea that particle-matrix is strong in XD composites, where there is direct contact between the atoms of the two phases.

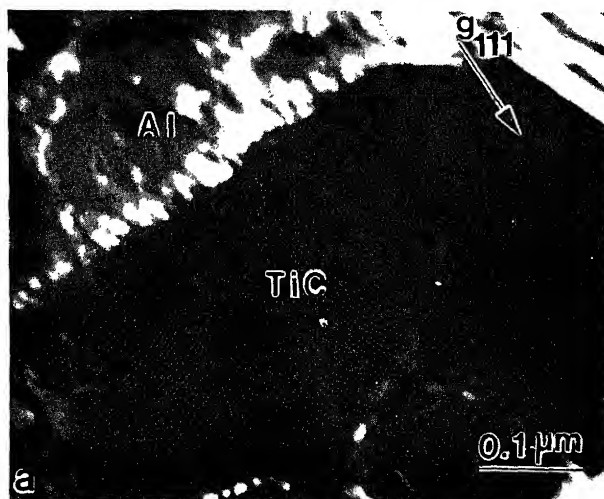
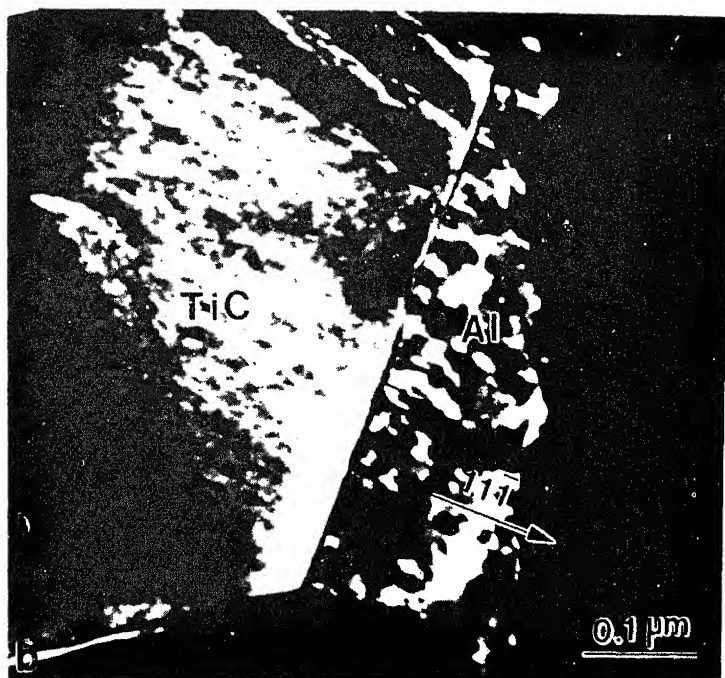


Figure 13a.



**Figure 13.** a-b. Dark-field TEM micrograph of a semicoherent interface between an Al subgrain and TiC particle in the XD Al/TiC composite. The composite was cold-rolled and annealed for recrystallization (Mitra 1993). Interface dislocations can be seen.

*In situ* composites have consistently shown higher modulus compared to those prepared by conventional techniques like casting and powder metallurgy (Westwood and Winzer 1987; Kuruvilla *et al* 1990). Young's modulus of Al/TiB<sub>2</sub> prepared by XD process at DMRL, Hyderabad (Kuruvilla *et al* 1990) is much higher as is clear from the bar chart for  $E(\text{expt})/E(\text{ROM})$  shown in figure 14. Young's modulus value of 15 vol% XD Al/TiC was found to be 94 GPa (Mitra *et al* 1993b), which is well within the lower and upper limits provided by Hashin–Shtrikman model (Hashin and Shtrikman 1963). Similar observations were made by Aikin for 15 vol% XD Al/TiB<sub>2</sub> (Aikin 1989). A significant improvement in Young's modulus over the monolithic metal or alloy is achievable mainly because of excellent chemical bond between atoms of metal and the reinforcement which are again in direct contact as has been seen in XD Al/TiC.

## 7. Effect of ageing and heat treatment

Ageing heat treatments in 7XXX and 2XXX Al–SiC composites, particularly the former, significantly alter the structure and chemistry of the interface (Manoharan and Lewandowski 1989). Interfacial segregation of Cu, Mg or Zn could be seen in both underaged as well as overaged conditions. In underaged 2XXX matrix composite, the region of segregation was in the form of a diffuse layer 20 nm into the matrix from the interface. The profiles of Mg and Cu were fairly broad and peaked away from the

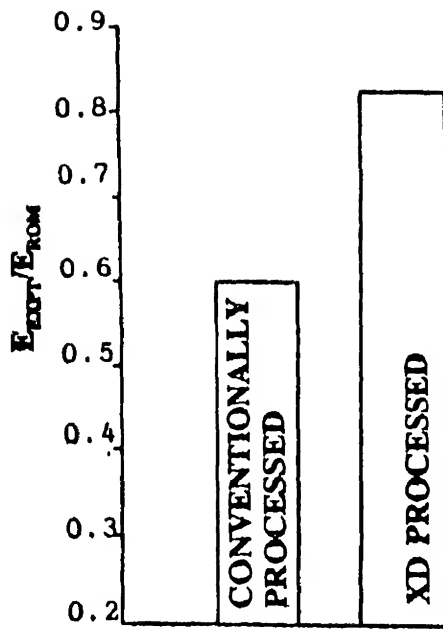


**Figure 14.** Comparison of  $E(\text{expt})/E(\text{ROM})$  ratios of Al/TiB<sub>2</sub> composites prepared by conventional P/M and XD process (Kuruville *et al* 1990). It is clear that the latter has higher modulus.

**Table 5.** Effect of isothermal annealing treatment (600°C) on tensile ductility of Al matrix composites.

Material	Time exposure (hours)	% Elongation	
		Initial	After exposure
Al/20 v/o B <sub>4</sub> C*	48	9.0	2.5
Al/20 v/o TiC*	96	6.8	0.8
Al/20 v/o SiC**	96	10.0	4.0
Al/20 v/o TiB <sub>2</sub> **	100	12.2	12.2

\*Vigorous reaction

\*\*No reaction

interface because of nonequilibrium segregation of vacancies. However, after over-aging, vacancies were segregated at the interface to meet the equilibrium conditions and the peak shifted to the interface. Similarly, a diffuse interface precipitate layer 10–20 nm wide was seen near the interface. On overaging, fairly regularly spaced particles Mg<sub>32</sub>(Al,Zn)<sub>49</sub> appeared with a distinct PFZ next to them extending 35–40 nm in the matrix, which is depleted in solute. In response to equilibrium vacancy segregation at the interface, there is a decrease in their concentration in the region where PFZ forms as solute atoms migrate by diffusion and segregate at the interface.

Recently, isothermal heat treatment of Al MMCs containing 20 vol% SiC, TiB<sub>2</sub>, B<sub>4</sub>C or TiC was performed at 600°C for different periods of time, and the results are shown in table 5 (Satyaprasad and Mahajan 1994). TiB<sub>2</sub> is thermodynamically stable

**Table 6.** Effect of heat treatment at 600°C for 96 h on properties of Al/SiC and Al/TiB<sub>2</sub> composites (Satyaprasad and Mahajan 1994).

Material	Young's modulus (GPa)		Yield strength (MPa)	
	Initial	Heat-treated	Initial	Heat-treated
Al/20 v/o SiC	97.5	100	115	190
Al/20 v/o TiB <sub>2</sub>			105	121

in Al at 600°C and obviously the elongation properties are not affected. TiC and B<sub>4</sub>C react extensively with Al resulting in reaction products at the interface (Al<sub>3</sub>Ti and Al<sub>4</sub>C<sub>3</sub> in case of TiC and Al<sub>4</sub>C<sub>3</sub> and AlB in case of B<sub>4</sub>C), which adversely affects tensile ductility. Al/SiC composite also shows lower elongation after heat treating and this is surprising as no reaction product could be seen at the interface using conventional TEM. However, some discontinuous precipitates of MgO and MgAl<sub>2</sub>O<sub>4</sub> could be seen, which possibly originated from Mg impurities in the matrix. Al SiC also showed some changes in Young's modulus and a significant change in yield strength after heat treating as shown in table 6. This suggests strengthening of the interfacial bond during heat treatment. It appears that at a temperature of 600°C (0.94  $T_m$ ) where diffusivity of Al is large, rearrangement on an atomic scale is possible near the interface leading to a structure closer to equilibrium. Slight but quite noticeable increase could be seen in the yield strengths of the Al/TiB<sub>2</sub> composite also (table 6). A detailed investigation of the interface is necessary to explain this. Recently, Warner and Stobbs (1989) noticed an increase in elastic modulus in Al-1.9% Mg 14 v/o SiC<sub>p</sub> composite on isothermal heat treatment, with the 0.2% yield stress remaining unchanged. Wu and Lavernia (1991) on the other hand, saw noticeable increase in yield and ultimate tensile strength of the MMCs prepared by spray deposition process on annealing at 560°C for 22 h prior to extrusion. It was observed that the failure mechanism involved fracture of SiC particles, rather than pull-out. This was explained based on the fact that annealing helped in improving the bond strength between matrix and reinforcement. Interdiffusion between Al and SiC was suggested as the reason for increase in bond strength. This was noticed earlier by Arsenault (1984).

## 8. Influence of the interface on physical properties

Interfaces play a significant role in determination of the physical and mechanical properties of the composite. The physical properties include coefficient of thermal expansion, thermal conductivity and damping.

Coefficient of thermal expansion is an important criterion for the design of dimensionally stable composites. Recently, the coefficients of thermal expansion were measured for 15 vol% XD Al/TiC composite with 0.7 or 4.0 µm particle size and it was observed that the former had smaller coefficient of thermal expansion (Xu *et al* 1994). The matrix being pure Al in either situation, it is surely due to more interface area in smaller-particle-size composite. The lattice distortion observed close to the matrix reinforcement interfaces in XD Al/TiC (Mitra *et al* 1993b) has been suggested to alter the behaviour of the interface with respect to thermal expansion. The coefficient of



thermal expansion of the composite  $\alpha_c$  can be expressed as

$$\alpha_c = \alpha_p V_p + \alpha_m V_m + \alpha_i V_i, \quad (6)$$

where  $\alpha_p$ ,  $\alpha_m$  and  $\alpha_i$  are coefficients of thermal expansion of particle, matrix and interfaces respectively, and  $V_p$ ,  $V_m$  and  $V_i$  are volume fractions of particle, matrix and interfaces.  $\alpha_i$  can be determined indirectly by using (6) for curve-fitting with the experimental data.

Hasselman and Donaldson (1992) reported thermal conductivity in Al/SiC metal matrix composites for particle sizes varying between 0.7 and 28  $\mu\text{m}$ . It was observed that thermal conductivity decreased with smaller particle size. This phenomenon can again be explained based on the fact that finer-particle-size composite has larger interface area. The interface acts as a thermal barrier. Thus for maximizing thermal conductivity, particle size needed is the largest possible as this will reduce the total interface area. Geiger *et al* (1993) observed that 6090 Al/SiC composites with 10.2 and 28  $\mu\text{m}$  particles had higher thermal conductivity than that of the unreinforced matrix. This was possible probably due to excellent bonding. However, with decrease in SiC particle size, thermal conductivity of the composite fell. Geiger and Jackson (1989) have also reported that 6061 Al/SiC shows higher thermal conductivity than 2124 Al/SiC. Besides the interface, the temper of the matrix alloy also affects the thermal conductivity and thus the above is difficult to explain.

Interfaces with reaction products or precipitates are likely to act as stronger barriers to heat conductivity than cleaner ones. This was investigated in detail by Reeves *et al* (1987) for the case of Ti/SiC composites, where the reaction products were a mixture of TiC and  $\text{Ti}_3\text{Si}_3$ . For a reaction layer of 0.5  $\mu\text{m}$  or thinner, the thermal conductivity of the composite was similar to that of the unreinforced matrix. This could be due to the fact that SiC particles possessed lower thermal conductivity than typical dense bulk SiC or because of the barrier created by the reaction layer. If the reaction layer was relatively thick (greater than 1  $\mu\text{m}$ ), thermal conductivity values of the composite were markedly reduced. The values were below those expected for composites reinforced with similar volume fractions of insulating particles.

To estimate the role of the interface, Hasselman and Johnson (1987) proposed a model for composite conductivity,  $K_c$ . This includes the interfacial heat transfer coefficient or thermal conductance,  $h$  ( $\text{Wm}^{-2}\text{K}^{-1}$ ).

$$K_c = K_M \frac{2f(K_I/K_M - K_I/rh - 1) + K_I/K_M + 2(K_I/rh) + 2}{f(1 - K_I/K_M + K_I/rh) + K_I/K_M + 2(K_I/rh) + 2}, \quad (7)$$

where  $f$  is the volume fraction of inclusions;  $C$ ,  $M$  and  $I$  refer to composite, matrix and inclusion respectively; and  $r$  is the radius of the inclusions assumed to be spherical. This equation is valid only for 'dilute' composites, in which disturbance to the thermal field around an inclusion does not overlap with the disturbance from surrounding inclusions.

The effect of reinforcement/matrix interface on the damping behaviour of the composites has been investigated by Zhang *et al* (1993). Schoek theory which was proposed to explain the phenomenon of internal friction in alloys has been used to

internal friction was found to be proportional to the volume fraction of reinforcement in the composite. In the MMCs, not only is the interface area large, but also CTE mismatch between particulates and matrix result in stress concentration at the incoherent interfaces, which increases the internal friction. At higher temperatures, when the matrix softens relative to the hard reinforcement, a reversible movement of vibrations is expected to occur at the interface and this can be used to explain increase in interface damping with temperature. In 2519 Al MMCs, the largest role of interface could be seen at temperatures between 250°C and 350°C.

## 9. Effect on yield strength and elongation

We have earlier discussed the effect of brittle reaction products at the interface on the load transfer efficiency of the interface which is adversely affected. Similarly, coarse intermetallic precipitates at the Al-Cu-Mg alloy/SiC interfaces are detrimental to all mechanical properties. The feedback from the above reports is that a clean interface is always desirable.

Even if there are no reaction products at the interface and the matrix, particle sizes and shapes are the same, the yield strength, modulus and tensile ductility vary based on the nature of chemical bond. This is evident from the data shown in table 7 for mechanical properties of pure Al and Al/SiC, Al/B<sub>4</sub>C, Al/TiC and Al/TiB<sub>2</sub> composites prepared by P/M process at DMRL.

It is obvious that the highest increase in yield and ultimate tensile strength is observed for Al/TiC. Improvement in strength is through load transfer at the interface as well as dislocation-particle and dislocation-dislocation interactions. Of course, the excellent bond integrity of Al/TiC interface explains why Al/TiC composite has the highest increase in yield and ultimate tensile strength.

The resistance of the interface to cracking even at high strains in the surrounding matrix is also essential for a significant role in load transfer. A brittle interface will crack at lower strains leading to little load transfer. In table 7, Al/TiC composite also shows maximum strain to fracture. Remarkable elongation of 20% or more has been seen in 15 vol% XD Al/TiC at room temperature, partly as the particles were equiaxed and also because interfacial bonding was excellent (Mitra 1993). Even after cold rolling to 75% reduction, cracks could be seen at only a few interfaces, where particles formed clusters. This is unlike the situation seen in many other interfaces like Al/Al<sub>2</sub>O<sub>3</sub> (Ruedl 1969) and Cu/SiO<sub>2</sub> and Cu/Al<sub>2</sub>O<sub>3</sub> (Humphreys and Stewart 1972). The regions around the interface are highly misoriented with respect to surrounding

**Table 7.** Tensile properties of some P/M as-extruded aluminium matrix composites (Kuruvilla *et al* 1989).

Composite	YS(MPa)	UTS(MPa)	Elongation (%)
Pure Al (P/M)	64	90	21
Al/20 v/o SiC	117	200	11.4
Al/20 v/o TiC	148	233	15.6
Al/20 v/o B <sub>4</sub> C	143	208	9.0
Al/20 v/o TiB <sub>2</sub>	121	166	14.8

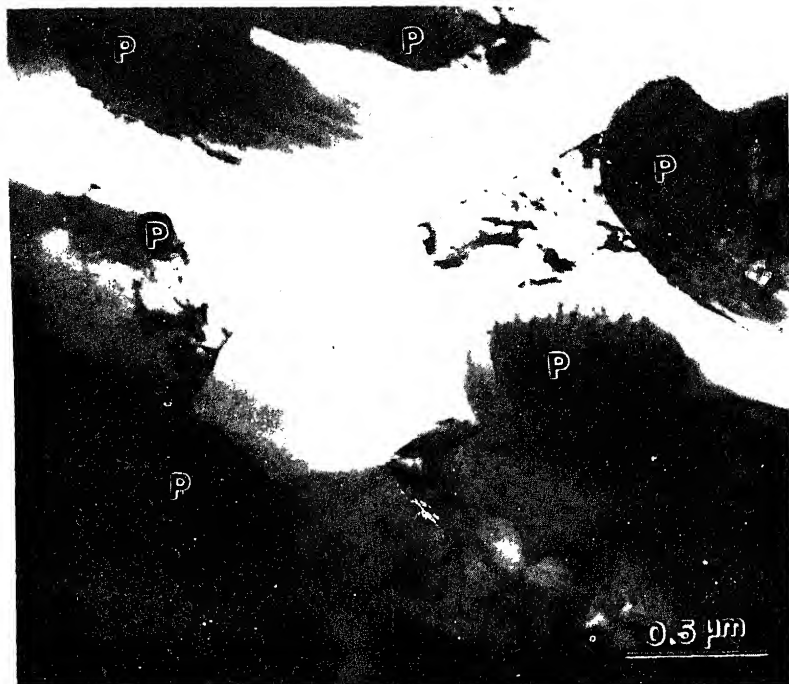


**Figure 15.** TEM micrograph of microstructure of XD Al/TiC composite after room-temperature tension test (area close to fracture surface). Regions around the particles are misoriented with respect to each other and hence the contrasts are different (Fine *et al* 1993).

regions resulting in local lattice rotation as shown in figure 15 (Fine *et al* 1993; Mitra 1993). The mechanism of local lattice rotation in dispersion-hardened alloys has been discussed by Ashby (1966) and Humphreys (1979). The high ductility of the Al/TiC interface can only be explained based on the metallic nature of bonding. In another investigation (Earvolino *et al* 1992), Al containing 15 vol% tetragonal  $\text{D0}_{23}$  structured  $\text{Al}_3\text{Zr}_{0.25}\text{Ti}_{0.75}$ , prepared by casting, was cold-rolled to 0.017% of the original thickness with a few intermediate anneals. While the intermetallic was fractured, the Al flow kept the interface intact and no cracks could be seen at Al-intermetallic interfaces. The Al/ $\text{Al}_2\text{O}_3$ , Cu/ $\text{SiO}_2$  and Cu/ $\text{Al}_2\text{O}_3$  interfaces, which are less ductile, will crack at smaller strains and not much local lattice rotation can take place as has been explained by Humphreys.

## 10. Effect on creep resistance

The creep threshold stress  $\sigma_0$  is the index of resistance to creep and for particle-reinforced composites this is given by

$$\sigma_0 = K \cdot (E_c/E_m)^m. \quad (\text{i})$$

$\sigma_0$  is independent of particle size and temperature, and increases with increase in the volume fraction of the reinforcement. The origin of  $\sigma_0$  is related to the load transfer at

the matrix–reinforcement interface, which of course depends on the interface bond integrity. This can be seen from table 8. The XD Al/TiB<sub>2</sub> composite has shown higher threshold stress compared to that prepared by conventional P/M process, which is due to stronger interface as well as finer particle size in the former. Al/SiC shows the highest creep threshold stress, as the matrix–reinforcement bonding is stronger than that in Al/TiB<sub>2</sub>, which is indicated by comparison of  $E(\text{expt})/E(\text{ROM})$  ratio (figure 3).

## 11. Interface engineering

It is well understood how important interfaces are in determining the performance of MMCs. We have seen how processing methods, ageing and heat treatments can affect the interfacial bond and properties. Hence there is a drive for developing the technology to tailor interfaces to achieve desired properties. Of course, processing methods and heat treatments can be devised and alloying elements can be added in order to modify interfaces. The other option is to treat the surfaces of the reinforcements, which play a crucial role in wetting. Some of the strategies to improve interfacial properties are outlined in table 9.

**Table 8.** Table reporting  $E(\text{expt})/E(\text{ROM})$  and  $\sigma_0$  values (Pandey 1993) for composites with different reinforcement and processing methods.

Material	$E(\text{expt})/E(\text{ROM})$	$\sigma_0$ (MPa)
PM Al/20 v/o SiC <sub>n</sub>	0.73	25.2
PM Al/20 v/o TiB <sub>2</sub>	0.60	14.3
XD Al/20 v/o TiB <sub>2</sub>	0.82	19.2

**Table 9.** Strategies to exploit full potential of metal matrix composites by tailoring interfaces.

Strategy	Example
1. Use of <i>in situ</i> processes	XD, reactive casting
2. Use of nonstoichiometric compounds as reinforcements	TiC <sub>1-x</sub> instead of TiC
3. Development and use of novel reinforcements with metallic bonding	Ti <sub>3</sub> Si <sub>3</sub> , TiSi <sub>2</sub> , Cr <sub>3</sub> C <sub>2</sub> , etc.
4. Novel techniques to modify reinforcement surfaces for improved bonding	Decarburization of TiC, Ion implantation, Irradiation
5. Matrix alloying for enhanced bonding	Addition of Ti, Cr, La, Ce, Li in Al/SiC system; Mg and Li to Al/Al <sub>2</sub> O <sub>3</sub> system
6. Development of innovative coating techniques for reinforcements	Sputtered coatings, duplex coatings, graded coatings, sol–gel coatings, <i>in situ</i> modification of coatings
7. Thermomechanical treatment	Deformation and recrystallization in XD Al/TiC composites led to higher degree of semicoherency at interfaces

Mcdonald and Ransley (1954) pretreated TiC particles by heating in moist hydrogen at 1000°C leading to removal of the oxide layer on the surface and partial decarburization of surfaces. This leaves a metallic Ti layer on the surface. It has already been discussed in an earlier section that TiC {111} surfaces ending with Ti have the same surface electronic structure as Ti {0001} and Ti sites on {100} surfaces are more active when these are carbon-deficient. Removal of oxide layer also probably resulted in establishment of direct contact and an equilibrium between the atoms of matrix and reinforcing phase and hence a strong chemical bond. Thus pretreatment with hydrogen resulted in significant increase in Young's modulus. This also proves once again our earlier proposition that metallic bonds result in a more efficient load transfer.

Another and quite popular surface modification method is coating with a third phase to improve wetting or prevent adverse chemical reaction. Coating material is normally wetted well by the Al matrix, such as Ni on TiC. TiB<sub>2</sub> coating applied by CVD, which is also an excellent wetting agent works on a different principle (Maruyama *et al* 1991). Bulk TiB<sub>2</sub> is not wetted as well by Al as CVD TiB<sub>2</sub> coating on SiC and C fibres is. It has been reported by Wu (1988) that CVD-deposited TiB<sub>2</sub> contains significant amounts of chlorine and wetting in C/Al system is related to the concentration of chlorine. Thus it was hypothesized that enhanced wetting action was due to the fluxing action of chlorine, which destabilized the surface aluminium oxide and allowed direct contact between liquid Al and the reinforcement.

Recently, Johnson and Sonup irlak (1993) investigated the effect of coating diamond particles (modulus = 1050 GPa) with SiC using chemical vapour infiltration. SiC not only helps in improving wettability, but retards formation of Al<sub>4</sub>C<sub>3</sub>, which is detrimental because of its tendency to corrode in moist environments. Also, Al<sub>4</sub>C<sub>3</sub> has poor thermal conductivity and it defeats the purpose of reinforcing with diamond for preparing composites having high thermal conductivity. The increase in SiC coating thickness of diamond reinforcements monotonously increases the thermal conductivity of the composites. It is visible that Young's modulus increases with increase in coating thickness; there is also an overall decrease in the coefficient of thermal expansion. These are due to changes in the interface bond due to coating as well as increase in volume fraction of SiC.

## 12. Conclusions

In this paper, we have analysed some of the existing information about interfaces in the composites of interest to understand their nature and relationship with mechanical properties. The variables controlling the characteristics of interfaces are quite large in number, such as processing (technique, temperature, etc.) as well as composition and chemical nature of matrix and reinforcement. Processing variables can be manipulated to enhance the wetting between matrix and reinforcement, like addition of alloying elements, pretreatment or coating of reinforcements, increase of temperature of molten metal, hot pressing the blended metal and ceramic powders above solidus temperature, etc. Ageing of the matrix with high solid solubility also affects the interface structure and chemistry.

The chemical bond at the interface can be through a chemical reaction or electronic. The former is detrimental as it leads to a brittle reaction product at the interface, whereas

the latter is desirable. For electronic bonding, intimate contact between the atoms of the matrix and of the ceramic phase is necessary and this is found more easily in the *in situ* composites. That is the reason some matrix-particle interfaces in XD composites are semicoherent and improvement in Young's modulus values are higher than those seen in composites prepared by conventional processes. Factors responsible for enhancement of interfacial bonding in metal/ceramic systems are: (i) presence of densely packed planes parallel to interface in either or both the reinforcement and the matrix phases, (ii) presence of charged defects close to interface, (c) substoichiometric composition of the reinforcement, and (d) lower heat of formation of the reinforcements.

Of a variety of reinforcements, the ones having metallic character form metallic bonds with the metal matrix. In such cases, the matrix-reinforcement interfacial bonding is stronger than in other metal-ceramic composites and this leads to a greater improvement in Young's modulus, yield and ultimate tensile strength values over those of the matrix material. Tensile ductility is also impressive in case of metallic bonding at interfaces as they can withstand higher strains. Although the incorporation of the reinforcements which give rise to metallic bonding at the interfaces results in superior properties compared to others, most of the potential ceramic reinforcements possess ionic or covalent bonding. Hence modification of interfaces is necessary to enhance the metallic character of the bond. Because of the critical role played by interfaces in the composites, it is necessary to plan the choice of matrix and reinforcement and processing conditions while keeping an eye on the nature of the interfaces expected.

## Acknowledgements

The authors gratefully acknowledge several useful discussions and research results from M/s V V Bhanuprasad, B V R Bhat, M K Jain, A B Pandey, V K Varma, Dr S V Kamat, K S Prasad and Dr A K Kuruvilla. One of the authors (RM) is thankful to Professor Morris E Fine and Professor Julia R Weertman for their guidance in successful completion of his PhD research at the Northwestern University, USA. Thanks are also due to Sri S L N Acharyulu, Director, Defence Metallurgical Research Laboratory, for his encouragement.

## References

- Aikin Jr R M 1989 NASA Contractor Report 4365, Contract NAS 1-18531
- Arsenault R J 1984 *Scr. Metall.* **18** 1131
- Arsenault R J 1994 *Composites* **27** 540
- Ashby M F 1966 *Philos. Mag.* **14** 1157
- Bhanuprasad V V, Prasad K S, Kuruvilla A K, Pandey A B, Bhat B V R and Mahajan Y R 1991 *J. Mater. Sci.* **26** 460
- Bonollo F, Guerriero R, Sentimenti E, Tangerini I and Jang L M 1991 *Advanced structural inorganic composites* (ed.) P Vincenzini (Amsterdam: Elsevier Science Publishers) p. 259
- Bradshaw A M, Van der Veen J F, Himpsel F J and Eastman D E 1980 *Solid State Commun.* **37** 37
- Brown N R 1993 *Effect of heat treatment on interfaces in magnesium metal matrix composites*, Ph D Dissertation, Northwestern University, Illinois, USA
- Calderon H A, Fine M E and Weertman J R 1988 *Metall. Trans.* **A19** 1135
- Carim A H 1991 *Mater. Lett.* **12** 153
- Chawla K K 1987 *Composite materials: Science and engineering* (New York: Springer Verlag) p. 83

- Chiou J -M and Chung D D L 1990 *Metal and ceramic matrix composites: Processing, modelling and mechanical behaviour* (eds) R B Bhagat, A H Clauer, P Kumar and A M Ritter (Warrendale, PA: TMS) p. 107
- Cisse J, Bolling G F and Keer H W 1972 *J. Cryst. Growth* **13/14** 771
- Clough R B, Biancianiello F S, Wadley H N G and Kattner U R 1990 *Metall. Trans.* **A21** 2747
- Date S K 1994 Private communication, NCL, Pune
- Delannay F, Froyen L and Deruyttere A 1987 *J. Mater. Sci.* **22** 1
- Dhingra A K 1980 *Philos. Trans. R. Soc.* **A294** 151
- Earvolino P A, Fine M E, Weertman J R and Parameswaran V R 1992 *Scr. Metall. Mater.* **26** 945
- Easterling K E, Fischmeister H F and Navara E 1973 *Powder Metall.* **16** 128
- Eid N M A and Thomason R F 1979 *Acta Metall.* **27** 1239
- Feng C R, Michael D J and Crowe C R 1991 *Mater. Sci. Eng.* **A145** 257
- Fine M E 1981 *Scr. Metall.* **15** 523
- Fine M E, Bourell D L, Eliezer Z, Persad C and Marcus H L 1988 *Scr. Metall.* **22** 907
- Fine M E, Mitra R and Weertman J R 1993 *Z. Metallkd.* **4** 282
- Finnis M W, Stoneham A M and Tasker P W 1990 *Metal-ceramic interfaces: Acta Scripta Metallurgica Proceedings Series* (eds) M Ruhle, A G Evans, M F Ashby and J P Hirth (New York: Pergamon Press) Vol. 4, p. 35
- Fuchs G E 1990 *Metal and ceramic matrix composites: Processing, modelling and mechanical behaviour* (eds) R B Bhagat, A H Clauer, P Kumar and A M Ritter (Warrendale, PA: TMS) p. 391
- Fuchs G E, Abonneau E, Treilleux M and Perez A 1989 *Mater. Sci. Eng.* **A109** 83
- Gao Y and Merkle K L 1992 *Structure and properties of interfaces in materials: MRS Symp. Proc.* (eds) W A T Clark, U Dahmen and C L Briant (Pittsburgh, PA: MRS) Vol. 238, p. 775
- Geiger A L, Hasselman D P H and Donaldson K Y 1993 *J. Mater. Sci. Lett.* **12** 420
- Geiger A L and Jackson M 1989 *Adv. Mater. Proc.* **7** 23
- Goretzki H 1967 *Phys. Status Solidi* **20** K141
- Goretzki H, Exner H E and Scheuermann W 1971 *Modern developments in powder metallurgy* (ed) H H Hausner **4** 327
- Hashin Z and Shtrikman S 1963 *J. Mech. Phys. Solids* **11** 127
- Hasselman D P H and Johnson L F 1987 *J. Compos. Mater.* **21** 508
- Hasselman D P H and Donaldson K Y 1992 *J. Am. Ceram. Soc.* **75** 3137
- Hawk J A, Mirchandani P K, Benn R C and Wilsdorf H G F 1988 *Dispersion strengthened aluminium alloys* (eds) Y -W Kim and W M Griffith (Warrendale, PA: TMS) p. 551
- Henager Jr C H, Brimhall J L and Hirth J P 1992 *Ceram. Sci. Eng. Proc.* **13** 596
- Henriksen B R and Gionnes J 1991 *Advanced structural inorganic composites* (ed.) P Vincenzini (Amsterdam: Elsevier Sci. Pub.) p. 251
- Homeny J, Neergard L J, Harasek K R, Donner J T and Bradley S A 1990 *J. Am. Ceram. Soc.* **73** 102
- Howe J M 1993 *Inter. Mater. Rev.* **38** 233
- Humphreys F J 1979 *Acta Metall.* **27** 1801
- Humphreys F J and Stewart A T 1972 *Surf. Sci.* **31** 389
- Iseki T, Kameda T and Maruyama T 1984 *J. Mater. Sci.* **19** 1692
- Jain M K, Bhanuprasad V V, Kamat S V, Pandey A B, Varma V K, Bhat B V R and Mahajan Y R 1993 *Int. J. Powder Metall.* **29** 267
- Johnson W B and Sonuparlak B 1993 *J. Mater. Res.* **8** 1169
- Jones C, Kiely C J and Wang S S 1989 *J. Mater. Res.* **4** 327
- Kimura Y, Mishima Y, Umekawa S and Suzuki I 1984 *J. Mater. Sci.* **19** 3107
- Kocak M J and Kumar K S 1989 U S Patent 4, 808, 372
- Konitzer D G and Loretto M H 1989a *Acta Metall.* **37** 397
- Konitzer D G and Loretto M H 1989b *Mater. Sci. Technol.* **5** 627
- Kuruville A K, Bhanuprasad V V, Prasad K S and Mahajan Y R 1989 *Bull. Mater. Sci.* **12** 495
- Kuruville A K, Prasad K S, Bhanuprasad V V and Mahajan Y R 1990 *Scr. Metall.* **24** 873
- Krock R H 1966 *Modern developments in powder metallurgy* (ed.) H H Hausner (New York: Plenum Press) p. 105
- Lagace H and Lloyds D J 1989 *Canadian Met. Quart.* **28** 145
- Lee D J, Vaudin M D, Handwerker C A and Kattner U A 1988 *Mater. Res. Soc. Symp. Proc.* **120** 357
- Levi C G, Abbaschian G J and Mehrabian R 1978 *Metall. Trans.* **A9** 697
- Lim C B, Yano T and Iseki T 1989 *J. Mater. Sci.* **24** 4144

- Lloyd D J and Jin I 1988 *Metall. Trans.* **A19** 3107
- Lucas J P, Yang N Y C and Stephens J J 1992 *Structure and properties of interfaces in materials* (Mater. Res. Soc. Symp. (eds) W A T Clark, U Dahmen and C L Briant (Pittsburgh, PA: MRS) Vol. 238, p. 377
- Lyle J P Jr 1967 *Aluminum* (ed.) K R Van Horn (Metals Park, OH: ASM) Vol. 1, Ch. 10, p. 337
- Mader W 1992 *Structure and properties of interfaces in solids* (MRS Symp. Proc. (eds) W A T Clark, U Dahmen and C L Briant (Pittsburgh, PA: MRS) p. 763
- Mahajan Y R and Rama Rao P 1992 *New materials* (eds) S K Joshi, C N R Rao, T Tsuruta and S Nagai (New Delhi: Narosa Pub. House) p. 322
- Manning C R and Gurganus T B 1969 *J. Am. Ceram. Soc.* **52** 115
- Manoharan M and Lewandowski J J 1989 *Scr. Metall.* **23** 301
- Marcus H L and Rabenberg L K 1987 ONR Contract N00014-84-K-0687, Technical Report 1 To MRS, p. 160
- Maruyama B, Barrera E V and Rabenberg L 1991 *Metal matrix composites: Processing and materials* (eds) R K Everett and R J Arsenault (San Diego, CA: Academic Press) p. 181
- McDonald N F and Ransley C E 1954 *Metal powder review: Symp. on powder metallurgy*, p. 242
- Meschter P J and Schwartz D S 1989 *JOM* **41** 52
- Mitra R 1993 *Microstructure and interfaces in XD Al/TiC metal matrix composites*, PhD Dissertation, Northwestern University, Illinois, USA
- Mitra R, Chiou W-A, Weertman J R, Fine M E and Aikin Jr R M 1992a *Structure and properties of interfaces in materials* (MRS Symp. Proc. (eds) W A T Clark, U Dahmen and C L Briant (Pittsburgh, PA: MRS) Vol. 238, p. 871
- Mitra R, Weertman J R, Fine M E and Aikin Jr R M 1992b *Developments in ceramic and metal matrix composites* (ed.) K Upadhy (Warrendale, PA: TMS) p. 125
- Mitra R, Fine M E and Weertman J R 1993a *J. Mater. Res.* **8** 2370
- Mitra R, Chiou W A, Fine M E and Weertman J R 1993b *J. Mater. Res.* **8** 2380
- Mitra R, Mahajan Y R, Prasad N E, Chiou W A and Ganguly C 1995 *Key engineering materials: Metal and ceramic matrix composites* (ed.) F H Wohlbiel (Switzerland: Trans Tech Publications)
- Nicholas M G 1987 *Fundamentals of diffusion bonding* (ed.) Y Ishida (New York: Elsevier) p. 25
- Ning X G, Pan J, Hu K Y and Ye H Q 1992 *Structure and properties of interfaces in solids* (eds) W A T Clark, U Dahmen and C L Briant (Pittsburgh, PA: MRS) Vol. 238, p. 865
- Nogi K, Tsujimoto M K, Ogino K and Iwamoto N 1992 *Acta Metall. Mater.* **40** 1045
- Norman J H, Reynolds G H and Brewer L 1990 *Mater. Res. Soc. Symp. Proc.* (Pittsburgh, PA: MRS) p. 369
- Nutt S R 1986 *Interfaces in metal matrix composites* (eds) A K Dhingra and S G Fishman (Warrendale, PA: TMS) p. 157
- Nutt S R and Carpenter R W 1985 *Mater. Sci. Eng.* **75** 169
- Oh S Y, Cornie J A and Russel K C 1989 *Metall. Trans.* **A20** 533
- Ohuchi F S 1987 *Interface science and engineering: J. Phys.* (eds) R Raj and S L Sass (New York: AIP) p. 783
- Pandey A B 1993 *Creep behaviour of particulate reinforced aluminium matrix composites*, PhD Dissertation, Banaras Hindu University, Varanasi
- Quigley B F, Abbaschian G J, Wunderlin R and Mehrabian R 1982 *Metall. Trans.* **A13** 93
- Rack H J 1988 *Dispersion strengthened aluminium alloys* (eds) Y-W Kim and W M Griffith (Warrendale, PA: TMS) p. 649
- Radmilovic V, Thomas G and Das S K 1991 *Mater. Sci. Eng.* **A132** 171
- Ramqvist J V 1965 *Int. J. Powder Metall.* **1** 2
- Ratnaparkhi P L and Howe J M 1992 *Scr. Metall. Mater.* **27** 133
- Reeves A J, Stobbs W M and Clyne T W 1987 *Metal matrix composites - Processing, microstructure and properties* (eds) N Hansen, D Juul Jensen, T Leffers, H Liholt, T Lorentzen, A S Pedersen, O B Pedersen and B Ralph (Roskilde, Denmark: Riso National Laboratory Press) p. 631
- Reeves A J, Taylor R and Clyne T W 1991 *Mater. Sci. Eng.* **A141** 129
- Reuss A 1929 *Z. Angew. Math. Mech.* **9** 55
- Rhee S K 1970 *J. Am. Ceram. Soc.* **53** 386
- Ribes H, Da Silva R, Suery M and Bretheau T 1990 *Mater. Sci. Tech.* **6** 621
- Ruedl F 1969 *J. Mater. Sci.* **4** 814



- Skinner D J 1988 *Dispersion strengthened aluminum alloys* (eds) Y -W Kim and W M Griffith (Warrendale, PA: TMS) p. 181
- Sritharan T, Xia K, Heathcock J and Mihelich J 1990 *Metal and ceramic matrix composites: Processing, modelling and mechanical behaviour* (eds) R B Bhagat, A H Clauer, P Kumar and A M Ritter (Warrendale, PA: TMS) p. 13
- Samsonov G V, Panasyuk A D and Kozina G K 1968 *Sov. Powder Metall. Met. Ceram.* **71** 874
- Schroder V, Kainer K U and Mordike B L 1989 *Developments in the science and technology of composite materials: Proc. of the third European conf. on composite materials, Bordeaux, France* (eds) A R Bunsell, P Lamicq and A Massiah (Amsterdam: Elsevier Applied Science) p. 221
- Schroder J, Kainer K U and Mordike B L 1991 *Proc. P/M 91: Int. conf. on P/M aerospace materials, Lausanne, Switzerland*
- Skinner D J, Zedalias M S, Frazier W E, Kockzak M J and Sahoo P 1990 *Metal and ceramic matrix composites: Processing, modelling and mechanical behaviour* (eds) R B Bhagat, A H Clauer, P Kumar and A M Ritter (Warrendale, PA: TMS) p. 535
- Stoneham A M and Tasker P W 1985 *J. Phys.* **C18** L543
- Sunwoo H, Fine M E, Meshi M and Stone D H 1982 *Metall. Trans.* **A13** 2035
- Suzuki M, Nutt S R and Aikin R M Jr 1993 *Mater. Sci. Eng.* **A162** 73
- Tombrello T A 1984 *Mater. Res. Soc. Symp. Proc.* **25**
- Van Den Burg M and De Hosson J Th M 1992 *Acta Metall. Mater.* **40** S281
- Voight W 1928 *Lehrbuch der Kristallphysik* (Leipzig: Teubner) p. 716
- Wang L and Arsenault R J 1991 *Metall. Trans.* **A22** 3013
- Warner T J and Stobbs W M 1989 *ICCM: Proc. 7th Int. conf. on comp. mater.* (eds) Wu Yunshu, Gu Zhenlong and Wu Renjie (New York: International Academic Press and Pergamon Press) Vol. 1, p. 503
- Warwick M and Clyne R T W 1989 *Developments in the science and technology of composite materials: Third European conf. on composite materials* (eds) A R Bunsell, P Lamicq and A Massiah (France: Elsevier Applied Science) p. 205
- Webster D 1982 *Metall. Trans.* **A13** 1511
- Weimin S, Pengxing L and Geyang L 1991 *Composites: Design, manufacturing and application, Proc. ICCM/VIII* (eds) S Tsai and G S Springer (Covina, CA: SAMPE) 19k3
- Westwood A R C 1988 *Metall. Trans.* **A19** 749
- Westwood A R C and Winzer S R 1987 *Advancing materials research* (eds) P A Paras and H D Langford (Washington, D.C.: Nat. Acad. Press) p. 225
- White J, Willis T C, Hughes I R and Jordan R M 1983 *Dispersion strengthened aluminium alloys* (eds) Y -W Kim and W M Griffith (Warrendale, PA: TMS) p. 693
- Wu R 1988 *Interfaces in polymer, ceramic and metal matrix composites* (ed.) H Ishida (New York: Elsevier) p. 43
- Wu Y and Lavernia E J 1991 *JOM* **43** 16
- Xia K, Nieh T G, Wadsworth J and Langdon T G 1990 *Fundamental relationships between microstructure and mechanical properties of metal-matrix composites* (eds) P K Liaw and M N Gungor (Warrendale, PA: TMS) p. 543
- Xu Z R, Chawla K K, Mitra R and Fine M E 1994 *Scr. Metall. Mater.* **31** 1525
- Yokokawa H, Sakai N, Kawada T and Dokiya M 1991 *Metall. Trans.* **A22** 3075
- Young T 1805 *Trans. R. Soc.* **94** 65
- Zedalias M S, Ghate M V and Fine M E 1985 *Scr. Metall.* **19** 647
- Zhang J, Perez R J, Gupta M and Lavernia E J 1993 *Scr. Metall.* **28** 91

## Crystal engineering of high- $T_c$ and related oxide films for future electronics

HIDEOMI KOINUMA

Center for Ceramics Research, Research Laboratory of Engineering Materials, Tokyo Institute of Technology, 4259 Nagatsuta, Midori-ku, Yokohama 226, Japan

**Abstract.** Advanced technology and future prospect of oxide-based electronic materials are described with a focus on the significance of atomically controlled epitaxy of high- $T_c$  superconductors and related oxide films. Problems in suitably forming the oxides whose power is potentially superior to silicon's are discussed to stimulate technology development for engineering oxide film growth on an atomic scale. Our experimental results on controlled epitaxial growth of oxide films are presented with respect to pulsed laser deposition of  $\text{YBa}_2\text{Cu}_3\text{O}_{7-\delta}$  films as well as laser MBE growth of  $\text{SrTiO}_3$  homoepitaxy and  $\text{CeO}_2$  heteroepitaxy on Si substrates.

**Keywords.** Crystal engineering; high- $T_c$  superconductor; oxide electronics; laser MBE; atomic layer epitaxy.

### 1. Introduction: New era of oxide research

Electronics is the driving force of civilization and innovation today and this situation is likely to continue in the 21st century. The most important material in current electronics is silicon, and this status of silicon is also likely to remain for centuries. Nevertheless, we are tempted from time to time to pose the question whether we will find or develop an electronics material superior to silicon.

Electronics application of oxide materials includes use as insulators, capacitors, piezo- and pyroelectric devices, solid ionics, varistors and transparent conductors, as well as magnets and optical devices. These oxides are used in both bulk form and as thin films mostly in polycrystalline phase. The so-called fine ceramics technology is based on the control of grain size in micrometre scale. With progress in microelectronics, much attention has been focussed on the fabrication of thin films, especially in high-quality single-crystal (epitaxial) phase. A current concern in the development of larger integrated silicon electronics is focussed on high-dielectric oxide films for capacitors and nonvolatile memories. In this respect, especially interesting is the heteroepitaxial growth of perovskite-type oxide films on silicon substrates. Extensive studies are being conducted for this purpose by using various methods such as vacuum evaporation, sputtering, chemical vapour deposition (CVD), sol-gel process, pulsed laser deposition, and molecular beam epitaxy (MBE). Films so far fabricated are, however, not so extraordinary, since they have crystal structures of known perovskite type or a slight modification and their properties are within our imagination.

In today's most advanced electronics research, much attention is paid to the fabrication of artificially designed structures to verify new device concepts based on quantum effects. As these are primarily important technology, intensive studies are performed on atomic-scale control and characterization of semiconductor thin films and heterostructures. In contrast, until recently we had neither a strong need for atomically engineered oxide films nor a theoretical background for predicting charac-

few people were interested in developing the technology of fabricating atomically regulated oxide films.

The discovery of high- $T_c$  oxide superconductors (Bednorz and Muller 1986) changed the situation. The high- $T_c$  superconductivity in layered cuprates was beyond our imagination and this surprising quantum effect suggested further potential of complex oxides in which electrons and spins are strongly correlated. As a systematic experimental approach to the exploration of potential and mystery of oxides, people started realizing the significance of atom technology of oxides (Koinuma and Yoshimoto 1994). This article is intended to stimulate and discuss the possibility of oxides as new innovative electronic materials with focus on the following features:

- (i) Intrinsic properties of oxides compared with silicon
- (ii) Crystal engineering of oxides for the fabrication of artificially designed crystal lattices and heterostructures including high- $T_c$  superconducting tunnel junction (Koinuma 1994)
- (iii) Combination with silicon electronics
- (iv) Exploration of novel functionalities in oxides.

## 2. Silicon versus oxides

Compound semiconductors were once considered good candidates to displace the position of silicon because of their compositional and functional versatilities. However, they are still far from replacing silicon in the electronics market. One of the main reasons is the lack of high-quality insulators that can be combined with them in device fabrication. From a materials science viewpoint, the great success of silicon electronics rests on relatively simple features: (i) the availability of large-size and defect-free single crystals, (ii) valence control by impurity doping, and (iii) the presence of high-quality  $\text{SiO}_2$  insulators. The third advantage of  $\text{SiO}_2$ , may no longer exist in further integrated silicon devices due to the low dielectric constant of  $\text{SiO}_2$  and the existence of defects at the interface between crystalline silicon and amorphous  $\text{SiO}_2$ .

Oxides have a far broader spectrum of structures and properties than does silicon. Oxides with similar crystal lattices may have insulating, semiconducting, metallic and

**Table 1.** Characteristics of silicon and oxides.

	Si/ $\text{SiO}_2$	Oxides
Components	SiO	Various metals, O
Intrinsic properties	Semiconductor (Si) Insulator ( $\text{SiO}_2$ )	Insulator; semiconductor; metal; superconductor; ferro-; piezo-; pyro-electricity; ferromagnetism; optical functions; nonlinearity in electric, magnetic and optical properties,...
Doping	Substitutional	Cation substitution Oxygen nonstoichiometry (chemical)
Crystal structure	Diamond (Si) Amorphous ( $\text{SiO}_2$ )	Versatile: rock salt, fluorite, zinc blende, spinel, perovskite, etc.

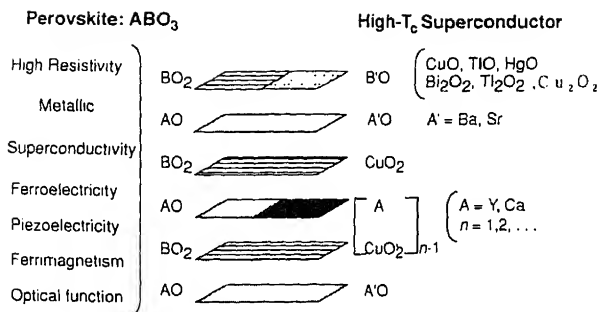


Figure 1. Unified layered lattice structure of perovskite-based functional oxides.

superconducting properties, as well as other functional properties, as summarized in table 1. Based on sophisticated crystal engineering techniques for oxides, it would be possible to fabricate all epitaxial hybrid devices and multiply stacked modules. Among a variety of oxides, special emphasis should be placed on perovskite oxides because this group of compounds represent functional ceramics and have good lattice matching among themselves as well as with silicon. Figure 1 represents the lattice structures of typical perovskite and high- $T_c$  superconductors. Although many new high- $T_c$  cuprate superconductors have been claimed to be discovered, their crystal lattices can be unified into a modified perovskite structure in which there is slight change in one or two atomic layers in the repeating unit. Hence, layered lattices related to high- $T_c$  cuprates could be reconstructed and/or modified if we establish the technology of assembling two-dimensional lattices of one to several atomic layers with designed compositions.

### 3. Crystal engineering of oxides: Why and how?

Ever since our first success in superconducting La-Sr-Cu-O film deposition in early 1987 (Koinuma *et al* 1987), extensive studies have been conducted on the fabrication of high- $T_c$  oxide films and devices. Success has been achieved to some extent in relatively simple devices using plain superconducting films or grain-boundary (Dimos *et al* 1988) and step-edge junctions (Daly *et al* 1991). Nobody, however, has succeeded in fabricating an SIS (superconductor-insulator-superconductor) tunnel junction that shows a clear hysteresis in  $I$ - $V$  characteristics at a temperature above 77 K. Such a junction is presumably the key to the wide electronic device application of high- $T_c$  superconductors, for example for switching devices expected to work much faster than conventional semiconductor transistors.

#### 3.1 Elementary processes for SIS tunnel junction

The difficulty in fabricating SIS tunnel junction originates, evidently, from the very short (3–20 Å) coherence lengths of high- $T_c$  superconductors. This necessitates not only high-quality but also atomic-scale engineering of both superconducting and insulating films. Such thin-film technology is almost established in semiconductors,

**Table 2.** Criteria of SIS device quality superconductor and insulator.*Superconductor*

1. *Bulk*  
Good electronic properties
2. *Surface*  
No deterioration in superconductivity  
Homogeneity in superconductivity  
Atomically flat  
*Particle free*

↓  
*Well equilibrated and  
relaxed lattice matrix*

*Insulator*

- Good insulator
- Surface flatness in atomic scale
- Perfect interface with YBCO
- Thickness control in atomic scale

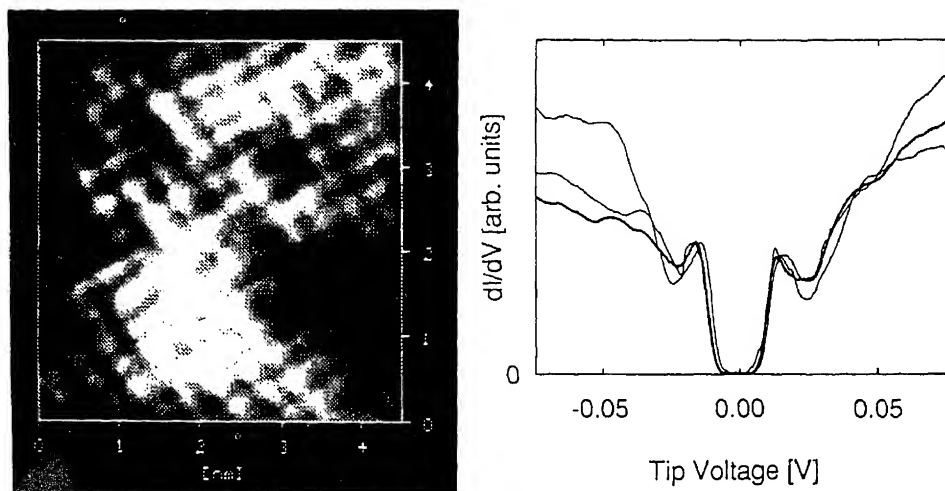


**Figure 2.** (Left) STM image of YBCO (001) surface taken at a constant current of 15 pA and a tip bias voltage of 500 mV. (Right) Tunnelling spectra taken at a set point current of 4 nA and a tip bias voltage of  $-100$  mV.

but similar methods cannot be simply applied to high- $T_c$  oxides due to some specific features originating from the ionic bond character, the multicomponent nature of the material, and mobile oxygen in the crystals. Other problems include the lack of high-quality single-crystal substrates and immaturity of supporting technologies such as substrate cleaning.

Problems to be solved for the fabrication of SIS tunnel junction (if possible) are listed in table 2. Most of these hurdles are presumed to have been overcome judging from the results we have accumulated. Some such results are exemplified in figures 2, 3, 5–7. Chemical stability and superconductivity even at the topmost surface were verified by the simultaneous observation of atomic image and superconducting

energy gap in the cryogenic STM/STS measurements on an air-exposed  $c$ -axis-oriented  $\text{YBa}_2\text{Cu}_3\text{O}_{7-\delta}$  (YBCO) film (figure 2) (Nantoh *et al* 1994). This highly crystalline and stable film was fabricated by pulsed KrF-excimer laser deposition under conditions optimized to give a well-relaxed (quasi-equilibrated) structure and a high oxygen content ( $0 < \delta < 0.1$ ). Although the  $c$ -axis-oriented YBCO films exhibit good superconductivity ( $T_c > 90\text{ K}$ ,  $J_c > 10^6\text{ A/cm}^2$  at  $77\text{ K}$ ), they have a very short coherence length ( $\sim 3\text{ \AA}$ ) and are apt to have a lot of precipitates on the surface especially in high-quality films (Gong *et al* 1994).  $a$ -Axis-oriented films have much less precipitates on the surface and a longer coherence length than  $c$ -oriented films, but instead they tend to have cracks and poor superconductivity. By controlling the deposition conditions and using an appropriate substrate, we could prepare high-quality  $a$ -oriented films with smooth surfaces and  $T_c$  exceeding  $85\text{ K}$  (figure 3) (Koinuma *et al* 1994).

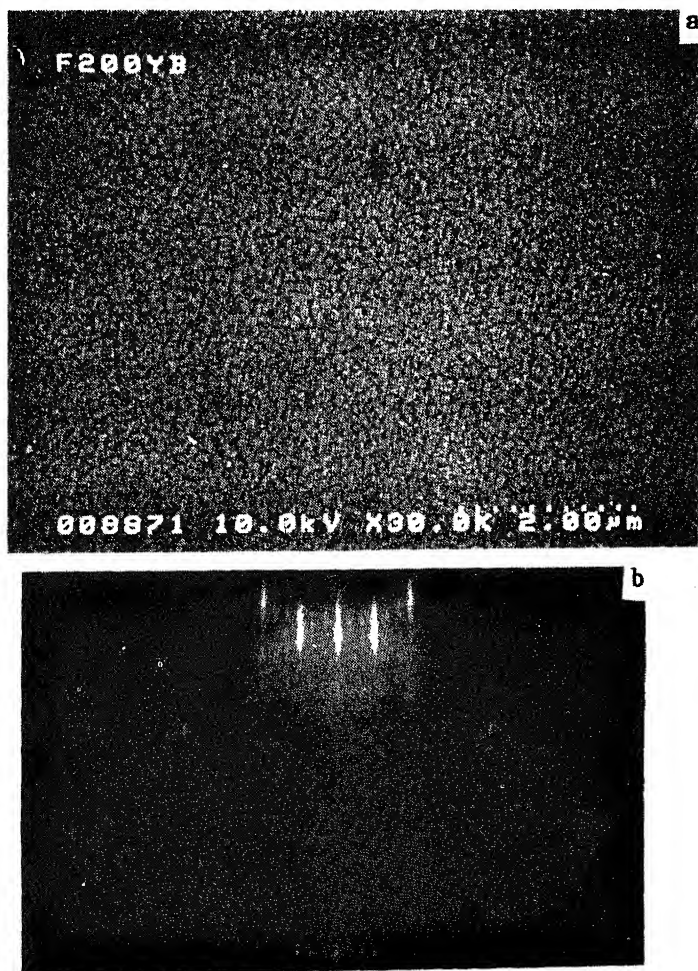


**Figure 3.** SEM (a) and RHEED (b) patterns of  $a$ -oriented YBCO film prepared by temperature gradient PLD (pulsed laser deposition) method.

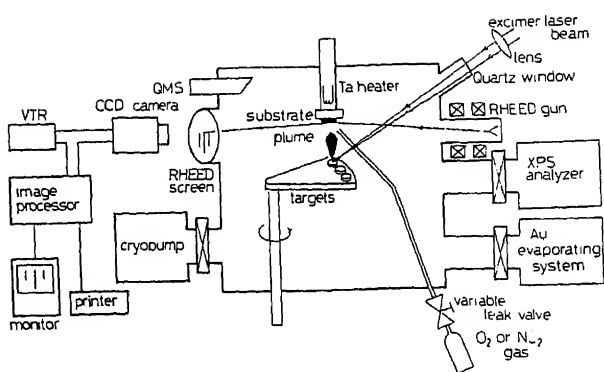


Figure 4. Laser MBE system equipped with *in situ* RHEED and XPS.

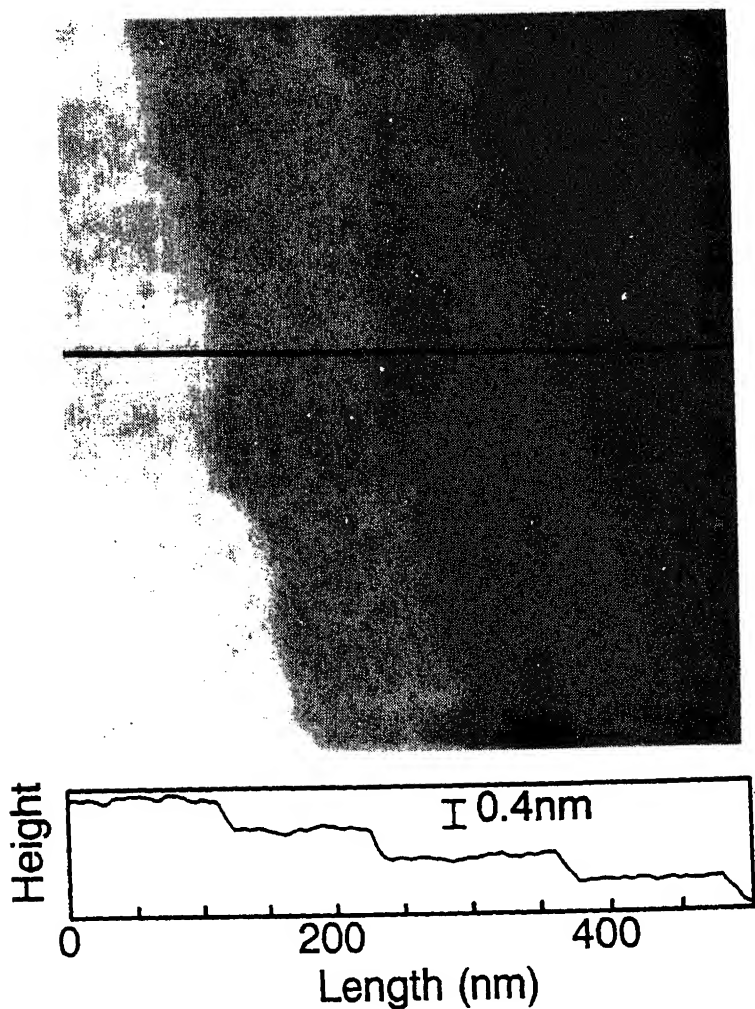
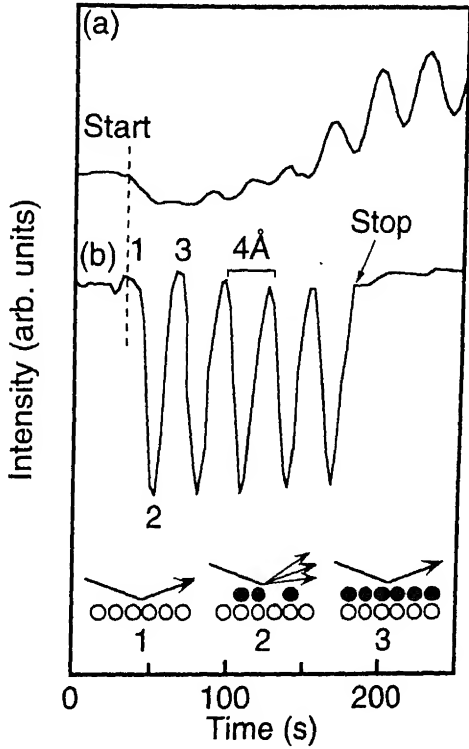
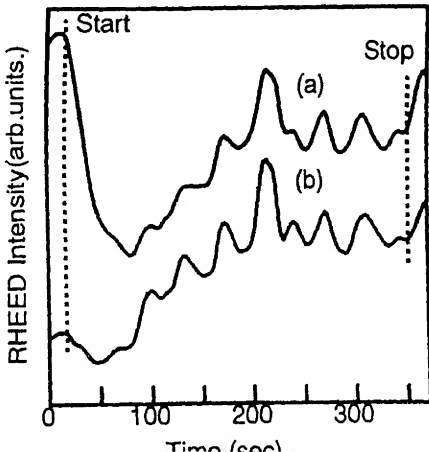


Figure 5. AFM image of BHF (NH<sub>4</sub>F-HF)-treated SrTiO<sub>3</sub> substrates. The vertical profile was taken along the line indicated in the image. The BHF-treated substrate exhibited atomically flat terraces and 0.4-nm-high steps.



**Figure 6.** The RHEED intensity variation during homoepitaxial growth of  $\text{SrTiO}_3$  by laser MBE (a) on the commercial  $\text{SrTiO}_3$  and (b) on the BHF-treated  $\text{SrTiO}_3$ .





In view of such a short coherence length even in *a*-oriented film, I (insulator) layer thickness must be regulated on an atomic scale. Elementary processes to fulfil this requirement are summarized in table 3, and can be achieved by the laser MBE (pulsed laser deposition in ultrahigh vacuum condition), which we employed for the first time for oxide film deposition (Yoshimoto *et al* 1990). The thermodynamical problem of oxidizing metal components in high vacuum can be overcome by the use of such a highly oxidizing agent as ozone or NO<sub>2</sub>. Homo- and some heteroepitaxial growth of oxides were performed by the laser MBE system illustrated in figure 4. In the system, a reflection high-energy electron diffraction (RHEED) apparatus, an X-ray photoelectron spectrometer (XPS), and a metal evaporator are installed for *in situ* measurements of growth process, composition and valence analyses of film, and electrode deposition without exposing the film in air, respectively.

RHEED intensity oscillation, which verifies atomically regulated layer-by-layer epitaxial growth, was confirmed for laser MBE growth of SrTiO<sub>3</sub> and so-called infinite layers of ACuO<sub>2</sub> (A = Ca, Sr, Ba, or mixtures) on SrTiO<sub>3</sub> substrates as well as for CeO<sub>2</sub> growth on Si(111) substrate. The oscillations, however, were not so sharp and damped gradually when the films were grown on the substrates supplied commercially and treated with the conventional cleaning procedures. Then we developed new surface treatment procedures to make single-crystal SrTiO<sub>3</sub> and sapphire surfaces composed of atomically smooth terraces and steps of one or two atomic layers in height. Figure 5 shows the atomic force microscopy (AFM) image of SrTiO<sub>3</sub> surface defined atomically by a wet cleaning treatment. The use of this substrate enabled us to observe the RHEED intensity oscillation as perfect as those in matured MBE growth of semiconductors during homoepitaxial laser MBE growth of SrTiO<sub>3</sub> (see figure 6) (Kawasaki *et al* 1994). The oscillation periodicity corresponds well with one unit cell growth (3.9 Å). Oscillation was also observed as shown in figure 7, although not so perfect as in figure 6, during the laser MBE growth of SrTiO<sub>3</sub> on *a*-oriented YBCO film. Thus, we can regulate SrTiO<sub>3</sub> layer thickness digitally by counting the oscillation peaks and use this technology for the formation of SIS junction.

### 3.2 Approach to new materials and phenomena

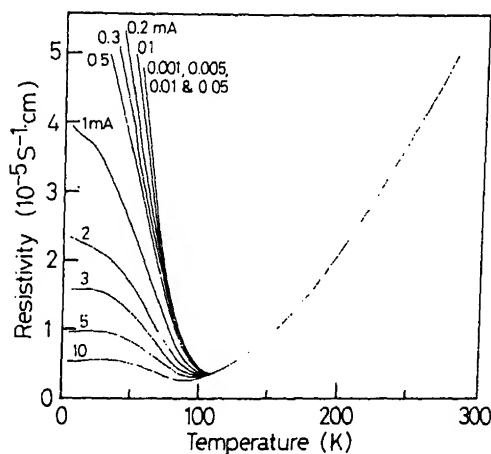
High-*T<sub>c</sub>* oxides have a tendency of increasing *T<sub>c</sub>* with increase in the number of CuO<sub>2</sub> plane in a layered perovskite unit cell structure, represented in figure 1. Thus the atomically controlled epitaxy of oxides is also promising for the exploration of new

**Table 3.** Elementary processes and characterization of ceramic layer epitaxy.

Process	Characterization
Oxidation in UHV	Thermodynamics and kinetics XPS
Epitaxial growth	RHEED pattern XRD
Lateral growth	RHEED oscillation
Atomic and valence control in as-grown film and interface	XPS ( <i>in situ</i> )

**Table 4.**  $\text{CeO}_2$  film orientation prepared by laser MBE on Si substrate at  $600^\circ\text{C}$ .

Film	Substrate	Orientation	
$\text{CeO}_2$	Si-O/Si	$\text{CeO}_2(111)$	In-plane random
	Si(001)	$\text{CeO}_2(110) \parallel \text{Si}(001)$	$\text{CeO}_2[110] \parallel \text{Si}[110]$ and $\text{CeO}_2[001] \parallel \text{Si}[110]$
	Si(110)	$\text{CeO}_2(111) \parallel \text{Si}(110)$	$\text{CeO}_2[001] \parallel \text{Si}[110]$
	Si(111)	$\text{CeO}_2(111) \parallel \text{Si}(111)$	$\text{CeO}_2[110] \parallel \text{Si}[110]$

**Figure 8.** Temperature dependences of resistivity for  $(\text{SrVO}_{3-x}:2 \text{ units}/\text{SrTiO}_{3-y}:1 \text{ unit})_9$  superlattice measured using currents varied from 0.001 mA to 10 mA.

superconducting materials. Infinite-layer cuprates,  $\text{ACuO}_2$  ( $A$  = alkaline earth metal), were prepared by atomic and unit-cell-layer epitaxies using conventional and laser MBE to examine their superconductivity (Kawai *et al* 1993).

Key factors and process parameters for constructing artificially designed crystal lattices should include lattice matching between the bottom and growth layers, Coulomb interaction at the heterointerface to be formed, oxygen control under the film deposition conditions, and setting conditions for surface migration to achieve two-dimensional growth. This crystal engineering technology is more advanced than the conventional sequential deposition by multitarget sputtering or pulsed laser deposition. *In situ* diagnosis of the surface reactions and interface characterization are indispensable for quantitative control and evaluation of the film growth. Once we have this new materials technology, we can even use it to search for new properties and physical phenomena. Besides high- $T_c$  superconductivity, a few interesting phenomena have been observed and predicted in recent years on bulk complex oxides as well as on thin films and layered hetero-structures. Figure 8 shows the anomalous conducting behaviour we detected in the digitally controlled superlattice of  $\text{SrTiO}_3/\text{SrVO}_3$ . This apparent metal-semiconductor transition at about 100 K can be regarded as one of the new phenomena in low-dimensional conductive oxides (Koinuma *et al* 1991).

An atomically controlled formation of hetero-junctions between oxides and semiconductors is desired for the development of highly integrated devices. The growth of high-dielectric or ferroelectric perovskite oxides on silicon is extensively studied for use in capacitors and gate insulators. SOI (silicon on insulator) also attracts much interest to stack layers of silicon devices.

$\text{CeO}_2$  has a fluorite structure with excellent lattice matching with Si (99.6% at room temperature).  $\text{CeO}_2$  can be used as a buffer layer for the epitaxial growth of high- $T_c$  superconducting films on Si. The lattice mismatches between cuprate superconductors and Si are less than 1% in their  $a$ - $b$  planes. For the deposition of oxide films on Si, we encounter such a contradicting process condition as oxygen control without oxidizing the Si surface.  $\text{CeO}_2$  was considered suitable for film deposition on Si because the oxygen affinity of Ce is high enough to form  $\text{CeO}_2$  in ultrahigh vacuum. Thermodynamically,  $x$  in  $\text{CeO}_x$  is higher than 1.99 at 1000°C under  $7.6 \times 10^{-9}$  torr of oxygen.

Films were grown on clean Si substrates heated at 600–800°C by ablating a  $\text{CeO}_2$  target under  $10^{-9}$  torr pressure. Table 4 summarizes the growth behaviour of  $\text{CeO}_2$  films on Si single crystals. The epitaxial  $\text{CeO}_2$  films were obtained on Si(111) but not on Si(001) or Si(110). These results are well explained in terms of preferential arrangement

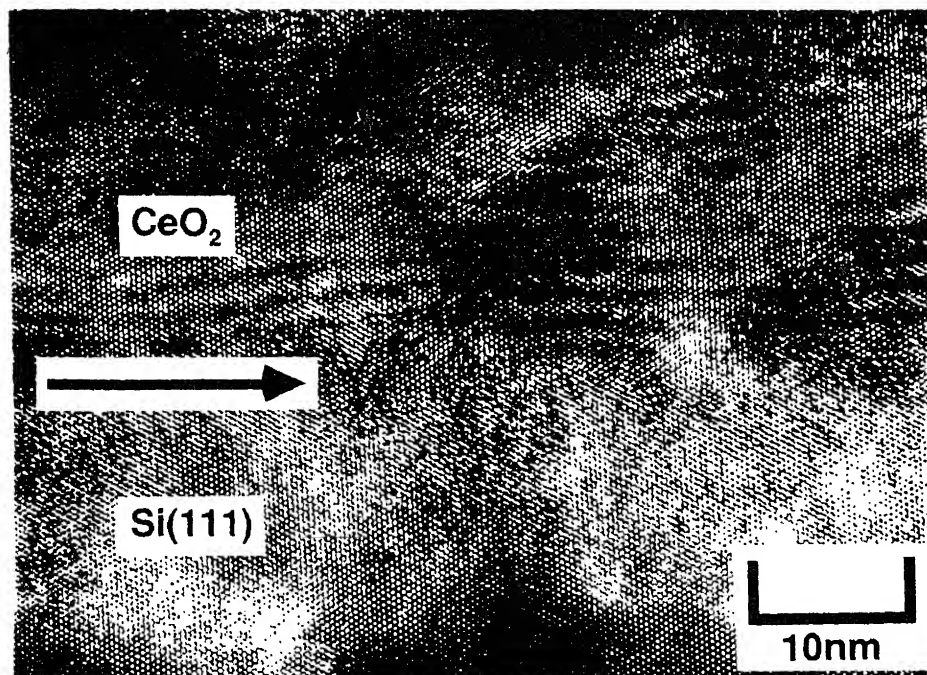


**Figure 9.** Cross-sectional lattice image at the interface observed from  $\langle 110 \rangle$  direction for the  $\text{CeO}_2$  film grown on Si(111) at 20°C. The arrow indicates the interface.  $\text{CeO}_2$  film grew epitaxially with the same crystallographic orientation as that of Si(111). No boundary amorphous layer was formed at the interface.

of the first plane of growing  $\text{CeO}_2$  by its Coulomb interaction with the topmost Si surface. Some other oxides such as  $\text{SrTiO}_3$  and yttria-stabilized zirconia (YSZ) were grown epitaxially on Si substrate. Epitaxial growth of  $\text{CeO}_2$  on Si(111) at room temperature was recently achieved by laser MBE to give such a sharp interface as depicted in figure 9. The interface is hardly distinguishable by transmission electron microscopy. This epitaxial  $\text{CeO}_2$  film has a dielectric constant much higher than that of  $\text{SiO}_2$  and a very high breakdown voltage.

## 5. Conclusion

Sophisticated pulsed laser technology has been used successfully to fabricate atomically controlled films of high- $T_c$  superconductors and related complex oxides as verified by the observation of RHEED intensity oscillation persisting for more than 300 cycles during homoepitaxial  $\text{SrTiO}_3$  growth. Such technology could be extended to the deposition of oxide films on silicon with almost perfect heteroepitaxial interface. Such crystal engineering of oxides is expected to lead to the fabrication of high- $T_c$  Josephson tunnel junction, and to be useful in advanced silicon VLSI technology and furthermore in novel electronics based on all epitaxial oxide films.

## Acknowledgements

The research described in this article was done in collaboration with my colleagues Drs M Yoshimoto and M Kawasaki as well as with graduate students T Maeda, N Kanda, K Fujito, K Takahashi, R Tsuchiya and T Ohnishi, to whom I would like to express my sincere thanks. The research was supported in part by a Grant-in-Aid for Scientific Research from the Ministry of Education, Science and Culture of Japan.

## References

- Bednorz J G and Muller K A 1986 *Z. Phys.* **B64** 189
- Daly K P, Dozier W D, Burch J F, Coons S B, Hu R, Platt C E and Simon R W 1991 *Appl. Phys. Lett.* **58** 543
- Dimos D, Chaudhari P, Mannhart J and LeGoues F K 1988 *Phys. Rev. Lett.* **61** 219
- Gong J P *et al* 1994 *Phys. Rev.* **B50** 3280
- Kawai M, Liu Z, Sekine R and Koinuma H 1993 *Jpn J. Appl. Phys.* **32** L1208
- Kawasaki M *et al* 1994 *Science* **266** 1540
- Koinuma H (ed.) 1994 *MRS Bull.* **19** 21
- Koinuma H and Yoshimoto M 1994 *Appl. Surf. Sci.* **75** 308
- Koinuma H, Kawasaki M, Funabashi M, Hasegawa T, Kishio K, Kitazawa K, Fueki K and Nagata S 1987 *J. Appl. Phys.* **62** 1524
- Koinuma H, Yoshimoto M, Nagata H and Tsukahara T 1991 *Solid State Commun.* **80** 9
- Koinuma H, Fujito K, Tsuchiya R and Kawasaki M 1994 *Proc. 8th CIMTEC, Florence*
- Nantoh M *et al* 1994 *J. Superconductivity* **7** 349
- Yoshimoto M, Nagata H, Tsukahara T and Koinuma H 1990 *Jpn J. Appl. Phys.* **29** L1199
- Yoshimoto M *et al* 1995 *Jpn J. Appl. Phys.* **34** L688



## Use of microwaves for the synthesis and processing of materials

K J RAO\* and P D RAMESH

Materials Research Centre, Indian Institute of Science, Bangalore 560 012, India

**Abstract.** An overview of the synthesis of materials under microwave irradiation has been presented based on the work performed recently. A variety of reactions such as direct combination, carbothermal reduction, carbidation and nitridation have been described. Examples of microwave preparation of glasses are also presented. Great advantages of fast, clean and reduced reaction temperature of microwave methods are emphasized. The example of  $\text{ZrO}_2$ - $\text{CeO}_2$  ceramics has been used to show the extraordinarily fast and effective sintering which occurs in microwave irradiation.

**Keywords.** Microwave synthesis; nitridation reaction; carbidation; glasses; microwave sintering.

### 1. Introduction

Synthesis and consolidation are two vital aspects of materials science particularly in respect of ceramics. One of the most important and attractive developments in this context is the use of microwaves for both synthesizing and sintering ceramics. The range of frequencies from 0.3 to 300 GHz in electromagnetic spectrum (wavelengths ranging from 1 m to 1 mm) constitute microwaves. Microwaves are coherent and polarized. Only two frequency windows of microwaves are available for industrial use and most microwave work reported to date is based on the use of 2.45 GHz sources. Microwave ovens which work at this frequency and at power levels of about a kW are in wide use (Osephchuk 1984).

It is generally believed that microwaves couple effectively with lossy materials and the primary action of microwaves occurs through very rapid heating. However, both physical and chemical characteristics seem to affect microwave coupling and hence microwave heating. This is amply illustrated in the literature particularly by microwave coupling of various forms of carbon. One important characteristic of microwave heating is that the entire volume of particles get heated up since generally the penetration depths are quite high. Thus the bulk heating and minimization of thermal gradients lead to modes of reaction as yet incompletely understood. Several materials couple effectively above a certain temperature probably because of the temperature dependent increase of dielectric loss. However, the phenomena enables immediate use of this aspect in microwave processing of pre-heated ceramic materials. The pre-heating itself could be accomplished by use of an inert second material which couples to microwaves at room temperature.

In this article, we first present the currently popular ideas about interaction of microwaves with matter. We then present examples of the preparation of several materials through different types of reactions assisted by use of microwaves. We also discuss consolidation of an important class of  $\text{ZrO}_2$  ceramics which illustrates the usefulness of the technique microwave sintering. The sections are subtitled

The most notable effect of microwave irradiation is the heating effect. In microwave heating, unlike in conventional heating, heat is generated within the material itself instead of heat supplied from external sources. As a result of this internal and volumetric heating, thermal gradients and flow of heat during microwave processing are quite different from those observed in conventional heating. The schematic of conventional and microwave heating processes are shown in figure 1. The various advantages of microwave process over conventional heating have been discussed in great depth by Sutton (1989).

Microwaves obey the laws of optics—they are transmitted, reflected or absorbed depending on the nature of materials. Figure 2 describes briefly the action of microwaves in different types of materials. Generally insulators which have low dielectric loss are transparent and those with high dielectric loss absorb microwaves and get heated. Many insulators which are microwave transparent at room temperature absorb microwaves at higher temperatures. Also, inclusions of conductive and magnetic phases in transparent materials enhance microwave absorption.

Microwave coupling is related to complex permittivity of the material by the relation

$$\epsilon'' = \epsilon' - j\epsilon'' = \epsilon_0(\epsilon'_r - j\epsilon''_{\text{eff}}), \quad (1)$$

where  $j = (-1)^{1/2}$ ,  $\epsilon_0 = 8.86 \times 10^{-12}$  F/m, permittivity of free space,  $\epsilon'_r$  is the relative dielectric constant and  $\epsilon''_{\text{eff}}$  is the effective dielectric loss factor.

When microwaves propagate through the material, an electric field is generated within the target material and it induces translational and rotational motions of the free and bound charges. They also excite the rotational modes of charge complexes such as dipoles. The resistance to the induced motions causes loss of microwave intensity in the material. The losses are frequency dependent and they attenuate the electric field which results in heating. The loss parameters are all combined into an effective relative dielectric loss factor,  $\epsilon''_{\text{eff}}$ . The loss tangent is defined in term of  $\epsilon''_{\text{eff}}$  as

$$\tan \delta = \frac{\epsilon''_{\text{eff}}}{\epsilon'_r} = \frac{\sigma}{2\pi f \epsilon'_r \epsilon_0}, \quad (2)$$

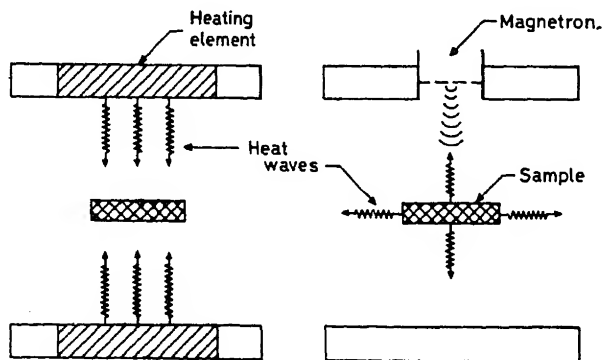


Figure 1. Representation of conventional and microwave heating patterns (schematic).

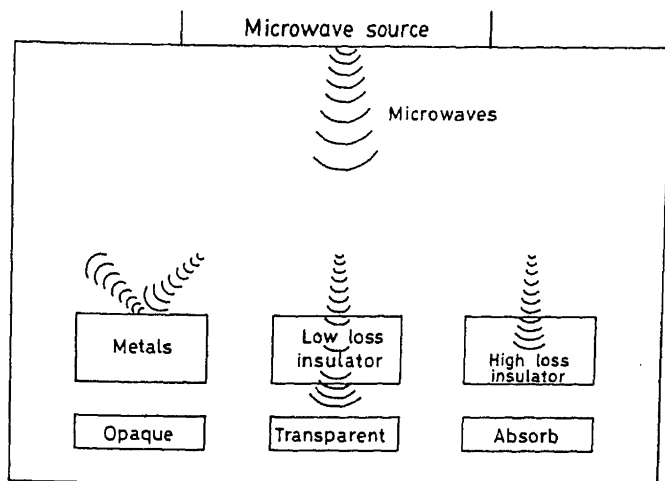


Figure 2. Behaviour of different types of materials in the microwave field (schematic).

where  $\sigma$  is the total effective conductivity (S/m) caused by conduction and displacement currents and  $f$  the frequency (GHz) of microwaves.

The power absorbed by unit volume,  $P$  is given by

$$P = 2\pi f \epsilon_0 \epsilon'_r \tan \delta E^2, \quad (3)$$

where  $E$  (V/m) is the magnitude of the field. Therefore power absorbed varies linearly with the applied frequency, dielectric constant ( $\epsilon_r$ ) of the material and the effective loss factor ( $\tan \delta$ ). It also varies with the square of internal electric field ( $E$ ). The parameters  $\epsilon'_r$ ,  $\tan \delta$  and  $E$  are all also not entirely independent of each other. Electric field generated in the material further depends on its size, geometry, its location within the microwave cavity and the design on the cavity itself. Equation (3) indicates the nature of variables which determine the value of  $P$ .

A parameter  $D$  which denotes the depth of microwave penetration in the material at which the incident power is reduced by one half is given by the equation

$$D = \frac{3\lambda_0}{8.686\pi \tan \delta (\epsilon'_r/\epsilon_0)^{1/2}}, \quad (4)$$

where  $\lambda_0$  is the incident (or) free space wavelength. Thus  $D$  is higher for higher wavelengths or lower frequencies. But lower frequencies result in lower induced electric field ( $E$ ) in the material which in turn causes less heating (see (3)). Thus there is an optimal range of useful microwave frequencies for material processing. The most commonly used microwave frequencies for materials processing are 0.915 GHz and 2.45 GHz. The loss factor of the material denoted by  $\tan \delta$  varies with temperature. It is also temperature dependent. Generally  $\tan \delta$  increases slowly initially up to a temperature  $T_{\text{crit}}$  above which it increases steeply. Above  $T_{\text{crit}}$ , therefore  $\tan \delta$  begins



runaway often causes undesirable hot spots in the material. By controlling the microwave power it is possible to prevent thermal runaway phenomenon in the material. Kenkre *et al* (1991) discussed thermal runaway phenomena in materials quantitatively.

The primary consequence of interaction of microwaves with materials appears to be rapid heating albeit with differences in details as compared to conventional heating.

### 3. Synthesis of materials

Microwave heating provides a uniquely advantageous method for the synthesis and sintering of materials. In the following we present synthesis of materials by different routes and induced by microwave irradiation.

#### 3.1 Direct combination

**3.1a Chalcogenides:** Chalcogenides constitute a rich category of inorganic solids with many technological applications such as solar cells. The conventional solid state synthesis of chalcogenides is quite complex. Preparation of PbTe by conventional method involves cumbersome heating in rotary furnaces for several hours. In microwave assisted synthesis (Vaidhyanathan *et al* 1995a), it is accomplished very simply by mixing together stoichiometric quantities of metal and chalcogenide powders in sealed evacuated ( $5 \times 10^{-5}$  torr) quartz tubes and subjecting them to microwave irradiation in a kitchen microwave oven operating at 2.45 GHz (maximum power 980 W)\*. Fine metal powders absorb microwaves and eddy currents are generated in the particles which result in heating. Exposure times varied from 5–20 min for complete reaction. Given in figure 3 is the X-ray diffractogram (XRD) of chalcogenide products (PbSe, PbTe, ZnS, ZnSe and Ag<sub>2</sub>S) obtained in this manner. Notable is the high phase purity of the products. The lattice parameters matched very well with the reported values.

**3.1b Metal vanadates:** Vanadates like Bi<sub>4</sub>V<sub>2</sub>O<sub>11</sub> and PbV<sub>2</sub>O<sub>6</sub> exhibit interesting electrical properties like ferroelectricity and are therefore technologically important materials. Conventional methods for their preparation are very tedious. Metal vanadates (Vaidhyanathan *et al* 1995a) of bismuth (Bi<sub>4</sub>V<sub>2</sub>O<sub>11</sub>) and lead (PbV<sub>2</sub>O<sub>6</sub>) have been prepared starting with reagent grade materials of V<sub>2</sub>O<sub>5</sub>, Bi<sub>2</sub>O<sub>3</sub> and PbO. The reactions were carried out by placing stoichiometric mixtures of component oxides in a quartz crucible which was placed in a microwave oven and irradiated for 15 min. V<sub>2</sub>O<sub>5</sub> absorb microwaves efficiently and the temperatures reach up to 1000 K. The products were allowed to anneal in the furnace for 2 h. The XRD patterns of metal vanadates prepared by microwave irradiation are shown in figure 4. The products exhibited high phase purity and the lattice parameters are as follows: Bi<sub>4</sub>V<sub>2</sub>O<sub>11</sub>:  $a = 16.86 \text{ \AA}$ ,  $b = 16.62 \text{ \AA}$  and  $c = 15.33 \text{ \AA}$  and PbV<sub>2</sub>O<sub>6</sub>:  $a = 9.799 \text{ \AA}$ ,  $b = 3.670 \text{ \AA}$  and  $c = 12.712 \text{ \AA}$ . These are in very good agreement with literature reports (Varma *et al* 1990).

It was confirmed that annealed Bi<sub>4</sub>V<sub>2</sub>O<sub>11</sub> sample exhibits an endothermic  $\alpha \rightarrow \beta$  transformation around 725 K as reported by Abraham *et al* (1988) by using

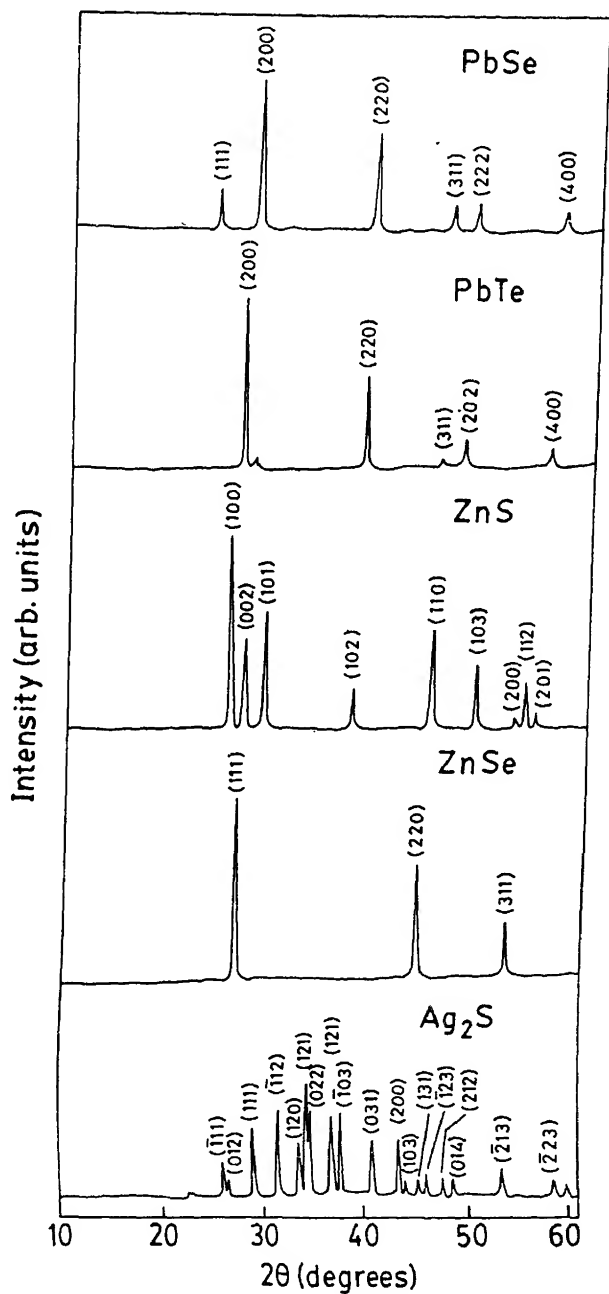


Figure 3. X-ray diffractograms of microwave prepared metal chalcogenides.

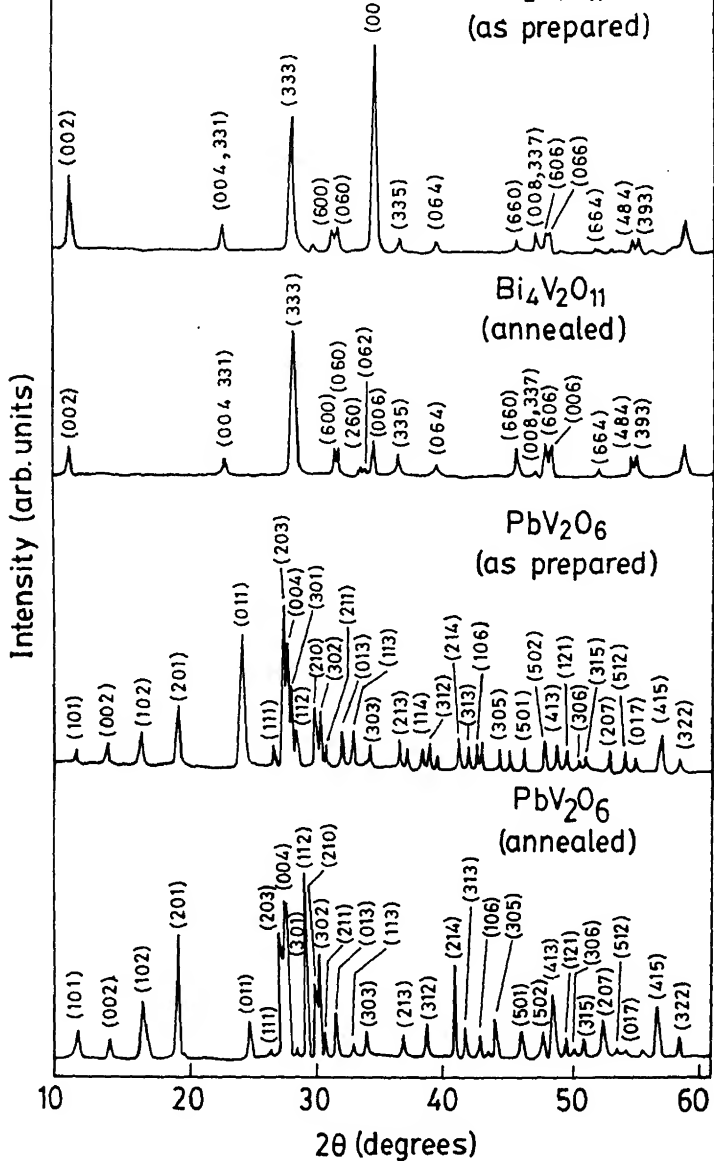


Figure 4. X-ray diffractograms of the metal vanadates prepared by microwave method.

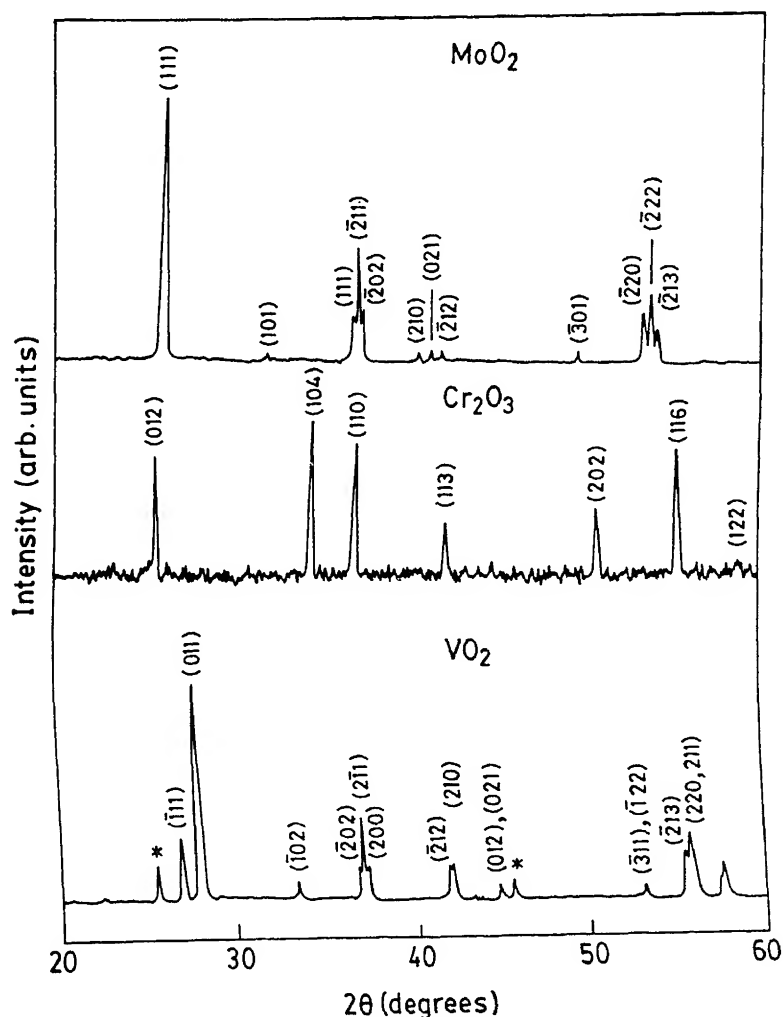
#### 4. Carbothermal reduction

##### 4.1 Deoxygenation of layer and chain containing oxides

Some of the industrially important oxides like  $\text{MoO}_2$  and  $\text{Cr}_2\text{O}_3$  are generally obtained by reduction of corresponding higher valent oxides like  $\text{MoO}_3$  and  $\text{CrO}_3$ . It

found that carbothermal reduction under microwave irradiation is an amazingly fast and simple method for this purpose provided higher valent oxides have layered structure or consists of chains of oxide polyhedral units. Many layered oxides namely  $\text{MoO}_3$ ,  $\text{V}_2\text{O}_5$ ,  $\alpha\text{-VOPO}_4 \cdot 2\text{H}_2\text{O}$  and  $\text{Ag}_6\text{Mo}_{10}\text{O}_{33}$  are reduced to  $\text{MoO}_2$ ,  $\text{VO}_2$ ,  $\text{VOPO}_4$  and  $(\text{Ag} + \text{MoO}_2)$  respectively by graphitic carbon under microwave irradiation (Vaidhyanathan 1995b). Similarly  $\text{CrO}_3$  which consists of chains of tetrahedrally coordinated chromium atoms is reduced to  $\text{Cr}_2\text{O}_3$ . The products were characterized using XRD, DSC, IR and ESR spectroscopies.

Experiments have been carried out using analar grade chemicals of  $\text{MoO}_3$ ,  $\text{V}_2\text{O}_5$  and  $\text{CrO}_3$  (for preparation of  $\text{MoO}_2$ ,  $\text{VO}_2$  and  $\text{Cr}_2\text{O}_3$ ) and high purity graphitic carbon.  $\alpha\text{-VO}_4\text{PO}_4 \cdot 2\text{H}_2\text{O}$  was prepared by the procedure described by Johnson *et al*



(1982).  $\text{Ag}_6\text{Mo}_{10}\text{O}_{33}$  was prepared by heating the mixture of  $\text{Ag}_2\text{MoO}_4$  and  $\text{MoO}_3$  in air (Rosner and Lagaly 1984). Initially the powders were thoroughly mixed with graphitic carbon in 3:1 weight ratio and exposed to microwaves in a silica crucible for 4 to 5 min. Remaining carbon can either be washed out or burnt in air. Experiments reveal (Vaidhyanathan *et al* 1995b) that these reactions occur entirely in the solid state.

XRD of the products formed are shown in figure 5. Lattice parameters of the microwave synthesized reduced compounds have been compared with the existing data and are given in table 1. The DSC trace of  $\text{VO}_2$  exhibits a clear endothermic transition at 340 K which corresponds to semiconductor metal transition of  $\text{VO}_2$ . The room temperature electron spin resonance (ESR) signal of  $\text{V}^{4+}$  in  $\alpha\text{-VOPO}_4 \cdot 2\text{H}_2\text{O}$  shows anisotropic hyperfine structure which compares well with the reported spectrum (refer figure 6). The product  $\text{VPO}_4$  exhibits a much simpler ESR spectrum due to a  $\text{V}^{3+}$  ion which compares well with the spectrum of  $\text{V}^{3+}$  of  $\text{V}_2\text{O}_3$ . Matching of ESR spectrum of microwave synthesized  $\text{Cr}_2\text{O}_3$  and commercial  $\text{Cr}_2\text{O}_3$  has provided additional confirmation.

It is interesting to note that though  $\text{MoO}_3$  and  $\text{WO}_3$  are chemically similar only layered  $\text{MoO}_3$  undergoes reduction reaction. It is clear demonstration of how structural chemistry plays an important role in these reactions. Also the non-layered materials such as  $\text{TiO}_2$ ,  $\text{SnO}_2$ ,  $\text{Nb}_2\text{O}_5$  and  $\text{ZrO}_2$  are not reduced by carbon in similar microwave experiments.

It is likely that the unshared oxygen which is connected to Mo weakly through the longer Mo–O bond of distance 2.33 Å is reacted away by the graphitic ( $sp^2$ ) carbon resulting in the reduction of  $\text{MoO}_3$ . A similar mechanism is suggested for  $\text{V}_2\text{O}_5$  also. In dehydrated  $\alpha\text{-VOPO}_4$ , the  $\text{VO}_5$  square pyramids are connected by interlayer oxygen which can readily react with carbon which results in the formation of  $\text{V}^{3+}$  phosphate. Removal of oxygens from interlayer region in  $\text{Ag}_6\text{Mo}_{10}\text{O}_{33}$  destabilizes the structure and it undergoes a complete decomposition to  $\text{Ag} + \text{MoO}_2$ . Presumably,  $\text{Ag}^+$  is also reduced to  $\text{Ag}^0$ . Similar reduction appears to occur in  $\text{CrO}_3$  which consists of  $[\text{CrO}_{2/2}\text{O}_2]$  chains. Microwave route thus provides an elegant and

**Table 1.** Lattice parameters of the microwave prepared lower valent oxides.

Compound	Lattice parameters		Reference
	Calculated	Reported	
$\text{MoO}_2$	$a = 5.615 \text{ \AA}$	$5.607 \text{ \AA}$	(NBS Monograph 1981)
	$b = 4.859 \text{ \AA}$	$4.860 \text{ \AA}$	
	$c = 5.533 \text{ \AA}$	$5.537 \text{ \AA}$	
	$\beta = 119^\circ 35'$	$\beta = 119^\circ 35'$	
$\text{Cr}_2\text{O}_3$	$a = 4.962 \text{ \AA}$	$4.959 \text{ \AA}$	(McMurdie 1987)
	$c = 13.582 \text{ \AA}$	$13.594 \text{ \AA}$	
$\text{VO}_2$	$a = 5.742 \text{ \AA}$	$5.743 \text{ \AA}$	(Anderson 1954)
	$b = 4.519 \text{ \AA}$	$4.517 \text{ \AA}$	
	$c = 5.377 \text{ \AA}$	$5.375 \text{ \AA}$	
	$\beta = 112^\circ 56'$	$\beta = 122^\circ 60'$	
$\text{VPO}_4$	$a = 5.220 \text{ \AA}$	$5.245 \text{ \AA}$	(Tudo and Carton 1979)
	$b = 7.770 \text{ \AA}$	$7.795 \text{ \AA}$	
	$c = 6.266 \text{ \AA}$	$6.285 \text{ \AA}$	

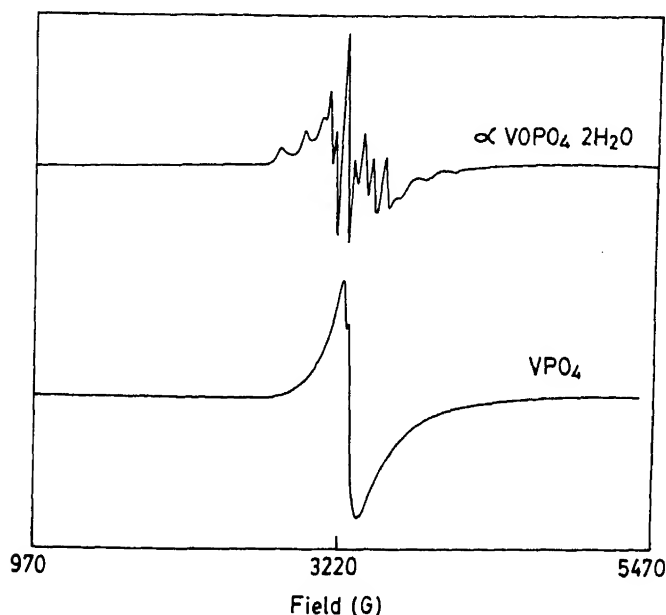


**Figure 6.** Room temperature ESR spectra of  $\alpha$ - $\text{VPO}_4 \cdot 2\text{H}_2\text{O}$  (reactant) and  $\text{VPO}_4$  (product).

structure selective method of reduction in solid state. Further the method is very fast (min) compared to long (such as 90–100 h for the preparation of  $\text{MoO}_2$ ) and tedious conventional methods.

### Carbide reaction

Silicon carbide (SiC) is one of the most important ceramics used in several applications. It can be prepared by irradiating a well prepared mixture of pure silicon and charcoal powders with 2.45 GHz microwaves. In our experiments the mixture was taken in a quartz container and exposed to microwaves up to a maximum of 10 min. Reaction was carried out in both air and iodine as ambients. The details of these have been discussed by Ramesh *et al* (1994). All the samples were identified by XRD. The reaction in air (particularly with excess carbon) leads to formation of silica up to about 15% which could be removed by chemical leaching. But silicon–carbon reaction carried out in iodine atmosphere gave only  $\beta$ -SiC of good phase purity (refer figure 7). Iodine atmosphere was created by carrying out a reaction between KI and  $\text{O}_2$  in a separate crucible along side (Si + C) mixture.

Maximum temperature attained by silicon–carbon mixture at 980 W power is 1733 K. This temperature is far less than the temperature (1673 K) required for initiation of silicon–carbon reaction in conventional process. Microwave heating carried out separately revealed that silicon is a poor microwave absorber whereas carbon is a good absorber.

It has been suggested (Ramesh *et al* 1994) that the rapidity of the reaction is likely to

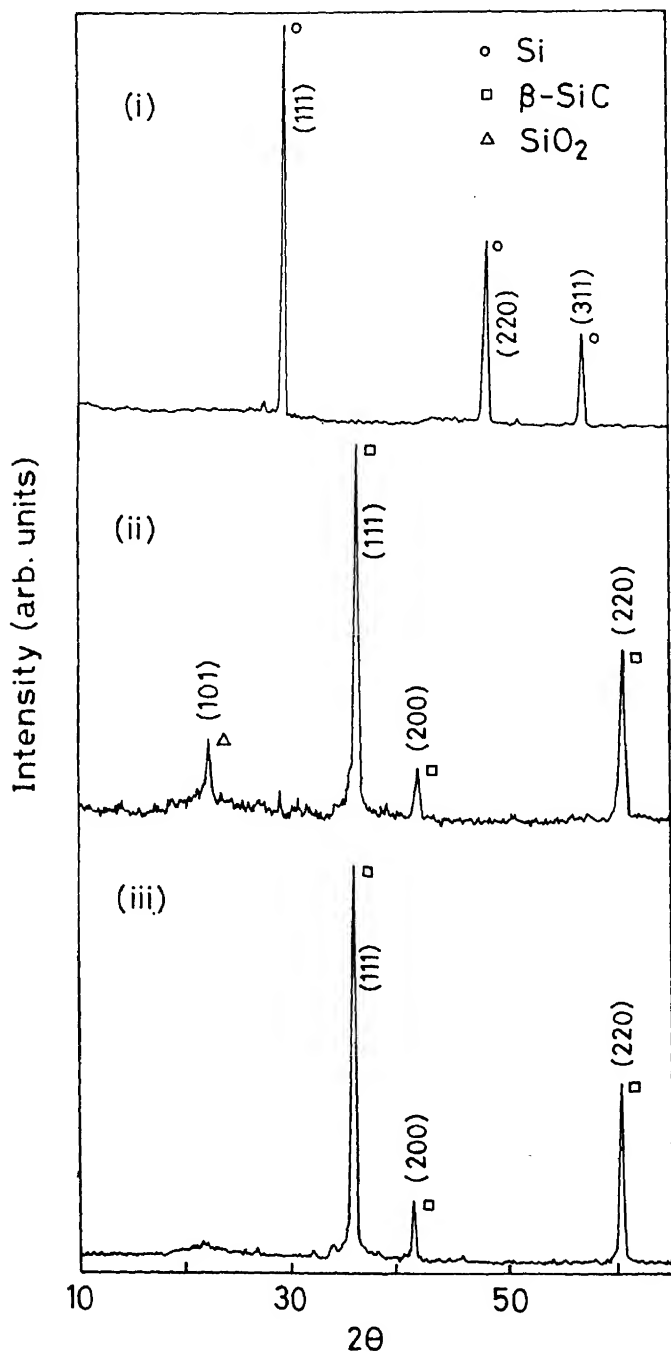


**Figure 7.** X-ray diffractogram of (i) silicon-carbon initial reactant mixture, (ii) reaction products formed in air after 10 min and (iii) reaction product formed in iodine atmosphere after 10 min.

reaction mixture. The local heating of the reactants which absorb microwaves are efficiently escalates the rate of reaction. The lower (1000 K) temperature of the reaction itself could be due to the possible microwave excitation of graphitic bonds during silicon-carbon reaction.

The microwave assisted preparation of SiC is notable for three aspects: (i) very short time scale of the reaction, (ii) lower reaction temperatures and (iii) very high phase purity of the product.

### Nitridation reaction

It was found that microwave irradiation assists nitridation reaction as well. Aluminium nitride is an important and high-cost ceramic required in the electronic industry (Leppard 1990). Besides, being an insulator, it possesses very attractive properties such as high thermal conductivity, low thermal expansivity and low dielectric constant. The method available for AlN synthesis involves high temperatures and handling of atomized Al powder (Weimer *et al* 1994). Preparation by carbothermal reduction and nitridation (Cho and Charles 1991) starting with  $\text{Al}_2\text{O}_3$  is also both cumbersome and time consuming. We have found (Ramesh and Rao 1995) that the synthesis of aluminium nitride can be achieved by the use of microwave irradiation of a mixture of aluminium and carbon powders in pure nitrogen. The details of the experiment and the possible reaction mechanisms are discussed by Ramesh and Rao (1995). The reaction between aluminium and nitrogen is highly exothermic. The temperature of the reaction varies between 1373 K and 1573 K. The reaction does not proceed to completion in one step since AlN layers are formed on the surface of aluminium particles, which prevents further nitridation. However, nitridation of aluminium powder occurs at surprisingly low temperatures (1200 K) and at exceedingly fast rates. The microwave irradiation was interrupted every 15 min and the powder was ground so that the surface covering with AlN was broken down. The effect of grinding on the product formation is shown in figure 8. In the first 15 min nearly 40% of the products were formed. But without grinding the converted amount remained essentially unaltered, even after 90 min. But with intermittent grinding nearly full conversion was achieved in about 120 min.

The resulting AlN powders were characterized using XRD, TEM, IR and particle size analysis.

The nitridation reaction was highly oxygen sensitive. Only when high pure nitrogen (99.95%) gas was used formation of pure AlN was observed. But even when 99.5% pure nitrogen was used considerable amount of  $\text{Al}_2\text{O}_3$  was found to form. AlN powders failed to reveal any XRD detectable oxide phase after burning out excess carbon at 973 K.

Infrared spectra of the microwave synthesized sample compared very well with the spectra of commercial AlN sample (see figure 9). Both give a strong and broad absorption band in the range of  $1100\text{--}350\text{ cm}^{-1}$  with a maximum at  $682\text{ cm}^{-1}$ . This corresponds to  $\text{Al-N}$  stretching vibration frequency in the wurtzite structure.

Some important features in microwave assisted synthesis are (i) the temperature does not rise beyond 1200 K; the silica ware remains unaffected, the charge becomes only red hot and no thermal runaway is observed, (ii) the aluminium particles, whose size is in the range of  $1\text{--}5\text{ }\mu\text{m}$ , do not agglomerate and (iii) the complete



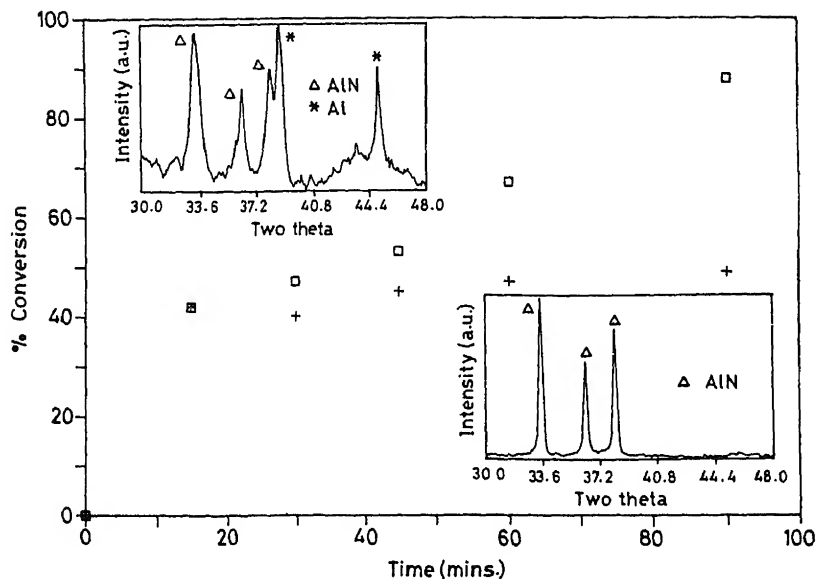


Figure 8. Amount of AlN formation against microwave exposure time; □, with intermediate grinding; +, without intermediate grinding. Top inset: X-ray diffractogram of the product mixture after 15 min of microwave exposure (no grinding). Bottom inset: X-ray diffractogram of the product mixture after 120 min of microwave exposure (ground eight times).

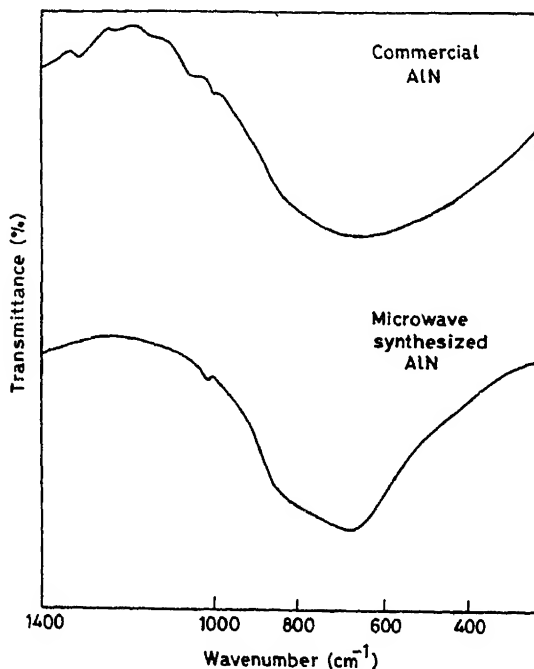


Figure 9. Infrared spectra of commercial AlN and AlN synthesized using microwaves.

It has been suggested that microwave coupling may be due to eddy current generation in aluminium particles and due to the high microwave susceptibility of carbon. However, the reaction appears to be directly microwave activated at the aluminium surface in an unclear manner and is not associated with the melting of aluminium particles. The product AlN is not a microwave absorber and hence apparently no further heating occurs. The process involves intermediate grinding and ensures formation of very fine (nanosized) AlN powder.

### Preparation of glasses

Glasses are very easily prepared by melting mixture of the ingredients if at least one of the ingredients is a microwave susceptor (Vaidhyanathan *et al* 1994). The melts are quenched between polished stainless steel plates. Various glasses prepared by this technique is given in table 2. The  $T_g$ 's of glasses determined using DSC are in good agreement with literature values (table 2). We have observed that oxides such as  $\text{SiO}_2$ ,  $\text{WO}_3$ ,  $\text{CuO}$ ,  $\text{ZnO}$  and  $\text{SiO}_2$  gel and halides like AgI and CuI efficiently couple with microwaves and temperatures of up to  $\approx 1000$  K are easily attained. Homogeneity in heating is achieved by fine mixing of the initial powders. The process is extremely fast. Undesirable aspects such as loss of materials and oxidation by ambient air etc are easily avoided.

In the preparation of CuI containing glasses by conventional procedure, copper is known to oxidize to the extent of 12–15%. But when melted by using microwaves the maximum extent of  $\text{Cu}^{2+}$  was found to be only 0.9%. In another procedure in which the melting was performed in  $\text{NH}_3$  atmosphere the oxidation of copper to  $\text{Cu}^{2+}$  was further reduced to 0.69% (ammonia atmosphere was created by heating a mixture of ammonium metavanadate and  $\text{V}_2\text{O}_5$  in another crucible kept in the microwave oven).  $\text{Cu}^{2+}$  was estimated using ESR.

But the most important observation in this procedure is that the temperatures level off once the mixtures are melted and at different values for different mixtures. Since melting alters the chemistry of the mixtures and also its physical state the microwave absorption characteristics change. This feature acts as an autocontrol and the temperature of glass forming melts level off even when the microwave power is on.

### Sintering of $\text{ZrO}_2$ – $\text{CeO}_2$ ceramics

As noted earlier, one important advantage of microwave irradiation is the rapid heating rate. This leads to short processing durations and low power requirements as compared to conventional heating. It is therefore obvious that microwaves can be employed for sintering applications. Reports (Sutton 1989) exist on microwave sintering of many ceramic materials. We discuss here a method of sintering ceramics which are not good microwave susceptors at ordinary temperatures. The method can be of quite general utility.

$\text{ZrO}_2$ – $\text{CeO}_2$  ceramics are known for their excellent mechanical properties. It is known that  $\text{CeO}_2$  toughened  $\text{ZrO}_2$  ceramics are potential electrode materials due to

Table 2. List of glasses formed using microwave heating.

No.	Glass system	Preparation conditions				Reference
		$T_g$ (K)	Time (min)	Crucible used	Type of quenching	
1	$x\text{PbO}:(100-x)\text{V}_2\text{O}_5 [x = 40-50]$	520-522	5	S	SSPQ	(Denton <i>et al</i> 1954; Tsuzuki <i>et al</i> 1992)
2	$50\text{GeO}_2:50\text{V}_2\text{O}_5$	491	6	S	SSPQ	(Denton <i>et al</i> 1954)
3	$33\text{BaO}:67\text{V}_2\text{O}_5$	551	5	S	SSPQ	(Denton <i>et al</i> 1954)
4	$30\text{Na}_2\text{O}:30\text{B}_2\text{O}_3:40\text{V}_2\text{O}_5$	470(468)	6	S	SSPQ	(Muthupari <i>et al</i> 1994)
5	$50\text{AgI}:25\text{Ag}_2\text{O}:25\text{MoO}_3$	348(340)	5	S	QPQ	(Shastry and Rao 1989)
6	$50\text{AgI}:25\text{Ag}_2\text{O}:25\text{WO}_3$	419(427)	6	S	QPQ	(Shastry and Rao 1989)
7	$50\text{AgI}:25\text{Ag}_2\text{O}:25\text{CrO}_3$	298(294)	3	S	QPQ	(Shastry and Rao 1989)
8	$50\text{AgI}:33\text{Ag}_2\text{O}:17\text{GeO}_2$	392(402)	5	S	QPQ	(Minami <i>et al</i> 1980)
9	$60\text{AgI}:20\text{Ag}_2\text{O}:10\text{MoO}_3:10\text{WO}_3$	345	3	S	QPQ	(Prasad and Radhakrishna 1988)
10	$40\text{AgI}:30\text{Ag}_2\text{O}:15\text{WO}_3:15\text{B}_2\text{O}_3$	460	5	S	QPQ	(Sidhu <i>et al</i> 1991)
11	$60\text{AgI}:20\text{Ag}_2\text{O}:10\text{MoO}_3:10\text{V}_2\text{O}_5$	351	2	S	QPQ	(Sathyanarayana and Radhakrishna 1988)
12	$30\text{CuI}:35\text{Cu}_2\text{O}:35\text{MoO}_3$ (in air)					
	(in $\text{NH}_3$ atm.)	390	3	S	SSPQ	
13	$x\text{B}_2\text{O}_3:(45-x)\text{PbO}:55\text{V}_2\text{O}_5 [x = 0-20]$	393(404)	10	S	SSPQ	(Machida <i>et al</i> 1988)
14	$x\text{SiO}_2:(45-x)\text{PbO}:55\text{V}_2\text{O}_5 [x = 0-15]$	520-515	7	S	SSPQ	(El-Sharkawy <i>et al</i> 1988)
15	$x\text{ZnO}:(45-x)\text{PbO}:55\text{V}_2\text{O}_5 [x = 0-40]$	520-531	5	PZ	SSPQ	
16	$x\text{MoO}_3:(45-x)\text{PbO}:55\text{V}_2\text{O}_5 [x = 0-35]$	520-541	5	S	SSPQ	
17	$x\text{CuO}:(45-x)\text{PbO}:55\text{V}_2\text{O}_5 [x = 0-20]$	520-515	5	S	SSPQ	
18	$x\text{WO}_3:(45-x)\text{PbO}:55\text{V}_2\text{O}_5 [x = 0-15]$	520-536	5	S	SSPQ	
19	$x\text{Bi}_2\text{O}_3:(45-x)\text{PbO}:55\text{V}_2\text{O}_5 [x = 0-10]$	520-531	5	S	SSPQ	
		520-537	4	S	SSPQ	

SSPQ, Stainless steel plate quenching; QPQ, quartz plate quenching; S, silica crucible; PZ, porous zirconia crucible.

sceptibility at high temperatures ( $> 773$  K). Thus a secondary microwave absorber which does not react with either  $\text{ZrO}_2$  or  $\text{CeO}_2$  can be used to raise the temperature initially to  $\approx 800$  K above which  $\text{ZrO}_2$  and  $\text{CeO}_2$  themselves couple to microwave field. Such a secondary absorption is provided by  $\beta$ -SiC which is itself readily prepared by microwave methods (see earlier section).

Detailed experimental procedure is given elsewhere (Ramesh *et al* 1995). Commercial  $\text{ZrO}_2$  and  $\text{CeO}_2$  powders were used as starting materials. The pellets were made from the powder mixtures of  $\text{ZrO}_2$  and  $\text{CeO}_2$  of various compositions over the entire composition range. Green densities were measured. These pellets were placed inside  $\beta$ -SiC powder which was kept in a quartz crucible and irradiated with microwaves of 2.45 GHz frequency. Generally, the duration of sintering was 35 min. Sintered samples were characterized using XRD, SEM and density measurements. Microhardness and fracture toughness values were also measured using variable loads.

Entire range of compositions between  $\text{ZrO}_2$  and  $\text{CeO}_2$  were found to be readily sintered (figure 10). In most of the cases, sintering densities were well above 95%. It was observed that the sintering densities vary linearly with mole fraction of  $\text{CeO}_2$ . Thus although direct sintering of  $\text{ZrO}_2$  and  $\text{CeO}_2$  is not possible as their microwave

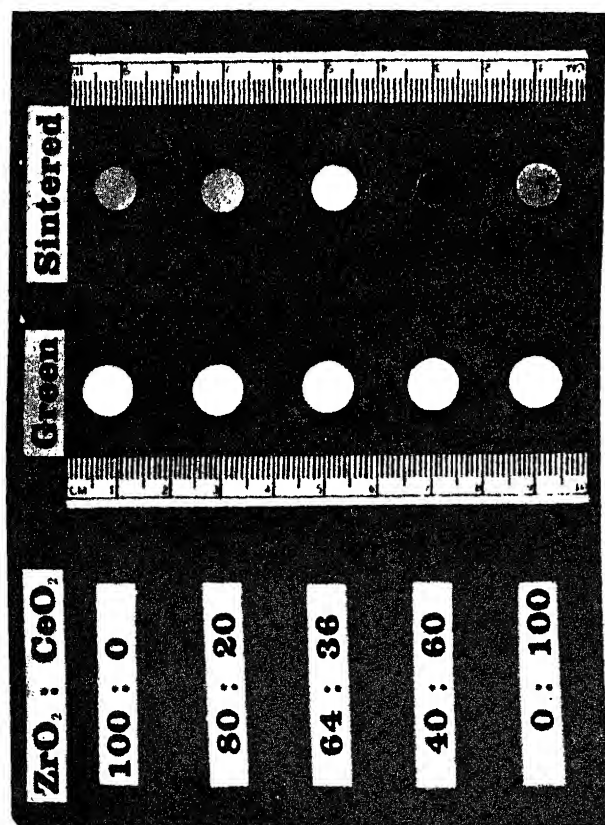


Figure 10. Photograph of  $\text{ZrO}_2$ - $\text{CeO}_2$  pellets (both green and sintered) with different compositions.

absorption is poor at room temperatures, microwave heating of  $\beta$ -SiC in which they are immersed preheats the pellets which absorb microwaves at elevated temperatures. A similar trend was observed with  $\text{CeO}_2$ . The temperatures of the pellets have been found to shoot up to 1773 K.

The phase field of sintered products were found to be similar to those observed in conventional sintering. Peak intensities of the (111) peak of monoclinic, (101) of tetragonal, and (111) of cubic phases were considered for phase content calculations. The variation of phase contents with ceria percentage is shown in figure 11. Even at 4%  $\text{CeO}_2$  tetragonal phase ( $T_{ss}$ ) is found to be present along with monoclinic ( $M_{ss}$ ) phase. Above 20% only tetragonal phase ( $T_{ss}$ ) is present.  $T_{ss}$  phase extends up to 44%  $\text{CeO}_2$  above which both cubic and tetragonal phases appeared till 76%  $\text{CeO}_2$ . Above this percentage of ceria only cubic solid solutions were found to form. The lattice parameters were calculated using PROSZKI software and is given in table 3.  $\phi$ -phase ( $\text{Ce}_2\text{Zr}_3\text{O}_{10}$ ) formation was not observed in any of the compositions which confirms the observations of Tani *et al* (1983).

We have also noted that phase formation in certain compositions depends strongly on the sintering duration. In the  $M_{ss} \rightarrow T_{ss}$  phase field with 12%  $\text{CeO}_2$ , sintering for 35 min results in 60% monoclinic and 40% tetragonal phases. The proportion of tetragonal phase increases with sintering time and about 95% tetragonal phase has formed after sintering for 105 min. Scanning electron micrograph of the etched top surface of this pellet is shown in figure 12. Thus phase boundaries in figure 11 obtained using 35 min should be treated as only approximate.

The hardness values are low for monoclinic phase whereas the Vickers hardness number (VHN) value increases and attains a maximum in the mixed tetragonal and cubic phase region. A maximum value of  $\approx 1200$  is reached in this region. For pure cubic phase the hardness values were again low. The scanning electron micrographs indicate the presence of microphases in the sintered samples. Hence fracture toughnesses,  $K_{IC}$ , are in fact microstructure dependent and only an apparent fracture

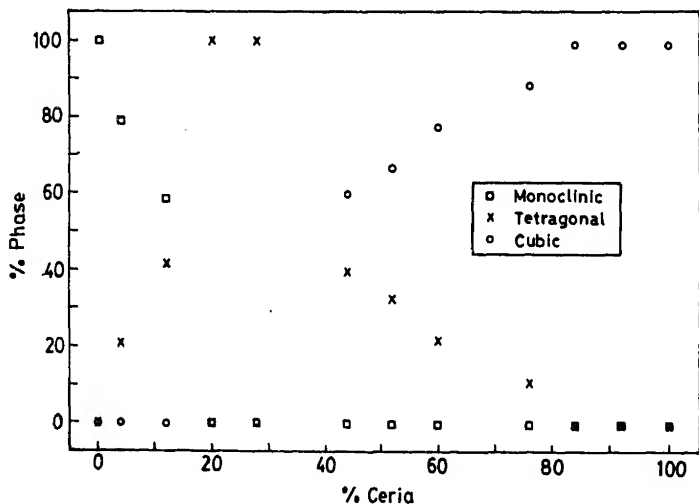


Figure 11. Variation of phase contents with ceria percentage.

Table 3. Sintering of  $\text{ZrO}_2\text{-CeO}_2$  pellets by use of microwave irradiation.

Sample code	Composition $\text{ZrO}_2\text{:CeO}_2$	Time of sintering (min)	Volume change (%)	Green density (g/cc)	Sintered density (g/cc)	Relative density (%)
A0	100:0	35	32.4	3.53	5.66	95
A1	96:4	35	29.2	3.55	5.33	90
A2	88:12	35	30.2	3.69	5.93	95
A3	80:20	35	34.4	3.67	6.08	99
A4	72:28	35	27.6	3.74	6.16	98
A5	64:36	35	32.0	3.80	5.96	94
A6	56:44	35	35.0	3.82	5.87	91
A7	48:52	35	33.6	3.94	6.29	96
A8	40:60	35	31.3	4.00	6.39	96
A9	32:68	35	31.4	4.26	6.49	96
A10	24:76	35	30.4	4.35	6.77	99
A11	16:84	35	28.8	4.25	6.41	92
A12	8:92	35	32.7	4.28	7.01	99
A13	0:100	35	27.8	4.39	6.69	93
G0	100:0	35	35.3	3.44	5.63	95
G1	97:3	35	30.2	3.59	5.70	95
G2	94:6	35	32.9	3.60	5.70	95
G3	91:9	35	30.8	3.59	5.85	97
G4	88:12	35	27.0	3.57	5.84	96
G5	85:15	35	27.0	3.72	5.72	94
Ce(3)	95:5	35	34.1	3.58	5.60	94

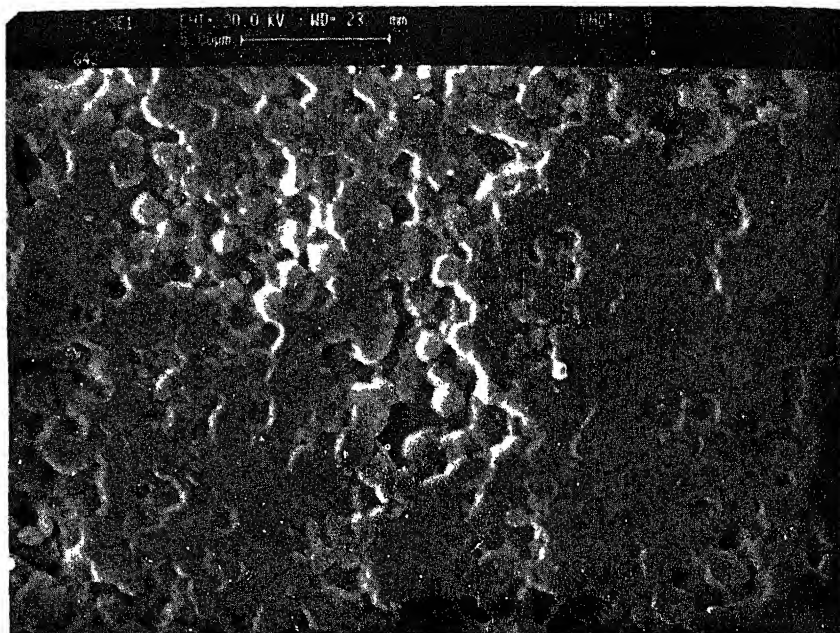


Figure 12. Scanning electron micrograph of the top surface of an etched pellet with 88  $\text{ZrO}_2$ :12  $\text{CeO}_2$  composition.

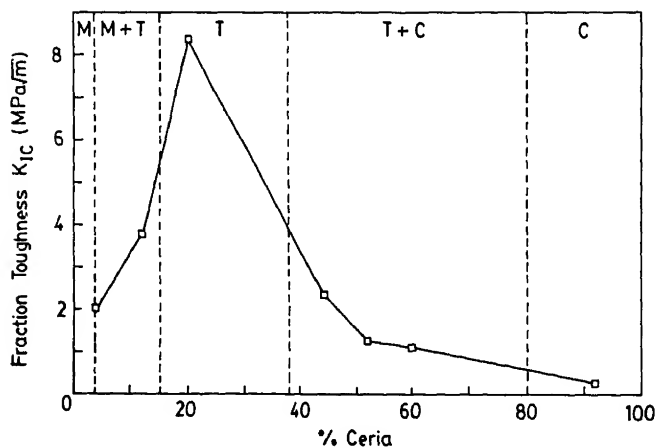


Figure 13. Variation of apparent fracture toughness values with ceria percentage.

toughness value of  $K_{IC}$  is assigned. Apparent fracture toughness value is maximum for the tetragonal phase particularly around 20%  $\text{CeO}_2$  content (figure 13). The rather high apparent fracture toughness value of  $8 \text{ MPa} \sqrt{m}$  could be due to the attendant  $M_{ss} \rightarrow T_{ss}$  phase transition.  $K_{IC}$  is severely reduced when tetragonal phases are partly substituted by either cubic or monoclinic phase.

We conclude that microwave irradiation provides the fastest means of sintering  $\text{FeO}_2\text{-CeO}_2$  ceramics. Theoretical densities well over 95% are achieved in very short durations (35 min) by this method. Micrographs indicate that interparticle sintering could have preceded by thermal shock pulverization. Use of secondary susceptors such as  $\beta\text{-SiC}$  provides general method to elevate the temperatures of materials which then couple with microwaves at higher temperatures.

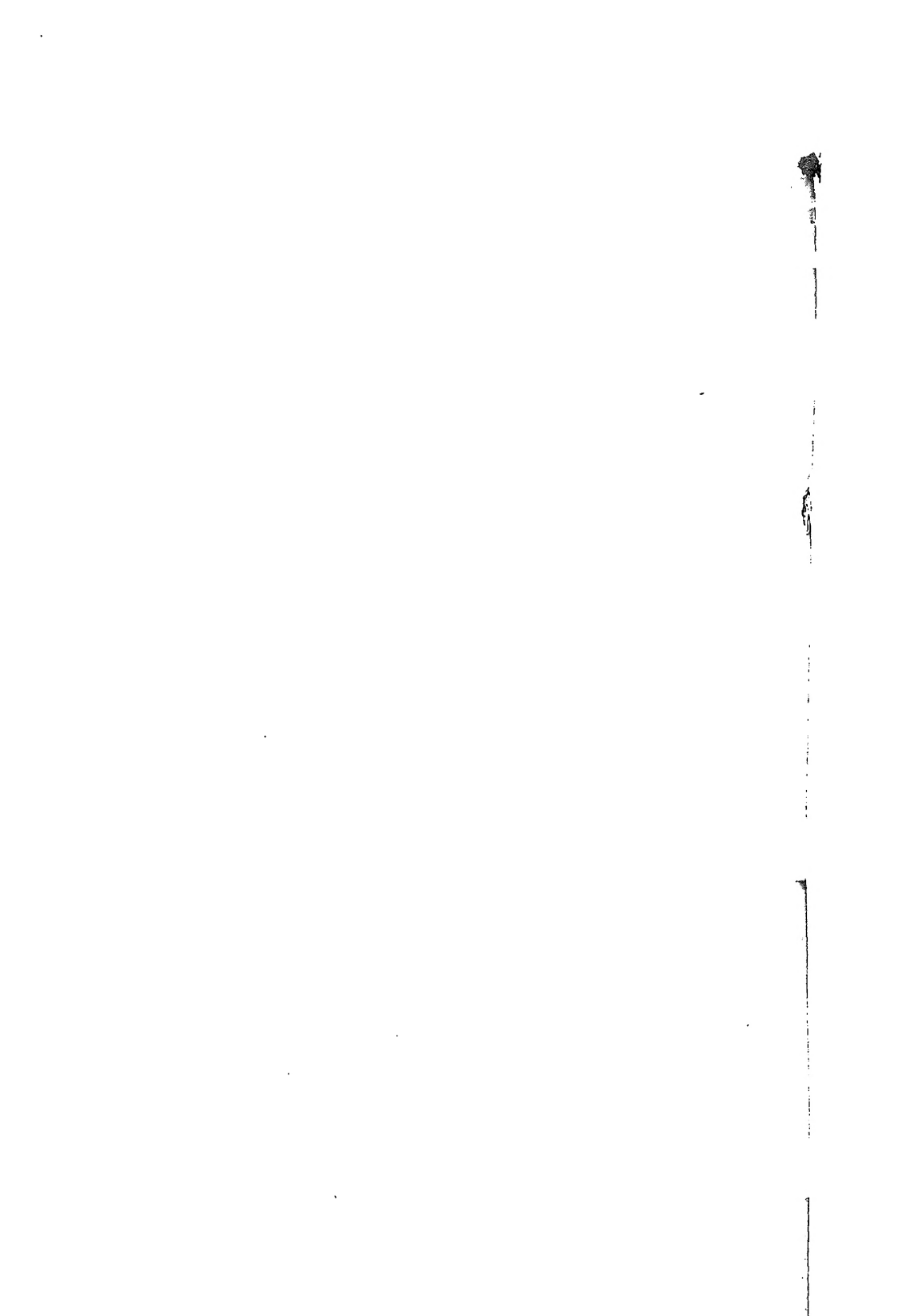
## Acknowledgements

JR expresses his thanks to DST, India and JSPS, Japan for financial support to attend Indo-Japan seminar on new materials held in Tokyo. The authors thank Mr B Vaidhyanathan and Miss Munia Ganguli who have worked on the materials reported in this paper. Thanks are also due to Prof. C N R Rao and Prof. P Rama Rao for their kind encouragement.

## References

- Graham F, Debruille-Gresse M F, Mairesse G and Nowogrocki G 1988 *Solid State Ionics* **28-30** 529
- Anderson 1954 *Acta Chem. Scand.* **8** 1599
- Ho Y W and Charles J A 1991 *Mater. Sci. & Tech.* **7** 495
- Anton E P, Rawson H and Stanworth J E 1954 *Nature* **172** 1030
- Sharkawy A A, Abousehly A M, Abou-el-Azm A M, Wasfy M H and Dakroury A Z 1988 *J. Mater. Sci. Lett.* **7** 1178
- Johnson J W, Jacobson A J, Brody F and Rich S M 1982 *Inorg. Chem.* **21** 3820
- Linker V M, Skala L, Weiser M W and Katz J D 1991 *J. Mater. Sci.* **26** 2483
- Ichida N, Mizuho C and Minami T 1988 *J. Non-Cryst. Solids* **101** 70
- McMurdie H 1987 *Powder Diffraction Journal* **2** 45
- Minami T, Imazawa K and Tanaka M 1980 *J. Am. Ceram. Soc.* **63** 627
- Mathupari S, Prabakar S and Rao K J 1994 *J. Phys. Chem.* **98** 2646
- NBS 1975 *Nat. Bur. Stand. (U.S.) Monogr.* 1981 **25** 44
- Leppchuk J M 1984 *IEEE Trans. Microwave Theory and Techniques* **32** 1200
- Das P S S and Radhakrishna S 1988 *Solid State Ionics* **28-30** 814
- Mesh P D and Rao K J 1995 *Adv. Mater.* **7** 177
- Mesh P D, Vaidhyanathan B, Munia Ganguli and Rao K J 1994 *J. Mater. Res.* **9** 3025
- Mesh P D, Pankaj Sarin, Siddharth Jeevan and Rao K J 1995 *Ceram. Int.* (accepted)
- Snider C and Lagaly G 1984 *J. Solid State Chem.* **53** 92
- Vaidhyanathan N and Radhakrishna S 1988 *Solid State Ionics* **28-30** 811
- Das P S S and Rao K J 1989 *Solid State Ionics* **37** 17
- Leppard L M 1990 *Am. Ceram. Soc. Bull.* **69** 1801
- Chen K S, Singh S, Sekhon S S, Chandra S and Kumar A 1991 *Phys. Chem. Glasses* **32** 255
- Anton W H 1989 *Am. Ceram. Soc. Bull.* **68** 376
- Yamamoto E, Yoshimura M and Somya S 1983 *J. Am. Ceram. Soc.* **66** 506
- Uzaki A, Kani K, Watari K and Torii Y 1992 *J. Mater. Sci.* **27** 5091
- Do J and Carton D 1979 *C. R. Acad. Sci. C. Paris* **289** 219
- Vaidhyanathan B, Munia Ganguli and Rao K J 1994 *J. Solid State Chem.* **113** 448
- Vaidhyanathan B, Munia Ganguli and Rao K J 1995a *Mater. Res. Bull.* (in press)
- Vaidhyanathan B, Munia Ganguli and Rao K J 1995b *J. Mater. Chem.* (communicated)
- Rama K B R, Subbanna G N, Guru Row T N and Rao C N R 1990 *J. Mater. Res.* **5** 2718
- Meier A W, Cochran G A, Eisman G A, Henley J P, Hook B D, Mills L K, Gupton T A, Knudsen A K, Nicholas N R, Volmering J E and Moore W G 1994 *J. Am. Ceram. Soc.* **77** 3





chemical approaches to the synthesis of inorganic materials, 1994, C N R Rao (New Delhi: Wiley-Eastern Ltd. and New Age International Ltd.) pp 1-102.

Synthesis is the key step in successful development of materials. Both in industry and academia development of novel materials with tailored properties is a constant activity. The community of practising solid state chemists, teachers and students will therefore warmly welcome this *petit* book on synthesis of inorganic materials. The book fills a gap in the solid state literature and fulfils a need long felt by materials scientists. Professor C. N. R. Rao has put together rather succinctly the quientessential aspects of the chemical approaches to synthesis of a variety of inorganic materials, simple or complex, stable or metastable, known or novel.

The book is set conveniently in 20 short chapters—better called sections. Chapters 1-14 discuss different methods of chemical synthesis while chapters 16-19 describe synthesis of some important classes of materials. Chapter 15 is a write up on formation of intergrowth structures which is perhaps a synthetic happenstance of great interest to chemists. Synthesis of nanomaterials is of significant current interest and has been treated in section 20. *Chimie douce* methods have been treated in chapter 15 but chapter 7 could as well be under this title. Addition of details of physical phenomena, of characterization (e.g. section 15), and of experimental set-up (e.g. sections 11-14) wherever essential is a feature which will be liked by the readers. Significant features of the syntheses of high  $T_c$  superconductors, microporous solids, high temperature ceramics, bifunctional catalysts, semiconductors etc. have been described. Materials from aerogels to zero expansion ceramics, from clay to clathracil have all found mention at appropriate places. Wide ranging techniques such as sol-gel, high pressure, self propagating flame, high temperature, vapour phase transport, electro-chemical deposition etc. have been described, although briefly, in this little book of 102 pages. There are more than 300 compounds mentioned by name and used as examples to illustrate the synthetic strategies. Close to 240 references covering literature reports up to 1994 make this a very valuable reference book for both students and teachers.

One may find that in these days of fabulous printing techniques, quality of production could have been better. However the technical editing has been excellent. The coverage could have been more complete if microwave synthesis had found a place in this book.

On the whole the book is written with superb clarity and brevity by an eminent author whose writings are quite well known to the scientific community. The book is highly recommended for all solid state scientists.

K J RAO

Solid State and Structural Chemistry Unit  
Indian Institute of Science  
Bangalore 560 012

ANNOUNCEMENT

IUPAC CHEMRAWN IX

World Conference on Sustainable Production, Use, Disposal and Recycling of Materials and The Role of Advanced Materials in Sustainable Development.

September 1—6, 1996  
Seoul, Korea

Cosponsored by International Union of Pure and Applied Chemistry and The Korean Chemical Society.

For details, please contact:

Organizing Committee & Secretariat  
IUPAC CHEMRAWN IX (Chemical Research Applied to World Needs)  
Tongwon B/D 6th Fl. 128-27 Tangju-dong, Chongno-ku  
Seoul 110-071, KOREA